RUNDSCHAU
radex
RADENTHEIN, IM MÄRZ 1986

Inhalt

Heft 1

Die Österreichisch-Amerikanische Magnesit Aktiengesellschaft ist eine Tochtergesellschaft der General Refractories Company, USA.

Die Radex-Rundschau wird in enger Zusammenarbeit mit den Hauptbüros der General Refractories Company und deren Forschungsinstituten herausgegeben.

The Austro-American Magnesite Company is a wholly owned subsidiary of General Refractories Company, USA.

This periodical is published in close cooperation with the headoffices of General Refractories Company and their respective research institutions.

La Compagnie Austro-Américaine de Magnésie appartient exclusivement à la General Refractories Company, USA.

Cette revue est publiée en coopération étroite avec la direction de la General Refractories Company et ses laboratoires de recherches.

MA-Spinellsteine im Glasofenregenerator

Paul Kettner und Gerhard Christof, Radenthein

Magnesiumaluminat-Spinell ist gegen den Angriff von SO_3 und Alkalisulfat sehr beständig und stellt somit ein geeignetes ff.-Material für den mittleren Temperaturbereich von Glasofenregeneratoren dar. Spinellsteine auf Basis Magnesiumaluminat gewinnen umso mehr an Bedeutung als der Einsatz chromerzhältiger Steine in den Regeneratoren aus Umweltgründen problematisch erscheint.

Es wird über Aufbau, Eigenschaften und Anwendung von Spinellsteinen aus 100% Magnesiumaluminat sowie von Steinen, die aus Periklas und Magnesiumaluminat-Spinell zusammengesetzt sind und über die bisherigen praktischen Erfahrungen mit diesen Steinen berichtet.

MA-Spinel Brick in Glass Furnace Regenerators

Magnesiumaluminate spinel is highly stable against attack by SO_3 and alkali sulfate and therefore presents itself as an apt refractory for the area of mean temperatures of glass tank regenerators. Spinel brick based on magnesium aluminate increasingly gain importance insofar as the use of chrome-containing bricks in regenerators becomes problematic out of environmental reasons.

It is reported on composition, properties and application of spinel bricks, made of 100% magnesium aluminate, as well as of brick composed of periclase and magnesium aluminate spinel, and on to-date experience gained with those brick in practical use.

Emploi des réfractaires de spinelle d'aluminate de magnésium dans les régénérateurs des fours de verrerie

Le spinelle d'aluminate de magnésium est un matériau très résistant à l'attaque par SO_3 et par les sulfates alcalins, de sorte qu'il constitue un réfractaire convenant à la zone des températures moyennes des régénérateurs de fours de verrerie. Les réfractaires de spinelle à base d'aluminate de magnésium prennent d'autant plus d'importance que l'emploi des réfractaires de chromite dans les régénérateurs semble poser des problèmes sur le plan de l'environnement.

On donne des indications sur la structure, les propriétés et les applications de réfractaires de spinelle constitués de 100% d'aluminate de magnésium ou bien de périclase et de spinelle d'aluminate de magnésium. Les résultats pratiques obtenus jusqu'à présent sont discutés.

Der mittlere Temperaturbereich der Regenerativkammern von Glasschmelzöfen ist eine Schwachstelle, die die Betriebszeiten einer Wanne sehr wesentlich beeinflußt.

Während sich die staubförmigen Gemengebestandteile hauptsächlich auf den oberen Lagen der Regenerativkammern ablagern, sind es im mittleren Temperaturbereich der Regeneratoren vor allem die verflüchtigten Gemengekomponenten und die Verbrennungsprodukte der Energieträger, die die feuerfesten Steine angreifen. Besondere Bedeutung kommt hiebei dem Angriff durch Alkalisulfate und -oxide sowie dem Schwefeltrioxid-Angriff zu.

Bei SO_3-Angriff, mit dem bei ölbeheizten Anlagen immer zu rechnen ist, sind Magnesitsteine für den mittleren Kammerbereich nicht das geeignete Feuerfestmaterial – die Bildung von $MgSO_4$ ist erst oberhalb von etwa 1125 °C auszuschließen – sodaß hier häufig korundhaltige Steine, Schamottesteine, Forsteritsteine sowie Steine auf Spinellbasis – sowohl Chromit- als auch MA-Spinell-

The area of mean temperatures in the regenerative chambers of glass furnaces represents a weak spot considerably influencing the service life of a tank.

While the dust parts of the feed mixture mainly settle out on the upper layers of the regenerative chambers, in the area of mean temperatures there are mostly the volatilized components of the feed mix and the combustion products of the fuels that attack the refractory bricks. Of special importance is the attack by alkali sulfates and -oxides, as well as the sulfur trioxide attack.

Regarding SO_3-attack – which has always to be taken into account in oil-fired installations – magnesia bricks are not the suitable refractory for the middle area of the chambers; formation of $MgSO_4$ can only be excluded at temperatures above approximately 1125 Centigrade, so that for this area frequently corundum containing brick, chamotte brick, forsterite brick, as well as brick based on spinel – as well chrome – as also MA-spinel – are used. Those brick, however, are sub-

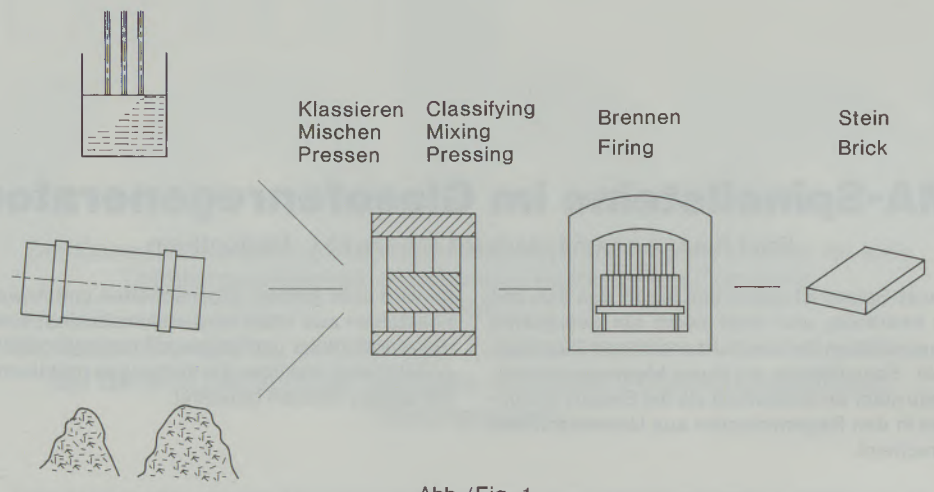

Abb./Fig. 1
Vormaterial: elektrisch geschmolzener Spinell
Simultansinterspinell
Mischung aus MgO + Al_2O_3-Träger
Starting material: electrically fused spinel
dead-burned simultan spinel
mixture of MgO + Al_2O_3 carrier

steine – Anwendung finden. Diese Steine unterliegen jedoch einem mehr oder weniger starken Verschleiß durch Alkalisulfat. Einerseits führen die durch die zyklischen Temperaturwechsel hervorgerufenen Vorgänge von Kondensieren und Verdampfen, Erstarren und Schmelzen der in die Steine infiltrierten Sulfatverbindungen – der Schmelzpunkt von Na_2SO_4 liegt bei 884 °C – zu einer Schwächung des Steingefüges und zu einer Abnahme der Temperaturwechselbeständigkeit, andererseits können auch chemische Reaktionen stattfinden, die zu Korrosionserscheinungen Anlaß geben.

Magnesiumaluminat-Spinell ist gegen den Angriff sowohl von SO_3 als auch von Alkalisulfat sehr beständig. Korrosionsversuche, bei denen MA-Spinell bei Temperaturen von 900 bis 1000 °C einer Na_2SO_4-Schmelze ausgesetzt waren, aber auch Versuche unter praxisnahen Bedingungen in unserem Glasgitterfunktionstest haben die hohe chemische Resistenz der MA-Spinellphase bewiesen.

MA-Spinellsteine werden im allgemeinen aus drei verschiedenen Arten von Vormaterial hergestellt (Abb. 1).

- Beim elektrisch geschmolzenen Spinell wird der Stein aus 100% Schmelzvormaterial hergestellt und bildet praktisch ein monomineralisches Produkt.
- Beim Simultansinterspinell wird Magnesiumkarbonat und Tonerde gemeinsam in einem Rotier- oder Schachtofen gebrannt. Bei diesem Brand bildet sich der Sinterspinell, welcher weiter zu einem Stein verarbeitet wird.
- Bei der dritten Herstellmethode wird MgO + Al_2O_3 gemeinsam zu Stein verarbeitet, wobei sich erst im Steinbrand der Spinell ausbildet.

ject to more or less substantial wear by alkali sulfate. On one hand, the processes caused by the cyclic temperature changes – condensating, vaporizing, solidification and fusion – of the sulfate compounds infiltrated into the brick (the fusion point of Na_2SO_4 is at 884 Centigrade) lead to a weakening of the brick structure and a reduction of the spalling resistance; on the other hand, chemical reactions may take place that may cause corrosion phenomena.

Magnesium-aluminate spinel is highly resistant against attack by SO_3 and also by alkali sulfate. Corrosion tests during which MA-spinel was exposed to a Na_2SO_4 melt at temperatures from 900 to 1000 Centigrade, as well as also tests under near operational conditions in our glass checker functioning test have proven the high chemical resistivity of the MA-spinel phase.

MA-spinel brick in general are made of three different starting materials (fig. 1).

- When electrically fused spinel is used, 100% fused starting material is taken, practically yielding a mono-mineralic product.
- For simultan dead-burned spinel, magnesium carbonate and alumina are simultaneously fired in a rotary or shaft kiln. During this burning process a dead-burned spinel is formed, that in the following is processed into a brick.
- In the third method of production, MgO and Al_2O_3 is processed together into a brick, whereby the spinel forms during the firing of the brick.

In the following, only the first two types of brick will be investigated more closely.

MA-fused spinel (fig. 2) is electrically fused out of highly pure MgO and Al_2O_3 carriers under stoichio-

In der weiteren Folge werden nur die beiden erstgenannten Steintypen näher untersucht.

MA-Schmelzspinell (Abb. 2) wird aus hochreinen MgO- und Al_2O_3-Trägern im stöchiometrischen Verhältnis elektrisch geschmolzen. Ein aus diesem Material hergestellter Stein hat folgende chemische und physikalische Prüfdaten (Tabelle 1).

Aus der chemischen Analyse ist ersichtlich, daß neben der Magnesiumaluminat-Phase nur in ganz untergeordnetem Maße Verunreinigungen vorliegen. Bei diesen Verunreinigungen handelt es sich um Silikatphasen, vor allem Merwinit (C_3MS_2), ganz vereinzelt Gehlenit (C_2AS).

Unter dem Mikroskop ist eine sehr homogene Verteilung der Korn- und Mehlkomponenten (Abb. 3 und 4) bei gleichzeitig ausgezeichneter Verfrittung der Mehlpartikel (Abb. 5) zu erkennen. Die ausgeprägte Versinterung des Mehles mit der Kornkomponente (Abb. 6) in Verbindung mit der Verfrittung der Mehlpartikel untereinander weist auf eine hervorragende keramische Bindung hin, die eine hohe Festigkeit der Steine garantiert.

Als praktisch monomineralisches Produkt werden MA-Schmelzspinellsteine von angreifendem Alkalisulfat zwar rasch durchtränkt, da für die eindringende Sulfatschmelze ein einheitliches Benetzungsverhalten vorliegt, die MA-Spinellphase verhält sich dem Alkalisulfat gegenüber jedoch äußerst resistent. Die Silikatphasen, die mit Alkalisulfat in Reaktion treten können, sind in so geringer Menge vorhanden, daß keine nennenswerten Korrosionserscheinungen auftreten. Da für die Festigkeit des Steines ausschließlich die keramische Bindung zwischen den MA-Kristallen und nicht die Silikatphase verantwortlich ist, behält

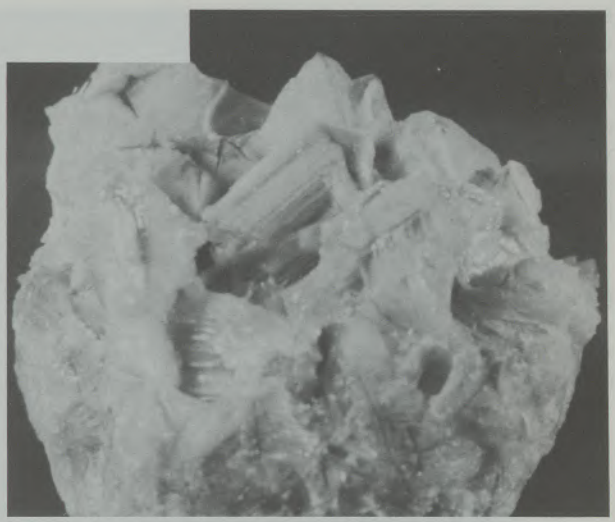

Abb./Fig. 2

metric conditions. A brick made of this material shows the following chemical and physical data (table 1).

From the chemical analysis it can be seen that aside from the magnesium-aluminate phase, impurities are present only in minute quantities. Those impurities are silicate phases, especially merwinite (C_3MS_2); rather rarely there is some gehlenite (C_2AS).

Under the microscope very homogeneous distribution of the grain and fines components (figs. 3 and 4) with simultaneous excellent fritting of the fines particles (fig. 5) may be observed. The expressed co-sintering of the fines with the grain component (fig. 6) in the connection of the inter-

Tabelle 1

Chemische und physikalische Prüfdaten von MA-Spinellsteinen, hergestellt aus 100% elektrisch geschmolzenem Vormaterial.

Steinsorte	MA-Schmelzspinellstein
Rg, g/cm³	2,85–3,00
Ps, %	16–20
KDF, N/mm²	30–60
HBF, N/mm²	
1260 Grad Celsius	9,8
1480 Grad Celsius	2,4
DFB	
t_a	>1700 Grad Celsius
t_b	>1700 Grad Celsius
Chemische Analyse, %	
SiO_2	0,3
Fe_2O_3	0,2
Al_2O_3	69,5
CaO	0,4
MgO	29,5

Table 1

Chemical and physical data of MA-spinel bricks made of 100% electrically fused starting material

Type of brick	fused MA-spinel brick
density, g/cm³	2.85–3.00
porosity, %	16–20
CCS, N/mm²	30–60
HBS, N/mm²	
1260 Centigrade	9.8
1480 Centigrade	2.4
Hot compressive strength	
t_a	>1700 Centigrade
t_b	>1700 Centigrade
Chemical analysis	
SiO_2	0.3
Fe_2O_3	0.2
Al_2O_3	69.5
CaO	0.4
MgO	29.5

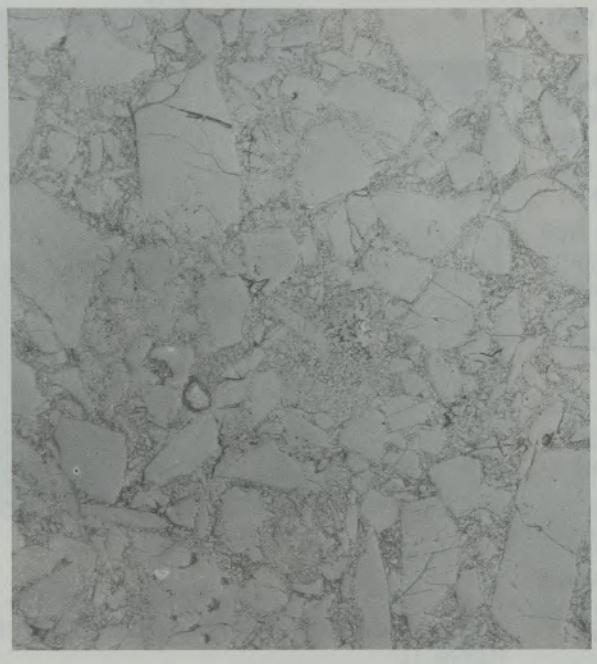

Abb./Fig. 3

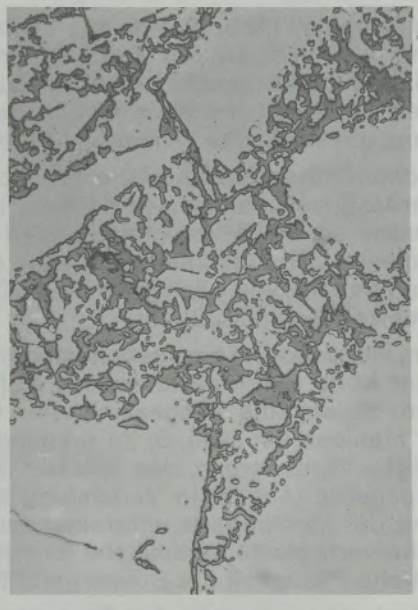

Abb./Fig. 4

Homogene Verteilung der Mehl- und Kornkomponenten im MA-Schmelzspinellstein
Homogeneous distribution of fines and grain components in fused MA-spinel brick

der Stein auch bei starker Alkalisulfat-Infiltration eine ausreichende Heißfestigkeit. Herr Dr. Küstner hat bezüglich der Heißfestigkeit dieser MA-Schmelzspinellsteine bei seinem Vortrag im Fachausschuß II der DGG am 30. November 1983 in Würzburg aufgrund von Untersuchungen der Heißspaltzugfestigkeit von mit Alkalisulfat infiltrierten Steinen ähnliche Feststellungen getroffen. Auch die Praxis, wo MA-Schmelzspinellsteine seit zehn Jahren in Gitterungen von Hohlglaswannen im Temperaturbereich zwischen 900 und 1200 °C mit

fritting of the fines-particles indicates an excellent ceramic bond, granting high mechanical strength of the brick.

Since for infiltrating sulfate melts there is a uniform wetting behavior, the practically mono-mineralic products – fused MA-spinel-brick – are quickly quenched by attacking alkali sulfate, however, the MA-spinel phase is highly resistant against alkali sulfate. The silicate phases that may also react with alkali sulfate are only present

Tabelle 2

Periklas-Spinellstein

RG	2,85–3,00 g/cm³
PS	16–20 %
KDF	30–70 N/mm²
HBF bei	
1260 Grad Celsius	11,0 N/mm²
1480 Grad Celsius	1,0 N/mm²
DFB	
t_a	> 1600 Grad Celsius
t_b	> 1700 Grad Celsius
Chemische Analyse, %	
SiO_2	3,2
Fe_2O_3	3,5
Al_2O_3	15
CaO	1,3
MgO	76

Table 2

Periclase – spinel brick

Density	2.85–3.00 g/cm³
Porosity	16–20 %
CCS	30–70 N/mm²
HBF at	
1260 °C	11.0 N/mm²
1480 °C	1.0 N/mm²
Hot compressive strength	
t_a	> 1600 Centigrade
t_b	> 1700 Centigrade
Chemical analysis	
SiO_2	3.2
Fe_2O_3	3.5
Al_2O_3	15
CaO	1.3
MgO	76

Erfolg eingesetzt werden, hat die hohe Verschleißresistenz dieser Steine bewiesen.

Neben reinen Spinellsteinen wird auch der Einsatz von Periklas-Spinellsteinen im Glasofenregenerator diskutiert. Solche Steine werden im allgemeinen aus stöchiometrisch zusammengesetztem MA-Spinell und einer MgO-Komponente hergestellt, was ein Grundgefüge aus Periklaskristallen ergibt, in das MA-Spinellnester eingelagert sind.

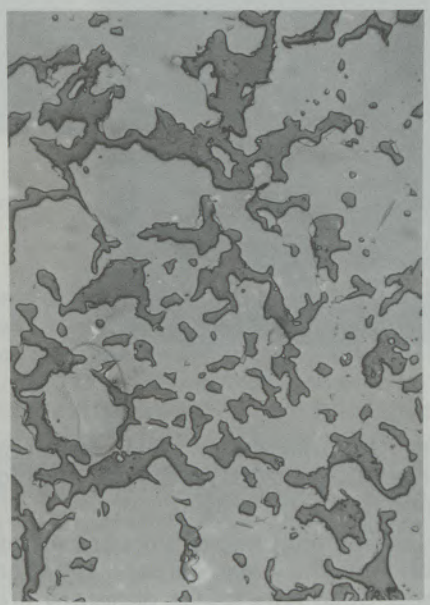

Abb./Fig. 5
Verfrittung der Mehlpartikel im MA-Schmelzspinellstein
Inter-fritting of the fines particles in a fused MA-spinel brick

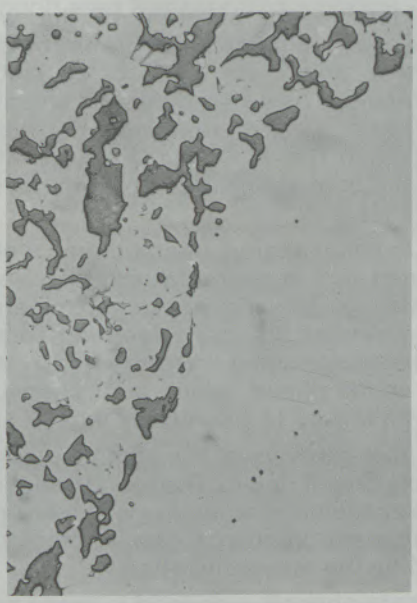

Abb./Fig. 6
Ausgeprägte Versinterung des Mehles mit Kornkomponente im MA-Schmelzspinellstein
Well developed sintering of the fines with the grain component in fused MA-spinel brick

in such small quantities that no significant signs of corrosion show up. Since for the strength of the brick exclusively the ceramic bond between the MA-crystals and not the silicate phase is responsible, the brick retains sufficient hot strength also upon strong alkali sulfate infiltration. Dr. Küstner has made similar statements regarding the hot strength of those fused MA-spinel brick during his lecture given at the Fachausschuß II of the German Ceramic Society at Würzburg, November 30, 1983, based on investigations of the hot cleaving strength of brick infiltrated by alkali sulfate. Also, in practical service, where fused MA-spinel brick have been successfully used for ten years in

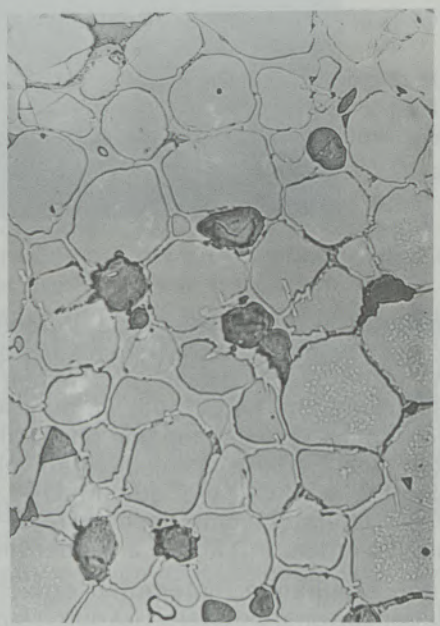

Abb./Fig. 7

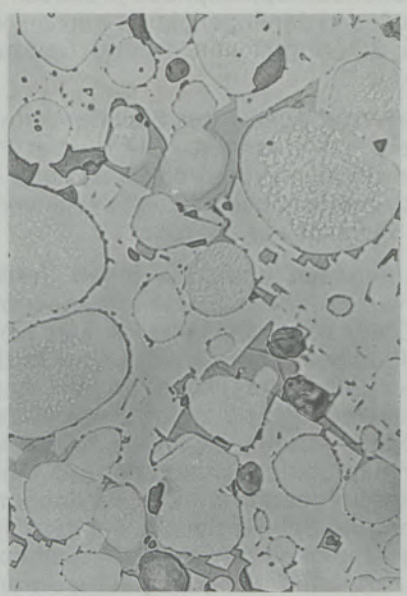

Abb./Fig. 8

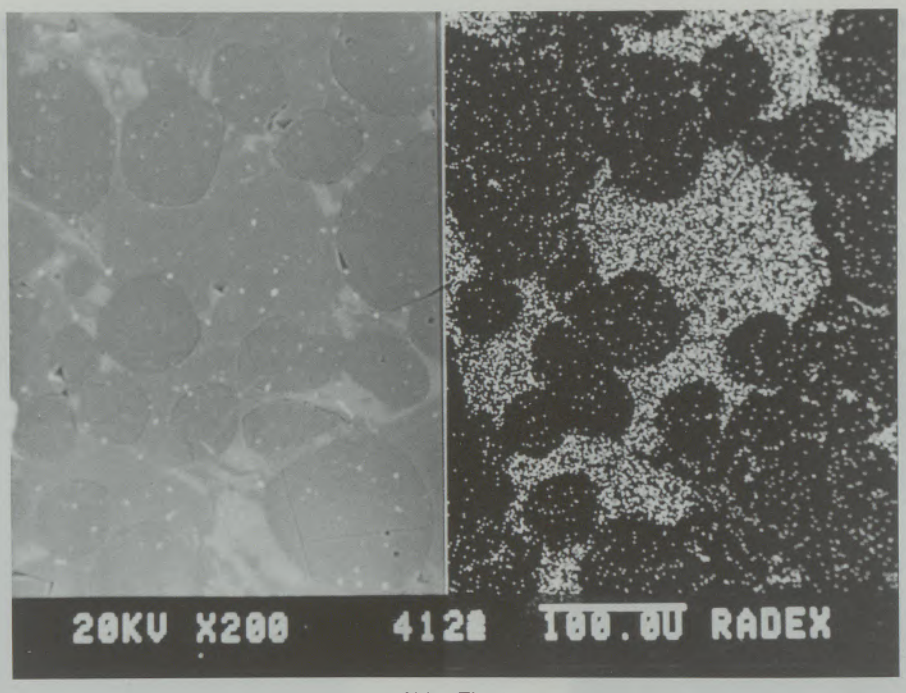

Abb./Fig. 9

Eine wesentliche Verbesserung der Verschleißresistenz von Periklas-Spinellsteinen kann erreicht werden, wenn diese Steine aus einem MgO-Al_2O_3-Simultansinter hergestellt werden. Als Beispiel werden die chemischen und physikalischen Prüfdaten von Periklas-Spinellsteinen mit 76% MgO und 15% Al_2O_3, die aus MgO-Al_2O_3-Co-Klinker mit überstöchiometrischem MgO-Gehalt hergestellt wurden, in Tabelle 2 wiedergegeben.

Durch den simultanen Sinterbrand erreicht man ein Gefüge, das charakterisiert ist durch eine sehr gleichmäßige Verteilung der Magnesiumaluminat-Spinellphase, wobei die Periklase von der zwickelfüllenden Spinellphase praktisch vollständig umhüllt und damit geschützt werden, was speziell bei SO_3-Angriff von größter Bedeutung ist (Abb. 7 und 8).

In Abb. 9 ist der Aufbau des Simultansintersteines besonders gut erkennbar. Die runden Periklase sind, wie die Aluminium-Verteilung unter dem Rasterelektronenmikroskop zeigt, vollkommen von der MA-Spinellphase umgeben.

An Silikatphasen enthalten diese Periklas-Spinellsteine Forsterit (M_2S) und untergeordnet Monticellit (CMS). MA-Spinell und Periklas sind gegen Alkalisulfate recht beständig, und was die Resistenz der Silikatphasen gegen den Angriff von Alkalisulfat betrifft, so steigt diese in der Reihe C_2S – C_3MS – CMS – M_2S bekanntlich stark an. Von Periklas-Spinellsteinen, die aus MgO-Al_2O_3-Co-Klinker hergestellt werden, ist daher nicht nur eine sehr gute SO_3-Resistenz, sondern auch eine hohe Beständigkeit gegen den Angriff von Alkalisulfat zu erwarten. Mineralogische Untersuchungen von solchen Periklas-Spinellsteinen nach eicheckers of bottle glass tanks in temperature zones from 900 to 1200 Centigrade, the high wear resistance has been proven.

Next to pure spinel brick, the use of periclase-spinel brick in the glass furnace regenerator is discussed. Such type bricks generally are made of stoichiometrically composed MA-spinel and an MgO-component, resulting in a basic structure of periclase crystals, into which nests of MA-spinel are embedded.

A considerable improvement of the wear resistance of periclase-spinel brick may be obtained when these bricks are made of an MgO-Al_2O_3-simultan-sinter. As an example, the chemical and physical data of periclase-spinel-brick containing 76% MgO and 15% Al_2O_3, made of MgO-Al_2O_3-Co-clinker with over-stoichiometric contents of MgO, shown in table 2.

Thanks to simultaneous dead-burning a structure is obtained that is characterized by a very even distribution of the magnesium-aluminate-spinel phase, whereby the periclases are practically completely surrounded and protected by the intertwining spinel phase, which is of special importance with regard to SO_3-attack (figs. 7 and 8).

In fig. 9 the structure of the simultan-sinter brick is especially well visible. The round periclases are – as the aluminum distribution is shown under the scanning electron microscope – completely surrounded by the MA-spinel phase.

The silicate phases contained in these periclase spinel bricks are forsterite (M_2S) and, to a reduced extent, monticellite (CMS). MA-spinel and periclase are rather resistant against alkali sulfates; regarding the resistance of silicate phases

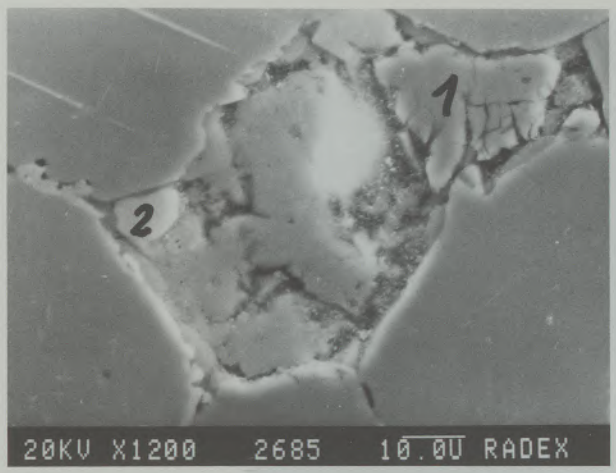

Abb./Fig. 10

1 M_2S Forsterit

2 Na-Ca-Sulfat Thenardit

nem von der British Glass Industry Research Association (BGIRA) bei Angriff von Na-Sulfat im zyklischen Temperaturwechsel zwischen 950 und 1100 °C durchgeführten Test haben dies bestätigt. Unter dem Rasterelektronenmikroskop zeigte sich, daß lediglich der CMS-Anteil der silikatischen Bindephase und auch dieser nur teilweise durch Na-Sulfat angegriffen wurde, wobei es zur Bildung von Forsterit und Na-Ca-Sulfat gekommen ist, während der M_2S-Anteil der Bindephase keinen Angriff erkennen läßt (Abb. 10).

Die geringen Mengen an neugebildetem M_2S und Na-Ca-Sulfat beweisen, daß nur ein geringer Teil des Bindephasengefüges zerstört wurde.

Neben ihrer Beständigkeit gegen SO_3 und Alkalisulfat-Angriff sind Periklas-Spinellsteine, die aus MgO-Al_2O_3-Co-Klinker hergestellt werden, auch gegen den Angriff von staubförmigen Gemengepartikeln sehr widerstandsfähig, was durch einen Test in unserem Glasgitterfunktionsaggregat gezeigt werden konnte. Weiters zeichnen sie sich durch gute Heißfestigkeiten, 11 N/mm² bei 1260 °C sowie durch eine exzellente Temperaturwechselbeständigkeit aus. Sie stellen demnach eine sehr gute Alternative zu herkömmlichen Magnesia-Chrom-Qualitäten für den Einbau in Glasofenregeneratoren, speziell im mittleren Temperaturbereich dar. Bisher wurden von diesem Steintyp erst Versuchseinbauten in kleinem Rahmen durchgeführt.

Wie bereits eingangs erwähnt, sind MA-Schmelzspinellsteine seit zehn Jahren in Gitterungen von Glasofenregeneratoren mit bestem Erfolg im Einsatz. Um bei Glasöfen eine optimale Wärmeausnutzung zu erreichen, werden heute vielfach zweizügige Kammern errichtet. Ein besonderes Problem bei diesen Regeneratoren stellen die Tragbögen der Gitterung dar, welche hohen Temperaturen von ca. 1000 °C, hohen Druckbelastungen durch die Gitterung sowie chemischem Angriff durch Alkalisulfat ausgesetzt sind.

against alkali sulfates, it is known that it strongly rises in the series C_2S – C_3MS_2 – CMS – M_2S. Periclase-spinel-brick made of MgO-Al_2O_3-Co-clinker therefore let anticipate not only a very good resistance against SO_3, but also a high immunity against the attack of alkali sulfate. Mineralogical investigations of such periclase-spinel brick conducted after a test of the British Glass Industry Research Association (BGIRA) upon attack of Na-sulfate in a cyclic temperature change between 950 and 1100 Centigrade, have proven this assumption; under the Scanning Electron Microscope it can be seen that only the CMS-portion if the silicatic binding phase – and also this only partially – is attacked, whereby formation of forsterite and Na-Ca-sulfate had been formed, while the part of the M_2S of the binding phase does not show any sign of an attack (fig. 10).

The small quantities of newly developed M_2S and Na-Ca-sulfate prove that only a minor part of the binding phase structure had been destroyed.

Aside from their resistance against SO_3 and alkali-sulfate attacks, the periclase-spinel bricks made of MgO-Al_2O_3-Co-clinker also are highly resistant against the attack of dusty particles of the mix, which could be shown in our glass checker functioning apparatus. Also, they are characterized by good hot strengths of 11 N/mm² at 1260 Centigrade, as well as by an excellent spalling resistance. Therefore, they represent a very good alternative to the usually used magnesia-chrome types of brick for installation in glass furnace regenerators, especially for the areas of mean temperatures. Until now, only small panel tests have been installed with this type of brick.

As already mentioned at the beginning, fused MA-spinel-bricks have been in use in glass furnace regenerators with optimum results for 10 years. In

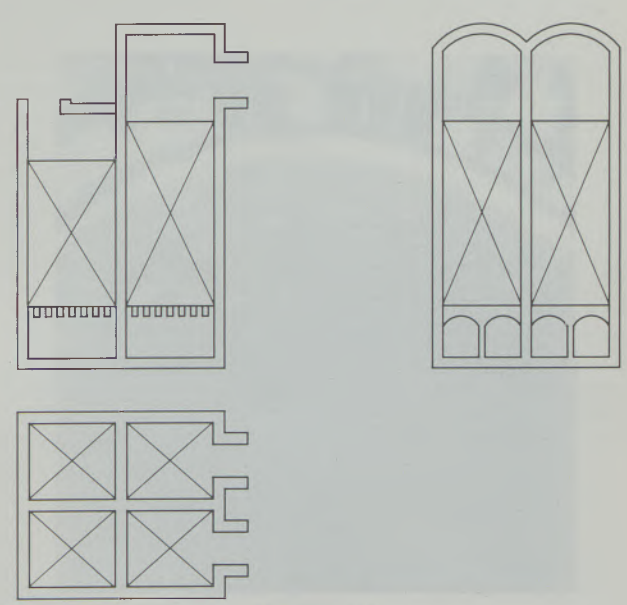

Abb./Fig. 11

Abb./Fig. 12

Im Sommer des Jahres 1985 wurden erstmals bei einer U-gefeuerten Wanne mit zwei Kammerzügen diese Tragbögen mit MA-Schmelzspinellsteinen zugestellt. Berechnungen der Kammertemperaturen nach dem HVG-Rechenmodell ließen Temperaturen von 1100 bis 1200 °C erwarten, sodaß der Einsatz von Schamottequalitäten nicht in Frage kam. Ermutigt durch die Erfolge in der Gitterung wird dieser exponierte Bereich mit MA-Schmelzspinellsteinen zugestellt (Abb. 11).

In Abb. 11 ist der Kammeraufbau im Prinzip dargestellt. Die Tragbogen sind aufgrund der Kammerbreite von 3,7 m zweigeteilt ausgeführt, sodaß die Druckbelastung durch die 8,0 m hohe Gitterung leichter aufgenommen werden kann.

Zur Abrundung dieses Themas noch ein paar Aufnahmen der Tragbögen, die während der Zustellung gemacht wurden (Abb. 12, 13, 14).

order to obtain an optimal heat efficiency, to-day frequently twin-draft chambers are built. A special problem of these regenerators is presented by the support arches of the checkers that are exposed to high temperatures around 1000 Centigrade, high pressure loads by the checkers, as well as chemical attack by alkali sulfate.

In summer this year 1985, for the first time those support arches of a U-fired tank with twin draft chambers were lined with fused MA-spinel bricks. Calculations of the chamber temperatures according to the HGV-computer model let expect temperatures from 1100 to 1200 Centigrade, so that the use of chamotte brick was prohibitive. Encouraged by the success in the checkers, this exposed area now is lined with fused MA-spinel brick (fig. 11).

In fig. 11 the construction of the chamber is presented in its principle. The support arches are built in two sections because of the width of the chamber of 3.7 meters, so that the pressure load of the 8.0 m high checkers can be reasonably distributed.

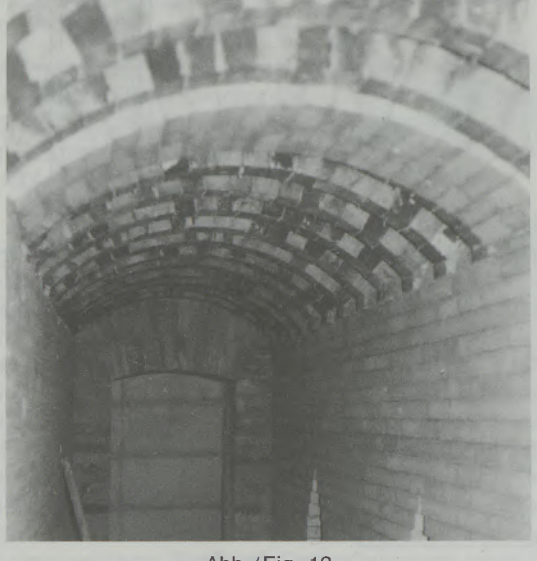

Abb./Fig. 13

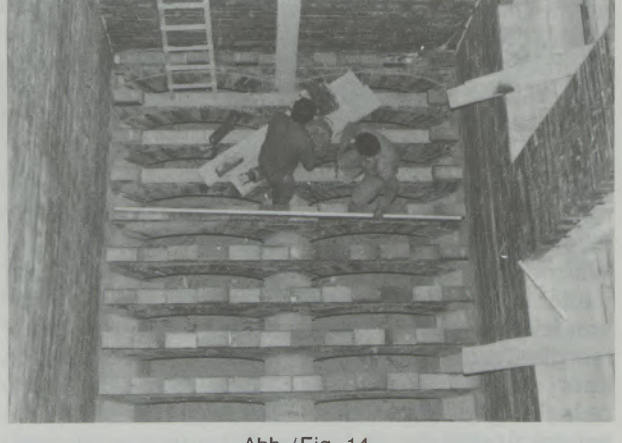

Abb./Fig. 14

Spinellsteine auf Basis $MgO\text{-}Al_2O_3$ haben im Glasofenregenerator sicher ihre Berechtigung und auch eine Zukunft in jenen Fällen, wo starke chemische Angriffe zu erwarten sind und aus Umweltschutzgründen auf Magnesitchromsteine verzichtet werden muß.

To round off the theme, we present a few additional photos of the support arches that were made during the construction (figs. 12, 13 and 14).

Spinel brick on basis of $MgO\text{-}Al_2O_3$ certainly are well in place in the glass furnace regenerator, and also have a future in those cases, where strong chemical attack may be anticipated, and where because of environmental reasons magnesite-chrome brick must not be used.

Model Investigations about the Influence of the Structure of Permeable Plugs on the Formation of Gas Bubbles

Bernd Grabner, Radenthein, Wolfgang Polanschütz, Leoben*)

The analysis of physical processes during the injection of inert gases in metal melts causes the requirement to inject high amounts of inert gas distributed as finely as possible. The presently used types of permeable plugs are described and the influence of the structure of these plugs on the formation of gas bubbles are discussed. The necessity of model investigations is easily concluded, the methods of these investigations are described and the theory of similarity for the transition of the water model to realistie melts is discussed. In the water model with test samples of defined size the most important parameters like packing density of bubbles, bubble diameter and the critical amount of gas are determined. The critical amount of gas defining the transition from the formation of bubbles to a gas jet is determined for all types of permeable plugs by repeated measurements. To estimate the parameters of permeable plugs characteristical data were calculated to characterize the transition of the status of single bubbles to a gas jet and by using these characteristical datas the critical amount of gas and the sizes of the bubbles can be determined under realistic conditions.

Modelluntersuchungen über den Einfluß des Gefüges von Gasspülsteinen auf die Ausbildung der Gasblasen

Die Analyse der physikalischen Vorgänge beim Einbringen von Inertgasen in Stahlschmelzen führt zu der Forderung, möglichst hohe Gasmengen, jedoch in feinstverteilter Form, in die Schmelze einzubringen. Die derzeit im Einsatz befindlichen Typen von keramischen Gasspülsteinen werden beschrieben und die Rolle der Blasenbildung als Funktion des Gefüges diskutiert. Hieraus ist die Notwendigkeit von Modelluntersuchungen zu erkennen, die Untersuchungsmethoden werden beschrieben und ähnlichkeitstheoretische Betrachtungen für die Übertragung des Wassermodells auf Schmelzen angestellt. Im Wassermodell werden an Prüfkörpern bestimmter Größe die wichtigsten Parameter wie Blasendichte, Blasendurchmesser und die kritische Gasmenge als steinabhängige Größen gemessen. Die kritische Gasmenge, die den Übergang vom Einzelblasenbereich zum geschlossenen Gasstrahl definiert, wurde für die einzelnen Spülsteintypen durch wiederholte Messungen bestimmt. Zur Abschätzung der charakteristischen Parameter von Spülsteinen wurden Kennziffern ermittelt, die für jeden bestimmten Steintyp als kennzeichnend für den Übergang des Einzelblasenbereiches zum geschlossenen Gasstrahl anzusehen sind und mit deren Hilfe die kritischen Gasmengen und die Blasengrößen unter definierten realen Bedingungen ermittelt werden können.

Etudes sur modèles de l'influence de la structure des réfractaires de buses pour injection de gaz inerte sur la forme des bulles gazeuses

L'étude de l'injection de gaz inertes dans les bains d'acier conduit à la conclusion qu'il est nécessaire d'introduire dans l'acier des quantités de gaz aussi élevées que possible tout en leur conservant une forme de distribution extrêmement fine. On décrit les types de buses céramiques actuellement utilisés à cet effet et on discute la rôle de le formation des bulles en tant que fonction de la structure du réfractaire. On a pu ainsi reconnaître la nécessité d'effectuer des études sur modèles dont on a décrit les méthodes et pour lesquelles on a discuté les théories de similitude afin de transposer le modèle à eau aux bains d'acier. On a mesuré sur un modèle à eau avec des éprouvettes de dimensions déterminées, la valeur des principaux paramètres tels que la densité des bulles, leur diamètre, ainsi que la quantité critique de gaz, en fonction du réfractaire utilisé. Cette quantité critique de gaz, qui définit le passage du domaine des bulles individuelles au jet de gaz fermé, a été déterminée par mesures répétées sur différents types de réfractaires pour buses. Pour évaluer les paramètres caractéristiques de ces derniers, on a calculé des indices s'appliquant à chaque type de réfractaire et désignant le passage du domaine de la bulle isolée au jet de gaz fermé. Ces indices permettent de déterminer les quantités critiques de gaz et les grosseurs des bulles dans des conditions réelles définies.

*) Dipl.-Ing. Dr.-Ing. Bernd Grabner, ÖAMAG, A-9545 Radenthein
Univ.-Doz. Dipl.-Ing. Dr. techn. Wolfgang Polanschütz, VOEST-Alpine AG, A-8700 Leoben

1. Metallurgical purpose of inert gas treatment

The treatment of metal melts with inert gas by means of permeable plugs is well known, many publications are describing the marginal conditions of purging. Fundamental papers about the quantitative description of the flow and mixing processes in ladles as well as the formation of gas bubbles were published by several authors (1) – (13). Also the interaction between metallurgical processes and inert gas bubbling were described (14) – (20).

For purging metal melts with inert gases by means of permeable plugs kinetic and metallurgical effects can be defined. Under kinetic effects the bath agitation processes can be summarized caused by the impulse of the rising gas bubbles. Under metallurgical effects essentially the transport of liquid and solid impurities and the degassing effect by the gas bubbles is understood.

The injection of gases may essentially be characterized by two physical parameters – of gas flow rate and bubble size. Generally the metallurgical effect of a defined amount of gas can be improved by the reduction of the bubble size because of the fact that interaction and transport capacity of the gas is increasing with higher surface – volume relation.

For the effect of homogenization and the support of metallurgical reactions e. g. dissolution of alloys and additions, the gas bubbling is used only for the supply of energy for the mixing processes.

For metallurgical and degassing reactions the size of the bubbles and the packing density of the bubbles at a defined amount and pressure of gas is of great importance.

According to H. K n ü p p e l (20) the following equation relation is characteristic for the degassing effect of a bulk of gas bubbles:

$$K_F \cdot \frac{F}{V} = \frac{0{,}0131}{d_{32}} \cdot \frac{H_o}{B} - 0{,}261 \cdot W_L^{0{,}91}$$

From this equation it may be concluded, that decreasing mean bubble diameters improve the degassing effect.

2. Structure of purge plugs

According to the process technology the purge plugs have to meet the requirements to inject high amounts of gas as finely distributed as possible.

For the production of purge plugs for inert gas bubbling there are presently three possibilities known and also approved in various plants:

A) Plugs with high open porosity – this can be achieved by a special grain structure or an addition of burn out materials.

B) Plugs resp. brick with channels of small diameters – "directed porosity".

C) Dense ceramic products, where the gas is pressed through fine joints in the plug itself or between plug and metal case. For higher amounts of gas also metal sheets in the plugs as well as grooves are used.

All three types show a different ceramic structure as well as different bubble characteristics. In the ceramic structure type B and C are equivalent to dense ceramic brick, no matter if burnt, chemically or carbon bonded, where the gas is injected through channels or grooves into the melt. In the type A) the gas is pressed through the open pore volume over the whole cross-section of the plug. The pore diameter of type A) is appr. 0,3 mm, because the plug has to meet the requirements of sufficient strength and resistance against erosion and penetration of metal melts and slag components.

For this paper all three types of plugs were tested in model trials to investigate the properties of the ceramic structure being relevant for the bubbling characteristics.

2.1. Type A-plugs with high open porosity

This type can be characterized by following physical data: Bulk density, open porosity, permeability and the relevant strength values. But there is no reference of these data to the average pore diameters or the average pore distance – characteristic values for the brick structure and important for the formation of gas bubbles.

The determination of the average pore diameters by means of penetration of mercury is not applicable for pore diameters being penetrated by hydrostatic pressure of mercury alone. Pore diameters of appr. 400 μm which often occur in purge brick, cannot be measured by these methods. An approximative information is possible by means of optical measurement.

Accepting the assumption that for the permeability a pore diameter of 100 μm as minimum is significant, it is possible to quantify these data by optical methods. For each type of purge brick there were performed 300 single determinations, which is in general too low, but an approximative characteristic for the properties of the structure being relevant for the formation of gas bubbles.

For five different purge bricks the following data were determined:

Table 1

Data of brick with high open porosity

brick	B. D. Pukall (g/cm³)	water adsorption (%)	open porosity (%)	permeability (nPm)
1	2,68	10,8	29,0	129,2
2	3,04	6,7	20,4	70
3	2,51	12,2	30,6	223
4	2,49	11,8	29,4	120,5
5	2,23	15,6	34,8	661,3

There are already publications about the physical data and first results in steel casting ladles (21). The single types of group A purge brick may be described by following structure characteristics:

Brick 1: Purge brick with high open porosity, based on mag-chrome co-clinker where burning out materials were added before the ceramic burning process. In a relatively coarse grain sizing a structure with fine pores can be seen (fig. 1A1–1A/2–4), there are only few pores with higher diameter. The fines consist of single periclase crystals and chrome ore particles (higher reflection) as ceramic structure. Therefore the average pore diameter is the lowest of all investigated samples with <0.2 mm.

Brick 2: High-fired low iron MgCr-brick with direct bond and special grain sizing. Compared with brick 1 the distribution of the pore diameters is more homogeneous and the average pore diameter higher. In the structure of the fines the network of single periclase crystals does not occur (fig. 2A/1–5).

Brick 3: Low iron magnesia brick, high-fired with special grain sizing. In the structure of this sample the tendency is even more distinct that the ceramic bond occurs mostly by contacts of the finest periclase crystals and causes greater pore volumes (fig. 3A/1–5).

Brick 4: Corundum brick with high permeability and special grain structure. This brick has a finer grain size compared with the magnesia brick, the sintering behaviour during the firing process being favorable for the formation of finer pores (fig. 4A). Therefore the average pore distance and pore diameter are lower than these of brick 2 and 3.

Brick 5: Corundum brick with extremely high permeability and special grain sizing. This sample produced for high permeability and porosity shows almost only grain-grain contacts (5A/1–4), but because of the fine grain structure the average pore distance is rather low.

For these 5 samples the average pore distances and the amount of pores $> 100\,\mu$ were determined (table 2).

With the exception of brick no. 1, the percentages of pores above 100 μm are from 38% to 62%. On account of different analytical methods, the percentages of coarse pores cannot be brought into relation to the open porosity determined.

2.2. Type B – purge brick with "directed porosity"

About the application of brick with "directed porosity" in ladles as well as in BOF-shops there are already some publications (21), (22), (23).

Table 2

Measured medium pore distances

brick	medium pore distance (mm)	percentage of pores $>110\,\mu$m
1	0,2	14
2	1,525	62,7
3	1,505	40,0
4	0,875	38,0
5	1,00	54,0

For the trials described in this publication the channel diameter was varied between 0.7 mm and 2 mm, although according to previous experiences for steel casting ladles the maximum channel diameter has to be lower than 1 mm.

As ceramic materials corundum as well as mag-chrome bricks were used, the physical properties of these samples are given in table 3.

Table 3

Data of purge brick with directed porosity

brick	B. D. Pukall (g/cm³)	Al_2O_3 (%)	MgO (%)	Cr_2O_3 (%)
6 (0,7 mm)	2,85	82		
7 (0,9 mm)	2,85	82		
8 (1,0 mm)	2,95		54	20

Brick 6: Is based on corundum raw materials and consists of channels with 0.7 mm diameter and a minimum distance of 5 mm. The channels are surrounded by the dense ceramic material without weakening the brick structure (fig. 6A–1–3). This is also valid for.

Brick 7: (0.9 mm channel diameter) and

Brick 8: (1 mm diameter) – fig. 7A, 8A, latter based on mag-chrome co-clinker. There were also tried samples with 2 mm channel diameters, but the results were not included in the evaluation.

2.3. Type C-brick with joints

Of these types two alternative possibilities were tried:

A cylindric part of a dense burnt brick was cut into three pieces and thin steel sheets were put into the joints in order to keep constant distance between the ceramic parts.

The cylinder then was encased in a steel sheet with mortar. It can be seen from the fig. 10A/1–3, that the width of the joint is between 0.15 and 0.30 mm. As ceramic material a low iron burnt magnesia brick was used (brick No. 10).

For the other type a dense cylindric part was encased in a steel sheet without mortar, the width of the joint between the ceramic cylinder and the steel case being appr. 0.2 mm (brick No. 11).

3. Model investigations on purge brick

The formation of bubbles in liquids is, besides the physical properties of the gas and the liquid, depending on the interfacial properties of the liquid and the material of the emersion orifice and the geometrical properties of the gas detachement like the cross sections and the distance of the emersion orificies (24), (25).

The detachement of gas from purge brick can be interpreted as similar to processes on single emersion orifices characteristic for the amount of gas carried through. With low amounts of gas single bubbles of a constant size are formed. With higher amounts of gas this process is transformed into a regime of constant frequency of bubble formation and incrasing bubble volume. Above a critical amount of gas the bubble volume in quickly increasing by coalescence of the single bubbles. During the separation of bubbles the regime of single bubbles is transformed into a gas jet. If the aim of inert gas treatment is not only the kinetic effect but also an efficient metallurgical effect, the amount of gas should be below the critical gas flow rates Q_K.

For the qualitative investigation of the formation of bubbles from purge brick water is useful as model liquid. A direct measurement of the bubble size is possible as well as a prompt determination of the critical amount of gas.

For the physical investigation of the purge effect of the above described samples a water model as described in fig. 12 was built up. The diameter of the model was 570 mm, the height of the bath 650 mm, in the middle of the bottom the sample of the purge brick of 50 mm diameter are fixed. As gas air is used. The amount of gas is measured by an orifice gauge with a DMS-based pressure transformer. The bubble formation can be observed and photographed through a window in the model for evaluation and documentation. For the observation of bubble formation a stroboscopic light was used. The flash light photos were taken with open shutter and single exposure time of appr. 10^{-4} sec.

The photographs of the bubble shapes were put in the fig. 1–11 in comparison to the brick structure. The four characteristical phases of bubble formation were registered:

I regime of constant bubble size
II regime of constant bubble frequency
III transition into gas jet
IV regime of gas jet

The three types of purge brick show different bubble characteristics, where also within the single group varieties differences can be observed.

In the type A brick the differences in the structure of the brick 1 are clearly visible also the bubble characteristics compared with brick 2–5. Brick 1 shows a more inhomogeneous bubble formation than with the other type A brick.

The brick of type B shows a differential characteristics of bubble formation – with increasing channel diameter the size of the bubbles does not increase accordingly. The formation of the bubble swarm in this type B brick group seems to be more inhomogenious (fig. 6B, 7B, 8B, 9B). It has to be mentioned that this model covers the formation and detachement of bubbles at low pressures and low amounts of gas compared to steel plant practice.

The two type C brick (fig. 10B, 11B) diverge to a high degree from the bubble characteristics of the types described above. The plug blowing in the periphery of the cylinder additionally shows a gas penetration through the open porosity of the magnesia brick (fig. 11B, III).

A fundamental presupposition for the scale-up of the informations obtained with the water model about the bubble formation on purge brick is the similarity of the wettability conditions. In wettable systems the bubble diameter depends on the orifice diameter (pore diameter), in non-wettable systems the distance of the orifices (pore distance) is characteric for the bubble size. In order to create in the model non wettable conditions, all 8 purge brick samples were impregnated with a paraffin solution, so that a comparably high wetting angle could be achieved.

As main measurable variables in this model experiment the critical gas flow – the amount of gas where the first bubble packages of appr. five times of the bubble diameter are detached – and the medium bubble diameter $\bar{D}_B$ at 0.95 Q_K critical gas flow are determined. Additionally, the packing density of bubbles detached from the purge brick is determined at 0.95 Q_K under the assumption of a hexagonal dense packing of the bubbles. This value represents the area distribution (density) of the active orifices of the δ_F-purge brick. For the type C-brick (purging through joints) the number of active orifices is determined according to the length of the joint δ_L. In order to compare the effectiveness of the various types of purge brick the critical gas flow $\bar{Q}_{KP}$ related to the total number of active orifices of the sample is determined as characteristic for the gas flow of the transition regime.

The results of the model investigations are summed up in table 5. It can be registered, that brick

Table 4

Relation of channel- and bubble diameters of brick with "directed porosity" in the model trials

channel diameter	bubble diameter
0,7 mm	5,4 mm
0,9 mm	6,0 mm
1,0 mm	6,6 mm
2,0 mm	9,2 mm

1/1 6×

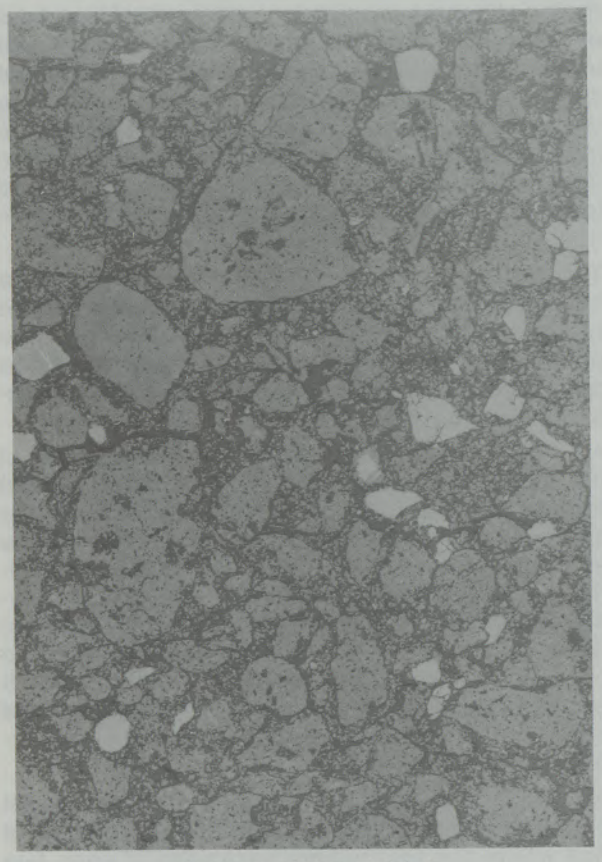

Structure of purge brick 1

Fig. 1 **PART A**

1/2 55×

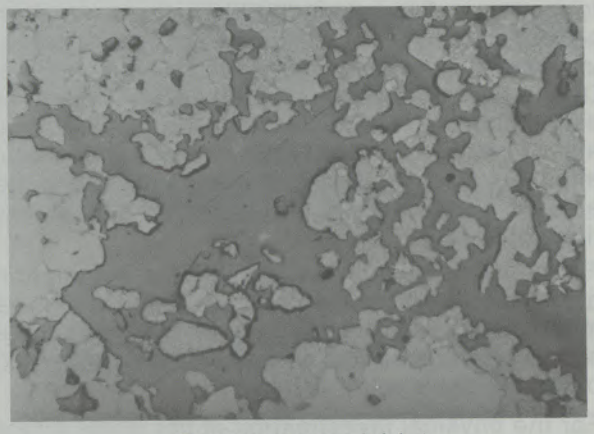

Structure of purge brick 1

1/3 55×

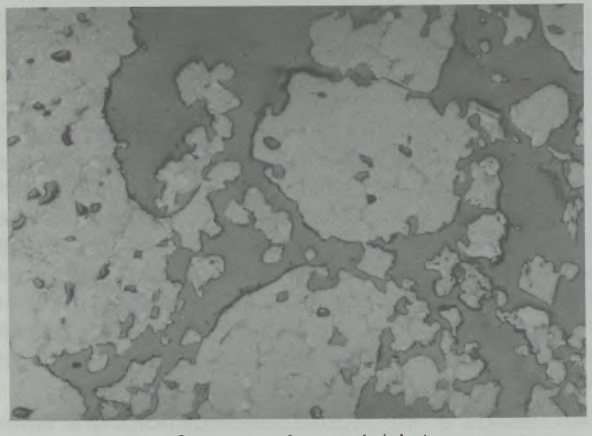

Structure of purge brick 1

1/4 55×

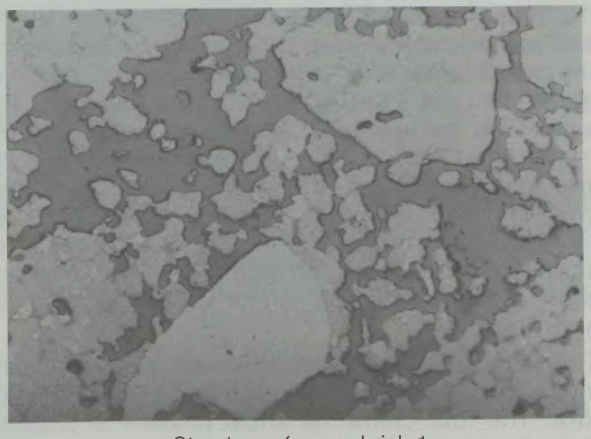

Structure of purge brick 1

with high open porosity and corresponding high δ_F cause the smallest bubble sizes, nevertheless with low critical gas flow for the single orifice. According to these model assuptions the brick 2 of type A turns out as optimal.

The type C brick show a high bubble diameter but also a high critical gas flow for the active singele orifice. Brick with directed porosity (type B) show relatively high bubble diameters and lower critical gas flow of the single active orifice.

The high $\bar{Q}_{KP}$ value of sample No. 8 can be explained by the low number of active orifices. Because of the fact that in orifices with low distances also a horizontal coalescence may occur, above a certain distance of the active orifices there will be only a vertical coalescence of bubbles. The transition regime will therefore occur with higher gas flow rates. It has to be mentioned, that this behaviour is an important information for optimizing the distance of active orifices of purge brick.

Fig. 1 **PART B**

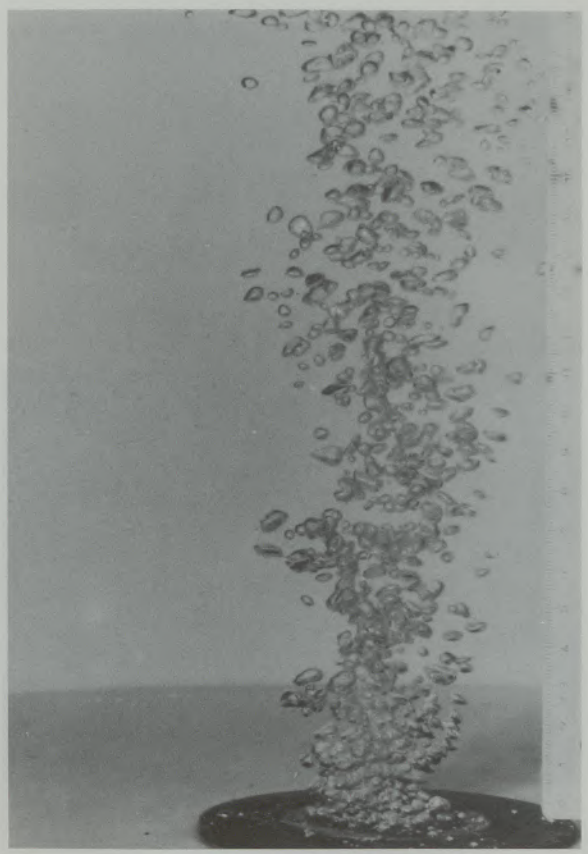

Regime of bubble formation I

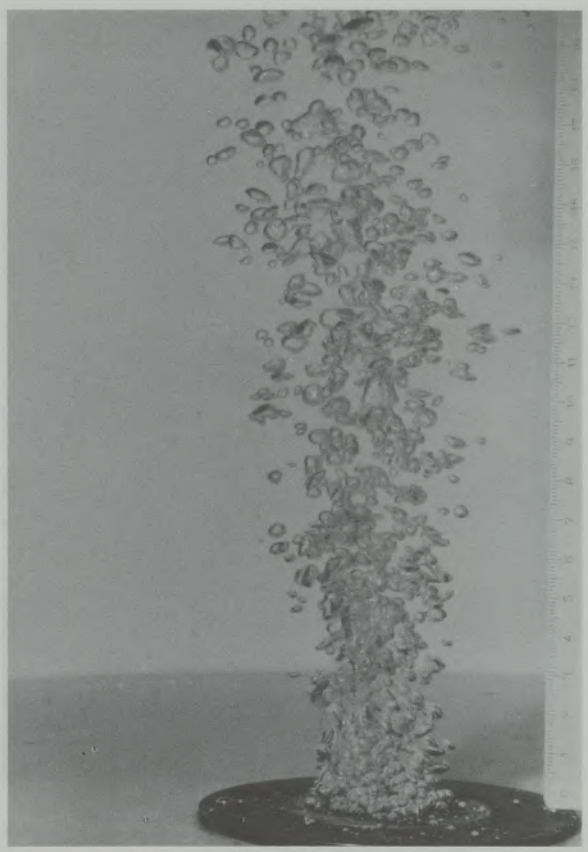

Regime of bubble formation II

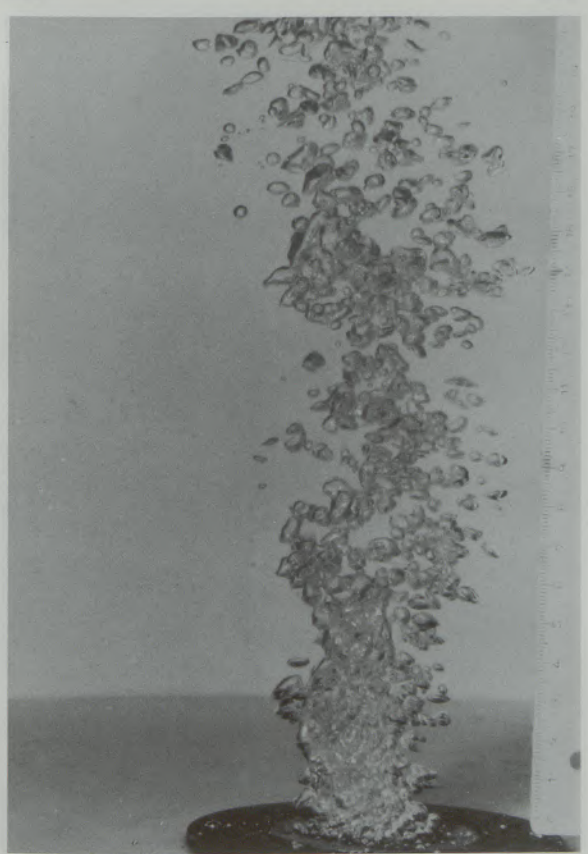

Regime of bubble formation III

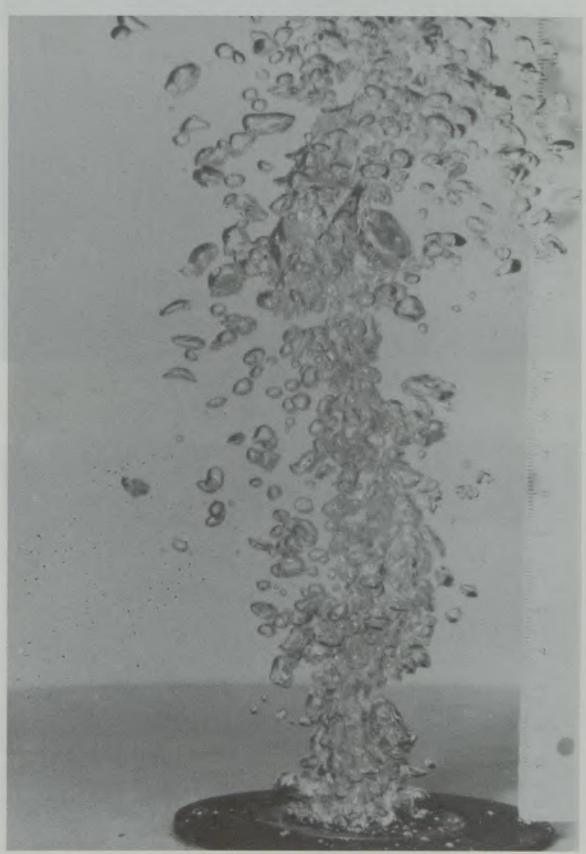

Regime of bubble formation IV

2/1 6×

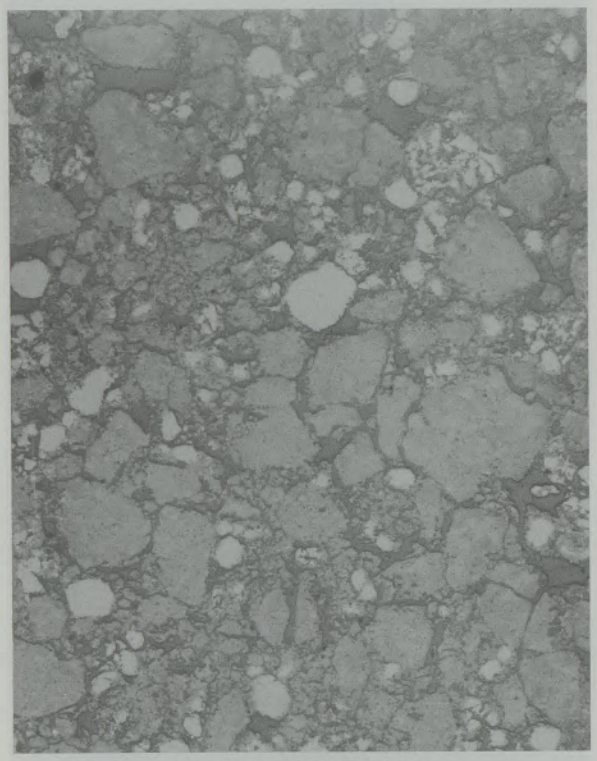

Structure of purge brick 2

2/3 55×

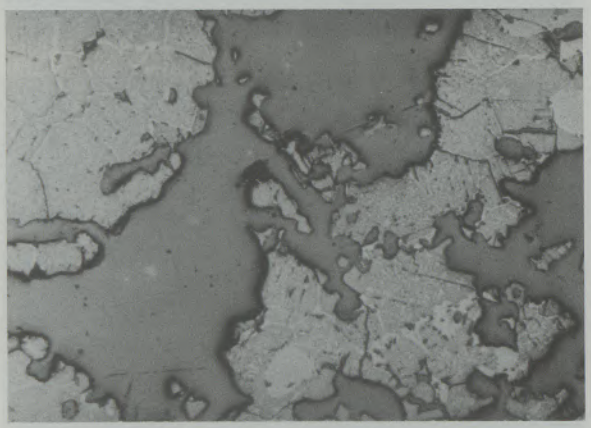

Structure of purge brick 2

2/4 55×

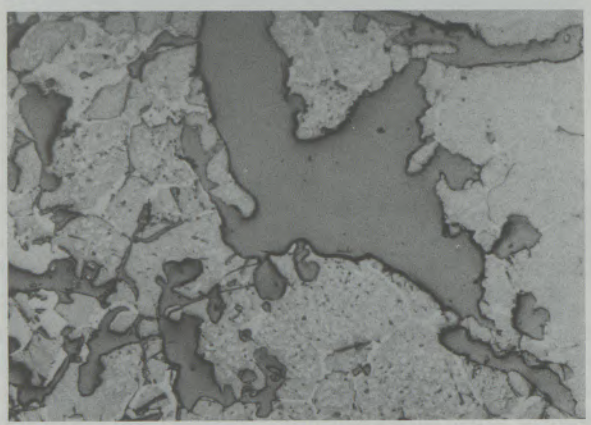

Structure of purge brick 2

Fig. 2 **PART A**

2/2 55×

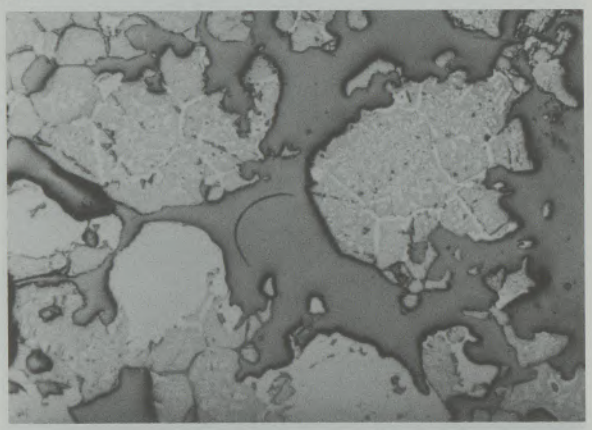

Structure of purge brick 2

2/5 55×

Structure of purge brick 2

Fig. 2 **PART B**

Regime of bubble formation I

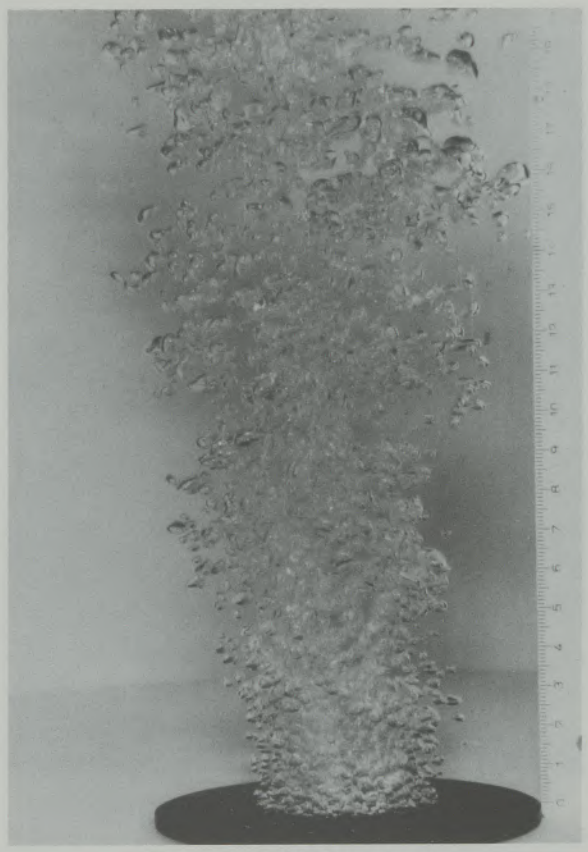

Regime of bubble formation II

Regime of bubble formation III

Regime of bubble formation IV

Fig. 3 **PART A**

3/1 6×

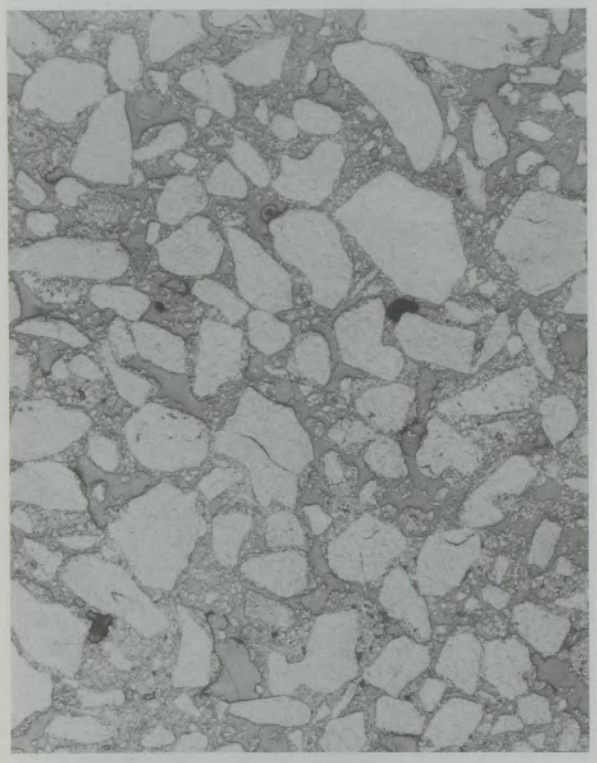

Structure of purge brick 3

3/2 55×

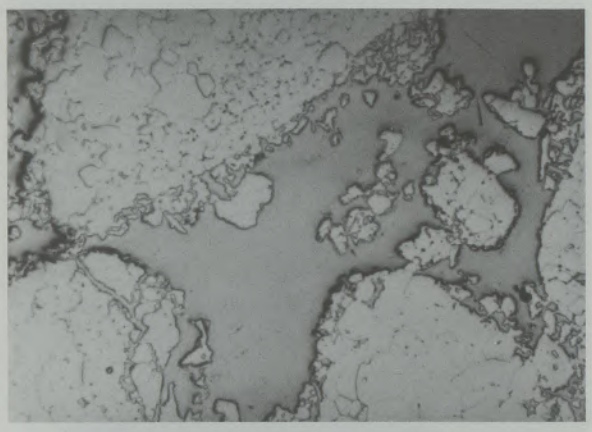

Structure of purge brick 3

3/3 55×

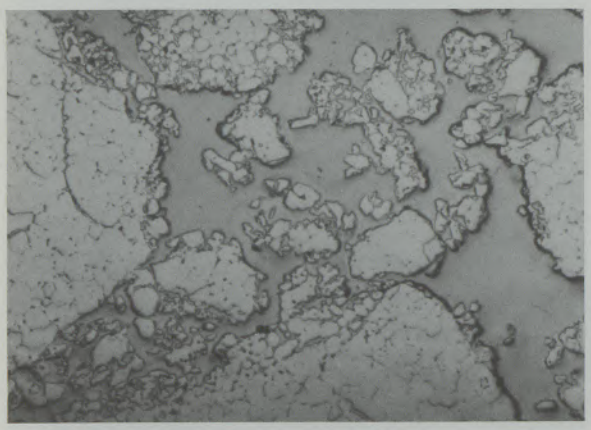

Structure of purge brick 3

3/4 55×

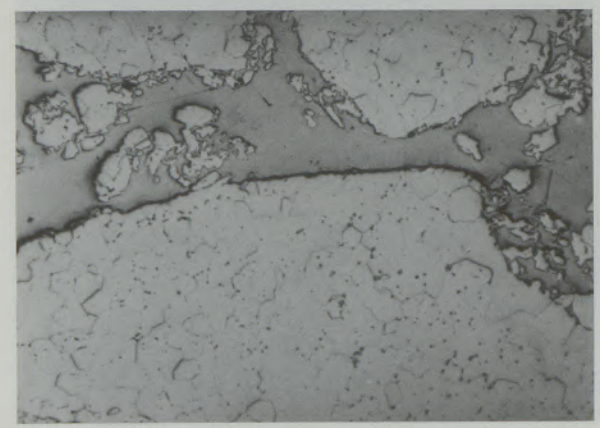

Structure of purge brick 3

3/5

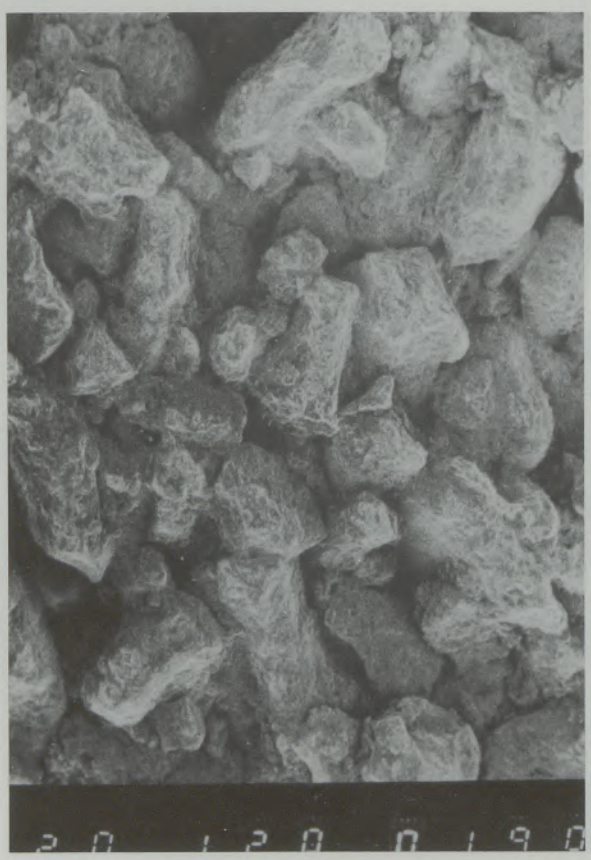

Structure of purge brick 3

Fig. 3 **PART B**

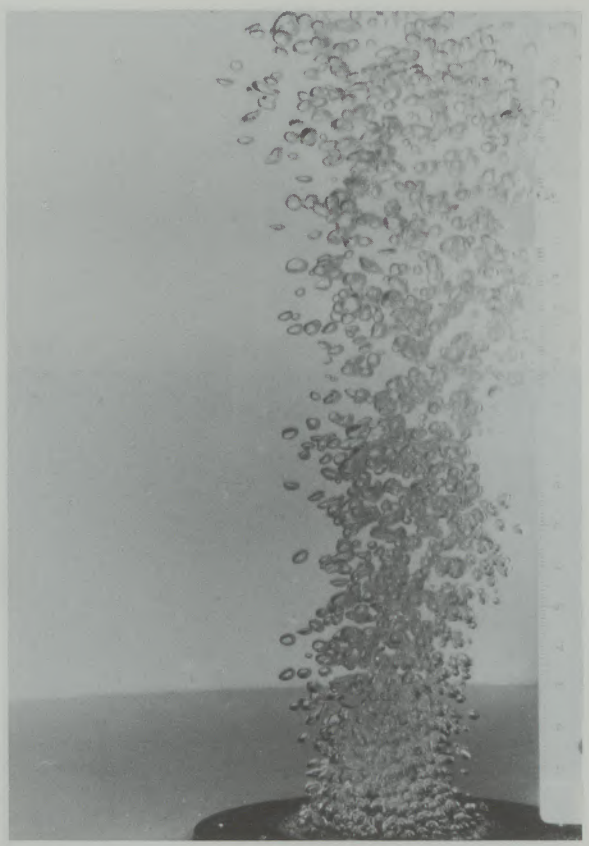

Regime of bubble formation I

Regime of bubble formation II

Regime of bubble formation III

Regime of bubble formation IV

Fig. 4 **PART A**

4/1 6×

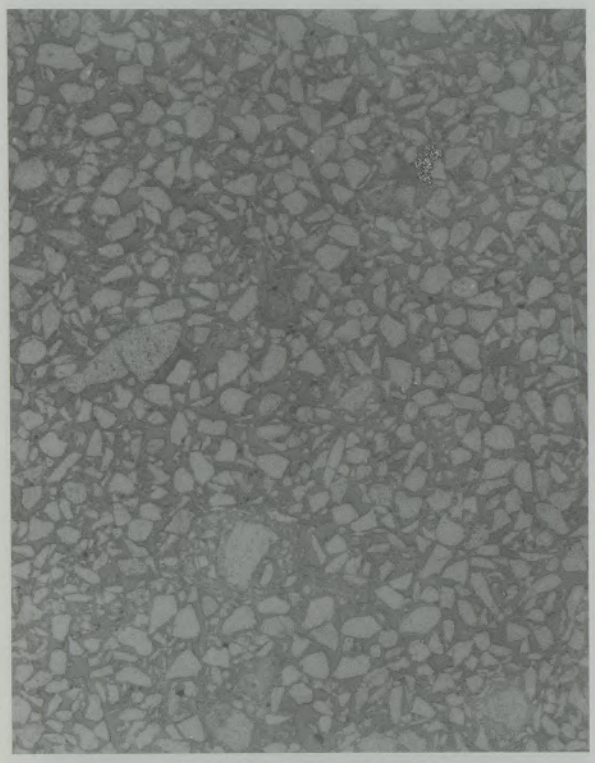

Structure of purge brick 4

4/2 55×

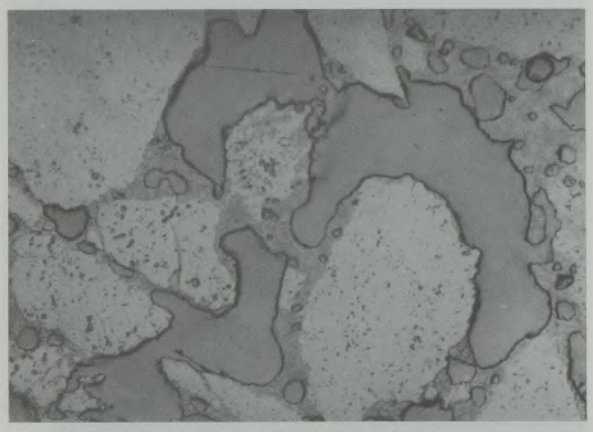

Structure of purge brick 4

4/3 55×

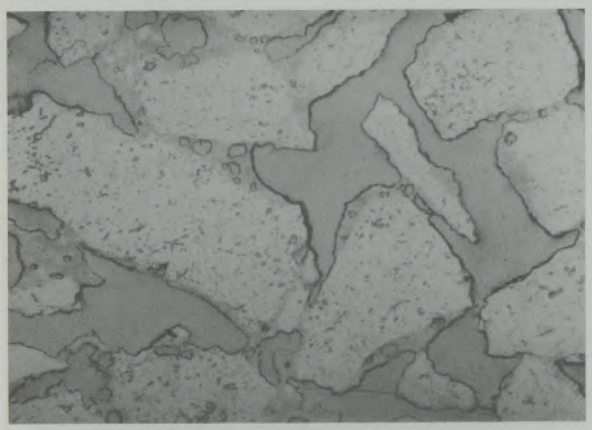

Structure of purge brick 4

4/4 55×

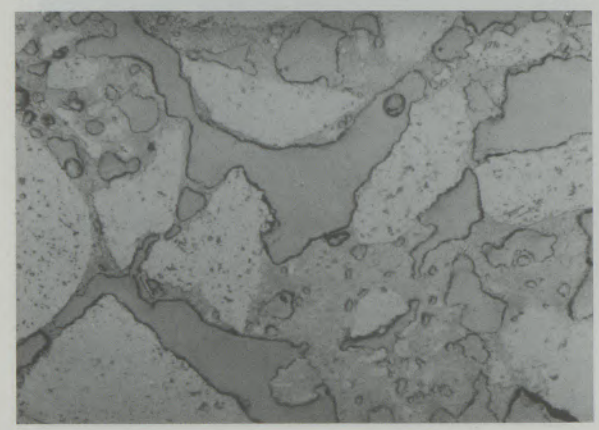

Structure of purge brick 4

4/5

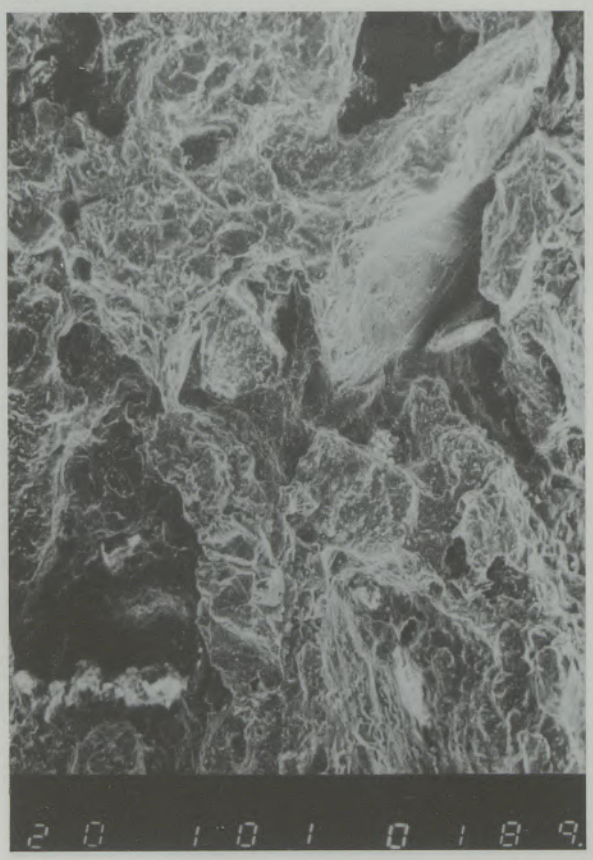

Structure of purge brick 4

Fig. 4 **PART B**

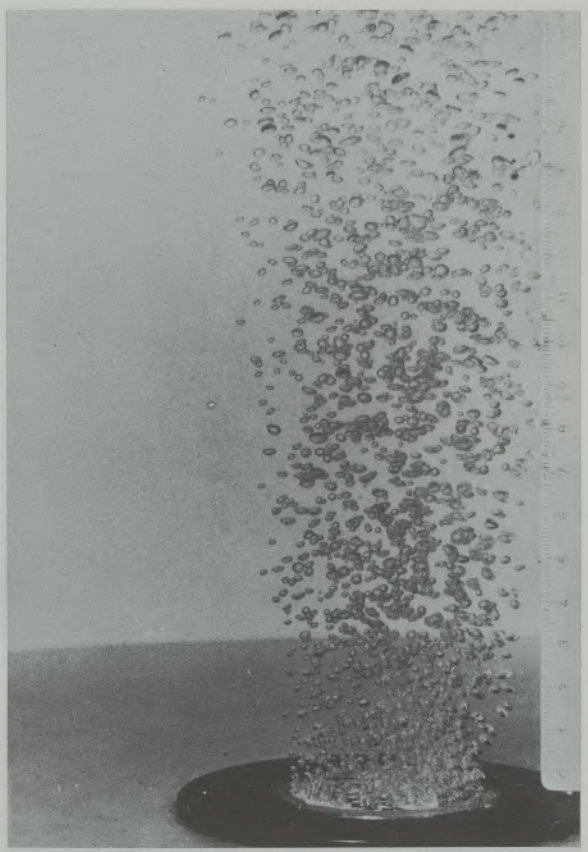

Regime of bubble formation I

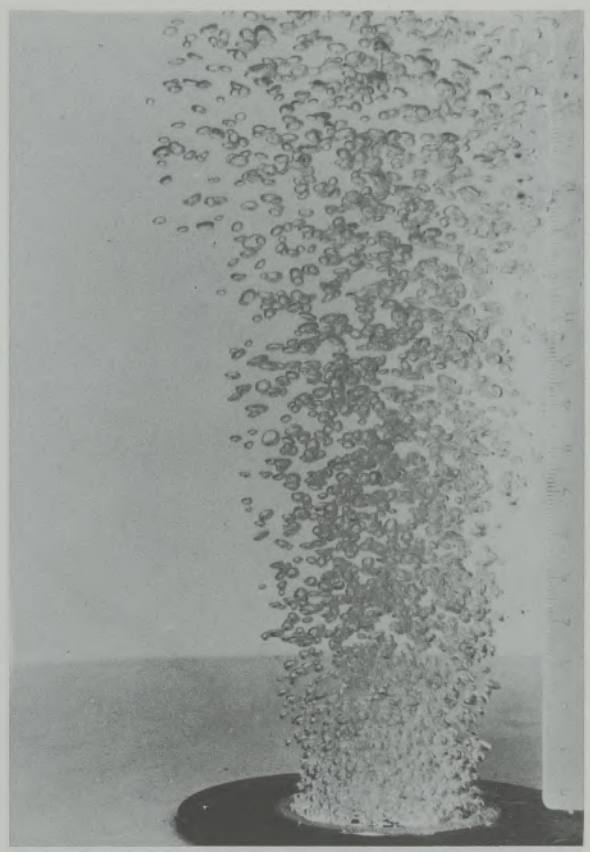

Regime of bubble formation II

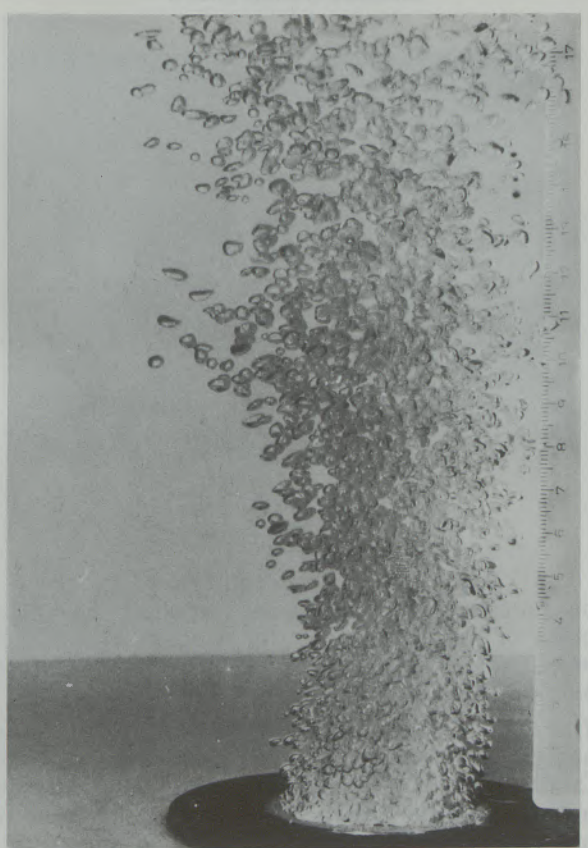

Regime of bubble formation III

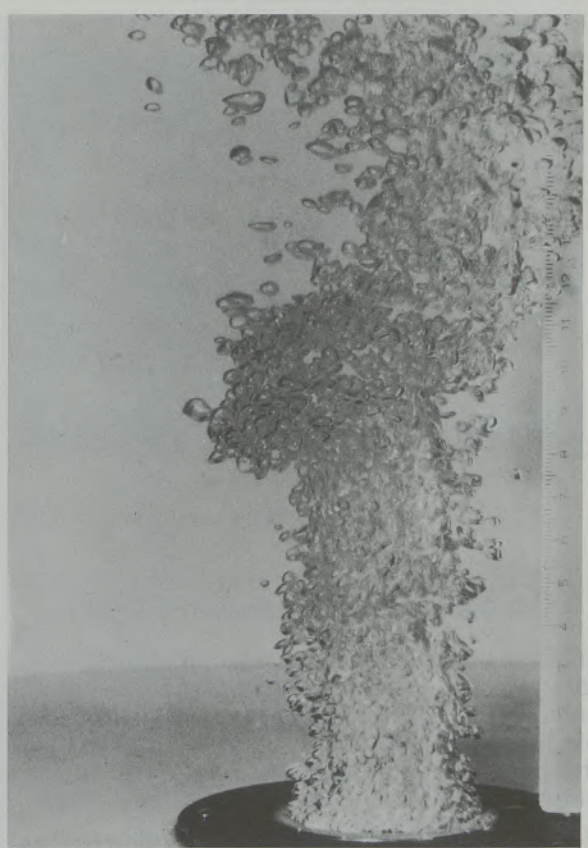

Regime of bubble formation IV

5/1 6×

Structure of purge brick 5

Fig. 5 **PART A**

5/2 55×

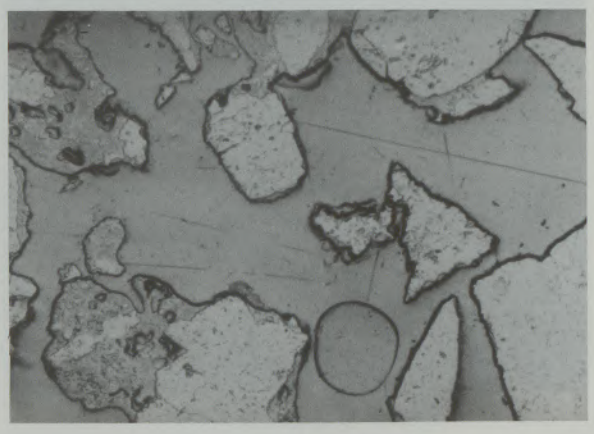

Structure of purge brick 5

5/3 55×

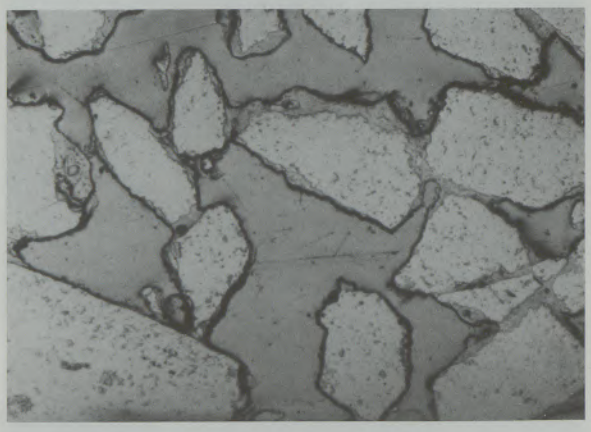

Structure of purge brick 5

5/4 55×

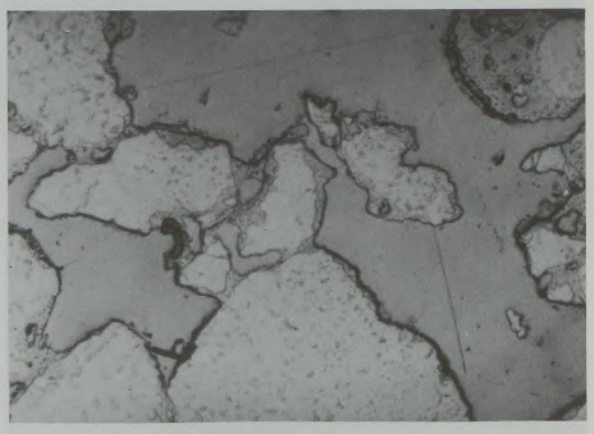

Structure of purge brick 5

4. Consideration of similarity theory

In order to estimate the characteristical parameters of purge brick in metal melts also quanitatively, besides the qualitative evaluation of the bubble formation a similarity theoretical analysis of the bubble formation at the transition regime of single bubbles to the gas jet was performed.

For this purpose the equation according to P a w l o w s k y (27) for the derivation of non-dimensional characteristic quantities was applied. As initial point of the discussion the results of a model investigation about the formation of bubbles from single orifices were used (25–29).

The investigation based on the similarity theory shows, that besides the objective values D_B and $\overline{Q}_{KP}$ the surface tension of the liquid σ defining the adhesion of the bubbles, the difference of density between liquid and gas and the gravitation g defining the buoyancy force are the values relevant

Fig. 5 **PART B**

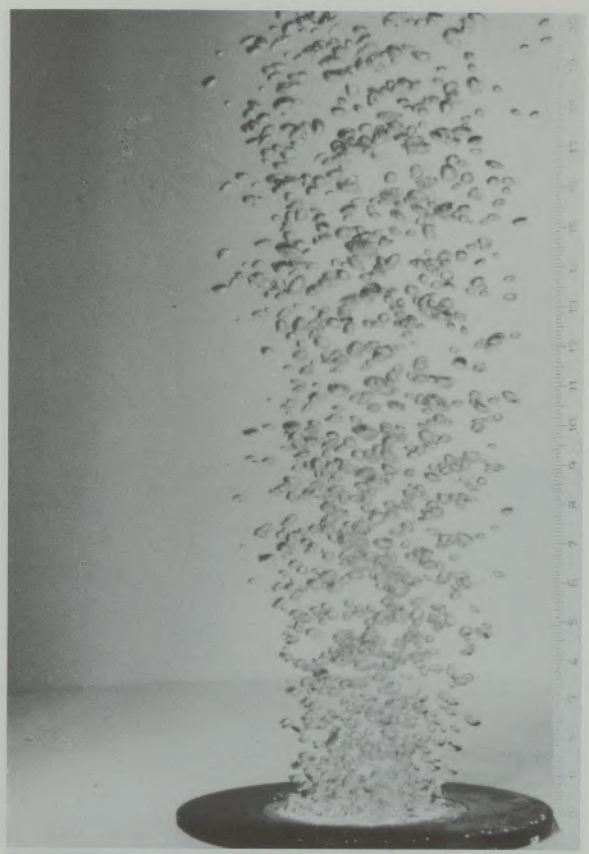

Regime of bubble formation I

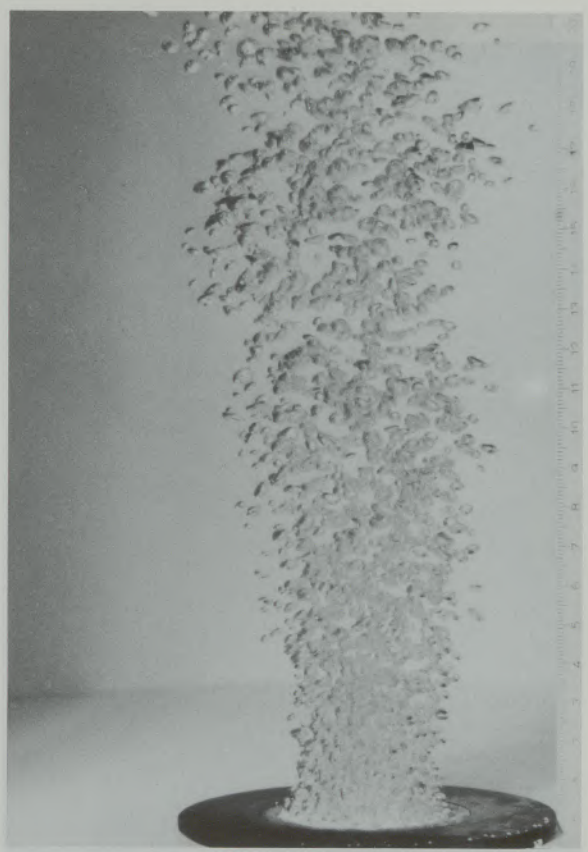

Regime of bubble formation II

Regime of bubble formation III

Regime of bubble formation IV

Fig. 6 **PART A**

6/1 6×

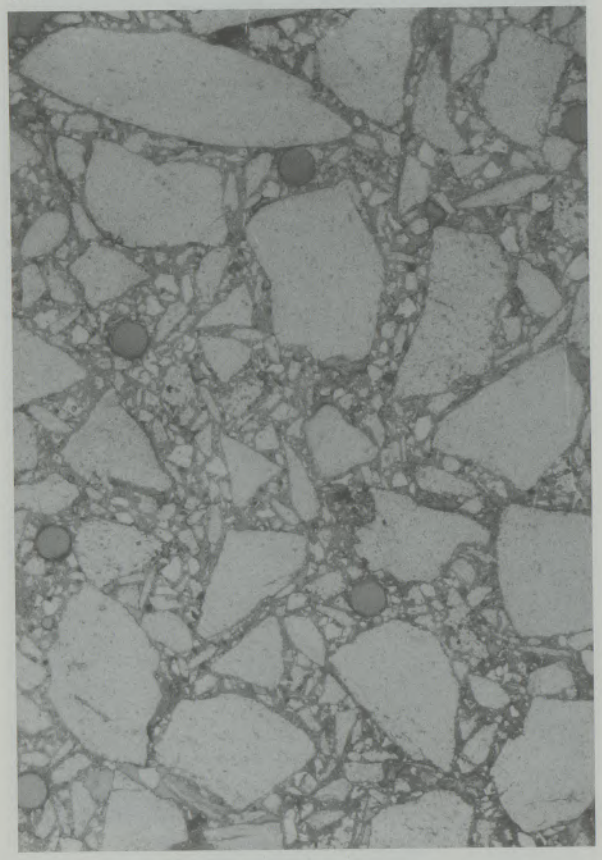

Structure of purge brick 6 with directed porosity with 0.7 mm channel diameter

6/2 55×

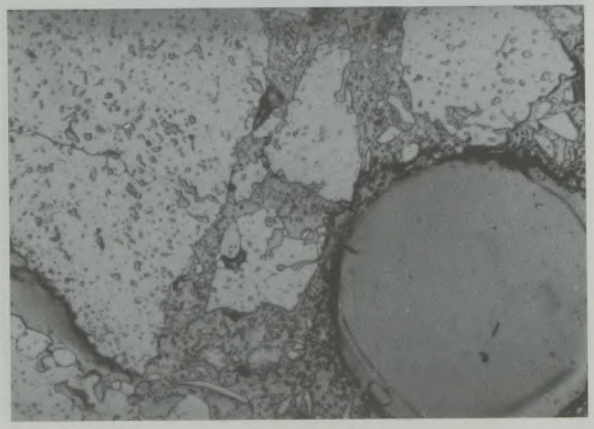

Structure of purge brick 6 with directed porosity with 0.7 mm channel diameter

6/3

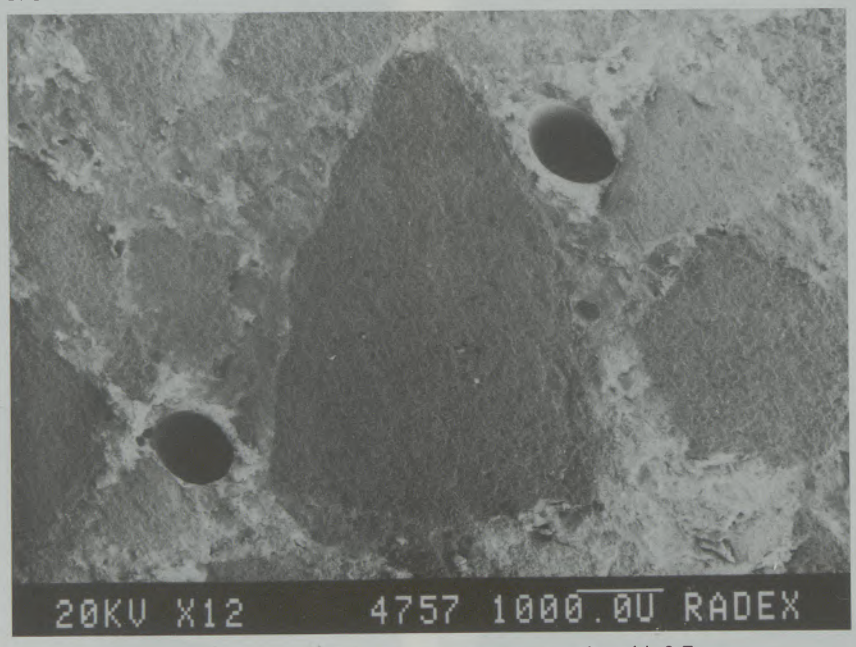

Structure of purge brick 6 with directed porosity with 0.7 mm channel diameter

Fig. 6 **PART B**

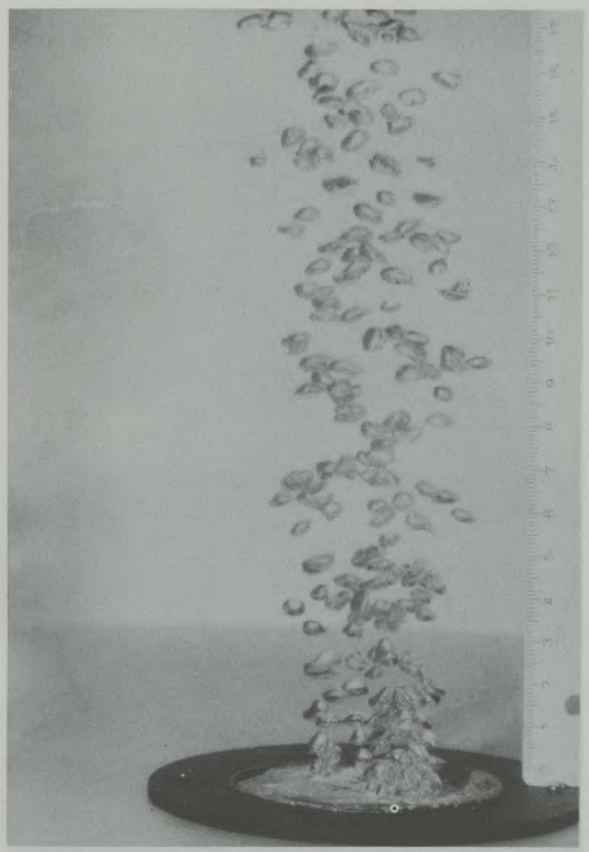

Regime of bubble formation I

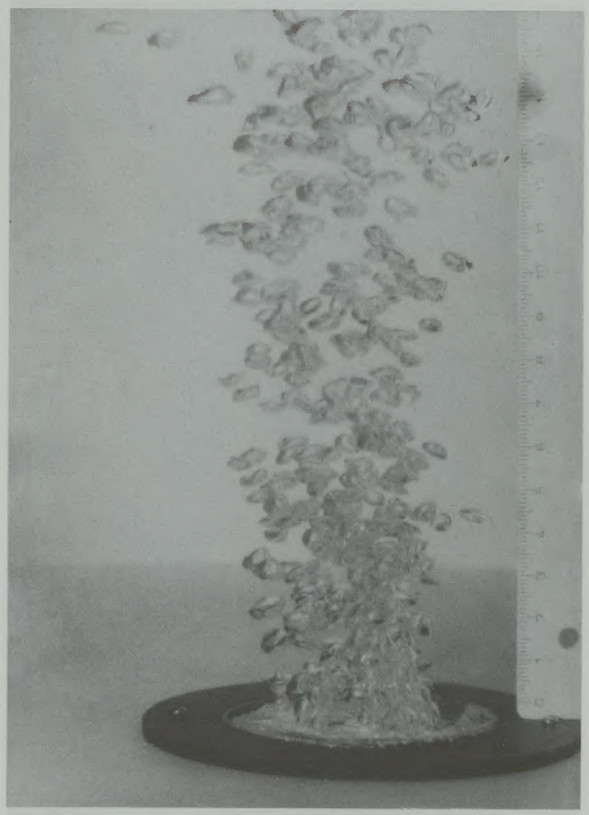

Regime of bubble formation II

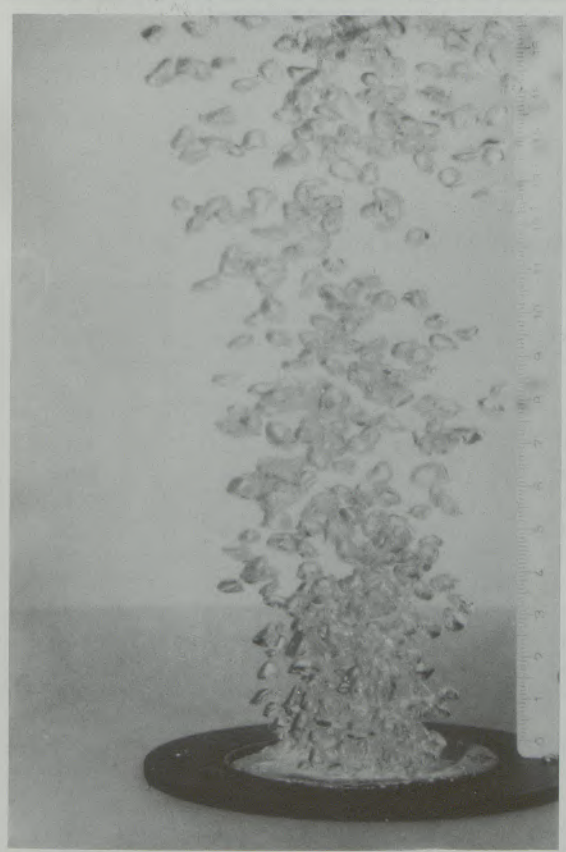

Regime of bubble formation III

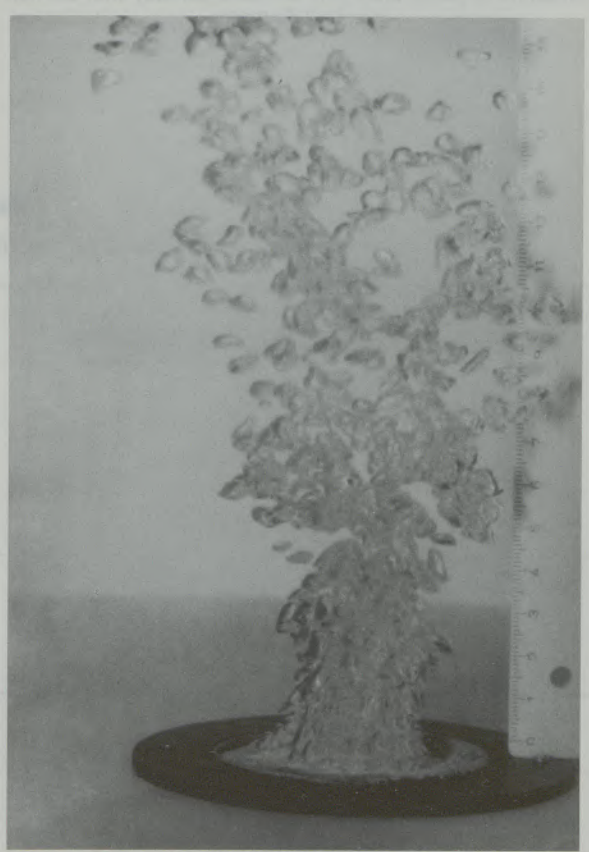

Regime of bubble formation IV

7/1 6×

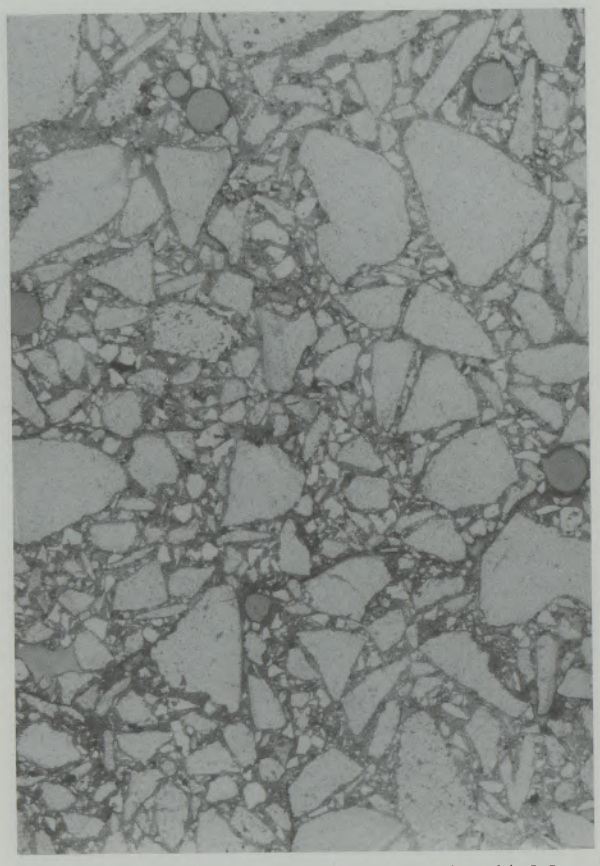

Structure of purge brick with directed porosity with 0.9 mm channel diameter

Fig. 7 **PART A**

7/2 55×

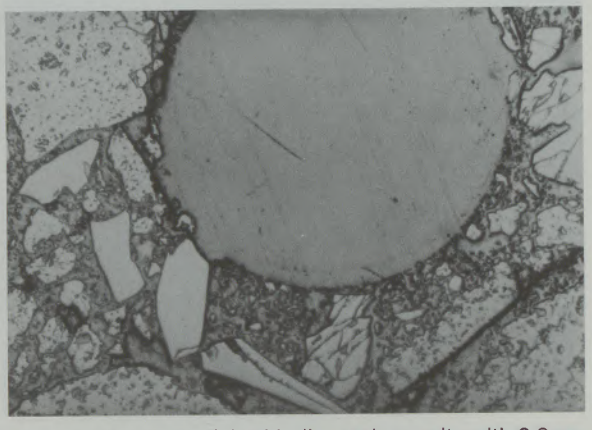

Structure of purge brick with directed porosity with 0.9 mm channel diameter

Table 5

Characteristic values of the model investigation of purge brick

no.	type of brick		$\overline{D}_B$ 10^{-3} (m)	σ_F 10^4 (m^{-2})	$\overline{Q}_{KP}$ 10^{-6} (m^3s^{-1})	Z_I (–)	Z_{II} (–)
brick with high open porosity							
1			4,0	19,7	0,5	40,2	18,4
2			3,2	12,4	1,28	2,0	1,41
3			4,0	10,9	1,51	4,4	2,05
4			3,2	20,3	0,36	25,4	18,4
5			3,4	11,8	0,89	5,6	3,60
brick with directed porosity							
6	channel diameter	0.7	5,4	7,6	0,53	160	40,2
7	channel diameter	0.9	6,0	6,6	0,75	136	27,5
8	channel diameter	1.0	6,6	2,6	3,1	12,8	2,12
no.	type of brick		$\overline{D}_B$ 10^{-3} (m)	σ_L 10^2 (m^{-1})	$\overline{Q}_{KP}$ 10^{-6} (m^3s^{-1})	Z_I (–)	Z_{II} (–)
9	purge brick with joints	S	5,6	1,6	1,45	25,7	6,0
10	purge brick with joints	R	6,4	1,6	1,26	66,3	11,9

Fig. 7 **PART B**

Regime of bubble formation I

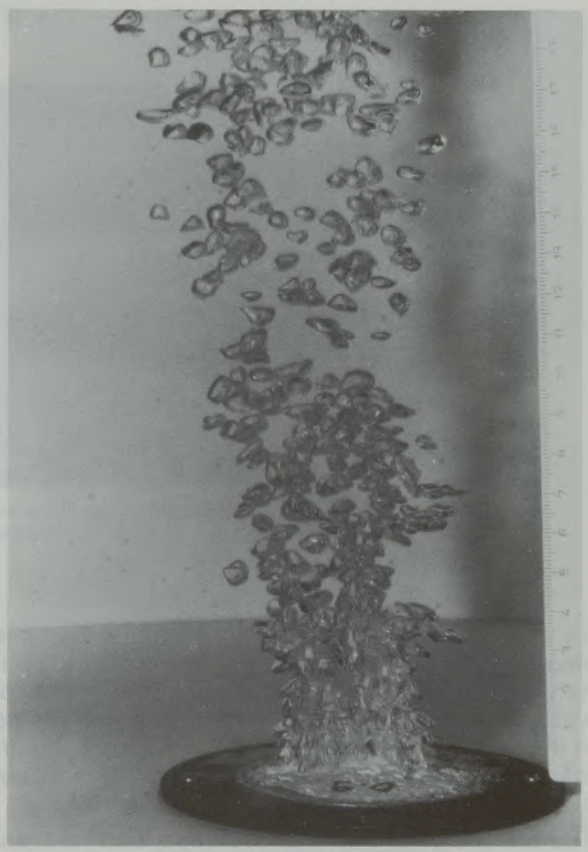

Regime of bubble formation II

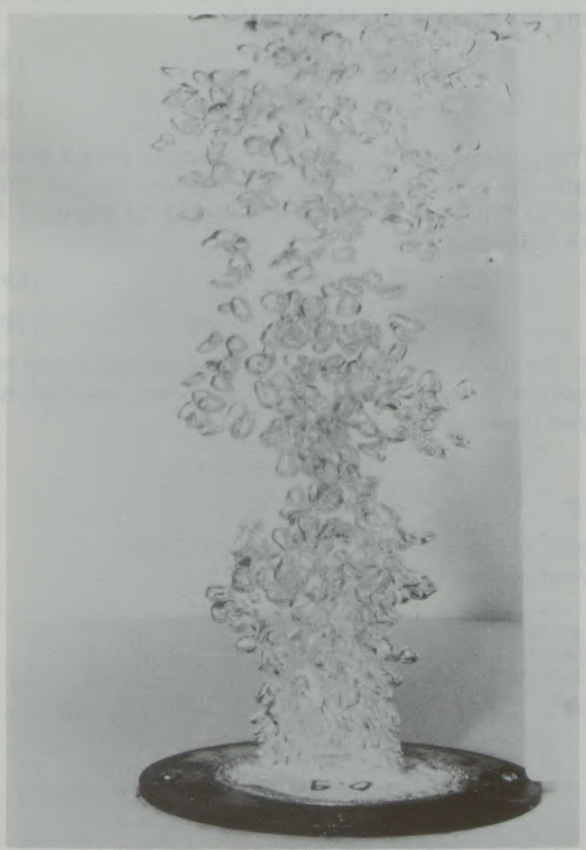

Regime of bubble formation III

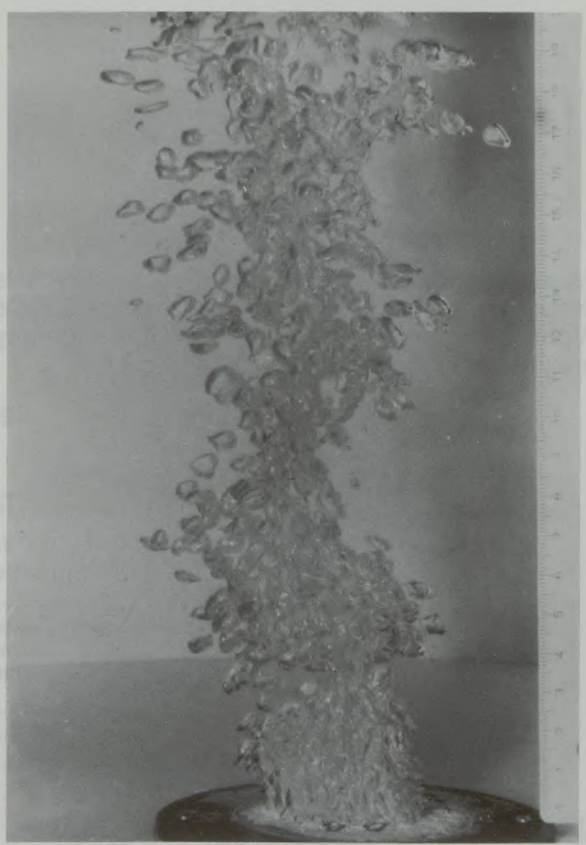

Regime of bubble formation IV

Fig. 8 **PART A**

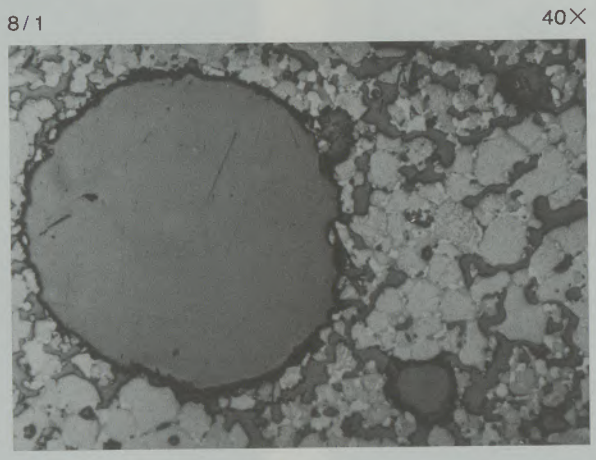

Structure of purge brick with directed porosity with 1 mm channel diameter

for this problem. The influence of the dynamic viscosity in the investigated regimes is almost negligeable. This was the result of mixtures of water and glycol, where the viscosity was varied in the range of a power of ten. This is also confirmed by the results of model investigations about bubble formation on single orifices (29).

The dimensional matrix of the described relevant data list is therefore:

Table 6

Dimensional matrix acc. to (27)

	$\overline{D}_B$	$\overline{Q}_{KP}$	Δ_ϱ	g	O
L	1	3	−3	1	0
Z	0	−1	0	−2	−2
M	0	0	1	0	1

As already shown in the formulation, the grade is three. Accordingly, after performance of Gauß's Algorithmus and after formulation of the identity matrix two non-dimensional coefficients.

$$Z_I = g\,\overline{D}^5/\overline{Q}^2_{KP} \qquad [2]$$

and $$Z_{II} = \sigma\,\overline{D}^3/\overline{Q}^2_{KP}\Delta\varrho \qquad [3]$$

can be derived. They are together with the coefficient σ_F resp. σ_L significant for the transition of the bubble regime into a gas jet.

The coefficients determined from the results of the water model are listed up in table 1.

It is possible to calculate the objective numbers for the various purge brick types by supposition of the surface tension and the difference in the density in real metal gas systems:

$$\overline{D} = (Z_I\sigma/Z_{II}\Delta\varrho g)^{1/2} \qquad [4]$$

$$\overline{Q}_{KP} = (Z_I^3\sigma^5/Z_{II}^5\,\Delta\varrho^5 g^3)^{1/4} \qquad [5]$$

The critical gas flow rate for a single purge brick can be calculated under consideration of the purge brick area A resp. the length of the joint 1 as following:

$$Q_K = \overline{Q}_{KP}\,\sigma_F A \qquad [6a]$$

$$Q_K = \overline{Q}_{KP}\,\sigma_L 1 \qquad [6b]$$

In liquid steel resp. pig iron melts the medium bubble diameters are appr. doubled, the critical gas flow rates tripled.

Table 7

Correlation of the relevant brick data of type A with the characteristical values of the model investigation

brick	water-adsorpt. (%)	open porosity (%)	medium pore distance	permeability (nPm)	bubble diameter (mm)	packing density of bubbles (cm^3)	volume (mm^3)	Q krit. (Nl/min.)	P krit. (bar)	Z_I	Z_{II}
1	10,8	29,0	0,2	129,2	4,0	19,7	33,5	5,7	0,12	40,2	33,5
2	6,7	20,4	1,525	70	3,2	12,4	17,2	15,2	0,76	2,0	17,2
3	12,2	30,6	1,505	223	4,0	10,9	33,5	15,7	0,21	4,4	33,5
4	11,8	29,4	0,875	120,5	3,2	20,3	17,2	7,0	0,14	25,4	17,2
5	15,6	34,8	1,00	661,3	3,4	11,8	29,6	10,1	1,3	5,6	29,6

Fig. 8 **PART B**

Regime of bubble formation II

Regime of bubble formation III

Fig. 9 **PART B**

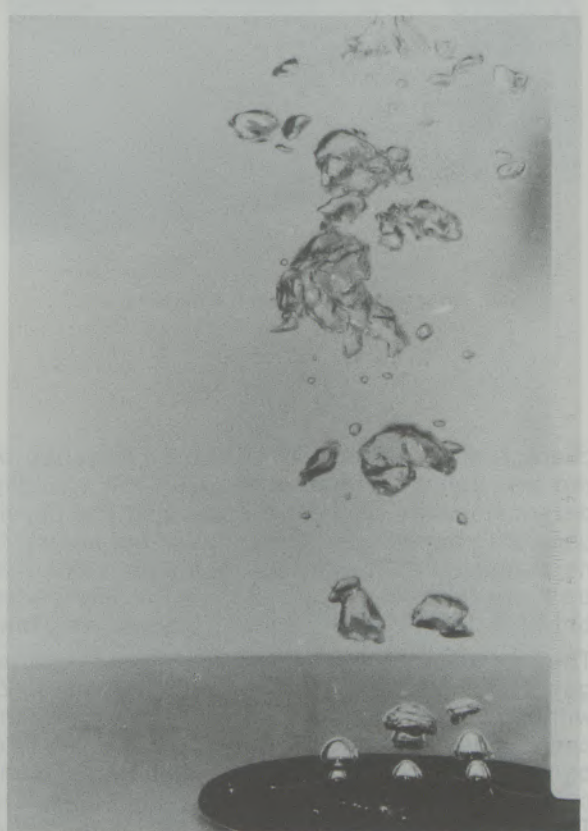

Regime of bubble formation II

Regime of bubble formation III

Fig. 10 **PART A**

10/1 6×

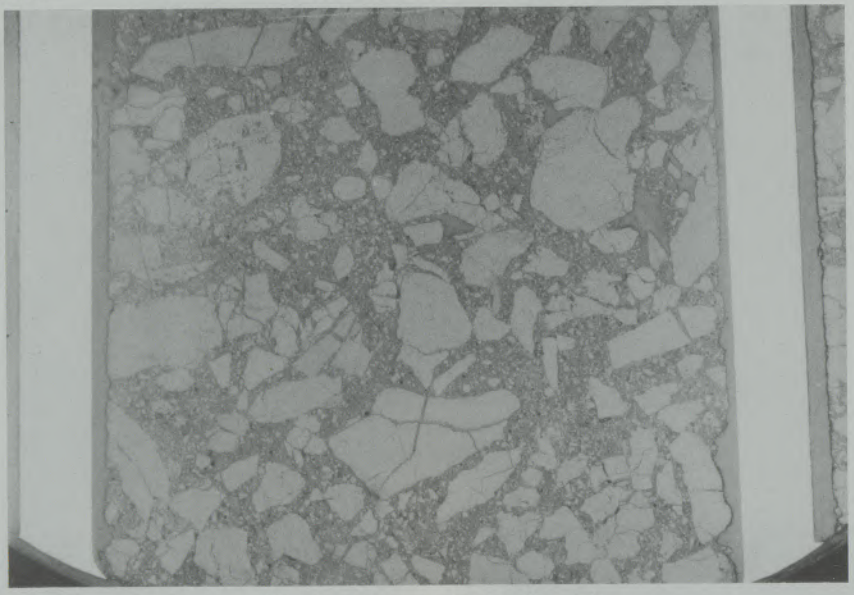

Structure of purge brick with joints

10/2 55×

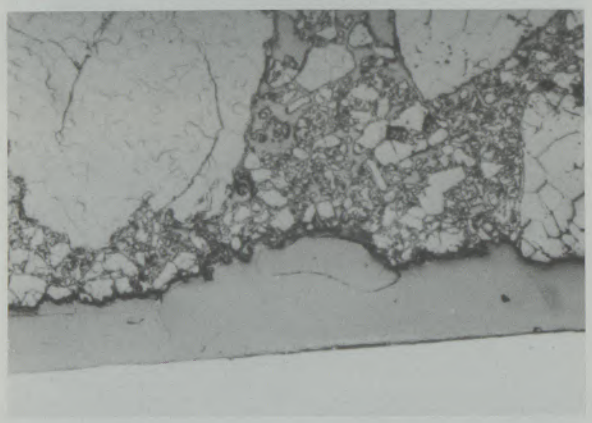

Structure of purge brick with joints

10/3 55×

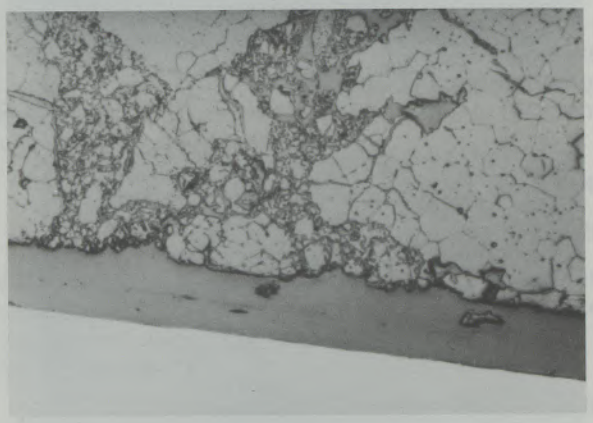

Structure of purge brick with joints

5. Discussion of the results

Besides the differences in bubble formation of the various types of purge brick it was the purpose of the trials described in this paper to achieve quantitative criteria for the evaluation of the bubbling behaviour of purge brick. This is possible by the correlation of characteristic values determined in the model investigation and derived by means of the similarity theory and physical data resp. characteristical structure values determined by means of optical measurement.

With the brick type A the water adsorption, open porosity and permeability do correspond to the gas flow rates but there is no reference to the characteristics of bubble formation. Because of the fact that a correlation between the optically determined rate of coarse pores and the physically determined open porosities is not possible, no statement about this characteristic value can be made. In addition to these facts the differences between the brick types 2 and 5 are relatively low.

The correlation between the measured critical gas flow rates resp. the characteristic values ZI with the optically determined medium pore distances seems to be significant (table 7, fig. 13). The brick types 2 and 3 with high medium pore distances also show the highest critical gas flow rates. This is referring to the assumption, that under the given conditions in these brick types neighbouring

Fig. 10 **PART B**

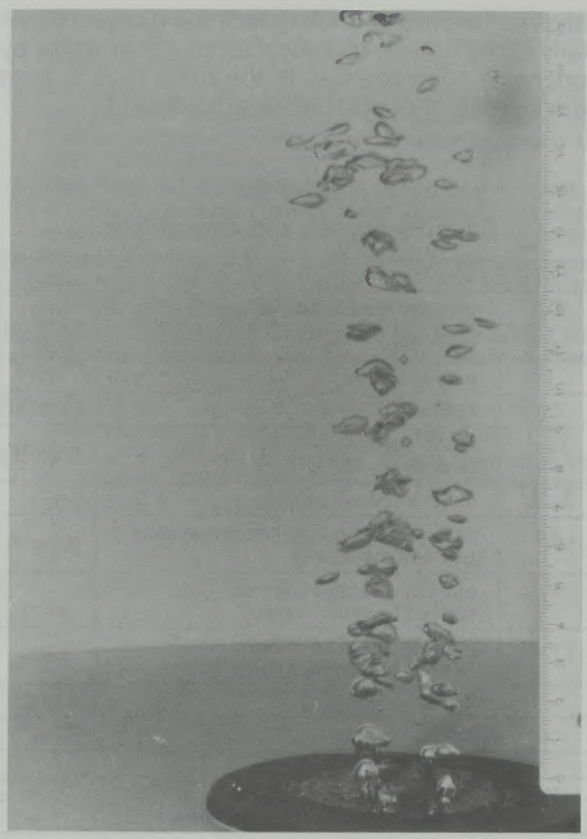

Regime of bubble formation II

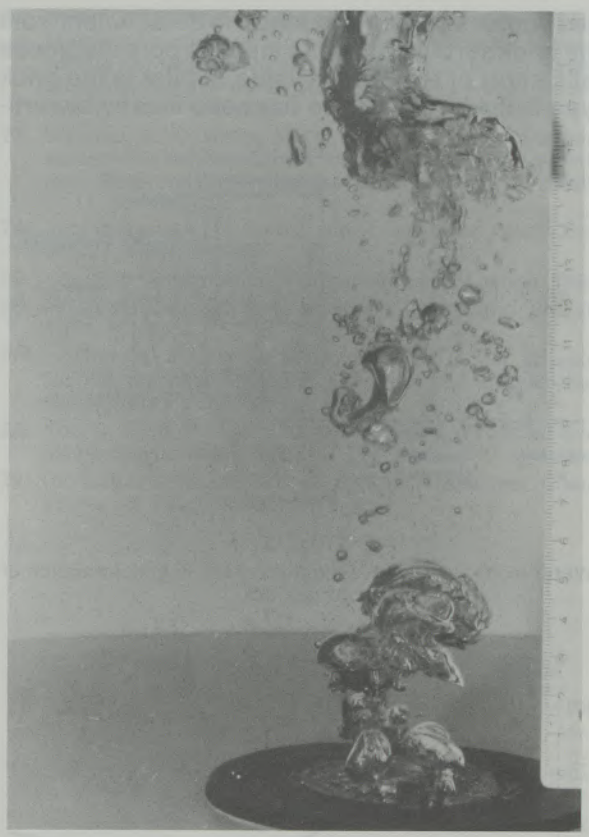

Regime of bubble formation III

Fig. 11 **PART B**

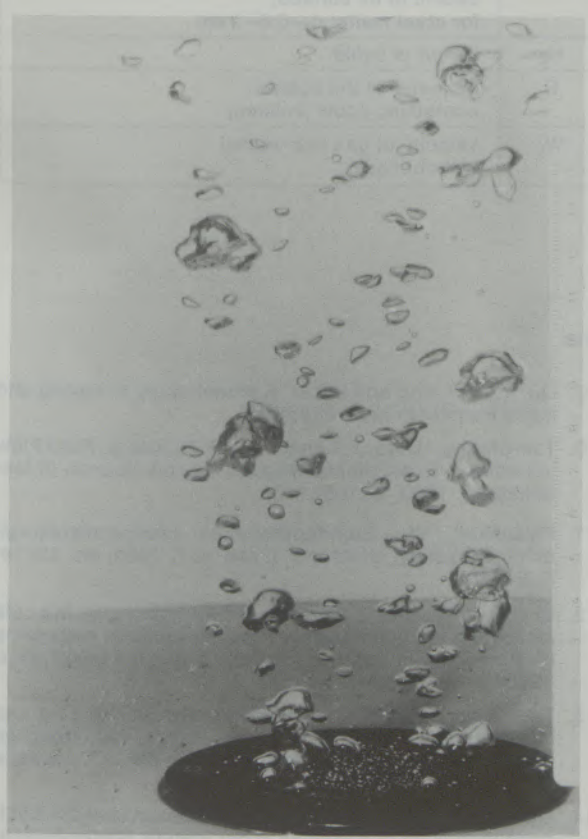

Regime of bubble formation II

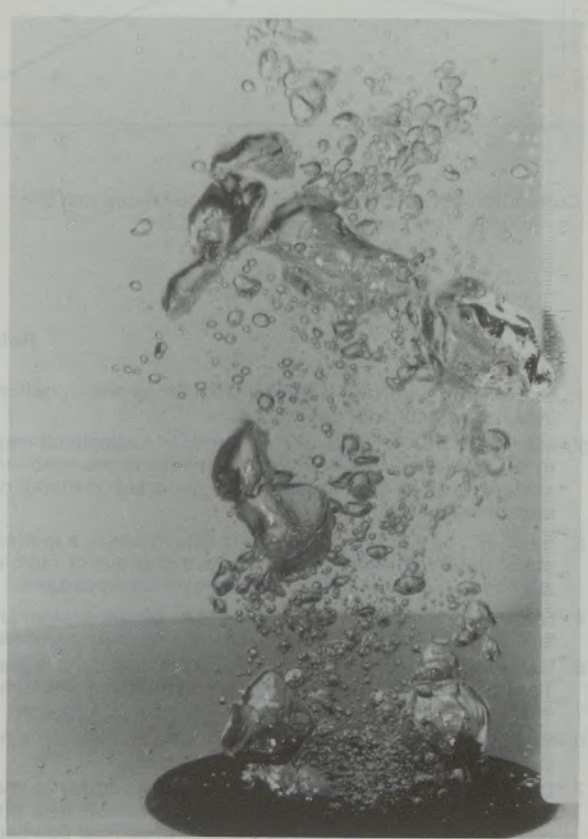

Regime of bubble formation III

gas bubbles coalesce during the detachment from the brick surface when the medium pore distances falls short of a minimum value. Whilst in the brick type B the coalescence happens mostly in vertical direction, in the brick type A the gas jet, especially in the critical regime is formed preferably by horizontal coalescence. In the brick type C both possibilities of coalescence are present.

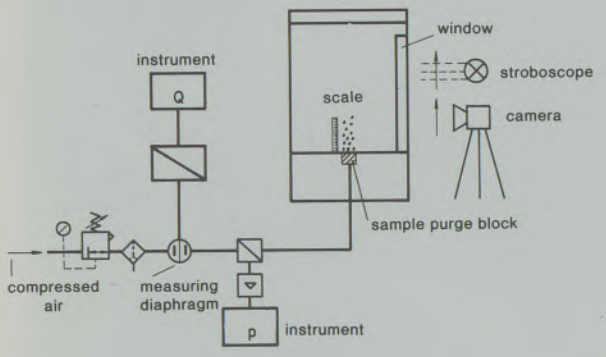

Fig. 12
Water model for the investigation of the bubble formation of purge brick

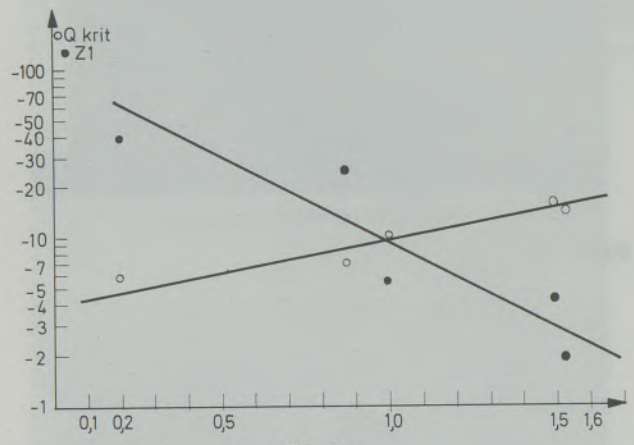

Fig. 13
Correlation between the medium pore distances and the critical gas flow rate resp. ZI

Table 8

Formula figures and dimensions

A	area of sample surface	(m^2)
$\overline{D}_B$	medium bubble diameter	(m)
g	gravitation	(ms^{-2})
l	length of joint	(m)
Q_K	critical gas flow	(m^3s^{-1})
$\overline{Q}_{KP}$	mean critical gas flow of active orifices	(m^3s^{-1})
Z_I, Z_{II}	dimensionless values	(–)
Δp	difference of density between inert gas and metal melt	(kg m^{-3})
σ_F	number of active orifices related to sample area	(m^{-2})
σ_L	number of active orifices related to length of the joints	(m^{-1})
η	dynamic viscosity	(Nsm^{-2})
σ	surface tension	(N m^{-1})

K_F	mass transfer coefficient into liquid phase of one bubble
d_{32}	diameter acc. to sauter; hypotetic diameter relating the volume of the bubble swarm to its surface; for steel melts: d_{32}-0,5–1 cm
H_O	height of liquid
B	diameter of the bubble containing liquid (volume)
W_L	velocity of gas in a vessel without liquid

References

1. Szekely, J., and N. El-Kaddah: Turbulence and agitation in ladle metallurgical operations.
2. Marchi, G. de, P. Costa and B. Canepa: A simplified way to determine the main flow characteristics in gas injection systems and its application to the generalized model of ladle metallurgy processes.
3. Sano, M., and K. Mori: Circulating flow model in a molten metal bath with special respect to behaviour of bubble svarms and its application to gas injection processes.
4. Oeters, F., H.-C. Drömer and J. Kepura: Model studies on fluid flow and particle behaviour during injection process.
5. Robertson, D. G. C., S. Ohguchi, B. Deo and A. Willis: Theoretical and laboratory studies of injection phenomena.
6. McNallan, M. J., J. O. Park and Y. W. Chang: Fluid dynamics of gas-particle injection into liquid metal.
7. Don You, B., W. Polanschütz and H. Hiebler: Study on the bubble formation and penetration of the melt into the nozzle during the injection of gas with or without powder.
8. Guthrie, R.: Alloy injection practises and mixing.
9. Qu, Y., Y. Liang and L. Liu: A model study of mixing and mass transfer in ladle injection.
10. Tse-Chiang, Hsiao, T. Lehner and B. Kjellberg: Fluid Flow in Ladles – Experimental Results, Scand. Journal of Metallurgy 9, **1980**, S. 105–110.
11. Pluschkell, W.: Grundoperationen pfannenmetallurgischer Prozesse, Stahl und Eisen 101, **1981**, Nr. 13/14, S. 97–103.
12. Shifrin, V. M., and E. I. Kadinov: Investigating by the cold simulation method the effectiveness of metal degassing by injection with Argon in the ladle, Steel the USSR, Dez. **1975**, S. 662–664.
13. Tse-Chiang, Hsiao, and Xu Kwang Di: Discharging and mixing behaviours of gas jets in liquids, Ber. Injection Phenomena in Extraction and Refining, Univ. of Newcastle upon Tyne.
14. Deilmann, W., and E. Klimanek: Erfahrungen bei der Spülgasbehandlung des Stahles in der Pfanne, Radex-Rdsch. **1968**, H. 2, S. 127–137.

15. Sperl, H., R. A. Weber and H. E. Wiemer: Betriebsergebnisse mit der Spülhandlung von Stahl in der Gießpfanne, Stahl und Eisen 96, **1976**, Nr. 21, S. 1056–1060.
16. Rentizelas, G., K. W. Lange and D. Papamantellos: Einfluß von Legierungselementen auf die Spülentgasung von Stahlschmelzen mit Argon, Arch. Eisenhüttenwesen 48, **1977**, S. 261–266.
17. Pluschkell, W., B. Redenz and E. Schürmann: Kineties of aluminium oxidation during argon injection into liquid steel, Arch. Eisenhüttenwesen 52, **1981**, Nr. 3, S. 85–90.
18. Peterkov, E. G., and S. I. Filippov: Principles of supplementary refining of steel by argon injection, Steel in the UdSSR, **1975**, 3, S. 152–153.
19. Grip, C. E., B. Tivelius, T. Sohlgren and P. Gossas: Ladle Metallurgy in SSAB, Scand. Journ. of Metallurgy 9, **1980**, S. 121–127.
20. Knüppel, H.: Desoxidation und Vakuumbehandlung von Stahlschmelzen, Verlag Stahleisen, Düsseldorf, **1983**.
21. Grabner, B., and H. Höffgen: Einsatz und Verschleiß von Spülsteinen in der Sekundärmetallurgie. Radex-Rdsch. **1983**, H. 3, S. 179–209.
22. Hütter, U., B. Grabner and M. Heinricher: Konverterspülsteine mit gerichteter Porosität. Ein Beitrag zur Verbesserung der Metallurgie und Wirtschaftlichkeit der Sauerstoffaufblasverfahren zur Stahlherstellung. Radex-Rdsch. **1981**, H. 3, S. 499–517.
23. Weidner, A., U. Hütter and B. Grabner: Konverterbodenspüler – ein weiterer Schritt zur Perfektion des LD-Verfahrens. Berg- und Hüttenmännische Monatshefte 127, **1982**, H. 11, S. 415–420.
24. Satyanaryan, A., R. Kumar and N. R. Kuloor: Chem. Eng. Sci. 24, **1969**, S. 749.
25. You, B. D.: Dissertation, Montanuniversität Leoben, **1983**.
26. McCann, D. J., and R. G. H. Prince: Chem. Eng. Sci. 26, **1971**, S. 1505.
27. Pawlowski, J.: Die Ähnlichkeitstheorie in der physikalisch-technischen Forschung; Springer-Verlag Berlin, Heidelberg, New York, **1971**.
28. You, B. D., W. Polanschütz and H. Hiebler: Proc. 3rd Scaningject Conf. Lulea, **1983**.
29. Davidson, J. F., and B. O. G. Schüler: Trans. Inst. Chem. Engrs. 38, **1960**, S. 335.

Rheologische Grundlagen des Spritzens feuerfester Massen

Walter M. Siegl, Radenthein

Der Spritzprozeß wird durch physikalische Modelle beschrieben, wobei die Masse aus Korn und einem viskosen Fluid bestehend gedacht wird. Die Modelle beschreiben insbesondere die zentrale Rolle der Viskosität beim Auftreffen der einzelnen Körner sowie auch für die Stabilität der gespritzten Schicht. Es wird gezeigt, daß für eine optimale Verdichtung eine niedrige Viskosität, für eine hinreichende Stabilität dagegen eine hohe Viskosität erforderlich ist. Beide Forderungen werden nur von einem strukturviskosen Fluid mit einer ausgeprägten Fließgrenze erfüllt.

Rheological Basis of Gunning Refractories

The gunning process is described by physical models, whereby the mix is assumed to consist of grains and a viscous fluid. The models especially describe the central part played by the viscosity during the impact of the single grains, as well as for the stability of the gunned layer. It is shown that for optimum densification low viscosity is necessary, for sufficient stability, however, high viscosity is required. Both requirements only are met by a fluid with structural viscosity with a well defined yield point.

Fondements rheologiques du gunitage de pisés réfractaires

Le processus de projection est décrit au moyen d'un modèle de nature physique, le réfractaire projetable étant représenté par des grains et un fluide visqueux. Les modèles utilisés décrivent surtout le rôle essentiel de la viscosité lors de l'impact de chaque grain et aussi son influence sur la stabilité de la couche projetée. On montre que pour obtenir une densification optimale il faut que la viscosité soit faible, alors que par contre une viscosité élevée est nécessaire pour que la stabilité soit suffisante. Ces deux conditions ne sont remplies que par un fluide à structure visqueuse avec une limite élastique étendue.

Einleitung

Das Spritzverfahren ist eine heute weit verbreitete Technik zur Reparatur und Zustellung feuerfester Auskleidungen. Die Anwendung basischer Pflegemassen wurde in einer vorausgehenden Veröffentlichung (1) ausführlich dargestellt. Die darin zusammengefaßte jüngere Fachliteratur über (basische) Spritzmassen zeigt, daß hinsichtlich der Rolle der Viskosität beim Spritzen noch viele Unklarheiten bestehen. Die Kenntnis der Grundlagen des Spritzverfahrens und dessen primäre Einflußgrößen bildet eine Voraussetzung für die Verbesserung basischer Pflegemassen. Mit der vorliegenden Arbeit soll der Zusammenhang zwischen den Abläufen beim Spritzprozeß und den rheologischen Eigenschaften basischer Pflegemassen anhand physikalischer, rheologischer Modelle hergestellt werden. Eine erste Mitteilung über diese Modellvorstellungen wurde bereits beim International Symposium on New Developments of Monolithic Refractories der American Ceramic Society (Pittsburgh 1984) gemacht (2).

Im Zusammenhang mit der Zähigkeit einer Spritzmasse stellen sich zwei Fragenkomplexe:

- Wie verläuft die Umsetzung der kinetischen Energie des auftreffenden Kornes in Verformungsarbeit bzw. Reibungsarbeit?

Introduction

Today, gunning is a widespread technique for repairing and lining of refractory linings. The application of basic maintenance mixes has been extensively described in a previous publication (1). The more recent special literature compiled there on (basic) gunning mixes shows that with regard to the part of viscosity during gunning there still are many uncertainties. The knowledge of the basics of the gunning process and its primary parameters is a prerequisite for improvements of basic maintenance mixes. The paper presented here is to show the interconnections between the phenomena of gunniting and the rheological properties of basic maintenance mixes on hand of physical, rheological models. A first notice on these model ideas has been presented at the International Symposium on New Developments of Monolithic Refractories of the American Ceramic Society (Pittsburgh, 1984) (2).

In connection with the viscosity of a gunning mix the following two complexes of questions arise:

- How is the transformation of kinetic energy of the impacting grain into resilience work, resp. friction work performed?
- How viscous has the mix to be, in order not to run off the vertical wall?

– Wie zäh muß die Masse sein, damit sie von der senkrechten Wand nicht abläuft?

Für die Beantwortung dieser Fragen ist es zweckmäßig, die Masse als ein viskoses Fluid zu denken, in das grobe Körner eingebettet sind. Das viskose Fluid ist eine Suspension feiner Partikel in Wasser. Es ist klar, daß bei einem kontinuierlichen Kornband, wie es in realen Spritzmassen meist vorliegt, die Zuordnung eines Teilchens mittlerer Größe zur Suspension oder zum darin eingebetteten Korn problematisch ist. Die Praxis hat jedoch gezeigt, daß Suspensionen von Teilchen unter 125 μm plastisch und einigermaßen stabil sind, während Suspensionen von Teilchen über 315 μm rasch sedimentieren und wenig bildsam sind. Daher erscheint es sinnvoll, Teilchen unter 200 μm der Suspension und solche über 200 μm dem Korn zuzurechnen (Abb. 1).

1. Die Rolle der Viskosität beim Auftreffen des Kornes

1.1. Auftreffen im Fluid

Wird eine Kugel vom Radius r mit der Geschwindigkeit v in einem Fluid bewegt, muß der Strömungswiderstand F_w überwunden werden. Das Newton'sche Gesetz des Strömungswiderstandes lautet

$$F_w = c_w \cdot r^2\pi \cdot \frac{v^2}{2} \cdot \varrho \qquad [1]$$

c_w = Widerstandsbeiwert (dimensionslos)
ϱ = Dichte des Fluids

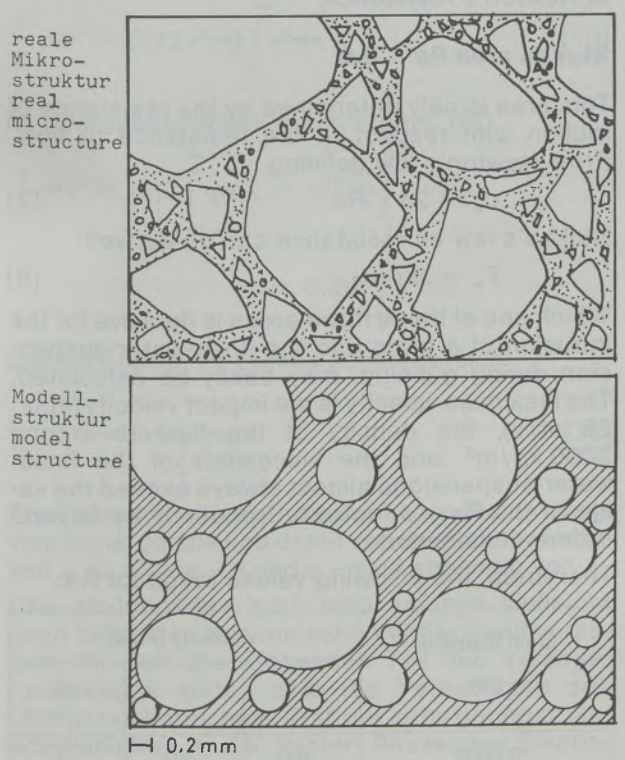

Abb./Fig. 1
Reale und idealisierte Struktur einer Spritzmasse
Real and idealized structure of a gunning mix

To answer these questions, it is useful to assume the mix as a viscous fluid into which coarse grains are embedded. The viscous fluid is a suspension of fine particles in water. It is clear that with a continuous grain size distribution – as it is mostly prevailing in actual gunning mixes – it is difficult to attribute a particle of mean size to the suspension or to the grains embedded therein. In practice, it has been found, however, that a suspension of particles below 125 microns is plastic and rather stable, while suspension of particles above 315 microns show fast sedimentation and are little plastic. It seems meaningful to attribute particles of below 200 microns to the suspension, and those above 200 microns to the grains (fig. 1).

1. Part of the viscosity during impact of a grain

1.1. Impacting within the fluid

If a ball with the radius r is moved with the velocity v in a fluid, the flow resistance F_w has to be overcome. Newton'law on the flow resistance is:

$$F_w = c_w \cdot r^2\pi \cdot \frac{v^2}{2} \cdot \varrho \qquad [1]$$

c_w = resistance coefficient (without dimension)
ϱ = density of the fluid

The resistance coefficient c_w is a function of Reynold's number $Re = v \cdot d \cdot \varrho / \eta$ (fig. 2).

η = dynamic viscosity
d = grain diameter

Newton' area $10^3 < Re < 2.5 \cdot 10^5$

In this area that in the field of beneficiation is also called Newton-Rittinger area, c_w is nearly constant and is appr. 0.44. The resistance to flow is here caused by the backing up pressure $v^2\varrho/2$ and is independent on the viscosity. There is

$$F_w = 0{,}22\, r^2\pi v^2 \varrho \qquad [2]$$

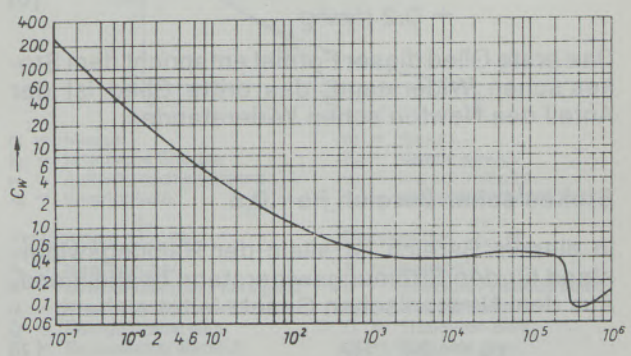

Abb./Fig. 2
c_w = f(Re) für Kugeln (nach Schubert (3))
c_w = f(Re) for balls (acc. to Schubert (3))

Der Widerstandsbeiwert c_w ist eine Funktion der Reynoldszahl $Re = v \cdot d \cdot \varrho / \eta$ (Abb. 2).

η = dynam. Viskosität
d = Korndurchmesser

Newton'scher Bereich $10^3 < Re < 2{,}5 \cdot 10^5$

In diesem Bereich, der in der Aufbereitung auch Newton-Rittinger-Bereich genannt wird, ist c_w nahezu konstant und beträgt rund 0,44. Der Strömungswiderstand wird hier durch den Staudruck $v^2\varrho/2$ hervorgerufen und ist unabhängig von der Viskosität. Es gilt

$$F_w = 0{,}22\, r^2 \pi v^2 \varrho \qquad [2]$$

Übergangsbereich $0{,}6 < Re < 10^3$

Bei abnehmender Reynoldszahl gewinnt der Reibungsanteil gegenüber dem Druckanteil an Einfluß. Der Zusammenhang $c_w = f(Re)$ wurde mit verschiedenen Näherungsformeln analytisch darzustellen versucht, wobei häufig folgender Ansatz gewählt wurde:

$$c_w = A/Re + B/Re^C + D \qquad [3]$$

Wie Schubert (3) genauer ausführt, liegen die Konstanten innerhalb folgender Grenzen:

A = 21–24 C = 0,537–0,25
B = 2,8–6 D = 0–0,4

Eine hinreichend genaue Annäherung ist gegeben mit

$$c_w = 24/Re + 4/Re^{1/2} + 0{,}4 \qquad [4]$$

Die Widerstandskraft im Übergangsbereich errechnet sich aus [3] in allgemeiner Form:

$$F_w = \frac{A}{4} r\pi v\eta + \frac{B}{2^{1+C}} r^{2-C} \pi v^{2-C} \varrho^{1-C} \eta^C + \frac{D}{2} r^2 \pi v^2 \varrho \qquad [5]$$

Setzt man c_w nach Gleichung [4] ein, ergibt sich

$$F_w = 6\, r\pi v\eta + 2^{1/2} r^{3/2} \pi v^{3/2} \eta^{1/2} \varrho^{1/2} + 0{,}2\, r^2 \pi v^2 \varrho \qquad [6]$$

Das erste Glied dieser Formel entspricht dem Stokes'schen Widerstand, das dritte Glied ist der Anteil des Newton'schen Widerstandes.

Stokes'scher Bereich $Re < 0{,}6$

In diesem Bereich ist allein der Reibungswiderstand für den Strömungswiderstand bestimmend. Aus dem Newton'schen Gesetz leitet sich mit

$$c_w = 24 / Re \qquad [7]$$

das Stokes'sche Widerstandsgesetz ab:

$$F_w = 6\, r\pi v\eta \qquad [8]$$

Transition area $0.6 < Re < 10^3$

With decreasing Reynold's number the part of the friction decreases in influence vs. the part of pressure. The connection $c_w = f(Re)$ was analytically described by means of several approximation formulas, where frequently the following statement was used:

$$c_w = A/Re + B/Re^C + D \qquad [3]$$

As Schubert (3) more precisely states, the constants are within the following limits:

A = 21–24 C = 0.537–0.25
B = 2.8–6 D = 0–0.4

A sufficiently precise approximation is reached with

$$c_w = 24/Re + 4/Re^{1/2} + 0{,}4 \qquad [4]$$

The force of resistance in the transition area is calculated from [3] in general way:

$$F_w = \frac{A}{4} r\pi v\eta + \frac{B}{2^{1+C}} r^{2-C} \pi v^{2-C} \varrho^{1-C} \eta^C + \frac{D}{2} r^2 \pi v^2 \varrho \qquad [5]$$

If c_w is inserted according to equation (4), the following results:

$$F_w = 6\, r\pi v\eta + 2^{1/2} r^{3/2} \pi v^{3/2} \eta^{1/2} \varrho^{1/2} + 0{,}2\, r^2 \pi v^2 \varrho \qquad [6]$$

The first member of this formula corresponds to Stokes's resistance, the third member is the part of Newton's resistance.

Stokes area $Re < 0.6$

This area is only determined by the resistance of friction with respect to the resistance to flow. From Newton's law defining

$$c_w = 24 / Re \qquad [7]$$

Stokes's law on resistance can be derived:

$$F_w = 6\, r\pi v\eta \qquad [8]$$

Which one of these three areas is decisive for the intrusion of a grain into the fines-water-suspension during gunning, may easily be calculated. The maximum velocity is the impact velocity (appr. 25 m/s), the density of the fluid is around 2000 kg/m³, and the viscosities of the fines-water-suspensions almost always exceed the value of 0.1 Pa · s, actually frequently by several orders of magnitude.

Therefrom, the following values result for Re:

grain diameter (m)	viscosity (Pa.s)		
	0,1	1	10
0,0002	100	10	1
0,001	500	50	5
0,004	2000	200	20

Welcher dieser drei Bereiche für das Eindringen eines Kornes in die Mehl-Wasser-Suspension beim Spritzen bestimmend ist, kann leicht errechnet werden. Die maximale Geschwindigkeit ist die Auftreffgeschwindigkeit (ca. 25 m/s), die Dichte des Fluids liegt bei rund 2000 kg/m³, und die Viskositäten der Mehl-Wasser-Suspensionen übertreffen fast immer den Wert von 0,1 Pa · s, und zwar meist um Größenordnungen.

Damit ergeben sich folgende Werte für Re:

Korndurchmesser (m)	Viskosität (Pa.s)		
	0,1	1	10
0,0002	100	10	1
0,001	500	50	5
0,004	2000	200	20

Für die Verzögerung des Kornes ist somit hauptsächlich der Übergangsbereich bestimmend (Abb. 3).

Beim Eindringen eines Kornes der Masse m in das Fluid bis zur Eindringtiefe x_e wird die kinetische Energie zum Überwinden des Strömungswiderstandes F_w verbraucht.

$$\frac{1}{2}mv^2 = \int_0^{x_e} F_w dx = \frac{1}{2}r^2\pi\varrho\int_0^{x_e} c_w v^2 dx \qquad [9]$$

Im Newton'schen Bereich gilt

$$\frac{1}{2}mv^2 = 0{,}22\, r^2\pi\varrho\int_0^{x_e} v^2 dx. \qquad [10]$$

Im Übergangsbereich (nach Formel [6])

$$\frac{1}{2}mv^2 = r\pi\left(6\int_0^{x_e}\eta v dx + \sqrt{2r\varrho}\int_0^{x_e}\sqrt{\eta v^3}dx + 0{,}2r\varrho\int_0^{x_e} v^2 dx\right) \qquad [11]$$

und schließlich im Stokes'schen Bereich:

$$\frac{1}{2}mv^2 = 6r\pi\int_0^{x_e}\eta v dx \qquad [12]$$

Die Viskosität eines strukturviskosen Fluids hängt vom Schergefälle und damit von der Geschwindigkeit v ab. Beide – η und v – sind abhängig von x.

Das eindringende Korn wird anfangs vielleicht noch durch den Newton'schen Widerstand verzögert, für den überwiegenden Teil des Verzögerungsweges gelten aber die Verhältnisse des Übergangsbereiches. Erst bei sehr geringer Geschwindigkeit in der letzten Phase des Eindringens kommt schließlich allein der Stokes'sche Widerstand zum Tragen. Sowohl für den Übergangsbereich als auch für den Stokes'schen Be-

For the deceleration of the grain, mainly, the transition area is determining (fig. 3).

Upon intrusion of a grain with the mass m into the fluid down to an intrusion depth of x_e, the kinetic energy is used up to overcome the resistance to flow F_w.

$$\frac{1}{2}mv^2 = \int_0^{x_e} F_w dx = \frac{1}{2}r^2\pi\varrho\int_0^{x_e} c_w v^2 dx \qquad [9]$$

For Newton's area the following holds:

$$\frac{1}{2}mv^2 = 0{,}22\, r^2\pi\varrho\int_0^{x_e} v^2 dx. \qquad [10]$$

In the transition area (according to formula [6])

$$\frac{1}{2}mv^2 = r\pi\left(6\int_0^{x_e}\eta v dx + \sqrt{2r\varrho}\int_0^{x_e}\sqrt{\eta v^3}dx + 0{,}2r\varrho\int_0^{x_e} v^2 dx\right) \qquad [11]$$

and finally, in Stokes's area:

$$\frac{1}{2}mv^2 = 6r\pi\int_0^{x_e}\eta v dx \qquad [12]$$

The viscosity of a structural viscous fluid depends on the shearing gradient and with this, on the velocity v. Both – η and v – depend on x.

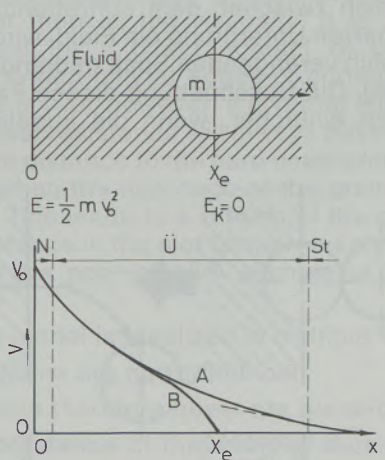

m = Masse
E_k = kinetische Energie
v_o = Auftreffgeschwindigkeit
x_e = Eindringtiefe

Verzögerung $\frac{dv}{dx}$ bei

A = Newtonscher
B = strukturviskoser Flüssigkeit
N = Newtonscher Bereich
Ü = Übergangsbereich
St = Stokesscher Bereich

m = mass
E_k = kinetic energy
v_o = impact velocity
x_e = depth of intrusion

Deceleration $\frac{dv}{dx}$ at

A = Newton's
B = structural-viscous liquid
N = Newton's area
Ü = Transition area
St = Stokes's area

Abb./Fig. 3
Die Verzögerung des Kornes im fluiden Medium
Deceleration of the grain in the fluid medium

reich gilt, daß die Eindringtiefe (bei gegebenen Kornabmessungen, Dichten und Auftreffgeschwindigkeiten) umso größer ist, je niedriger sich die Viskosität in unmittelbarer Umgebung des bewegten Kornes einstellt.

Diese Modellvorstellung ist insoferne idealisiert, als

a) reale Teilchen keine Kugelform aufweisen und daher andere c_w-Werte haben,

b) die Verhältnisse unmittelbar beim Eindringen in das Fluid nicht berücksichtigt sind (dort ist der Widerstand geringer), und

c) die Viskosität des Fluids nicht nur von der Schergeschwindigkeit, sondern auch noch von der Zeit (d. h. vom Alter der Suspension) und von der Temperatur abhängt.

1.2. Korn-Korn-Stoß

Nur in sehr mehlreichen Mischungen ist mit einem unbehinderten Eindringen des auftreffenden Kornes zu rechnen. Normalerweise kommt es unmittelbar beim Auftreffen auf die Spritzschicht oder nach einem kurzen Eindringen in das Fluid zu einem Korn-Korn-Stoß.

Befindet sich zwischen dem Korn und dem Untergrund kein Fluid, handelt es sich um einen elastischen Stoß, und das Korn prallt zurück (Abb. 4).

Der elastische Stoß führt vor allem am Beginn der Spritzung zu einer erhöhten Rückprallrate, solange das Fluid eine erforderliche Mindeststärke noch nicht erreicht hat („Mehlbett").

Befindet sich zwischen dem auftreffenden Korn und dem harten Untergrund ein Fluid, wird dieses aus dem sich verengenden Spalt gedrängt (plastischer Stoß). Die Beschreibung dieses Falles gestaltet sich einfacher, wenn die kugelförmigen

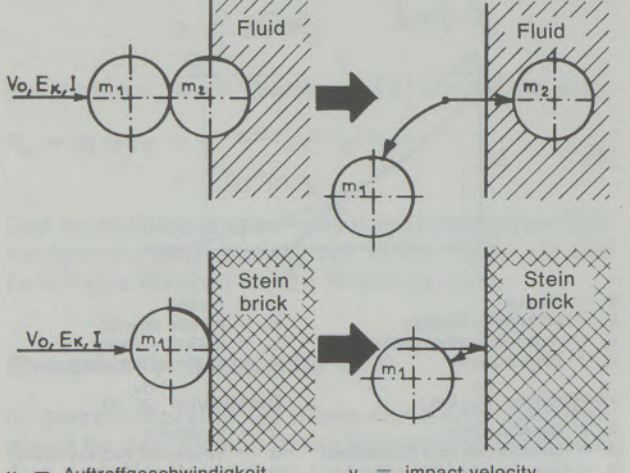

v_o = Auftreffgeschwindigkeit
E_k = kin. Energie $1/2\ m_1 v_o^2$
I = Impuls $m_1 v_o$

v_o = impact velocity
E_k = kinetic energy $1/2\ m_1 v_o^2$
I = impulse $m_1 v_o$

Abb./Fig. 4
Der elastische Korn-Korn-Stoß
Resilient grain-grain impact

Initially, the intruding grain may probably be retarded by the Newton resistance, for the overwhelming part of the distance of deceleration the conditions of the transition area are holding. Only at small velocity during the final phase of the intrusion, in the end, Stokes's resistance alone becomes effective. As well for the transition area, as also for Stokes's area it is applicable that the depth of intrusion (at given grain dimensions, densities and velocities of impact) is the greater, the smaller the viscosity is arranging itself in the immediate surroundings of the grain in motion.

This model construction is idealized insofar, as

a) real parts are not ball-shaped and their c_w-values are different;

b) the conditions immediately upon intrusion into the fluid have not been considered (the resistance is lower there), and

c) the viscosity of the fluid does not only depend on the shearing velocity, but also on time (i.e. the age of the suspension) and temperature.

1.2. Grain-grain impact

Only within mixes very high in fines, an unimpeded intrusion of the impacting grain may be expected. Normally, immediately after impacting on the gunned layer, or after short intrusion into the fluid, grain-grain impact occurs.

If there is no fluid between grain and underground, a resilient impact occurs and the grain rebounces (fig. 4).

Especially at the beginning of the gunning, the resilient impact causes an increased rate of rebouncing, as long as the fluid has not reached the needed minimum thickness ("bed of fines").

If there is a fluid between the impacting grain and the hard underground, this fluid is pressed out of the narrowing slot (plastic impact). The description of this case is made more simple, if the ball-shaped grains of the model are replaced by cylinder-shaped bodies, hitting each other with their

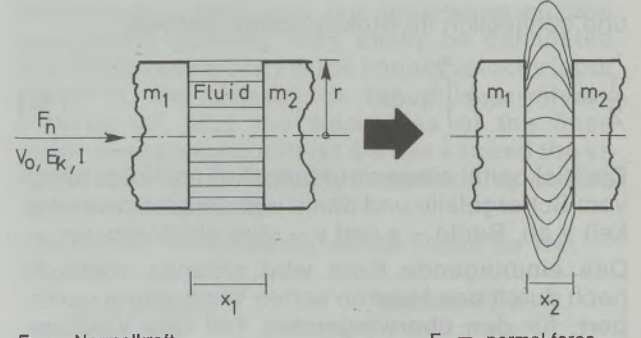

F_n = Normalkraft
v_o = Auftreffgeschwindigkeit
E_k = kinetische Energie
I = Impuls

F_n = normal force
v_o = impact velocity
E_k = kinetic energy
I = impulse

Abb./Fig. 5
Der Korn-Korn-Stoß im viskosen Medium
The grain-grain impact in viscous medium

Körner im Modell durch zylinderförmige Körper ersetzt werden, die mit den Stirnseiten aufeinandertreffen. (Die flächenparallele Annäherung ist in der Praxis die Regel, weil die Körner dazu neigen, sich parallel auszurichten, was weiter unten begründet wird.) (Abb. 5)

Zu diesem Zeitpunkt der Annäherung wirkt auf das Fluid im Spalt eine Normalkraft F_n. Sie beträgt (nach Becker (4))

$$F_n = \frac{3\eta v r^2 A}{2x^3} = \frac{3\eta v r^4 \pi}{2x^3}, \qquad [13]$$

sie steigt also mit der dritten Potenz der sinkenden Spaltweite x.

η = dyn. Viskosität (mPa · s)
v = Geschwindigkeit (m/s)
r = Radius der kreisförmigen Spaltfläche A (m)
x = Spaltweite (m)

Die zur Verformung bzw. Verdrängung des Fluids nötige Energie bei einer Verringerung der Spaltweite von x_1 auf x_2 ergibt sich aus der Integration der Normalkraft:

$$\frac{1}{2} mv^2 = \int_{x_1}^{x_2} F_n dx \qquad [14]$$

$$\frac{1}{2} mv^2 = \frac{3\eta r^4 \pi}{2} \int_{x_1}^{x_2} \frac{v(x)}{x^3} dx \qquad [15]$$

Die Arbeit zum Verdrängen des Fluids aus der Fuge ist also proportional dem Widerstand des Fluids (= Viskosität η), und sie nimmt mit abnehmender Spaltweite sehr stark zu. Die durch 1/2 mv^2 limitierte Energie des Kornes führt zu umso größerer Annäherung, je höher die Geschwindigkeit v(x) und je niedriger die Viskosität sind, sie reicht aber für eine direkte Berührung einzelner Körner nicht aus. Lediglich die Berührung an Ecken oder Kanten ist denkbar ($r^4 \rightarrow 0$), aber eher unwahrscheinlich. Bei nicht paralleler Annäherung der Körner wird stets dort, wo der Abstand zum harten Untergrund am geringsten ist, der höchste Widerstand auftreten. Das führt zu einer Drehung des Kornes, bis der Widerstand im Spalt annähernd gleichmäßig verteilt ist, also zu einer annähernd parallelen Ausrichtung der Kornflächen.

Auch dieses Modell ist in mehrfacher Weise idealisiert:

a) reale Körner sind nicht zylinderförmig,
b) die Spalten sind daher nie planparallel,
c) der Widerstand des außerhalb des Spaltes befindlichen Materials wurde nicht berücksichtigt,
d) die Energie zum Drehen der Teilchen wurde ebensowenig berücksichtigt wie der Strömungswiderstand des Fluids, in dem sich das Teilchen bewegt.

front faces. (The plane-parallel approaching is the rule in practice, since the grains tend to orient themselves parallely – which will be substantiated lateron) (fig. 5).

At any given time during the approach a normal force F_n takes effect on the fluid in the slot. According to Becker (4) it is

$$F_n = \frac{3\eta v r^2 A}{2x^3} = \frac{3\eta v r^4 \pi}{2x^3}, \qquad [13]$$

and rises with the third power of the falling slot diameter x, as can be seen.

η = dyn. viscosity (mPa · s)
v = velocity (m/s)
r = radius of the circular slot area A (m)
x = slot diameter (m)

The energy needed to deform or replace the fluid upon reducing the slot diameter from x_1 to x_2 results by integrating the normal force:

$$\frac{1}{2} mv^2 = \int_{x_1}^{x_2} F_n dx \qquad [14]$$

$$\frac{1}{2} mv^2 = \frac{3\eta r^4 \pi}{2} \int_{x_1}^{x_2} \frac{v(x)}{x^3} dx \qquad [15]$$

The work to replace the fluid from the joint is proportional to the resistance of the fluid (= viscosity η), and strongly increases with decreasing diameter of the slot. the energy of the grain which is limited by 1/2 mv^2 leads to the higher approximation, the higher there is the velocity v(x), and the lower there is the viscosity; it is, however, insufficient for a direct contact of the single grains; contact only at edges or corners may be assumed ($r^4 \rightarrow 0$), however, it is rather improbable. The highest resistance will always develop there, where the distance to the hard underground is the lowest, when the approach of the grains is non-parallel. This leads to a turning of the grain until the resistance in the slot is near-evenly distributed, i.e. to a near-parallel aligning of the grain faces.

Also this model is idealized in multiple ways:

a) real grains are not cylindrical,
b) the slots therefore never are plane-parallel,
c) the resistance of the material outside of the slot was not duly considered,
d) also, the energy for turning the particles was not considered, as well as the resistance to flow of the fluid in which the particle is moved.

In reality, the resistance to flow of the fluid, and the resistance of the grain-grain impact superimpose, resp. add up. It is certainly not possible to clearly classify this impact as either resilient or plastic, because, either with small quantities of fluid or with the rather unusual edge or corner contact, remaining energies may lead to rebounce despite plastic deformation.

In der Realität überlagern bzw. summieren sich der Strömungswiderstand des Fluids sowie der Widerstand beim Korn-Korn-Stoß. Dieser selbst ist keineswegs so klar mit elastisch oder plastisch zu klassifizieren, da – sei es bei geringen Fluidmengen, sei es beim seltenen Kanten- oder Eckenkontakt – trotz plastischer Verformung noch Restenergien zum Rückprall führen können.

Für eine dichte Packung wird eine größtmögliche Eindringtiefe und ein minimaler Teilchenabstand angestrebt. Beides hat zur Voraussetzung, daß die Viskosität möglichst niedrig ist.

2. Die Stabilität der gespritzten Schicht

Die Frage lautet hier: Unter welchen Bedingungen fließt die gespritzte Schicht von der senkrechten Wand nicht ab? (Abb. 6)

In jeder Schichttiefe x wirkt eine Schubspannung τ_x gleich dem Gewicht der Masse bis x pro Flächeneinheit:

$$\tau_x = x \cdot \varrho \cdot g \qquad [16]$$

x = Schichttiefe (m)
ϱ = Raumgewicht der Spritzschicht (kg/m³)
g = Gravitationskonstante (9,81 ms^{-2})

Ohne Fließgrenze fließt ein Fluid ab, und zwar mit der Schergeschwindigkeit:

$$D_x = \frac{\tau_x}{\eta_s} = \frac{x \cdot \varrho \cdot g}{\eta_s} \qquad [17]$$

Durch Integration von $D = \frac{dv}{dx}$ ergibt sich die Abfließgeschwindigkeit. Sie beträgt an der Stelle x

$$v_x = \frac{(X^2 - x^2) \cdot \varrho \cdot g}{2\,\eta_s} \qquad [18]$$

X = Spritzschichtstärke (m)

η_s sei hierin die scheinbare Viskosität der gespritzten Schicht, die sich von der Viskosität η des Fluids unterscheidet.

Je höher die scheinbare Viskosität ist, desto langsamer fließt die Schicht ab.

Strukturviskose Fluide haben häufig eine Fließgrenze. Sie liegt dann vor, wenn bei einer sehr niedrigen Schergeschwindigkeit D_o von fast 0 die Viskosität η_o sehr hoch ist, sodaß eine relativ hohe Schubspannung τ_o resultiert. Solange $\tau > \tau_x$, bleibt die Schicht stabil. Es existiert eine kritische Schichtdicke x_c, die nicht überschritten werden darf.

$$x_c = \frac{\tau_o}{\varrho\, g} \qquad [19]$$

Im Falle eines homogenen, strukturviskosen Fluids gibt die Viskositätsmessung direkt Auskunft über das zu erwartende Fließverhalten der Schicht (5) (S. 76ff.). Die gespritzte Schicht einer basischen Pflegemasse besteht aber nicht nur aus dem Fluid (= wäßrige MgO-Mehl-Suspen-

For dense packing a maximum intrusion depth and a minimum particle distance is aimed at. For both it is required that the viscosity be as low as possible.

2. The stability of the gunned layer

The question here now is: Under which conditions will the gunned layer not flow down from the vertical wall? (fig. 6)

At any given depth x of the layer a shearing stress τ_x is in force that is equal to the weight of the mass up to x per unit area:

$$\tau_x = x \cdot \varrho \cdot g \qquad [16]$$

x = depth of layer (m)
ϱ = bulk density of the gunned layer (kg/m³)
g = gravitational constant (9.81 m/s^{-2})

Without a yield point a fluid flows with a shearing velocity of:

$$D_x = \frac{\tau_x}{\eta_s} = \frac{x \cdot \varrho \cdot g}{\eta_s} \qquad [17]$$

By integrating $D = \frac{dv}{dx}$ the shearing velocity results at point x with:

$$v_x = \frac{(X^2 - x^2) \cdot \varrho \cdot g}{2\,\eta_s} \qquad [18]$$

X = thickness of gunned layer (m)

η_s is the apparent viscosity of the gunned layer, which is different from the viscosity η of the fluid.

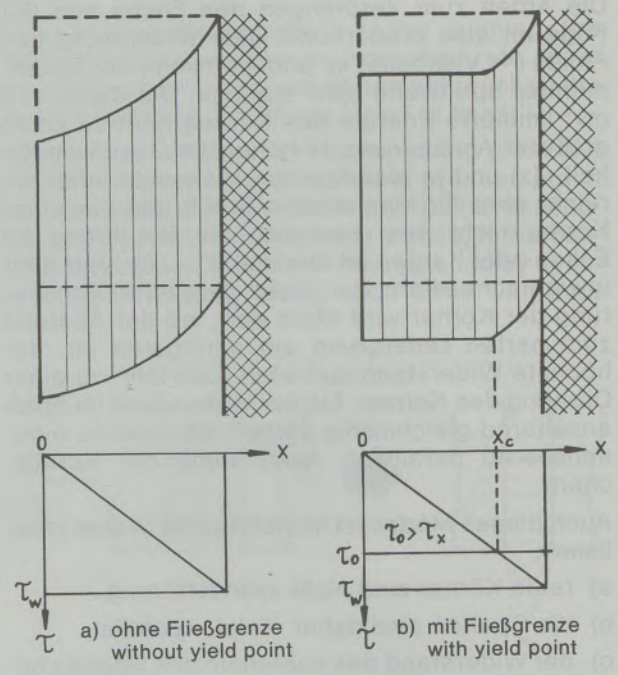

x_c = krit. Schichtdicke
τ_o = Schubspannung an der Wand
τ_w = Schubspannung an der Fließgrenze

x_c = crit. thickness of layer
τ_o = shearing stress at the wall
τ_w = shearing stress at yield point

Abb./Fig. 6
Die Stabilität der gespritzten Schicht an der vertikalen Wand
The stability of the gunned layer at the vertical wall

sion), sondern sie enthält zusätzlich noch Korn, d. h. Teilchen, die nach der eingangs getroffenen Abgrenzung gröber als 0,2 mm sind. Die feuchte Masse stellt daher ein sogenanntes „verdünntes System" dar, dessen scheinbare Viskosität η_s höher sein wird als die Viskosität η des Fluids, weil der Einbau starrer Teilchen einer Verringerung der Spaltweite gleichzusetzen ist. In der Literatur (siehe Tabelle 1) finden sich zahlreiche Formeln, in denen die scheinbare Viskosität η_s dargestellt wird als Funktion von η und der Volumskonzentration φ der eingelagerten Teilchen:

$$\varphi = \frac{c}{\varrho} \cdot \frac{1}{\left(\frac{c_f}{\varrho_f} + \frac{c}{\varrho}\right)} \qquad [20]$$

c = Feststoffgehalt (%)
c_f = Fluidgehalt (%)
ϱ = Dichte des Kornes (kg m^{-3})
ϱ_f = Dichte des Fluids (kg m^{-3})

Die Gleichungen gelten für Fluide mit eingelagerten, starren Kugeln. Eine Vielzahl weiterer Formeln wurden erarbeitet für nichtkugelförmige und/oder nichtstarre Teilchen (Ellipsoid, Hantel, Stäbchen, Platten, Fäden, Knäuel . . .). Die scheinbare Viskosität ist laut Reiner (6) unabhängig von der Korngröße. In der Praxis läßt sich aber immer wieder der Einfluß der Korngrößenverteilung auf die scheinbare Viskosität nachweisen.

Eine genaue Untersuchung des Einflusses der Volumskonzentration gebrochener Körner auf die scheinbare Viskosität einer strukturviskosen, wäßrigen Mehlsuspension steht noch aus.

3. Praktische Konsequenz

Aus dem theoretischen Ansatz sind folgende Forderungen für eine Spritzmasse abzuleiten:

a) Die Viskosität des Fluids soll in unmittelbarer Umgebung des auftreffenden Kornes möglichst niedrig sein, um ein tiefes Eindringen und eine enge Zusammenlagerung der Körner zu gewährleisten.

b) Die Viskosität des Systems Fluid + Korn soll möglichst hoch und mit einer möglichst ausgeThe higher the apparent viscosity, the slowlier the layer flows down.

Structural viscous fluids frequently show a yield point. It is then present, when at a very low shearing velocity D_o of nearly zero the viscosity η_o is very high, so that a relatively high shearing stress results. As long as $\tau > \tau_x$, the layer stays stable. There is, however, a critical thickness x_c of the layer, that must not be exceeded:

$$x_c = \frac{\tau_o}{\varrho\, g} \qquad [19]$$

In case of a homogeneous, structurally viscous fluid, the measurement of the viscosity gives a direct information on the flow-behaviour to be expected from the layer ((5) p. 76). The gunned layer of a basic maintenance mix does not only consist of the fluid (= aqueous MgO-fines suspension), but it additionally contains grains, i.e. particles that according to the initial definition are coarser than 0.2 mm. The moist mix therefore represents a so called "diluted system", whose apparent viscosity η_s will be higher than the viscosity η of the fluid, since the inclusion of rigid particles may be considered equal to reducing the slot diameter. In the literature (see table 1) many formulas may be found in which the apparent viscosity η_s is described as a function of η and volume concentration φ of the included particles:

$$\varphi = \frac{c}{\varrho} \cdot \frac{1}{\left(\frac{c_f}{\varrho_f} + \frac{c}{\varrho}\right)} \qquad [20]$$

c = percentage of solids (%)
c_f = percentage of fluid (%)
ϱ = grain density (kg m^{-3})
ϱ_f = fluid density (kg m^{-3})

The equations hold for fluids with embedded rigid balls. A variety of additional formulas have been developed for non-ball-shaped and/or non-rigid particles (ellipsoid, dumbbel, rods, plates, strings, tangles . . .). According to Reiner (6), the apparent viscosity is independent on the grain size. In practice, however, always the influence of the grain size distribution on the apparent viscosity may be proven.

Tabelle/Table 1

Scheinbare Viskosität verdünnter Systeme
Apparent viscosity of diluted systems

Formel / Formula	Autor / Author	Literatur / Reference
$\eta_s = \eta\,(1 + 2{,}5\,\varphi)$	Einstein	(7), S. 229
$\eta_s = \eta\,(1 + 2{,}5\,\varphi + 10{,}6\,\varphi^2)$	Eirich/Rieseman	(4), S. 14
$\eta_s = \eta\,(1 + 2{,}5\,\varphi + 12{,}6\,\varphi^2)$	Simha	(4), S. 14
$\eta_s = \eta\,(1 + 2{,}5\,\varphi + 14{,}1\,\varphi^2)$	Mark	(7), S. 229
$\eta_s = \eta\,(1 + 2\,\varphi)\,(1 - \varphi)$	Frank	(4), S. 14
$\eta_s = \eta \exp(2{,}5\,\varphi\ /\ [1 - k\,\varphi])$, $1 < k < 2$	Mooney	(4), S. 14

prägten Fließgrenze ausgestattet sein, damit die Spritzschicht an der senkrechten Wand stabil ist.

Beide Erfordernisse lassen sich nur vereinen, wenn das Fluid ein strukturviskoses Fließverhalten (mit Fließgrenze) zeigt.

An exact investigation of the influence of the volume concentration of crushed grains on the apparent viscosity of a structurally viscous aqueous suspension of fines still has to be conducted.

3. Practical consequences

From the theoretical statement the following claims have to be derived for a gunning mix:

a) The viscosity of the fluid within the immediate surroundings of the impacting grain should be at a minimum to allow maximum intrusion and close aggregation of the grains.

b) The viscosity of the system fluid plus grains should be as high as possible and fitted with a well expressed yield point in order to allow the gunned layer to remain stable at the vertical wall.

Both requirements are only compatible, if the fluid shows structural viscous flow behavior (with a yield point).

Literaturverzeichnis / References

1. Siegl, W.: „Aufbau und Verarbeitung basischer feuerfester Pflegemassen"; Radex-Rdsch. 4/**85**, S. 706–723.
2. Siegl, W.: "Viscosity and Gunning of Basic Specialties"; Proc. Intern. Symp. on New Developments in Monolithic Refractories, Pittsburgh, PA, April 30, **1984.** Advances in Ceramics No. 14, American Ceramic Society 1985, S. 175–191.
3. Schubert, H.: „Aufbereitung fester mineralischer Rohstoffe", Bd. I, 3. Auflage, S. 241ff.; VEB Deutscher Verlag für Grundstoffindustrie, Leipzig.
4. Becker, E.: „Technische Strömungslehre"; 5. Aufl. Verlag B. G. Teubner Stuttgart **1982**; ISBN 3-519-33019-9, S. 92–93.
5. Schramm, G.: „Einführung in die praktische Viskosimetrie"; Haake GmbH (**1981**).
6. Reiner, M.: „Rheologie in elementarer Darstellung"; 2. Aufl. Carl Hanser Verlag, München **1969.**
7. Schurz, J.: „Einführung in die Strukturrheologie"; Verlag Berliner Union, Stuttgart.

Verbesserte Pfannenmetallurgie in slowenischen Stahlwerken

V. Prešern, Ljubljana; P. Bračun, Štore*)

Ein Verfahren der Stahlherstellung in ŽR Štore wird beschrieben, wobei der Stahl auf einer 4-Strang-Anlage für kontinuierliches Gießen von Knüppeln mit Abmessungen 100×100 mm oder 140×140 mm abgegossen wird. Wegen der kleinen Abmessungen der Knüppel war es nicht möglich, den Stahl mit Aluminium zu beruhigen. Um einen Stahl von höherer Reinheit mit weniger Einschlüssen und modifizierter Zusammensetzung der Einschlüsse zu erreichen, wurde ein System zum Einblasen von CaSi eingeführt.

Die Ergebnisse bzw. der Einfluß des eingeblasenen CaSi auf den Gehalt einiger Elemente im Al-beruhigten Stahl (Schwefel, Sauerstoff, Silizium, Aluminium) und auf die Zahl, Form und Art nichtmetallischer Einschlüsse werden gezeigt.
Die neue Rahmentechnologie zur Herstellung einiger Stahlgüten wird behandelt.

Improvements on Ladle Metallurgy in Slovenian Steel Plants

A process of steel making practice in the Steel Plant Štore is described, where the steel is poured into a continuous casting plant with four strands producing billets of 100×100 mm or 140×140 mm. Because of the small dimensions of the billets it was not possible to kill the steel with aluminum. In order to obtain steel with higher purity and fewer inclusions, a system for injecting CaSi was introduced.

The results of, resp. the influence of the injected CaSi on the contents of some elements in Al-killed steel (sulfur, oxygen, silicon, aluminum) and on the number, shape and kind of nonmetallic inclusions are demonstrated. The new basic technology for the manufacture of some steel qualities is discussed.

Procédé amélioré de traitement des aciers en poche dans les aciéries slovaques

On décrit un procédé de production de l'acier appliqué à l'aciérie Store comportant une installation de coulée continue à 4 barres de 100×100 mm ou 140×140 mm de section. Les dimensions de ces barres rendaient impossible le calmage de l'acier avec de l'aluminium. Afin d'obtenir un acier présentant une propreté élevée avec peu d'inclusions et une composition modifiée de celles-ci, on a mis en oeuvre un système d'injection de CaSi.

Les résultats obtenus sont discutés, ainsi que l'influence des injections de CaSi sur les teneurs en certains éléments de l'acier calmé à l'Al (soufre, oxygène, silicium, aluminium) et sur le nombre, la forme et la nature des inclusions non métalliques. On donne un aperçu de la nouvelle technologie des cadres utilisée pour la production de certaines nuances d'aciers.

Einleitung

In SŽ-Železarna Štore wird Stahl in zwei elektrischen Lichtbogenöfen mit Ofengröße 40 t (Birlec) und 50 t (BBC) erzeugt.

Das Produktionsprogramm umfaßt hauptsächlich Federstähle, kohlenstoffarme Stähle, Stähle mit mittleren Kohlenstoffgehalten, niedriglegierte Einsatzstähle und Vergütungsstähle.

Die gesamte Menge des erzeugten Stahles wird auf einer 4-Strang-Gießanlage (Concast) in Knüppel mit Querschnitten Quadrat 100 mm oder Quadrat 140 mm abgegossen.

*) Doz. dr. mag. Vasilij Prešern, dipl. ing. met., SŽ-Metalurški inštitut Ljubljana, Lepi pot 11, Jugoslavija
Dipl. ing. met. Peter Bračun, SŽ-Železarna Štore, Štore pri Celju, Jugoslavija

Introduction

In SŽ-Železarna Štore the steel is produced in two electric arc furnaces of 40 t (Birlec) and 50 t (BBC).

Our production program mainly consists of spring steels, low carbon steels, steels with medium carbon contents, low-alloyed case hardening steels and heatable steels.

The total quantity of the steel produced is poured through a four-strand continuous casting plant (Concast) into billets 100 or 140 mm square.

Because of the very small cross sections, technological standards do not permit to kill the steels with aluminum (max. up to 0.006%).

In order to obtain higher purity, to improve the casting properties and to increase the productivity of the electric arc furnaces, it was decided

Wegen der sehr kleinen Querschnitte ist es von der technologischen Norm her nicht erlaubt, Stähle mit Aluminium (max. bis 0,006%) zu beruhigen.

Um eine höhere Reinheit zu erreichen, die Gießbarkeit zu verbessern und die Produktivität der Stahlerzeugung in den elektrischen Lichtbogenöfen zu erhöhen, wurde die Entscheidung getroffen, das Verfahren von CaSi-Einblasen in den flüssigen Stahl in der Pfanne einzuführen.

Zahlreiche diesbezügliche ausländische und heimische Artikel (1), (2), (3) haben aufgezeigt, daß die Einführung dieses Verfahrens angebracht ist. Die wichtigsten Ergebnisse des Verfahrens sind:

- CaSi-Behandlung des Stahles ist mit der vorher gefertigten Schmelze mit kompletter Al-Desoxidation verbunden. Im Vergleich zu Si-Desoxidation bedeutet das natürlich wesentlich niedrigere Gehalte an Sauerstoff und weniger Oxideinschlüsse.
- Zusätzliche Entschwefelung wird erreicht, wodurch die Raffination im Ofen verkürzt wird.
- Reine Al_2O_3-Einschlüsse vergrößern das Schmieren von Abgüssen. Diese Einschlüsse treten in herkömmlich erzeugten Stählen oft in sehr ausgeprägter scharfer und gerichteter Form auf. Nach CaSi-Behandlung liegen nur runde unplastische komplexe Einschlüsse vom Typ $CaO\text{-}Al_2O_3$ vor, mit einem Schmelzpunkt unter 1873 K (1600 °C), die während der Weiterverarbeitung brechen.
- Die Möglichkeit der Seigerungsrisse wird wegen der Mn-Sulfide in kohlenstoffarmen Stählen auf ein Minimum gebracht, da die restlichen Einschlüsse stark entschwefelt und modifiziert werden.
- Als Folge guter Desoxidation, Entschwefelung und Modifikation der Einschlüsse werden sehr reiner Stahl und gute Oberfläche der kontinuierlich gegossenen Knüppel erzielt.

Es gibt viele ausländische Firmen, die ihre Systeme für Einblasen von Feinkornstoffen anbieten. Der Preis solcher Angebote liegt jedoch über 300.000 US-Dollar. Deshalb wurde die gesamte Anlage in Jugoslawien konstruiert und gebaut. Das Hauptprojekt wurde von der Firma INŽENIRING Bled ausgefertigt, die Anlage selbst wurde aber in Laško gebaut. Im Mai 1984 wurden bereits die ersten Tests an der Anlage vorgenommen. Es soll erwähnt werden, daß diese Anlage wenigstens dreimal weniger gekostet hat als eine ausländische und daß die bisherigen Ergebnisse beweisen, daß sie imstande ist, außerordentlich erfolgreich zu arbeiten.

Beschreibung des Vorganges

Bis jetzt wurden in Štore mehrere tausend Tonnen des mit CaSi behandelten Stahles in der Pfanne erzeugt. Durch Anfangsversuche wurden die

to introduce the process of injecting CaSi into the liquid steel in the ladle.

A series of foreign and domestic publications (1), (2), (3) have convinced us that the introduction of this procedure is justified. The most important results of the process are:

- CaSi treatment of the steel is connected with the previously made melt with complete Al-desoxidation. Compared with Si-desoxidation this naturally means considerably lower oxygen contents and fewer oxide inclusions.
- Additional desulfurization is achieved, thus reducing refining time in the furnace.
- Pure Al_2O_3-inclusions increase the clogging of nozzles by casting. These inclusions frequently appear in conventionally produced steels in well expressed precise and directed form. After CaSi treatment only non-plastic, round, complex inclusions of the type $CaO\text{-}Al_2O_3$ are present, with a melting point of below 1873 K (1600 °C) that break up during further processing.
- The possibility of liquation cracks is brought to a minimum because of the Mn-sulfides in low-carbon steels, since the remaining inclusions are highly desulfurized and modified.
- Due to good desoxidation, desulfurization and modification of the inclusions, very pure steel and good surfaces of the continuously cast billets are obtained.

There are many foreign companies offering their systems for injecting fine-grained materials. Prices of such offers range above US-$ 300,000. Therefore, the complete installation was designed and built in Yugoslavia. The main project was made by the company INŽENIRING, Bled. The installation itself was built in Laško. Already in May 1984, the first trials were run with the plant. It should be mentioned that this installation has been at least three times cheaper than a foreign one, and the results obtained until now prove that it is capable of operating extremely successfully.

Description of the Process

Until now, several thousand tons of CaSi-treated steel have been produced in the ladle. The basic characteristics of the new process were defined by initial tests:

- such operational conditions were defined that guarantee sufficiently quiet and practically 100% secure operation of the plant;
- at corresponding, res. apt operational conditions CaSi is injected at a rate of 20–25 kgs CaSi/min;
- the necessary duration of the injection is from 3 to 6 minutes (corresponding to a quantity of 1.5–2.5 kg CaSi p.t. of steel;
- during the CaSi-injection the temperature of the steel drops by 3–5 °C/min.

grundlegenden Charakteristiken des neuen Vorganges festgelegt:

- Solche Betriebsbedingungen wurden bestimmt, die ein genügend ruhiges und praktisch 100% sicheres Arbeiten der Anlage garantieren;
- bei entsprechenden bzw. passenden Betriebsbedingungen wird CaSi mit einer Geschwindigkeit von 20–25 kg CaSi/min eingeblasen;
- die notwendige Dauer des Einblasens beträgt 3–6 Minuten (da es einer CaSi-Menge von 1,5–2,5 kg/t Stahl entspricht);
- während des CaSi-Einblasens fällt die Stahltemperatur um 3–5 °C/min.

Wegen Einführung des CaSi-Einblasens war es nötig, die Raffinationstechnologie im elektrischen Lichtbogenofen anzupassen, um so eine Möglichkeit zum Erreichen optimaler Ergebnisse zu sichern.

Es hat eigentlich keinen Sinn, die nicht mit Aluminium beruhigten Stähle mit CaSi zu behandeln. Die Sauerstoffmenge in einem solchen Stahl ist nämlich so groß, daß das eingeblasene Calcium vor allem für zusätzliche Desoxidation verbraucht wird, was natürlich zu teuer kommt.

Deshalb wurde mit gestuftem Al-Zugeben in den Ofen und in die Pfanne begonnen, und zwar bei einigen Stahlsorten, die für die CaSi-Behandlung ausgesucht wurden.

Diese Stähle wurden in folgende vier Gruppen geteilt:

- Stähle mit niedrigerem Kohlenstoffgehalt als 0,30%;

On account of the introduction of the CaSi-injection it became necessary to adapt the refining technology in the electric arc furnace, in order the secure reaching of optimum results.

There is practically no sense in treating steels not killed with aluminum with CaSi. The quantity of oxygen in such a steel is so high that the calcium injected is primarily used for additional desoxidation, thus raising costs excessively.

It was therefore begun with staggered Al additions in the furnace and the ladle, actually with several types of steel that had been selected for CaSi-treatment.

These steels were divided into four groups:

- steels with carbon contents of below 0.30%;
- steels with carbon contents from 0.30 to 0.50%;
- low-alloyed steels containing Cr, Ni, Mo, V;
- spring steels.

The technological rules for the manufacture of the single grades were adapted to the results of the use of Al and the injection of CaSi. Special attention had to be given to the influence of the furnace slag. It was shown that despite drawing off of the oxidation slag such a quantity of that slag remained that during casting and the following CaSi-treatment most of the aluminum burned off. We therefore decided to add a mixture of lime and fluorspar into the ladle and to keep the furnace slag in the furnace as long as possible. This procedure proved to be very successful. Thus we reached a practically constant Al-content during

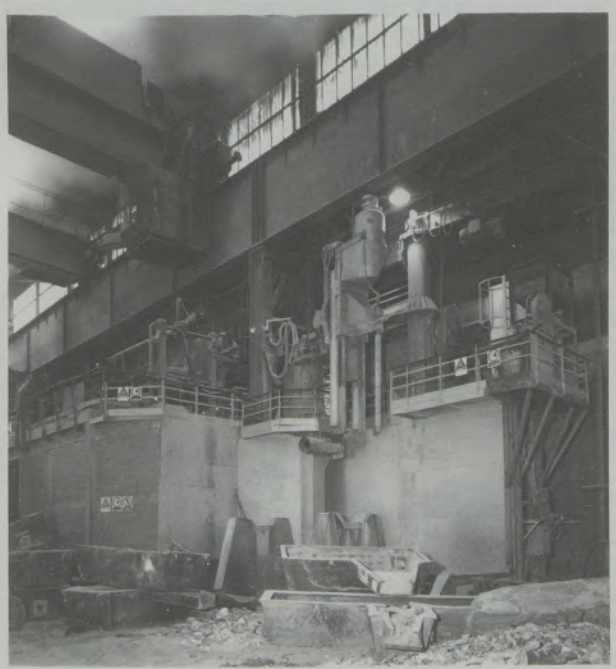

Abb./Fig. 1
Aussehen der Anlage
View of the plant

Abb./Fig. 2
Anlage während des Betriebes
Plant during operation

- Stähle mit Kohlenstoffgehalt 0,30–0,50%;
- niedriglegierte Stähle mit Cr, Ni, Mo, V;
- Federstähle.

Technologische Vorschriften zur Erzeugung einzelner Güteklassen wurden den erreichten Ergebnissen der Al-Anwendung und des CaSi-Einblasens angepaßt. Besondere Aufmerksamkeit mußte auch dem Einfluß der Ofenschlacke gewidmet werden. Es zeigte sich nämlich, daß trotz Abziehens der Oxidierungsschlacke im Ofen eine solche Menge dieser Schlacke zurückblieb, daß beim Abstich und später bei der CaSi-Behandlung das meiste Aluminium abbrannte. Deshalb entschloß man sich, in die Pfanne eine Mischung aus Kalk und Flußspat zuzugeben und die Ofenschlacke beim Abstich möglichst lange im Ofen zu halten. Diese Handlungsweise zeigte sich sehr erfolgreich. Dadurch wurde erreicht, daß sich der Al-Gehalt während des CaSi-Einblasens, wo es zum kräftigen Mischen des Stahles und der Schlacke kommt, praktisch konstant bleibt.

Die neue Schlacke vermeidet das Risiko des Nichterreichens vorgegebener chemischer Zusammensetzung, da es zu keiner Reduktion von Mn, Si und P kommt.

In der Pfanne wird jedenfalls Schlacke gebraucht, welche die Aufgaben hat (4), (5), (6):

- Produkte von Desoxidations- und Entschwefelungsreaktionen während des CaSi-Einblasens zu binden;
- den Zutritt des Atmosphärensauerstoffes zu verhindern;
- unkontrollierte Reaktionsabläufe zwischen Schlacke und Stahl zu verhindern.

the injection of CaSi, where an intensive mixing of the steel and the slag occurs.

The new slag avoids the risk of not reaching a predetermined chemical composition, since no reduction of Mn, Si and P occurs.

In the ladle a slag is needed that has the following function (4), (5), (6):

- to bind products of the desoxidation and desulfurization reactions during the injection of CaSi;
- to stop the access of atmospheric oxygen;
- to avoid uncontrolled reactions between slag and steel.

The appearance of the plant for injecting CaSi and the plant in operation can be seen from figures 1 and 2. Figs. 3 and 4 schematically show the process technology Č. 4732 (DIN 42CrMo4) according to conventional and new technology applying aluminum and CaSi.

Technological results of the manufacture of several types of steel are listed in table 1.

Analysis of the Results

Desoxidation

The introduction of the CaSi-injection process is intricately connected with optimizing refining in the electric arc furnace.

The main goal of the new process and the changed refining with aluminum is to secure increased purity of the steel. Another scope is the possibility

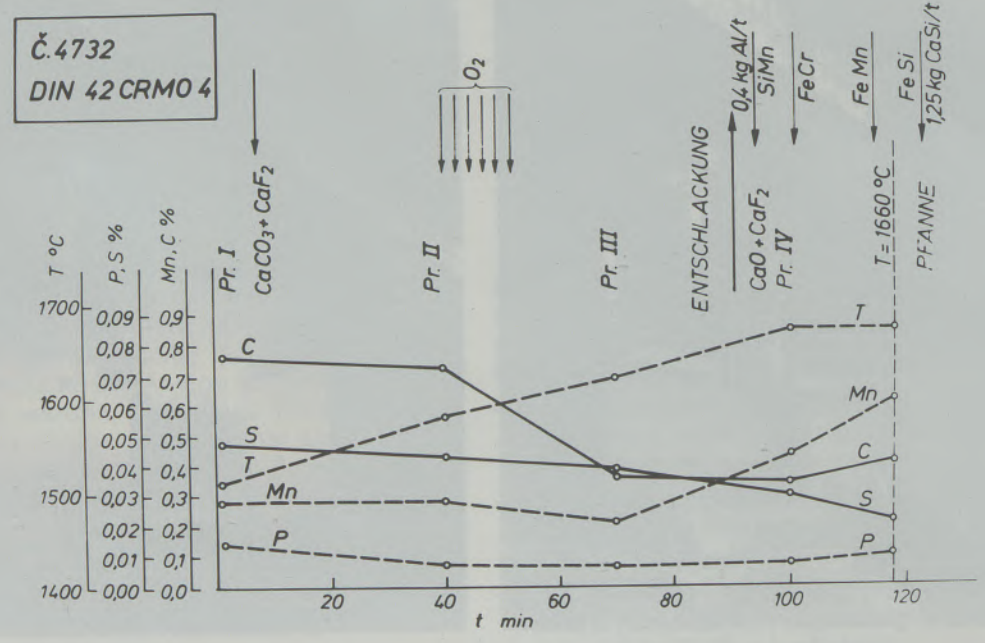

Abb./Fig. 3
Herstellungstechnologie für Stahlgüte 42 CrMo4
Production technology for steel quality 42 CrMo4

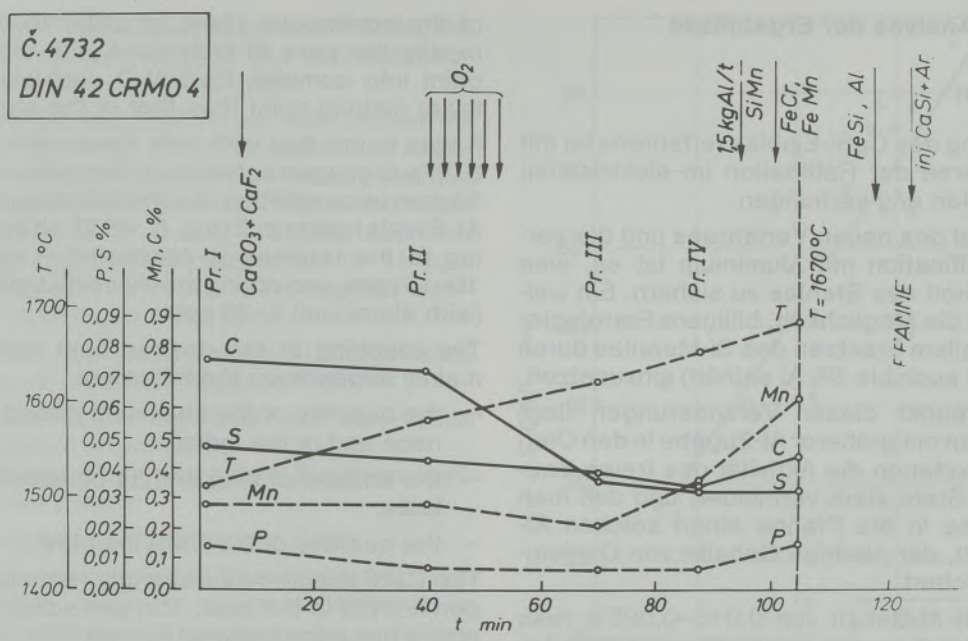

Abb./Fig. 4
Neue Technologie für Stahlgüte 42 CrMo4
New technology for steel quality 42 CrMo4

Das Aussehen der Anlage zum Einblasen von CaSi und diese Anlage während des Betriebes sind den Abb. 1 und 2 zu entnehmen. Die Abb. 3 und 4 zeigen schematisch die Herstellungstechnologie für die Stahlgüte Č. 4732 (DIN 42CrMo 4) nach herkömmlicher und neuer Technologie mit Aluminium und CaSi.

Technologische Ergebnisse der Erzeugung von einigen Schmelzen sind in der Tabelle 1 zusammengestellt.

to use cheaper ferro-alloys (especially to replace Si-metal by FeSi 75 that contains up to 3% Al).

The main scope of these changes is to reduce the activity of free oxygen in the steel by increased Al-additions in the furnace during pre-desoxidation and by achieving such an Al-content by adding Al in the ladle, that will secure lower contents of oxide inclusions.

Steel with an Al-content of 0.015 to 0.025% (which is our goal) has to be treated with CaSi because

Tabelle/Table 1

Technologische Ergebnisse der Erzeugung von einigen Schmelzen
Technological results of some heats produced

Schmelze heat	Qualität quality	Chemische Analyse / chemical analysis						CaSi		
		C %	Si %	Al_{tot} %	S %	O_{tot} %	ΔS %	O_a (ppm) vor before	O_a (ppm) nach after	CaSi kg/t
15128	CK 15	0,19	0,22	0,016	0,007	0,0061	72	24,3	11,9	1,1
15178	CK 15	0,17	0,40	0,021	0,011	0,0052	59	20,5	8,8	1,1
15422	50CrV4	0,51	0,38	0,020	0,011	0,0062	63	10,4	5,0	1,5
25966	50CrV4	0,50	0,34	0,016	0,006	0,0059	78	12,7	5,2	1,9
15125	50CrV4	0,52	0,32	0,014	0,008	0,0065	58	13,9	6,4	2,2
25668	42CrMo4	0,42	0,31	0,017	0,005	0,0061	71	12,9	5,8	2,1
25669	CK 45	0,47	0,29	0,026	0,003	0,0049	73	10,3	4,6	2,1
25968	60SiCr7	0,58	1,56	0,020	0,006	0,0056	63	7,1	4,5	1,6
25969	60SiCr7	0,58	1,44	0,015	0,005	0,0055	75	4,6	3,6	1,6
15426	60SiCr7	0,60	1,84	0,014	0,003	0,0058	87	6,7	3,6	1,6

Analyse der Ergebnisse

Desoxidation

Die Einführung des CaSi-Einblasverfahrens ist mit dem Optimieren der Raffination im elektrischen Lichtbogenofen eng verbunden.

Das Hauptziel des neuen Verfahrens und der veränderten Raffination mit Aluminium ist es, eine höhere Reinheit des Stahles zu sichern. Ein weiteres Ziel ist die Möglichkeit, billigere Ferrolegierungen (vor allem Ersetzen des Si-Metalles durch FeSi 75, das auch bis 3% Al enthält) einzusetzen.

Der Schwerpunkt dieser Veränderungen liegt darin, daß man mit größerer Al-Zugabe in den Ofen bei Vordesoxidation die Aktivität des freien Sauerstoffes im Stahl stark vermindert und daß man mit Al-Zugabe in die Pfanne einen solchen Al-Gehalt erzielt, der niedrige Gehalte von Oxideinschlüssen sichert.

Der Stahl mit Al-Gehalt von 0,015–0,025% (was das Ziel ist) muß wegen der kontinuierlichen Anlage CaSi-behandelt werden, damit die reinen Al-Einschlüsse mit hohem Schmelzpunkt in kom-

of the continuous plant, in order to be able to modify the pure Al inclusions with high melting point into complex $CaO\text{-}Al_2O_3$ inclusions with a lower melting point than that of the steel.

It was found that with soft steels with less than 0.30% C oxygen activities in the ladle reach 20 to 30 ppm upon addition of corresponding addition of Al. Steels higher in C (e.g. Č. 4830) show – according to the technology presented – activities of 10–15 ppm, and spring steels made using FeSi 75 (with aluminum) 5–10 ppm.

The reaching of the desired final content of Al mainly depends on the following:

- the quantity of the aluminum added in the furnace and in the ladle;
- the amount of slag and its composition in the ladle;
- the quantity of the CaSi injected.

The CaSi injected has strongly reduced the oxygen activity in the steel. Oxygen activity in spring steels has been reduced by over 50% (to an average of 4.0 ppm) by CaSi. For other grades of steel, regularly values ranging from 5 to 10 ppm (fig. 5) are measured. These values are so small that they most certainly guarantee sufficient purity (7), (8). This is also confirmed by investigations on the total oxygen content in the steel (table 1), whereby it is interesting to note that despite open casting the final oxygen contents only are higher by appr. 10% than the oxygen contents in the ladle!

However, it must be stressed than in the continuously operated plant, steel is re-oxidized because of the open casting. A precise analysis of the re-oxidizing intensity is under way, in Štore closed casting of billets of 140 mm square is introduced as of spring 1985.

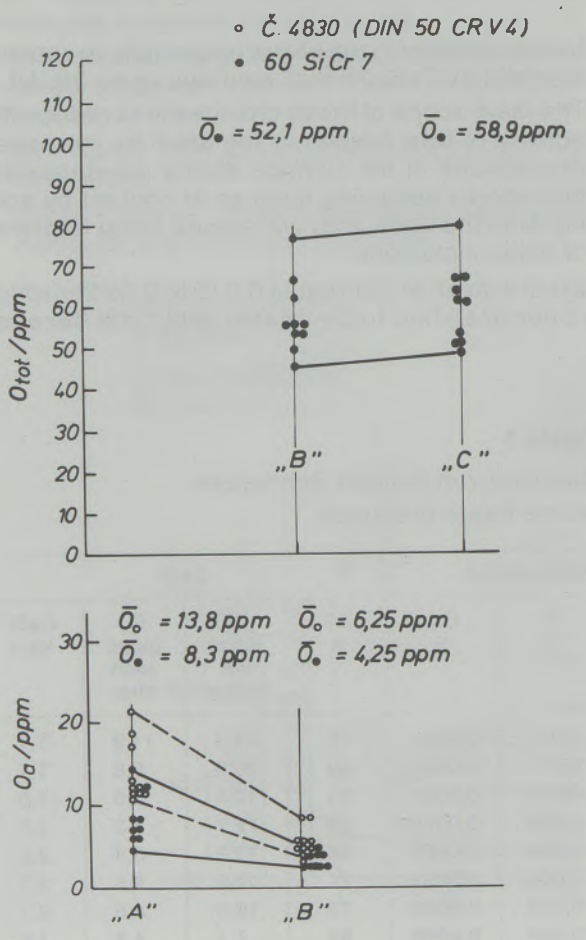

Abb./Fig. 5
Sauerstoffbewegung bei CaSi-Einblasen
Oxygen development during injection of CaSi

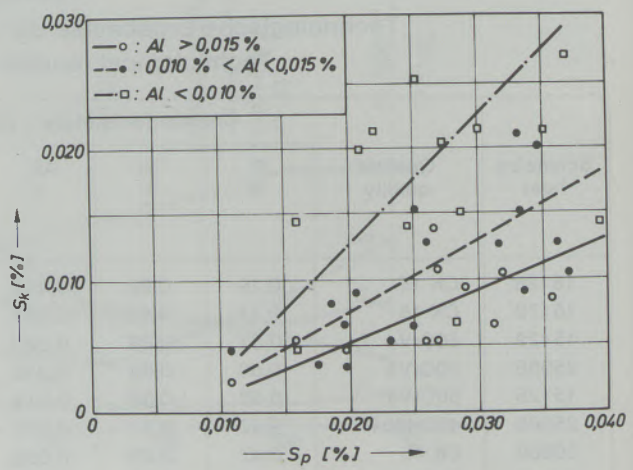

Abb./Fig. 6
Al-Einfluß auf den Schwefelendgehalt (S_k)
Influence of Al on final sulfur content (S_k)

plexe $CaO\text{-}Al_2O_3$-Einschlüsse mit einem Schmelzpunkt, der niedriger liegt als der Stahlschmelzpunkt, modifiziert werden können.

Es wurde festgestellt, daß bei weichen Stählen mit weniger als 0,30% C mit entsprechender Al-Zugabe Sauerstoffaktivitäten in der Pfanne zwischen 20 und 30 ppm erreicht werden. Stähle mit höheren C-Gehalten (z. B. Č. 4830) zeigen nach der vorgelegten Technologie Aktivitäten 10–15 ppm und die mit Einsatz von FeSi 75 erzeugten Federstähle (mit Aluminium) 5–10 ppm.

Das Erreichen des gewünschten Al-Endgehaltes hängt hauptsächlich von folgendem ab:

- der Menge des in den Ofen und die Pfanne zugegebenen Aluminiums;
- der Schlackenmenge und ihrer Zusammensetzung in der Pfanne;
- der Menge des eingeblasenen CaSi.

Das eingeblasene CaSi hat in ausreichend beruhigten Stählen auch die Sauerstoffaktivität im Stahl stark herabgesetzt. So ist die Sauerstoffaktivität in Federstählen durch CaSi um mehr als 50% vermindert worden (auf durchschnittlich 4,0 ppm). Auch bei anderen Stahlgüten werden regelmäßige Werte zwischen 5 und 10 ppm (Abb. 5) gemessen. Diese Werte sind schon so klein, daß sie ganz sicher genügende Reinheit garantieren (7), (8). Das wird auch durch Untersuchungen der gesamten Sauerstoffgehalte im Stahl bestätigt (Tabelle 1), wobei es interessant ist, daß trotz des offenen Gießens die Endsauerstoffgehalte nur um ca. 10% höher liegen als die Sauerstoffgehalte in der Pfanne.

Es muß jedoch betont werden, daß auf der kontinuierlich arbeitenden Anlage wegen des offenen Gießens die Reoxidation des Stahles auftritt. Die genauere Analyse der Reoxidationsintensität ist im Gange, in Štore wird aber schon im Frühling 1985 für Knüppel 140 mm Quadrat ein geschlossenes Gießen eingeführt werden.

Entschwefelung

Es ist bekannt, daß durch das CaSi-Einblasen in Al-beruhigten Stahl in Pfannen gute Entschwefelung erreicht werden kann (9), (10), (11).

Abb. 6 und 7 zeigen den Al-Einfluß im Stahl auf den Schwefelendgehalt und auf den erreichten Entschwefelungsgrad.

Es ist ersichtlich, daß Aluminium den Entschwefelungsverlauf stark bzw. entscheidend beeinflußt und daß es zum Erreichen von niedrigen Schwefelgehalten nicht einmal wichtig ist, ob in genügend beruhigten Stahl 1,5 oder 2 kg CaSi/t eingeblasen werden.

Der Abb. 6 ist zu entnehmen, daß man beim S-Ausgangsgehalt von 0,020–0,35% im Ofen folgende durchschnittliche S-Endgehalte erreicht:

- 0,021% bei Al-Gehalt <0,010%;

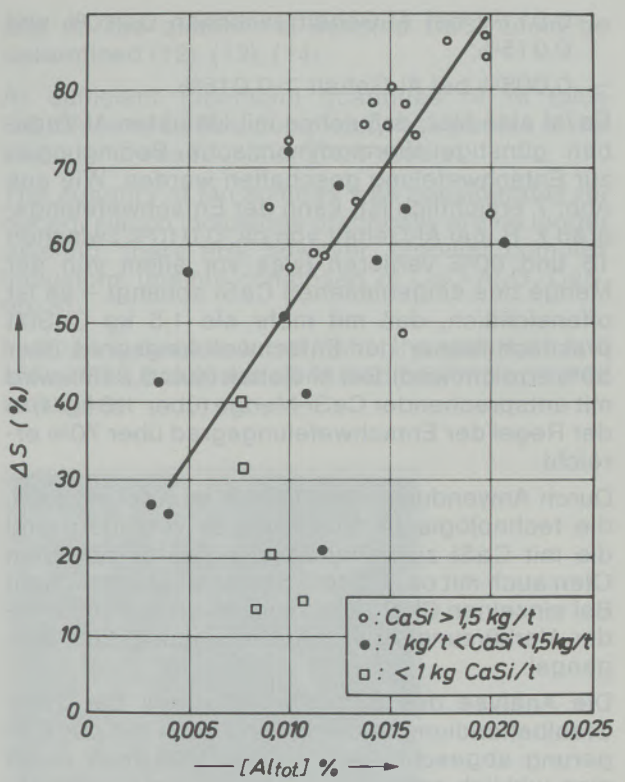

Abb. / Fig. 7
Al- und CaSi-Einfluß auf den Entschwefelungsgrad
Influence of Al and CaSi on degree of desulfurization

Desulfurization

It is known that by injecting CaSi into Al-killed steel in ladles (9), (10), (11) good desulfurization is reached. Figs. 6 and 7 show the Al-influence in the steel on the final sulfur content and on the degree of desulfurization reached.

It can be seen that the aluminum strongly, resp. decidingly influences the course of the desulfurization and that – in order to reach low sulfur contents – it is not even important, whether into sufficiently killed steel 1.5 or 2 kg CaSi/t are injected.

From fig. 6 it can be seen that with an initial S-content of 0.020 to 0.35% in the furnace, the following average final S-contents are reached:

- 0.021% with Al-content <0.010%;
- 0.011% with Al-content between 0.010% and 0.015%;
- 0.008% with Al-content >0.015%.

It therefore is clear that already with smallest Al-additions favorable thermodynamic conditions for desulfurizing are created. As can be seen from fig. 7, the desulfurizing degree at e.g. Al-content of appr. 0.010% may vary from 15 to 80% (which mainly depends on the quantity of CaSi injected – it is obvious that with more than 1.5 kg CaSi/t practically always a desulfurization degree of plus

– 0,011% bei Al-Gehalt zwischen 0,010% und 0,015%;
– 0,008% bei Al-Gehalt >0,015%.

Es ist also klar, daß schon mit kleinsten Al-Zugaben günstige thermodynamische Bedingungen zur Entschwefelung geschaffen werden. Wie aus Abb. 7 ersichtlich ist, kann der Entschwefelungsgrad z. B. bei Al-Gehalt von ca. 0,010% zwischen 15 und 80% variieren (was vor allem von der Menge des eingeblasenen CaSi abhängt – es ist offensichtlich, daß mit mehr als 1,5 kg CaSi/t praktisch immer der Entschwefelungsgrad über 50% erreicht wird). Bei Al-Gehalt über 0,015% wird mit entsprechender CaSi-Menge (über 1,5 kg/t) in der Regel der Entschwefelungsgrad über 70% erreicht.

Durch Anwendung von CaSi ist es jetzt möglich, die technologische Vorschrift zu verändern und die mit CaSi zu behandelnden Stähle aus dem Ofen auch mit ca. 0,040% Schwefel abzustechen! Bei einzelnen Chargen kommt es so zu bedeutender Verkürzung bzw. zur Verbilligung des Vorgangs!

Die Analyse des Schwefelverhaltens bei CaSi-Stahlbehandlung in der Pfanne kann mit der Folgerung abgeschlossen werden, daß man damit eine wirklich erfolgreiche Maßnahme zur wirksamen und sicheren Entschwefelung bekam. Die Grundbedingungen für den Erfolg dieses Verfahrens sind:

– genügend beruhigter Stahl (Al-Gehalt im Stahl in der Pfanne mehr als 0,015%);
– richtige Schlackenzusammensetzung und richtige Schlackenmenge in der Pfanne;
– ausreichende Menge und optimale Geschwindigkeit des CaSi-Einblasens.

Metallographische Untersuchungen

Es wurden die Durchschnittslängen und Gehalte der Sulfid-, Silicat- und Aluminateinschlüsse in ausgewalzten Stäben bestimmt. Nur Einschlüsse länger als 0,01 mm in der Mitte wurden berücksichtigt. Starke Abhängigkeit des Einschlußtypes und ihrer Menge von der Al-Menge im Stahl und von der eingeblasenen CaSi-Menge wurde festgestellt (12), (13), (14).

Bei genügenden (optimalen) Al- (über 0,015%) und CaSi-Mengen wurde in Štore-Stählen ein ganz neues Bild von Einschlüssen gefunden.

Die Menge der Mn-Sulfide wurde wesentlich vermindert, Siliciumeinschlüsse sind praktisch nicht mehr vorhanden, es liegen aber globulare komplexe Einschlüsse vor (mit vorwiegender Zusammensetzung von CaO-Al_2O_3-CaS, Abb. 8).

Bei richtig hergestellten Schmelzen wurden die Aluminat- und Mn-Sulfideinschlüsse in komplexe Einschlüsse modifiziert.

Es wird angenommen, daß die Anzahl der Einschlüsse bei einigen Stahlgüten um mehr als 50%

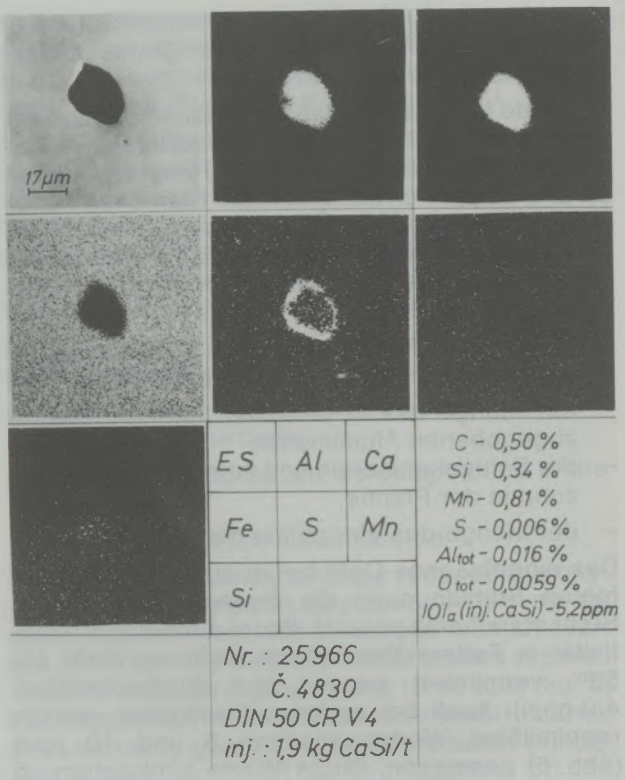

Abb./Fig. 8
Form und Zusammensetzung von Einschlüssen
Shape and composition of inclusions

50% is reached). At an Al-content of plus 0.015%, as a rule, a desulfurization degree of plus 70% is reached with the corresponding quantity of CaSi.

By applying CaSi it now is possible to change technological rules and to tap steels treated with CaSi from the furnace also with appr. 0.040% sulfur! For the single heats this leads that way to considerable time cuts and cost savings.

The analysis of the behaviour of the sulfur during CaSi treatment of the steel in the ladle may be finished with the conclusion that with this a really successful weapon became available for an effective and secure desulfurization. The basic conditions for the success of this process are:

– sufficiently killed steel (Al-content in the steel in the ladle plus 0.015%);
– proper slag composition and proper slag quantity in the ladle;
– sufficient quantity and optimum speed of the CaSi-injection.

Metallographic Investigation

The average lengths and contents of the sulfide, silicate, and aluminate inclusions in rolled rods were determined. Only inclusions exceeding 0.01 mm in length in the middle were considered. High dependability of the type of inclusion and their quantities on the quantity of Al in the steel

vermindert wurde, bei einigen Stählen (z. B. Federstählen) ist die Anzahl um 30–50% kleiner.

Die Modifikation der Einschlüsse wurde auch durch Bruchanalysen bestätigt. Die Abb. 9 und 10 zeigen, wie die Brüche bei einigen Stählen aussehen. Wie ersichtlich, sind Brüche für die Stähle mit perlitischer Mikrostruktur charakteristisch. Einschlüsse liegen nur selten vor, sie haben meist eine kugelige Form mit Durchmesser unter 15 μm.

Schlußfolgerungen

Es war die Absicht, eine Möglichkeit zu wesentlicher Erhöhung der Reinheit im Stahl und zum Abstand on the quantity of injected CaSi could be determined (12), (13), (14).

At sufficient (optimum) quantities of Al (plus 0.015%) and CaSi, a completely new picture of the inclusions was found in Store-steels.

The quantity of Mn-sulfides was considerably reduced, silicon inclusions practically are no longer existing, there are, however, globular complex inclusions (mainly composed of $CaO\text{-}Al_2O_3\text{-}CaS$, fig. 8).

In properly manufactured melts, the aluminate and Mn-sulfide inclusions were modified into complex inclusions.

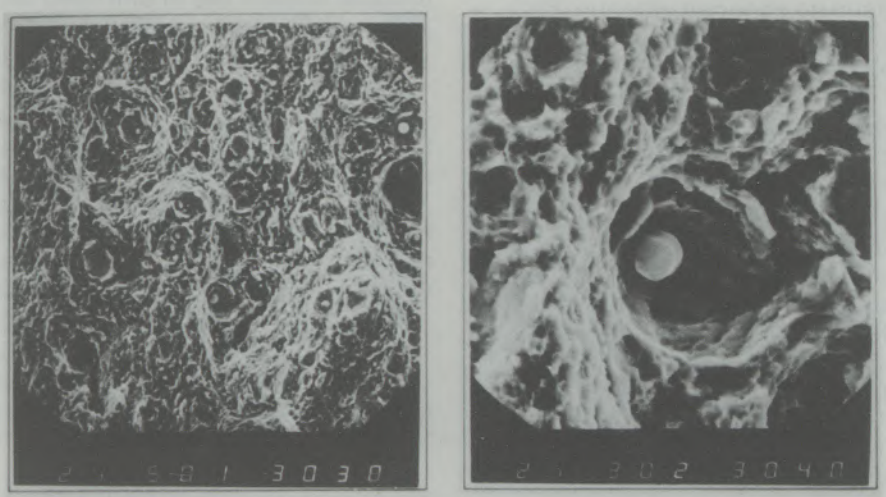

Mag. 500x Mag. 3000x

Nr. 25966 (Č. 4830, DIN 50 CR V 4) inj. 1,9 kg CaSi/t
C-0,50%, Si-0,34%, S-0,006%, Al_{tot}-0,016%, O_{tot}-0,0059%

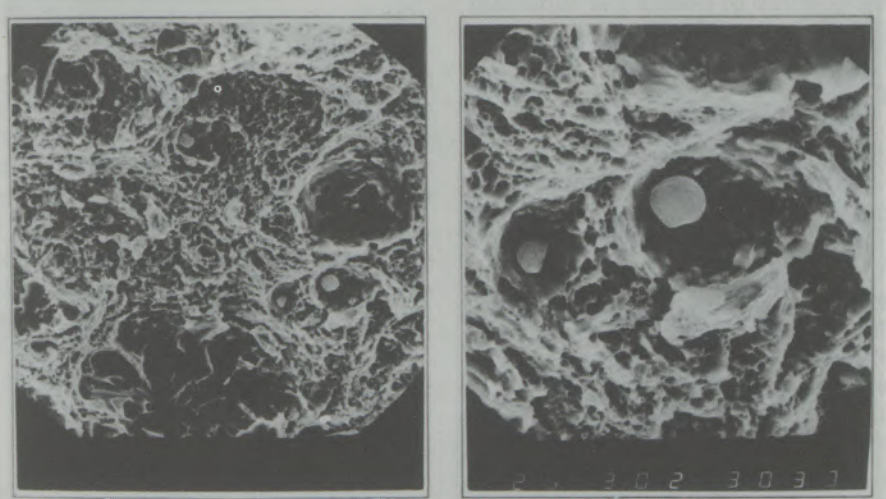

Mag. 500x Mag. 3000x

Nr. 15422 (Č. 4830, DIN 50 CR V 4) inj. 1,5 kg CaSi/t
C-0,51%, Si-0,38%, S-0,017%, Al_{tot}-0,020%, O_{tot}-0,0062%

Abb./Fig. 9
Aussehen der Brüche
Appearance of fracture

gießen aluminiumberuhigten und mit CaSi behandelten Stahles auf einer kontinuierlich arbeitenden Gießanlage in Železarna Štore nachzuweisen. Eine neue Anlage zum CaSi-Einblasen wurde eingeführt und optimiert und die Stahlherstellungstechnologie im Lichtbogenofen dem neuen Verfahren angepaßt.

Die optimal festgelegten Parameter des Einblasens sind:

- Geschwindigkeit des CaSi-Einblasens ca. 25 kg/min;
- Verbrauch des Trägergases Argon 400–600 Nl/min;

It is assumed that the number of inclusions in some qualities of steels had been reduced by over 50%, with some steels (e.g. spring steel) the number is by 30 to 50% smaller.

The modification of the inclusions also was confirmed by fracture analysis. Figs. 9 and 10 show, what the fractures of some steels look like. Ruptures of steels with perlitic microstructure are oviously characteristic. Inclusions appear rarely, they show mostly a ball-like shape with a diameter of below 15 μm.

Mag. 500x

Mag. 3000x

Nr. 15098 (Č. 8330, DIN ST 52-V) inj. 1,5 kg CaSi/t
C-0,24%, Si-0,30%, S-0,015%, Al_{tot}-0,015%, O_{tot}-0,0062%

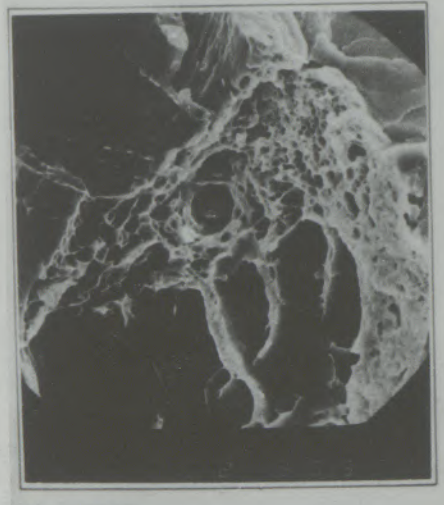

Mag. 3000x

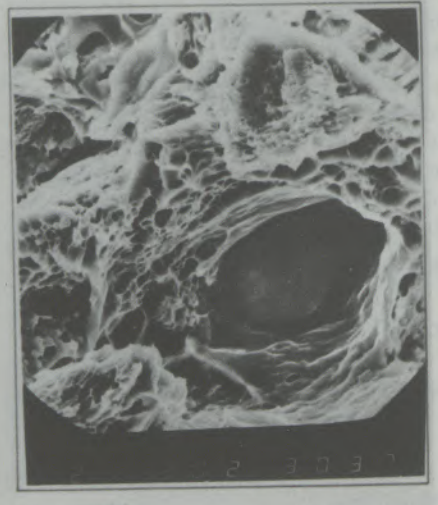

Mag. 3000x

Nr. 15426 (60 Si Cr 7) inj. 1,6 kg CaSi/t
C-0,58%, Si-1,44%, S-0,005%, Al_{tot}-0,015%, O_{tot}-0,0053%

Abb./Fig. 10
Aussehen der Brüche
Appearance of fracture

- CaSi-Menge ist von der Qualität abhängig und variiert zwischen 1,2 und 2 kg/t Stahl;
- Temperaturgefälle im Stahl während des Einblasens beträgt bis zu 30 °C;
- aufgezählte Parameter können nur mit richtig kombiniertem Drücken des Träger-, Misch- und Dispensergases erreicht werden.

Da die optimalen Ergebnisse der Anwendung von CaSi-Einblasverfahren nur bei Al-beruhigten Stählen erreicht werden, wurde stufenweise die neue Technologie der Vordesoxidation im Ofen und der Enddesoxidation mit Aluminium in der Pfanne eingeführt.

Es wurde nachgewiesen, daß es mit entsprechender Al-Menge im Ofen und in der Pfanne möglich ist, sehr niedrige Sauerstoffgehalte zu erzielen, die aber später während der CaSi-Behandlung reduziert werden.

Um stabile Ausbeutebedingungen des in der Pfanne zugegebenen Aluminiums mit Hinsicht auf das spätere starke Durchmischen von Schlacke und Stahl während des Einblasens zu sichern, wurde das Abstechen von Stahl aus dem Ofen ohne Schlacke eingeführt. In die Pfanne werden Kalk und Flußspat zugegeben, um eine neue Schlackendecke zu bilden.

Erwartungsgemäß sind in Stählen mit genügendem Al-Gehalt bzw. mit genügend kleiner Sauerstoffaktivität und mit entsprechender Menge des eingeblasenen CaSi auch die S-Endgehalte sehr niedrig.

Wegen des guten Entschwefelungsgrades (auch 90% vom Ofen zum Knüppel) wurde vorgeschrieben, die mit CaSi behandelten Stähle aus dem Ofen mit einem Schwefelgehalt, der nicht niedriger als 0,040% S liegt, abzustechen. Das kann natürlich die Raffinationsdauer ziemlich verkürzen!

Wegen des hohen Entschwefelungsgrades wird die Menge der Mn-Sulfide im Stahl sehr reduziert (interessanterweise waren die Schwefelabdrucke manchmal fast ganz weiß). Deshalb können auch die Seigerungsrisse in kohlenstoffarmen Stählen nicht so leicht gebildet werden.

Modifikationen der Aluminat-Einschlüsse in Al-beruhigten Stählen wurden nachgewiesen; wodurch das Abgießen solcher Stähle auf der Konti-Gießanlage für Knüppel ermöglicht wird.

Abschließend kann festgestellt werden, daß mit der neuen Stahlherstellungstechnologie in SŽ-Železarna Štore die Möglichkeit geboten wurde, Stähle wesentlich höherer Qualität zu erzeugen, was sich auch in neuen Ausfuhrmöglichkeiten dieser Stähle spiegelt.

Conclusions

It was our intention to present a possibility for a considerable increase of the purity of steel and for tapping aluminum killed and CaSi treated steel with a continuous casting plant at Železarna Štore. A new unit for injecting CaSi was introduced and optimized, and the steel manufacturing technology of the electric arc furnace accordingly adapted to the new process.

The optimum parameters defined for injection are the following:

- rate of the CaSi-injection appr. 25 kg/min;
- carrier gas consumption (Argon) 400–600 Nl/min;
- CaSi quantity depends on quality, varying from 1.2 to 2 kg/t of steel;
- temperature gradient in the steel during injection is up to 30 °C;
- parameters listed may only be reached through properly combined pressures of the carrier-, mixing- and dispenser gases.

Since the optimum results of the application of the CaSi-injection process were obtainable only with Al-killed steels, the new technology of pre-desoxidation in the furnace and final desoxidation with aluminum in the ladle was introduced.

It was proven that using the proper amount of Al in the furnace and in the ladle it is possible to obtain very low oxygen contents, that lateron are reduced during CaSi treatment.

To secure stable conditions of recovery of the aluminum added in the ladle with respect to the lateron following strong mixing of slag and steel during injection, tapping the steel from the furnace without slag was introduced. In the ladle, lime and fluorspar are added to develop a new slag-cover.

As expected, the final S-contents of steels with sufficient Al-content, resp. with sufficiently low oxygen activity and with proper quantity of CaSi injected are very low.

On account of the good degree of desulfurization (also 90% from furnace to billet) it was prescribed to tap the steels from the furnace with a sulfur content not lower than 0.040%. This is a way to considerably shorten the time of refining!

Because of the high degree of desulfurization the quantity of Mn-sulfides in the steel is strongly reduced (it was interesting to note that the sulfur prints occasionally were almost completely white). Therefore, the liquation cracks are not so easily formed in low-carbon steels.

Modifications of the aluminate inclusions were proven in Al-killed steels; this permits casting such steels with our continuous casting plant for billets.

Finally we may state that thanks to the new steel making technology in SŽ-Železarna Štore the possibility is offered to produce steels of considerably higher quality which is also reflected by the new exportation possibilities of those steels.

Literaturverzeichnis/References

1. Prešern, V., F. Kandare, T. Mlakar: Radex-Rdsch., Heft 1/2, **1982,** 771–779.
2. Prešern, V., J. Arh, T. Mlakar: SCANINJECT III, P6:1–P6:20, Lulea, Sweden, June 15–17, **1983.**
3. Prešern, V., J. Arh: CCC 84, Voest-Alpine Continuous Casting Conference **1984,** Paper No. 24.
4. Carlsson, G., T. Lehner: Radex-Rdsch., **1981,** Heft 1/2, 374–379.
5. Szekely, J., N. El-Kaddah: Symposium on Injection in Extraction and Refining, Proc. Symp. at University of Newcastle Upon Tyne, **1982,** R1–42.
6. Holappa, L. E. K.: SCANINJECT II, Paper 1, Lulea, Sweden, June **1980.**
7. Jeanneau, M., M. Poupon: Revue de Metallurgie, Juin **1981,** 517–524.
8. Tähtinen, K., R. Vainola: Modern developments in Steelmaking, Paper 7.5.1.–7.5.15, 16–18 February **1981,** Jamshedpur, India.
9. Holappa, L. E. K.: International Metals Reviews, **1982,** Vol. 27, No. 2, 53–76.
10. Gruner, H.: Stahl und Eisen, 1979, 99(4), 725–737.
11. Grimm, W., J. Feller: Radex-Rdsch., **1981** (1/2), 455–465.
12. Yoshimura, M., S. Yoshikawa: Scaninject II Conf., Lulea, June **1980,** Paper 28.
13. Stubbs, P.: 40th Electric Furnace Conf. Proceedings, Kansas City, Dec. **1982,** 285–288.
14. Turkdogan, E. T.: Arch. Eisenhüttenwes. 54 **(1983),** Nr. 1, Januar, 1–10.

Eigentümer, Herausgeber und Verleger: **Österreichisch-Amerikanische Magnesit A. G., Radenthein, Kärnten**
Verantwortlicher Schriftleiter: Prok. Obering. Karl Hajek, Radenthein, Kärnten
Titelfoto: Kurt Maier
Druck: Carinthia, Klagenfurt

RUNDSCHAU
radex

RADENTHEIN, IM JUNI 1986

Inhalt — Heft 2/3

Geleitwort

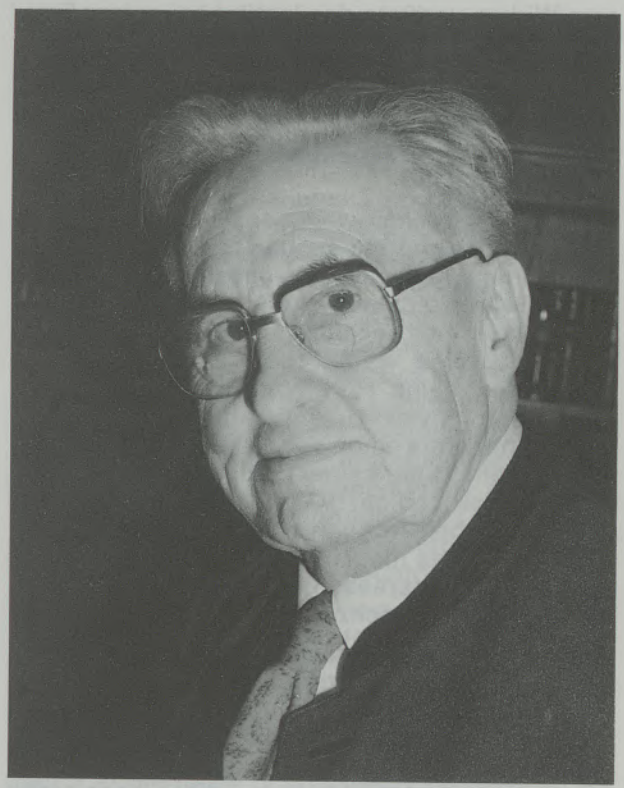

Wenn das vorliegende Heft der RADEX-Rundschau als Sonderheft erscheint, so geschieht dies aus einem ganz besonderen Anlaß. Am 28. August dieses Jahres feiert Univ.-Prof. Dr. phil. Franz Lihl seinen 80. Geburtstag, eine willkommene Gelegenheit für seine Freunde, Kollegen, Mitarbeiter und Schüler, an seinem Lebensweg das Beispiel eines erfolgreichen, allgemein hoch verehrten Menschen und Wissenschafters aufzuzeigen.

Ausgestattet mit einem soliden humanistischen Grundwissen wandte sich Franz Lihl im Jahre 1925 dem Studium der Physik, Chemie und Mathematik an der Universität in Wien zu. Seiner hohen Begabung und seinem Fleiß war es zuzuschreiben, daß er bereits nach fünf Jahren Studienzeit zum Doktor der Philosophie promoviert wurde. In der anschließenden Zeit als wissenschaftlicher Assistent und später als stellvertretender Leiter an der staatlichen Versuchsanstalt für röntgentechnische Materialuntersuchungen in Wien setzte er sich grundlegend mit der Röntgenphysik auseinander. Seine ersten größeren Veröffentlichungen behandeln daher die Abbildungsgeometrie bei der Röntgenstrahlenbeugung an Kristallpulvern.

Nach neunjähriger erfolgreicher Tätigkeit an der staatlichen Versuchsanstalt übernahm Franz Lihl die Leitung der Abteilung Schweißtechnik und Materialprüfung der Firma Waagner-Biro in Graz. Damit wechselte er nicht nur den Arbeitsplatz, sondern auch sein Arbeitsgebiet von der Röntgenkunde zur Metallurgie, Schweißtechnik und Werkstoffprüfung. Es gelang ihm innerhalb kürzester Zeit, sich fachliche Grundlagen dieses neuen Arbeitsgebietes anzueignen, wobei er viele Abendstunden im Metallurgielabor verbrachte, um sich fundamentale praktische Kenntnisse als Werkstoffingenieur zu erwerben und damit die Leitungsposition in seiner Abteilung nicht nur bekleiden, sondern echt ausfüllen zu können.

Nach mehrjähriger Erfahrung in der Praxis wandte sich Franz Lihl ganz der Wissenschaft zu und nahm im Jahre 1942 die Stelle eines wissenschaftlichen Assistenten am Institut für Metallkunde und Materialprüfung der Bergakademie Freiberg in Sachsen an. Dort habilitierte er sich im Jahre 1943 für das Fach „Theoretische Metallkunde, Metallphysik und Röntgenkunde". Im Jahre 1946 wurde Franz Lihl mit der Supplierung der Hauptvorlesung für Physikalische Chemie betraut – eine Herausforderung für ihn, die er durch eine gründliche Auseinandersetzung mit Physik und Chemie zu meistern wußte.

Nach einem kurzen Intermezzo auf dem Gebiet der Pulvermetallurgie bei den Sintermetallwerken Bernard Berghaus Mitterberghütten kehrte Franz Lihl im Jahre 1948 nach Wien zurück, wo er am Institut für Chemische Technologie Anorganischer Stoffe der damaligen Technischen Hochschule als Assistent und Lehrbeauftragter und später dann als a. o. Hochschulprofessor bis zum Jahre 1958 tätig war. In dieser Zeit arbeitete er auf den verschiedensten Gebieten der Werkstoffchemie und Werkstoffphysik. Er untersuchte nicht nur die katalytischen Eigenschaften von Metallen, neue weich- und hartmagnetische Werkstoffe, sowie den Sprödbruch von Metallen, sondern entwickelte auch ein neues Verfahren zur Legierungsherstellung bei niedrigen Temperaturen – das Amalgamverfahren. Diese letztgenannte Entwicklung ist ein glänzendes Beispiel für die Symbiose von Technik und Wissenschaft, wie sie von Franz Lihl meisterhaft beherrscht wurde und Gegenstand breiter Anerkennung in der Fachwelt war. Er etablierte dieses neue Fachgebiet am Institut für Chemische Technologie Anorganischer Stoffe und untersuchte mit seinen Mitarbeitern eine ganze Reihe von Metallsystemen.

Nicht zuletzt führten diese wissenschaftlichen Erfolge im Jahre 1958 zur Berufung als ordentlicher Hochschulprofessor an die damalige Technische Hochschule in Wien. Er übernahm damit auch die Leitung des Institutes für Angewandte Physik.

Zum Zeitpunkt der Übernahme des Institutes bestand dieses im wesentlichen aus ein paar desolaten Kellerräumen mit veralteten wissenschaftlichen Geräten. Franz Lihl verstand es, mit dynamischer Aquisitionsdiplomatie und mit großer Umsicht das Institut auszubauen und es mit wissenschaftlichen Aktivitäten zu beleben, die aktuellen Forschungszielen dienten. Nach achtzehnjähri-

gem Wirken verfügte das Institut bei seiner Emeritierung über modernste Forschungseinrichtungen zur wissenschaftlichen Forschung im Bereich der plastischen Verformung von Werkstoffen, der Elektronenmikroskopie, der Tiefentemperaturphysik und des Magnetismus sowie der Dünnschichtphysik.

Nicht minder intensiv waren seine Bemühungen in der Lehre. Seine Vorlesungen brachten eine ausgezeichnete Auswahl des umfangreichen Lehrstoffes, waren didaktisch hervorragend aufgebaut und wurden mit exakter, sprachlich brillanter Ausdrucksweise vorgetragen. Damit gelang es ihm immer, seine Hörer für Probleme der angewandten Physik zu begeistern. Sein Institut hatte daher stets einen beachtlichen Zustrom von Mitarbeitern. Unter seiner Leitung führten ca. 350 Diplomanden und ca. 100 Dissertanten ihre wissenschaftlichen Arbeiten an seinem Institut durch. Dadurch war es möglich, einer Vielzahl von wissenschaftlich interessanten Problemen der angewandten Physik nachzugehen.

Auf Grund seiner Persönlichkeit in Wissenschaft und Lehre war es für Franz Lihl ein ernstes Anliegen, jeden seiner Schüler nach besten Kräften und gegebenen Möglichkeiten zu fördern. Seine Mitarbeiter betraute er mit verantwortlichen Forschungs- und Lehrtätigkeiten und gab ihnen große Freiräume für ihre persönliche und fachliche Entfaltung. Damit hat Franz Lihl viele seiner Schüler und Mitarbeiter geprägt, die heute verantwortungsvolle Stellen an Universitäten, Forschungsinstituten und Industriebetrieben im In- und Ausland bekleiden.

Anerkennung fand sein Wirken an der Technischen Universität Wien in der Wahl zum Dekan der Naturwissenschaftlichen Fakultät in den Jahren 1962 bis 1964 und in der Betrauung mit einer Vielzahl von akademischen Funktionen bis zu seiner Emeritierung im Jahre 1976.

Franz Lihl ist in wissenschaftlicher Hinsicht ein sehr vielseitiger Forscher auf den Gebieten der Physik und Chemie, wie es auch in seinem wissenschaftlichen Werk von weit über hundert Publikationen zum Ausdruck kommt. Es kann mit Recht behauptet werden, daß es nur noch wenige Wissenschafter gibt, die über ein so umfassendes Wissen im Bereich der Physik und Chemie verfügen.

In menschlicher Hinsicht sind seine Bescheidenheit, seine absolute Aufrichtigkeit und seine Hilfsbereitschaft charakteristische Eigenschaften; jede Diskussion, jede Zusammenarbeit, jeder menschliche Kontakt mit ihm ist ein Gewinn.

Alle gratulieren herzlich dem Jubilar zum hohen Geburtstag und wünschen für die vor ihm liegenden Jahre Gesundheit und frohe Schaffenskraft, sodaß er auch weiterhin am Gedeihen seiner ehemaligen Forschungsgebiete sowie an seinen lange vernachlässigten Hobbys Freude finden kann.

Walter Kemmerling

O. Univ.-Prof. Dr. Walter Kemmerling
Rektor der Technischen Universität Wien

Foreword

This issue of the RADEX-Rundschau appears in honour of Prof. Dr. Franz Lihl, who is celebrating his 80th birthday on August 28, 1986. Therefore, his friends, colleagues, co-workers and former students take this opportunity to record some of the most important steps in the life of this successful and highly respected man and scientist.

Building on a solid classical education Franz Lihl began to study physics, chemistry and mathematics at the University of Vienna in 1925. His outstanding talent and his diligence enabled him to finish his studies with the Doctor phil. after only five years of study. He became a scientific assistant and the second head of the State Department of X-ray Material Research (Staatliche Versuchsanstalt für röntgentechnische Materialuntersuchungen) in Vienna. There he obtained his profound knowledge as an X-ray physicist. Thus his first important publications dealt with the geometry of X-ray diffraction image patterns in crystal powders.

After nine years of successful work at the Staatliche Versuchsanstalt Franz Lihl became head of the Department for Welding-Technique and Materials Testing (Abteilung Schweißtechnik und Materialprüfung) of the Waagner-Biro company in Graz.

This change of position meant that he also changed his field of work from X-ray physics to metallurgy, welding technique and material testing. Within a short time he learnt the fundamentals of these sciences, spending many evenings in his metallurgy laboratory in order to study the practical problems of material engineering. Thus he became a fully qualified head of this department.

After several years in industry, Franz Lihl turned to research and accepted a position as a scientific assistant at the Institute for Metallurgy and Materials Science (Institut für Metallkunde und Materialprüfung) at the Bergakademie Freiberg in Sachsen. There he qualified as a university lecturer for theoretical metallurgy, metal physics and

X-ray physics ("Theoretische Metallkunde, Metallphysik und Röntgenkunde"). After 1946 Franz Lihl gave lectures on physical chemistry; this was a challenge for him which he met by a thorough study of physics and chemistry.

After a short interlude in the field of powder metallurgy at the Sintermetallwerke Bernhard Berghaus Mitterhütten, Franz Lihl returned to Vienna in 1948, working as an assistant and lecturer at the Institute of Chemical Technology of Inorganic Materials at the Technische Hochschule and later as an associate professor until 1958. During this time he worked in various fields of materials chemistry and materials physics. He not only investigated the catalytic properties of metals, new soft- and hard-magnetic materials, as well as the brittle fracture of metals, but also developed a new technique to produce alloys at low temperatures – the amalgam process. This later development is an outstanding example of Franz Lihl's ability which was widely recognized by experts in these fields. He established this new special field at the Institute of Chemical Technology for Inorganic Materials and investigated a series of metal-systems together with his co-workers.

These scientific successes resulted in an appointment as full professor at the Technische Hochschule, later the Technical University of Vienna, in 1958. Simultaneously he became head of the Institute for Applied Physics.

At the time when he took over the institute, it essentially consisted of a few desolate basement rooms with antiquated scientific instruments. With his forethought and great persuasive ability Franz Lihl was able to improve and modernize the institute and to make it live with scientific activities serving modern goals of research. After eighteen years of his work the institute had the best-equipped laboratories for scientific research in the fields of plastic deformation of materials, electron-microscopy, low-temperature physics, magnetism and thin layer physics.

No less intensive were his efforts in teaching. In his lectures, Franz Lihl presented an excellent overview of and selection from the very broad field of applied and technical physics. His lectures were didactically perfect and were formulated in precise and brillant language. This helped him to fascinate his students with the problems of applied physics. His institute therefore always attracted many scholars. Under his guidance about 350 students worked to obtain their diplomas and some 100 students worked at his institute to do their doctoral theses. This made it possible to investigate a wide variety of scientifically interesting problems of applied physics.

Being a great man and scientist, it was one of Franz Lihl's first and most important aims to help all his students in their careers as far as possible. He entrusted his co-workers with highly important research and teaching activities, giving them wide freedom for their personal and scientific development. Thus Franz Lihl shaped many of his students and assistants who today hold responsible jobs at universities, research institutions, and industrial enterprises in this country and abroad.

His work at the Technical University Vienna found recognition by his election to dean of the Faculty of Natural Sciences in the years 1962–1964, and with a variety of other academic functions until his retirement in 1976.

As a scientist, Franz Lihl is a very versatile investigator in the fields of physics and chemistry, as shown in his published work which consists of more than a hundred publications. It could be claimed that there are only a few scientists in the world with such an extensive knowledge of physics and chemistry.

As a man, Franz Lihl is characterized by his absolute sincerity, helpfulness and modesty. Every discussion, every co-operation and every contact with him is a genuine pleasure.

We all congratulate Professor Franz Lihl cordially on his 80th birthday and wish him health and happy creative power for the years ahead, so that he many enjoy the prosperous growth of his former fields of research and the hobbies which he has had to neglect for so long.

Prof. Dr. Walter Kemmerling
President of the Technical University Vienna

New Developments in the Field of Permanent Magnetic Materials

Josef Fidler and Peter Skalicky, Wien*)

Dedicated to the 80th birthday of Prof. Dr. Franz Lihl

The increasing importance of newly developed permanent magnetic materials in many electro-, magnetomechanical and electronic applications can be attributed to the drastic improvement of the magnetic energy density product and coercivity of the new materials. The influence of the microstructure of the magnets on their magnetic properties will be discussed in this review paper.

Neue Entwicklungen auf dem Gebiet dauermagnetischer Werkstoffe

Die zunehmende Bedeutung von neu entwickelten dauermagnetischen Werkstoffen in zahlreichen elektro-, magnetomechanischen und elektronischen Anwendungen ist auf eine Verbesserung des Energiedichteproduktes und der Koerzitivfeldstärke zurückzuführen. Der Einfluß der Mikrostruktur der Magnete auf ihre magnetischen Eigenschaften wird in diesem Übersichtsartikel diskutiert.

Produits nouveaux dans le domaine des aimants permanents

L'importance croissante des aimants permanents nouvellement développés, dans de nombreuses applications électro- et magnétomécaniques et électroniques, doit être attribuée à l'amélioration du produit de densité d'énergie et de l'intensité du champ coercitif. On résume et on discute dans cet article l'influence de la microstructure des aimants sur leurs propriétés magnétiques.

Introduction

The history of permanent magnetism reaches to the ancient Greece, where the ability of the loadstone to attract iron having been discovered. With the development of special alloy steels the modern history of permanent magnetic materials starts with the end of the last century. The intrinsic coercivity and the energy density product of such magnetic steel materials were rather low compared to recently developed hard magnetic materials. Table 1 shows the historical development of the intrinsic coercivity and the magnetic energy density product of hard magnetic materials. In the year 1931 Mishima discovered in Japan an alloy of 58 wt% Fe, 30 wt% Ni and 12 wt% Al with a coercivity of about double that of the best magnet steel material (30–40 wt% Co plus W and Cr) which was available at that time. Soon it was discovered that the addition of cobalt and copper improved the properties of the Mishima alloy leading to various types of AlNiCo magnetic materials. After second world war hard magnetic materials based on ceramic hexaferrites were developed particulary in Holland.

Since the 1960s most of the developments of permanent magnetic materials have been done on the improvment of the magnetic properties. The search for new materials has been shifted from shape anisotropy to crystal anisotropy. The new hard magnetic materials based on rare earth intermetallic compounds exhibit a considerably higher

Table 1

Historical development of coercivity and energy density product of hardmagnetic materials

magnet	coercivity	energy density product	year
magnetic carbon-steel	1 kA/m	2 kJ/m³	1890
AlNiCo	10 kA/m	15 kJ/m³	1940
AlNiCo	100 kA/m	90 kJ/m³	1955
hardferrites	200 kA/m	20 kJ/m³	1960
SmCo 1:5	1000 kA/m	200 kJ/m³	1975
SmCo 2:17	2000 kA/m	260 kJ/m³	1982
NdFeB	2000 kA/m	400 kJ/m³	1985

*) Univ.-Doz. Dr. Josef Fidler, o. Prof. Dr. Peter Skalicky, Institut für Angewandte und Technische Physik, Technische Universität Wien, Karlsplatz 13, A-1040 Wien, Austria

coercive force and energy density product than the traditional AlNiCo-alloys and hardferrites. In the late 1960s the high magnetocrystalline anisotropy, the basis for a good permanent magnet material, was discovered in the USA under the leadership of K. Strnat (1) in several rare earth – cobalt intermetallic compounds. Soon it was discovered that the combination of the high magnetic moments of iron and/or cobalt with the high magnetic moment of heavy rare earths leads to high magnetocrystalline anisotropy and retains the high magnetic ordering temperature particularly in the system samarium – cobalt. The rare earth permanent magnets were discovered in the USA, but recent developments in this field have come from Japan, especially by the invention of rare earth – iron based permanent magnets (2) having the best magnetic properties so far achieved, in the year 1983.

The magnetic hardness of permanent magnet materials depends critically on the microstructure of the individual magnets. In the light of the historical development of the coercivity and the energy density product of hard magnetic materials the improvement of the energy density product is closely connected with a better understanding of the mechanisms leading to higher coercive forces of the magnets. The coercive force of hard magnetic materials is determined either by the nucleation of reversed magnetic domains at magnetic fields which are lower than the theoretical maximum

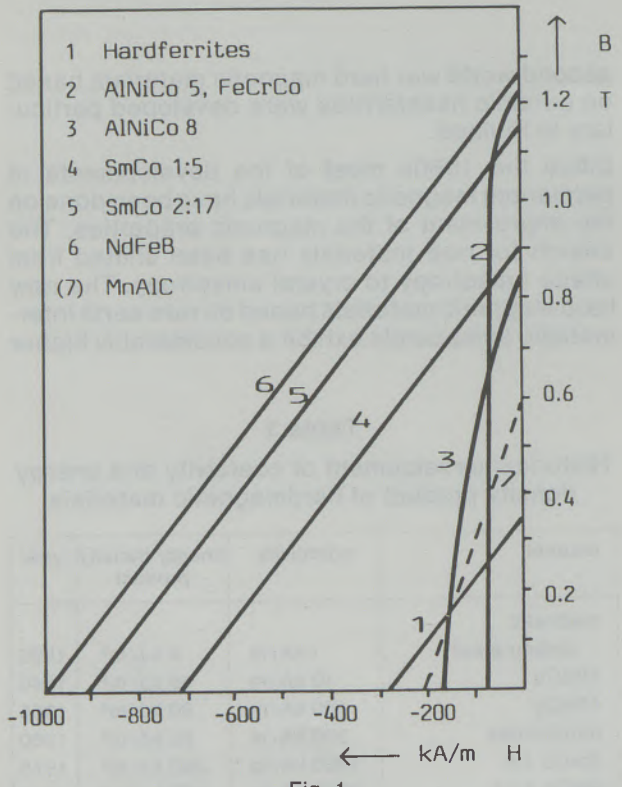

Fig. 1
Room temperature demagnetization curves of commercial hardmagnetic materials

Table 2

Magnetic properties of commercial hardmagnetic materials
(at room temperature)

magnet	$(B \cdot H)_{max}$ kJ/m³	B_r T	${}_BH_c$ kA/m	${}_JH_c$ kA/m	T_C °C
hardferrites	25	0.35	280	320	450
$AlNiCo_5$	60	1.30	60	62	850
FeCrCo	60	1.30	60	62	850
$AlNiCo_8$	55	0.85	140	145	850
SmCo 1:5	200	0.90	720	2500	720
SmCo 2:17	260	1.15	920	3000	820
NdFeB	400	1.25	1000	2000	310

value of the anisotropy-field, or by the strong pinning of domain walls at crystal lattice defects and precipitates during the magnetization reversal (3). Analytical investigations for the characterization of the microstructural parameters, such as grain size distribution, phase determination, chemical homogeneity of the grains, crystal lattice defects and precipitates, are necessary for a better knowledge of the limiting factors of the coercivity.

As it has been the tradition for many years, special emphasis of our institute has been laid on the measurement of the hard magnetic properties and on the investigation of the microstructure of newly developed hard magnetic materials. Using high resolution and analytical electron microscopy together with X-ray microanalysis and metallography the microstructure of various magnetic materials were characterized.

1. New hard magnetic materials

Commercially available permanent magnet materials may be divided into seven groups. Fig. 1 shows the demagnetization curves of hardferrites, AlNiCo, rare earth permanent magnet materials and MnAlC magnets. The corresponding magnetic properties, such as energy density product, remanence, coercive forces and Curie temperature are summarized in Table 2. Magnets based on samarium-cobalt intermetallic compounds have gained an increased importance for the last 10 years and are strictly speaking not only limited to samarium. Depending on the producer a mixture of one or more rare earth elements with cobalt is used for the preparation of the magnets. In the following we distinguish two types of rare earth – cobalt magnets: the SmCo 1:5 and the SmCo 2:17 magnets, according as the main phase of the magnet exhibits the $SmCo_5$- or the Sm_2Co_{17}-structure.

Nevertheless, from the point of view of mass production the hardferrites and AlNiCo-magnets are the most important ones. Fig. 2 shows the estimated amount of Hardferrite, AlNiCo, REPM (rare earth permanent magnets) and other magnet materials to the western world production (Japan,

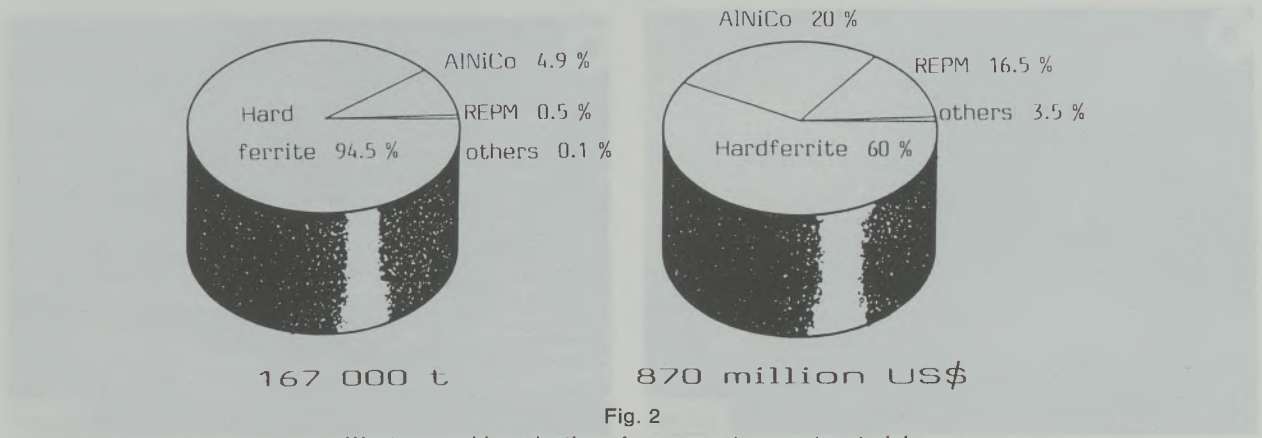

Fig. 2
Western world production of permanent magnet materials in the year 1984

USA and Europe) in the year 1984. Because of high raw material and production costs the cobalt based rare earth permanent magnets share only less than 20% of the annual total turnover, whereas the annual growth of this group has been in the order of more than 30% for the last few years. Through the invention of rare earth – iron based magnets which are less expensive from the raw material point of view, the annual growth of rare earth permanent magnets is expected to be increased worldwide. The production of the inexpensive ceramic Hardferrites increases annually in the order of 20%, whereas the one of AlNiCo magnets is slightly decreasing.

The drastic increase of the energy density product of newly developed hard magnetic materials (Table 2) enabled the invention of many new applications of permanent magnets. Permanent magnets are primarily used in magneto- and electromechanical applications and increasingly in beam guiding systems. Generally the magnetic field strength in the air gap of a magnetic circuit, containing a permanent magnet, is proportional to the energy density product and to the volume of the magnet, according to:

$$H_{air\ gap} \sim \sqrt{\frac{(B \cdot H)_m \cdot V_m}{V_{air\ gap}}} \qquad [1]$$

It is evident that the increase of the energy density product reduces besides the volume also the weight of the permanent magnet containing device and new designs of dynamic devices (motors, generators, etc.) and static devices (charged beam guiding systems) are possible.

2. Microstructure and properties of permanent magnets

2.1 Conventional magnets (Hardferrite and AlNiCo magnets)

Besides the *barium- and strontium-hardferrites* the group of AlNiCo magnets have been the most dominant commercial permanent magnet materials for many years (fig. 2). The hexagonal crystal structure of the hardferrites imparts a strong magnetocrystalline anisotropy. Magnets are made by sintering of aligned particles of about 10–100 μm in diameter. Metallographic investigations show that the shape of the demagnetization curve and therefore also the coercivity strongly depends on the grain size of the final magnet (4). The coercivity is controlled by the nucleation of reversed domains at low anisotropy regions. After the abrupt reversal of the magnetization in the individual grains after applying of an opposite external magnetic field, the further expansion of the reversed magnetic domains might be hindered by the pinning of domain walls at the grain boundary region. Finally, the coercivity of the individual magnet depends on the processing parameters (milling and annealing) and is directly correlated to the microstructure of the material.

The *AlNiCo magnets* are hard and brittle and are manufactured by casting of a liquid alloy, leading to the large grain size up to the order of millimeters, or by pressing and sintering metal powders leading to small grain sizes. Fig. 3a is an optical micrograph showing a large grain size of a cast AlNiCo 5 magnet. The transmission electron micrograph of this magnet (fig. 3b) shows a duplex microstructure of Fe-Co rich α_1-phase and a Ni-Al rich α_2-matrix phase. Depending on the type of the AlNiCo magnet different multi-stage heat treatments, including magnetic field anneals, are necessary to produce optimum properties. The effect of adding small amounts of Ti, Nb or Ta is to increase the coercivity but to decrease the remanence (AlNiCo 8). Depending on the cooling condition rodlike, coherent precipitates of the bcc-crystal structure type are formed parallel to the external magnetic field direction during cooling. The cause of the magnetic hardness of AlNiCo magnets is primarily the shape anisotropy of the rod-shaped and strongly magnetic Fe-Co rich α_1-phase and the difference of the magnetization between the two phases. The rods of the α_1-phase of the AlNiCo 5 magnet of fig. 3b are of the order

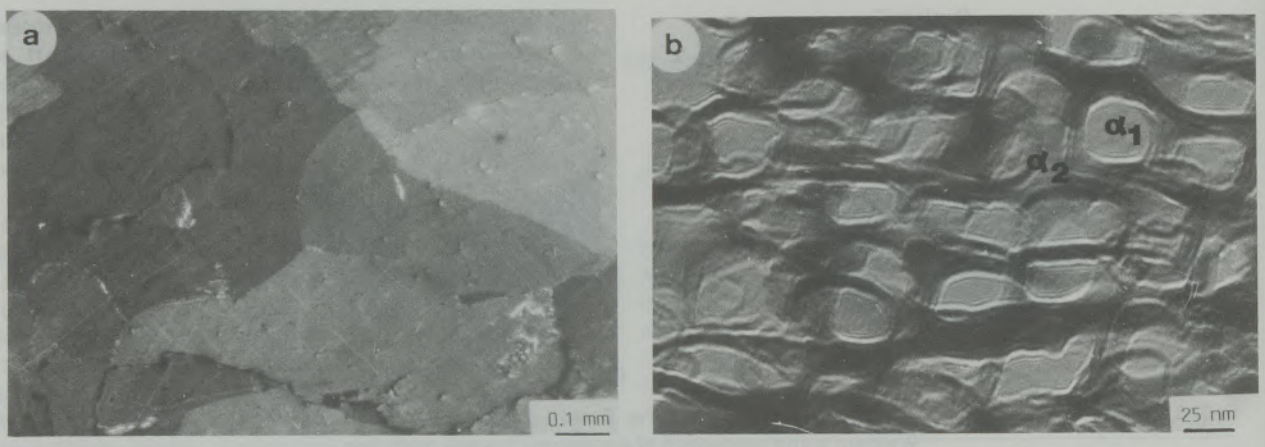

Fig. 3
Optical (a) and electron (b) micrographs showing the grainsize distribution and the duplex microstructure of a cast AlNiCo 5 magnet

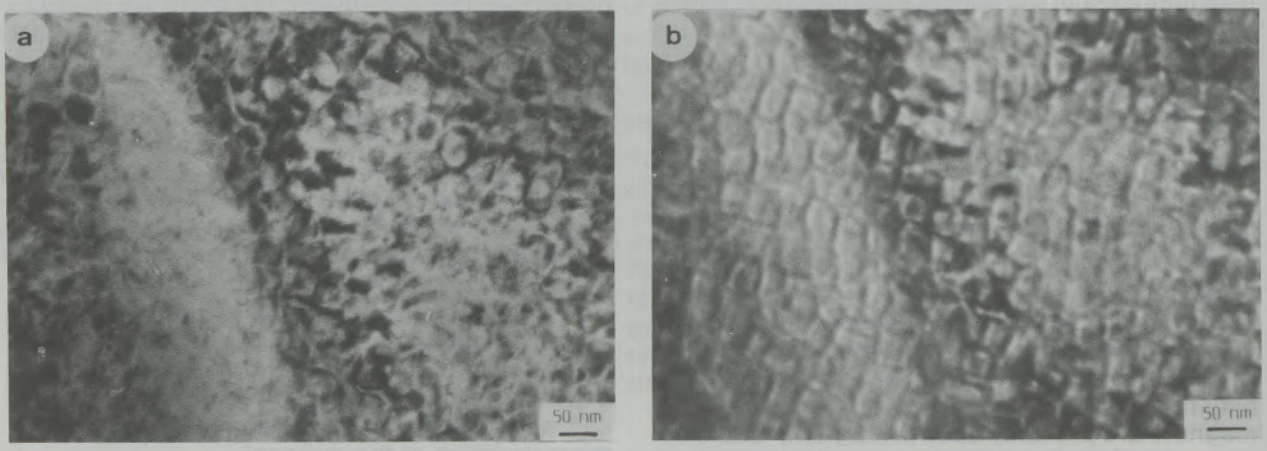

Fig. 4
Transmission electron micrographs of a cast AlNiCo 5 magnet. Magnetic domain walls are visible within the weak magnetic Al-Ni rich matrix phase in the defocused Fresnel image (b)

of 30x30x120 nm^3. From the Lorentz electron micrograph of fig. 4b showing magnetic domain walls within the weakly magnetic α_2-matrix phase, it is evident that the influence of the Ni-Al phase on the moving domain walls during the magnetization reversal must be taken into account. Electron microscopic investigations (fig. 5) show that titanium additions change the shape of the α_1-rods and decrease the volume fraction of the strongly magnetic Fe-Co rich α_1-phase and therefore change the coercivity and remanence. The interpretation of the coercivity of AlNiCo magnets is based on the combination of magnetization reversal models of single domain particles with domain wall motion models of interacting domains (5), (6), (7).

Ductile permanent magnet alloys based on the *Fe-Cr-Co* system have received considerable attention to be hot or cold worked into wire, sheet

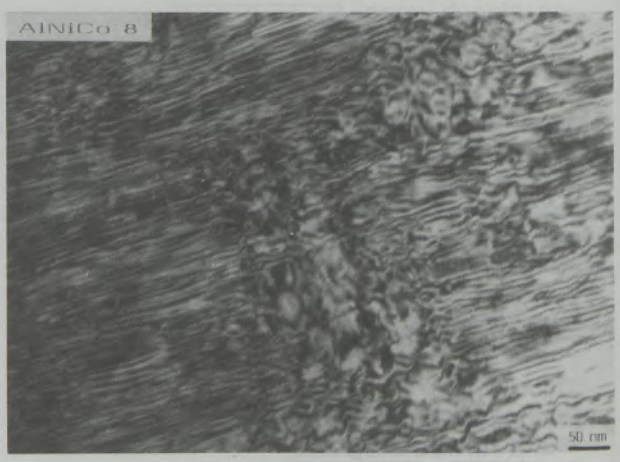

Fig. 5
Transmission electron micrograph of a cast Ti-containing AlNiCo 8 magnet

or other forms. The magnetic properties and the microstructure are quite similar to AlNiCo 5 magnets. During cooling the alloy decomposes spinodally into the Fe rich α_1-phase and the Cr rich α_2-phase. Similar to the AlNiCo magnets the particle morphology (shape anisotropy) of the strongly magnetic α_1-phase predominatly determines the coercivity. The magnetic characteristics have been gradually improved by adding various minority elements such as Mo-Si, Nb, Al, V, T, and Cu (8), (9).

2.2 Rare earth permanent magnets (REPM)

According to the phase diagrams of rare earth intermetallic compounds five compounds ($RECo_2$, $RECo_3$, RE_2Co_7, $RE_5 19_{19}$ and $RECo_5$) appear in the composition range 66.7–83.3 at% Co (10). The crystal structures of these phases are closely related with each other and are based on a regular stacking of two kinds of layers, one is a layer of $SmCo_2$-laves phase structure and the other is that of $SmCo_5$-structure. There exist two groups of REPM, the *RE-cobalt magnets* and the recently developed *RE-iron magnets.* The RE-cobalt magnets can be divided into five types depending on wether the magnet has a single-phase or a two-phase microstructure. The ideal microstructure of the single phase magnets consists of aligned single-domain particles with a $SmCo_5$- or Sm_2Co_{17}-crystal structure. Two types of precipitation hardened magnets can be distinguished: the one type contains 2:17-precipitates in a 1:5-matrix, the other type has 1:5-precipitates in a 2:17-matrix. Besides these magnets there are the bonded magnets, in which the single domain particles are embedded in a non magnetic phase. Rare earth-cobalt magnets are produced by a powder metallurgical process, whereas rare earth-iron magnets can be produced either by a powder metallurgical process (11) or derived from rapidly solidified melt-spun ribbons (12). The main process steps for the production of sintered rare earth permanent magnets are shown in fig. 6. The

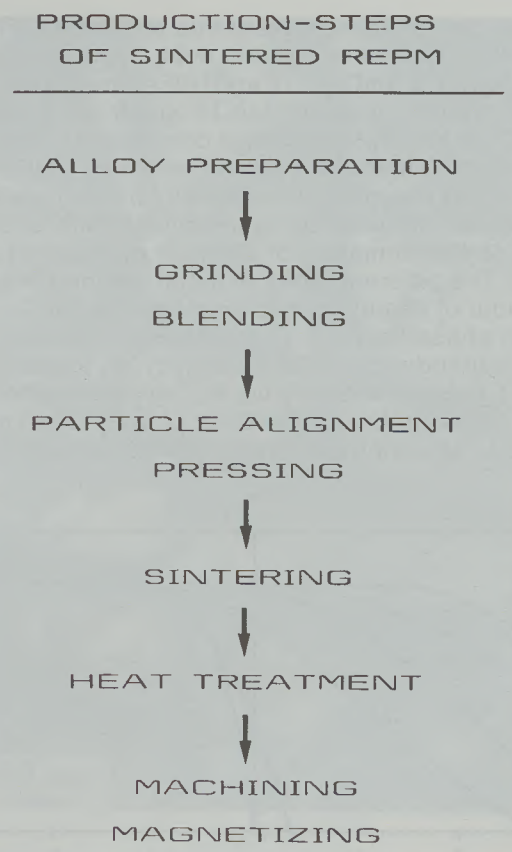

Fig. 6
Main process steps for the production of sintered rare earth permanent magnets

general production steps include alloy preparation, milling, composition control and adjustment, particle alignment and pressing, sintering and aging, machining and final magnetizing. Besides the parameters which determine the composition of the phases within the magnets there are also processing parameters, particularly during sintering and annealing steps such as sintering temperature, cooling rate, aging temperature and time (fig. 7), which must carefully be controlled in order

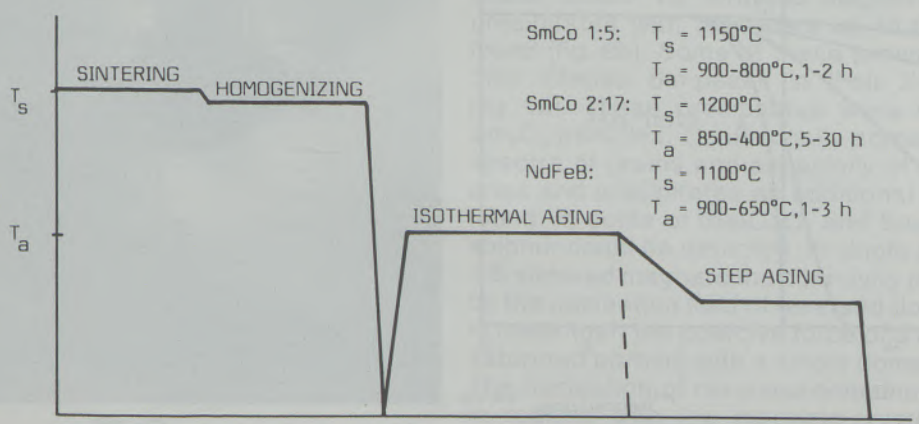

Fig. 7
Schematic sintering and post-sintering heat treatment curves of rare earth permanent magnets

to achieve maximum magnetic properties. Fig. 7 shows a typical schematic heat treatment curve of SmCo 1:5 SmCo 2:17 and NdFeB magnets. The heat treatment sequence to sinter multi-phase SmCo 2:17 magnets is more complicated and time consuming than the ones for sintering SmCo 1:5 or NdFeB magnets. The reason for different heat treatment sequencies for the different materials is due to the formation of different microstructures (13). The different types of initial magnetizing behaviour of demagnetized single phase SmCo 1:5, multi phase SmCo 2:17 and NdFeB magnets and the dependence of the coercivity on the magnetizing fields is shown in fig. 8. The different behaviour of the SmCo 1:5, SmCo 2:17 and NdFeB magnets is caused by different microstructures.

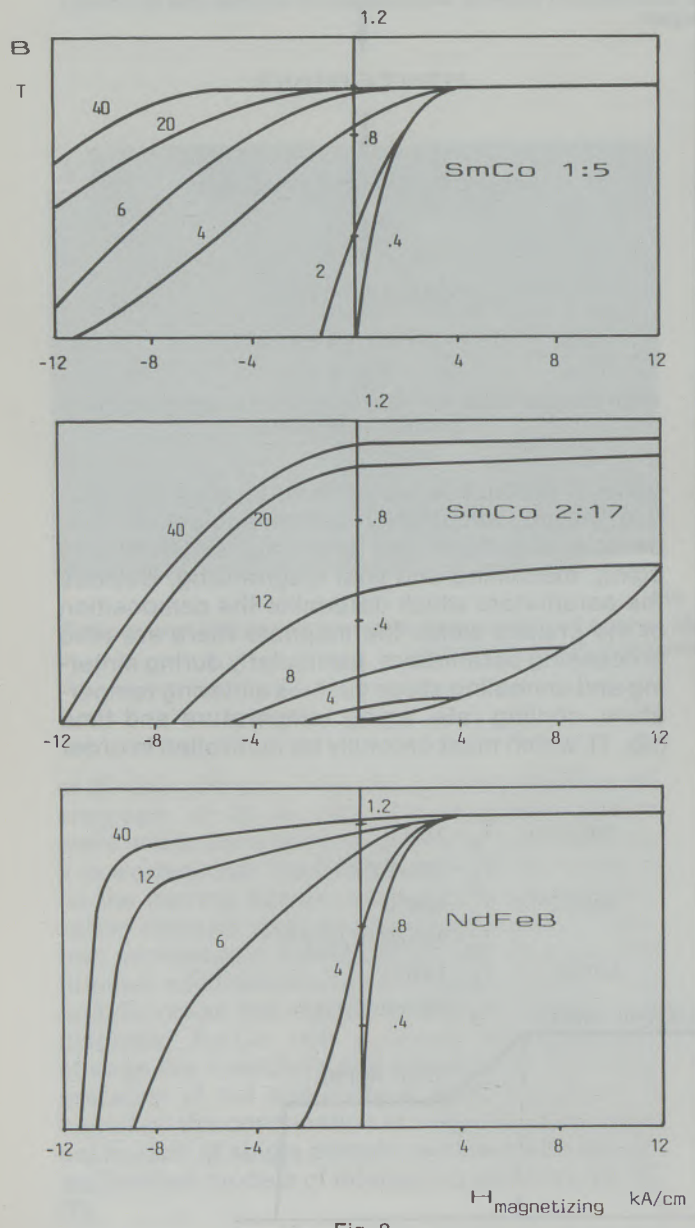

Fig. 8

Initial magnetization curves and dependence of the coercive force on the magnetizing external fields of different types of rare earth permanent magnet materials

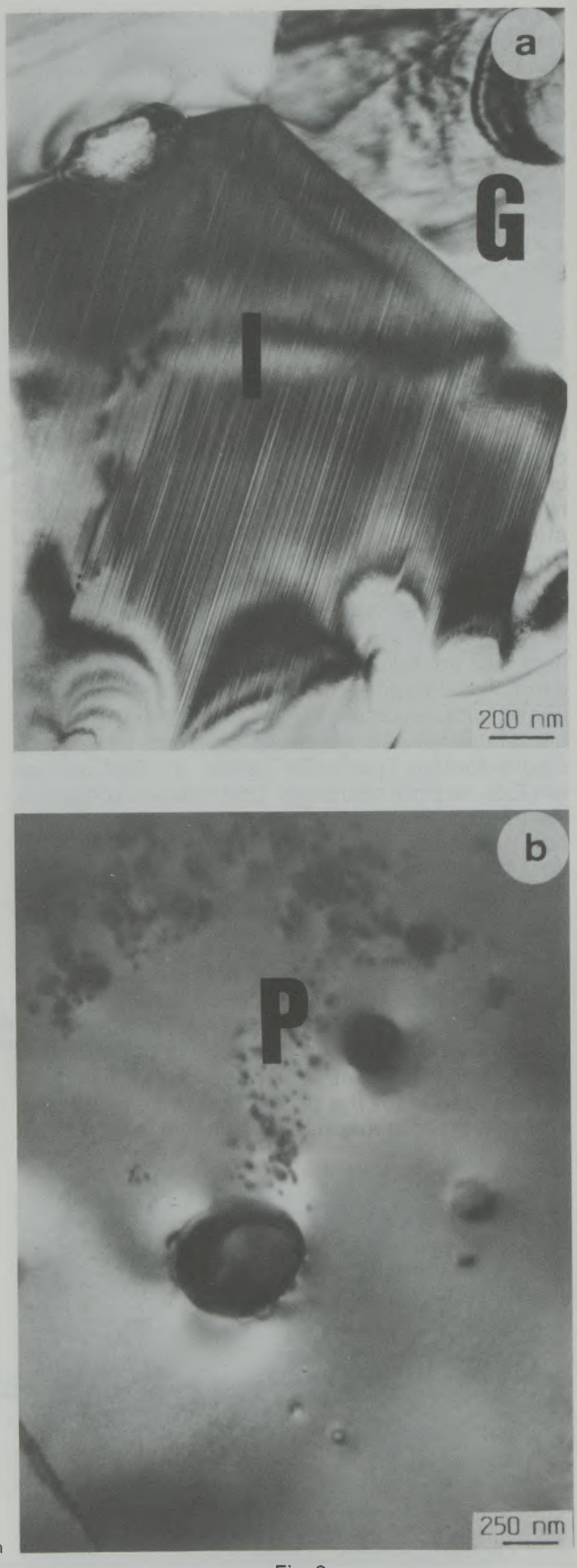

Fig. 9

Electron micrographs showing a grain with densly packed planar faults (a) and small precipitates (b) of a sintered SmCo 1:5 magnet

For the understanding of the different magnetization behaviour of demagnetized SmCo 1:5, SmCo 2:17 and NdFeB magnets we have used transmission electron microscopy and X-ray microanalysis together with optical metallography to characterize crystal defects, precipitates and different phases and to study the magnetic domain structure and their interaction with crystal lattice defects and precipitates. The microstructure of *single phase SmCo 1:5 magnets* consists of grains oriented parallel to the alignment direction, of precipitates with diameters comparable to the grain size and of precipitates with diameters up to 500 nm (14). Most of the $SmCo_5$ grain interiors show a low defect density and their grain diameter exceeds the theoretical single domain size (1:2 μm) and is in the order of 5–10 μm. Except isolated grain boundary inclusions, partly identified as a CaO-phase, our electron microscope investigation does not show a preferential segregation of a second phase at grain boundaries. Besides 1:5-grains also grains with densly packed, parallel

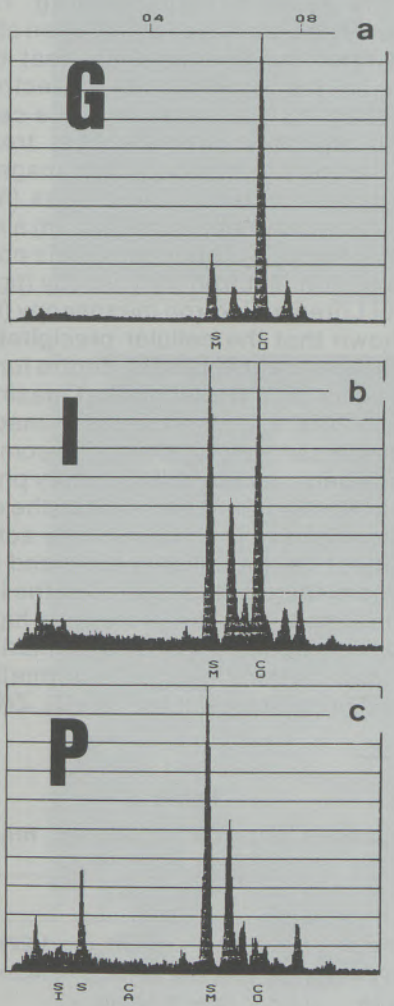

Fig. 10
Energy dispersive X-ray spectra of a hard magnetic grain G, of a rare earth-rich phase I and of a rare earth-oxide phase P of a sintered SmCo 1:5 magnet

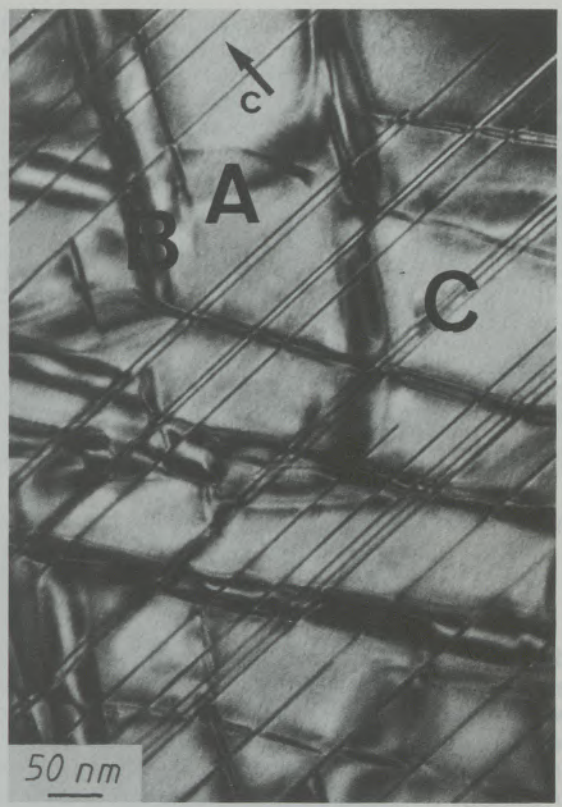

Fig. 11
Electron micrograph showing the cellular precipitation structure of a sintered SmCo 2:17 magnet. Rhombic cells – phase A – are separated by a cell boundary phase B. In high coercivty magnets a platelet phase C is found

stacking faults perpendicular to the hexagonal c-axis are observed (fig. 9a). Such basal stacking faults correspond to a transformation of the 1:5-crystal structure into the Sm-rich Sm_2Co_7 and Sm_5Co_{19} structure types. Using high resolution electron microscopy together with X-ray STEM microanalysis the different polytypes and structural modifications of these Sm-rich phases can be distinguished (15), (16). In all of the single phase SmCo 1:5 sintered magnets incoherent precipitates with diameters up to 0.5 μm were found (fig. 9b). Some of these precipitates show only intense Sm-peaks in their X-ray spectra (fig. 10). These precipitates were identified as Sm_2O_3-particles. Occasionally some of the X-ray spectra of grains and especially of grain boundaries and precipitates an additional Si-peak was found. In some of the CaO- and Sm_2O_3-particles sulphur could be detected. In single phase SmCo 1:5 sintered magnets the coercivity is determined by the nucleation field of reversed domains which is lower than the coercive force of a magnetically saturated particle with a single domain structure. The nucleation of reversed domains takes place in regions with low magneto-crystalline anisotropy. Rare earth-rich precipitates mainly deteriorate the coercivity of the final magnet. The reason for the formation of these phases is due to the

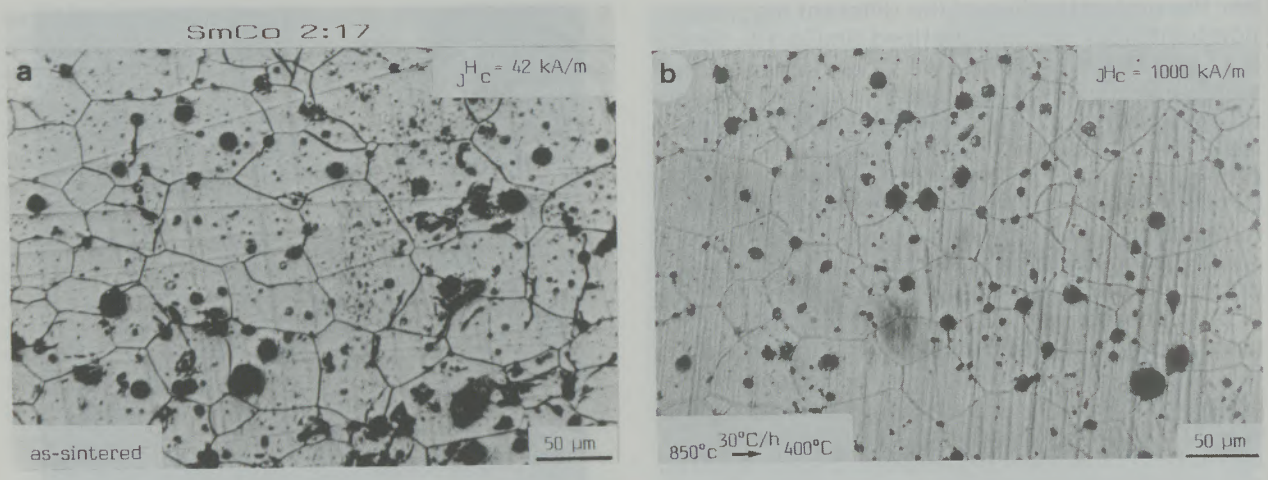

Fig. 12
Optical micrographs show no difference in the grain size distribution in the as-sintered and after an optimum post-sintering heat treatment of a SmCo 2:17 magnet

addition of a rare earth-rich sintering aid phase before the sintering process. The coercivity can be improved by adding small amounts of transition metal powders or transition metal oxides. Microstructural investigations on (CeMM,Sm)Co_5 and (Pr,Sm)Co_5 sintered magnets showed similar results as in the case of single phase $SmCo_5$ sintered magnets (16), (17). The corresponding X-ray spectra of the different phases showed a mixture of rare earth elements due to their ratio of the nominal composition of the magnet. Our analytical electron microscope study shows that the chemical composition, the size distribution and the impurity content of the starting powder material are important factors for the magnetic properties of SmCo 1:5 sintered magnets.

Copper containing cobalt rare earths with a composition of $Sm(Co,Fe,Cu,TM)_{6-8}$ TM = Zr,Ti,Hf show a fine scale, cellular microstructure (18), (19). Rhombic cells of the type $Sm_2(Co,Fe,TM)_{17}$ – phase A – are separated by a $Sm(Co,Cu,TM)_5$ cell boundary phase – phase B (fig. 11). In magnets with high coercivities (> 1000 kA/m) thin platelets are found perpendicular to the hexagonal c-axis. Our high resolution electron microscope investigations (18) show that the crystal structure of the platelet phase C is close to the hexagonal Sm_2Co_{17} structure with a c-crystal parameter of 0.8 nm, which is in agreement with metallurgical considerations (20). The development of the cellular precipitation structure of highest coercivity magnets is controlled by the growth process and the chemical redistribution process and is determined by the direction of zero deformation strains due to the crystal lattice misfit between the different phases (21). Growth occurs primarily during the isothermal aging procedure and involves the diffusion of samarium. The cellular precipitation structure is formed during the isothermal aging procedure, whereas the chemical redistribution of the transition metals during the step aging procedure increases the coercivity of the final magnet (fig. 7). The optical micrographs of fig. 12 show no difference in the grain size distribution after sintering and after the postsintering heat treatment, whereas in the corresponding electron micrographs of fig. 13 the formation of the cellular precipitation structure after the heat treatment is shown. Contrary to high coercivity magnets which contain large crystallographic twins (fig. 14a) in low coercivity magnets (<500 kA/m) a microtwinning within the cell interior phase A is observed by high resolution electron microscopy (fig. 14b). By means of Lorentz electron microscopy (fig. 15) we have shown that the cellular precipitation structure acts as attractive pinning centre for magnetic domain walls (21). We found that maximum coercivities (~2000 kA/m) occurred in magnets with cell diameters of about 200 nm. The compositional difference between the cell boundary phase B and the cell interior phase A determines the coercivity. The platelet phase C predominately acts as diffusion path for the transition metals and leads to a better chemical redistribution after the isothermal aging treatment and therefore to a higher coercivity of the magnet. Impurities, primarily such as oxygen and carbon, lead to the formation of macroscopic precipitates of the Sm_2O_3, ZrC, TiC etc.

Table 3

Phases in sintered $Nd_{15}Fe_{77}B_8$ magnets

				MH
A	$Nd_2Fe_{14}B$	tetr.	a = 0.88 nm, c = 1.22 nm	950
B	$Nd_{1+\varepsilon}Fe_4B_4$	tetr.	a = 0.71 nm, c = 14.5 nm	1430
C	Nd-rich	f.c.c.	a = 0.52 nm	360
D	Nd-oxides	hex.	a = 0.38 nm, c = 0.60 nm	
E	α – Fe	b.c.c.	a = 0.29 nm	190

Not detected: Nd_2Fe_{17}, $NdFe_2$ / MH . . . microhardness

and therefore impede the formation of the platelet phase C and finally impede the chemical redistribution process.

Sintered *NdFeB magnets* with a nominal composition $Nd_{15}Fe_{77}B_8$ exhibit the highest energy density products so far (3). These magnets show magnetization curves according to the nucleation of reversed domains (fig. 8). As result of our microstructural investigations an identical microstructure in various magnets, supplied by different producers, was observed. The following phases were detected by analytical electron microscopic techniques and are summarized in table 3. The optical (fig. 16a) and the electron (fig. 16b) micrographs show three different types of phases, each with a different chemical composition, occurring in sin-

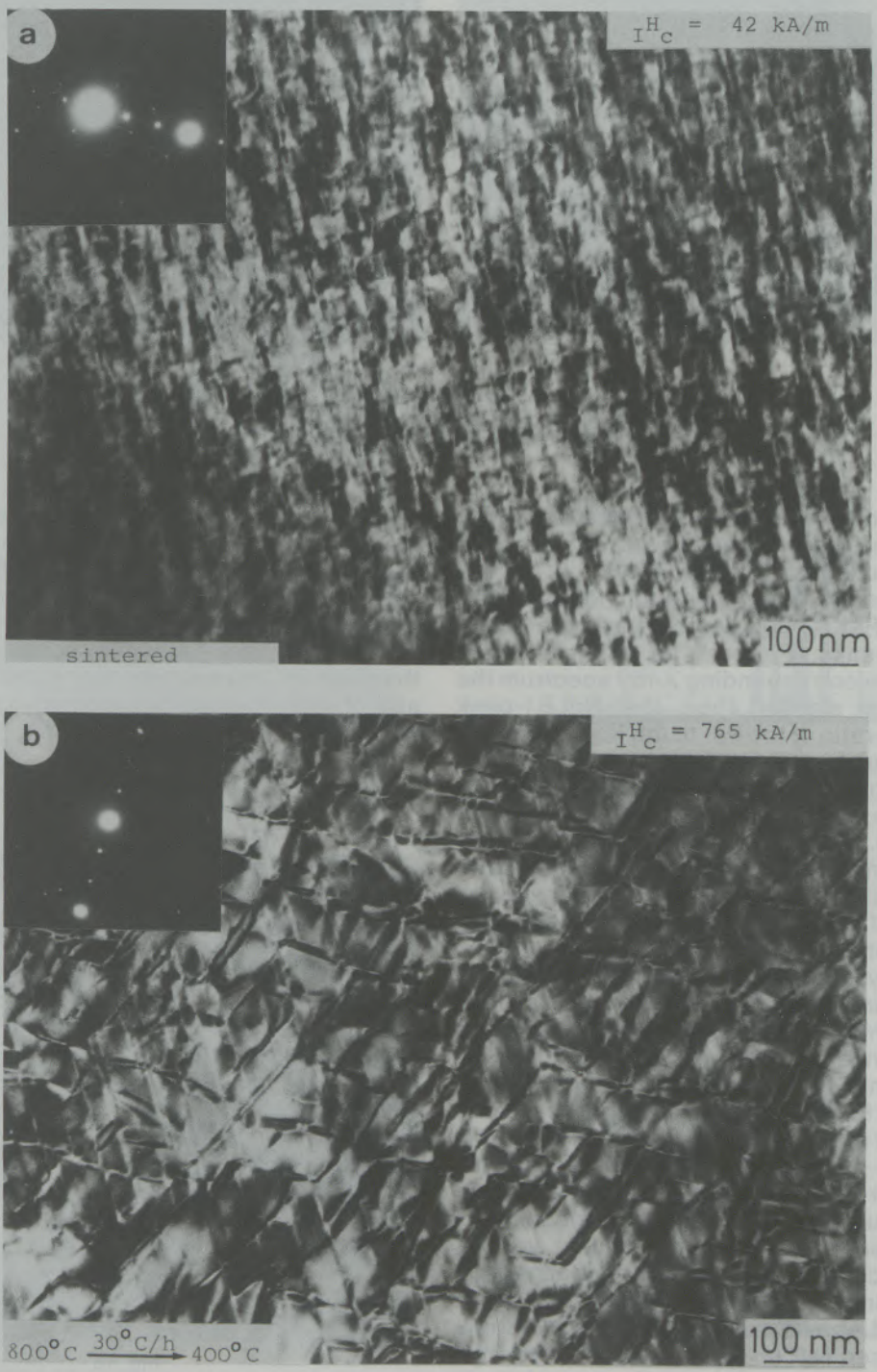

Fig. 13
Electron micrographs showing the influence of the heat treatment on the cellular microstructure and therefore on the coercivity of the magnets of fig. 12

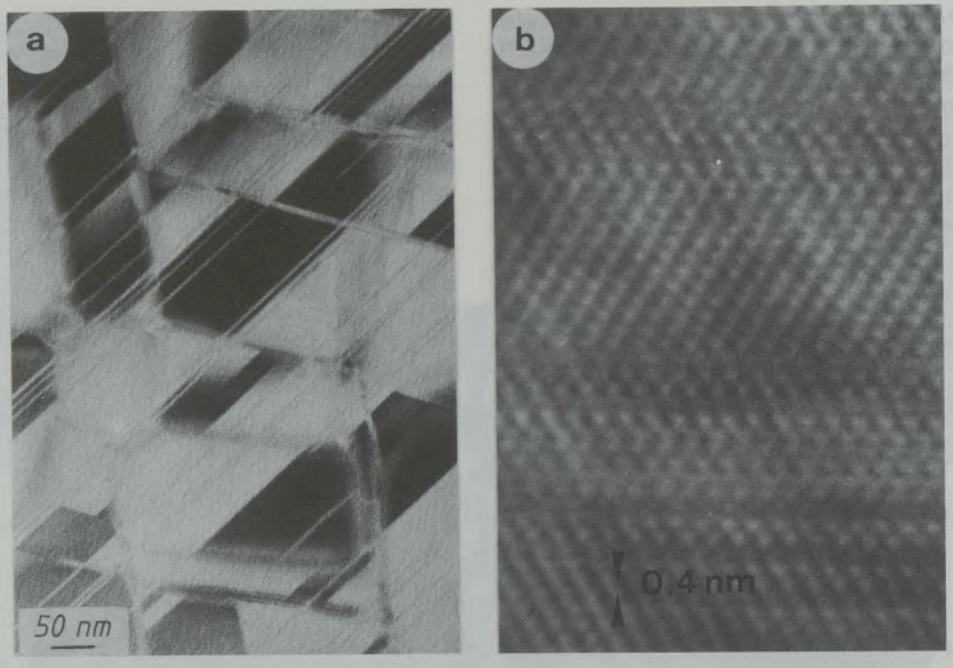

Fig. 14
Bright field (a) and high resolution (b) electron micrographs showing the twinning in high coercivity (1000 kA/m) and low coercivity (400 kA/m) SmCo 2:17 magnets

tered NdFeB magnets. Phase A is always found to be free of crystal lattice defects and corresponds to the hard magnetic boride $Nd_2Fe_{14}B$. In the energy dispersive X-ray spectrum of phase A (fig. 17a) the FeKB-peak lies between the NdLA- and NdLB1-peaks. Phase B is Nd-richer than phase A. In the corresponding X-ray spectrum the FeKB-peak is smaller than the NdLB1-peak (fig. 17b). The ratio of the Fe- to the Nd-concentration (in at%) was found to be in the range 3.6 to 3.9. Our high resolution electron studies revealed a crystal lattice periodicity of 0.4 nm, 4.8 nm and 14.5 nm (22). Both results, obtained by X-ray STEM microanalysis and high resolution electron microscopy, are in agreement with structural and compositional data of the phase $Nd_{1.109}Fe_4B_4$ (23). The grain interior of phase B shows a high crystal defect density, which explains the large value of the microhardness (see table 3). Phase C is found to be a Nd-rich sintering aid phase. The ratio of the Nd- to Fe-concentration (in at%) determined by X-ray microanalysis is about 6 corresponding to about 85 at% Nd. This phase may also occur with some content of oxygen and/or boron. Phase C is mainly found as isolated inclusions near grain boundaries or as layer phase along grain boundaries. It should be mentioned that depending on the raw material used by the producer various impurities such as silicon, chlorine, phosphorus, niobium, platinum, tin etc. are found in all of the phases listed above. As result of our investigations of sintered NdFeB magnets, produced by a powder metallurgical process, the coercivity is primarily determined by the magnetization reversal within the hard magnetic $Nd_2Fe_{14}B$ grains and is limited by the nucleation and expansion field for reversed domains. The layer phase, separating the hard magnetic grains, contributes also to the coercivity. Replacing neodymium by dysprosium (Nd:Dy = 10:1) increases the coercivity, but does not show any drastic effect on the composition of the different phases, whereas generally the grain size of such magnets is considerably smaller than in magnets without dysprosium.

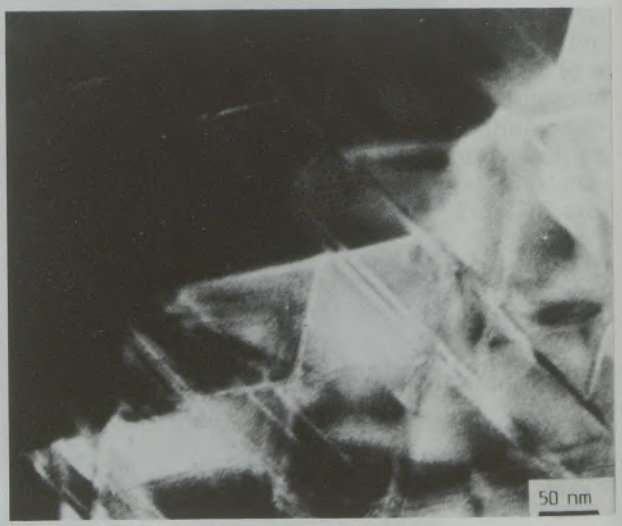

Fig. 15
Foucault electron micrograph showing the pinning of a magnetic domain wall at the continuos cellular precipitation structure

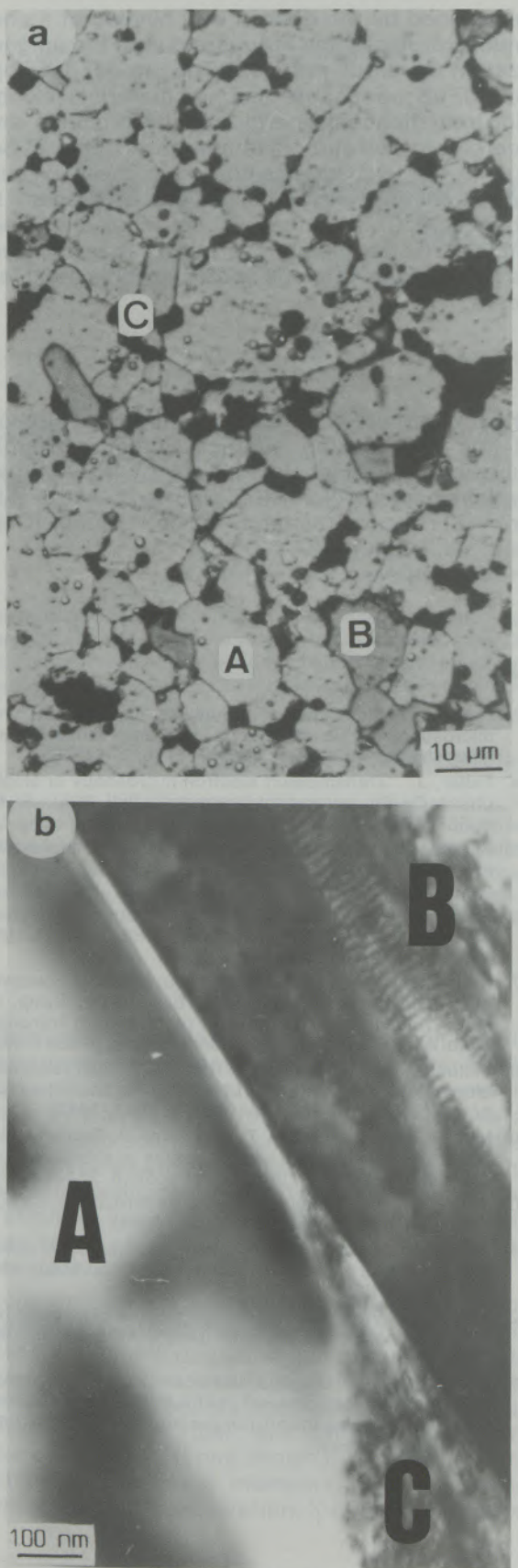

Fig. 16
Optical (a) and transmission electron (b) micrographs showing various phases in a sintered $Nd_{15}Fe_{77}B_8$ magnet

3. Conclusions

Newly developed magnetic materials such as rare earth permanent magnets are increasingly used in many magneto- and electromechanical and electronic applications. One of the reasons is a better understanding of the microstructure of the materials which determines besides the processing parameters the magnetic properties of the magnets (fig. 18). Effectively the magnetic energy density product and the coercivity could be improved drasticly during the last ten years. As result of analytical investigations it is evident that the coercivity is closely related to the individual microstructure of the magnets. In the case of shape anisotropy materials (AlNiCo, FeCrCo) the magnetocrystalline anisotropy is relatively small and the coercivity is controlled by shape anisotropy, the volume fraction of the strongly magnetic phase and the difference of the magnetization of the different phases. In hardferrites, SmCo 1:5 and NdFeB magnets the high coercive forces are primarily obtained by the high magnetocrystalline

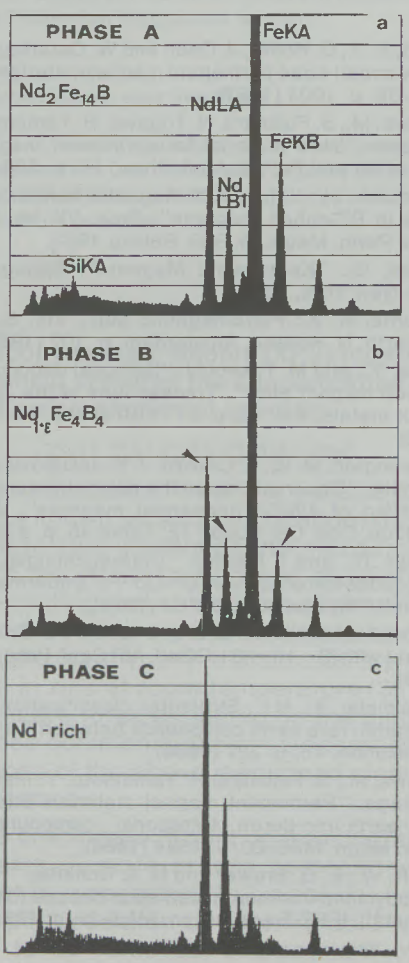

Fig. 17
Energy dispersive X-ray spectra taken by STEM-microanalysis of the various phases of a sintered $Nd_{15}Fe_{77}B_8$ magnet

anisotropies and are limited by the nucleation and expansion of reversed domains. In precipitation hardened SmCo 2:17 magnets the coercivity is determined by the domain wall pinning at a continuous precipitation structure during the magnetization reversal process. The newly developed NdFeB permanent magnet materials exhibit high remanences, energy density products and coercive forces at room temperature (table 2), but due to the low Curie temperature the maximum operation temperature is limited at present to about 120 °C. It can be expected that this upper limit of the operation temperature can be increased by a further magnetic hardening in the next few years.

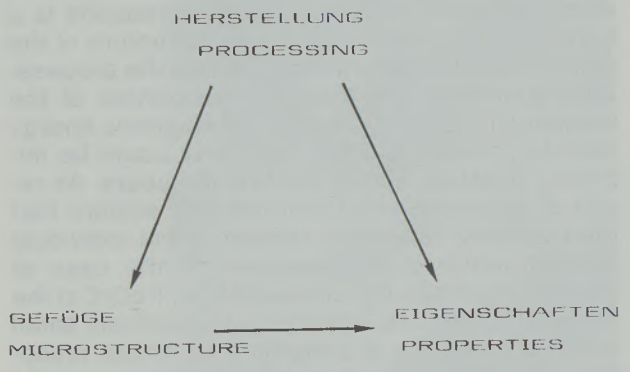

Fig. 18
The magnetic properties of permanent magnet materials are primarily determined by processing parameters and by the microstructure

Acknowledgement

The authors are grateful for the financial support of this work by the Austrian Forschungsförderungsfonds (Project No. P4640), by the Austrian Nationalbank (Projekt No. 2088) and by the U.S. Army European Research Office, London (Contract No. DAJA 45-84-C-0010).

References

1. Strnat, K. J., G. Hoffer, J. Oson and W. Ostertag: "A family of new cobalt-base permanent magnet materials", J. Appl. Phys. 38, p. 1001 (**1967**).
2. Sagawa, M., S. Fujimura, N. Togawa, H. Yamamoto and Y. Matsuura: "New material for permanent magnets on a base of Nd and Fe", J. Appl. Phys., 55, p. 2083 (**1984**).
3. Kronmüller, H.: "Theory of magnetic hardening mechanisms in RE-cobalt magnets", Proc. VII. Int. Workshop RE-Co Perm. Magn., p. 339, Beijing **1983.**
4. Heimke, G.: "Keramische Magnete", Springer Verlag, Wien, New York, **1976.**
5. McCurrie, R. A.: Ferromagnetic Mat., Vol. 3, ed. E. P. Wohlfarth, N. Holland, Amsterdam, p. 107 (**1982**).
6. Iwama, Y., and M. Takeuchi: "Spinodal decomposition in AlNiCo8 magnet alloy", Transactions of the Japan Institute of metals, Vol. 15, p. 371 (**1974**) and Vol. 17, p. 399 (**1976**).
7. Hetherington, M. G., A. Cerezo, J. P. Jakubovics and G. D. W. Smith: "Observations on the microstructure and magnetization of AlNiCo permanent magnets", Journal de Physique, Coll. C9, Cuppl. 12, Tome 45, p. 429 (**1984**).
8. Cremer, R., and I. Pfeiffer: "Untersuchungen zum Ausscheidungsverhalten von Cr–Co–Fe Dauermagnetlegierungen", Physica 8OB, p. 164 (**1975**).
9. Kaneko, H., M. Homma and M. Okada: "Fe–Cr–Co ductile magnet with (B · H) = 8 HGOe", AIP Conf. Proc. 29, p. 620 (**1975**).
10. Stadelmaier, H. H.: „Structural classification of transition-metal/rare earth compounds between T and T_5R", Z. Metallkunde, 75, p. 227 (**1984**).
11. Sagawa, M., S. Fujimura, H. Yamamoto, Y. Matsuura and K. Hiraga: "Permanent magnet materials based on the rare earth-iron-boron tetragonal compounds", IEEE Trans. Magn. MAG-20, p. 1584 (**1984**).
12. Lee, R. W., E. G. Brewer and N. A. Schaffel: "Processing of neodymium-iron-boron melt-spun ribbons to fully dense magnets", IEEE-Trans. Magn. MAG-21, p. 1958 (**1985**).
13. Fidler, J., P. Skalicky and F. Rothwarf: "Analytical electron microscopy of rare-earth permanent magnet materials", Mikrochimica Acta (Wien), Suppl. 11, p. 371 (**1985**).
14. Fidler, J.: "Transmission electron microscopy of single-phase Co_5Sm permanent magnets", Phil. Mag., B 46, p. 565 (**1982**).
15. Fidler, J., and P. Skalicky: "Microanalysis and microstructure of cobalt-containing permanent magnets", Metallurgie, in press.
16. Ghandehari, M. H., and J. Fidler: "Microstructural studies of oxide doped $PrCo_5$ magnets", IEEE Trans. Magn., MAG-21, p. 1973 (**1985**).
17. Rodewald, W., and J. Fidler: "Improvement of coercivity of (CeMM, Sm)Co_5-magnets", Proc. 3rd Int. Symp. on Magn. Anisotropy and Coercivity of Rare Earth Transition Metal Alloys (J. Fidler, ed.), Baden/Austria, p. 339 (**1982**).
18. Fidler, J., P. Skalicky and F. Rothwarf: "High resolution electron microscope study of $Sm(Co, Fe, Cu, Zr)_{7.5}$ magnets", IEEE-Tran. Magn. MAG-19, p. 2041 (**1983**).
19. Mishra, R. K., G. Thomas, T. Yoneyama, A. Fukuno and T. Ojima: "Microstructure and properties of step aged rare earth alloy magnets", J. Appl. Phys. 52, p. 2517 (**1981**).
20. Ray, A. E.: "Metallurgical behavior of $Sm(Co, Fe, Cu, Zr)_z$ alloys", J. Appl. Phys., 55, p. 2094 (**1984**).
21. Fidler, J.: "Coercivity of precipitation hardened cobalt rare earth 17:2 permanent magnets", J. Magn. Magn. Mat. 30, p. 58 (**1982**).
22. Fidler, J.: "Analytical microscope studies of sintered Nd-Fe-B magnets", IEEE Trans. Magn. MAG-21, p. 1955 (**1985**).
23. Bezinge, A., H. F. Braun, J. Muller and K. Yvon: "Tetragonal rare earth-iron borides $R_1 + \varepsilon Fe_4B_4$ ($\varepsilon \cong 0.1$) with incommensurate rare earth and iron substructures", Solid State Commun., in press.

Surface Investigations of Hot-Dip Galvanized Steel Sheets

Wolfgang Gröger, Michael Mayr, Horst Ebel and Johann Wernisch, Wien*)

Dedicated to the 80th birthday of Prof. Dr. Franz Lihl

Hot-dip galvanized steel sheets become stained after a period of storage. The evidence are dark areas in zinc-spangles. The first occurence and the degree of darkening depends on the conditions of storage, atmosphere, temperature and besides on the thickness of zinc-layer and the way of passivation. Surface analytical techniques provide clear evidences for the contribution of precipitated metallic lead to this phenomenon.

Oberflächenuntersuchungen an feuerverzinkten Stahlblechen

Feuerverzinktes Stahlblech zeigt nach einer bestimmten Lagerungszeit ein Auftreten dunkler Flächen in Zinkblumen. Die Art der Lagerung, umgebende Atmosphäre, Temperatur und darüber hinaus Dicke der Zinkschicht und Art der Passivierung beeinflussen das erste Auftreten bzw. das Ausmaß der Dunkelfärbung. Mittels oberflächenanalytischer Methoden konnte eindeutig der Einfluß von ausgeschiedenem metallischen Blei auf dieses Phänomen festgestellt werden.

Etude des surfaces de tôles d'acier galvanisées par trempé

Au bout d'un certain temps de stockage, les tôles en acier galvanisé par trempé présentent des taches foncées parmi les efflorescences de zinc. Les facteurs agissant sur la première apparition on sur l'étendue de ces zones de coloration foncée sont: le mode de stockage, l'atmosphère environnante, la température et aussi l'épaisseur de la couche de zinc et le mode de passivation. Des méthodes d'analyse de surfaces ont permis d'établir nettement l'influence, sur ce phénomène, de plomb métallique précipité.

Introduction

White rust is formed on the surface of hot-dip galvanized steel sheets when stored under humid atmosphere. A description of the phenomenon is given by Leroy (1): "During such storage metal ions go into solution at anodic areas and hydrogen is evolved at cathodic areas. A saturated zinc hydroxide solution is formed from which solid may precipitate when the water evaporates. This may then react chemically with oxygen and carbon dioxide in the atmosphere."

Protection against white rust is frequently done by a passivation treatment (2). Dipping into chromic acid for example causes a thin chromi-chromate layer on the outmost surface of the zinc layer. The protective components against corrosion in this chromi-chromate film are chromium-(VI)-compounds. Leroy (1) has shown the in-depth distribution of significant elements of zinc coating without and with passivation. X-ray photoelectron spectroscopy measurements (XPS) together with Ar-ion etching provided the concentration profiles of the following elemental species:

$$Zn^{2+}\ Zn^{\circ}\ Cr^{3+}\ O\ Al^{3+}\ Pb^{\circ}$$

(and of course carbon from the surface contamination). As known an addition of about 0.2 wt% of aluminum to zinc influences the mechanical properties of the interface between steel-substrate and zinc-coating and an addition of about 0.1 wt% of lead reduces the crystallite size of zinc. Since there exists hardly any solid solubility of both elements in zinc at room temperature (3), (4) precipitations are to be expected on the plating surface. These comments explain measured indepth distributions of the above mentioned elements as given by tab. 1.

Thus, the precipitate is built up from metallic lead and alumina. A more or less homogeneous alumina layer is – according to Leroy (1) – responsible for poor reaction of chromic acid with zinc and has to be removed. A treatment of a few seconds with soda-solution decreases the alumina content from 8 to 1 mg per m² and in addition to it dissolves zinc oxide, allowing chromic acid to react more effectively with zinc. Such an additio-

*) Dr. Wolfgang Gröger, Dr. Michael Mayr, o. Univ.-Prof. Dr. Horst Ebel, Univ.-Doz. Dr. Johann Wernisch, Institut für Angewandte und Technische Physik, Technische Universität Wien, A-1040 Wien, Karlsplatz 13

Table 1

In-depth distribution of different elements as published by Leroy (1)

detected atomic species	without passivation	with passivation
Zn^{2+}	<10 nm	<40 nm
Zn^{o}	>10 nm	>40 nm
Cr^{3+}		<20 nm
O	<20 nm	<40 nm
Al^{3+}	<20 nm	<40 nm
Pb^{o}	<20 nm	<60 nm
C	< 1 nm	< 5 nm

nal preparation of hot-dip galvanized steel in advance of passivation led to a remarkable improvement of corrosion resistance.

As will be shown by our investigations the passivation procedure does not only influence the onset of white rust formation. Applying the normal procedure to hot-dip galvanized steels without removal of alumina causes staining in the course of storage. Dark zinc spangles appear. This is also observed on surfaces without passivation, but the probability of its occurence increases under the mentioned circumstances.

Darkening

Our experiments included the following techniques:

Auger electron spectroscopy (AES)
Scanning Auger electron spectroscopy
X-ray photoelectron spectroscopy (XPS)
Secondary ion mass spectroscopy (SIMS)
Atomic absorption spectroscopy (AAS)
Surface roughness measurements
Texture determination by X-ray diffraction
Scanning electron microscopy combined with electron probe micro analysis (SEM)

From AES we learned about the existence of C, O, Zn, Cr and Cl on the surface and scanning Auger electron spectroscopy gave an idea of imperfect passivation layer. In areas with low chromium signal we found strong zinc signals and vice versa. XPS-results were much more fascinating. A broad oxygen signal indicates a number of different oxygen compounds, zinc and chromium are in bright areas about twice as much as in dark ones. Lead, aluminium and sulfur are stronger represented in dark areas. According to Wagner (5) the line position of sulfur is an evidence for sulfate. The in-depth profiles from SIMS gave comparable values to Leroy's investigations (1). Lead is found down to a depth of about 50 to 100 nm and chromium ranges in between zero and 10 nm. Especially the latter result supports again the assumption of a poor passivation layer. An ultrasonic treatment in distilled water helped us to remove those products from the surface just having a loose contact to it. AAS measurements of the washed out substance showed a much higher amount of zinc from dark areas compared to bright areas. Therefore, the dark substance seems to be a product consisting of a zinc compound. In dark portions surface roughness is also much more pronounced. The result of texture measurements is described by the spatial distribution of the zinc-

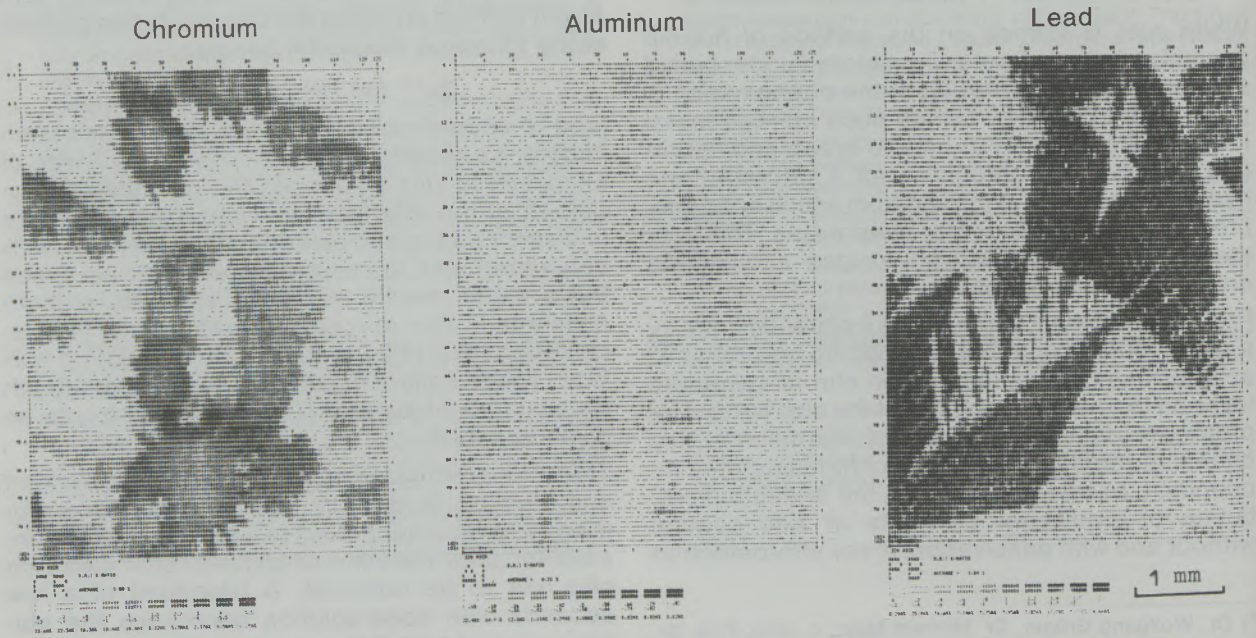

Fig. 1
Elemental distribution of lead, chromium and aluminum within an area of 4×5.5 mm²

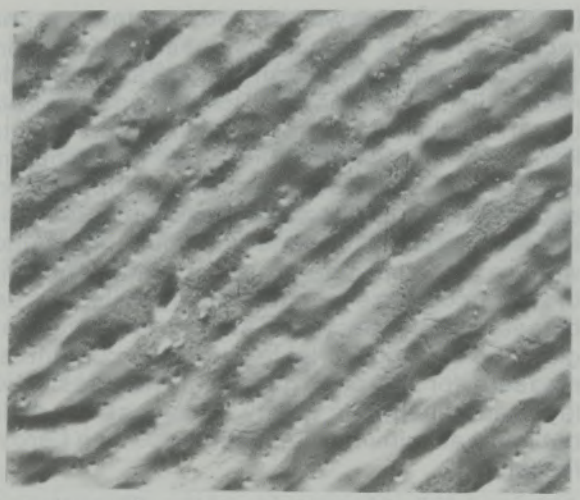

SE

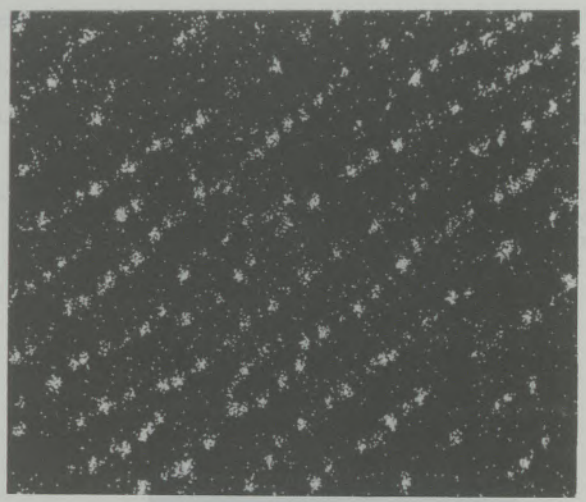

Pb

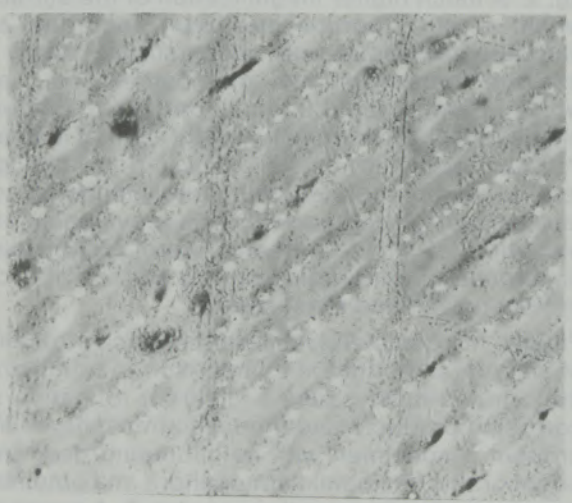

BE

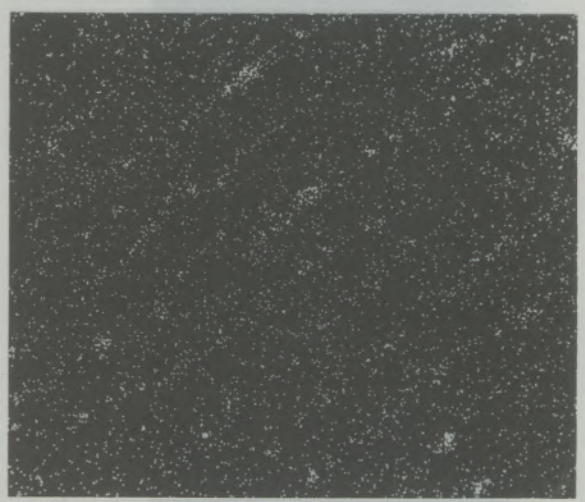

Cr

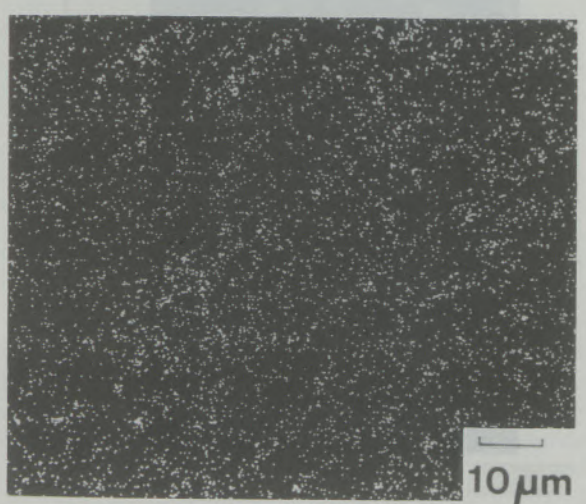

Al

Fig. 2
Rough portion of plating, magnified 1000×. Secondary electron backscattered electron image, aluminum, chromium and lead distribution

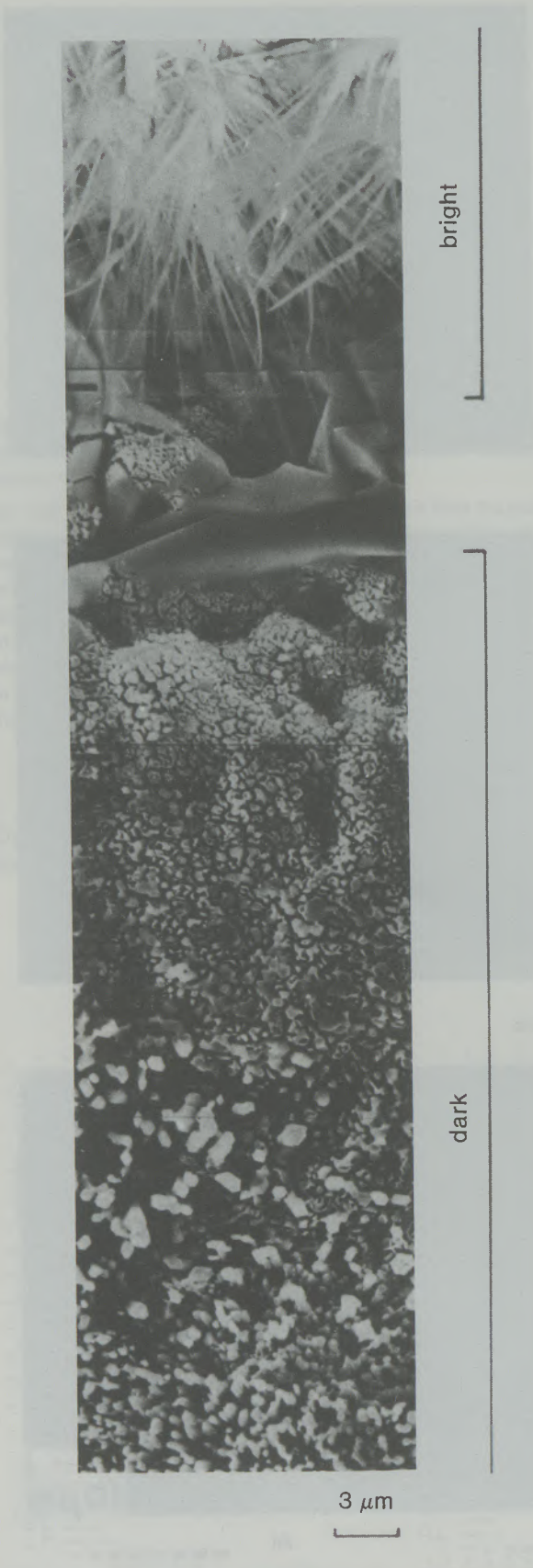

Fig. 3
SEM micrographs. The upper portion illustrates an advanced state of corrosion within a bright grain and the lower within a dark grain

(002)-plane. Grains with a smooth surface are characterized by a distribution nearly at random, whereas grains with rough surface show a preferential distribution parallel to the surface of plating. The influence of the crystallographic orientation on the precipitation behaviour is demonstrated by fig. 1. A new technique (6) developed by one of the authors of this paper enabled us to depict the lead-, aluminium- and chromium distribution within a selected surface area of a few mm in spite of their occurence in extremely thin films. As can be seen, lead reflects the structure of zinc spangles, the strongly variable chromium content is a measure for the poor quality of the passivation layer and finally the nearly homogeneous distribution of aluminum is in accordance with Leroy's findings (1).

A more detailed impression of the different precipitation of lead and aluminum is obtained from fig. 2. A much higher magnification of the surface within a rough portion has been performed by standard technique and demonstrates again a homogeneous aluminum distribution and lead which is precipitated in small particles. This explains in fact the surprising XPS-result of lead as Pb° and aluminum as Al^{3+}. Thick zinc coatings tend to precipitate their comparably higher absolute amount of lead as well. This provides an explanation of the faster and more pronounced occurence of dark grains on the surface of such hot-dip galvanized steel sheets.

Finally, the completely different surface structure of smooth and bright in comparison to rough and dark grains must cause a different formation of corrosion products under humid atmosphere. We brought a specimen with neighbouring dark and bright grains into humid atmosphere and obtained a surface structure as shown in fig. 3. A series of micrographs has been put together in order to give an idea on the difference of the corrosion products as created under identical conditions.

Conclusion

The corrosion resistance of hot-dip galvanized steels is determined by the quality of the passivation layer. Dark zinc spangles can be found on surfaces without passivation too, but together with a passivation treatment this phenomenon becomes more probable. From the elemental distribution and physical properties it must be concluded that elemental lead acts as local element thus causing dark staining of hot-dip galvanized steels stored under certain conditions.

Acknowledgement

One of the authors (H. E.) would like to express his gratitude to the "Hochschuljubiläumsstiftung der Stadt Wien" for granting financial support for the Project "Untersuchungen früher Stadien der Korrosion" which enabled us to buy an electron detector.

References

1. Leroy, V.: "Metallurgical Applications of Surface Analytical Techniques", Materials Sciences and Engeneering, 42.289 (**1980**).
2. Zinktaschenbuch, Metall Verlag GmbH, Berlin, Grunewald (**1959**).
3. A Handbook of Lattice Spacings and Structure of Metals and Alloys, Pearson W. B., Pergamon Press (**1958**), p. 389 ff.
4. Constitution of Binary Alloys, Hansen M. and Anderko K., McGraw Hill Book Company Inc. (**1958**), p. 148 ff.
5. Wagner, C. D., W. M. Riggs, L. E. Davis, J. F. Moulder and G. E. Muilenberg: "Handbook of X-Ray Photoelectron Spectroscopy, Perkin Elmer Corp., Eden Prairie (**1979**).
6. Mayr, M., and J. Angeli: "Concentration Mapping – a Software Package for the Quantitative Determination of Two-Dimensional Elemental Distribution by an Electron Probe "Microanalyser", XRS 14, 89 (**1985**).

Magnetic Ordering in $Y(Fe,M)_2$ Laves Phases M = Al, Co, Rh, Ir

Walter Steiner and Michael Reissner, Wien*)

Dedicated to the 80th birthday of Prof. Dr. Franz Lihl

The magnetic properties of cubic Laves phases $Y(Fe, M)_2$, M = Al, Co, Rh and Ir are discussed. Pauli paramagnetism is obtained for all four YM_2 compounds. The appearance of a percolation limit for the onset of long range magnetic order, which depends strongly on the matrix susceptibility, is characteristic for all investigated series $Y(Fe,M)_2$. Mictomagnetic behavior can be deduced from magnetic, Mössbauer and neutron depolarization measurements below the percolation limit.

Magnetische Ordnungszustände in $Y(Fe, M)_2$ Lavesphasen, M = Al, Co, Rh, Ir

Die magnetischen Eigenschaften der kubischen Lavesphasen $Y(Fe, M)_2$, M = Al, Co, Rh and Ir werden diskutiert. Für die vier Verbindungen YM_2 ist Pauliparamagnetismus zu beobachten. In allen untersuchten Reihen $Y(Fe, M)_2$ ist für das Einsetzen einer langweitreichenden magnetischen Ordnung das Auftreten einer Perkolationsgrenze, die von der Matrixsuszeptibilität bestimmt wird, charakteristisch. Aus den magnetischen, Mössbauer- und Neutronendepolarisationsmessungen ist auf Mictomagnetismus bzw. Clusterglasverhalten unterhalb der Perkolationsgrenze zu schließen.

Etats d'ordre magnétique dans les phases de laves $Y(Fe, M)_2$ avec M = Al, Co, Rh, Ir

On discute les propriétés magnétiques de phases cubiques de laves du système $Y(Fe, M)_2$ avec M = Al, Co, Rh ou Ir. Pour les quatres composés de type YM_2, on observe le paramagnétisme de Pauli. Dans toutes les séries du système $Y(Fe, M)_2$ étudiées on note l'existence caractéristique, pour l'installation d'un ordre magnétique de longue portée, une limite de percolation qui dépend de la susceptibilité de la matrice. D'après les mesures d'effet Mössbauer et de dépolarisation de neutrons, on consclut à un mictomagnétisme ou à un comportement de verre aggloméré au-dessous de la limite de percolation.

1. Introduction

Yttrium forms a number of intermetallic compounds with 3d- and 4d-transition metals, which offer the interesting possibility to exchange iron with one of the transition metal atoms without changing the crystal structure. Furthermore, compounds with the same crystal structure are formed, where the transition metals are substituted by aluminum. Therefore pseudo-binary mixed crystal series allow a detailed investigation of the exchange interactions between the iron and the transition metal atoms as well as between the iron atoms themselves.

Striking discrepancies arise from a comparison of Y_xFe_{1-x} with Y_xCo_{1-x}. The magnetic moments of the Fe atoms decrease approximately linearly with increasing x, whereas the ordering temperatures increase with x after a first sharp drop at $x \sim 0.11$. In YFe_2 the Fe atoms still have a magnetic moment. Contrary to that both the Co moment and the ordering temperatures decrease with increasing x for the Y-Co compounds. On the other hand, in the amorphous state the ordering temperature increases in (Y, Co)-alloys and decreases in (Y, Fe)-alloys and the transition metal moment increases in both systems (1), (2), (3). Thus the vanishing of the Co moment observed in YCo_2 seems to be connected with the crystalline state, since for amorphous compounds a Co moment of 1.6 μ_B was obtained (4). These results have stimulated the investigation of magnetic order caused by the substitution of iron in pseudo-binary cubic Laves phases with the nominal composition YM_2, which fullfill the condition that Fe can be substituted for the M atoms over a large concentration range without destroying the crystal structure.

The unit cell of Laves phases is relatively simple and exhibits high symmetry. In this cell the Y atoms are arranged in a diamond lattice and the M atoms form tetrahedras with the point symmetry $\bar{3}m$. Each Y atom is surrounded by 4 Y and 12 M atoms as nearest neighbors. The distance between Y atoms is only 4% larger than the distance between Y and M atoms. Every M atom has 6 nearest and 12 next nearest M neighbors and is

*) Univ.-Doz. Dr. Walter Steiner, Dipl.-Ing. Michael Reissner, Institut für Angewandte und Technische Physik, Technische Universität Wien, Karlsplatz 13, A-1040 Wien

surrounded by 6 Y nearest neighbors. Fe which substitutes the M atoms is therefore situated on well defined lattice sites in magnetically different matrix materials.

This paper attempts to compile the experimental data in a comprehensive form in order to contribute to the understanding of the magnetic order caused by this iron substitution in cubic Laves phases $Y(Fe, M)_2$, M = Al, Co, Rh and Ir. A more detailed description, and above all a complete list of references can be found in the original papers concerned with $Y(Fe, Al)_2$ (5), (6), (7), $Y(Fe, Co)_2$ (7), (8), (9), $Y(Fe, Rh)_2$ (10) and $Y(Fe, Ir)_2$ (11).

2. $Y(Fe, Al)_2$

Although both compounds YFe_2 and YAl_2 form the cubic $MgCu_2$ structure type, the hexagonal $MgZn_2$ structure type was observed in the intermediate concentration range (12), (13), (14). Tendencies for a preferential accomodation for Fe on one of the crystallographically nonequivalent lattice sites (6h and 2a in the Wyckoff notation) of the hexagonal $MgZn_2$ structure type are reported (12), (13). Therefore the hexagonal compounds have been omitted in our investigations. For the cubic compounds the lattice constants increase approximately linearly with increasing Al content. On the Fe-rich side single phased samples could only be prepared with a Y excess of 10–15wt% over the stoichiometric composition. In this concentration range the line widths of the Bragg-peaks obtained from X-ray diffraction measurements are approximately twice those measured for the calibration standard (quartz). An exception was the sample with x = 0.65 for which a broadening of roughly 30% was recorded. On the Al-rich side for all Fe containing samples the diffraction peaks were not only broadened but also structurized. Since no additional lines could be detected, the existence of regular multilayers sequences, reported for Laves phases which exhibit a structural change from the cubic to the hexagonal structure type (15) must be excluded. An analysis by taking into account a distortion of the $MgCu_2$ structure type was not successful. Generally a distortion of approximately 1% was sufficient to obtain the observed line broadenings, however the resulting line intensities for the different diffraction peaks are in disagreement with the theoretically calculated ones for every selected type of distortion. From this the existence of regions with different Fe-concentrations might be a possible explanation. From the linear concentration dependence of the lattice spacings an upper limit can be estimated of 3–7% for these concentration differences. These fluctuations are independent of both the conditions of the sample preparation and the excess of Y.

YAl_2 shows a nearly temperature independent paramagnetic behavior with a room temperature susceptibility value of $\chi = 0.8 \cdot 10^{-6}$ cm^3/g. From bulk magnetic measurements no magnetic order was detected in $Y(Fe_xAl_{1-x})_2$ for $x \leq 0.78$ at temperatures ≥ 2K but magnetically split ^{57}Fe Mössbauer (MB) spectra were recorded at 5K (fig. 1). For $Y(Fe_{0.7}Al_{0.3})_2$ no magnetic long range order could be detected down to 30mK (16), neither was magnetic order observed for Al-rich alloys (14), (17–21). The low field magnetization versus temperature curves show maxima (T_M) for $x < 0.8$. The shape of these maxima broadens with increasing x. Furthermore, characteristic irreversible phenomena (magnetic history effects, displaced hysteresis loops and time dependence of the magnetization) occur at temperatures below T_M. The temperatures T_A defined as the temperatures for which the magnetic hyperfine splitting disappears are in reasonably good agreement with T_M. The shape of the MB spectra of $Y(Fe_{0.7}Al_{0.3})_2$ measured at 5K does not change for fields of 1.72T and only minor changes occur for spectra recorded after cooling in the applied field. These facts point to a mictomagnetic or cluster glass like behavior.

For $x \geq 0.78$ the susceptibility data above T_C exhibit Curie-Weiss behavior. In the cubic Al-rich concentration range downward curvatures are observed in these curves. The susceptibility data were thus analyzed by a least squares fit procedure to the relation

$$\chi = \chi_0 + C/(T-\Theta) \qquad [1]$$

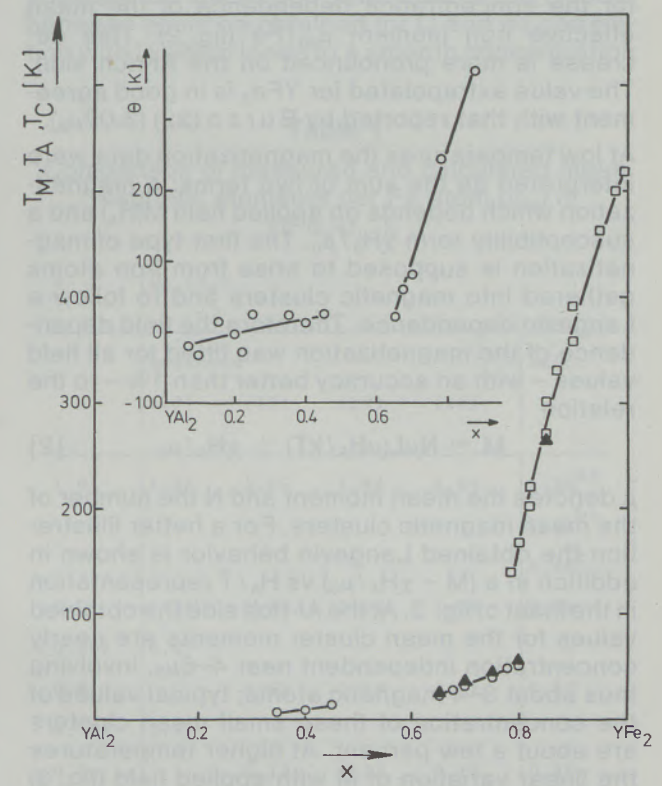

Fig. 1

Concentration dependence of T_C (□) determined by $M^2(H_A/M)$ diagrams, T_A (▲) determined by the vanishing of the magnetic hyperfine splitting and T_M (○) determined by the maximum in the temperature dependence of the magnetization measured in low fields of $Y(Fe_xAl_{1-x})_2$. Inset: Curie-Weiss temperature Θ

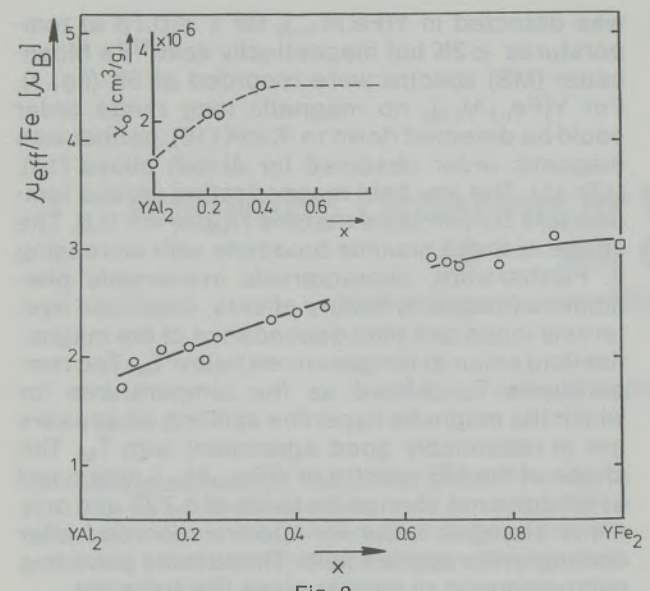

Fig. 2

Mean effective iron moment of $Y(Fe_xAl_{1-x})_2$ (□, after Burzo (22)). Inset: matrix susceptibility; the broken curve represents the values used for the calculations

where χ_0 accounts for the observed curvature through a Pauli-type susceptibility and includes the matrix contribution (inset fig. 2). A slow decrease with increasing Al content was obtained for the concentration dependence of the mean effective iron moment μ_{eff}/Fe (fig. 2). This decrease is more pronounced on the Al-rich side. The value extrapolated for YFe_2 is in good agreement with that reported by Burzo (22) (3.02μ_B).

At low temperatures the magnetization data were interpreted as the sum of two terms: a magnetization which depends on applied field $M(H_A)$ and a susceptibility term $\chi H_A/\mu_0$. The first type of magnetization is supposed to arise from iron atoms gathered into magnetic clusters and to follow a Langevin dependence. Therefore the field dependence of the magnetization was fitted for all field values – with an accuracy better than 1% – to the relation

$$M = N\mu L(\mu H_A/kT) + \chi H_A/\mu_0 \qquad [2]$$

μ denotes the mean moment and N the number of the mean magnetic clusters. For a better illustration the obtained Langevin behavior is shown in addition in a $(M - \chi H_A/\mu_0)$ vs H_A/T representation in the inset of fig. 3. At the Al-rich side the obtained values for the mean cluster moments are nearly concentration independent near 4–6μ_B, involving thus about 3–4 magnetic atoms; typical values of the concentration of these small mean clusters are about a few percent. At higher temperatures the linear variation of M with applied field (fig. 3) reflects that this short range order has disappeared. The magnetic behavior is then to be ascribed to the sole large susceptibility term which as described above includes a magnetic term and a band-like susceptibility.

The saturation magnetization was calculated according to $M_s = N\mu$. Large differences exist in the M_s values on both sides of the hexagonal domain (fig. 4). It must be mentioned that a smooth connection between the two cubic regions is possible for the mean unit cell volume, the mean isomer shift and the mean effective iron moment.

Strong changes of the MB spectra recorded at 5K caused by the Al-substitution are observable even for small amounts of Al. The large mean hyperfine fields indicate that Fe moments have to be present, evidencing a complex magnetic ordering. If only the influence of nearest neighbors is considered the details of the recorded spectra cannot be obtained by the fitting procedure. Therefore the different surroundings of a particular Fe atom were taken into account by means of a binomial distribution – P(n, m) – for nearest (n) and next nearest (m) neighbors, assuming that neither Y nor Al contribute to the hyperfine interaction. For a chosen x value the intensity ratios are calculated from this binomial distribution and kept unchanged throughout the fitting procedure. The hyperfine fields decrease with both decreasing num-

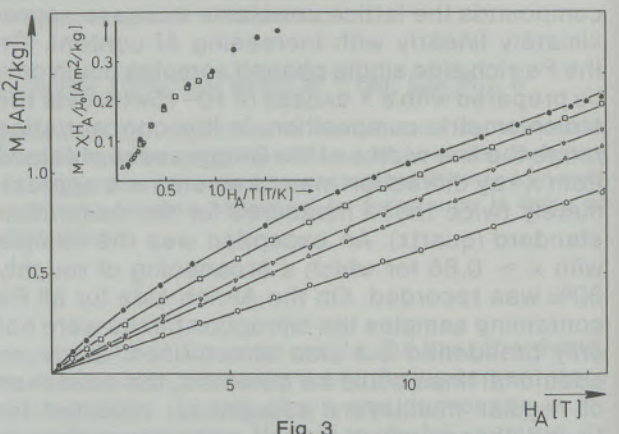

Fig. 3

Field dependence of the magnetization of $Y(Fe_{0.1}Al_{0.9})_2$ at 4.2 (●), 8.7 (□), 18.9 (▽), 28.8 (△) and 57.0 K (○). Inset: $(M - \chi H_A/\mu_0)$ against H_A/T

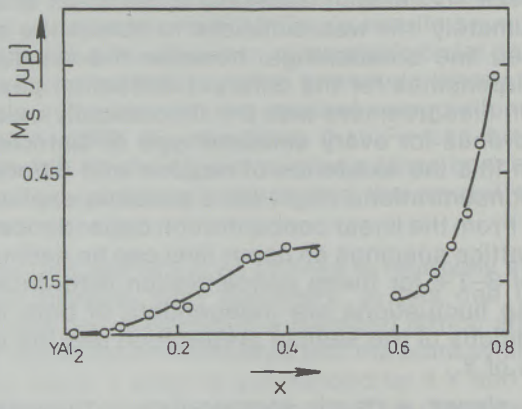

Fig. 4

Concentration dependence of the saturation moment $M_s = N\mu$ (N is the number and μ the moment of the mean cluster) for $Y(Fe_xAl_{1-x})_2$ at 4.2 K

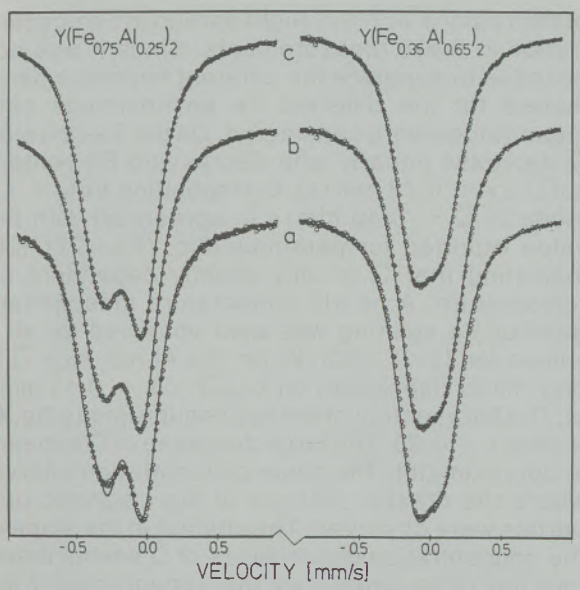

Fig. 5

Room temperature ^{57}Fe Mössbauer transmission spectra of typical $Y(Fe, Al)_2$ samples. Full lines: spectra fitted by a superposition of two subspectra (a), a superposition of up to five subspectra with intensity ratios according to a binomial distribution taking into account nearest Fe neighbor environments (b) and a quadrupole distribution (c)

ber of nearest and next nearest Fe neighbors and increasing Al content. The mean reduction in the hyperfine field for substitution of one nearest Fe neighbor by Al is approximately 18%.

The hyperfine field in $Y(Fe, Al)_2$ compounds may be calculated from

$$H_{hf} = A_{3d}\mu_d + A_s\mu_s \qquad [3]$$

where the first term represents the core polarization with the hyperfine coupling constant $A_{3d} = -12.5\,T/\mu_B$ deduced by Watson and Freeman (23) and the second the Fermi contact interaction, with $A_s = 178\,T/\mu_B$ estimated by Campbell (24). Assuming that:

(I) no 3d electrons are transferred to Al,

(II) the hyperfine coupling constants are concentration independent and

(III) the polarization of the conduction electrons can be taken into account by a mean value deduced from YFe_2 ($\mu_s = -0.03\ \mu_B$) (25),

the 3d moments for different surroundings can be calculated using the measured $H_{hf}^{(n,m)}$ values by

$$\mu_{3d}^{(n,m)} = 1/A_{3d}\,(H_{hf}^{(n,m)} - A_s\mu_s) \qquad [4]$$

using

$$\mu = \sum_{n,m} P(n, m)\mu_{3d}^{(n,m)} + \mu_s \qquad [5]$$

these values can be compared with the mean moments obtained from bulk magnetic measurements (tab. 1). In spite of the overall error resulting from the uncertainties of the hyperfine fields due to the small resolution of the measured spectra, the agreement is very good. Any correction due to dipolar contributions was omitted. From this analysis a decrease of the Fe moments with both decreasing number of nearest and next nearest neighbors as well as increasing Al content must be concluded.

For $0.10 \leq x \leq 0.85$ quadrupole split MP spectra were recorded at room temperature. The asymmetry of the shape of the spectra strongly depends on x (fig. 5), pointing to an influence of the different environments of the Fe atoms not only on the hyperfine fields at low temperatures but also on the electrostatic interactions far above T_A. Therefore three different methods were used to fit the spectra. As a first approximation they have been analyzed with a superposition of two subspectra. Because of the different values of the quadrupole splitting (Q) and isomer shift (Is), observed at the Fe-rich and Al-rich side of the series, the spectrum with the larger value of Q was correlated with the lower value of Is. The intensity ratio of the two subspectra continuously varies with x. However, always some small deviations from the measured spectra remain (fig. 5). Therefore an analysis taking into account the different environments of nearest Fe neighbors by means of a binomial distribution was performed. The agreement of the fits is excellent (fig. 5). On the Fe-rich side the Q values of the different environments decrease monotonically with decreasing x and can be correlated with Is as in the former analysis. On the Al-rich side however no smooth behavior could be obtained for Q and no correlation with Is which leads to a smooth concentration

Table 1

Comparison of measured and calculated mean magnetic moments per Fe atom (μ_{Fe}) in $Y(Fe_xAl_{1-x})_2$

x	$\mu_{Fe}(\mu_B)$				
	measured				calc.
	(18)	(17)	(19)	(14)	
1.0	1.45	1.45	1.44	1.55	1.36[a]
					1.42[b]
					1.48[c]
0.9	1.29	1.39	1.03	1.04	1.09
0.802	0.67				
0.8		0.61	0.50	0.52	0.67
0.701	0.19				
0.7		0.13	0.13	0.15	0.45

a) Using the mean hyperfine field determined by Dariel et al. (53) and Barb et al. (27).

b) Using the mean hyperfine field determined by Nikitin et al. (54).

c) After Oppelt and Buschow (25).

dependence was possible. Nevertheless the mean quadrupole splitting ($\overline{Q}$) and the mean isomer shift ($\overline{Is}$) are in good agreement with those of the first fitting procedure (fig. 6). These results strongly point to a quadrupole distribution which is also inferable from the $MgCu_2$ structure, if the Al substitution and only nearest neighbor interactions are taken into account. For x = 0.75 and x = 0.35 a fit according to such a quadrupole distribution (26) was performed. The allowed Q values varied inbetween 0.00 (0.15) mm/s and 0.70 (0.30) mm/s on the Fe-(Al-)rich side. In accordance with the calibration measurements the half width of the Lorentzian lines was allowed to vary between 0.22 and 0.26 mm/s. It was not possible to fit the spectra with only one value for Is. Therefore as a first approximation a linear dependence of Is on Q according to

$$Is = A \cdot (Q - Q_{min}) + B \qquad [6]$$

was used leading to a quadrupole distribution which strongly depends on these two parameters. The shape of the resulting distribution, which is only meaningful if the mean square deviation is a minimum, is similar to a Gaussian one and about three times broader on the Fe-rich side than on the Al-rich. The $\overline{Q}$ and $\overline{Is}$ values are in agreement with those of the other fitting models (fig. 6). On the Al-rich side the quadrupole distribution is small. The differences in the Is values which result from the spread in the Fe concentration according to the X-ray investigations are also small compared with the line widths of the MB measurements. Therefore it is not possible to resolve the influence of the regions with the slight spread in Fe concentration in these measurements. Since it was not possible to separate the different hyperfine parameters for the different Fe environments only mean values were considered. On the Fe-rich side $\overline{Q}$ decrease linearly with decreasing Fe content ($\Delta\overline{Q}/\Delta x = 0.78$ mm/s). Extrapolating to x = 1.0 leads to $\overline{Q} \sim 0.49$ mm/s in agreement with the value reported for paramagnetic YFe_2 (27), (28) indicating that $\overline{Q}$ is only slightly dependent on temperature. A nearly temperature independent quadrupole splitting was also observed for all x values for $T_A < T < 300$ K. On the Al-rich side $\overline{Q}$ is only mildly dependent on x ($\Delta\overline{Q}/\Delta x = 0.11$ mm/s). The intersection of the two linear regions (fig. 6) is near x = 0.68. The large decrease of $\overline{Q}$ appears in approximately the same concentration interval where the drastic changes of the magnetic properties were observed. The change in the slope of the concentration dependence of $\overline{Q}$ seems therefore not to be caused by the appearance of the hexagonal structure type. The linear increase of the lattice parameter with decreasing x points to a concentration dependent volume available for the Fe atoms. A plot of the increase in $\overline{Is}$ against the volume change, both taken relative to YFe_2, leads to a straight line indicating that a charge transfer from the substituted Al to the Fe atoms is of minor importance and that the increase in $\overline{Is}$ with decreasing Fe content is mainly caused by the change in volume.

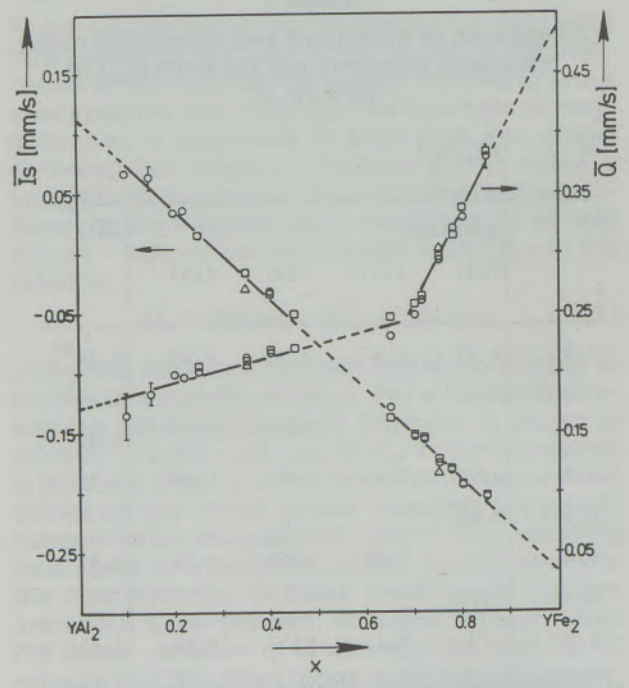

Fig. 6

Concentration dependence of the mean quadrupole splitting $\overline{Q}$ and the mean isomer shift $\overline{Is}$ (relative to ^{57}CoPd) at room temperature (spectra fitted with two subspectra ○, binomial distribution □, quadrupole distribution △)

The system may thus be qualitatively divided into three regions. On the Fe-rich side, the compounds are ferromagnetic. This long range order disappears however rapidly; magnetization and Curie temperatures go to zero at about x = 0.78. In this concentration range T_A and T_M are in agreement. The susceptibility follows a Curie-Weiss law with positive Θ. At lower Fe concentrations typical mictomagnetic or cluster glass behavior is observed. The magnetic clusters, originated from the statistical replacement of Al for Fe, subsist down to the lowest Fe concentrations investigated. In this concentration range the susceptibility follows a modified Curie-Weiss law with Weiss parameters which scatter around zero (inset fig. 1). In a limited concentration range around 80% Fe T_C values can be determined from the high field part of $M^2(H_A/M)$ diagrams. However the low field magnetization curves are still indicative of freezing phenomena for $T < T_M$. Whereas T_A and T_M are in reasonable agreement, much higher values are obtained for T_C (e.g. T_M = 52K, T_A = 57K, T_C = 165K for $Y(Fe_{0.8}Al_{0.2})_2$, (fig. 1)) pointing towards the existence of a very complex magnetically ordered state.

3. $Y(Fe,Co)_2$

YCo_2 especially is one of the most interesting compounds within these series. To explain the magnetic properties, ferromagnetism as well as antiferromagnetism was assumed. However, at

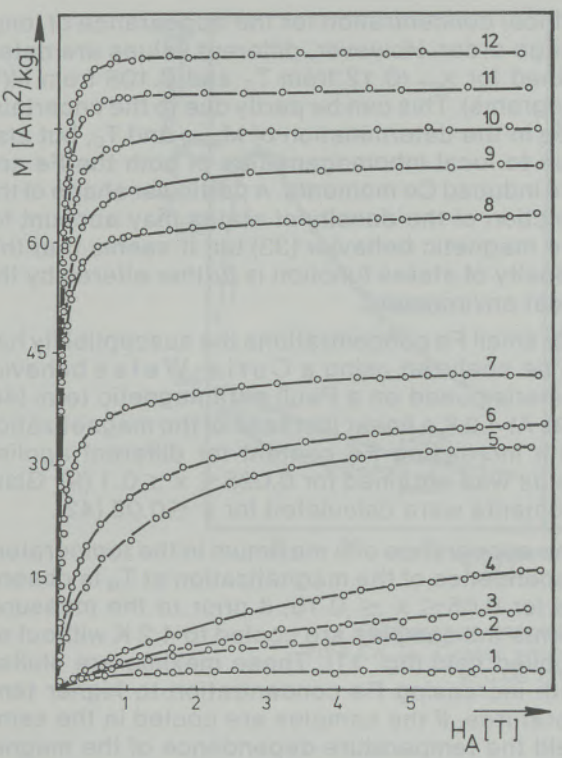

Fig. 7

Field dependence of the magnetization at 4.2 K for $Y(Fe_xCo_{1-x})_2$. (1) x = 0.025, (2) x = 0.05, (3) x = 0.075, (4) x = 0.106, (5) x = 0.129, (6) x = 0.13, (7) x = 0.15, (8) x = 0.20, (9) x = 0.25, (10) x = 0.30, (11) x = 0.40, (12) x = 0.50

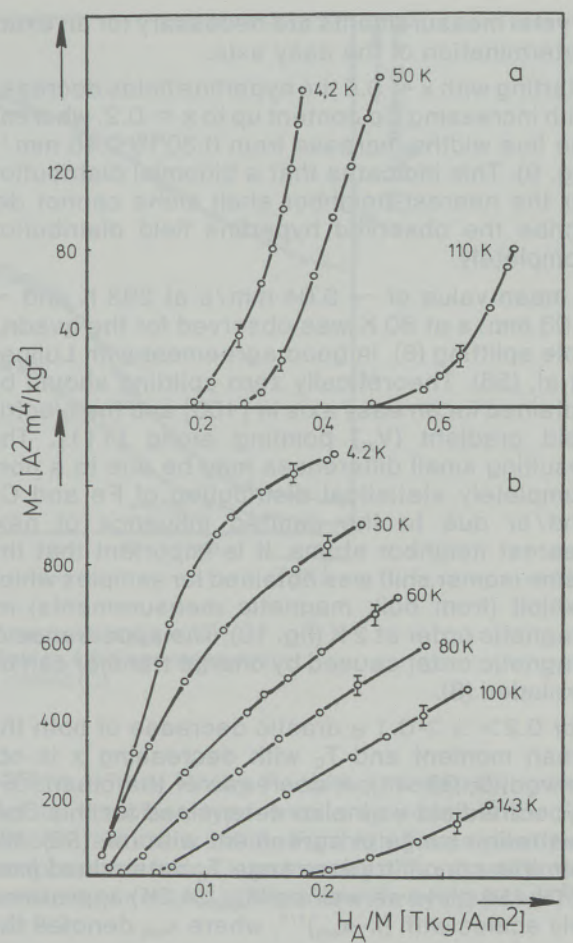

Fig. 8

$M^2(H_A/M)$ for $Y(Fe_xCo_{1-x})_2$. (a) x = 0.106, (b) x = 0.129

present it has been established that YCo_2 is an exchange enhanced Pauli paramagnet exhibiting a broad maximum in the temperature dependence of the susceptibility at approximately 250K (9), (29), (30). The magnetic properties have been explained by means of the model of weak induced itinerant magnetism (31), (32). Within this model application of a field would lead to a first order transition from a small Co moment to a large value of aligned spins. The value of this critical field was estimated to be somewhere between 62 T and 380 T (7), (31), (33–37).

In $Y(Fe_xCo_{1-x})_2$ the field dependence of the magnetization is completely altered for $x \leq 0.1$ (fig. 7). For all samples within this concentration region no positive intersection could be obtained from plots $M^2(H_A/M)$ indicating that no long-range order is present. Furthermore, the $M^2(H_A/M)$ diagrams for $0.129 \leq x \leq 0.2$ are curved making a clear decision for T_c very difficult (fig. 8).

A change of the easy axis from [111] in YFe_2 to [100] in $Y(Fe_{0.5}Co_{0.5})_2$ was obtained from an analysis of the MB spectra taking into account the different environments by means of a binomial distribution. This is supported by X-ray investigations of aligned powder samples (8). However, textures of this kind are readily obtained in cubic Laves phase compounds with low crystalline anisotropy by the alignment process alone and single

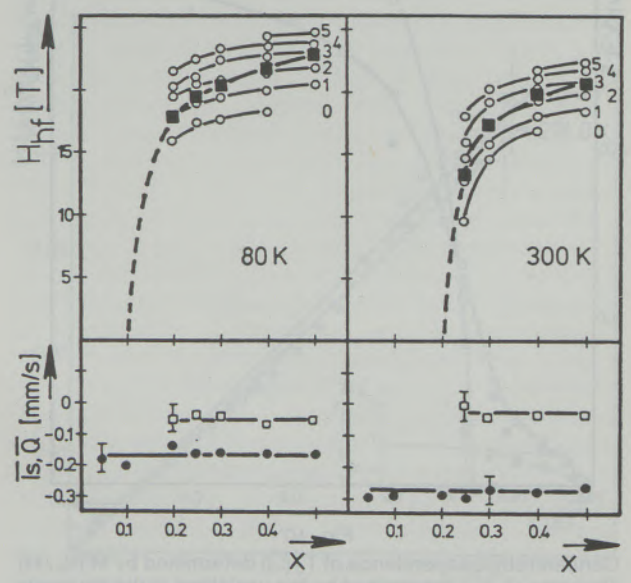

Fig. 9

Concentration dependence of the hyperfine field (○) (the numerals denote the number of nearest Fe neighbors), weighted mean hyperfine field (■), mean isomer shift relative to ^{57}CoPd (●) and quadrupole splitting (□) for $Y(Fe_xCo_{1-x})_2$

crystal measurements are necessary for an exact determination of the easy axis.

Starting with x = 0.5 the hyperfine fields decrease with increasing Co content up to x = 0.2, whereas the line widths increase from 0.30 to 0.46 mm/s (fig. 9). This indicates that a binomial distribution for the nearest neighbor shell alone cannot describe the observed hyperfine field distribution completely.

A mean value of ~ 0.04 mm/s at 293 K and ~ 0.03 mm/s at 80 K was observed for the quadrupole splitting (8), in good agreement with Luijpen et al. (38). Theoretically zero splitting should be obtained for an easy axis in [100] and the electric field gradient (V_{zz}) pointing along [111]. The resulting small differences may be due to a non-completely statistical distribution of Fe and Co and/or due to the omitted influence of next nearest neighbor atoms. It is important that the same isomer shift was obtained for samples which exhibit (from bulk magnetic measurements) no magnetic order at 2 K (fig. 10). The appearance of magnetic order caused by charge transfer can be excluded (8).

For $0.2 > x > 0.1$ a drastic decrease of both the mean moment and T_C with decreasing x is observed (9, 39–41). A decrease of the mean ^{57}Fe hyperfine field was also determined for this concentration range in agreement with ref. (38). Within this concentration range T_C determined from $M^2(H_A/M)$ plots as well as $M_{spont}(4.2K)$ approximately scales with $(x-x_{crit})^{1/2}$, where x_{crit} denotes the critical concentration for the appearance of long-range order. However, different values are determined for x_{crit} (0.12 from T_C and 0.105 from M(T) diagrams). This can be partly due to the uncertainties in the determination of M_{spont} and T_C, but also due to local inhomogeneities of both the Fe and the induced Co moments. A particular shape of the function of the density of states may account for the magnetic behavior (33) but it seems that this density of states function is further altered by the local environment.

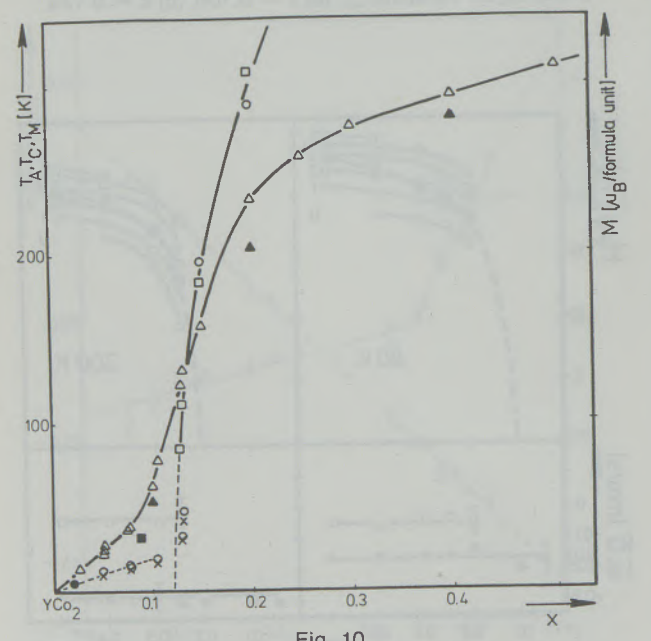

Fig. 10

Concentration dependence of T_C (□) determined by $M^2(H_A/M)$ diagrams, T_A (○) determined by the vanishing of the magnetic hyperfine splitting, T_M (×) determined by the maximum in the temperature dependence of the magnetization measured in low fields and M (△) measured at 4.2 K and 6.6 T for $Y(Fe_xCo_{1-x})_2$. (●) after Corson et al. (43), (■) after Luijpen et al. (38), (▲) after Burzo (40)

For small Fe concentrations the susceptibility has to be analyzed using a Curie-Weiss behavior superimposed on a Pauli paramagnetic term (40, 42). At 4.2 K a linear increase of the magnetization with increasing Fe content for different applied fields was obtained for $0.025 \leq x \leq 0.1$ (9). Giant moments were calculated for $x \leq 0.02$ (42).

The appearance of a maximum in the temperature dependence of the magnetization at T_M is observed for $0.05 \leq x \leq 0.15$, if prior to the measurements the samples are cooled to 4.2 K without an applied field (fig. 11). These maxima are shifted with increasing Fe concentration to higher temperatures. If the samples are cooled in the same field the temperature dependence of the magnetization coincides for $T > T_M$, but appreciable higher values are obtained for $T < T_M$. The resulting differences at 4.2 K as well as the relative heights of the maxima decrease with increasing applied fields. Furthermore a strong time dependence of the magnetization is observed at 4.2 K.

At 5 K magnetically split MB spectra are recorded for $0.05 \leq x \leq 0.2$ which exhibit a broad hyperfine field distribution. The width of the distribution increases with increasing x for $x \leq 0.129$ and decreases for $x \geq 0.13$. It was not possible to analyze these spectra using a binomial distribution taking into account the different numbers of nearest Fe neighbors. Corson et al. (43) reported magnetically split spectra for x = 0.022 at 0.15 K. This clearly indicates the existence of Fe moments even at this low concentration. The presence of Fe moments was tested for $Y(Fe_{0.1}Co_{0.9})_2$ by measurements in external fields up to 1.72 T at $T > T_A$. No decision as to different moments for Fe surrounded by a different number of Fe atoms was possible. Although the saturation hyperfine field could not be determined, the slope of the induced hyperfine field (H_{in}) versus H_A/T ($dH_{in}/d(H_A/T)$ = 120 K) refers to Fe moments in this compound.

No change of the overall shape of the MB spectrum measured in 1.72 T compared to that measured without a field was observed at 5 K. Contrary to this for x = 0.129 at 5 K a strong polarization effect due to the applied field is observed. For this sample a T_C value could also be obtained from $M^2(H_A/M)$ diagrams.

The temperatures T_A and T_M coincide nearly for $0.05 \leq x \leq 0.1$ (fig. 10). For further increasing x large deviations occur and for $x \geq 0.15$ T_A and T_C determined from bulk magnetic measurements

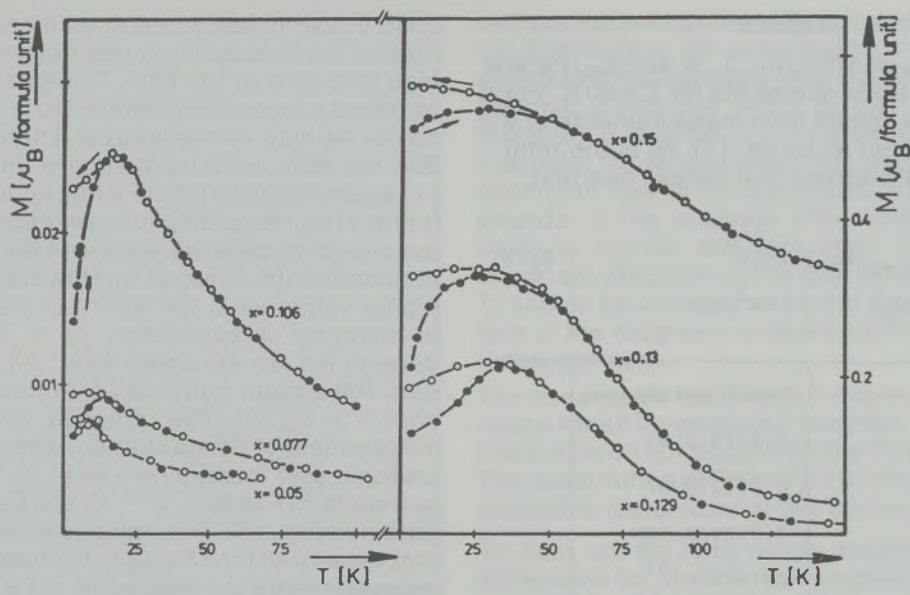

Fig. 11
Temperature dependence of the magnetization for $Y(Fe_xCo_{1-x})_2$. Cooled without any field to 4.2 K and measured in 0.06 T (●), field cooled (○)

are in rough agreement. Nevertheless, discrepancies up to approximately 20 K are still observed for this concentration range.

These results indicate that for $x \leq 0.1$ the magnetic behavior is characteristic for mictomagnetic or cluster glass alloys.

The magnetic properties of $Y(Fe,Co)_2$ can be summarized as follows: YCo_2 is an exchange enhanced Pauli paramagnet. Substituting Fe for Co leads to a polarization of the surrounding Co atoms. Giant moments are obtained for low Fe concentrations. Depending on the number of Fe atoms in the neighbor shells, magnetic clusters are formed and up to 10% Fe mictomagnetic or cluster glass behavior is observed. Further increasing x leads to a coupling of these clusters. T_C values are determinable from bulk magnetic measurements and the width of the hyperfine distribution decreases. For $x \geq 0.2$ the MB spectra indicate that different local environments of the Fe atoms are of minor importance, since for this concentration range the Co atoms carry also a moment.

4. $Y(Fe,Rh)_2$

For YRh_2 at all temperatures a linear dependence of the magnetization on applied field is observed. The magnetization measured at 6.69 and 0.168T decrease slightly with increasing temperature (fig. 12). For comparable temperatures the values are in agreement with Loebich and Raub (44) (tab. 2). The small temperature dependence of the susceptibility might be caused by the impurities of Y used for the samples. Therefore, Pauli paramagnetism can be concluded for YRh_2.

Substitution of Rh by Fe without destroying the $MgCu_2$ structure type was only possible for Fe concentrations $x \leq 0.3$. For high Fe content the sample preparation is extremely difficult and small amounts of second phases are always present for $x \geq 0.2$.

No indication for the appearance of long range magnetic order was obtained for $Y(Fe_xRh_{1-x})_2$, $0.1 \leq x \leq 0.3$, neither from plots $M^2(H_A/M)$ nor from

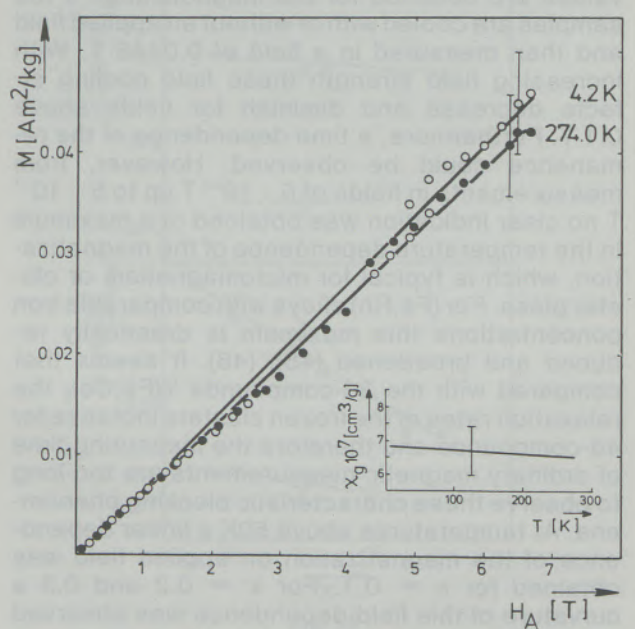

Fig. 12
Field dependence of the magnetization of YRh_2. Inset: temperature dependence of the susceptibility

Table 2

Magnetic data of $Y(Fe_xRh_{1-x})_2$. Θ and μ_{eff}/Fe are obtained from Curie-Weiss fits for T>80 K. For x $\geq$ 0.1 χ is determined from measurements at 4.2 K by eq. [2] and N_1 by eq. [7]. N_0 is the total number of Fe atoms. For details see text.

x	Θ(K)	μ_{eff}/Fe (μ_B)	$\chi*10^7$ (cm^3/g)	N_1/N_0
0.0	-	-	Pauli paramagnet	-
			6.87(4.2 K)	
			6.47(274 K)	
			4.7(room temperature)[a]	
			4.0[b]	
0.1	-25	3.50	205	0.08
	-28	3.50	208	0.08
0.2	-28	3.64	285	0.05
	-27	3.73	286	0.05
0.3	-25	3.90	440	0.04

a) After Loebich and Raub (44).
b) After Buschow (47).

ac-susceptibility measurements. Nevertheless, MB spectra with magnetic hyperfine splitting are recorded at 5K (fig. 13), indicating that some kind of magnetic order has to be present. Different values are obtained for the magnetization if the samples are cooled with or without an applied field and than measured in a field of 0.0145 T. With increasing field strength these field cooling effects decrease and diminish for fields above 0.1 T. Furthermore, a time dependence of the remanence could be observed. However, from measurements in fields of $5 \cdot 10^{-4}$ T up to $5 \cdot 10^{-1}$ T no clear indication was obtained of a maximum in the temperature dependence of the magnetization, which is typical for mictomagnetism or cluster glass. For (Fe,Rh) alloys with comparable iron concentrations this maximum is drastically reduced and broadened (45), (46). It seems that compared with the 3d-compounds $Y(Fe,Co)_2$ the relaxation rates of the frozen clusters increase for 4d-compounds and therefore the measuring time of ordinary magnetic measurements are too long to observe these characteristic blocking phenomena. At temperatures above 50K a linear dependence of the magnetization on applied field was obtained for x = 0.1. For x = 0.2 and 0.3 a curvature of this field dependence was observed for small applied fields. However, for fields larger than 1 T a linear dependence is always found in these samples. Assuming that the unknown second phase is saturated at all measuring temperatures the susceptibility was determined from the high field part of the $M(H_A,T)$ measurements. The obtained susceptibility obeys Curie-Weiss behavior at high temperatures. Therefore for T > 80K the data were least square fitted to relation [1] again assuming that Fe has no orbital momentum in YRh_2. According to the expected error in the susceptibility data there exists a large uncertainty concerning the value of χ_0. However, because for higher values of χ_0 the errors of the least square fit increase unreasonable, $\chi_0 = \chi_{YRh_2}$ could be determined as an upper limit. All susceptibility data have been corrected by this value and are shown in fig. 14. The obtained values for Θ are independent of concentration, whereas μ_{eff}/Fe increases with increasing x (tab. 2). From a linear extrapolation versus x = 0 μ_{eff}/Fe = 3.25μ_B is obtained (fig. 15). This value is in agreement with that measured for YFe_2 (22). Furthermore from MB measurements the existence of Fe moments can be concluded. The increasing μ_{eff}/Fe with increasing x indicates that a polarization of the surrounding Rh atoms is caused by the substituted Fe atoms.

At low temperatures the dependence of the magnetization on applied field was analyzed using relation [2]. The mean square deviations are below 1%, indicating that the basic assumption of this fitting procedure, that at low temperatures the sample consists of noninteracting magnetic clusters, is valid. No Curie-Weiss behavior is observed for the susceptibility at low temperatures (fig. 14). Since at 4.2K the values are much larger than χ_0 estimated from the high temperature fit the number of Fe atoms not included in the mean

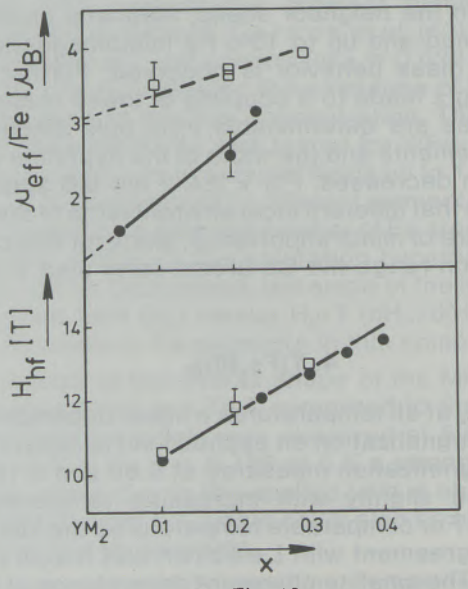

Fig. 13
Concentration dependence of the mean effective Fe moment and of the mean hyperfine field for $Y(Fe_xM_{1-x})_2$, M = Rh (□), Ir (●)

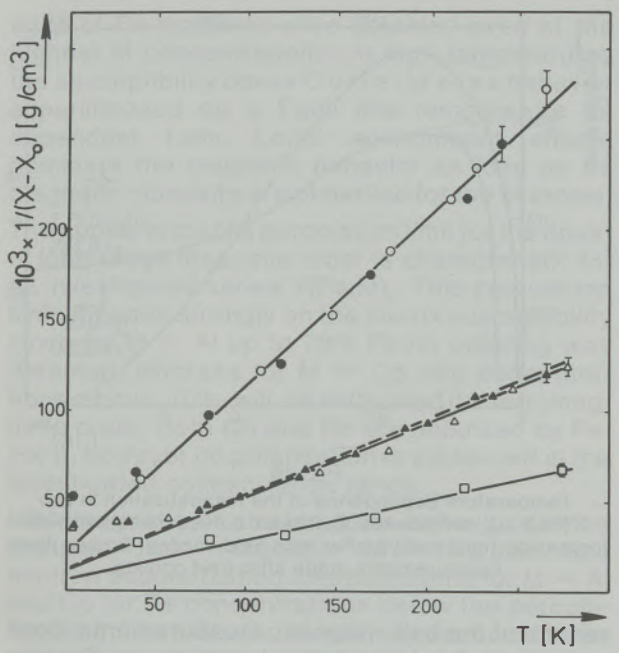

Fig. 14
Reciprocal susceptibility of $Y(Fe_xRh_{1-x})_2$. (○, ●) x = 0.1, (△, ▲) x = 0.2, (□) x = 0.3, $\chi_0 = 6.87 * 10^{-7}$ (cm^3/g)

clusters determined by the Langevin-function (N_1) are calculated using

$$\chi(x) = N_1\mu^2_{eff}/Fe(x)/3kT + \chi_0 \qquad [7]$$

assuming that both χ_0 and μ_{eff}/Fe are the same as obtained at high temperatures. The ratio N_1/N_0 (N_0 is the total number of Fe atoms) decreases with increasing x (tab. 2).

Contrary to the susceptibility the values of N and μ strongly depend on the number of points included in the fitting procedure. Therefore the absolute values are rather uncertain. Generally, both n and μ increase with increasing x, indicating that the number of Fe atoms involved in these clusters increases and that at the same time the number of clusters increases too. However, the largest amount of Fe (x = 0.3) which could be substituted without destroying the $MgCu_2$ structure type is not enough to reach the critical concentration for long range magnetic order.

At room temperature and at 80 K for all x values MB spectra exhibiting a quadrupole splitting are recorded. The isomer shift is independent of the Fe concentration (fig. 15), although the lattice parameters decrease with increasing x. Since the volume changes due to the Fe substitution are below 1% the volume dependence of the isomer shift could not be determined. Nevertheless the isomer shift indicates that the substitution of Rh by Fe causes only minor changes in the electron density at the Fe nucleus. This supports the assumption of a constant iron moment which is introduced for the analysis of the magnetic measurements.

At 5K spectra exhibiting a broad hyperfine field distribution are observed. For x = 0.1 a spectrum with pure quadrupole splitting is superimposed on the distribution. No contribution of this kind was detectable for samples with higher iron concentrations. Since the width of the hyperfine field distribution is large, a strong dependence of the magnetic hyperfine interaction upon the local environment has to be concluded for the Rh-compounds, if the analysis with different hyperfine fields is correct and relaxation effects are not important. Because of the lack of long range order T_A should be interpreted as the freezing temperature of the magnetic clusters which are formed in these samples.

The quadrupole splitting is independent of temperature for all investigated samples. The observed linewidths do not depend on the Fe concentration. The substitution of Rh by Fe therefore causes only negligible distortions of the surrounding lattice.

To sum up: No long range magnetic order was detectable for $x \leq 0.3$. The magnetization and MB measurements indicate mictomagnetic or cluster-glass behavior, although it was not possible to observe the maximum in the temperature dependence of the magnetization measured in low applied fields. Fe moments have to be concluded from the Curie-Weiss behavior and the increase of the effective moment indicates that a polarization of the surrounding Rh atoms is caused by the substituted Fe atoms.

5. $Y(Fe,Ir)_2$

YIr_2 is Pauli paramagnetic ($\chi_0 = 1.35 \cdot 10^{-4}$ cm^3/mole (48)). Contrary to $Y(Fe,Rh)_2$ a complete solid solubility is reported for $Y(Fe,Ir)_2$ (41), (49), how-

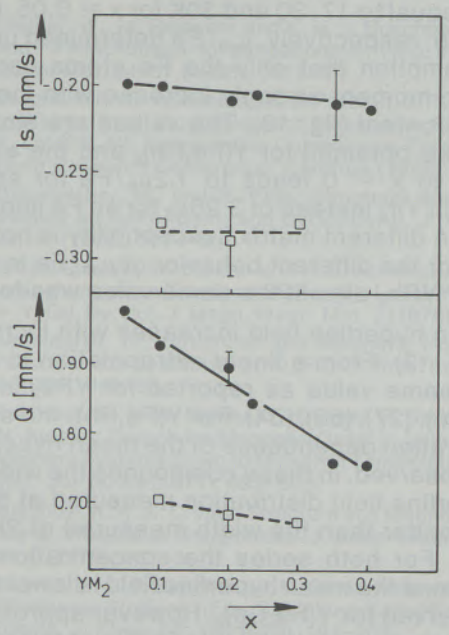

Fig. 15
Concentration dependence of the isomer shift (Is) relative to ^{57}CoPd and the quadrupole splitting (Q) in $Y(Fe_xM_{1-x})_2$, M = Rh (□) and Ir (●) at room temperature

ever our investigations were restricted to $0.05 \leq x \leq 0.4$

No positive intersections were obtained in $M^2(H_A/M)$ for compounds with $x \leq 0.235$. At low temperatures the $M(H_A)$ curves are strongly curved, pointing to some kind of short range magnetic order. For compounds with $x \geq 0.35$ the $M^2(H_A/M)$ plots are different, because of small amounts of second phases. Therefore in these cases no clear conclusion concerning the appearance of a long range magnetically ordered state can be obtained. Nevertheless the sharp increase of the magnetization with increasing field points to magnetic order.

For all samples (with the exception of $x = 0.05$) field cooling effects and associated with it, strong time dependences of the magnetization at 4.2K were observed. Such behavior is reminiscent of mictomagnets or cluster glasses. The temperature dependence of the magnetization of zero field cooled samples shows a maximum, the location of which is independent of the applied field H_A (fig. 16). No correlation between the values of T_A and the temperatures corresponding to these maxima (T_M) was observed. Further, also unusual for mictomagnetic materials, the difference of the magnetization measured at 4.2K between samples cooled with and without field (ΔM) increases with increasing H_A. This behavior is different from that obtained for $Y(Fe,Rh)_2$.

The linear part of the $M(H_A)$ curves was used to determine the susceptibility $\chi(T)$ using relation [1]. As discussed for $Y(Fe, Rh)_2$ $\chi_0 = \chi_{YIr_2}$ was used for all fitting procedures. For alloys with $x \leq 0.235$, $\chi(T)-\chi_0$ follows a Curie-Weiss behavior above about 100K. The corresponding values of Θ are equal to 17, 30 and 30K for $x = 0.05$, 0.20 and 0.235, respectively. μ_{eff}/Fe determined under the assumption that only the Fe atoms carry a magnetic moment strongly increase with increasing Fe content (fig. 13). The values are smaller than those obtained for $Y(Fe,Rh)_2$ and the extrapolation to $x = 0$ leads to $1.2\mu_B$/Fe for an Fe impurity in YIr_2 instead of $3.25\mu_B$ for an Fe impurity in YRh_2. A different matrix susceptibility is not the reason for the different behavior of μ_{eff}/Fe in YIr_2, since for YRh_2 almost the same value was found.

The mean hyperfine field increases with increasing x (fig. 13). From a linear extrapolation to $x = 1.0$ the same value as reported for YFe_2 is obtained (25), (27), (53), (54). For $Y(Fe,Rh)_2$ the same concentration dependence of the mean hyperfine field is observed. In these compounds the width of the hyperfine field distribution measured at 5K is much broader than the width measured at 2K for $Y(Fe,Ir)_2$. For both series the concentration dependence of the mean hyperfine field is lower than that observed for $Y(Fe,Co)_2$. However approximately the same mean hyperfine field is obtained for all series by extrapolating versus diminishing Fe content. It can therefore be suggested that the polarization of the Rh atoms, indicated by the results of the bulk magnetic measurements, does not affect the hyperfine interaction on Fe very much.

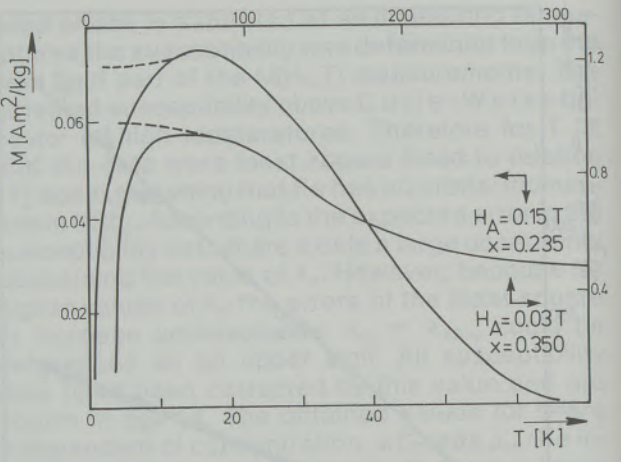

Fig. 16

Temperature dependence of the magnetization in two $Y(Fe_xIr_{1-x})_2$ compounds. Full lines: curves measured with increasing temperature after zero field cooling. Broken lines: measurements made after field cooling

The quadrupole splittings observed at 295K are extremely large for intermetallic compounds and larger than in $Y(Fe,Rh)_2$. They decrease with increasing x (fig. 15). For a fixed x value the splitting is independent of temperature. The isomer shift depends only slightly on composition (fig. 15) and can be correlated to the change in volume, indicating that the substitution of Ir for Fe causes only minor changes in the electron density at the Fe nucleus.

The magnetic behavior of $Y(Fe,Ir)_2$, can be summarized as follows: Long range magnetic order occurs only for Fe concentrations in excess of $x = 0.3$. For $x \leq 0.235$ the magnetization and MB measurements point to the occurence of short range magnetic order. Field cooling effects, strong time dependencies of the magnetization at 4.2K and the maximum in the magnetization of zero field cooled alloys would characterize these materials in this concentration range as mictomagnets or cluster glasses. However, the large difference between T_M and T_A, the field independent maxima of the magnetization and the increase of M with increasing H_A are unusual. They were not observed in the other Laves phases described above.

6. Conclusion

Pauli paramagnetism is obtained for all four YM_2 compounds where M = Al, Co, Rh and Ir. For YFe_2 selfconsistent spin-polarized energy band calculations have predicted a ferrimagnetic order with spatially localized Fe moments and extended negative spin densities around the Y sites (36), (50), (51). From our experiments no information about this polarized spin density could be obtained.

For all series from both Mössbauer and magnetic measurements indications for the pres-

ence of Fe moments were obtained even at the highest M concentrations. At high temperatures the susceptibility obeys Curie-Weiss behavior superimposed on a Pauli like temperature independent term. Local environment effects dominate the magnetic behavior as long as no magnetic moments are observed for the M atoms.

The appearance of a percolation limit for the onset of long range magnetic order is characteristic for all investigated series $Y(Fe,M)_2$. This percolation limit depends strongly on the matrix susceptibility since for M = Al up to 78% Fe no ordering was detected, whereas for M = Co iron concentrations above 10% will already lead to ferromagnetic order. Both Co and Rh are polarized by Fe. For Ir, however no polarization is evidenced in the investigated concentration range.

Mictomagnetic or cluster glass behavior can be deduced from magnetic, Mössbauer and neutron depolarization measurements for M = Al and Co for Fe concentrations below the percolation limit. The following model may account for the magnetic behavior within this concentration range. All substituted Fe atoms have magnetic moments. For higher Fe concentrations magnetically ordered clusters are formed due to statistical fluctuations of the number of nearest Fe neighbors leading to the observed moments. Following Beck (52), a magnetic interaction between the cluster moments and the randomly frozen moments of the matrix can lead to a blocking of the reorientation of the cluster moments at a certain temperature T_M. Increase of energy due to increasing temperature overcomes this blocking energy. Therefore the susceptibility increases with increasing temperature. At higher temperatures the moments are able to rotate and some reorientation with respect to an applied field is possible. Cooling the sample in this field therefore leads to higher values of the magnetization. The appearance of magnetically hyperfine splitting takes place since most of the Fe moments are frozen below T_M. For M = Rh a similar behavior should occur as indicated by the dependence of the magnetization upon the magnetic pretreatments as well as by the magnetically split Mössbauer spectra, although no maxima of the low field magnetization as a function of the temperature are observed for these samples. A behavior reminiscent of mictomagnetism or cluster glasses is also observed for M = Ir. However, the large differences between T_M and T_A, the increase of the difference of the magnetization measured at 4.2K between samples cooled with and without field and above all the field independent maxima in the temperature dependence of the magnetization are unusual and point to a very complex magnetic order, which needs further investigations both experimentally and theoretically for a complete explanation.

Acknowledgement

We want to acknowledge the continuous interest of Prof. F. Lihl and valuable discussions with him during the initial phase of these investigations.

References

1. Heiman, N., and N. Kazama: Magnetic Properties of Amorphous Alloys of Fe with La, Lu, Y and Zr. Phys. Rev. B19, 3 (**1979**), 1623–32.
2. Forester, D. W., N. C. Koon, J. H. Schelleng and J. J. Rhyne: Spin-Glass and Magnetic Blocking Transitions in Amorphous YFe_2. Sol. Stat. Comm. 30 (**1979**), 177–80.
3. Chappert, J., R. Arrese-Boggiano and J. M. D. Coey: Appearance of Magnetism in Amorphous $Y_{1-x}Fe_x$. J. Magn. Mat. 7 (**1978**), 175–7.
4. Buschow, K, H. J.: On the Difference in the Magnetic Properties of Amorphous Alloys and Intermetallic Compounds. J. Magn. Mat. 28 (**1982**), 20–8.
5. Reissner, M., W. Steiner, J. P. Kappler, P. Bauer and M. J. Besnus: Magnetic Behaviour of $Y(Fe_xAl_{1-x})_2$ Alloys. J. Phys. F14 (**1984**), 1249–59.
6. Reissner, M., and W. Steiner: Electrostatic Hyperfine Interactions in $Y(Fe, Al)_2$. Hyperfine Interactions 28 (**1986**), 1017–20.
7. Steiner, W.: Magnetization Processes Caused by Iron Substitution in Cubic Laves Phases. J. Magn. Magn. Mat. 14 (**1979**), 47–79.
8. Ortbauer, H., W. Steiner and R. Haferl: Mössbaueruntersuchungen an $Y(Fe_xCo_{1-x})_2$ im Bereich kleiner Fe-Konzentrationen. Phys. Stat. Sol. (a) 39 (**1977**), 157–65.
9. Steiner, W., und H. Ortbauer: Magnetische Messungen an $Y(Fe_xCo_{1-x})_2$ im Bereich kleiner Fe-Konzentrationen. Phys. Stat. Sol. (a) 26 (**1974**), 451–7.
10. Hrubec, J., W. Steiner and M. Reissner: Magnetization and Mössbauer Studies of $Y(Fe, Rh)_2$. J. Magn. Magn. Mat. 37 (**1983**), 93–100.
11. Steiner, W., M. Reissner and K. H. J. Buschow: Magnetic and ^{57}Fe Mössbauer Investigations on $Y(Fe, Ir)_2$. J. Magn. Magn. Mat. 54–57 (**1986**), 1079–80.
12. Dwight, A. E., C. W. Kimball, R. S. Preston, S. P. Taneja and L. Weber: Crystallographic and Mössbauer Study of (Sc, Y, Ln) $(Fe, Al)_2$ Intermetallic Compounds. Proc. 10th Rare Earth Research Conference, Carefree (**1973**).
13. Österreicher, H., and R. Pitts: Structural and Magnetic Studies on $DyFe_2$-$DyAl_2$ and $DyCo_2$-$DyAl_2$. J. Appl. Phys. 43, 12 (**1972**), 5174–9.
14. Grössinger, R., W. Steiner und K. Krec: Magnetische Untersuchungen an Ternären $SE(Fe, Al)_2$ Laves-Phasen (SE = Y, Gd, Dy, Ho). J. Magn. Magn. Mat. 2 (**1976**), 196–202.
15. Kanematsu, K.: Structural and Magnetic Properties of Pseudobinary System $(Zr_{1-x}Nb_x)Fe_2$. J. Phys. Soc. Jap. 27, 4 (**1969**), 849–56.
16. Goblirsch, R., H. W. Weber, G. Hilscher, R. Grössinger and W. Steiner: Search for Magnetic Order in Selected Pseudobinary Systems Down to Milikelvin Temperatures. Phys. Stat. Sol. (a) 44 (**1977**), 593–600.
17. Buschow, K. H. J.: Crystal Structure and Magnetic Properties of $YFe_{2x}Al_{2-2x}$ Compounds. J. Less-Common Metals 40, 3 (**1975**), 361–3.
18. Besnus, M. J., P. Bauer and J. M. Génin: Magnetic and ^{57}Fe Mössbauer Study of $Y(Fe_{1-c}Al_c)_2$ Alloys: Local Environment Effects. J. Phys. F8, 1A (**1978**), 191–204.
19. Muraoka, Y., M. Shiga and Y. Nakamura: Magnetic Properties and Mössbauer Effect of $A(Fe_{1-x}B_x)_2$ (A = Y or Zr, B = Al or Ni) Laves Phase Intermetallic Compounds. Phys. Stat. Sol. (a) 42 (**1977**), 369–374.

20. Hilscher, G., R. Grössinger, V. Sechovsky and P. Nozar: The Extent of Localization of the Fe Moment in $Y(Fe_{1-x}Al_x)_2$ and $Zr(Fe_{1-x}Al_x)_2$ – a Comparison of the Magnetic Properties. J. Phys. F12 (**1982**), 1209–26.
21. Kraan, A. M. van der, P. C. M. Gubbens and K. H. J. Buschow: Mössbauer Effect Study of $Y(Fe, Al)_2$. Proc. Int. Conf. on Mössbauer Effect Boukarest **1977**.
22. Burzo, E.: High Temperature Magnetic Behaviour of $(Gd_xY_{1-x})Fe_2$ Compounds. Sol. Stat. Phys. 20 (**1976**) 565–8.
23. Watson, R. E. and A. J. Freeman: Origin of Effective Fields in Magnetic Materials. Phys. Rev. 123 (**1961**), 2027–47.
24. Campbell, I. A.: Hyperfine Fields on Impurities in Ferromagnetic Metals. J. Phys. C2, 2 (**1969**), 1338–51.
25. Oppelt, A., and K. H. J. Buschow: NMR Investigations of the Hyperfine Interactions in $Y(Fe_{1-x}A_x)_2$ (A: Al, Co, Pt). Phys. Rev. B13 (**1976**), 4698–704.
26. Caer, G. Le, and J. M. Dubois: Evaluation of Hyperfine Parameter Distributions from Overlapped Mössbauer Spectra of Amorphous Alloys. J. Phys. E12 (**1979**), 1083–90.
27. Barb, D., E. Burzo and M. Morariu: The Temperature Dependence of the Mössbauer Parameters and the Magnetic Properties of the RFe_2 (R = Y or Rare-Earth) Compounds. Proc. 5th Intern. Conf. Mössbauer Spectroscopy, Part 1 (**1973**), 37–40.
28. Nishihara, Y., T. Katayama and S. Ogawa: Mössbauer Study of Amorphous and Crystalline YFe_2. J. Phys. Soc. Jap. 51, 8 (**1982**), 2487–92.
29. Lemaire, R.: Magnetic Properties of the Intermetallic Compounds of Cobalt with the Rare Earth Metals and Yttrium. Cobalt 32 (**1966**), 132–40, 33 (**1966**), 201–11.
30. Burzo, E.: Crystallographic, Magnetic and E. P. R. Studies of Rare-Earth and Yttrium – Cobalt Laves Phases. Jahrestagung DPG Freudenstadt (**1972**).
31. Voiron, J.: Métamagnétisme en champ interne: Application aux composés TCo_2. These, Univ. Grenoble (**1973**).
32. Wohlfahrt, E. P., and P. Rhodes: Collective Electron Metamagnetism. Phil. Mag. 7 (**1962**), 1817–24.
33. Cyrot, M., D. Gignoux, F. Givord and M. Lavagna: Magnetism of the Rare Earth, 3d – Theoretical Review. J. de Phys. 40 (**1979**), C5-171 – 6.
34. Wohlfarth, E. P.: Itinerant Metamagnetism in $TiBe_2$. J. Physique Letts. 41 (**1980**), L563–5.
35. Schwarz, K., and P. Mohn: Itinerant Metamagnetism in YCo_2. J. Phys. F14 (**1984**), L129–34.
36. Yamada, H., and M. Shimizu: Metamagnetic Transition of YCo_2. J. Phys. F15 (**1985**), L175–80.
37. Bloch, D., D. M. Edwards, M. Shimizu and J. Voiron: First Order Transitions in ACo_2 Compounds. J. Phys. F5 (**1975**), 1217–26.
38. Luijpen, M. G., P. C. M. Gubbens, A. M. van der Kraan and K. H. J. Buschow: Mössbauer Effect Study of $Y(Fe, Co)_2$. Physica 86–88B (**1977**), 141–2.
39. Abel, A. W., and R. S. Craig: Magnetic and Structural Characteristics of $TiCr_2$, $ZrCr_2$, $HfCr_2$ and the $TiCo_2$–$ZrCo_2$ and YFe_2–YCo_2 Alloy Systems. J. Less-Common Metals 16 (**1968**), 77–83.
40. Burzo, E.: On the Magnetic Properties of $Y(Fe_xCo_{1-x})_2$ Compounds. Sol. Stat. Comm. 25 (**1978**), 525–9.
41. Dongen, J. C. M. van, G. J. Nieuwenhuys, J. A. Mydosh, A. M. van der Kraan and K. H. J. Buschow: Magnetic Properties and Electrical Resistivity of Transition Metal Laves Phase Compounds: $Y(Co_{1-x}Fe_x)_2$, $Y(Ir_{1-x}Fe_x)_2$ and $Hf(Co_{1-x}Fe_x)_2$. Inst. Phys. Conf. Ser. 55 (**1980**), 275–8.
42. Ikeda, K.: Role of Substitutional Iron Atoms Affecting the Paramagnon Scattering in Co_2Y. J. Less-Common Metals 52 (**1977**), 101–8.
43. Corson, M. R., B. Kolk, G. Hoy, G. O. Zimmermann, A. M. van der Kraan and P. C. M. Gubbens: Mössbauer Effect Study of $Y(Fe_{0.22}Co_{0.978})_2$ at Temperatures between 0.15 and 4.2K. Hyperfine Interactions 4 (**1978**), 411–4.
44. Loebich, O., Jr. und E. Raub: Magnetische Eigenschaften der Legierungen des Rhodiums mit Lanthaniden. Mat. Res. Bull. 10 (**1975**), 1017–22.
45. Murani, A. P., and B. R. Coles: Interactions between Anomalous Local Moments: Magnetic Ordering in Rhodium-Iron Alloys. J. Phys. C3, 2 (**1970**), S159–68.
46. Vogt, E., F. Bölling und W. Treutmann: Magnetisches Verhalten der Mischkristallreihe vom Rhodium und Ruthenium mit Eisen und Kobalt. Ann. Phys. 25, 3 (**1970**), 280–98.
47. Buschow, K, H. J.: private communication.
48. Buschow, K, H. J.: Intermetallic Compounds of Rare-Earths and Non-Magnetic Metals. Rep. Prog. Phys. 42 (**1979**), 1373–1477.
49. Kraan, A. M. van der, P. C. M. Gubbens and K. H. J. Buschow: Magnetic Behaviour of $Y(Fe, Ir)_2$. J. de Phys. 40 (**1979**), C2–190.
50. Mohn, P., and K. Schwarz: Binding Mechanism and Itinerant Magnetism of $ZrFe_2$ and YFe_2. Physica 130B (**1985**), 26–8.
51. Yamada, H., J. Inoue, K. Terao, S. Kanada and M. Shimizu: Electronic Structure and Magnetic Properties of YM_2 Compounds (M = Mn, Fe, Co and Ni). J. Phys. F14 (**1984**), 1943–60.
52. Beck, P. A.: Comments on Mictomagnetism. J. Less-Common Metals 28 (**1972**), 193–99.
53. Dariel, M. P., U. Atzmony and D. Lebenbaum: Dipolar Contributions to Magnetic Hyperfine Fields in $Er_xY_{1-x}Fe_2$ and $Tb_xY_{1-x}Fe_2$ Compounds. Phys. Stat. Sol. (b) 59 (**1973**), 615–20.
54. Nikitin, S. A., V. A. Vasil'kovskii, H. M. Kovtun, A. K. Kupriyanov and V. F. Ostrovskii: Hyperfine Fields at Fe^{57} Nuclei in $Gd_xY_{1-x}Fe_2$ Alloys. Sov. Phys. JETP 41, 2 (**1975**), 285–6.

Fundamental Parameter Approaches in Quantitative X-Ray Fluorescence Analysis

Michael Mantler and Norbert Tupy, Wien*)

Dedicated to the 80th birthday of Prof. Dr. Franz Lihl

Fundamental parameter equations for primary and secondary fluorescent count rates from bulk materials, single layer thin films and multilayer thin films as well as equations for single and double scattered coherent and incoherent radiations are presented. Discussed aspects of applications include "no standard" analysis of bulks, simultaneous determination of concentrations and thicknesses of single and multi layer thin films and the computation of the backscattered image of a tube spectrum.

Fundamentale Parameter-Näherungen bei der quantitativen Röntgenfluoreszenz-Analyse

Es wurden die fundamentalen Parameter Gleichungen für primär und sekundär angeregte Fluoreszenzstrahlung für kompaktes Material sowie für einfache und mehrfache dünne Schichten zusammengestellt und Gleichungen für kohärente und inkohärente Einfach- und Mehrfachstreuung vorgestellt. Die besprochenen Anwendungen umfassen eichprobenfreie Analyseverfahren bei Kompaktproben, die gleichzeitige Bestimmung von Konzentrationen und Schichtdicken bei einfachen und mehrfachen dünnen Schichten sowie die Berechnung der Intensitätsverteilung des rückgestreuten Röhrenspektrums.

Approximations fondamentales de paramètres en analyse quantitative par fluorescence X

On a présenté des équations de paramètres fondamentales pour le rayonnement d'excitation primaire et secondaire, dans le cas de matériaux compacts et de couches minces simples et multiples. On a également établi les équations de dispersion simple et multiple, cohérente ou incohérente. Les applications discutées comportent l'analyse sans étalon dans le cas d'échantillons compacts et la détermination simultanée des concentrations et des épaisseurs de couches dans le cas de couches minces simples ou multiples, ainsi que le calcul de la distribution d'intensité de dispersion réfléchie du spectre du tube.

Introduction

X-ray fluorescence analysis is a widely used method for qualitative and quantitative elemental analysis of various kinds of materials in industrial and scientific applications. It is generally nondestructive, fast, and applicable to all elements between uranium and sodium. Special methods have been developed to extend the method to the ultra soft x-ray region in order to analyze boron (which is important in the glass industry), carbon (for example in steel), and other light elements.

In most cases specimens are made from bulk material by mechanical cutting and grinding or prepared as glassy pellets by fusion techniques. Pressed or loose powders, liquids or filter precipitates can be used as well, but require special consideration in the interpretation of count rate data. In addition, analysis of thin film materials, including multiple thin film layers, became an important industrial application in the electronics industries and others.

For the conversion of count rate data into weight fractions of elements in the specimen the application of empirical parameter equations constitutes the most widely used method. It is, however, restricted to bulk materials including glassy pellets and pressed powders and it requires an adequate number of standard specimens, preferably with a similar qualitative and quantitative composition as the unknown.

Thin film analysis is often based on a linear relationship between concentration and/or film thickness versus count rate, but such approximations are restricted to the case of very thin single layer films. Data from small amounts of precipitates or loose powders as well as low concentrations of an analyte in liquids can also be evaluated by such linear relationships.

*) Univ.-Doz. Dr. Michael Mantler, Norbert Tupy, Institut für Angewandte und Technische Physik, Technische Universität Wien, Karlsplatz 13, A-1040 Wien

An alternative to the empirical parameter techniques is the fundamental parameter method, which requires only a few calibration standards. It is applicable to all kinds of bulk specimens as well as to thin films and multiple thin film packages without (mathematical) restrictions to low thicknesses or concentrations.

While these techniques constitute a more or less accurate relationship between count rate ratios and elemental concentrations, the general goal of a mathematical / physical model is to compute the whole measured spectrum, including all lines of the elements rather than one single "analyte line" as well as the complete background spectrum from a specimen based on the knowledge of its elemental composition (in the case of thin film layers packages, also of its thicknesses) and the experimental conditions.

This paper describes and discusses the mathematical equations and computer methods used for the numerical evaluation of fluorescent intensities from thin films and multiple thin films as well as of intensities of background radiation due to single and double coherent and incoherent scattering.

Primary and Secondary Excitation

The theories for primary fluorescent radiation (excited by polychromatic primary radiation) and secondary fluorescent radiation (excited by primary fluorescent radiation within the same specimen) for bulk material and single layer thin films have been developed by Sherman (1), Shiraiwa and Fujino (2), and Pollai et al. (3), and extended for multiple thin film layers by Mantler (4).

1. Fluorescent Radiation from Bulk Specimens

The theoretical count rate for the primary fluorescent radiation from the analyte, i, as a function the concentrations, $c_1, c_2, \ldots, c_n$, is

$$n_{prim,i} = A \cdot B_i \cdot c_i \cdot \eta_i \cdot \frac{1}{\sin\psi_1} \cdot \int_{E_i}^{E_0} \frac{x(E) \cdot \tau_i(E)}{\frac{\mu(E)}{\sin\psi_1} + \frac{\mu(i)}{\sin\psi_2}} \cdot dE$$

$$\left(B_i = p_i \cdot W_i \cdot \frac{S_i - 1}{S_i} \cdot \frac{\Omega}{4\pi} \right) \qquad [1]$$

and the count rate of secondary fluorescent radiation from the analyte, i, excited by primary fluorescent radiation, j, within the same specimen:

$$n_{sec,i} = A \cdot B_i \cdot B_j \cdot c_i \cdot c_j \cdot \eta_i \cdot \frac{1/2}{\sin\psi_1} \cdot \int_{E_j}^{E_0} \frac{x(E) \cdot \tau_i(j) \cdot \tau_j(E)}{\frac{\mu(E)}{\sin\psi_1} + \frac{\mu(i)}{\sin\psi_2}} \cdot$$

$$\left\{ \frac{\sin\psi_1}{\mu(E)} \cdot \ln\left[1 + \frac{\mu(E)}{\mu(j) \cdot \sin\psi_1} \right] + \frac{\sin\psi_2}{\mu(i)} \cdot \ln\left[1 + \frac{\mu(i)}{\mu(j) \cdot \sin\psi_2} \right] \right\} dE \qquad [2]$$

2. Fluorescent Radiation from single Thin Film Layers

For single layer thin films, the count rate from primary fluorescent radiation differs only by the exponential term (1–exp(. . .)) from that for bulk material:

$$n_{prim,i} = A \cdot B_i \cdot c_i \cdot \eta_i \cdot \frac{1}{\sin\psi_1} \cdot \int_{E_i}^{E_0} \frac{x(E) \cdot \tau_i(E)}{\frac{\mu(E)}{\sin\psi_1} + \frac{\mu(i)}{\sin\psi_2}} \cdot$$

$$\left\{ 1 - \exp\left[-T \cdot \rho \cdot \left(\frac{\mu(E)}{\sin\psi_1} + \frac{\mu(i)}{\sin\psi_2} \right) \right] \right\} dE \qquad [3]$$

The equation for secondary fluorescent radiation is, however, not such a simple extension of that for primary fluorescence. An additional numerical integration step is required:

$$n_{sec,i} = A \cdot B_i \cdot B_j \cdot c_i \cdot c_j \cdot \eta_i \cdot \frac{1}{2 \cdot \sin\psi_1} \int_{E_j}^{E_0} x(E) \cdot \tau_i(j) \cdot \tau_j(E) \cdot$$

$$\cdot \int_{\varphi=0}^{\pi/2} \frac{\cos\varphi}{\sin\varphi} \cdot (F_1 - F_2 + F_3 - F_4) \cdot d\varphi \cdot dE$$

$$F_1 = \frac{1 - \exp\left[-T \cdot \rho \cdot \left[\frac{\mu(E)}{\sin\psi_1} - \frac{\mu(j)}{\sin\psi_2} \right] \right]}{\left[\frac{\mu(E)}{\sin\psi_1} + \frac{\mu(j)}{\sin\varphi} \right] \cdot \left[\frac{\mu(i)}{\sin\psi_2} - \frac{\mu(j)}{\sin\varphi} \right]}$$

$$F2 = \frac{1 - \exp\left[-T \cdot \rho \cdot \left[\frac{\mu(E)}{\sin\psi_1} + \frac{\mu(i)}{\sin\psi_2} \right] \right]}{\left[\frac{\mu(E)}{\sin\psi_1} + \frac{\mu(i)}{\sin\psi_2} \right] \cdot \left[\frac{\mu(i)}{\sin\psi_2} - \frac{\mu(j)}{\sin\varphi} \right]}$$

$$F_3 = \frac{1 - \exp\left[-T \cdot \rho \cdot \left[\frac{\mu(E)}{\sin\psi_1} - \frac{\mu(i)}{\sin\psi_2} \right] \right]}{\left[\frac{\mu(i)}{\sin\psi_2} + \frac{\mu(j)}{\sin\varphi} \right] \cdot \left[\frac{\mu(E)}{\sin\psi_1} + \frac{\mu(i)}{\sin\psi_2} \right]} \qquad [4]$$

$$F_4 = \frac{\exp\left[-T \cdot \rho \cdot \left[\frac{\mu(i)}{\sin\psi_2} - \frac{\mu(j)}{\sin\varphi} \right] \right]}{\left[\frac{\mu(i)}{\sin\psi_2} + \frac{\mu(j)}{\sin\varphi} \right] \cdot \left[\frac{\mu(E)}{\sin\psi_1} - \frac{\mu(j)}{\sin\varphi} \right]} -$$

$$- \frac{\exp\left[-T \cdot \rho \cdot \left[\frac{\mu(E)}{\sin\psi_1} - \frac{\mu(i)}{\sin\psi_2} \right] \right]}{\left[\frac{\mu(i)}{\sin\psi_2} + \frac{\mu(j)}{\sin\varphi} \right] \cdot \left[\frac{\mu(E)}{\sin\psi_1} - \frac{\mu(j)}{\sin\varphi} \right]}$$

φ is an angle related to the direction of the primary fluorescent radiation which excites the secondary fluorescent radiation within the specimen.

The thin film equations developed above are valid for free standing films and for such cases where the interaction with a substrate is negligible; otherwise, secondary enhancement by substrate radiation has to be considered. The secondary

fluorescent film count rate excited by primary substrate radiation, j, is:

$$n_{sec,i} = A.B_i.B_j.c_i.c_j.\eta_i.\frac{1}{2.\sin\psi_1}\int_{E_j}^{E_0} x(E).\tau_i(j).\tau_j(E).$$

$$.\exp(-T.\rho.\frac{\mu(E)}{\sin\psi_1}).\int_0^{\pi/2} ctg\varphi.F_5.d\varphi.dE \qquad [5]$$

$$F_5 = \frac{\exp\left[-T.\rho.\frac{\mu(i)}{\sin\psi_2}\right] - \exp\left[-T.\rho.\frac{\mu(i)}{\sin\varphi}\right]}{\left[\frac{\mu^{sub}(E)}{\sin\psi_1}+\frac{\mu^{sub}(j)}{\sin\varphi}\right]\left[\frac{\mu(j)}{\sin\varphi}-\frac{\mu(i)}{\sin\psi_2}\right]}$$

3. Fluorescent Radiation from the Substrate (Single Thin Film Layer)

It is sometimes desirable to compute the count rates from substrate radiation as a function of (shielding) film thickness and film composition. Primary fluorescent radiation, secondary fluorescent radiation excited by primary fluorescent radiation within the substrate, and secondary fluorescent radiation excited by primary radiation from the thin film layer have then to be computed.

The primary fluorescent count rate from the substrate is easily derived from equation [1] by considering absorption of primary radiation (tube radiation) and primary fluorescent radiation by the thin film:

$$n^{sub}_{prim,i} = A.B_i.c_i.\eta_i.\frac{1}{\sin\psi_1}.\int_{E_i}^{E_0}\frac{x(E).\tau_i(E)}{\frac{\mu(E)}{\sin\psi_1}+\frac{\mu(i)}{\sin\psi_2}}.$$

$$.\exp\left[-T.\rho.\left[\frac{\mu^{film}(E)}{\sin\psi_1}+\frac{\mu^{film}(i)}{\sin\psi_2}\right]\right]dE \qquad [6]$$

The same correction has to be applied to the secondary fluorescent count rate of analyte radiation, i, excited by primary fluorescent radiation, j, within the substrate:

$$n^{sub}_{sec,i} = A.B_i.B_j.c_i.c_j.\eta_i.\frac{1/2}{\sin\psi_1}.\int_{E_j}^{E_0}\frac{x(E).\tau_i(j).\tau_j(E)}{\frac{\mu(E)}{\sin\psi_1}+\frac{\mu(i)}{\sin\psi_2}}.$$

$$.\exp\left\{-T.\rho.\left[\frac{\mu^{film}(E)}{\sin\psi_1}+\frac{\mu^{film}(i)}{\sin\psi_2}\right]\right\}. \qquad [7]$$

$$.\left\{\frac{\sin\psi_1}{\mu(E)}.\ln\left[1+\frac{\mu(E)}{\mu(j).\sin\psi_1}\right]+\frac{\sin\psi_2}{\mu(i)}.\right.$$

$$\left.\ln\left[1+\frac{\mu(i)}{\mu(j).\sin\psi_2}\right]\right\}dE$$

The contribution of primary fluorescent radiation, j, from the thin film layer to the analyte radiation, i, from the substrate is

$$n^{film,sub}_{sec,i} = A.B_i.B_j.c_i.c_j.\eta_i.\frac{1}{2.\sin\psi_1}\int_{E_j}^{E_0} x(E).\tau_i(j).\tau_j(E).$$

$$.\int_0^{\pi/2}\frac{\exp\left[-T.\rho.\frac{\mu^{film}(j)}{\sin\varphi}\right]-\exp\left[-T.\rho.\frac{\mu^{film}(E)}{\sin\psi_1}\right]}{\left[\frac{\mu^{film}(E)}{\sin\psi_1}-\frac{\mu^{film}(j)}{\sin\varphi}\right]\left[\frac{\mu(j)}{\sin\varphi}+\frac{\mu(i)}{\sin\psi_2}\right]}ctg\varphi.d\varphi.dE \qquad [8]$$

4. Fluorescent Radiation from Multiple Thin Film Layers

The equation for the primary fluorescent count rate from layer m of a multiple thin film package is derived from the single layer thin film equation by correcting for absorption of primary radiation and primary fluorescent radiation by the shielding (m − 1) layers above the layer under consideration:

$$n_{prim,i} = A.B_i.c_i.\eta_i.\frac{1}{\sin\psi_1}.\int_{E_i}^{E_0}\frac{x(E).\tau_i(E)}{\frac{\mu(E)}{\sin\psi_1}+\frac{\mu(i)}{\sin\psi_2}}.$$

$$.\exp\sum_{k=1}^{m-1}\left[-T^k.\rho^k.\left[\frac{\mu^k(E)}{\sin\psi_1}+\frac{\mu^k(i)}{\sin\psi_2}\right]\right]. \qquad [9]$$

$$.\left\{1-\exp\left[-T^m.\rho^m.\left[\frac{\mu^m(E)}{\sin\psi_1}+\frac{\mu^m(i)}{\sin\psi_2}\right]\right]\right\}.dE$$

In a similar way the secondary fluorescent count rate excited by primary fluorescent radiation, j, within the same thin film layer can be derived from the corresponding single layer equation:

$$n^m_{sec,i} = A.B_i.B_j.c_i.c_j.\eta_i.\frac{1}{2.\sin\psi_1}\int_{E_j}^{E_0} x(E).\tau_i(\ ).\tau_j(E).$$

$$.\exp\sum_{k=1}^{m-1}\left[-T^k.\rho^k.\left[\frac{\mu^k(E)}{\sin\psi_1}+\frac{\mu^k(i)}{\sin\psi_2}\right]\right]$$

$$.\int_0^{\pi/2}\frac{\cos\varphi}{\sin\varphi}.(F_6-F_7+F_8-F_9).d\varphi.dE \qquad [10]$$

$$F_6 = \frac{1-\exp\left[-T^m.\rho^m.\frac{\mu^m(E)}{\sin\psi_1}+\frac{\mu^m(j)}{\sin\varphi}\right]}{\left[\frac{\mu^m(E)}{\sin\psi_1}+\frac{\mu^m(j)}{\sin\varphi}\right].\left[\frac{\mu^m(i)}{\sin\psi_2}-\frac{\mu^m(j)}{\sin\varphi}\right]}$$

$$F_7 = \frac{1-\exp\left[-T^m.\rho^m.\frac{\mu^m(E)}{\sin\psi_1}+\frac{\mu^m(i)}{\sin\psi_2}\right]}{\left[\frac{\mu^m(E)}{\sin\psi_1}+\frac{\mu^m(i)}{\sin\psi_2}\right].\left[\frac{\mu^m(i)}{\sin\psi_2}-\frac{\mu^m(j)}{\sin\varphi}\right]}$$

$$F_8 = \frac{1 - \exp\left[-T^m.\rho^m.\left(\frac{\mu^m(E)}{\sin\psi_1} + \frac{\mu^m(i)}{\sin\psi_2}\right)\right]}{\left[\frac{\mu^m(i)}{\sin\psi_2} + \frac{\mu^m(j)}{\sin\varphi}\right].\left[\frac{\mu^m(E)}{\sin\psi_1} + \frac{\mu^m(i)}{\sin\psi_2}\right]}$$

$$F_9 = \frac{\exp\left[-T^m.\rho^m.\left(\frac{\mu^m(i)}{\sin\psi_1} + \frac{\mu^m(j)}{\sin\varphi}\right)\right]}{\left[\frac{\mu^m(i)}{\sin\psi_2} + \frac{\mu^m(j)}{\sin\varphi}\right].\left[\frac{\mu^m(E)}{\sin\psi_1} - \frac{\mu^m(j)}{\sin\varphi}\right]} - \frac{\exp\left[-T^m.\rho^m.\left(\frac{\mu^m(E)}{\sin\psi_1} - \frac{\mu^m(i)}{\sin\psi_2}\right)\right]}{\left[\frac{\mu^m(i)}{\sin\psi_2} + \frac{\mu^m(j)}{\sin\varphi}\right].\left[\frac{\mu^m(E)}{\sin\psi_1} - \frac{\mu^m(j)}{\sin\varphi}\right]} \qquad [10]$$

Secondary enhancement effects caused by fluorescent radiation from other layers require correction for absorption of primary radiation on its path to layer g, where primary fluorescent radiation, j, is excited; for absorption of primary fluorescent radiation, j, to layer m, where it excites secondary fluorescent radiation; and for absorption of secondary fluorescent radiation, i, on its path to the detector through the (m − 1) layers above.

The resulting equation consists of two components related to the cases g>m and g<m:

$$n^{g,m}_{sec,i} = n^{g>m,m}_{sec,i} + n^{g<m,m}_{sec,i}$$

$$n^{g<m,m}_{sec,i} = A.B_i.B_j.c_i^m.c_j^g.\eta_i.\frac{1}{2.\sin\psi_1}.$$

$$\int_{E_j}^{E_o} x(E).\tau_i(j).\tau_j(E).\int_0^{\pi/2} ctg\varphi\,\frac{F_{10}.F_{11}.F_{12}}{F_{13}}.d\varphi.dE$$

$$F_{10} = \exp\left\{-\frac{1}{\sin\psi_1}\sum_{k=1}^{g-1}T^k.\rho^k.\mu^k(E) - \frac{1}{\sin\varphi}\sum_{k=g}^{m-1}T^k.\rho^k.\mu^k(j) - \frac{1}{\sin\psi_2}\sum_{k=1}^{m-1}T^k.\rho^k.\mu^k(i)\right\}$$

$$F_{11} = 1 - \exp\left[-\frac{1}{\sin\psi_2}.T^m.\rho^m.\mu^m(i) - \frac{1}{\sin\varphi}.T^m.\rho^m.\mu^m(j)\right]$$

$$F_{12} = 1 - \exp\left[\frac{1}{\sin\varphi}.T^g.\rho^g.\mu^g(j) - \frac{1}{\sin\psi_1}.T^g.\rho^g.\mu^g(E)\right]$$

$$F_{13} = \left[\frac{\mu^g(E)}{\sin\psi_1} - \frac{\mu^g(j)}{\sin\varphi}\right]\left[\frac{\mu^m(j)}{\sin\varphi} + \frac{\mu^m(i)}{\sin\psi_2}\right] \qquad [11a]$$

continued...

$$n^{g>m,m}_{sec,i} = A.B_i.B_j.c_i^m.c_j^g.\eta_i.\frac{1}{2.\sin\psi_1}.$$

$$\int_{E_j}^{E_o} x(E).\tau_i(j).\tau_j(E).\int_0^{\pi/2} ctg\varphi\,\frac{F_{14}.F_{15}.F_{16}}{F_{17}}.d\varphi.dE$$

$$F_{14} = \exp\left\{-\frac{1}{\sin\psi_1}\sum_{k=1}^{g-1}T^k.\rho^k.\mu^k(E) - \frac{1}{\sin\varphi}\sum_{k=m}^{g-1}T^k.\rho^k.\mu^k(j) - \frac{1}{\sin\psi_2}\sum_{k=1}^{m-1}T^k.\rho^k.\mu^k(i)\right\}$$

$$F_{15} = 1 - \exp\left[-\frac{1}{\sin\psi_2}.T^m.\rho^m.\mu^m(i) + \frac{1}{\sin\varphi}.T^m.\rho^m.\mu^m(j)\right]$$

$$F_{16} = 1 - \exp\left[-\frac{1}{\sin\varphi}.T^g.\rho^g.\mu^g(j) - \frac{1}{\sin\psi_1}.T^g.\rho^g.\mu^g(E)\right]$$

$$F_{17} = \left[\frac{\mu^g(E)}{\sin\psi_1} + \frac{\mu^g(j)}{\sin\varphi}\right]\left[\frac{\mu^m(j)}{\sin\varphi} + \frac{\mu^m(i)}{\sin\psi_2}\right] \qquad [11b]$$

The effect of enhancement by primary fluorescent radiation from the substrate is derived from equation [11b] by assuming layer g to be infinitely thick:

$$n^{sub,m}_{sec,i} = A.B_i.B_j.c_i^m.c_j^{sub}.\eta_i\,\frac{1}{2.\sin\psi_1}.$$

$$\int_{E}^{E_j} x(E).\tau_i(j).\tau_j(E).\int_0^{\pi/2} ctg\varphi\,\frac{F_{14}.F_{15}}{F_{17}}.d\varphi.dE \qquad [12]$$

(with index g in the equations for F_{14} and F_{17} indicating "substrate")

5. Fluorescent Radiation from the Substrate (Multiple Thin Film Layers)

The equations for primary and secondary fluorescent radiations can be derived from equations [1] and [2] by considering absorption by the thin film layers similar to the derivation of equations [6] and [7]:

$$n^{sub}_{prim,i} = A.B_i.c_i^{sub}.\eta_i.\frac{1}{\sin\psi_1}.\int_{E_i}^{E_o}\frac{x(E).\tau_i(E)}{\frac{\mu^{sub}(E)}{\sin\psi_1} + \frac{\mu^{sub}(i)}{\sin\psi_2}}.\exp\left\{-\sum_{k=1}^{L}\left[T^k.\rho^k.\left[\frac{\mu^k(E)}{\sin\psi_1} + \frac{\mu^k(i)}{\sin\psi_2}\right]\right]\right\}dE \qquad [13]$$

$$n^{sub}_{sec,i} = A.B_i.B_j.c_i.c_j.\eta_i.\frac{1/2}{\sin\psi_1}.\int_{E_j}^{E_0}\frac{x(E).\tau_i(j).\tau_j(E)}{\frac{\mu(E)}{\sin\psi_1}+\frac{\mu(i)}{\sin\psi_2}}.$$

$$.\exp\left\{-\sum_{k=1}^{L}\left[\tau^k.\rho^k.\left[\frac{\mu^k(E)}{\sin\psi_1}+\frac{\mu^k(i)}{\sin\psi_2}\right]\right]\right\}.$$

$$.\left\{\frac{\sin\psi_1}{\mu(E)}.\ln\left[1+\frac{\mu(E)}{\mu(j).\sin\psi_1}\right]+\frac{\sin\psi_2}{\mu(i)}.\right.$$

$$\left.\ln\left[1+\frac{\mu(i)}{\mu(j).\sin\psi_2}\right]\right\}dE \qquad [14]$$

The contribution of primary fluorescent radiation, j, in layer g above the substrate is derived from equation [11a] by assuming layer m to be infinitely thick:

$$n^{g,sub}_{sec,i} = A.B_i.B_j.c_i^{sub}c_j^{g}.\eta_i.\frac{1}{2.\sin\psi_1}.$$

$$\int_{E_j}^{E_0}x(E).\tau_i(j).\tau_j(E).\int_0^{\pi/2}ctg\varphi\,\frac{F_{10}.F_{12}}{F_{13}}\,.d\varphi\,.dE \qquad [15]$$

(with index m in the equations for F_{10} and F_{13} indicating "substrate")

SCATTERING EFFECTS

Scattering effects are rarely quantitatively considered in practical applications of x-ray fluorescence analysis (at least in the case of excitation by photons). A few papers, however, have been published on Monte Carlo techniques dealing with single and multiple scattering (5), (6) and an approach based upon the classical fundamental parameter equations has recently been published (7).

Two cases have to be distinguished: The contribution of scattered radiation to the enhancement of fluorescent radiation as well as backscattering of primary radiation into the detector causing most of the observed background. Concerning the latter case, single scattering effects (coherent and incoherent scattering) as well as double scattering have to be covered by a theoretical treatment.

1. Single Scattering

The derivation of the intensity equation for scattered radiation (single scattering) requires only a slight modification of the fundamental parameter equation for the primary fluorescent intensity. The term

$$B_i = p_i.W_i.\frac{S_i-1}{S_i}.\frac{\Omega}{4.\pi} \qquad [16]$$

in equations [1], [3], [6], [9] and [13] (all of which describe primary fluorescent count rates) has to be replaced by

$$B_i' = d\sigma(E,\Theta)/d\Omega \qquad [17a]$$

$$d\Omega = 2.\pi.\sin\Theta.d\Theta \qquad [17b]$$

$d\sigma(E,\Theta)/d\Omega$ is the differential (mass-) scattering cross section defined as the probability, that a photon of energy E in a beam penetrating the equivalent of unit mass thickness is scattered by an angle Θ into the differential solid angle $d\Omega$. The scattering angle Θ is defined by the incidence angle of the primary radiation, ψ_1, and the take off angle of the fluorescent radiation, ψ_2:

$$\Theta = \psi_1 + \psi_2 \qquad [18]$$

In the case of coherent scattering $d\sigma(E,\Theta)/d\Omega$ is given by

$$d\sigma(E,\Theta)/d = \frac{N}{A}.r^2.\frac{1+\cos^2\Theta}{2}.F_i^2(E,\Theta).10^{-24} \qquad [19]$$

$$[\sigma] = [cm^2/g]$$

While these equations should be correct for completely amorphous material, errors are to be expected when applied to cristalline specimens, where diffraction effects occur. However, no comprehensive theoretical treatement of this factor has been given so far for XRFA applications.

The differential (mass-) cross section for incoherent scattering is given by the Klein-Nishina folmulae (8): [20]

$$d\sigma(E,\Theta)/d = \frac{N}{A}.\frac{r_0^2}{2}.\left[\frac{E'}{E}\right]^2.\left[\frac{E}{E'}+\frac{E'}{E}-\sin^2\Theta\right].10^{-24}$$

and the energy of a photon after incoherent scattering, E', is

$$E' = \frac{m_0.c^2}{1-\cos\Theta+m_0.c^2/E} \qquad [21]$$

In both, coherent and incoherent scattering, the primary beam is assumed to be unpolarized; the scattered radiation is polarized.

2. Double Scattering: Geometrical Considerations

The primary radiation is assumed to penetrate the specimen under an incidence angle ψ_1. At point B_1 (see fig. 1) within the specimen a photon is scattered by an angle Θ_1 into a new direction. At point C_1 a second scattering event occurs; the scattering angle is Θ_2 and the new direction points into the detection system.

It is feasible to describe the scattering angles as functions of angular coordinates φ and ε which can later be used as integration variables in order to cover all possible scattering directions (see equs. [26], [28]). The instrument is assumed to detect

all double scattered photons with directions (in three dimensional space) parallel to direction CD (fig. 1). This is equivalent to the condition that the incident beam (primary radiation) and detected radiation lie in planes which are parallel to each other and perpendicular to the specimen surface, and corresponds closely to the geometrical situation in a crystal spectrometer where the angular directions are defined by a collimator and the reflection characteristics of the crystal (in the case of a point source – point detector geometry slight modifications of equations [22], [23] and [25] are necessary). The scattering angles described as functions of φ and ε are then:

$$\Theta_1 = \arccos\left(\sin\psi_1 . \sin\varepsilon + \cos\varphi . \cos\psi_1 . \cos\varepsilon\right) \quad [22]$$

$$\Theta_2 = \arccos\left(-\sin\psi_2 . \sin\varepsilon + \cos\varphi . \cos\psi_2 . \cos\varepsilon\right) \quad [23]$$

3. Double Coherent Scattering

Each scattering event causes polarization of the scattered photon. In the case of double scattering an already polarized photon undergoes an additional polarization step.

The polarization factor for the second scattering event is a function of the two scattering angles Θ_1 and Θ_2, and of the angle ϱ between the two scattering planes (defined by ABC and BCD in fig. 1 (9):

$$P = \left(\cos^2\Theta_1 . \cos^2\varrho + \sin^2\varrho\right) . \cos^2\Theta_2 + \\ + \cos^2\Theta_1 . \sin^2\varrho + \cos^2\varrho \quad [24]$$

The angle ϱ can be described as a function of Θ_1 and Θ_2 under the same assumptions as for Θ_1 and Θ_2:

$$\varrho = \arccos\left(\frac{1}{\sin\Theta_1 . \sin\Theta_2} . \right. \\ \left. . \left(\cos\Theta_1 . \cos\Theta_2 - \cos(\psi_1 + \psi_2)\right)\right) \quad [25]$$

The count rate from double coherent scattering is then:

$$dn_{sec,i} = A . c_i . c_j . \eta_i . \frac{\Omega}{4\pi} . x(E) . dE . \\ \int_{\varphi=0}^{2\pi} \int_{\varepsilon=-\pi/2}^{\pi/2} \frac{d\sigma(\Theta_1)}{d\Omega'} . \frac{d\sigma(\Theta_2)}{d\Omega'} . P . \frac{\operatorname{ctg}\varepsilon}{\sin\psi_1} . \\ . \frac{1}{\left(\frac{\mu(E)}{\sin\psi_1} - \frac{\mu(E)}{\sin\varepsilon}\right)\left(\frac{\mu(E)}{\sin\psi_2} + \frac{\mu(E)}{\sin\varepsilon}\right)} . d\varepsilon . d\varphi \quad [26]$$

4. Double Incoherent Scattering

The situation in the case of double incoherent scattering is more complicated than that of coherent scattering because of the energy shifts involved and because of more complicated (energy dependent) relationships between the two polarization states.

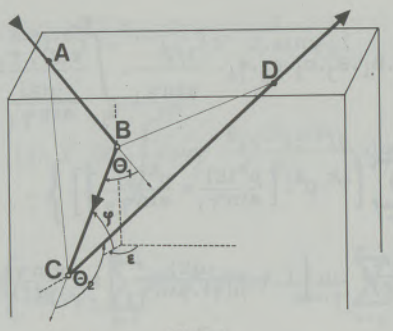

Fig. 1
Double Scattering: Geometrical situation.

The combined scattering factor for double incoherent scattering is (10)

$$S(\Theta_1,\Theta_2,E) = \frac{1}{4} . \frac{e^2}{m_o . c^2} \left[\frac{E'}{E}\right]^2 . \\ . \left(\int_{01} . \int_{02} - \int_{01} . \sin^2\Theta_2 - \int_{12} . \sin^2\Theta_1 + 2 . \sin^2\Theta_1 . \sin^2\Theta_2 . \cos^2\varrho\right)$$

$$\int_{01} = \frac{E'}{E} + \frac{E}{E'} \quad ; \quad \int_{12} = \frac{E''}{E'} + \frac{E'}{E''} \quad [27]$$

and the count rate from double incoherent scattering

$$dn_{sec,i} = A . c_i . c_j . \eta_i . \frac{\Omega}{4\pi} . x(E) . dE . \\ \int_{\varphi=0}^{2\pi} \int_{\varepsilon=-\pi/2}^{\pi/2} S(\Theta_1,\Theta_2,E) . \frac{\operatorname{ctg}\varepsilon}{\sin\psi_1} . \\ \frac{1}{\left(\frac{\mu(E)}{\sin\psi_1} - \frac{\mu(E)}{\sin\varepsilon}\right)\left(\frac{\mu(E)}{\sin\psi_2} + \frac{\mu(E)}{\sin\varepsilon}\right)} . d\varepsilon . d\varphi \quad [28]$$

NUMERICAL CONSIDERATIONS

1. Quantitative Analysis of Bulk Material

Equations [1] and [2] are based on the assumption, that the beam of primary radiation has a cross section of 1 cm² and that the spectral distribution of the photons is defined by a function x(E). The calibration factor A is required in order to obtain the numbers corresponding to an actual measurement carried out with a specific instrument with a given mA-setting of the x-ray tube. Theoretically this factor should be independent of type and composition of the specimen, of the analyzed element, and of the experimental parameters except the tube current. Only one calibration measurement should be required for a full knowledge of all factors affecting the fluorescent intensities.

Under this assumption, quantitative analysis of bulk specimens is possible without any standard specimens. Such "no standard-techniques"

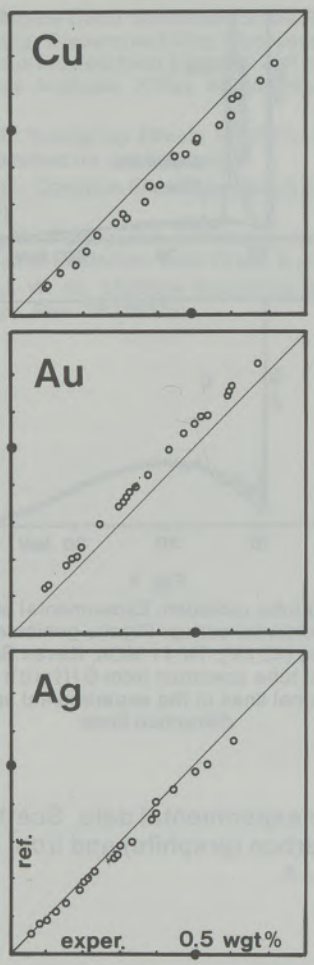

Fig. 2
Results from "No Standards"-analysis. Specimens were Ag-Au-Cu alloys. Chemical Reference data: ÖGUSSA Vienna (manufacturer). Experimental conditions: Rigaku goniometer, Cr-target fine focus tube (45 kV), TN-11 multi channel analyzer, Kevex Si(Li) detector

entirely depend on the accuracy of the fundamental parameters envolved; in practice, relatively good results (absolute errors around 2–5 wt % abs) are obtained for the transition elements if K-lines are analyzed. Analysis of L-lines and other elements is often much less accurate, mainly because of poor available data for transition probabilities and fluorescent yields (11). An example for practical results is shown in fig. 2.

All element specific constants which are not a function of concentration and energy can be concluded in a single element specific constant, B_i (see equ. [16]). It can be eliminated by using calibration standards for each element in the unknown specimen. The usual way is to build count rate ratios where these B_i's as well as the general calibration constant A cancel, at least in the mathematical terms for primary fluorescence counts. The transition probabilities for the elements causing secondary enhancement (the j's in equation [2]) remain however unaffected by this calibration step. A more accurate way is to specifically determine the factors A and B_i by calibration standards and to use their values in the terms for primary and secondary fluorescent counts when computing the unknown concentrations.

Any kind of standards can be used for the determination of the constants A and B_i and there is no advantage of restricting the concentrations of the standards to values silimar to those of the unknown. There are, however, also uncertainities involved in the data for absorption coefficients and in the function x(E) describing the spectral distribution of the primary radiation. In order to compensate for these errors it is also feasible to build count rate ratios, but for this purpose standards with a similar qualitative and quantitative composition as the unknown should be used.

2. Quantitative Analysis of Thin Films

In thin film analysis the count rates are not only a function of elemental concentrations but also of film thickness(es). In the case of single film layers any set of computed count rates is related in a unique way to the composition of a film and its thickness. It is therefore possible to determine concentrations and thickness simultaneously from a single set of thin film count rate data (the constant A and, for better accuracy, the B_i's, must have been determined from standards).

In the case of multiple thin films the relationship between count rate data and configuration of the thin film package is generally not unique and restrictions have to be applied. One possibility is to require any chemical element to appear in only one layer and the qualitative composition of all layers to be known. In this case all concentrations and thicknesses can be determined simultaneously from a single set of count rate data (again A and, for better accuracy the B_i's, must be known).

Examples for results from computations concerning thin films are given in fig. 3 (13).

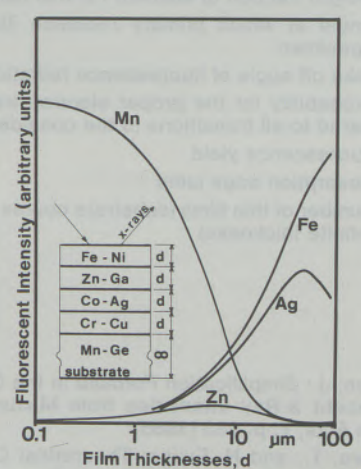

Fig. 3
Prediction of intensities of multiple thin film packages

3. Computation of Scattered Intensities

Computation of scattered intensities requires the differential cross sections to be known. In the case of coherent scattering, the cross sections are a function of the atomic scattering factors, which are tabulated as functions of $\sin\frac{\theta}{2}/\lambda$ or can be computed from polynominal fit functions (12). The energy range of such tables is usually restricted to values between $0 < \sin\frac{\Theta}{2}/\lambda < 2$ corresponding to an energy of about 25 keV for backscattering ($\Theta = 180°C$). This does not constitute much of a problem in practical applications because incoherent scattering by far exceeds coherent scattering at these energies.

The computation of incoherent cross sections is directly possible by using the Klein-Nishina formulae. It should be carried in mind, that in this simplified formulae the assumption is made that the photon energy is comparable to the rest energy of an electron (which exceeds by far the energy range of fluorescence analysis) and that binding effects of the electrons can therefore be neglected. For more accurate results more complex quantum mechanical considerations are required.

As an example for the application of fundamental parameter equations for scattering, the backscattered spectral images of the primary radiation from an Cu-target x-ray tube were computed and compared to experimental data. Scattering materials were carbon (graphite) and iron. Results are shown in fig. 4.

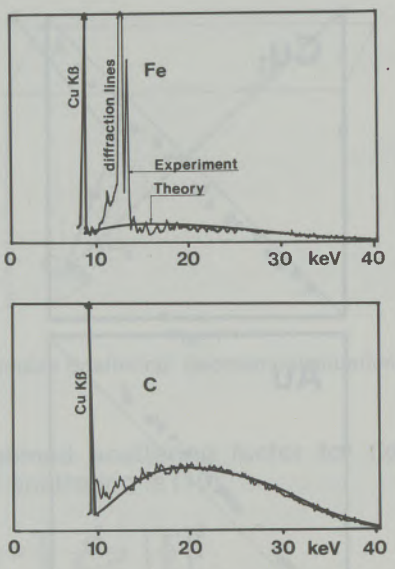

Fig. 4

Backscattered tube radiation: Experimental and theoretical spectra. Experimental set-up: Rigaku goniometer, Cu-target fine focus tube (45 kV), TN-11 MCA, Kevex Si(Li) detector. Theoretical tube spectrum from Gilfrich et al. (14). The additional lines in the experimental spectra are diffraction lines

Nomenclature

$\mu_i(E)$	mass absorption coefficient for radiation energy E in element i
$\mu(E)$	mass absorption coefficient for energy E in a sample
$\mu^m(E)$	mass absorption for energy E in thin film m
$\mu(i)$	mass absorption coefficient for analyte line i
τ	photoabsorption coefficient
T, T^m	thin film thicknesses (m indicates layer)
c_i	weight fraction of element i
$c^m{}_{,i}$	weigth fraction of element i in thin film m
ψ_1	angle at which primary radiation illuminates the specimen
ψ_2	take off angle of fluorescence radiation
p_i	probability for the proper electron transition compared to all transitions to the considered shell
w_i	fluorescence yield
S_i	absorption edge jump
L	number of thin films (substrate counts as a film with infinite thickness)
Ω	solid angle at which radiation is detected
$\eta(i)$	detector efficiency for analyte line i
ϱ^m	density of specimen or (with index) of thin film m
F_i	atomic scattering factor
A	calibration constant
n_i^k	count rate from analyte line i (a selected line from element i) (index k may be used to indicate origin of radiation in a specified layer)
$n_i^{g,k}$	secondary fluorescence count rate from analyte i in layer k excited by primary fluorescence originating in layer g
E	energy of a photon
E_i	absorption edge energy of analyte line i
x(E)	spectral distribution function of primary radiation; $x(E) \cdot dE$ is the number of photons with energies between E and $E+dE$ in a beam with a cross section of 1 cm^2 impinging the specimen surface per second.

References

1. Sherman, J.: Simplification Formula in the Correlation of Fluorescent X-Ray Intensities from Mixtures. Spectrochimica Acta, 7, p. 283 (**1955**).
2. Shirariwa, T., and N. Fujino: Theoretical Calculation of Fluorescent X-Ray Intensities in Fluorescent X-Ray. Spectrochemical Analysis Jap. J. Appl. Phys. 5, 10, p. 886 (**1966**).
3. Pollai, G., M. Mantler and H. Ebel: Die Sekundäranregung bei der Röntgenfluoreszenzanalyse ebener dünner Schichten. Spectrochim. Acta, 26 B, p. 747 (**1971**).
4. Mantler, M.: Quantitative X-Ray Fluorescent Analyses of Multiple Thin Film Layers. American Chemical Abstracts (accepted for publication).

5. Armc, F.: Monte Carlo Simulation of the Backscatter Region in Energy Dispersive X-Ray Fluorescence Spectra of Homogenous Multielement Samples with an Application to Quantitative Analysis. X-Ray Spectrometry, 13, p. 103 (**1984**).
6. Mantler, M.: Scattering Effects in XRFA. X-Ray Spectrometry (submitted for publication).
7. Evans, R. D.: Compton Effect. Handbuch der Physik 34, p. 218 (**1954**).
8. Azaroff, L. V.: Polarization Correction for Crystal-Monochromatized X-Radiation. Acta Cryst. 8, p. 701 (**1955**).
9. Dumond, J. W. M.: Multiple Scattering in the Compton Effect. Phys. Rev. 36 (**1930**).
10. Wightman, W.: Note on the Polarization Effects in Compton Scattering. Phys. Rev. 74, 12 (**1948**).
11. Mantler, M., and H. Ebel: No Standard X-Ray Fluorescence Analysis. X-Ray Spectrometry, 9, p. 148 (**1980**).
12. International Tables for Crystallography IV, Kynoch Press, (**1969**).
13. Mantler, M.: LAMA III – A Computer Program for Quantitative XRFA of Bulk Specimens and Thin Film Layers. Advances in X-Ray Spectrometry 27, p. 433 (**1984**).
14. Gilfrich, J. V., and L. S. Birks: Spectral Distribution of X-Ray Tubes for Quantitative X-Ray Fluorescence Analysis. Anal. Chem. 40, p. 1077 (**1968**).

Slow Fatigue Crack Growth under Spectrum-Loads in RSt 37-2 Steel

Elmar K. Tschegg*), Stefanie E. Stanzl**) and Herwig Mayer*)

Dedicated to the 80th birthday of Prof. Dr. Franz Lihl

The fatigue crack growth behavior of the structural steel RSt 37-2 has been studied in constant amplitude, eight-step and random loading tests at a mean stress equal to zero ($R = -1$) and in the range of low crack growth rates. The results, plotted versus the root mean square (RMS)-value of the cyclic stress intensity (K_{rms}), show that the crack growth curves coincide for the different load spectra in the Paris-regime. This is not the case for the threshold regime. In constant amplitude and eight step tests, pronounced thresholds are detected. For random-loading, however, a threshold in the conventional sense cannot be observed but a lower limit for the stress intensity range might be defined, below which crack growth rates do not exceed a certain value, for example 10^{-12}m/cycle. Comparison of experimentally determined crack growth rates and results from model-calculations reveal that neither remarkable crack retardation nor acceleration occurs at the mean stress zero ($R = -1$).

Langsame Ermüdungsrißausbreitung bei verschiedenen Beanspruchungsspektren im Stahl RSt 37-2

Der Baustahl RSt 37-2 wurde hinsichtlich seiner Ermüdungsrißausbreitungseigenschaften im Konstantamplituden-, Achtstufen- und Random-Versuch mit einem Mittelspannungswert null ($R = -1$) im Bereich langsamer Rißgeschwindigkeiten untersucht. Die Ergebnisse, dargestellt in Abhängigkeit vom quadratischen Mittelwert der Spannungsintensität, K_{rms}, zeigen, daß die Rißausbreitungskurven der verschiedenen Beanspruchungsspektren im Paris-Bereich zusammenfallen. Dies ist hingegen nicht der Fall für den Schwellwertbereich. Bei der Konstantamplituden- und bei der Achtstufen-Beanspruchung zeigen sich ausgeprägte Schwellwerte. Bei der Random-Beanspruchung wird ein Schwellwert im herkömmlichen Sinne nicht beobachtet, und es kann nur eine untere Schranke des Spannungsintensitätswertes bei z. B. einer Rißgeschwindigkeit von 10^{-12}m/Lastwechsel angegeben werden. Ein Vergleich der experimentell bestimmten Rißausbreitungskurven mit solchen aus Modellrechnungen zeigt, daß bei einer Beanspruchung mit einem Mittelspannungswert null ($R = -1$) keine nennenswerten Rißverzögerungs- und Beschleunigungseffekte auftreten.

Croissance lente de criques de fatigue sous charges spectrales dans l'acier RSt 37-2

On a étudié les caractéristiques de propagation des criques de fatigue dans l'acier de construction RSt 37-2 à des amplitudes constantes, au moyen d'essais à huit paliers et d'essais au hazard, pour une valeur moyenne de contrainte zéro ($R = -1$), dans le domaine des vitesses lentes de propagation des criques. Les résultats, établis en fonction de la valeur quadratiques moyenne de l'intensité de contrainte, K_{rms}, montrent que les courbes de propagation des criques des divers spectres de sollicitation concordent dans le régime de Paris. Par contre il n'en est pas ainsi dans le régime du seuil. Dans le cas des essais à amplitude constante, ou de la sollicitation à huit paliers, on note des valeurs marquées des seuils. Pour la sollicitation au hazard, on n'observe pas de seuil proprement dit et on ne peut indiquer qu'une limite inférieure de l'intensité de contrainte pour une vitesse de contrainte, par exemple, de 10^{-12}m/cycle. La comparaison entre les courbes de propagation de criques déterminées expérimentalement avec celles obtenues au moyen de calculs modèles montre que, pour une sollicilation à contrainte moyenne zéro ($R = -1$), il ne se produit pas de retard ou d'accélération notable des criques.

1. Introduction

All technical materials contain small defects. These may act as crack initiation sites, if the material is fatigue-loaded. After a small crack reaches a certain critical length, it grows until fracture of the whole component occurs. This may cause accidents with loss of human life or at least environmental damage and high financial costs.

In order to avoid such accidents crack growth predictions are often made (1). These are as important as calculations of the static strength of any pre-cracked component. Specific material properties such as the fatigue crack growth rates versus the cyclic stress intensity are the basis for such calculations. These crack growth curves have to be obtained experimentally. Usually they are measured in one-step tests (i.e. with constant amplitudes and constant mean stress) (2), (3). Life times of a pre-cracked component are calculated

*) Univ.-Doz. Dr. Elmar K. Tschegg, Dipl.-Ing. Herwig Mayer, Institute for Applied and Technical Physics, Technical University Vienna, Austria

**) Univ.-Doz. Dr. Stefanie E. Stanzl, Institute for Solid State Physics, University of Vienna, Austria

then by integration of the crack growth curve under the assumption that the component is loaded with constant stress-amplitude and constant mean-value. However, this kind of loading is not too usual in practice; there, the amplitudes vary usually radomly (4).

In such case, the crack growth rate does not only depend on the momentary cyclic stress intensity and R-value. Actual measurements show that the crack growth rate depends on the load-sequence; crack growth retardations as well as accelerations may occur. In order to understand load-sequence effects and especially to separate the different parameters, numerous investigations with various load-sequences have been performed. Examples are given in (5), (6), (7) where tests at constant amplitude and mean-stress with single or repeated positive or negative overloads are reported. Such changes of constant-amplitude loading cause crack growth retardations which depend essentially on the height of a peak load, on the number of peaks, the R-value and the cyclic stress intensity of the constant amplitude background loading.

Similar results have been observed for block-loading – at the transition from a high-amplitude-block to a low one (or from a high mean-load to a low mean-load-block) and from low to high (8), (9). For complex load-sequences, crack retardation and acceleration interact in a complex manner and it is difficult to predict the consequencies (5). If the load-sequencies consist of blocks, crack retardations or accelerations effects may still be registered, whereas during random-loading retardations and accelerations are continously interrupted so that these contrasting effects are neutralized partly or completely. Therefore, it has been tried to correlate the fatigue crack growth behavior under random loading in some way with constant-amplitude crack growth (5), (10). An "equivalent" cyclic stress intensity has been introduced which should yield the same crack growth rates under constant amplitude loading:

$$da/dN = f(\Delta K_{\text{constant amplitudes}}) = f(\Delta K_{\text{random loading}})$$

It has been attempted to introduce the root-mean-square (RMS) as the equivalent cyclic stress intensity for the constant-amplitude value. The crack growth curve is then given by:

$$da/dN = C(\Delta K_{rms})^n$$

where $\Delta K_{rms} = (\sum_{i=1}^{N} \Delta K^2_i / N)^{1/2}$, and C, n are the constants of the Paris equation. In several cases the RMS value was proved to be a good correlation parameter (11).

Though good results could be obtained in the midrange of cyclic crack growth, no systematic studies exist on material behavior in the threshold regime during random loading. As many components are stressed with low varying amplitudes in practice, knowledge in this field would be desirable. However, extremely long testing times are needed with conventional fatigue machines for such measurements. For a reliable measurement of threshold values during random loading, at least 10^8 to 10^9 cycles are needed for one data-point; with conventional hydraulic fatigue machines which work between 10–100 Hz such a test is almost impossible.

This paper attempts to narrow this gap of knowledge about fatigue crack growth behavior during random loading. Crack growth studies have been performed on RSt 37 steel with different amplitude distributions using the time-saving ultrasound technique (12), which has been adapted for variable-amplitude loading conditions (13), (14).

2. Material and method

In order to characterize crack growth behavior at very low crack growth rates during complex loading sequencies, the carbon steel RSt 37-2 (Din 17100-80) has been used. This steel can be easily welded electrically and is used for machine constructions or bridges. It is commercially available in form of rods or sheets. The material for this work was cut from 10 mm sheet metal, parallel and transverse to the rolling direction. The chemical composition and the mechanical properties of the cold-rolled material are summarized in table 1. The mechanical properties in longitudinal and transverse rolling direction are only slightly different and are therefore not separately given in table 1.

For work with resonance machines given specimen dimensions must be used. Dumbbell-shaped flat specimens with a thickness of 2,5 mm in the center where the maximum of stress is attained were tested in longitudinal and transverse rolling direction. A notch of 1 mm was introduced in the center. One broad side of the specimens was polished and the growing crack was observed there during fatigue loading with a video camera. Thus crack propagation can be measured conveniently on a monitor and also may be recorded on a tape for further evaluation. The magnification on the monitor used for these measurements was

Table 1

Chemical composition of RSt 37-2 steel

element	C	Mn	P	S	Al	N
amount (wt%)	0.11	0.41	0.013	0.016	0.04	0.005

Average tensile properties of RSt 37-2 steel at ambient temperature

Ultimate tensile strength	R_m	= 386 MPa
Yield strength 0.2% offset	$R_{p0.2}$	= 255 MPa
% reduction in area	A_5	= 38.5%

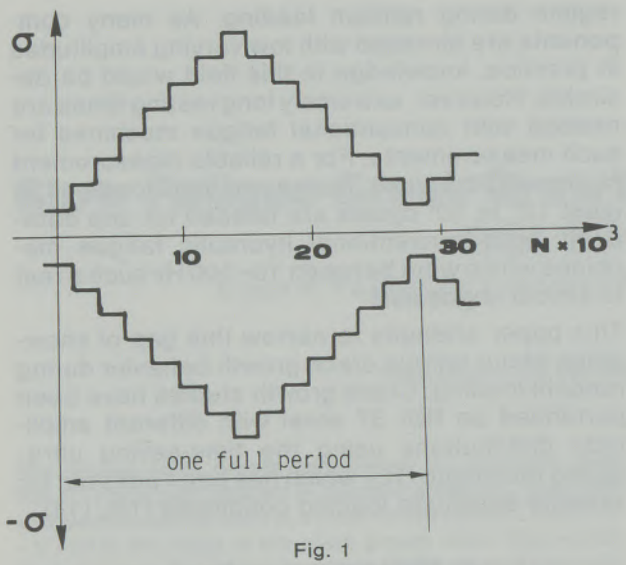

Fig. 1
Amplitude (stress)-distribution in eight-step test

130; therefore crack increments of some μm could be detected. Usually crack increments of 100 μm or at most 200 μm at high stress amplitudes were evaluated for each data point.

Fatigue loading was performed with an ultrasound machine which has been described in detail elsewhere (13), (14). Therefore, only the most essential features are mentioned in this paper. The specimens were stressed in resonance at 21 kHz with fully reversed push-pull loading ($R = -1$). Strains are measured in the center of the specimens with micro-strain gauges. A coil-magnet assembly serves as feedback control for amplitude measurement and control. The control unit furnishes the amplitude sequences which are generated by a computer. The computer controls pre-given amplitudes, number of cycles within a pulse and length of pauses between the pulses. In addition the computer does not only serve to control the process but also stores and evaluates the data. For example, pre-given amplitudes, actually performed strain-amplitudes, frequency and number of cycles are registered. It is typical of resonance machines that they cannot perform single cycles with a certain amplitude like hydraulic machines. A number of cycles is always needed to build up a certain amplitude and also to let it fade out. Therefore, ultrasound machines cannot produce single cycles either; in this work, pulses containing 1000 cycles were performed:

Three different load-programs were used for the St-37 steel.

a) a constant amplitude program
b) an eight-step sequence
c) a test with random distribution of the amplitude (random-loading)

In the eight-step test the amplitude rises in steps and decreases after the maximum is obtained again in steps, as shown in fig. 1. The tests were begun with the lowest amplitude and stopped after a whole period was performed. Each step contained 2000 cycles. After each step a pause was introduced in order to avoid heating of the specimens due to damping processes. For the studies of this work a standard load sequence recommended and described by Fischer et al. (15) was used which yields an amplitude distribution with a Gauß'ian cumulative frequency.

The range of possible tensile stresses is divided into 16 steps. The irregularity factor (N/N_o) is 0.999 (N is the number of transitions through the mean stress = 0 and N_o is the number of amplitude maxima) and the mean stress is zero ($R = -1$). Analogous to the tensile range, the range of compressive stresses is devided into 16 steps, thus resulting in 32 stress levels on the whole. The division of the compressive-stress range need not be programmed separately, if loading is symmetric around the mean stress = 0 as in this work.

The pre-given amplitudes are calculated with the aid of a Markov-matrix (15). The as received amplitude sequence is a Markov sequence, where two following amplitudes are combined statistically, but where they do not depend on the other previous process. Details about calculating the amplitude series may be read in (15). The repeat sequence is 10^6 pulses. The amplitude distribution for these 10^6 pulses (where 1 pulse contains 1000 cycles) was calculated according to the Markov formalism and is shown in fig. 2.

As high stress values, especially those exceeding the yield stress, are often not fully obtained, it is important to determine the actually performed amplitudes. Therefore, in this work the actual as well as the pre-given amplitudes were recorded and evaluated. This procedure is also important in view of the fact that a full load sequence of 10^6 pulses cannot be accomplished for crack growth studies at higher amplitudes (where one sequence should cause crack increments exceeding the specimen width). For this reason, calculation of the RMS values was based on the actually performed amplitudes in this work. The values of K_{max} corresponding to a given crack length and loading amplitude were calculated from a theoretical analysis, as discussed in detail in (16), (17).

3. Results

The crack growth results on RSt 37-2 steel are presented in two ways; first, the measured crack growth rates are plotted versus (I) the maximum stress intensity obtained during a whole sequence and secondly (II) versus the root mean square (RMS) value of the cyclic stress intensity K_{rms}.

I) In fig. 3 the crack growth results are plotted vs. K_{max} for constant amplitude loading, for the eight-step test and for random loading. The crack

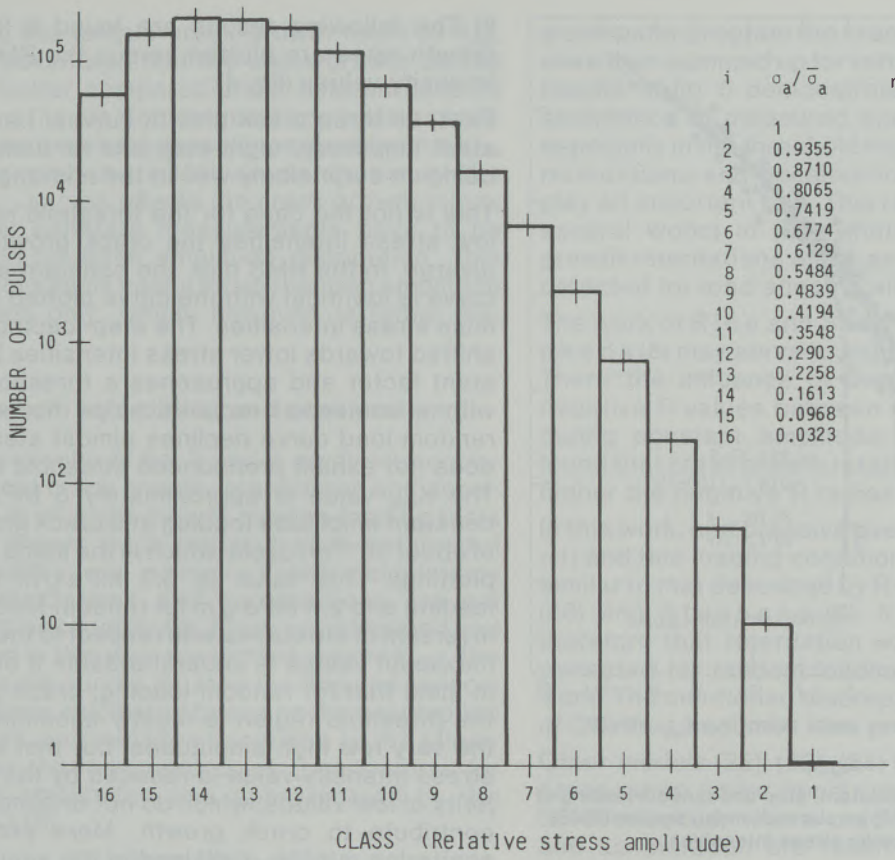

i	$\sigma_a/\bar{\sigma}_a$	number of pulses
1	1	1
2	0.9355	10
3	0.8710	47
4	0.8065	193
5	0.7419	698
6	0.6774	2230
7	0.6129	6305
8	0.5484	15728
9	0.4839	34524
10	0.4194	66423
11	0.3548	111327
12	0.2903	160995
13	0.2258	197493
14	0.1613	198535
15	0.0968	149976
16	0.0323	55768

Fig. 2
Stress spectrum in random loading tests according to the Markov-random program

growth curve for constant amplitude loading shows as expected the highest crack growth rates compared with the other types of loading. It is characterized by the typical transition from a midrange response to a threshold region as is also known from other materials (18). The datapoints exceeding 5.10^{-9}m/cycle may be approximated by a straight line (in this double logarithmic plot). The slope yielding the exponent n in the crack growth law is 2.5 and the threshold stress intensity is 5 MPa$\sqrt{m}$. (For calculation of the cyclic stress intensity only the tensile part of loading was used in this work.)

The differences between the crack growth rates parallel and transverse to the rolling direction were negligible. Only scattering is more pronounced for crack propagation parallel to the rolling direction; in the following, results are plotted only for the transverse direction.

The crack growth curve for step loading lies somewhat below the constant amplitude results, if the highest of the eight steps is plotted on the abscissa. As the maximum load is reached only in every forteenth pulse of a whole sequence, it is not surprising that somewhat lower crack growth rates result in comparison with the constant amplitude test. It is worth mentioning, that the step-loading curve runs almost parallel to the constant-amplitude curve at crack growth rates

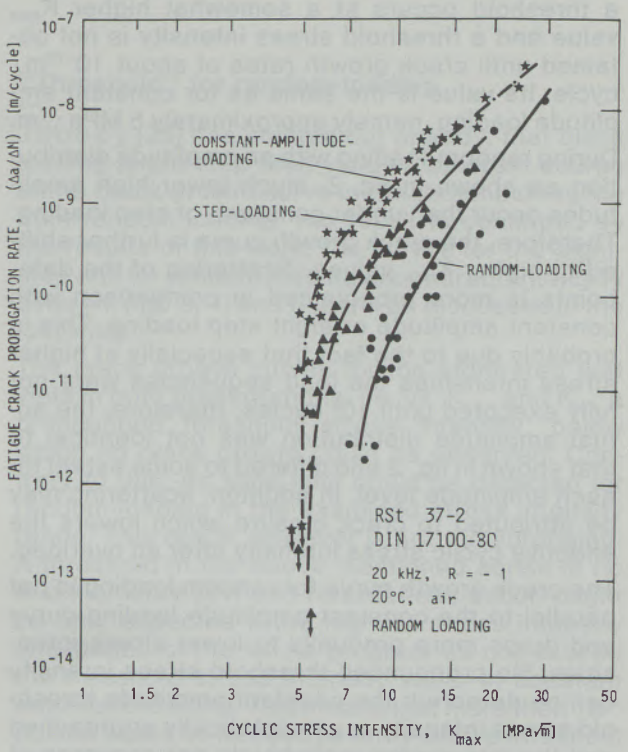

Fig. 3
Crack growth rates for constant, step and random loading of structural steel RSt 37-2 versus maximum cyclic stress intensities

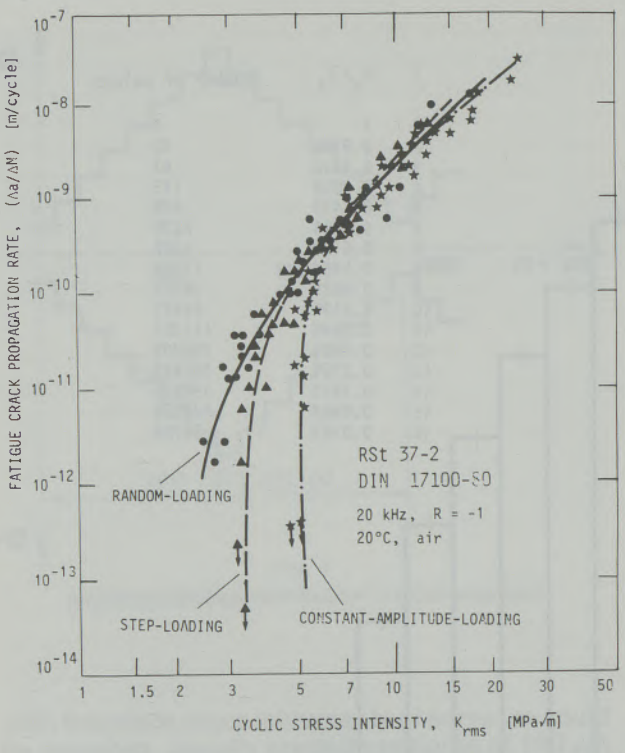

Fig. 4
Crack growth rates for constant, step and random loading of structural steel RSt 37-2 versus root mean square (RMS) values of cyclic stress intensities

above 5.10^{-9}m/cycle. However, the transition to a threshold occurs at a somewhat higher K_{max} value and a threshold stress intensity is not obtained until crack growth rates of about 10^{-12}m/cycle. Its value is the same as for constant amplitude loading, namely approximately 5 MPa$\sqrt{m}$.

During random-loading with an amplitude distribution as shown in fig. 2, much fewer high amplitudes occur than under constant- or step loading. Therefore, the crack growth curve is further shifted to higher K_{max} values. Scattering of the datapoints is more pronounced in comparison with constant amplitude or eight step loading. This is probably due to the fact that especially at higher stress intensities the load sequencies were not fully executed until 10^6 cycles; therefore, the actual amplitude distribution was not identical to that shown in fig. 2 and differed to some extent for each amplitude level. In addition, scattering may be attributed to crack closure which lowers the effective cyclic stress intensity after an overload.

The crack growth curve for random loading is not parallel to the constant-amplitude loading curve and drops more gradually to lower stress intensities. No pronounced threshold stress intensity can be detected; the constant-amplitude threshold stress intensity is asymptotically approached and the two curves probably do not converge at crack growth rates above approximately 10^{-14}m/cycle; such low crack growth rates are hardly obtainable even with an ultrasound machine.

II) The following results are found if the crack growth rates are plotted versus the RMS stress intensity values (fig. 4):

First, all three crack growth curves, i.e. for constant amplitude, eight-step and random loading, coincide surprisingly well in the midrange.

This is not the case for the threshold regime; at low stress intensities the crack growth curves diverge. In the RMS plot, the constant-amplitude curve is identical with the curve plotted vs. maximum stress intensities. The step-loading curve is shifted towards lower stress intensities by a constant factor and approaches a threshold value, with a somewhat reduced slope however. The random-load curve declines almost steadily and does not exhibit pronounced threshold behavior. The K_{rms} value is approximately 5 MPa$\sqrt{m}$ for constant amplitude loading at a crack growth rate of about 10^{-12}m/cycle (which is the same as in K_{max} plotting). This value is 3.3 MPa$\sqrt{m}$ for step-loading and 2.4 MPa$\sqrt{m}$ for random-loading. This inversion of the curves with respect to the plot with maximum values is understandable if one keeps in mind that for random-loading, crack growth in the threshold region is mostly accomplished by the very few high amplitudes, but that the RMS-stress intensity value is reduced by the high majority of low values, which do not or almost do not contribute to crack growth. More pronounced scattering may be explained in the same way as in I).

4. Discussion

Aspects of RMS and maximum value representation

Plotting the fatigue crack growth rates versus K_{rms} (fig. 4) shows that the results for constant-amplitude, step-loading and random-loading coincide in one curve within the midrange stress intensity region.

Similar results were obtained by Barsom (11) who studied 5 different American bridge steels with various random loading programs at crack growth rates between $2.5x10^{-6}$ and $2.5x10^{-8}$m/cycle. Based on the results of Barsom's and this work it seems reasonable to use the RMS values for characterizing crack growth of carbon steels used for machine construction under fatigue random-loading in the midrange stress intensity region; the curves appear to be independent of the load spectrum. In this case it would be necessary to measure just one crack growth curve under any load spectrum, and this could be used for predicting crack growth under changed load distributions.

In fact, Barsom (11) points out that the coincidence of the crack growth curves under different loading conditions probably is characteristic just for the studied bridge-steels, but that is seemed worth studying the applicability of the RMS value on other material, too.

Referring the fatigue crack growth rates to K_{max} has the advantage that the crack growth curves may be better compared under different loading conditions (fig. 3). For technical applications however, some drawbacks result compared with a K_{rms} plot. Changing the amplitude distribution at the same K_{max} values affects the crack growth curve; therefore, separate measurements have to be performed for each amplitude distribution. This sort of plot seems useful for unchanged amplitude distribution only, which, however, is rather seldom.

Crack growth retardation and acceleration

From the results of fig. 3 and 4 no direct conclusions about crack growth retardations and accelerations in an eight-step or random-loading tests may be drawn. Such information is obtained if these results are compared with calculations where retardations and accelerations are not taken into account. In fig. 5 curves calculated and measured in this way are plotted versus K_{rms}. The crack growth curves for step-loading and random loading were calculated based on the assumption of damage accumulation according to the Miner-rule. First the measured crack growth curve for constant amplitudes was approximated by the equation (19)

$$da/dN = C(K^n - K_{th}^n)$$

where da/dN is the fatigue crack growth rate and K_{th} the threshold stress intensity. With the aid of a computer program the crack growth increments were then summed up for variable amplitudes. The results of fig. 5 demonstrate rather good correspondence of measured and calculated curves, especially in the threshold region. This means that retardations and accelerations obviously do not play an important role. This result is in contrast to several works in (20) where remarkable crack growth retardations and – accelerations could be detected for load spectra with tensile overloads.

The work of Rice and Stephens (26) and Stephens (6) may serve to explain this discrepancy. There the influence of overloads with different negative R-values between 0 and –2 was tested during constant amplitude loading and it was found that crack growth retardation is reduced the higher the negative R radios are.

In this work, compressive overloads occured (R = –1) and this loading condition may be considered similar to that described by Rice and Stephens (26) and Stephens (6). It may be concluded therefore that retardation was reduced or compensated for random-loading at R = –1 in this work. The mentioned discrepancy with the results of (20) thus becomes less pronounced.

Other models (22), (23), (24) for calculating crack propagation under spectrum loading should not be overlooked, where crack growth retardation and acceleration are taken into account. However, as such phenomena were not observed in the results of this paper, they have not been further considered.

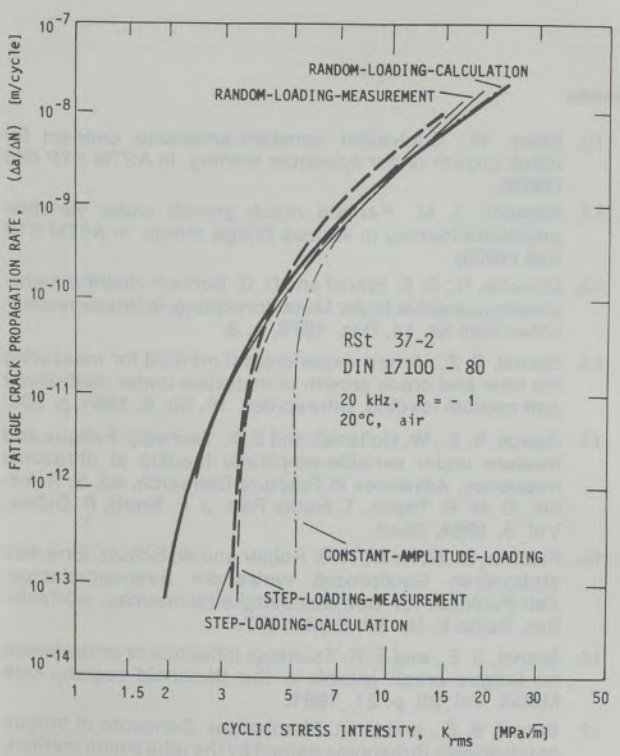

Fig. 5
Comparison of measured crack growth curves and calculated curves based on linear damage accumulation

"Threshold" for random-loading

Jacoby (25) has pointed out already, that block loading (eight-step test) yields a different course of the crack growth curve in the threshold regime from random-loading. His result is confirmed by the results of this work; the curves for the eight-step and for random loading are characteristically different (fig. 3, 4) and this will be discussed in the following.

The crack growth curves for the eight-step test yield in both presentations, i.e. vs. K_{max} and K_{rms} a pronounced threshold stress intensity, below which no crack growth could be observed. Contrary to this, no such limit could be detected for random-loading in the examined stress intensity range. This result, however is not too surprising. A threshold in the above mentioned sense (if no crack closure (21) and retardations occur) might be only expected if the highest stress intensity amplitudes of the whole program do not exceed the threshold stress intensity value at constant amplitude loading. This means that more than 10^{12} pulses would be needed to verify such a threshold value. However, even machines and components for long-time use are usually not stressed longer than with 10^{10} cycles. Therefore, measuring with 10^{12} and more cycles does not seem important.

Thus, the threshold in the conventional sense is not relevant any longer for crack growth under random-loading. It is only possible to determine a lower limit of the stress intensity range for random-loading, below which the crack growth rate falls below a defined limit, as for example 10^{-12}m/cycle.

5. Conclusions

Crack growth measurements on a structural steel RSt 37-2 under constant amplitude, eight step and random-loading conditions revealed the following results:

1. Plotting the results of various load-programs, versus the maximum stress intensity value of the whole sequence, K_{max} as reference value, yield a clear presentation of the crack growth behavior, but they do not help too much for practical application, especially if other load sequences are performed. If the results are plotted versus the root mean square (RMS) value of the cyclic stress intensity the crack growth curves coincide for the various amplitude spectra executed in this work in the midrange stress-intensity region. This means that the crack growth curve is a universal curve for different (at least the three performed in this work) amplitude sequences.
2. In the threshold regime however, the curves diverge. The curves for constant and block (8 step test) loading yield a pronounced threshold stress intensity in the conventional sense ($K_{th,\ const.\ ampl.,\ rms} = 5$ MPa$\sqrt{m}$, $K_{th,\ step\text{-}loading,\ rms} = 3{,}3$ MPa$\sqrt{m}$) whereas no such value is detected for random loading in plotting crack growth rates, whether versus K_{max} as versus K_{rms}. Therefore, for random loading a threshold stress intensity cannot be stated; instead a lower limit of the cyclic stress intensity, for example 2.3 MPa$\sqrt{m}$, where the fatigue crack growth rate falls below some specified value, for example 10^{-12}m/cycle, can be defined.
3. If experimental results and calculations according to a Miner summation based on constant amplitude results (neglecting crack growth retardation and acceleration) are compared good correspondence is found in the midrange and very good correspondence in the threshold region. Therefore it may be concluded that, in the case of the tested structural steel and at loading with mean stress equal to zero ($R = -1$), crack growth retardation or acceleration effects do not play a remarkable role.

Acknowledgment

The authors thank Prof. G. Ramberger and Fa. Waagner-Birò, Vienna, for their help in supplying the RSt 37 steel. The "Hochschuljubiläumsstiftung der Stadt Wien" is thanked for its support of the project.

References

1. Schütz, W.: Berechnung des Rißfortschritts bei betriebsähnlichen Beanspruchungen, Vortrag bei der 3. Sitzung des Arbeitskreises Betriebsfestigkeit, 14. 10. **1977**, Berlin DVM.
2. Rolfe, S. T., and J. M. Barsom: Fracture and Fatigue Control in Structures, Prentice-Hall, Englewood Cliffs, NJ, **1977**.
3. Schwalbe, K. H.: Bruchmechanik metallischer Werkstoffe, Carl Hanser Verlag, München–Wien, **1980**.
4. Jacoby, G.: Schwingfestigkeit, in Neuzeitliche Verfahren der Werkstoffprüfung, Verlag Stahleisen M.B.H., Düsseldorf, **1973**.
5. Schijve, J.: Observations on the prediction of fatigue crack growth propagation under variable-amplitude loading, in ASTM STP 595 (**1976**).
6. Stephens, R. I., D. K. Chen and B. W. Hom: Fatigue crack growth with negative stress ratio following single overloads in 2024–T3 and 7075–T6 aluminium alloys, in ASTM STP 595 (**1976**).
7. Bernhard, P. J., T. C. Lindley and C. E. Richards: Mechanisms of overload retardation during fatigue crack propagation, in ASTM STP 595 (**1976**).
8. Jacoby, G. H., H. Nowack and H. T. M. van Lipzig: Experimental results and a hypothesis for fatigue crack propagation under variable-amplitude loading, in ASTM STP 595 (**1976**).
9. Van Euw, E. F. J., R. W. Hertzberg and R. Robert: Delay effects in fatigue crack propagation, in ASTM STP 513 (**1972**).
10. Elber, W.: Equivalent constant-amplitude concept for crack growth under spectrum loading, in ASTM STP 595 (**1976**).
11. Barsom, J. M.: Fatigue crack growth under variable-amplitude loading in various bridge steels, in ASTM STP 595 (**1976**).
12. Mitsche, R., S. E. Stanzl and D. G. Burkert: Hochfrequenzkinematographie in der Metallforschung, in Wissenschaftlicher Film Nr. 14, Dez. **1973**, p. 3.
13. Stanzl, S. E.: A new experimental method for measuring life time and crack growth of materials under multi-stage and random loading, Ultrasonics, 19, No. 6, **1981**, p. 269.
14. Stanzl, S. E., W. Hollanek and E. K. Tschegg: Fatigue and fracture under variable-amplitude loading at ultrasonic frequency, Advances in Fracture Research, ed. S. R. Valuri, D. M. R. Taplin, T. Rama Rao, J. F. Knott, R. Dubey. Vol. 5, **1984**, 3645.
15. Fischer, R., M. Hück, H. G. Köbler and W. Schütz: Eine dem stationären Gaußprozeß verwandte Beanspruchungs-Zeit-Funktion für Betriebsfestigkeitsversuche, Fortschr. Ber. Reihe 5, Nr. 30, Sept. **1977**.
16. Stanzl, S. E., and E. K. Tschegg: Influence of environment on fatigue crack growth in the threshold region, Acta Metall, Vol. 29, p. 21, **1981**.
17. Stanzl, S. E., and H. M. Ebenberger: Concepts of fatigue crack growth thresholds gained by the ultrasound method, in Fatigue Crack Growth Threshold Concepts, ed. D. Davidson and S. Suresh, The metallurgical Soc. of AIME, **1984**, p. 399.

18. Speidel, M. O., S. E. Stanzl and E. K.Tschegg: Ermüdung von Stahl X20 Cr 13, Z. Werkstofftech. 11, **1980**, p. 305.

19. Klesnil, M., and P. Lukás: Influence of strength and stress history on growth and stabilisation of fatigue cracks, Eng. Frac. Mech., 4, **1972**, p. 77.

20. American Society for Testing and Materials, Symposium "Fatigue Crack Growth under Spectrum Loads" Montreal, Canada, 23–24 June **1975**, ed. R. P. Wei and R. I. Stephens, ASTM STP 595 (**1976**).

21. Suresh, S.: Micromechanism of fatigue crack growth retardation following overloads, Eng. Frac. Mech. Vol. 18, No. 3, **1983**, p. 577.

22. Willenborg, J., R. M. Engle and H. A. Wood: A crack growth retardation model using an effective stress concept, AAFDL TM–71–1–FBR.

23. Wheeler, O. E.: Crack growth under spectrum loading, General Dynamics, Report FZM 5602, 30. Juni **1979**.

24. Elber, W.: Fatigue crack closure under cyclic tension, Eng. Fract. Mech., 2 (**1970**), p. 37.

25. Jacoby, G.: Experimentelle Erfassung der Betriebsfestigkeit, ÖIZ **1975**, 18. Jg., Heft 7, p. 219.

26. Rice, R. C., and R. J. Stephens: Overload effects on subcritical crack growth in austenitic manganese steel, in Progress in Flaw Growth and Fracture Toughness Testing, ASTM STP 536, **1973**, p. 95.

Application of Different $\Phi(\varrho z)$ Distributions in Quantitative Electron Probe Microanalysis Without Standard Samples

Johann Wernisch, Wien*)

Dedicated to the 80th birthday of Prof. Dr. Franz Lihl

In the quantitative electron probe microanalysis (EPMA) without standard samples the accuracy of the results of the measurements depends strongly on the absorption correction and thus on the X-ray depth distribution function $\Phi(\varrho z)$. Three of the depth distribution functions now in use in the field of traditional microprobe analysis are used in the EPMA without standard samples and are tested on the basis of microanalytical data obtained in 230 measurements. The results shows that in the best case a standard deviation $\sigma = 7.78$ is reached.

Anwendung verschiedener $\Phi(\varrho z)$-Verteilungen bei der quantitativen Elektronenstrahl-Mikroanalyse ohne Eichproben

In der eichprobenfreien quantitativen Elektronenstrahlmikroanalyse (ESMA) hängt die Genauigkeit der Meßergebnisse sehr stark von der Absorptionskorrektur und damit von der Röntgentiefenverteilungsfunktion $\Phi(\varrho z)$ ab. Drei zurzeit in der herkömmlichen Mikrosondenanalytik verwendete Tiefenverteilungsfunktionen werden in der eichprobenfreien ESMA adaptiert und anhand 230 gemessener Microanalysendaten überprüft. Das Ergebnis zeigt, daß im optimalen Fall eine Standardabweichung $\sigma = 7.78$ erreicht wird.

Utilisation de différentes distributions de $\Phi(\varrho z)$ dans l'analyse quantitative à la microsonde électronique sans étalons

Dans l'analyse quantitative à la microsonde électronique sans étalons, la précision des résultats dépend très fortement de la correction d'absorption et par conséquent de la fonction de distribution des profondeurs de rayons X, $\Phi(\varrho z)$. Trois de ces fonctions actuellement utilisées dans l'analyse à la microsonde électronique ordinaire sont adaptées à l'analyse sans étalons et contrôlées au moyen de 230 résultats d'analyses. Les résultats montrent que dans un cas optimal on atteint un écart type de $\sigma = 7.78$.

Introduction

The quantitative electron probe microanalysis (EPMA) is based mainly on comparative measurements, but the knowledge of the spectrometer function also allows an EPMA without them (1). In both cases the concentration is calculated by means of an algorithm while taking in account the composition of the sample (Z), the absorption of the emerging radiation (A), and the fluorescence excitation in the sample (F). In the literature the various models of correction procedures are called "ZAF correction methods". As far as the absorption correction $f(\chi)$ is concerned, which is dealt with most often, in the literature different models and calculations are given that yield varying optimal results for low-atomic number elements and high-atomic number elements. In calculating $f(\chi)$, the determination of the depth distribution function $\Phi(\varrho z)$ indicating the distribution of the X-rays generated in the sample in relation to the mass depth ϱz, is of decisive significance.

The fraction of non-absorbed quanta $f(\chi)$ is given by

$$f(\chi) = \frac{\int_0^\infty \Phi(\varrho z) \cdot \exp(-\chi \varrho z)\, d(\varrho z)}{\int_0^\infty \Phi(\varrho z)\, d(\varrho z)}$$

with $\frac{\mu}{\varrho}$ = mass absorption coefficient

φ = take off angle

$$\chi = \frac{\mu}{\varrho} \cdot \frac{1}{\sin \varphi}$$

For the EPMA without standard samples there are not k ratios (net intensities of the characteristic X-rays from sample and standard) that are used, but only the net intensities of the K_α and L_α series of the elements of the sample to be investigated. The absorption correction determines the result linearly. The range of elements is limited to Mg–Bi because of the EDS-system that is used for these investigations.

*) Univ.-Doz. Dr. Johann Wernisch, Institut für Angewandte und Technische Physik, Technische Universität Wien, Karlsplatz 13, A-1040 Wien

The object of this work was to apply the absorption correction procedure now in use in the conventional EPMA, to the EPMA without standard samples and to investigate which Φ distribution function yields the best results with regard to the determination of the concentration of a given sample.

Theoretical

The following approaches were taken as comparisons:

1. $f(\chi)$ according to G. Love and V. D. Scott (2)
2. $\Phi(\varrho z)$ according to J. D. Brown and R. H. Packwood (3), (4)
3. $\Phi(\varrho z)$ according to G. F. Bastin, F. J. J. van Loo and H. J. M. Heijligers (5), (6)

ad 1. Love-Scott

In the EPMA without standard samples dealt with in lit. (1) an expression developed by Bishop (7) and further developed and improved by Love and Scott (2) is used for the absorption correction $f(\chi)$ in the following way (fig. 1):

$$f(\chi) = \frac{1 - \exp(-2\chi\overline{\varrho z})}{\chi\overline{\varrho z}}$$

$\overline{\varrho z}$ = mean ionization depth

ad 2. Brown-Packwood

The $\Phi(\varrho z)$ distribution function obtained from experimental results is shown in the following way (fig. 2):

$$\Phi(x) = \gamma_o\left[1 - \frac{\gamma_o - \Phi(0)}{\gamma_o} \cdot e^{-\beta x}\right] \cdot e^{-\alpha^2 x^2}$$

$$\alpha = 3.95 \cdot 10^5 \frac{Z^{0.95}}{A \cdot E_0^{1.25}} \left[\frac{\ln(1.166\, E_0/J)}{E_0 - E_c}\right]^{0.5}$$

$$\beta = 0.4 \cdot \alpha \cdot Z^{0.6}$$

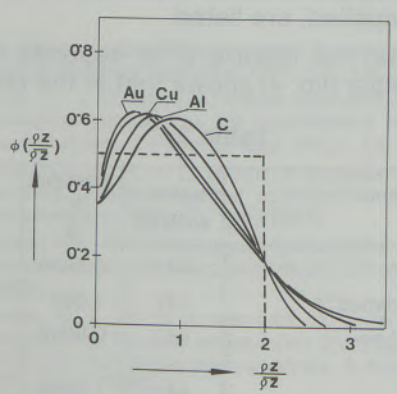

Fig. 1
Standardized depth distribution function for various elements with U = 10 (Monte-Carlo-calculations)

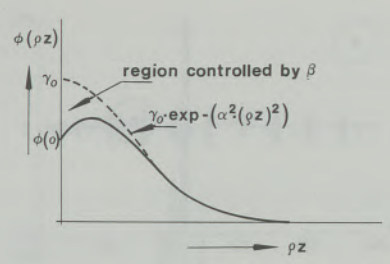

Fig. 2
Diagram of the Gaussian distribution for the depth distribution function $\Phi(\varrho z)$ and of the different influences of the parameters Φ_o, α, β, γ_o

$$\gamma_o = \frac{5\pi U_o}{(U_o - 1)\ln U_o} (\ln U_o - 5 + 5 \cdot U_o^{-0.2})$$

$$\Phi(0) = 1 + \frac{\eta}{1+\eta} (I(U_o) + G(U_o) \cdot \ln(1+\eta))$$

For $\Phi(0)$ which is the value for $\Phi(\varrho z)$ when $\varrho z = 0$, the expression developed by Love-Scott (2) is used.

ad 3. Bastin-van Loo and Heijligers

The $\Phi(\varrho z)$ distribution function is borrowed from Brown-Packwood, but with the newly optimized parameters α, β, γ_o (fig. 2).

$$\alpha = \frac{1.75 \cdot 10^5}{E_0^{1.25}(U_0 - 1)^{0.55}} \left[\frac{\ln(1.166\, E_0/J)}{E_c}\right]^{0.5}$$

$$\beta = 0.4 \cdot \alpha \cdot \frac{Z^{1.7}}{A} (U_o - 1)^{0.3}$$

$$\gamma_o = \frac{5\pi U_o}{(U_o - 1) \cdot \ln U_o} \cdot (\ln U_o - 5 + 5 \cdot U_o^{-0.2}) \cdot 0.98 \cdot e^{0.001 \cdot Z}$$

$\Phi(0)$ is taken over from Love-Scott (2)

The results of the comparative investigations

The results of the comparative investigations served the purpose of testing the method of analysis without standard samples according to lit. (1) with regard to the relative error depending on the atomic number and the acceleration voltage and

Table 1

authors of the $f(\chi)$ correction models	number of analysis	averages $\frac{c'}{c}$	σ_{rel}
Love-Scott	230	1.001	7.78
Brown-Packwood	230	0.998	8.49
Bastin-van Loo-Heijligers	230	1.005	8.42

Results of the averages and of the relative standard deviation σ_{rel} in quantitative EPMA without standards using different $f(\chi)$ correction models with the ZAF correction program developed by Wernisch.

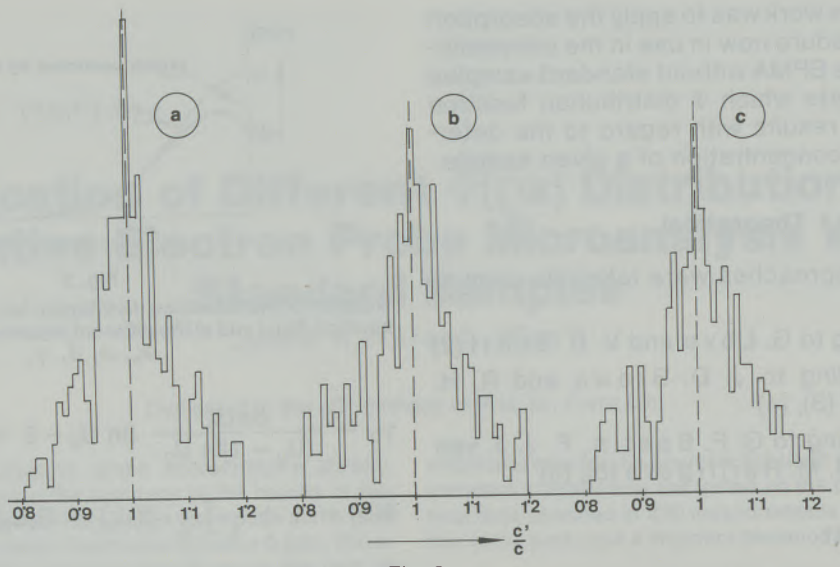

Fig. 3
Histogram of deviations of measured concentrations from results of chemical analysis ($\frac{c'}{c}$ = rel. error). Results obtained with the energy-dispersive system. a) Love-Scott, b) Brown-Packwood, c) Bastin-van Loo–Heijligers

with regard to the absolute error in the whole range of concentration. Besides, it is examined which one of the absorption correction f(χ) models mentioned yielding the best analytical results. In order to be able to compare the above mentioned absorption correction f(χ) models in EPMA without standard samples, 230 analyses of multi-component alloys were carried out. The combinations of the elements were selected in such a way that combinations of elements of similar atomic numbers as well as combinations of high-atomic number elements with low-atomic number elements were used for the analytical results. The acceleration voltage was varied between 15 and 30 kV. The concentration ranged from 1 to 99 wt-%.

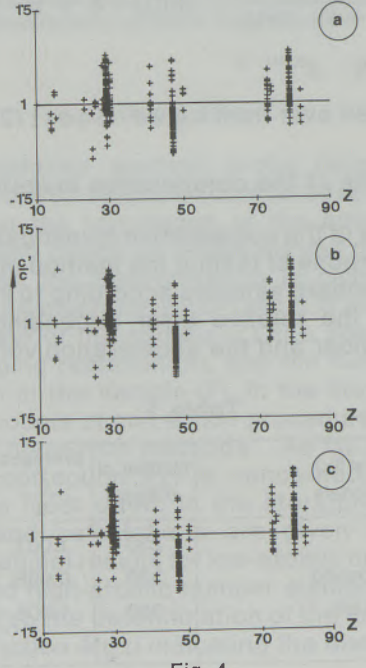

Fig. 4
The relative error $\frac{c'}{c}$ depending on the atomic number Z
a) Love-Scott, b) Brown-Packwood, c) Bastin-van Loo–Heijligers

Table 1 shows the mean values and the relative standard deviations of the analytical results. The respective histograms can be seen in fig. 3.

It can be seen that the model used in lit. (1) with a mean value of 1.001 and a standard deviation $\sigma = 7.78$ yields the best analytical results. The accuracy of the results of the measurements can well be compared with the accuracy calculated by means of the correction procedures with standard samples described in the literature. The values $\frac{k'}{k}$ and σ for the above mentioned models were calculated on the basis of microanalytical values that had been published, and they are shown in table 2. In addition, the values $\frac{k'}{k}$ and σ of an usual ZAF program, where the atomic number correction procedure of Duncumb and Reed (8), the absorption correction procedure of Philibert (9), and the fluorescence correction procedure of Reed (10), were applied, are listed.

The fact that the relative error depends on the atomic number (fig. 4) shows that in the range of

Table 2

ZAF correction programs	number of analysis	averages $\frac{k'}{k}$	σ_{rel}
Love-Scott*	441	0.9929	5.56
Brown-Packwood**	147	1.068	4.8
Bastin-van Loo-Heijligers*	441	0.9902	5.46
ZAF*	441	1.0240	6.30

RMS values and averages obtained with different ZAF correction programs (* lit. (6), ** lit. (4)).

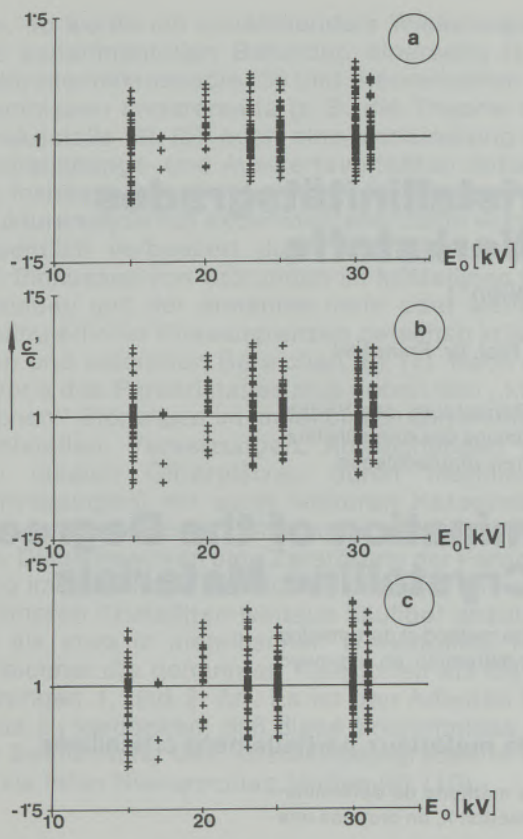

Fig. 5
The relative error $\frac{c'}{c}$ depending on the acceleration voltage E_0 (kV)
a) Love-Scott, b) Brown-Packwood, c) Bastin-van Loo–Heijligers

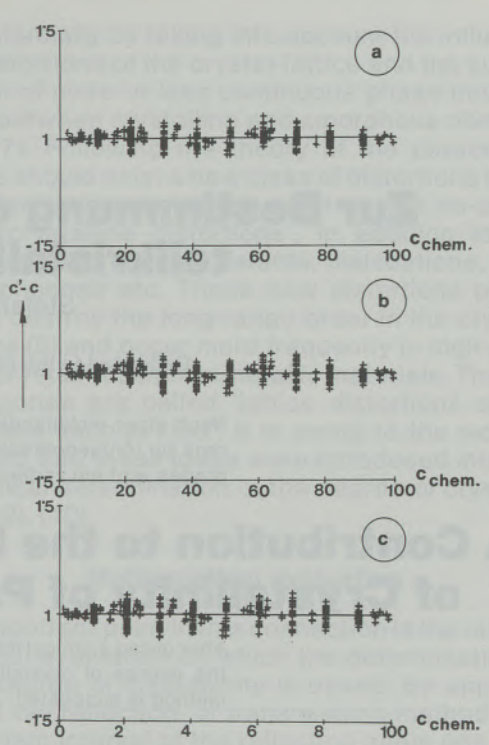

Fig. 6
The absolute error c' – c depending on the actual concentration c_{chem} (wt%)

atomic numbers starting with Z = 40, where L-spectra are used for the analysis, there is a systematic error in all models. In this range of atomic numbers the fundamental parameters for L-series show some major inaccuracies. In the SEM-analysis without standard samples only K_α- and L_α-spectra are used to calculate the concentrations. Besides, another source of error must be seen in the deconvolution of the L-series in the medium range of atomic numbers when using an energy dispersive X-ray system.

In all cases the relative error depending on the acceleration voltage (fig. 5) does not show any significant deviations.

The fact that the absolute error depends on the concentration of an element (fig. 6) shows that in the whole range of concentration the difference between the actual value and the measured value does not show any significant deviations from the mean value. The percentage of deviations is almost constant in the whole range of concentration except in the range of concentration below 10 wt-%.

References

1. Wernisch, J.: Quantitative electron microprobe analysis without standard samples, XRS, Vol. 14, No 3. (**1985**).
2. Love, G., V. D. Scott: A critical appraisal of some recent correction procedures for quantitative electron probe microanalysis, J. Phys. D. Appl. Phys. 13, 995 (**1980**).
3. Packwood, R. H., J. D. Brown: A Gaussian expression to describe Φ(oz) curves for quantitative electron probe microanalysis, XRS 10, 138 (**1981**).
4. Brown, J. D., R. H. Packwood: Quantitative electron probe microanalysis using Gaussian Φ(oz) curves, XRS 11, 187 (**1982**).
5. Bastin, G. F., F. J. J. van Loo, H. J. M. Heijligers: An evaluation of the use of Gaussian Φ(oz) curves in quantitative electron probe microanalysis. A new optimization, XRS 13, 91 (**1984**).
6. Bastin, G. F., H. J. Heijligers, F. J. J. van Loo: The performance of the modified Φ(oz) approach as compared to the Love and Scott, Ruste and standard ZAF correction procedures in quantitative electron probe microanalysis, Scanning Vol. 6, 58 (**1984**).
7. Bishop, H. E.: The prospectes for an improved absorption correction in electron probe microanalysis, J. Phys. D Appl. Phys. 7, 2009 (**1974**).
8. Duncumb, P., S. J. B. Reed: The calculation of stopping power and backscatter effects in electron probe microanalysis, In: Quantitative electron probe microanalysis (Ed.: K. F. J. Heinrich), NBS Spee Publ. No. 298, 133 (**1968**).
9. Philibert, J.: A method for calculating the absorption correction in electron probe microanalysis, 3rd Int. Symp. on X-ray optics and X-ray microanalysis, Stanford (**1962**) (Eds.: H. H. Pattee, V. E. Cosslett and E. Engström), Academic Press, New York **1963**, 379.
10. Reed, J.S. B.: Characteristic fluorescence correction in electron probe microanalysis, Brit. J. Appl. Phys. 16, 913 (**1965**).

Zur Bestimmung des Kristallinitätsgrades teilkristalliner Werkstoffe

Stefan Bauer, Wien*)

Dedicated to the 80th birthday of Prof. Dr. Franz Lihl

Nach einer einleitenden kritischen Betrachtung des Verfahrens zur röntgenographischen Bestimmung des Kristallinitätsgrades wird ein verbessertes Verfahren vorgeschlagen.

A Contribution to the Determination of the Degree of Crystallinity of Partly Crystalline Materials

After giving a critical introduction to the method of determining the degree of crystallinity by X-ray-diffraction an improved method is suggested.

Sur la détermination du taux de cristallisation de matériaux partiellement cristallisés

Après une introduction critique de la méthode de détermination du taux de cristallisation par diffraction X, on propose une méthode améliorée.

Einleitung

Der vorliegende Beitrag beschreibt eine Verbesserung des mathematischen Auswerteverfahrens zur Bestimmung des röntgenographischen Ordnungszustandes („Kristallinitätsgrades") nach der Theorie des parakristallinen Zustandes. Das angegebene Verfahren findet bei der Untersuchung von teilkristallinen Hochpolymeren Verwendung und steht am Institut für Angewandte und Technische Physik zur routinemäßigen Prüfung insbesondere von Proben aus isotaktischem Polypropylen (it-PP) zur Verfügung.

Theoretische Grundlagen

Der „Kristallinitätsgrad" ist im wesentlichen ein Maß für das Mengenverhältnis von (ev. polymorph-)kristalliner zu amorpher Phase in einem repräsentativen untersuchten Probenvolumen und stellt einen wichtigen technologischen Parameter dar (1) – insbesondere bei der Charakterisierung von hochpolymeren Werkstoffen (2).

Hatte man ursprünglich bei der physikalischen Beschreibung der Strukturen im hochpolymeren Festkörper mit einem Zwei-Phasen-Konzept, d. h. ideal amorphe Phase, ideal kristalline Phase, scharfe Phasengrenzen, das Auslangen gefun-

*) Dipl.-Ing. Stefan Bauer, Institut für Angewandte und Technische Physik, TU Wien

Introduction

The following paper describes an improved mathematical evaluation-method for the determination of the state of order (or 'degree of crystallinity') by X-ray diffraction methods following the basic theory of Ruland. The cited method is mainly used for the investigation of partly crystalline high-polymers and is a routine-method at the Institute of Applied Physics for specimens of isotactic Polypropylene (it-PP).

Basic theory

Basically the degree of crystallinity is a measure of the ratio of (possibly polymorphous-) crystalline to amorphous phase in an investigated representative volume of a specimen and is considered an important technological parameter (1) – esp. for the characterisation of high-polymer materials (2).

In earlier stages of the physical description of structures in the high-polymer solid body a two-phase concept was sufficient supposing an ideal amorphous phase, an ideal crystalline phase and sharp phase boundaries. But with growing state of knowledge from experimental facts on one side (e.g. electron-microscopy (3)) and theoretical considerations on the other side (e.g. the concept of the paracrystal (4), (5)) a refinement of the methods of investigation and evaluation became necessary. Especially the methods of X-ray diffraction in the experimental field could be improved

den, so wurde mit zunehmendem Wissensstand aus experimentellen Befunden einerseits (z. B. Elektronenmikroskopie (3)) und theoretischen Erkenntnissen andererseits (z. B. die Theorie des Parakristalls (4), (5)) auch eine Verfeinerung der Untersuchungs- und Auswerteverfahren notwendig. Insbesondere die Methoden der Röntgenfeinstrukturanalyse auf experimenteller Seite wurden wesentlich verbessert durch die Einbeziehung des Einflusses von Störungen im kristallinen Gitteraufbau und der Annahme mehr oder weniger kontinuierlicher Phasengrenzen zwischen kristallinen und amorphen Bereichen (6), (7). Nach der Theorie des Parakristalles muß neben den „klassischen" Störungen im molekularen Gitteraufbau (Fehlstellen, Versetzungen, Abweichungen von den idealen Gitterplätzen durch thermische Schwingungen) mit einer weiteren Kategorie – den „parakristallinen" Störungen gerechnet werden. Diese bewirken eine Zerstörung der Fernordnung im kristallinen Bereich (8) und sind im hochpolymeren Kristalliten weitaus häufiger anzutreffen als etwa in metallischen Werkstoffen. Man bezeichnet die genannten Kategorien als Gitterstörungen 1. und 2. Art. Es ist den Arbeiten Rulands zu verdanken, daß diese Erkenntnisse bei der Bestimmung des Kristallinitätsgrades in der Praxis ihren Niederschlag fanden (9), (10).

substantially by taking into account the influence of distortions of the crystal-lattice and the supposition of more or less continuous phase boundaries between crystalline and amorphous domains (6), (7). Following the theory of the paracrystal there should exist a new class of distortions in the regular molecular lattice-structure the so-called 'paracrystalline distortions', in addition to the classic distortions as defects, dislocations, thermal phonons etc. These new distortions principally destroy the long-range order in the crystal-lattice (8) and occur more frequently in high-polymer crystallites than in metallic materials. The two categories are called 'lattice distortions of the first and second kind'. It is owing to the work of Ruland that these ideas were introduced into the practical determination of the degree of crystallinity (9), (10).

Mathematical evaluation

An important point in this connection is the mathematical evaluation on which the determination of the degree of crystallinity is based. By applying the X-ray reflection- or transmission-method over a certain interval of the reflection angle one gets a characteristic spectrum of the diffracted intensity: $I = f(2\Theta)$ (fig. 1).

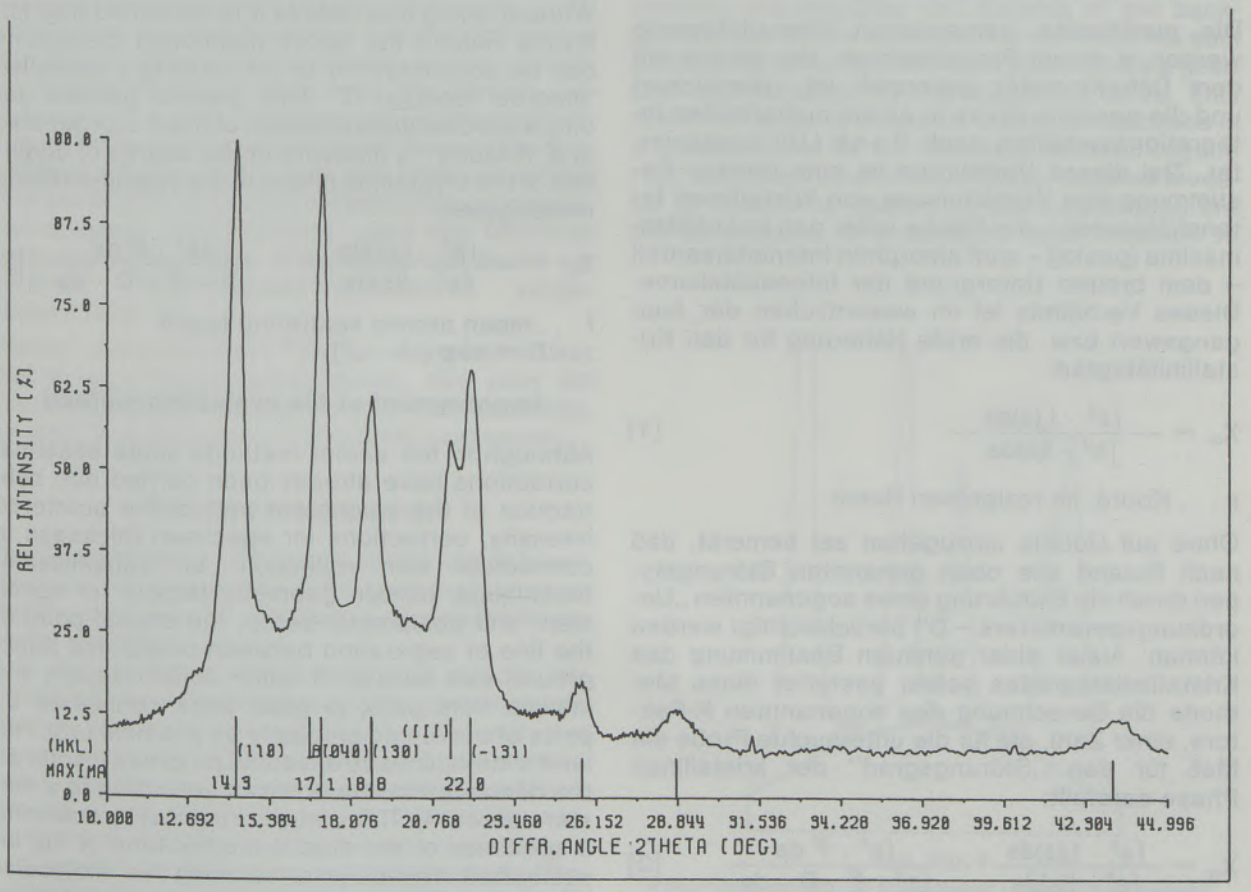

Abb./Fig. 1
Typisches Röntgenbeugungsspektrum von it-PP
X-ray spectrum, as typical of it-PP

Mathematische Auswertung

Worauf in diesem Zusammenhang näher eingegangen werden soll, ist die mathematische Auswertung, auf der die Bestimmung des Kristallinitätsgrades basiert. Durch die Anwendung des röntgenographischen Reflexions- oder Transmissionsverfahrens in einem geeigneten Winkelbereich erhält man eine für die Probe charakteristische Verteilung der gebeugten Strahlungsintensität als Funktion des Beugungswinkels: $I = f(2\Theta)$ (Abb. 1).

Kristallographisch gesehen stellt dies einen Schnitt vom Ursprung durch den reziproken Raum in einer bestimmten Richtung dar. Bei isotroper räumlicher Kristallitverteilung in der Probe ist die Intensitätsverteilung kugelsymmetrisch und alle Schnittrichtungen sind daher gleichberechtigt. Bei anisotroper Verteilung müssen Mittelungsverfahren angewendet werden (11). Für den speziellen Fall uniaxialer Symmetrie – von besonderer Bedeutung bei Faseruntersuchungen – steht am Institut eine Zusatzeinrichtung zum Goniometer zur Verfügung, die eine elektronische Mittelung in einer Koordinate ermöglicht:

$$I(r) = \int I(r, \varphi) \cdot \sin\varphi \, d\varphi$$

r, φ . . . Polarkoordinaten
r . . . senkrecht zur Faserachse

Die punktweise gemessenen Intensitätswerte werden in einem Prozeßrechner, der on-line mit dem Diffraktometer gekoppelt ist, gespeichert und die gesamte Kurve in einem numerischen Integrationsverfahren nach Vonk (12) ausgewertet. Ziel dieses Verfahrens ist eine genaue Bestimmung des Verhältnisses von kristallinem Intensitätsanteil – die Fläche unter den Intensitätsmaxima (peaks) – zum amorphen Intensitätsanteil – dem breiten Untergrund der Intensitätskurve. Dieses Verhältnis ist im wesentlichen der Ausgangswert bzw. die erste Näherung für den Kristallinitätsgrad:

$$X_{cr} = \frac{\int s^2 \cdot I_c(s) ds}{\int s^2 \cdot I(s) ds} \qquad [1]$$

s . . . Koord. im reziproken Raum

Ohne auf Details einzugehen sei bemerkt, daß nach Ruland alle oben genannten Störungstypen durch die Einführung eines sogenannten „Unordnungsparameters – D" berücksichtigt werden können. Außer einer genauen Bestimmung des Kristallinitätsgrades selbst gestattet diese Methode die Berechnung des sogenannten K-Faktors, einer Zahl, die für die untersuchte Probe ein Maß für den „Störungsgrad" der kristallinen Phase darstellt:

$$X_{cr} = \frac{\int s^2 \cdot I_c(s) ds}{\int s^2 \cdot I(s) ds} \cdot \frac{\int s^2 \cdot \bar{f}^2 \, ds}{\int s^2 \cdot \bar{f}^2 \cdot D \cdot ds} \qquad [2]$$

$\bar{f}$ . . . mittlerer Atomstreufaktor
$D = \exp(-K \cdot s^2)$

In crystallographic terms this is a cut from the origin of reciprocal space in a certain direction. For isotropic spatial distribution of the crystallites in the specimen the distribution of intensity is spherically symmetric and all directions render equal information. For anisotropy averaging methods have to be applied (11). For the special case of uniaxial distribution, important for investigating fibre materials, the institute's goniometer disposes of an electronic device for averaging in one coordinate:

$$I(r) = \int I(r, \varphi) \cdot \sin\varphi \, d\varphi$$

r, φ . . . polar coordinates
r . . . normal to fibre-axis

The stepwise measured intensity-values are stored in a computer coupled on-line to the diffractometer. The complete curve is thereafter evaluated by a numeric integration program developed by Vonk (12). This yields a good ratio of the intensity owing to the crystalline phase – the area under the peaks – to the amorphous intensity – the broad background of the intensity-curve. This ratio is a first approximation of the degree of crystallinity (d.o.c.):

$$X_{cr} = \frac{\int s^2 \cdot I_c(s) ds}{\int s^2 \cdot I(s) ds} \qquad [1]$$

s . . . coordinates in reciprocal space

Without going into details it is remarked that following Ruland the above mentioned distortions can be accounted for by introducing a so-called 'disorder-function D'. This method permits not only a precise determination of the d.o.c. but also of a 'K-factor', a measure of the degree of distortion of the crystalline phase of the specimen being investigated:

$$X_{cr} = \frac{\int s^2 \cdot I_c(s) ds}{\int s^2 \cdot I(s) ds} \cdot \frac{\int s^2 \cdot \bar{f}^2 \, ds}{\int s^2 \cdot \bar{f}^2 \cdot D \cdot ds} \qquad [2]$$

f . . . mean atomic scattering factor
. . . $D = \exp(-k \cdot s^2)$

Improvement of the evaluation method

Although in the earlier methods some essential corrections have already been carried out: subtraction of the incoherent part of the scattered intensity, corrections for specimen thickness in connection with reflection- or transmission-techniques, certain geometry factors for specimen- and goniometer-setup, the crucial point of the line of separation between peaks and background was always of some doubt. Usually the minima from peak to peak were connected by parts of curves as smoothly as possible (13). Ruland's method made essential progress insofar as the demarcation-line is drawn according to a master-curve (14). This curve is supplied by scanning a specimen of the atactic modification of the investigated high-polymer-asuming the molecular structure of this modification being more or less identic to that of the amorphous phase in the partly crystalline material.

Verbesserung des Auswerteverfahrens

Bei den früher verwendeten Auswertemethoden wurden zwar gewisse Korrekturen vorgenommen, wie: Subtraktion des inkohärenten Strahlungsuntergrundes, Korrekturfaktoren für die Probendicke in bezug auf Reflexions- oder Transmissionsverfahren, diverse Geometriefaktoren für Proben- und Strahlenanordnung etc. Der wesentliche Punkt, nämlich die Grenzlinie zwischen peaks und Untergrund, war in den älteren Verfahren jedoch stets eine Schwachstelle: Es erfolgte meist eine mehr oder weniger willkürliche Verbindung der Minima durch möglichst glatte Kurvenstücke (13). Das Verfahren von Ruland brachte insofern eine wesentliche Verbesserung, als hier die Trennungslinie in ihrer Form an eine Master-Kurve angeglichen wird (14). Diese erhält man durch einmalige Vermessung einer Probe der ataktischen Modifikation des untersuchten Hochpolymeren – da man annehmen kann, daß die Molekularstruktur dieser Modifikation mit derjenigen der amorphen Phase im teilkristallinen Material nahezu ident ist.

Kritischerweise muß jedoch festgestellt werden, daß diese Methode nur dann gute Ergebnisse liefert, wenn die einzelnen peaks so weit voneinander getrennt liegen, daß keine wesentliche Überlappung benachbarter Intensitätsmaxima erfolgt. Besonders bei hochpolymeren Werkstoffen (z. B. it-PP) ist dies jedoch häufig der Fall, zumindest bei den Hauptmaxima. Grund hierfür ist die geringe Kristallitgröße sowie Störungen des idealen Gitteraufbaues durch Defekte vom parakristallinen Typus. Beide bewirken in vielen untersuchten Probefällen eine Vergrößerung der Halbwertsbreite und damit eine Überlappung benachbarter peaks. Durch diese „Sattelbildung" wird das Minimum zwischen zwei peaks angehoben und damit ein erhöhter Strahlungsuntergrundanteil vorgetäuscht (Abb. 2).

Diesen unerwünschten Effekt auszuschalten war Ziel eines Computerprogrammes, das zwar die Grundzüge des Programmes von Vonk beibehält, es aber in puncto peak-Separation verbessert.

Meßkurvenanpassung

Das beschriebene Programm ist für die Auswertung von Messungen an it-PP geeignet, kann jedoch auch leicht für andere hochpolymere Werkstoffe adaptiert werden:
Aus der experimentellen Meßkurve werden die Positionen und Amplituden der Hauptmaxima bestimmt. Die Positionen der beiden Maxima, aus denen sich die Untergrundskurve zusammensetzt, sind fix vorgegeben. Im on-line-Betrieb werden dann am graphischen Terminal Halbwertsbreiten und Amplituden der Untergrundskurven so variiert, daß deren Summe zusammen mit den Einzelpeaks eine gute Näherung der Meßkurve ergibt. Die damit bestimmte Summe von zwölf analytischen Funktionen stellt die Ausgangsfunktion für

Critically it must be stated that this method leads to good results only when the single peaks are separated so far from each other that no great overlapping occurs. Especially for high polymers (e.g. it-PP) this is not the case for some of the main peaks. Reason for this is the small size of crystallites and distortions of the ideal lattice of the paracrystalline type. Both show the effect of peak-broadening and overlapping in many investigated specimens. Due to this 'saddle-effect' the minimum between two adjacent peaks is raised and thereby an increased portion of background-radiation is pretended (fig. 2).

To compensate this unwanted effect a computer program was written – based on the one by Vonk but improving it in the point of peak-separation.

Fitting the measured curve

The described program is written for the evaluation of specimens of it-PP, yet it can be easily adapted for other high-polymer substances:
From the experimental curve the positions and heights of the main peaks are determined. The positions of those two maxima composing the background curve are given in advance, taken from the master-curve. Monitored on a graphic terminal the breadths and heights of the background-curves are set in such a way that the sum of them together with the main peaks gives a good first approximation of the measured curve. This summed-up curve of twelve analytical functions is a starting point for the following iteration-routine (15). By the method of least-mean-squares a vector of solution is seeked whose coordinates are the parameters of a sufficient approximation to

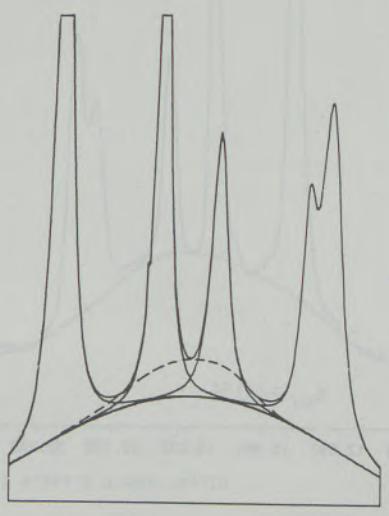

Abb./Fig. 2
Peak-Überlappung mit scheinbarer Untergrundanhebung (– – –)
Peak-overlapping, causing a seeming raise of the curve of background radiation (– – –)

das folgende Iterationsverfahren dar (15). Dieses sucht mit Hilfe der Methode der kleinsten Fehlerquadrate jenen Lösungsvektor, dessen Koordinaten die Kurvenparameter einer ausreichend guten Näherung an die vorgegebene Meßkurve darstellen. Es empfiehlt sich, die Anfangsparameter sorgfältig zu wählen, dadurch wird erstens das Iterationsverfahren (und damit die Rechenzeit) verkürzt und zweitens kann man ein „Verirren" des Algorithmus in unerwünschte Nebenminima und ein manchmal auftretendes Überschwingen der anzupassenden Funktion im allgemeinen verhindern. Für den Untergrund wurden Kurven vom Gauß-Typ gewählt, für die peaks solche vom Lorentz-Typ. Gaußkurven sind für die peak-Anpassung wegen der stärkeren Basisverbreiterung weniger geeignet. Ein absolutes Minimum wird bei diesem Iterationsverfahren wegen der großen Zahl der Meßpunkte: 550 und der Variablenzahl: 36 kaum erreicht, die Entscheidung, ob das Näherungsverfahren ausreichend ist, bleibt der subjektiven Beurteilung überlassen. Nach Abschluß des Verfahrens können die Kurvenparameter gespeichert werden, die Meßkurve ist damit durch eine Summe von analytischen Funktionen ersetzt. Im weiteren erfolgt die Bestimmung des Kristallinitätsgrades nach dem Verfahren von Ruland. Das Beispiel (Abb. 3) zeigt deutlich, daß bei Verwendung der Ersatzkurve der Einsattelungseffekt durch peak-Überschneidung kompensiert ist und sich ein deutlich korrigierter (erhöhter) Kristallinitätsgrad ergibt. Das angewandte Minimie-

the experimental curve. It is recommended to choose the starting-point properly – by doing so the computing-time of the iteration-routine is reduced and a 'going-astray' of the algorithm in unwanted subsidiary minima and possible oscillating of the function can be avoided. For fitting the background curves of the Gaussian type were chosen, Cauchy-type for the peaks. Gaussians are inadequate for peak-fitting because of the broadening of the basis. For the great number of measured points (550) and the number of variable parameters (max. 36) the absolute minimum is hardly reachable, the question whether the accuracy of the final approximation is sufficient is left to subjective opinion. After completion of the iteration-procedure the gained parameters can be stored, thus the experimental curve is substituted by a sum of analytical functions. Continuing the determination of the d.o.c. is executed by Ruland's method. The example (fig. 3) shows clearly that by using the fitted curve the saddle-effect by peak-overlapping is compensated and a different (increased) d.o.c. results. Besides the applied minimization procedure smoothes the statistical oscillations of the measured curve – an advantageous effect for specimen with low reflecting power and therefore poor counting-statistics.

Conclusion

Thanks to improved facilities of computerization (high calculation speed, graphic systems) it was

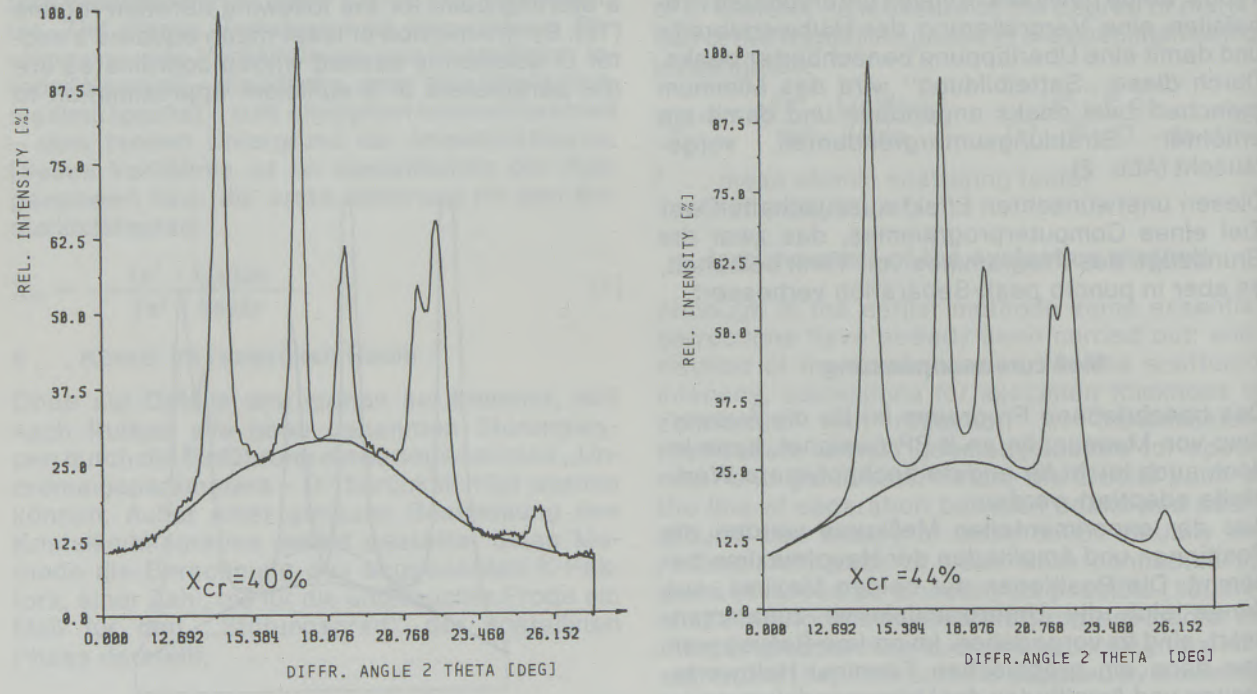

Abb./Fig. 3

a) Meßkurve mit Untergrund ohne Berücksichtigung der Peak-Überlappung

a) Spectrum with background, peak-overlapping not taken into account

b) Analytische Kurve mit korrigiertem Untergrund

b) Analytic curve with corrected background

rungsverfahren glättet außerdem die statistischen Schwankungen der Meßkurve, was bei Proben von geringer reflektierter Intensität und damit schlechter Zählerstatistik von Vorteil ist.

Zusammenfassung

Dank der verbesserten Möglichkeiten der Datenverarbeitung (hohe Rechnergeschwindigkeit, graphische Systeme) war es möglich, eine methodisch notwendige Verbesserung dieser wichtigen röntgenographischen Auswertemethode zu erreichen. Das Verfahren bietet außerdem die Möglichkeit, die bestimmten Kurvenparameter für weitere Analysen (Kristallitgröße, Gitterschwankungsparameter etc.) zu verwenden und so mehr Information im Sinne der parakristallinen Theorie über den teilkristallinen Aufbau in bestimmten Werkstoffen zu erhalten.

possible to achieve a methodical improvement of this important X-ray procedure. The method also offers the possibility to use the determined parameters for further analysis (crystallite-size, lattice-statistics, etc.) thus gaining more information about the structure in certain materials in the sense of paracrystalline-theory.

Literaturverzeichnis / References

1. Alexander, L. E.: X-Ray Diffraction Methods in Polymer-Science (Wiley, **1969**).
2. Kakudo, M., N. Kasai: X-Ray Diffraction by Polymers (Elsevier, **1968**).
3. Lovinger, A.: in J. Pol. Sci., Pol. Phys. Ed. 21 (**1983**), S. 97.
4. Hosemann, R., S. N. Bagchi: Direct Analysis of Diffraction by Matter (North Holland, **1962**).
5. Hosemann, R.: in Prog. Coll. & Pol. Sci. 66 (**1979**), S. 143.
6. Koberstein, J.: in J. Appl. Cryst. 13 (**1980**), S. 34.
7. Hosemann, R.: in Z. f. Physik 128 (**1950**), S. 465.
8. Ruland, W.: in Acta Cryst. 14 (**1961**), S. 1180.
9. Ruland, W.: in Brit. J. of Appl. Phys. 15 (**1964**), S. 1301.
10. Ruland, W.: in Faserforschung und Textilt. 15 (**1964**), S. 533.
11. Ruland, W.: in J. Sci. Instr. 44 (**1967**), S. 236.
12. Vonk, C.: in J. Appl. Cryst. 6 (**1973**), S. 148.
13. Rybnikar, J.: in Kunststoffe 57 (**1967**), Heft 3.
14. Vonk, C.: priv. Comm.
15. Nag Lib. der Prozeßrechenanlage, TU Wien.

Rare Earth Permanent Magnets

Roland Grössinger, Gerfried Hilscher and Hans Kirchmayr, Wien*)

Dedicated to the 80th birthday of Prof. Dr. Franz Lihl

The invention and development of different rare earth permanent magnets (REPM), based on the intermetallic compounds $SmCo_5$, Sm_2Co_{17} and $Nd_2Fe_{14}B$ is summarized. Emphasis is laid on the physical and metallurgical aspects of these materials, but also on the principles of the numerous possible applications. Since this field is exactly 20 years old, also the historical development is treated.

Seltene-Erd-Permanentmagnete

Es wird die Erfindung und Entwicklung der Seltenen-Erd-Permanentmagnete, die auf den intermetallischen Verbindungen $SmCo_5$, Sm_2Co_{17} und $Nd_2Fe_{14}B$ beruhen, übersichtsmäßig dargestellt. Ein Schwerpunkt wird auf die Darstellung der physikalischen und metallurgischen Eigenschaften dieser Materialien, aber auch auf die Prinzipien der zahlreichen möglichen Anwendungen gelegt. Da dieses Gebiet genau 20 Jahre alt ist, wird auch ein Überblick der historischen Entwicklung gegeben.

Aimants permanents de terres rares

On donne un aperçu de l'invention et du développement d'aimants permanents constitués de terres rares, à base de composés intermétalliques tels que $SmCo_5$, Sm_2Co_{17} et $Nd_2Fe_{14}B$. L'accent est mis surtout sur la description des caractéristiques physiques et métallurgiques de ces matériaux ainsi que sur les principes de leurs nombreuses applications possibles. Etant donné que cette découverte date exactement de 20 ans, on traite également de l'historique de ce développement.

Introduction

The rare earth permanent magnets are based on alloys between rare earth metals and 3d-transition metals. These 3d-transition metals comprise especially the elements iron, cobalt, but also other 3d-elements as Cr, Mn, Ni. By the word "rare earth (metals)" we mean the elements number 21 (Sc), 39 (Y) and 57 (La) through 71 (Lu). Because the majority of these elements possess an unfilled 4f-shell, the magnetic properties of the elements, compounds, intermetallics and alloys have always been in the focus of physical interest. In fact the magnetic properties of the rare earth metals and of the 3d-metals combined in a intermetallic compound are the basis for the good permanent magnetic properties.

Although no rare earth ores are available in Austria, Austria has contributed to the science and development of the rare earth. This is especially due to Dr. Carl Auer von Welsbach, who promoted the use of rare earth products scientifically and by founding industrial companies as the Treibacher Chemische Werke. In 1885 he found that didymium, a material believed to be an element up to this date, in fact consisted of two elements which he called praseodymium and neodymium. He also invented the thorium-cerium-gas-mantle and also in 1903 the cerium-flint-stone. Based on 70 wt-% cerium or cerium-Mischmetal and 30 wt-% iron. Numerous other scientific and technical inventions connected with the rare earth elements can also be contributed to Auer von Welsbach and his companies.

The first large scale use of metallic rare earth alloys was the above mentioned "Cerium-iron" and also "Mischmetal" i.e. a mixture of several rare earth metals in the ratio according to the natural abundance. Therefore metallic rare earth elements and their alloys have been in use since the turn of the century. The development of the rare earth permanent magnets, however, had to wait until thorough scientific investigations of the rare earth-intermetallic compounds took place. The rare earth-intermetallics form a special group of the many different intermetallics, present in the huge class of alloys. The term "alloy" can be used for any metallic mixture of phases, while the term "intermetallic compound" should be reserved for

*) Univ.-Doz. Dr. Roland Grössinger, Univ.-Doz. Dr. Gerfried Hilscher and o. Univ.-Prof. Dr. Hans Kirchmayr, Institut für Experimentalphysik, Technische Universität Wien, Karlsplatz 13, A-1040 Wien, Austria

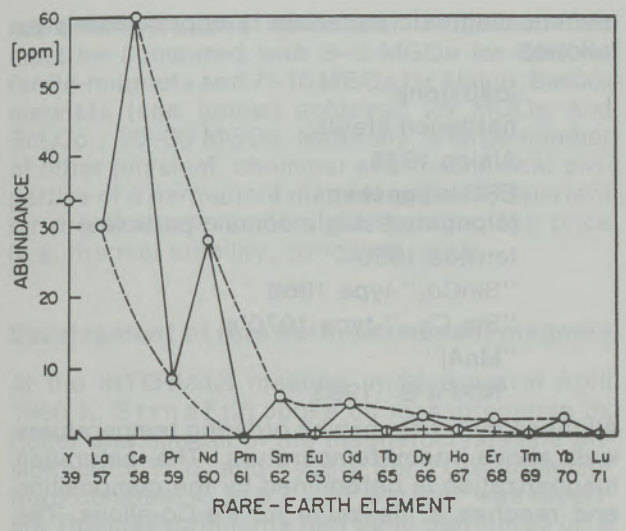

Fig. 1
Natural abundance of the rare-earth elements in the earth's crust (after Strnat et al. (3))

such a combination of metals for at least a combination of metals with metalloids with metallic properties, where a crystal structure and a distinct composition with limited reciprocal solubility of the components is observed. When in the late 1950's larger quantities of pure metallic rare earth elements became available, the phase-diagrams and the crystal structure of binary metallic systems have been systematically evaluated. Therefore, based on the knowledge of the basic features of the phase-diagrams and of the crystal structures, the main physical properties of isolated rare earth intermetallics could be studied systematically. In the USA especially scientists in Ames, Iowa and Ed. Wallace in Pittsburgh and his co-workers systematically studied intermetallic compounds of rare earth metals in the late 1950's.

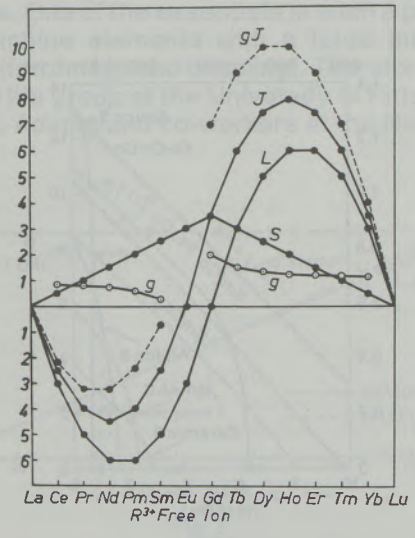

Fig. 2
Dependence of the quantum numbers S, L, J. g, gJ on the rare-earth elements (after Kirchmayr and Poldy (4))

In 1962 Karl Strnat, at the Air Force Materials Laboratory, Wright-Patterson Air Force Base, Dayton, Ohio, granted a research contract to o. Prof. F. Lihl of Technical University of Vienna. This contract started the work on rare earth elements in the physics department of the Technical University of Vienna. The subject of this contract was the preparation of rare earth intermetallic compounds by means of the so called "amalgam process". This process uses liquid mercury as a medium to form intermetallic compounds well below the melting point. Numerous new intermetallic compounds have been prepared between 1962 and 1969 and corresponding physical, especially magnetic properties have been established (1).

In 1966 K. Strnat and his co-workers (2) determined the huge magnetocrystalline anisotropy of YCo_5 (see also fig. 5) which started the field of the rare earth permanent magnets, later mainly based on $SmCo_5$.

Rare earth – 3d-intermetallics

The rare earth elements (R) are present in different ores, as e.g. monazzite, bastnasite, etc. The abundance is large for elements with an even atomic number. The light R (La through Gd) are much more abundant than the heavy ones (see fig. 1 after Strnat et al. (3)). Therefore, if possible, for large scale technical uses the light R are preferred. The R form numerous compounds with many other elements, but not a single intermetallic compound with the elements of the IV, V and VI group i.e. Ti, V Cr, Zr, Nb, Mo, Hf, Tl, W (Kirchmayr and Poldy (4)). However, numerous compounds are formed with the elements of group VII and VIII and especially with Mn, Fe, Co and Ni. In these intermetallics the valency of the R is usually 3^+. Therefore, the occupation of the 4f-shell is nearly equal to a_4R^{3+}-ion. This fact determines in a first approximation the magnetic moment of the R-atom in an intermetallic compound. Fig. 2 shows the different quantum numbers S, L, J, g and gJ, characterizing the R-elements (after Kirchmayr and Poldy (4)). The maximum magnetic moment J is observed for Ho and Er. However, because the heavy R always align their magnetic moments antiparallel to a 3d-moment, only the light R are important in order to achieve a large total magnetic moment for an intermetallic compound of the general formula R_aB_b (R . . . rare earth element, B . . . 3d-metal, a, b . . . integers).

Another important property of an intermetallic compound is its ordering temperature. The ordering temperatures of the system R-Mn, Fe, Co and Ni (where a 3d-element is present) almost exclusively correspond to the onset of magnetic order in which all 3d-moments are ferromagnetically coupled to one another. In addition, the R-moments are also coupled parallel to one another. The coupling between the B- and R-moments is such that the spins in all cases are antiparallel. This results in ferromagnetic coupling of the mag-

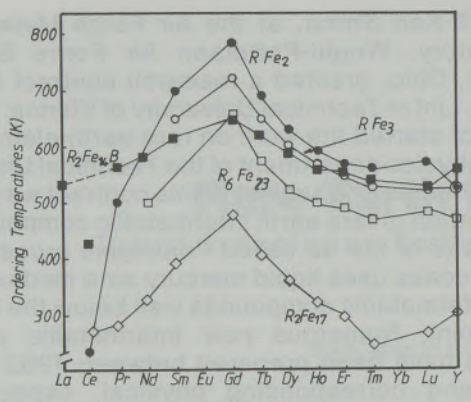

Fig. 3

The ordering temperatures of R-Fe and $R_2Fe_{14}B$ compounds (after Kirchmayr and Poldy (4) and Sinnema et al. (5))

netic moments for the light lanthanides and ferrimagnetic coupling of the heavy lanthinides, as has been mentioned above. The large magnetic moments of the heavy rare earths can therefore not be used in combination with 3d-metals in order to achieve alloys or intermetallic compounds with extremely high saturation magnetization.

In the R-Fe, R-Co and R-Ni system up to 10 different phases with distinct stoichiometry are present. In the R-Co and R-Ni systems the Curie temperatures increase with increasing Co and Ni content. In the R-Co series the RCo_5 compounds posses ordering temperatures above 800K (with the exception of $CeCo_5$, where Ce is tetravalent) while the R_2Co_{17} compounds are magnetically ordered below 1100K. These temperatures are high enough for most practical purposes. The R-Fe compounds however, show low ordering temperatures (see fig. 3 after Kirchmayr and Poldy (4) and Sinnema et al. (5)). Furthermore an increase in the Fe-content decreases the ordering temperature. This fact is probably due to the localized character of the Fe-moments compared to the itinerant character of the Co-moments. In fig. 3 it can also be seen that by preparing ternary $R_2Fe_{14}B$ compounds an increase of the ordering temperatures compared to the binary compounds with similar Fe-contents is observed. This is of the greatest importance for the recently developed $R_2Fe_{14}B$-magnets (Vide infra).

Principles of permanent magnets

A permanent magnet for practical use must fulfil at least the following requirements.

a) Ordering (Curie or Neel)-temperature, well above room temperature.

b) The highest possible coercive field $_IH_C$ and

c) a reasonably high saturation magnetization which is the basis for high remanence.

The history of permanent magnets dates back to ancient times. The historical sequence of the permanent magnetic materials is approximately as follows:

loadstone
hardened steels
Alnico 1935
ESD-magnets
(elongated single domain particles)
ferrites 1950
"$SmCo_5$"-type 1966
"Sm_2Co_{17}"-type 1970's
"MnAl"
"Nd-Fe-B" 1983

All these materials exhibit ordering temperatures well above room temperature. The saturation magnetization is determined by the composition and reaches a maximum for Fe-Co-alloys. The main improvement, however, concerns the intrinsic coercive field $_IH_C$ (kA/m or kOe, 1 kOe = 79,6 kA/m).

Ideally, at the operating temperatures $_BH_C$ shall numerically equal at least B_r. This means, that the ideal demagnetizing curve (B(H) in the second quadrant; see fig. 4) should be a straight line with a slope of 45°. From fig. 4, which shows the second quadrant of the B(H) curves of typical permanent magnets; it can be seen, that the improvement rests on $_BH_C$ and not on B_r. Since the area in a B(H) diagram is proportional to an energy density, the product GOe characterizes the magnetic energy stored in a permanent magnet. The $(B \cdot H)_{max}$ value is determined by the largest rectangle to fit under the B–H loop in the second quadrant. This procedure also defines the ideal geometry of the magnet and the working point. The $(B \cdot H)_{max}$ value of a permanent magnet therefore is a very important figure to characterize a magnet. The usual unit is 1 MGOe = 7,9577 kJ/m³. With the Nd-Fe-B magnets values beyond 45 MGOe at

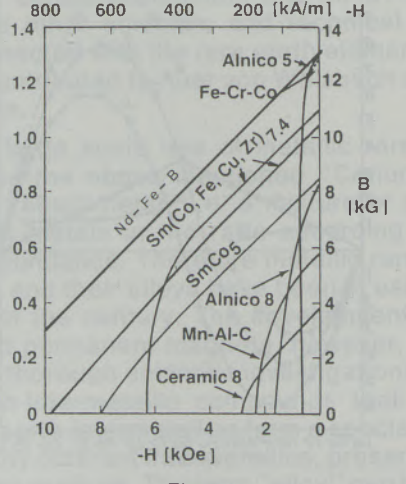

Fig. 4

Comparison of the demagnetization curves of various technical permanent magnets

room temperatures have been achieved. This must be compared with 3–5 MGOe for Barium-ferrite-magnets and 7–10 MGOe for Alnico. $SmCo_5$ magnets (see below) achieved 25 MGOe and Sm_2Co_{17} 30–35 MGOe. Naturally, a large number of other physical, chemical and mechanical properties of a permanent magnet are also important for practical application, disregarding the price (e.g. thermal stability, corrosion, etc.).

Development of rare earth permanent magnets

At the INTERMAG meeting in Stuttgart in April 1966 K. Strnat (2) spoke on measurements by Hoffer and himself of the magnetocrystalline anisotropy of YCo_5 and Y_2Co_{17}. For YCo_5 an anisotropy constant $K_1 = 5{,}7 \cdot 10^7$ erg/cm^3 was reported. The measurements had been performed on a single crystal of YCo_5 which was available for the first time. The essential result is summarized in fig. 5. This finding was identical with the statement that YCo_5 represents a material with extremely high uniaxially magnetocrystalline anisotropy. Strnat immediately drew the conclusion that "with this extremely high crystal anisotropy, a relatively high saturation moment and a Curie point of 630 °C, YCo_5 appears to be a promising material for producing fine-particle permanent magnets with very high energy product". This paper was the starting point for the development of REPMs although no YCo_5 permanent magnet exists today and the development of the mainly Sm-Co based REPMs was characterized by an enormous scientific and technical effort including many setbacks until the present high standard of development was achieved.

The initial finding of the high anisotropy of YCo_5 was not accidental. For some years several laboratories had been investigating R-3d metal compounds with the aim to explore new magnetic materials for applications as soft or hard magnetic materials. One of the essentials in such a process is to combine elements with a large magnetic moment (ferromagnetic coupling). Therefore, Wallace and his group at the University of Pittsburgh, Hubbard, Adams and co-workers at the Naval Research Laboratory, Nesbitt, Wernnick and co-workers at the Bell Laboratories and others performed systematical investigation on R-3d metals and compounds in order to increase the number of useful magnetic materials. One of the basic ideas in this connection was to combine the high magnetic moments of iron or cobalt with the high moment and the high anisotropy of one of the heavy rare earths, while retaining the high magnetic ordering temperature of the 3d-metals. Therefore, when Hubbard and co-workers (6) observed in 1960 for $GdCo_5$ a small magnetic moment where the Gd and Co moments almost cancel each other out, this was of no practical interest. The really exciting finding, however, that $GdCo_5$ powder showed a coercivity $_IH_C$ of 8 kOe (the highest coercivity field achieved at that time) was neglected because of the small moment of $GdCo_5$, which made $GdCo_5$ uninteresting as a permanent magnet material. The nowadays seemingly trivial conclusion, that if $GdCo_5$ had a high coercive force, perhaps other compounds of the same $CaCu_5$ structure, but with a higher saturation magnetization, would also have a comparable high coercive force and would therefore be interesting for practical applications, was not drawn at that time.

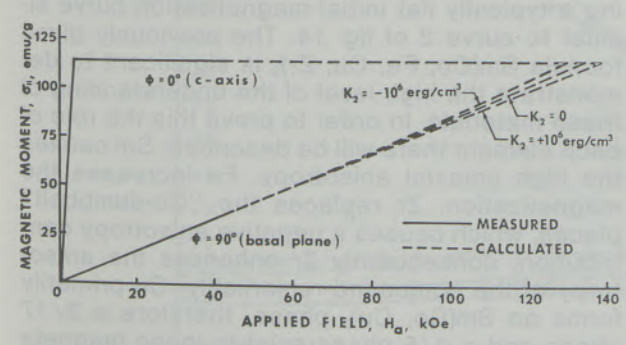

Fig. 5

Magnetization measurement of a YCo_5 single crystal at room temperature applying the external field parallel and perpendicular to the c-axis (after Hoffer and Strnat (2))

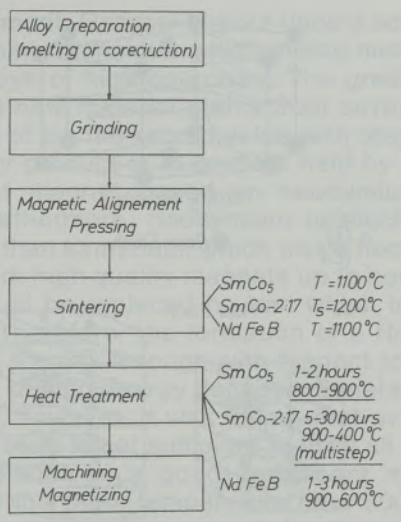

Fig. 6

Production steps of a R-3d metal sintered permanent magnet, e.g. based on Nd-Fe-B (after Ervens (7))

In 1966 Strnat (2) and co-workers independently made the observation of the high anisotropy of YCo_5, and they immediately recognized the relevance of this observation and the field of rare earth permanent magnets was opened.

It took, however, some time until the magnetic producers and especially the magnet users have been convinced, that a real breakthrough in the field of permanent magnets had occurred.

In the beginning, finely ground $SmCo_5$ grains were bonded together with some resin to form a magnet. In some instances this is still done today to

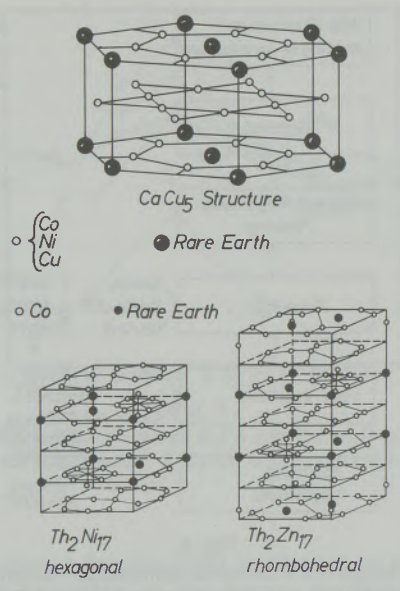

Fig. 7
Sketch of the $CaCu_5$ and the two possible Th_2Ni_{17} and Th_2Zn_{17} structures (after Buschow (8))

form an isotropic, or (when a magnetic field is used to align the particles) an anisotropic magnet. Since 1970, however, a sintering process has been developed. By this process, which is given schematically in fig. 6 (after Ervens et al. (7)) compact sintered permanent magnets can be formed. A large number of process parameter (composition of the alloy, grain size of the powder to be sintered, aligning field, sintering temperature, post sintering heat treatment etc.) must be observed in order to achieve the optimum result. The physical basis of the use of RCo_5 and especially $SmCo_5$ alloys is the large intrinsic magnetocrystalline anisotropy, which is linked to the special crystal structure ($CaCu_5$-type) of the RCo_5 compounds (see fig. 7). In this crystal structure layers of Co-atoms alternate with layers consisting of Sm- and Co-atoms. The high magnetocrystalline anisotropy can be explained as a superposition of the Co-sublattice anisotropy which is caused by an anisotropic exchange plus the crystal field caused anisotropy of the Sm ions.

The anisotropy field H_A is in $SmCo_5$ at room temperature approximately 300 kOe. This value is much higher than static magnetic fields which are achievable. The anisotropy is therefore generally determined by extrapolating M(H) (measured parallel and perpendicular to the easy axis) similar as was shown for YCo_5 in fig. 5. A better and more direct method for determining the anisotropy field H_A of such uniaxial materials is the SPD-(Singular Point Detection-)method, which was developed by Asti and Rinaldi (9). The advantages of this method were shown when studying various uniaxial materials (see e.g. (10)). This technique, which is generally used in pulsed fields, not only allows to determine H_A even on polycrystalline materials, but also to study H_A as a function of the temperature and to investigate spin-reorientations.

The development of $SmCo_5$ based magnets took more than 10 years, but can now be regarded as mature; the different steps of development are documented in the proceedings of the "International Workshop on Rare-Earth-magnets and their applications". The 8th of these workshops was held in Dayton, Ohio (11) in May 1985.

It had always been known that not only the RCo_5, but also the R_2Co_{17} intermetallics posses an appreciable anisotropy field. While, however, the development of the $SmCo_5$-magnets was more or less straight forward, many problems arose with the Sm_2Co_{17}-type magnets. A great general problem has always been the large discrepancy between H_A and the much lower $_iH_C$, which can be achieved. In the case of $SmCo_5$ H_A is approximately 300 kOe, but $_iH_C$ of only 10–15 kOe can be realized with some effort. This is 5% of the anisotropy field.

For Sm_2Co_{17} H_A is merly 70 kOe, but there a similar level of $_iH_C$ of 10–15 kOe should be reached. It took several years, until by special alloy compositions, heat treatments etc. also for Sm_2Co_{17} based alloys large $_iH_C$ values became available. Furthermore, in contrast to RCo_5 where no "RFe_5" counterpart exists, R_2Fe_{17} compounds exist forming solid solutions with the R_2Co_{17} compounds. The situation is, however, complicated, because two alternative crystal structures for the R_2Co_{17} and R_2Fe_{17} compounds (Th_2Ni_{17} and Th_2Zn_{17}) are available, depending on the nature of the compound and the temperature (see fig. 7). Two different methods have emerged to prepare $Sm_2(Fe, Co)_{17}$ based magnets. The first one is similar to the preparation of $SmCo_5$ magnets (see fig. 6). By careful sintering process and post sintering heat treatment beneficial magnetic properties can be achieved. The second method is based on a precipitation of hard magnetic particles in a softer matrix. A typical composition is $Sm(Co_{67}\ Fe_{22}\ Cu_8\ Zr_3)_8$. By a careful heat treatment $_iH_C$ values up to 30 kOe can be achieved. This coercivity is the result of a precipitation hardening process, causing a typically flat initial magnetization curve similar to curve 2 of fig. 14. The previously given formula Sm(Co, Fe, Cu, Zr)$_8$ is significant to demonstrate the high level of the understanding of these materials. In order to prove this the role of each element there will be described: Sm causes the high uniaxial anisotropy. Fe increases the magnetization. Zr replaces the "Co-dumbbell" places, which causes a negative anisotropy contribution, consequently Zr enhances the anisotropy of the compound remarkably. Cu primarily forms an Sm(Co, Cu)$_5$ phase, therefore a 2/17 phase and a 1/5 phase exist in these magnets which is important for the pinning of the domain walls causing high coercivity. This short description shows, that each substitution in this multi-

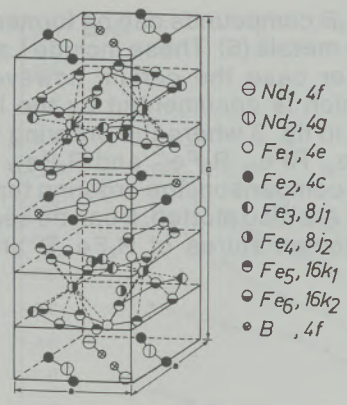

Fig. 8
Tetragonal unit cell of the $Nd_2Fe_{14}B$ structure (after Herbst et al. (16))

phase magnet is quite well understood. Until 1983, i.e. before the development of the Nd-Fe-B magnets the "Sm_2Co_{17}" magnets seemed to be the best permanent magnets which will ever be achieved.

$Nd_2Fe_{14}B$-type magnets

In 1983 Sagawa and co-workers from Sumitomo Special Metals Co. as well as Croat and co-workers from General Motors (12), (13) announced the development and production of permanent magnets based on ternary neodymium-iron-boron-alloys. Although the intermetallic compound which is responsible for the permanent magnetic properties is the same, the production routes are quite different. While Sumitomo uses a melting, grinding and sintering technique, followed by a heat-treatment, General Motors uses a so-called melt-spinning technique which yields microcrystalline alloys of high coercivity. The great interest in this new material stems from several factors: First of all, the record value with respect to the energy product is at present held by such a permanent magnet based on neodymium-iron-boron. Furthermore, neodymium is much more abundant than samarium, which was a necessary requisite for high quality magnets up to now. Also cobalt could be replaced by iron which is much cheaper. Therefore, the formation of a Nd-Fe-B-magnet is a break-through with respect to larger quantities of high energy density magnets. In the meantime, however, it was found, that even this ternary system is not sufficient to fulfill all necessary conditions of a good permanent magnet. Especially the Curie-temperature near 300 °C for $Nd_2Fe_{14}B$ is too low for many applications. Therefore, in the meantime a large variety of (Nd, Pr, Dy)$_2$(Fe, Co, M)$_{14}$(B, Si, X)-magnets has been developed (M, X . . . other elements). In various conferences (14), (15) the present status has been documented.

Basic feature of the Nd-Fe-B-magnets

The basis of the physical properties is the unique crystal structure, which has been determined independently by 3 research groups (16), (17), (18). The unique cell contains 4 $Nd_2Fe_{14}B$ units (68 atoms). The space group is tetragonal $P4_2/mnm$ (see fig. 8). There are two different sites available for Nd, six different sites for Fe and one site for B. The existence of such a ternary phase had been detected already by Chaban, Kuźma and co-

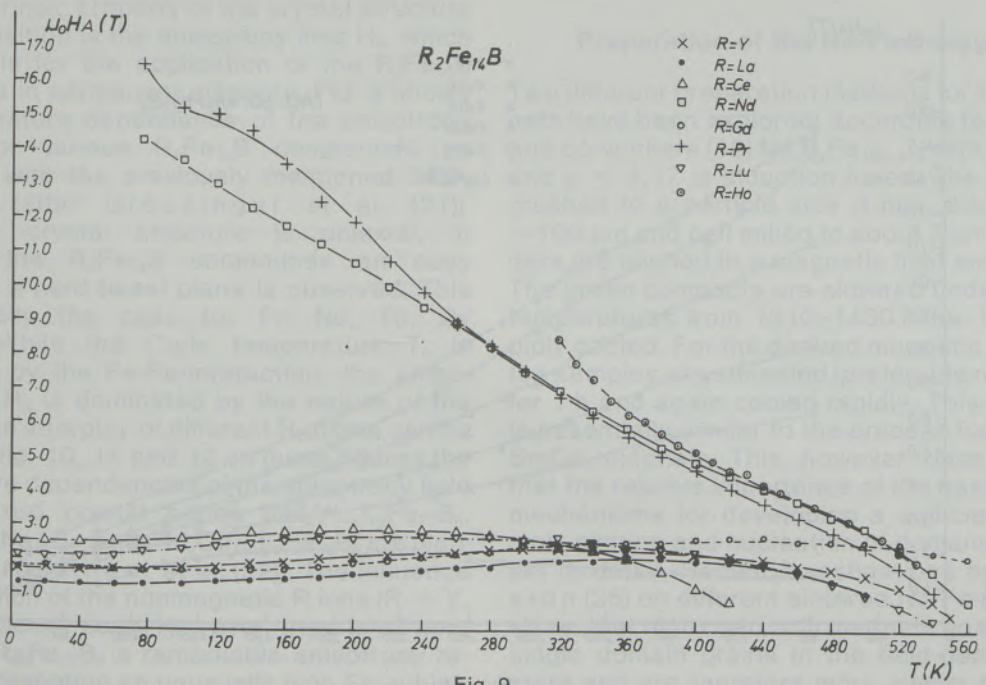

Fig. 9
Temperature dependence of the anisotropy field $\mu_0 H_A$ of $R_2Fe_{14}B$ (R = Y, La, Ce, Nd, Pr, Gd, Ho, Lu) after (21))

workers (19) in 1979, however with an incorrect stochiometry and without measuring the magnetic properties. A detailed discussion of the phase relations and ternary phase diagram has recently been given by Stadelmaier and co-workers (20). The $Nd_2Fe_{14}B$ phase does just not melt congruently, although single crystals can be extracted from the melt by the Czochalski-technique (17).

The $R_2Fe_{14}B$ compounds can be formed with most rare-earth metals (5). These include La and Ce, in which latter case the cerium however is tetravalent, which is documented by the lower T_C of $Ce_2Fe_{14}B$, in fig. 3 where the ordering temperatures of RFe_2, RFe_3, R_6Fe_{23} and R_2Fe_{17} have been given. For comparison, the ordering temperatures of $R_2Fe_{14}B$ are also plotted. It can be seen, that the ordering temperatures of $R_2Fe_{14}B$ are atypical.

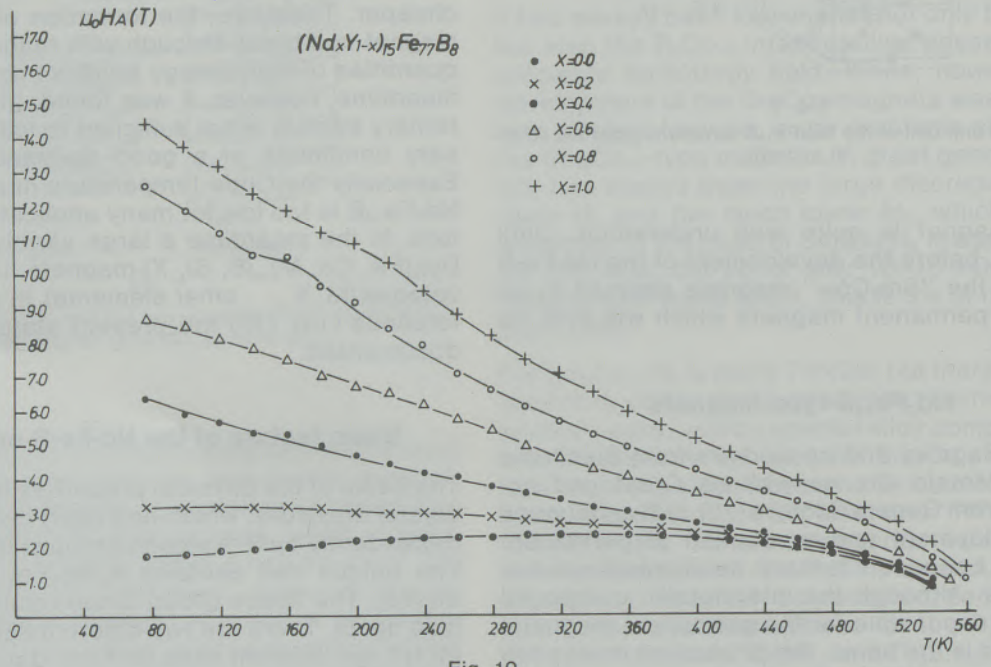

Fig. 10

Temperature dependence of the anisotropy field $\mu_0 H_A(T)$ of $(Nd_xY_{1-x})_{15}Fe_{77}B_8$ (after (22))

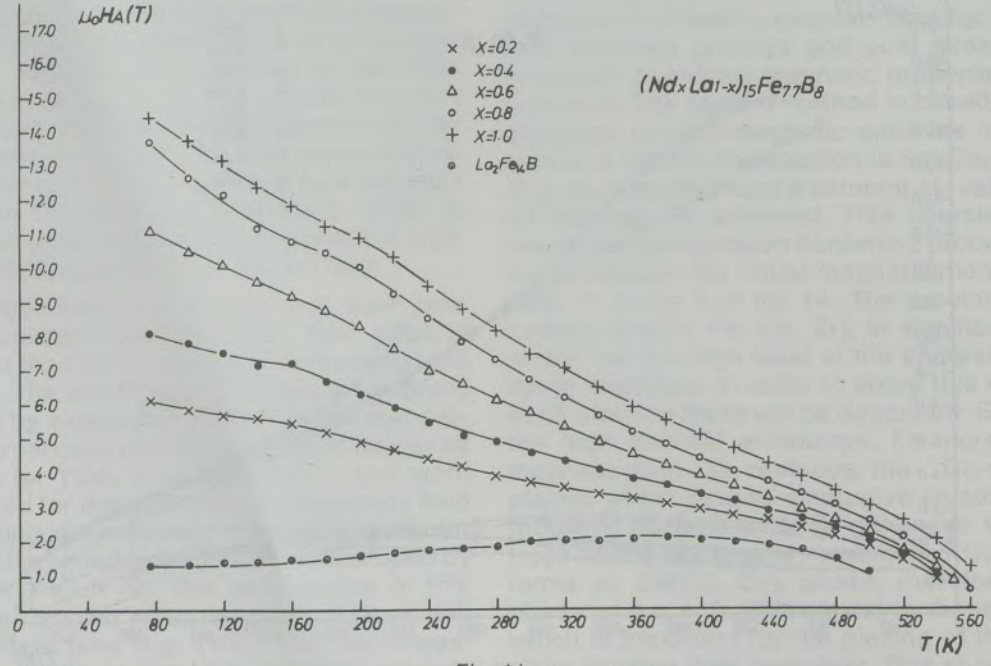

Fig. 11

Temperature dependence of the anisotropy field $\mu_0 H_A(T)$ of $(Nd_xLa_{1-x})_{15}Fe_{77}B_8$ (after (22))

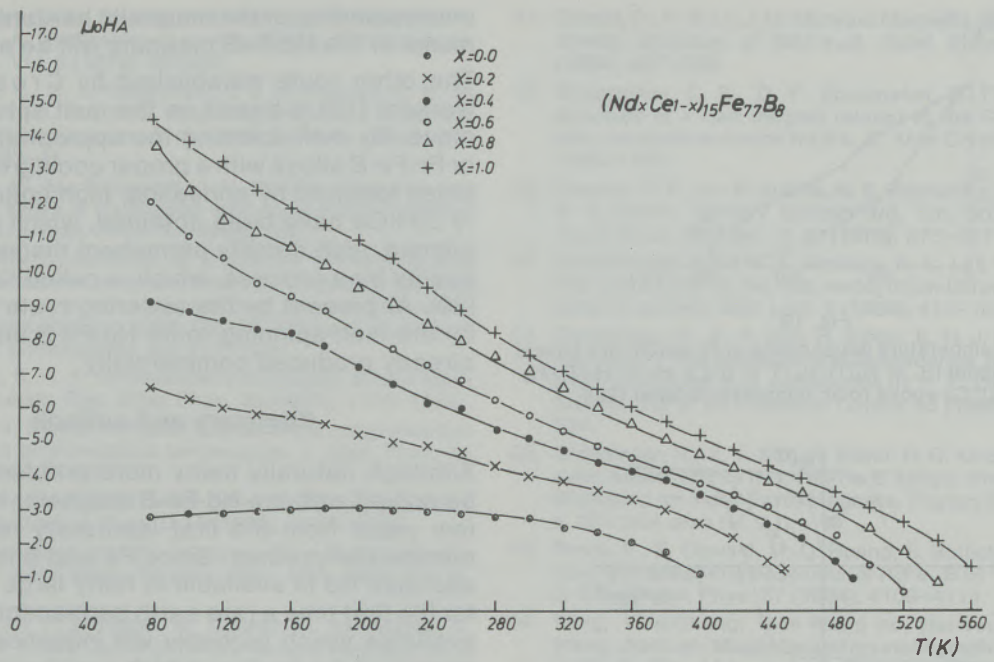

Fig. 12
Temperature dependence of the anisotropy field $\mu_0 H_A(T)$ of $(Nd_2Ce_{1-x})_{15}Fe_{77}B_8$ (after (22))

Although $Gd_2Fe_{14}B$ possesses the highest ordering temperature, the variation of the Curie temperature is small and even the $La_2Fe_{14}B$ compound has a fairly high ordering temperature. This shows that the $R_2Fe_{14}B$ compounds cannot be described as binary compounds with a small addition of B, but are truly ternary compounds with properties which cannot be deduced from the binary compounds.

Another intrinsic property of the crystal structure and composition is the anisotropy field H_A, which is the basis for the application of the $R_2Fe_{14}B$ compounds in permanent magnets. Fig. 9 shows the temperature dependence of the anisotropy field H_A of various $R_2Fe_{14}B$ compounds as measured with the previously mentioned SPD-technique (after Grössinger et al. (21)). Since the crystal structure is uniaxial, in some of the $R_2Fe_{14}B$ compounds an easy c-axis and a hard basal plane is observed. This is especially the case for Pr, Nd, Tb, Dy and Ho. While the Curie temperature T_c is dominated by the Fe-Fe-interaction, the anisotropy field H_A is dominated by the nature of the R-atom. The interplay of different R-atoms can be seen from fig. 10, 11 and 12. In these figures the temperature dependencies of the anisotropy field of the mixed crystal series $(Nd_xY_{1-x})_{15}Fe_{77}B_8$, $(Nd_xLa_{1-x})_{15}Fe_{77}B_8$ and $(Nd_xCe_{1-x})_{15}Fe_{77}B_8$ are plotted (after Grössinger et al. (22)). The influence of the addition of the nonmagnetic R ions (R = Y, La, Ce) is clearly seen. However, even in all nonmagnetic $R_{15}Fe_{77}B_8$ a remarkable anisotropy remains, representing an unusually high Fe-sublattice anisotropy.

Because of the great interest in the $R_2Fe_{14}B$ compounds, also other magnetic properties as e.g. the paramagnetic behavior of the $R_2Fe_{14}B$ systems (R = Pr, Nd, Dy or Er) (23) and the enhancement of the Curie temperature T_c by the addition of Co and the decrease of T_c by the replacement of Fe by Mn and Cr have been studied (24) respectively.

Preparation of the Nd-Fe-B-magnets

Two different preparation methods for these magnets have been explored: According to Sagawa and co-workers (12) $Nd_xB_yFe_{100-x-y}$ with x = 13,19 and y = 4,17 is induction fused. The ingots are crushed to a particle size ‹1 mm, disc milled to ~100 μm and ball milled to about 3 μm. The powders are aligned in a magnetic field and pressed. The green compacts are sintered under argon at temperatures from 1310–1430 K for 1 h and rapidly cooled. For the desired magnetic properties the samples are annealed (preferable near 900 K) for 1 h and again cooled rapidly. This procedure is essentially similar to the process for preparing $SmCo_5$ magnets. This, however, does not mean that the relative importance of the basic physical mechanisms for developing a sufficient $_iH_c$, namely pinning and nucleation of domains is known yet in detail. Recent investigations by Livingston (25) on different sintered Nd-Fe-B-magnets show, that high coercivity magnets possess more single domain grains in the field-demagnetized state and are therefore more similar to sintered $SmCo_5$ magnets than low coercivity magnets.

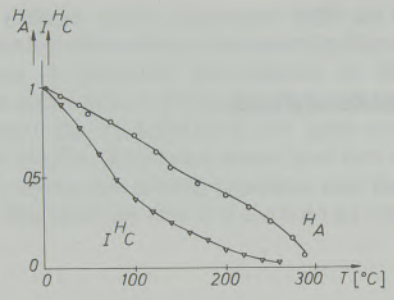

Fig. 13

Normalized temperature dependence of $_IH_C$ and H_A of a typical Nd-Fe-B magnet ($H_A = H_A(T)/H_A\ (T = 0°C)$, $_IH_C = {}_IH_C(T)/{}_IH_C\ (T = 0°C)$) above room temperature (after (27))

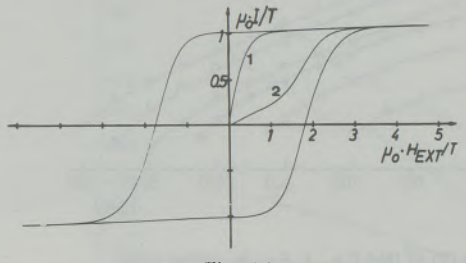

Fig. 14

Hysteresis loop of a $(Nd_{0.9}Dy_{0.1})_{15}Fe_{77}B_8$ permanent magnet at room temperature. The magnetic parameter are: $_IH_C = 18$ kOe, $4\pi/_R = 10{,}2$ kG, $(BH)_{max} = 24.3$ MGOe

1: Initial magnetization curve after thermal demagnetization (nucleation)

2: Initial magnetization curve after field demagnetization (pinning) (after (28))

By the sintering-route in the meantime Nd-Fe-B-magnets with energy products in excess of 45 MGOe have been prepared. Obviously, additions of Dy or Tb are beneficial for high coercivity. Unfortunately, the coercivity of the permanent magnets decreases faster with increasing temperature than the anisotropy field (26), (27). In order to demonstrate this behavior in fig. 13 the normalized temperature dependence of the coercivity and the anisotropy field above room temperature of a typical Nd-Fe-B magnet is shown (27). In fig. 14 (28) the full hysteresis loop and also the initial magnetization curve of a $(Nd_{0,9}Dy_{0,1})_{15}Fe_{77}B_8$ permanent magnet, prepared in this laboratory, is given. A thermally demagnetized magnet exhibits a steep rise of the magnetization with the applied field by nucleation of new domains (curve 1). If the same magnet, however, is demagnetized by an applied field, the domain walls still present are strongly pinned in the grain boundaries. Many further investigations will be necessary, until a full understanding of the magnetic hardening mechanisms in the Nd-FeB magnets will be available.

The other route established by Croat and coworkers (13) is based on the melt spinning technique. By melt-spinning the appropriate Nd-Fe-B or Pr-Fe-B alloys with a proper cooling rate, sometimes followed by annealing, high coercivities up to 20 kOe have been obtained, which resulted in aligned, high density permanent magnets of high quality by a process, which is called "die-upset" (29). At present by the sintering route as well as by the melt-spinning route Nd-Fe-B magnets are already produced commercially.

Summary and outlook

Although naturally many more problems have to be solved with the Nd-Fe-B magnets, it took only few years from the first laboratory results to a commercial product. Since Fe and B is abundant and also Nd is available in fairly large quantities for the first time a rare earth permanent magnet is available which probably will influence even the market of the ferrites, which are at present most widely used permanent magnets.

Because of the large energy product now available, a number of applications become now feasible for the first time. This is especially true for electric motors in the 1 kW – 100 kW range. In this case weight and size reductions by a factor 3 compared to conventional motors are foreseen. The best way to use these new materials in electric motors is to place the permanent magnets in the rotor. This necessitates, however, to alternate the current in the stator, which is best done by an electronic commutator. The many advantages, however, render this sophisticated design for many advanced applications. Many other applications of modern high quality magnets can be found in the already mentioned proceedings of the REPM-workshop (11).

The intimate collaboration between basic and applied scientists and engineers has therefore resulted in three families of REPMs based on "$SmCo_5$", "Sm_2Co_{17}" and "$Nd_2Fe_{14}B$". Each group of permanent magnets has its advantages and disadvantages and therefore its place in the market.

A lot of additional basic and applied research is still necessary in order to make the best use of these materials. However, the properties and qualities already achieved are so convincing, that many applications of REPM are possible only because of the existence of these modern tailor made materials.

References

1. Lihl, F.: Investigations of transition metal rare earth alloys, AFML–TR–69–245, Air force materials Labs., Wright-Patterson, Ohio, **1969.**
2. Hoffer, G., K. Strnat: Magnetocrystalline Anisotropy of YCo_5 and Y_2Co_{17}, IEEE MAG 2 (**1966**), 487.
3. Strnat, K.: Study and Review of Permanent Magnets of Electric Vehicl Propulsion Motors, NASA, CR–168278 DOE/NASA/0189–83/2.
4. Kirchmayr, H., C. Poldy: Magnetic properties of intermetallic compounds of rare earth-metals, chapt. 14 of the

"Handbook on the Physics and Chemistry of Rare Earth". Ed. by K. A. Gschneider Jr. and L. Eyring, North Holland, Publ. Co. Vol. 2 (**1979**), 55–230.

5. Sinnema, S., R. J. Radwanski, J. J. M. Franse, D. B. de Mooij, K. H. J. Buschow: Magnetic properties of ternary rare-earth compounds of the type $R_2Fe_{14}B$, JMMM 44, (**1984**), 333–41.
6. Hubbard, W. M., E. Adams, J. V. Gilfrich: Magnetic moments of alloys of Gadolinium with some of the transition elements, J. Appl. Phys. 31 (**1960**), 368.
7. Ervens, W.: Comparison of properties of Nd-Fe-B and Sm-Co permanent magnets. Proc. of a Workshop-meeting on Nd-Fe permanent magnets their present and future applications, Brüssel, **1984**, Ed. I. V. Mitchel Commission of Europ. Communities, pp. 111–122.
8. Buschow, K. H. J.: Intermetallic compounds of rare earth and 3d-metals. Rep. Prog. Phys. 40 (**1977**), 1179–1256.
9. Asti, G., S. Rinaldi: Singular points of the magnetization curve of a polycristalline ferromagnet. J. Appl. Phys. 45 (**1974**), 3600–3610.
10. Grössinger, R.: Pulsed fields: generation, magnetometry and application. J. Phys. D 15 (**1982**), 1548–1608.
11. Proc. 8th International Workshop on Rare-Earth-Magnets and their Application, Dayton, Ohio, May **1985**, Ed. K. Strnat.
12. Sagawa, M., F. Fujimura, N. Togawa, H. Yamamoto, Y. Matsuura: A new material for permanent magnets on a base of Nd and Fe. J. Appl. Phys. 55 (**1984**), 2083–87.
13. Croat, J. J., J. F. Herbst, R. W. Lee, F. E. Pinkerton: Pr-Fe and Nd-Fe-based materials: A new class of high performance permanent magnets. J. Appl. Phys. 55 (**1984**), 2078–82.
14. "Nd-Fe permanent magnets, their present and future application." Proc. of the Workshop held on Oct. 25, **1984** in Brüssel, ed. by I. V. Mitchell, Commission of Europ. Communities.
15. 30th-Annual Conf. on Magn. and Magn. Mat. Nov. 27–30, **1984**, San Diego, California, J. Appl. Phys. 57 (**1985**) (8).
16. Herbst, J. F., J. J. Croat, F. E. Pinkerton, W. B. Yelon: Relationship between crystal structure and magnetic properties in $Nd_2Fe_{14}B$. Phys. Rev. B29 (**1984**), 4176–4178.
17. Givord, D., H. S. Li, J. M. Moreau: Magnetic properties and crystal structure of $Nd_2Fe_{14}B$. Solid State Comm. 50 (**1984**), 497–499.
18. Shoemaker, C. B., D. P. Shoemaker, R. Fruchart: The structure of a new magnet related to the Sigma phase: iron, neodymium boride $Nd_2Fe_{14}B$, Acta Cryst. C40 (**1984**), 1665–1688.
19. Chaban, N. F., Yu. B. Kuźma, N. S. Bilonizhko, O. Kachmar, N. V. Petriv: Ternary System (Nd, Sm, Gd)-Fe-B. Dokl. Akad. Nauk, SSR Ser. A 10 (**1979**), 875–877.
20. Stadelmaier, H. H., N. A. Almesry, N. C. Liu, C. F. Cheng: The metallurgy of the iron-neodymium-boron permanent magnet system. Mat. Lett. 2 (**1984**), 411–15.
21. Grössinger, R., X. K. Sun, R. Eibler, K. H. J. Buschow, H. Kirchmayr: The temperature dependence of the anisotropy field in $R_2Fe_{14}B$ compounds (R = Y, La, Ce, Pr, Nd, Gd, Ho, Lu). J. de Physique Tomme 46 (**1985**), C 6–221–224.
22. Grössinger, R., X. K. Sun, R. Eibler, H. R. Kirchmayr: Magnetic Anisotropy of (Nd, RE)-Fe-B Alloys. Proc. of 8th Int. Workshop on Rare Earth Magnets, Dayton (USA) (**1985**), p. 553 (see also ref. 11).
23. Burzo, E., E. Oswald, M. Q. Huang, E. Boltich, W. E. Wallace: Paramagnetic behaviour of $R_2Fe_{14}B$ (R = Pr, Nd, Dy or Er). J. Appl. Phys. 57 (**1984**), 4109–4111.
24. Yang, Ying-Chang, Wen-Wang ho, Hai-Ying Chen, Jin Wang, Jian Lan: Magnetic and crystallographic properties of $Nd_{15}B_7$ $(Fe_{1-x}M_x)_{78}$. J. Appl. Phys. 57 (**1984**), 4118.
25. Livingston, J. D.: Magnetic domains in sintered Fe-Nd-B magnets. J. Appl. Phys. 57 (**1985**), 4137–39.
26. Grössinger, R., P. Obitsch, X. K. Sun, R. Eibler, H. Kirchmayr, F. Rothwarf, H. Sassik: The anisotropy of Nd-Fe-B magnets. Mat. Lett. 2 (**1984**), 539–543.
27. Grössinger, R., H. R. Kirchmayr, R. Krewenka, K. S. V. L. Narasimhan, M. Sagawa: High temperature behaviour of technical Nd-Fe-B permanent magnets. Proc. of 8th Int. Workshop on Rare-Earth Magnets, Dayton (USA) (**1985**), p. 565.
28. Heisz, S.: Diploma Thesis, TU Wien, **1985**.
29. Lee, R. W.: Hot pressed neodymium-iron-boron magnets. Appl. Phys. Lett. 48 (**1985**), 790–91.

Hydrogen Induced Change of the Magnetic Properties of Intermetallic Compounds

Günter Wiesinger and Gerfried Hilscher, Wien*)

Dedicated to the 80th birthday of Prof. Dr. Franz Lihl

A survey is given of the author's recent activities on the field of metal hydrides with emphasis laid on bulk magnetic properties and hyperfine interactions. Particularly the hydrides of $TiMn_2$, $Zr(Fe, Mn)_2$, Ti(Fe, Co) and $Nd_2Fe_{14}B$ are discussed.

Wasserstoffinduzierte Veränderung der magnetischen Eigenschaften intermetallischer Verbindungen

Die vorliegende Arbeit stellt einen Überblick über die Aktivitäten der Arbeitsgruppe „Metallhydride" am Institut dar, wobei das Hauptaugenmerk auf magnetische Eigenschaften und Hyperfeinwechselwirkungen gelegt wird. Besonders ausführlich diskutiert werden die Hydridsysteme von $TiMn_2$, $Zr(Fe, Mn)_2$, Ti(Fe, Co) sowie von $Nd_2Fe_{14}B$.

Modification, induite par l'hydrogène, des propriétés magnétiques de composés intermétalliques

On donne un aperçu des activités du groupe de travail «hydrures métalliques» en mettant principalement l'accent sur les propriétés magnétiques et les interactions hyperfines. On discute plus en détail les systèmes d'hydrures de $TiMn_2$, $Zr(Fe, Mn)_2$, Ti(Fe, Co) et $Nd_2Fe_{14}B$.

1. Introduction

In the last decade an enormous interest arouse with respect to the field of hydrides of intermetallic compounds. The remarkable storage properties of certain systems can be regarded as the main reason, $LaNi_5$, TiFe, $ZrMn_2$ serving as typical examples. About five years ago a group has been established at this institute, whose activities are particularly devoted to the study of the hydrogen induced change of bulk magnetic properties as well as of hyperfine interactions in intermetallic compounds (1)–(6). This work ended up with a comprehensive review which will be published in the near future (7).

When studying the bulk magnetic properties and the hyperfine interactions by magnetization- and susceptibility measurements and by Moessbauer spectroscopy respectively, one holds two experimental techniques (macroscopic and microscopic respectively) which form an ideal combination and completion in order to elucidate a great number of physical and chemical properties of intermetallic hydrides such as the chemical nature of hydrogen and its location, the formation and the stability of various structural phases and the influence of hydrogen absorption on electronic, magnetic, and superconducting properties of the host lattice. Moreover frequently, from studying the hydrides conclusions may be drawn upon properties of the parent system, particularly in case of the electronic structure and the magnetic interaction mechanism. Thus such kinds of studies have received considerable attraction not only in case of basic research but also from the applied point of view. Our recent investigations as far as metal hydride systems are concerned are summarized below. In order to gain more clarity we have chosen a division into a general part followed by a discussion of the experimental results.

2. Some general comments on magnetism and hyperfine interactions

Metallic magnetism covers a wide range of phenomena which are not only intimately correlated with the electronic structure but also with the metallurgy. This appears to become of particular importance for intermetallics and the binary and ternary metal hydrides. However no general prediction of the effect of hydrogen absorption upon the magnetic properties could be given so far.

In contrast to the magnetism of the 3d-metals, reflecting the old controversy of localized versus itinerant description, the magnetic properties of

*) Univ.-Doz. Dipl.-Ing. Dr. techn. Günter Wiesinger, Univ.-Doz. Dipl.-Ing. Dr. techn. Gerfried Hilscher, Institut für Experimentalphysik, TU Wien, Karlsplatz 13, A-1040 Wien

the rare earth (R) elements are successfully described in terms of the RKKY theory: because of the localized nature of the 4f-electrons there is no overlap of 4f-wave functions of different lattice sites and thus the magnetic coupling has to proceed indirectly via the spatially non-uniform polarization of the conduction electrons.

Unlike the binary 4f-hydrides no similar simple and convincing conclusions for changes of magnetism in terms of a protonic or anionic behaviour of hydrogen can be given in case of 3d-metals and their intermetallics. The only general statement which can be made is that changes in magnetic properties in the Fe compounds occur in the direction opposite from that in the Ni and Co compounds. Particulary, in Sc-, Y-, Hf- and R-Fe intermetallics the Fe moment is found to increase on hydrogen absorption while for the magnetic ordering temperatures changes can be obtained in either direction (8)–(11).

Currently, 3d-magnetism is best described by an improved theory based on the Stoner-Wohlfarth model (spin-polarized band theory (12), (13)).

The magnetic properties of 3d-metals crucially depend upon width and structure of the 3d-band and the density of states at the Fermi level. In a semi-empirical model Griessen and Feenstra (14) recently related the heat of formation of a metal hydride to the difference between the Fermi energy and the center of the s band of the host metal. For a deeper insight into the basic physical properties of parent intermetallics and their hydrides realistic band structure calculations are required.

TiFe, the pseudobinary alloy system Ti(Fe, Co), and $LaNi_5$ serve as a relevant example for intermetallic compounds, where hydrogen absorption affects not only the bulk 3d-magnetism but also the metallurgy giving rise to a decomposition at the surface. Apart from the complex 3d-magnetism, in the former systems the surface decomposition in Ti- and in Fe-clusters which, together with a change of so-called antistructure atoms (Fe atoms on Ti sites) contributes to the global magnetization, further complicates the analysis of the magnetization actually measured. This should demonstrate that the change of magnetic properties upon hydrogenation may have different origins which need not necessarily be correlated with a change of the bulk or intrinsic magnetic properties of the material.

Intermetallic compounds of 3d-metals (Mn, Fe, Co, Ni) with rare earth elements exhibit a large variety of interesting magnetic properties. In R-3d-intermetallics and their hydrides, where both the R- and the 3d-element are magnetic we can distinguish three main types of magnetic interactions which are quite different in nature: the magnetic interaction i) between the localized 4f-moments, ii) between the more itinerant 3d-moments and iii) between the 3d- and the 4f-moments. If in R-3d-intermetallics both the R- and the 3d-element are magnetic, it is generally observed that the magnetic interaction decreases in the following sequence: 3d–3d > 4f–3d > 4f–4f.

Depending upon the composition and the type of combination of these elements hydrogen absorption commonly leads to a weakening of the magnetic coupling between the 4f-moment and the 3d-moment and to substantial changes of the 3d-transition metal moment. In Co and Ni compounds hydrogen absorption results usually in a reduction of the 3d-moment, while the opposite is observed for R-Fe compounds. The weakening of the 4f–3d exchange interaction upon hydrogen absorption may be explained by a reduced overlap of the 3d-electron wave functions with the 5d-like ones which are polarized by the 4f-moment and thus transmit the interaction to the 3d-electrons. Hydrogen reaction can furthermore lead to atomic – and/or concentration fluctuations of H-atoms over a few atomic distances so that the electron concentration may differ from one R-site to the other and therefore changes of the magnetic coupling strength can be expected.

In view of results obtained from Moessbauer spectroscopy on R-nuclei and from UPS and XPS experiments it is now generally agreed that in these R-intermetallic hydrides hydrogen exists as a screened proton with a screening charge larger than one. The excess screening charge is due to charge transfer from R-atoms to hydrogen rather than from the 3d-atoms (9), (15)–(17).

When γ-rays are emitted or absorbed without recoil they suffer no energy loss, and the resulting lines exhibit the natural width (Moessbauer effect). Thus a resolution can be obtained sufficiently high in order to monitor the minute hyperfine interactions by periodically changing the Doppler velocity in the order of mm/s up to cm/s corresponding to energy changes of the order of a few μeV or even less.

Three of those interactions are known: An electrostatic one (Coulomb-like) between the nuclear charge and the electronic charge at the nucleus, causing a shift of the nuclear levels. Therefore we commonly observe deviations from the theoretical resonance frequency (isomer shift). The interaction between the nuclear quadrupole moment and the electric field gradient (EFG) at the nuclear site results in a partical (quadrupole-) splitting of the nuclear levels. The degeneracy of the nuclear states is, however, lifted completely, when the nuclear magnetic moments experience a magnetic field (nuclear Zeeman effect). Consequently, in the latter two cases we observe a splitting of the γ-ray pattern, i.e. multi-line Moessbauer spectra are obtained. Further parameters which can be derived from the analysis of a spectrum are the width of the Moessbauer line which can yield information about diffusion – or relaxation processes and the Moessbauer-Lamb (f) factor representing the fraction of recoil free emitted or absorbed γ-rays, thus giving insight into the dynamic behavior of the lattice.

The isomer shift simultaneously contains information about the difference in the nuclear radii (δR) of excited and ground state respectively and the difference in the charge at the nuclear site in absorber and source respectively. Because δR can be of either sign (e.g. <0 for ^{57}Fe, ^{155}Gd, >0 for ^{119}Sn) a shift of the resonance line to more positive (negative) energies corresponds in the former case to a smaller (larger) electron density, whereas the opposite is obtained in the latter case. The isomer shift depends upon valence state and chemical bonding. It can be influenced directly by altering the population of the s-like conduction electrons or indirectly via a shielding of the s electrons by those with d-character.

Already Wagner and Wortmann (18) had pointed to the problem of asigning the total hydrogen induced change in isomer shift to different origins. If the isomer shift S is considered as a function of hydrogen concentration n and volume v, the overall change after charging can be expressed as

$$\frac{dS}{dn} = \left(\frac{\partial S}{\partial \ln v}\right)_n \cdot \frac{d \ln v}{dn} + \left(\frac{\partial S}{\partial n}\right)_v \qquad [1]$$

dS/dn is measured by Moessbauer spectroscopy; $(\partial S/\partial \ln v)_n$ displays the pure volume dependence of S and can be obtained from high pressure data. The term $d\ln v/dn$ represents the hydrogen induced rise in volume and may be evaluated from X-ray diffraction data. The change at constant volume, $(\partial S/\partial n)_v$, depicting the actual effect of hydrogen on the electronic structure of the Moessbauer atom, can thus be readily calculated. It turns out that this term is rather small in magnitude, i.e. of the order of $+0.1$ mm/s. An appreciable 3d-charge transfer from Fe to H which frequently has been proposed in order to explain the hydrogen induced changes in the magnetic moment can by no means account for it, since this would even lead to a wrong sign of dS.

Very recently Gupta (19) interpreted the isomer shift of TiFe hydride by applying the APW method, yielding an excellent agreement with the experimental data. She proposed a depletion of the Fe 4s states in order to form a low lying metal-hydrogen band which in case of binary metal-hydrogen systems has already been suggested by Switendick (20). This finding is in complete accordance with XPS data recently reported by Schlapbach (21) for $ZrMn_2H_3$. He was able to experimentally verify this hydrogen induced band to lie 6.5 eV below the Fermi level. The shift of the Zr 3d levels towards higher energies can be regarded as a further hint to a charge transfer from Zr to H. The Fe 3d states seem to be minor affected by hydrogen absorption.

Buschow (9) questioned the justification of making the hydrogen induced change in isomer shift up from an electronic and a volume term. He suggested to use the model of Miedema and van der Woude (22) rather, where the differences in electronegativity and in the electron density at the atomic cell boundary have to be considered. An attempt was made to explain the isomer shift data for $Th_7Fe_3H_x$, however, no further confirmation has been reached yet.

3. Results and discussion

$TiMn_2$ (2), (4)

Three Ti-Mn intermetallics were found to be stable at low temperature: the C 14 Laves phase with a wide range of homogeneity reaching from $TiMn_2$ to $TiMn_{1.2}$, the Q-phase $TiMn_{1.17}$ and the Φ-phase $TiMn_{1.08}$. While all parent compounds exhibit temperature independent paramagnetism, the three hydrides are ferromagnetic with Curie temperatures of about 212 K, 87 K and 155 K respectively. The onset of ferromagnetism has been attributed to both volume expansion and increase in $N(E_F)$ upon hydrogen absorption. In context to the large homogeneity range of the Laves phase compound an increase of the lattice constants was observed when rising the Ti concentration. Simultaneously, the hydrogen capacity was found to grow, whereas stoichiometric $TiMn_2$ absorbs no hydrogen at all. Thus the existence of a critical range of the lattice dimensions for the absorption of hydrogen has been suggested which is in agreement with results obtained by Oesterreicher and Bittner (23) on (Ti, Zr)Mn_2, however, should not be generalized.

Moessbauer studies performed on $TiMn_{1.5}$ doped with ^{57}Fe yielded a non-symmetric quadrupole doublet with a comparatively small splitting which was strongly enhanced after hydrogenation. The shape of the spectrum furthermore had changed to complete symmetry with narrow lines. The non-symmetric doublet of the parent compound we attributed to a non-random distribution of the excess Ti atoms on the 2a sites, which later on has been confirmed by neutron diffraction experiments (24). The presence of only one hyperfine pattern after hydrogenation has been quoted to originate from the large lattice expansion ($\Delta V/V = 27\%$), which should release the space restriction for the (Ti, Mn)-tetrahedra. Thus reasons for lattice distortions are no longer provided and all Fe atoms are now assumed to experience the same EFG, very similar to that one in the isostructural $TiFe_2$. It should be pointed out that an alternative explanation for the occurance of narrow line widths after hydrogen absorption can be given by taking motional narrowing effects into account which are caused by rapid fluctuations of the hydrogen atoms.

In this work we furthermore made an attempt to determine the type of ferromagnetism in the ternary Ti-Mn hydrides. By means of the so-called Rhodes-Wohlfarth plot one is able to classify ferromagnetic order as being of localized or of itin-

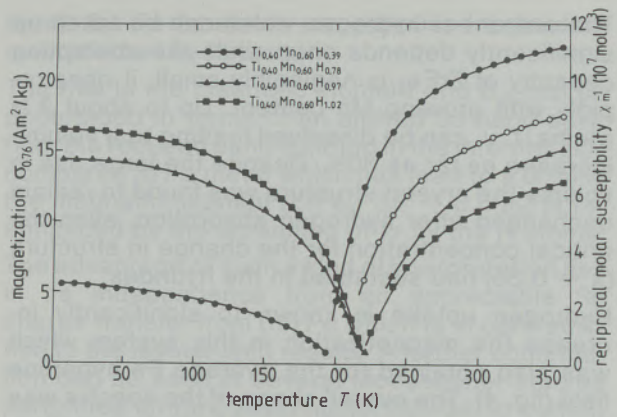

Fig. 1
Magnetization and reciprocal molar susceptibility vs. temperature for some $TiMn_{1.5}$ hydrides

erant type. We note that the crucial parameter within this model is given by the ratio of magnetic carriers in paramagnetic and in the ferromagnetic states, q_c/q_s as a function of the Curie temperature.

In terms of this analysis the Ti-Mn Laves phase turned out to exhibit localized moments which is confirmed by the fact that the Arrott-plots (σ^2 vs. B/σ) are not parallel. In case of the ϱ- and of the Φ-phase, however, the rather large values of q_c/q_s with the corresponding Curie temperatures fit well into the itinerant branch of the Rhodes-Wohlfarth plot which led us to the conclusion that these compounds might exhibit rather pure band ferromagnetism.

Comments were also made on the onset of ferromagnetism upon hydrogenation in the Laves phase $TiMn_{1.5}$ by considering the large increase of the temperature independent term of the paramagnetic susceptibility (fig. 1) as well as of the specific heat coefficient γ observed after hydrogen absorption. This finding has been correlated with an increased density of states at the Fermi level N (E_F) which is found to still grow in the hydride when the amount of hydrogen is increased further. Within the frame of this simple picture the high value of N (E_F) in the hydride was interpreted as one reason for the onset of ferromagnetism (Stoner criterion). Since the lattice expansion caused by hydrogen absorption brings about a narrowing of the d band and thus an increase of N (E_F), the interpretation of the results concerning YMn_2 by Buschow and Sherwood (25) emphasizing this lattice expansion, was proposed by us to fit within our picture.

Ti (Fe, Co) (1), (3)

The system Ti ($Fe_{1-x}Co_x$) (CsCl type of structure) exhibits unique magnetic properties: while the boundary compounds TiFe (x = 0) and TiCo (x = 1) are Pauli paramagnets, ferromagnetism is observed in an intermediate concentration range. On the other hand, Moessbauer spectra recorded on these ferromagnetic samples show a completely collapsed magnetic hyperfine interaction and thus give no evidence for the existence of a localized moment on the iron site. In subsequent theoretical and experimental studies the idea of so-called antistructure (AS) atoms, i.e. misplaced Fe (Co) atoms at the Ti sublattice, has been introduced. Since in such a case an Fe atom is surrounded by 8 Fe (Co) neighbors, a local magnetic moment may form on these atoms.

Until recently, however, no direct experimental evidence for AS atoms has been presented which is connected with the appearent puzzle regarding a zero hyperfine field within the ferromagnetic region. By Moessbauer measurements with an extended measuring time, yielding count rates of about 12 millions per channel, we finally succeded in resolving a weak magnetic hyperfine pattern which otherwise is buried in the background (fig. 2). Intensity and splitting are in good agreement with the values predicted from bulk magnetic measurements for the Fe AS atoms.

If the pseudobinary compounds are hydrided, they behave very similar to TiFe. Again α-, β- and γ-phase are found which exhibit equivalent Moessbauer spectra as has been observed for TiFe (26). The rise in T_c upon hydrogenation we tentatively interpreted as a negative pressure effect by comparing our results with high pressure magnetization data (27–29). This, however, could successfully be done for low Co-concentrations (small changes of T_c) only, in case of higher Co-content and larger increase in T_c (~40 K) no agreement could be obtained at all.

We want to recall that pressure experiments clearly point to the presence of localized moments in the Fe-rich regime, whereas for the Co-rich side of the system they point to itinerant ferromagne-

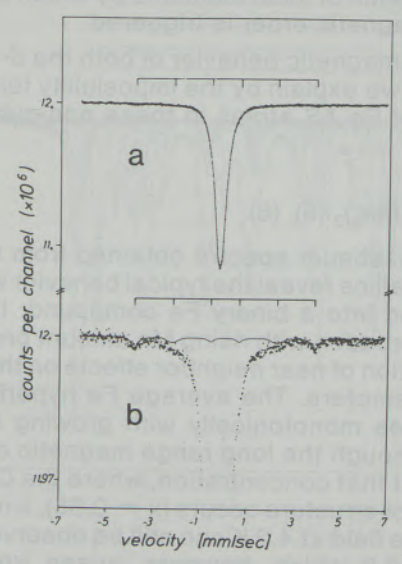

Fig. 2
Mössbauer spectrum of $TiFe_{0.6}Co_{0.4}$ recorded at 4.2 K; +++... experimental points, solid line ... computer fit; the bars on top of the spectrum indicate the line positions

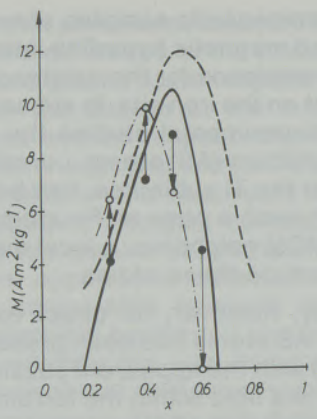

Fig. 3

Spontaneous magnetization (●, full curve) and magnetization taken at 7 T and 4.2 K (broken curve) for uncharged Ti ($Fe_{1-x}Co_x$) compared with the spontaneous magnetization of α phase hydrides (o, chain curve)

tism. The change of T_c and σ upon hydrogenation is positive for $x<0.45$ (Fe-rich) and negative for $x>0.45$ (Co-rich) (fig. 3). Therefore, not even a qualitative correlation between the hydrogen induced change of T_c and its pressure dependence can be experted for the Corich compounds. However, with the assumption that additional AS atoms are created upon hydrogenation the magnetic properties of the Ti (Fe, Co) hydrides could be explained at least qualitatively: the number of Fe AS atoms carrying the local moments decreases, while N (E_F) increases with the amount of Co. The occurence of two critical concentrations for the onset of ferromagnetism ($x = 0.25$ and $x = 0.65$) we suggest to be a consequence of these two competing phenomena. Finally, we conclude that despite the presence of surface segregations the dominating feature responsible for the complex magnetic behavior of this system is given by the presence of local moments by which the long-range magnetic order is triggered.

The paramagnetic behavior of both the β- and the γ-phase we explain by the imposibility for the formation of Fe AS atoms in these non-cubic compounds.

Zr ($Fe_{1-x}Mn_x$)$_2$ (5), (6)

The Moessbauer spectra obtained from the host intermetallics reveal the typical behavior when Mn is alloyed into a binary Fe compound: the lines rapidly broaden with rising Mn amount preventing a resolution of near neighbor effects on the hyperfine parameters. The average Fe hyperfine field decreases monotonically with growing Mn content. Although the long range magnetic order vanishes at that concentration, where the C15–C14 change of structure occurs ($x = 0.35$), a magnetic hyperfine field at 4.2 K can still be observed as far as $x \sim 0.9$ which, however, arises from short range magnetic order only. The concentration dependence of the average magnetic Fe hyperfine field is displaced in fig. 4.

The amount of hydrogen which can be taken up significantly depends on x: while the absorption capacity of $ZrFe_2$ is neglegibly small, it rises rapidly with growing Mn content. Up to about 3 H atoms/f. u. can be dissolved leading to a volume increase as far as 30%. Despite the large rise in volume the crystal structure was found to remain unchanged after hydrogen absorption, even the critical concentration for the change in structure ($x = 0.35$) had sustained in the hydrides.

Hydrogen uptake is known to significantly increase the magnetization in this system which was also obtained for the average Fe hyperfine field (fig. 4). The overall shape of the spectra was found to be only less influenced by hydrogenation. This is in agreement with the observations in case of Zr (Fe, V)$_2$H$_y$ made by Fujii et al (30). The hyperfine field distribution curves indicate an almost symmetrical arrangement of the hyperfine patterns with a peak width up to about 7 T which increases only insignificantly after hydrogen absorption. Concerning the enhancement of the magnetic order it should again be pointed out that for Mn concentrations exceeding $x = 0.4$ this order is only of the short range type. Compared to the host system this spin glass range in the hydrides has extended up to $x = 1$.

The quadrupole splitting is generally enhanced upon hydrogen absorption. This points to an increased disturbance of the local symmetry of the Moessbauer atoms. A change in the Fe 3d population which would be an alternative explanation for the rise in ΔE_Q is ruled out from reasons discussed below. The hydrogen induced positive rise in isomer shift δS is correlated with the amount of dissolved hydrogen and with the increase in volume and thus grows with the Mn concentration. δS values up to +0.53 mm/s have been obtained which corresponds to a pure electronic effect – $(\partial S/\partial n)_v$ – of about +0.1 mm/s (see also sect 2). Using the data of Walker et al. (31) this yields a reduction of only a few tenths of an s-like electron from a Fe atom. From reasons discussed in sec-

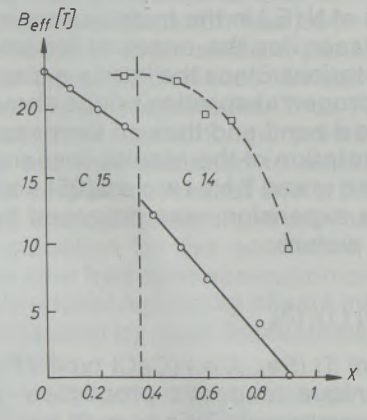

Fig. 4

Average hyperfine field taken at 4.2 K for uncharged Zr ($Fe_{1-x}Mn_x$)$_2$ (o, solid line) and for some hydrides (□, broken curve)

tion 2 the Fe 3d states are supposed to be only less affected by hydrogen.

The rise in the magnetic moment and B_{eff} can be understood in terms of an altered 3d band splitting: the reduced band splitting in the intermetallic compared to Fe metal which has lead to a drop in the magnetic moment ($ZrFe_2$: $\Delta\mu = 0.6\ \mu_B$) is re-enhanced by the screening of Zr by the H atoms.

The advantage of such a kind of interpretation lies in its independence from an appreciable 3d charge transfer from (to) Fe which is in contradiction to the isomer shift results. A further confirmation can be seen in several Moessbauer studies performed on rare earth nuclei (32–34) in certain series of intermetallic compounds. There it was commonly observed that the different ternary hydrides exhibited isomer shift values similar to the corresponding binary rare earth hydride. The various 3d partner elements were found to lead to almost identical changes in S which distinctly points to a d-like charge transfer from R to H rather than from TM to H (R . . . rare earth, TM . . . transition metal).

$R_2Fe_{14}B$ type compounds (7), (42)

Very recently the development of an outstanding hard magnetic material based on Co-free R-Fe-B alloys was successfully demonstrated by rapidly quenched ribbons (35), by sintered magnets (36) and lastly by a ternary diffusion path (37). Energy products up to 45 MGOe have already been reported. The principle source of the unique hard magnetic properties in Nd-Fe-B are the intrinsic properties of the tetragonal compound $Nd_2Fe_{14}B$ (space group $P4_2/mnm$, No. 136) which exhibits two Nd- and six Fe sublattices (38): the large saturation magnetization and the high uniaxial crystal anisotropy ($\mu_0 H_A = 7.5$ T, $\mu_0 M_S = 1.6$ T) at room temperature. Moreover, the metallurgical possibility for the formation of small crystallites of the Nd_2Fe_{14} B-phase gives rise to a high coercivity $_iH_C$. The easy axis of magnetization was determined to lie along the c-axis at room temperature, whereas below about 120 K a complex magnetic structure occurs. If another rare earth with the exception of Eu and Yb replaces Nd, the crystal structure remains unchanged.

According to the large number of inequivalent Fe-lattice sites rather complicated Moessbauer spectra are obtained. In some cases, however, they could reasonably well be analyzed by considering the relative site occupancy of the Fe atoms in the unit cell (see e. g. (39)).

Several compounds have already been examined with regard to their hydrogen absorption properties. For R = Nd up to 4 H atoms / f. u. were found to be dissolved leading to a rise not only in the Fe moment but also in the Curie temperature (40, 41). Upon charging with hydrogen the Moessbauer spectra reveal not only an increase in B_{eff} but also the occurrence of a pattern characteristic for α-Fe (fig. 5). In cases, where free metallic Fe was already present in the host compound this specific hyperfine pattern seems to exhibit an enlarged intensity after hydrogen absorption.

From the temperature dependence of the anisotropyc field H_A, measured by the so-called singular point detection technique for $Y_{15}Fe_{77}B_8$, $Nd_{15}Fe_{77}B_8$ and $Nd_{15}Fe_{77}B_8H_{3.8}$ (42) we deduce that for $T > 200$ K the contribution of the Nd sublattice to H_A is strongly reduced by hydrogen, leading to a drop of the global anisotropy of $Nd_{15}Fe_{77}B_8H_{29}$ even below that of $Y_{15}Fe_{77}B_8$. At low temperatures, however, the Nd contribution is estimated to still dominate the Fe sublattice contribution to H_A. A further indication for the persistence of the Nd anisotropy at low temperatures can be seen by the occurance of the spin reorientation even in the hydride. The shift of the reorientation temperature T_{SR} to lower values is suggested to originate from the weakened Nd anisotropy upon hydrogen absorption.

Hydrogen absorption and desorption may instead of milling be an alternative way to desintegrate bulk Nd-Fe-B into a fine powder which is required for the sintering process as well as for the production of polymer bonded magnets. Since Schlapbach (43) has proven by means of XPS that $Nd_2Fe_{14}B$ shows a selective oxydation of Nd, it is suggested by analogy to $LaNi_5$ that in this case the surface decomposes into Nd_2O_3 and precipitates of Fe. These precipitations may even be

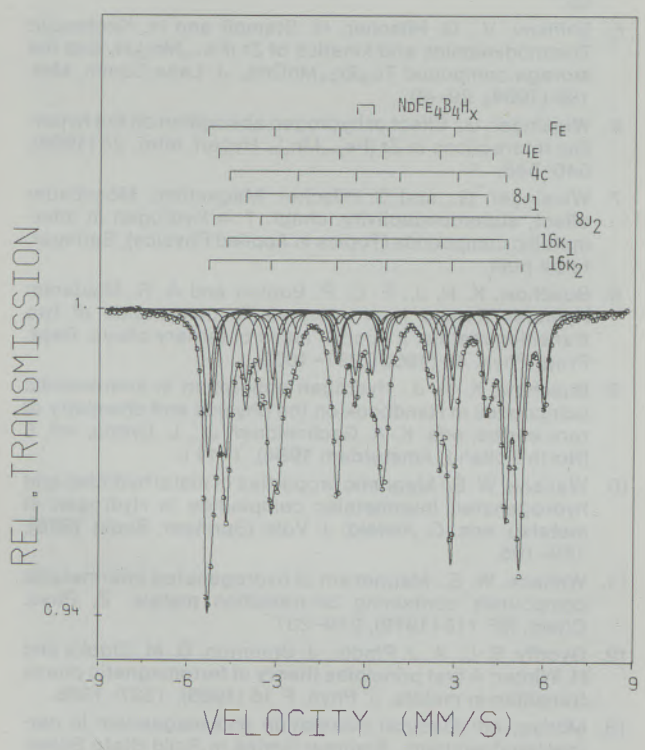

Fig. 5
Mössbauer spectrum of $Nd_2Fe_{14}B$ hydride recorded at room temperature; ooo . . . experimental points, solid line . . . computer fit

large enough to be detected by ^{57}Fe Moessbauer spectroscopy. In agreement with Harris et al. (44) up to now, we only obtained coercivities comparable in magnetitude with those from magnets produced by the standard milling and sintering technique. A further optimization of the parameters during the hydriding process is required in order to exceed the conventional techniques by the pulverization of the material by hydrogen absorption.

4. Conclusions

Some samples have been presented which should demonstrate the capability of the combination of magnetic measurements with Moessbauer spectroscopy in order to elucidate the complex problem of hydrogen induced change of the electronic properties in intermetallic compounds. Studying the material from both macroscopic and a microscopic point of view leads to a deeper insight into a physical problem. Although the absorption of hydrogen appearently seems to complicate the question after certain properties in fortunate cases hydriding can even help in understanding the nature of the parent compound.

Acknowledgement

This work has been supported by the Austrian Science Foundation (Fonds zur Förderung wissenschaftlicher Forschung) under grant No. 4431.

References

1. Hilscher, G., G. Wiesinger and E. Lebsanft: Magnetic and ^{57}Fe Mössbauer studies of hydrided Ti ($Fe_{1-x}Co_x$). J. Magn. Magn. Mat. 15–18 (**1980**), 1273–1274.
2. Hempelmann, R., and G. Hilscher: Ferromagnetism in Ti-Mn ternary hydrides. J. Less-Comm. Met. 74 (**1980**), 103–109.
3. Hilscher, G., G. Wiesinger and R. Hempelmann: Competition between local and itinerant magnetism in Ti ($Fe_{1-x}Co_x$) and Ti ($Fe_{1-x}Co_x$) hydrides. J. Phys. F 11 (**1981**), 2161–2177.
4. Hempelmann, R., E. Wicke, G. Hilscher and G. Wiesinger: Magnetism and hyperfine interactions in Ti-Mn intermetallic hydrides. Ber. Bunsenges. Phys. Chem. 87 (**1983**), 48–55.
5. Shitikov, V., G. Hilscher, H. Stampfl and H. Kirchmayr: Thermodynamics and kinetics of Zr ($Fe_{1-x}Mn_x)_2H_x$ and the storage compound $Ti_{0.8}Zr_{0.2}MnCrH_3$. J. Less-Comm. Met. 102 (**1984**), 29–40.
6. Wiesinger, G.: Effect of hydrogen absorption on the hyperfine interactions in Zr ($Fe_{1-x}Mn_x)_2$. Hyperf. Inter. 28 (**1986**), 545–548.
7. Wiesinger, G., and G. Hilscher: Magnetism, Mössbauer effect, superconductivity. chapt. 7 in Hydrogen in intermetallic compounds (Topics in Applied Physics), Springer, to be publ.
8. Buschow, K. H. J., P. C. P. Bouten and A. R. Miedema: Hydrides formed from intermetallic compounds of two transition metals: a special class of ternary alloys. Rept. Prog. Phys. 45 (**1982**), 937–1039.
9. Buschow, K. H. J.: Hydrogen absorption in intermetallic compounds in Handbook on the physics and chemistry of rare earths, eds. K. A. Gschneidner, Jr., L. Eyring, vol. 6 (North-Holland, Amsterdam **1984**), 1–111.
10. Wallace, W. E.: Magnetic properties of metal hydrides and hydrogenated intermetallic compounds in Hydrogen in metals I, eds. G. Alefeld, J. Völkl (Springer, Berlin **1978**), 169–195.
11. Wallace, W. E.: Magnetism of hydrogenated intermetallic compounds containing 3d-transition metals. Z. Phys. Chem. NF 115 (**1979**), 219–237.
12. Gyorffy, B. L., A. J. Pindor, J. Staunton, G. M. Stocks and H. Winter: A first principles theory of ferromagnetic phase transition in metals. J. Phys. F 15 (**1985**), 1337–1386.
13. Moriya, ed: Electron correlation and magnetism in narrow-band systems. Springer Series in Solid State Sciences, Vol. 29 (Springer, Berlin **1981**).
14. Griessen, R., and R. Feenstra: Volume changes during hydrogen absorption in metals. J. Phys. F 15 (**1985**), 1013–1019.
15. Bennet, P., and J. C. Fuggle: The electronic structure of PdH_x studied with photoemission and electron loss spectroscopy in Electronic structure and properties of hydrogen in metals, eds. P. Jena, C. B. Satterthwaite (Pelnum, New York **1983**), 223–228.
16. Schlapbach, L., and J. P. Burger: XPS/UPS study of the electronic structure of $PdH_{0.6}$ in Electronic structure and properties of hydrogen in metals, eds. P. Jena and C. B. Satterthwaite (Plenum, New York **1983**) 229–234.
17. Buschow, K. H. J.: Intermetallic compounds, amorphous alloys and ternary hydrides based on rare earth elements. J. Magn. Magn. Mat. 29 (**1982**), 91–99.
18. Wagner, F. E., and G. Wortmann: Mössbauer studies of metal-hydrogen systems in Hydrogen in Metals I, eds. G. Alefeld and J. Völkl (Springer, Berlin **1978**), 131–167.
19. Gupta, M.: Mössbauer isomer shifts of titanium iron hydrides. Sol. State Comm. 42 (**1982**), 501–504.
20. Switendick, A. C.: The change in electronic properties on hydrogen alloying and hydride formation in Hydrogen in Metals I, eds. G. Alefeld and J. Völkl (Springer, Berlin **1978**), 101–129.
21. Schlapbach, L.: Surface properties of $ZrMn_2$ and electronic structure of $ZrMn_2$ hydride. Phys. Lett. 91 (**1982**), 303–306.
22. Miedema, A. R., and F. van der Woude: A cellular atomic model for the Mössbauer isomer shift of ^{197}Au in alloys. Physica 100B (**1980**), 145–156.
23. Oesterreicher, H., and H. Bittner: Studies of hydride formation in $Ti_{1-x}Zr_xMn_2$. Mat. Res. Bull. 13 (**1978**), 83–88.
24. Fruchart, D., J. L. Soubeyroux and R. Hempelmann: Neutron diffraction in $Ti_{1.2}Mn_{1.8}$ denteride: structural and magnetic aspects. J. Less-Comm. Met. 99 (**1984**), 307–319.
25. Buschow, K. H. J., and R. C. Sherwood: Magnetic properties and hydrogen absorption in rare-earth intermetallics of the type RMn_2 and R_6Mn_{23}. J. Appl. Phys. 48 (**1977**), 4643–4648.
26. Swartzendruber, L. J., L. H. Bennett and R. E. Watson: Mössbauer studies of hydrided TiFe. J. Phys. F 6 (**1976**), L331–L334.
27. Hilscher, G., N. Buis and J. J. M. Franse: The transition from ferromagnetism to paramagnetism in Ti ($Fe_{1-x}Co_x$), Y_6 ($Fe_{1-x}Mn_x)_{23}$ and the effect of pressure. Physica 91B (**1977**), 170–174.
28. Beille, J., D. Bloch and F. Towfiq: High pressure magnetic properties of $Fe_xCo_{1-x}Ti$ alloys. Sol. State Comm. 25 (**1978**), 57–59.
29. Beille, J., D. Bloch, F. Towfiq and J. Voiron: The magnetic properties of $Fe_xCo_{1-x}Si$ and $Fe_xCo_{1-x}Ti$ alloys. J. Magn. Magn. Mat. 10 (**1979**), 265–273.

30. Fujii, H., T. Okamoto, W. E. Wallace, F. Pourarian and T. Morisaki: Influence of hydrogen absorption on magnetic properties of Zr $(Fe_{1-x}V_x)_2$ ternaries. J. Magn. Magn. Mat. 46 (**1985**), 245–253.
31. Walker, L. R., G. K. Wertheim and V. Jaccarino: Interpretation of the Fe^{57} isomer shift. Phys. Rev. Lett. 6 (**1961**), 98–101.
32. Buschow, K. H. J., R. L. Cohen and K. W. West: What is the mechanism of hydrogen absorption in rare-earth intermetallics? J. Appl. Phys. 48 (**1977**), 5289–5295.
33. Oliver, F. W., K. W. West, R. L. Cohen and K. H. J. Buschow: Mössbauer effect of ^{151}Eu in $EuNi_5$, $EuMg_2$ and their hydrides. J. Phys. F 8 (**1978**), 701–707.
34. Cohen, R. L., K. W. West, F. Oliver and K. H. J. Buschow: Mössbauer studies of hydrogen absorption in Dy, $DyMn_2$, $DyFe_2$, and $DyNi_2$. Phys. Rev. B 21 (**1980**), 941–944.
35. Croat, J. J., J. F. Herbst, R. W. Lee and F. E. Pinkerton: Pr-Fe and Nd-Fe based materials: A new class of high-performance permanent magnets. J. Appl. Phys. 55 (**1984**), 2078–2082.
36. Sagawa, M., S. Fujimura, N. Togawa, H. Yamamoto and Y. Matsuura: New material for permanent magnets on a base of Nd and Fe. J. Appl. Phys. 55 (**1984**), 2083–2087.
37. Stadelmaier, H. H., N. A. El Masry and S. R. Stallard: Alternative method of preparing high-coecivity neodymium-iron-boron-magnets. J. Appl. Phys. 57 (**1985**), 4149–4150.
38. Shoemaker, C. B., and D. P. Shoemaker: The structure of a new magnetic phase related to the sigma phase: iron neodymium boride $Nd_2Fe_{14}B$. Acta Cryst. C 40 (**1984**), 1665–1668.
39. Größinger, R., G. Hilscher, H. Kirchmayr, H. Sassik, R. Strnat and G. Wiesinger: Investigation of the magnetic properties of Nd-Fe-B based hard magnetic materials. Physica 130B (**1985**), 307–311.
40. L'Heritier, P., P. Chaudonet, R. Madar, A. Rouault, J.-P. Senateur and R. Fruchart: Une nouvelle série d'hydrures métalliques ferromagnétiques de type $Nd_2Fe_{14}BH_x$ ($0 < x < 5$). C. R. Acad. Sc. Paris 299 (**1984**), 849–852.
41. Oesterreicher, K., and H. Oesterreicher: Structure and magnetic properties of $Nd_2Fe_{14}BH_{2.7}$. Phys. Stat. Sol. (a) 85 (**1984**), K61–K64.
42. Wiesinger, G., G. Hilscher, R. Größinger, S. Heisz and H. Kirchmayr: Effect of hydrogen absorption on structural and magnetic properties of $Nd_2Fe_{14}B$. Int. J. Hydr. Energy, to be publ.
43. Schlapbach, L.: Hydrides of rare earth metals and intermetallics and topics in solid state science. J. Less-Comm. Met. 111 (**1985**), 291–294.
44. Harris, I. R., C. Noble and T. Bailey: The hydrogen decrepitation of an $Nd_{15}Fe_{77}B_8$ magnetic alloy. J. Less-Comm. Met. 106 (**1985**), L1–L4.

Development of Technical Nb_3Sn-Superconductors in Austria

Richard Eibler, Wien, Wolfgang Glätzle, Reutte, Gerfried Hilscher, Wien, und Hans Kirchmayr, Wien*)

Dedicated to the 80th birthday of Prof. Dr. Franz Lihl

We report on the development of technical Nb_3Sn-superconductors in Austria with four different technologies (multifilamentary-bronze-, externally tinned powdermetallurgical, internally tinned powdermetallurgical and internally tinned multifilamentary conductors respectively). The results show, that the critical current densities achieved international standard. The measurements of the a.c. losses indicate, that the powdermetallurgical superconductors are also suitable for technical use.

Die Entwicklung technischer Nb_3Sn-Supraleiter in Österreich

Es wird über die Entwicklung von technischen Nb_3Sn-Supraleitern in Österreich nach vier verschiedenen Verfahren (Multifilament-Bronze-, extern verzinnte pulvermetallurgische, intern verzinnte pulvermetallurgische und intern verzinnte Multifilamentleiter) berichtet. Die Ergebnisse zeigen, daß die kritischen Stromdichten internationalen Standard erreicht haben. Die Messungen der Wechselfeldverluste zeigten, daß auch die pulvermetallurgischen Supraleiter für einen technischen Einsatz geeignet sind.

Développement de supraconducteurs techniques de Nb_3Sn en Autriche

On décrit le développement de supraconducteurs techniques de Nb_3Sn en Autriche, selon quatre procédés différents (multifilament-bronze-, métallurgie des poudres à étamage extérieur, métallurgie des poudres à étamage intérieur et conducteur à multifilament étamé intérieurement). Les résultats montrent que les densités de courant critiques ont atteint la norme internationale. Les mesures de pertes de champ alternatif ont indiqué que les supraconducteurs obtenus par la métallurgie des poudres conviennent également pour les applications techniques.

1. Introduction

The rising importance of superconductivity led in the last years to an increasing interest on new production technologies for superconducting materials. The emphasis of our work was laid on the improvement of the physical properties of technical superconductors as the critical current density J_c, the critical field H_{c2} and the superconducting transition temperature T_C and on the economical manufacturing procedure for the magnet technology.

In spite of the many superconducting materials knwon up to now, only the ductile Nb-Ti alloys with nearly equal weight percentages of both elements and the two intermetallic A-15 compounds Nb_3Sn and V_3Ga have gained almost universal acceptance in magnet construction.

The technical superconductors used in magnet technology are composite conductors, which consist of fine, usually twisted filaments of superconducting material in normal metals (as e.g. copper) in order to increase their electromagnetic stability and to reduce the energy loss in time-varying magnetic field application.

Originally the superconducting materials used for magnet construction were restricted to the ductile superconducting alloys with excellent metallurgical properties, mainly Nb-Ti. The application of these ductile solid solution superconductors is, however, limited to magnetic fields up to about 8–9 T at 4.2 K and 10 T at 2 K. Owing to a need for improvements in the design of magnets exceeding the field range of 10 T for particle accelerators in high energy physics (e.g. CERN, LHC-project), fusion reactors, NMR tomography and in smaller magnet units for the recently discovered quantum hall effect (Klitzing (1)), complex metallurgical methods for producing such filamentary superconductors with the brittle intermetallic A-15 compounds were developed in the past years.

*) Dipl.-Ing. Dr. Richard Eibler, Univ.-Doz. Dr. Gerfried Hilscher, o. Univ.-Prof. Dr. Hans Kirchmayr, Institute of Experimental Physics, Technical University of Vienna, A-1040 Vienna, Karlsplatz 13
Dr. Wolfgang Glätzle, Metallwerk Plansee Ges.m.b.H., A-6600 Reutte

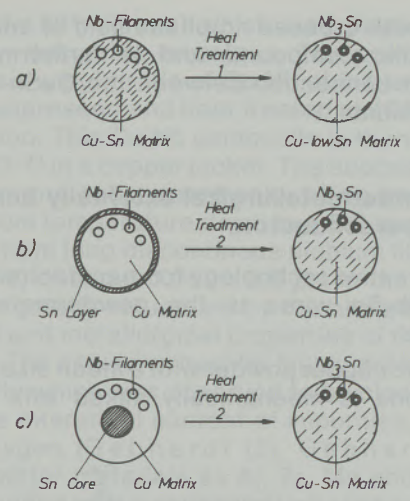

Fig. 1
Schematical Nb_3Sn-superconductor production processes investigated in this work
a) Bronzeprocess
b) External tin process
c) Internal tin process
Heat treatment 1: Only reaction Nb-Nb_3Sn
Heat treatment 2: Stepwise tin diffusion and reaction

The technical application of superconductors requires because of electromagnetic stability etc. not only the subdivision of the bulk superconducting materials into filaments of the order of 1 to 10 microns but also the fabrication of large lengths of the superconducting composite wire. The requirements can easily be fulfilled with the ductile Nb-Ti alloys since they can be coprocessed easily with matrix materials such as copper and copper-nickel.

In 1969-70 a method to fabricate such composite superconductors with the brittle intermetallic compounds Nb_3Sn and V_3Ga was successfully developed by Kaufmann (2) and Tachikawa (3) respectively, which is now called the bronze process. Since the discovery of the bronze process many small scale magnets have successfully been manufactured, while various large scale applications of these high field superconductors are in the state of design and test.

The continuously rising demands of high critical current densities in the field range of 10 to 16 T for laboratory magnets but also for large scale applications stimulated the activities in the past few years to develop new technologies for A-15 compounds, e.g. the powder technology with internal or external tin source, the „in-situ" technology and the multifilament technology with internal or external tin source.

The cooperation of the industry and university institutes in Austria was initiated by the so-called „Österreichischer Arbeitskreis Supraleitung" in 1975 in order to develop materials for use in superconducting electrical machinery. In this paper we report on the development of technical Nb_3Sn superconductors of various technologies, which was performed in close cooperation between Metallwerk Plansee and the Institute of Experimental Physics of the Technical University of Vienna.

2. Preparation of superconductors

The superconductors are manufactured by Metallwerk Plansee under use of industrial equipment. The heat treatment of the superconductors for the diffusion of the tin (internally and externally tinned powdermetallurgical conductors, internally tinned multifilamentary conductors) and the reaction of the niobium filaments into Nb_3Sn is performed at the Technical University of Vienna. The bronze-process and the internal and external tin process respectively are shown schematically in fig. 1.

2.1 Multifilament-bronze-conductor

The already mentioned bronze process (Kaufmann (2)) relies on the fact, that the brittle intermetallic A-15 compound Nb_3Sn can be formed at the interface between Nb and Cu-Sn (bronze) during a proper heat treatment of such composites.

In this technology, niobium rods are inserted in a hole matrix drilled in a bronze bolt. This niobium-bronze-bolt is hot extruded and then rolled down to a hexagonal cross section. These hexagonal subelements are bundled and inserted in a copper tube with a tantalum barrier inside (see fig. 2). This

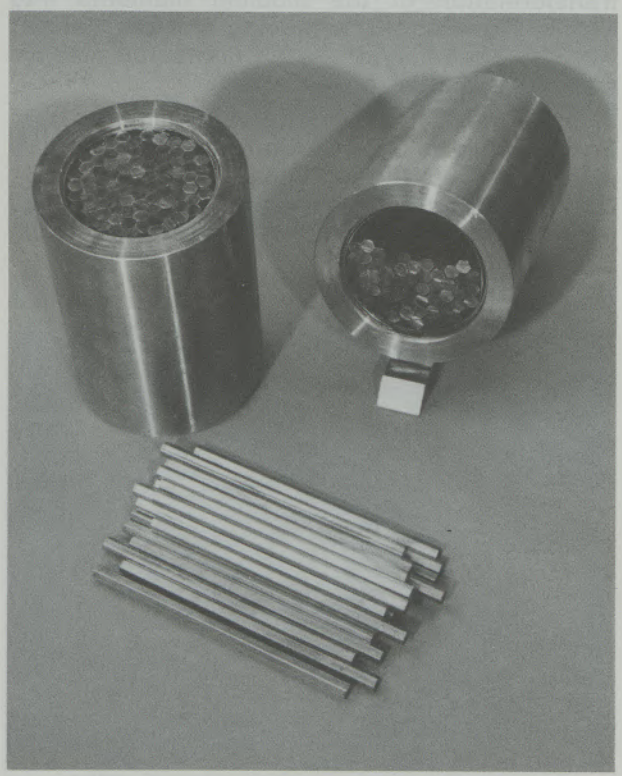

Fig. 2
The hexagonal bronze-niobium-subelements are inserted in an OFHC-copper tube with tantalum barrier

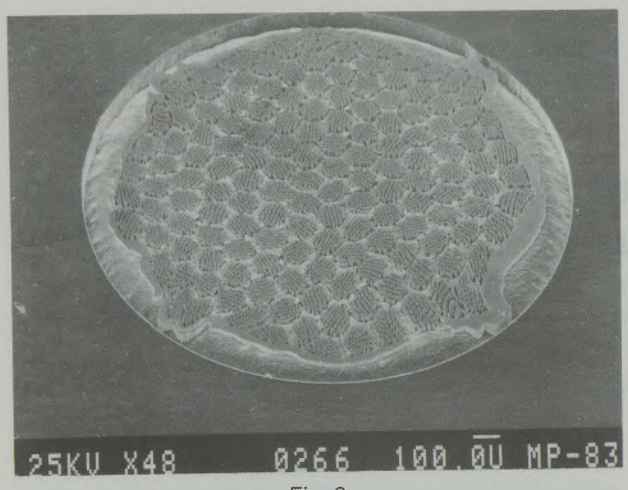

Fig. 3
Etched cross section of a finally deformed bronze-niobium-filament-composite conductor with 6580 niobium filaments, outer stabilizing OFHC-copper and tantalum barrier

composite is again hot extruded. The further reduction to the final diameter is done by rolling and drawing, where, because of the deformation hardening of the bronze matrix after every 50% area reduction, a softening heat treatment has to be performed.

The ready deformed bronze-niobiumfilament-composite conductor (see fig. 3) is properly heat-treated at approximately 550 to 750 °C for the transformation of the niobium filaments into Nb_3Sn. Fig. 4 shows a reacted niobium filament with the Nb_3Sn-layer and an unreacted niobium core in the center of the filament.

In the ternary system Cu-Nb-Sn the diffusion path from the solid solution Cu-Sn (α-phase) to the pure niobium passes the A-15 phase field (see fig. 5). Only the intermetallic compound Nb_3Sn is formed during a proper heat treatment, because this diffusion path crosses no phase field of another intermetallic compound and is furthermore the shortest connection between the CuSn-α-phase and niobium.

2.2 Powdermetallurgical externally tinned superconductors

An alternative technology for manufacturing technical Nb_3Sn wires is the powdermetallurgical method.

Dendritic copper powder with a mean size of about 4 microns is mechanically mixed with niobium

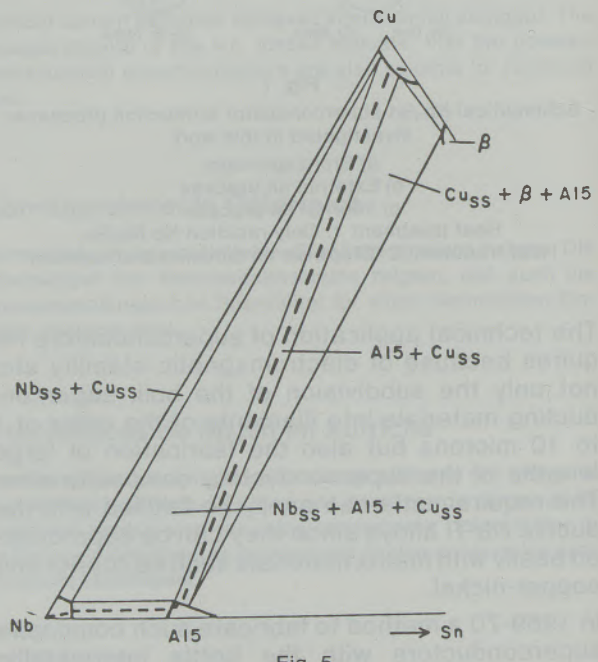

Fig. 5
Ternary phase diagram Cu-Nb-Sn at about 700 °C after Dew-Hughes (4) with the dashed-dotted-line diffusion path CuSn-α-bronze-niobium

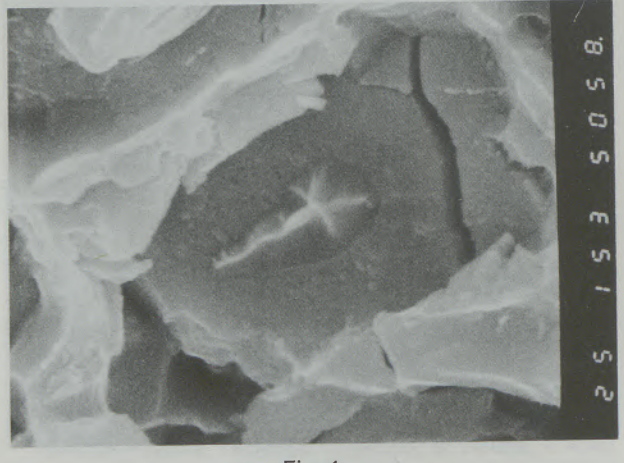

Fig. 4
Reacted niobium filament with the Nb_3Sn-layer and a central unreacted niobium core

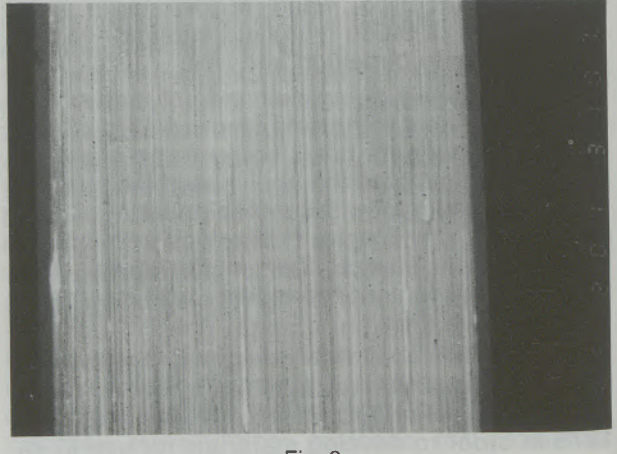

Fig. 6
Longitudinal microstructure of the finally deformed Cu-Nb powder composite conductor with niobium particles deformed into filaments (bright)

powder (<36 microns) which was produced by hydride – dehydride technique. The powder mixture with a weight ratio of Cu:Nb of 3:1 is isostatically compressed and heat treated at 1050 °C for purification. This Cu-Nb composite is then extruded at 700 °C in a copper jacket. The success of the extrusion and subsequent cold rolling and drawing at room temperature down to a 0.3 mm wire in order to form long discontinous niobium filaments (see fig. 6) of about 0.05 to 0.5 μm in the copper matrix is greatly influenced by the chemical, mechanical and metallurgical properties of the initial powder. The powders must be highly deformable, a property which was observed to be closly related to the interstitial content of impurities, particulary oxygen (Gebhardt (5), Gebhardt (6)). Proper getter materials as Al, Zr, Mg and Ti etc. may be added with a concentration of about 0.2–1 wt% in order to improve the deformation of the niobium particles into filaments. Before the galvanical tin plating of the conductor, a homogenization heat treatment according to Cogan (7) was performed in order to improve the final diffusion of tin into the wire during the following stepwise heating treatment to form Nb_3Sn.

This diffusion proceeds via a solid state reaction (Benz (8)) where in the first step below 227 °C (see fig. 7) the Cu_6Sn_5-η-phase and subsequently in the second step below 415 °C the Cu_3Sn-ε-phase is formed. Finally, in the last step at elevated temperatures of 500 to 700 °C, tin is completely diffused into the wire and the niobium filaments are reacted to Nb_3Sn.

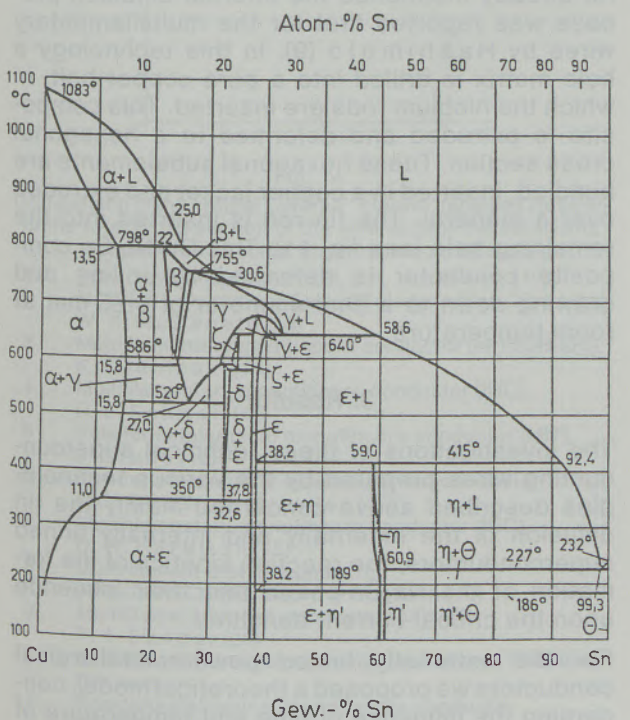

Fig. 7
Cu-Sn phase diagram

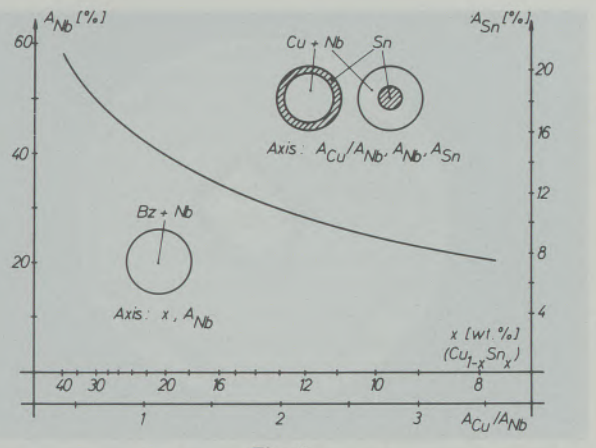

Fig. 8
Maximum niobium cross section portion which can be transformed into Nb_3Sn in a bronze-niobium composite and a copper-niobium-tin composite under the assumption, that no tin remains in the copper matrix

The advantage of this technology is the fairly easy deformation of the niobium powder particles into filaments without intermediate heat treatments and in the free choice of the composition ratio Cu:Nb:Sn compared with the bronze process. In the latter process only a limited Nb_3Sn-portion of the composite conductor can be achieved, since a tin bronze with more that 13 wt% tin practically cannot be deformed. The niobium cross section which can be transformed into Nb_3Sn is therefore limited to about 29% (see fig. 8). This corresponds to approximately 26 wt% niobium portion. However, the actual Nb_3Sn content is usually less than 26 wt% since due to reaction kinetics 2–3% tin remains in the copper matrix.

2.3 Internally tinned powdermetallurgical superconductors

A modification of the external diffusion process, the tin core process, was reported for multifilament technology and the powdermetallurgical route by Hashimoto (9) and Otubo (10) respectively.

The external tin process eliminated one of the major drawbacks of the bronze process namely that the tin content in the copper matrix is limited to 13 wt%. However in the external diffusion process problems have been encountered in the tin plating process and the subsequent heat treatment to diffuse the tin into the copper matrix. The primary difficulties are the mechanical stability of the tin layer, the delamination of the outer layer of the wire, particularly if the tin layer is greater than about 5 microns, and the occurance of Kirkendall voids. These drawbacks are eliminated in the internal diffusion process where the tin is contained at the center of the wire. The production of the Cu-Nb composite is similar to the external powder

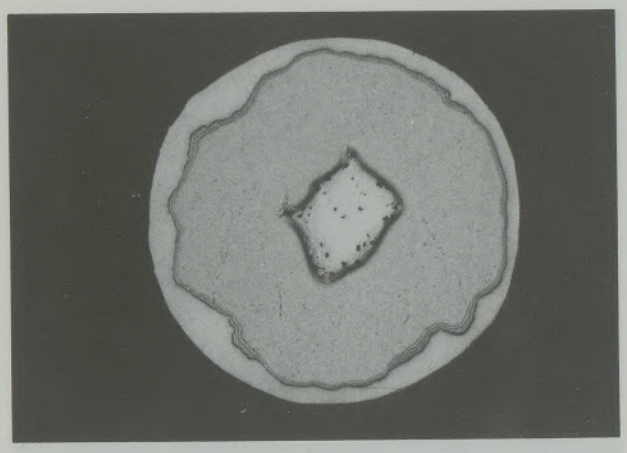

Fig. 9

Finally deformed internally tinned powdermetallurgical superconductor (diameter 0,5 mm) with outerside stabilizing copper, tantalum barrier and a central tin core

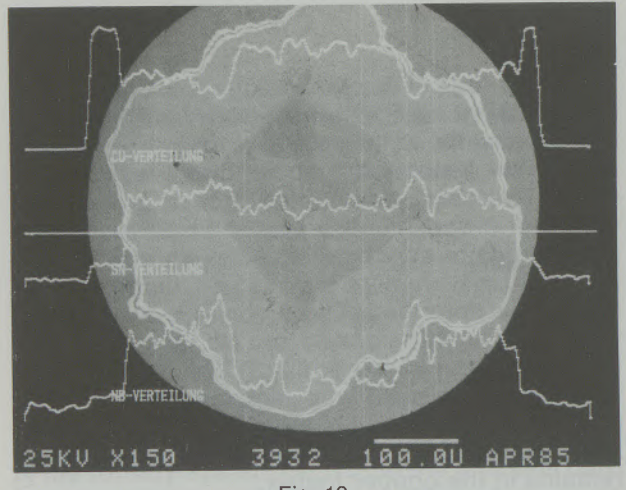

Fig. 10

Fully reacted internally tinned powdermetallurgical superconductor with the distributions of copper, niobium and tin

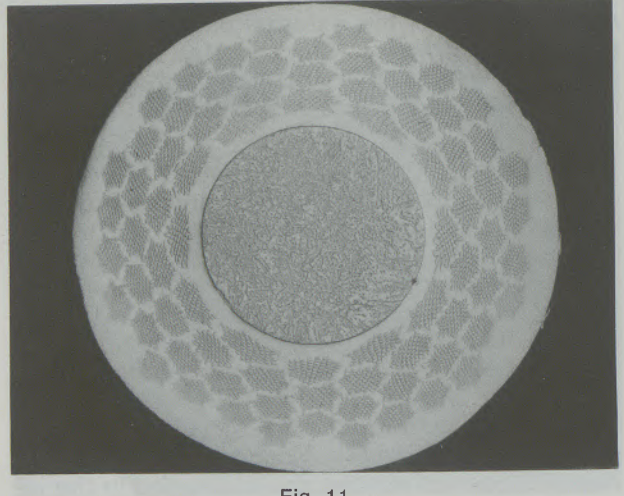

Fig. 11

Internally tinned multifilamentary superconductor after the extrusion process with a outer diameter of 14 mm, 2852 niobium filaments and central tin core

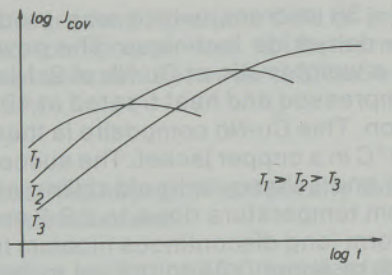

Fig. 12

Theoretical influence of temperature T and time t of the heat treatment upon the critical „overall" current density J_{cov}

metallurgical process, however, the main difference is, that the stabilizing copper and the tantalum barrier are placed outside the wire. Furthermore, the Cu-Nb composite is extruded over a mandrel. In the remaining hole of the extruded composite a tin rod is inserted. The further deformation is done by rolling and drawing at room temperature. The cross section of a final wire is shown in fig. 9.

The final Cu-Nb-Sn composite wire is heat treated stepwise in the same way as described for the externally tinned powdermetallurgical wire. During this heat treatment the tin core is completely filled with copper due to the counter running diffusion of copper and tin (see fig. 10).

2.4 Internally tinned multifilamentary superconductors

As already mentioned the internal diffusion process was reported first for the multifilamentary wires by Hashimoto (9). In this technology a hole matrix is drilled into a pure copper bolt, in which the niobium rods are inserted. This composite is extruded and deformed to a hexagonal cross section. These hexagonal subelements are bundled, inserted in a copper jacket and extruded over a mandrel. The tin rod is inserted into the remaining hole (see fig. 11). This Cu-Nb-Sn composite conductor is deformed by rolling and drawing down to a final diameter of 0.25 mm at room temperature.

3. Results

The investigations of these technical superconducting wires prepared by the various technologies described above concerned mainly the tin diffusion of the externally and internally tinned superconductors, the reaction kinetics of the formation of the Nb_3Sn-phase and their influence upon the critical current densities.

For the externally tinned powdermetallurgical conductors we proposed a theoretical model, concerning the influence of time and temperature of the heat treatment upon the critical „overall" current density (see fig. 12, Eibler (11)). The expe-

rimental results (fig. 13) are in good agreement with the model suggested, which states that for a decreasing filament size (which means a higher reduction ratio $q = A_o/A$) a higher degree of reaction of niobium into Nb_3Sn with the same reaction parameters is obtained, which consequently increases the „overall" current density. In order to achieve the same degree of reaction on smaller filaments the reaction temperature can be lowered yielding a finer Nb_3Sn grain size and consequently higher current densities (compare for this in fig. 13: $q = 12.844$, $t = 240$ h, $T = 560$, 600 °C respectively with $q = 26.677$, $t = 240$ h, $T = 560$, 600 °C respectively).

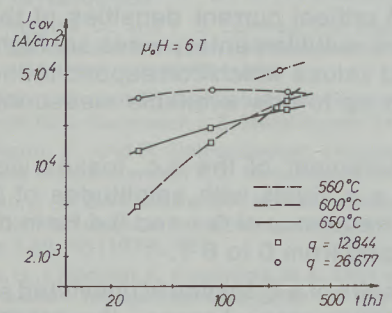

Fig. 13

Experimentally ascertained influence of temperature T and time t of the reaction heat treatment and the reduction ratio $q = A_o/A$ on externally tinned powdermetallurgical superconductors upon the critical "overall" current density J_{cov}

The results obtained on externally tinned powdermetallurgical superconductors concerning the tin diffusion and reaction kinetics can be applied to other manufacturing technologies (multifilament-bronze-, internally tinned powdermetallurgical and internally tinned multifilamentary conductors). A comparison of the critical "overall" current densities obtained (reference cross section is the total cross section without stabilizing copper area) with that of other authors (and firmes) is shown in fig. 14. The results demonstrate, that the international standard for current densities in the field range of 5 to 10 T could be achieved with properly heat treated superconducting wires produced by Metallwerk Plansee.

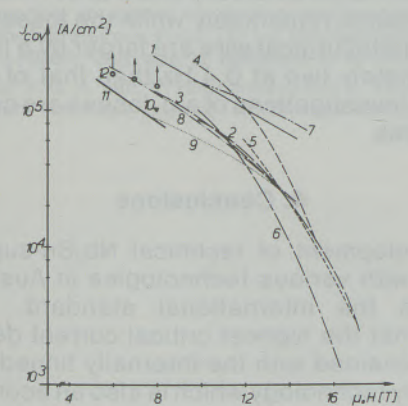

Fig. 14

Comparison of the critical „overall" current densities referred to the total cross section of the wire except the stabilizing copper area of some Nb_3Sn-superconductors

1 . . . ECN-conductor (HOLEC), A.C.A. van Wees (12)
2 . . . Modified-jelly-roll-conductor (Teledyne Wah Chang), W. K. McDonald (13)
3 . . . Multifilamentary multitincore conductor (MITSUBISHI), K. Yoshizaki (14)
4 . . . Multifilamentary monotincore conductor (IGC), R. E. Schwall (15)
5 . . . Powdermetallurgical monotincore conductor (MIT), J. Otubo (16)
6 . . . Powdermetallurgical external tinned conductor (GÖTTINGEN), K. Mrowiec (17)
7 . . . Multifilamentary monotincore conductor (IGC), D. W. Hazelton (18)
8 . . . Multifilament-bronze-conductor (VAKUUMSCHMELZE), H. Hillmann (19)
9 . . . Multifilament-bronze-conductor (AIRCO), P. A. Sanger (20)
10 . . . Multifilament-bronze-conductor (Metallwerk Plansee), this work
11 . . . Powdermetallurgical monotincore conductor (Metallwerk Plansee), this work
12 . . . Multifilamentary monotincore conductor (Metallwerk Plansee), this work

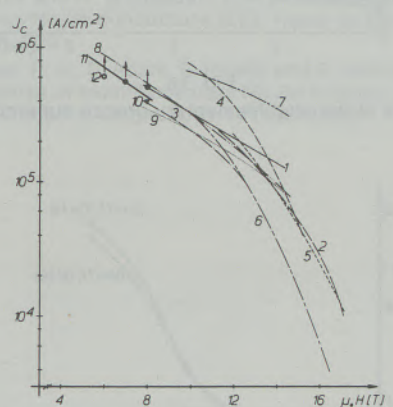

Fig. 15

Comparison of the critical current densities referred to the Nb_3Sn cross section (plus unreacted niobium core of the filaments) of some Nb_3Sn-superconductors

1 . . . ECN-conductor (HOLEC), A.C.A. van Wees (12)
2 . . . Modified-jelly-roll-conductor (Teledyne Wah Chang), W. K. McDonald (13)
3 . . . Multifilamentary multitincore conductor (MITSUBISHI), K. Yoshizaki (14)
4 . . . Multifilamentary monotincore conductor (IGC), R. E. Schwall (15)
5 . . . Powdermetallurgical monotincore conductor (MIT), J. Otubo (16)
6 . . . Powdermetallurgical external tinned conductor (GÖTTINGEN), K. Mrowiec (17)
7 . . . Multifilamentary monotincore conductor (IGC), D. W. Hazelton (18)
8 . . . Multifilament-bronze-conductor (VAKUUMSCHMELZE), H. Hillmann (19)
9 . . . Multifilament-bronze-conductor (AIRCO), P. A. Sanger (20)
10 . . . Multifilament-bronze-conductor (Metallwerk Plansee), this work
11 . . . Powdermetallurgical monotincore conductor (Metallwerk Plansee), this work
12 . . . Multifilamentary monotincore conductor (Metallwerk Plansee), this work

The comparison of the critical current density related to the Nb_3Sn cross section (exactly to say the Nb_3Sn area plus the unreacted niobium core of the filaments) is of interest from the physical point of view. It is shown in fig. 15 that these current densities internationally obtained lie close to each other with only one exception, the internally tinned multifilamentary superconductor from IGC. These up to now highest reported critical current densities for technical Nb_3Sn superconductors were achieved by an optimized deformation process and an optimized 5-step heat treatment respectively.

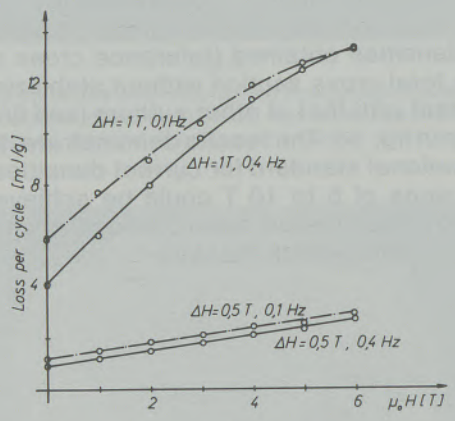

Fig. 16
AC-losses of the multifilamentary bronze superconductor

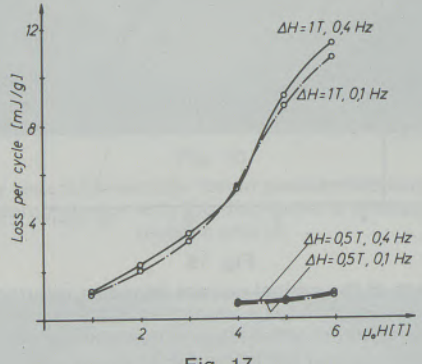

Fig. 17
AC-losses of the internally tinned multifilamentary superconductor

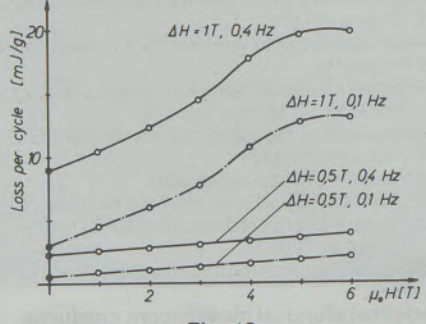

Fig. 18
AC-losses of the internally tinned powdermetallurgical superconductor

Furthermore we note, that our multifilamentary wire produced by the bronze process and both the multifilamentary and the powdermetallurgical wire produced by the internal diffusion process are currently under investigation and not yet fully optimized. The arrows in fig. 14 and 15 indicate that the actual critical current densities of the internally tinned multifilamentary wires are higher than our plotted values which correspond to the upper limit of our up to now available measuring capabilities.

The measurement of the a.c. losses were performed in a.c. fields with amplitudes of 0.5 and 1 T and a frequency of 0.1 and 0.4 Hz in d.c. bias fields ranging from 0 to 6 T.

Typical results of a.c. losses of untwisted samples of the multifilamentary bronze-, the internally tinned powdermetallurgical- and multifilamentary conductors are shown in the figs. 16–18. A comparison of these a.c. losses shows, that the losses of the powdermetallurgical wire are only larger by a factor of about 1.5 than that of the multifilamentary wires. We note, that the a.c. losses of the multifilamentary wires at 0.1 and 0.4 Hz do not change remarkably while the losses of the powder metallurgical wire are larger by a factor of approximately two at 0.4 Hz than that of 0.1 Hz. Detailed investigations of a.c. losses are currently in progress.

4. Conclusions

The development of technical Nb_3Sn-superconductors with various technologies in Austria approaches the international standard. It was shown, that the highest critical current densities can be obtained with the internally tinned multifilamentary technology which is also an economical manufacturing process. This technology appears to be currently the best procedure for the fabrication of technical Nb_3Sn superconductors.

The optimization of the manufacturing parameters and the heat treatment is still in progress, however, the results presented are very promising. Especially the loss measurements of the powdermetallurgical conductors show, that the a.c. losses of these conductors are higher but in the same order of magnitude as those of the conventional multifilamentary conductors and therefore seem suitable for a technical use with proper optimization.

Acknowledgement

This work was supported by the Austrian Ministry for Science and Research during several years at least under the contract number 77614/1-25/85. Additionally, this work was supported by the „Forschungsförderungsfonds für die gewerbliche Wirtschaft" under the contract number 6/370-I/P.

References

1. Klitzing, K. von, G. Dorda and H. Pepper: Realization of a resistance standard based on fundamental constants; Phys. Rev. Lett. 45 (**1980**), 494.
2. Kaufmann, A. R., and J. J. Pickett: Multifilament Nb_3Sn Superconducting wire; Bull. Am. Phys. Soc. 15 (**1970**), 838.
3. Tachikawa, K., and Y. Iwasa: Current capacities of superconducting V_3Ga tapes in high magnetic fields; Appl. Phys. Lett. 16 (**1970**), 230.
4. Dew-Hughes, D., and T. S. Luhman: The thermodynamics of A15 compound formation by diffusion from ternary bronzes; J. Mat. Sci. 13 (**1978**), 1868.
5. Gebhardt, E., und R. Rothenbacher: Untersuchungen im System Niob-Sauerstoff I; Z. Metallkunde 54 (**1963**), 443.
6. Gebhardt, E., und R. Rothenbacher: Untersuchungen im System Niob-Sauerstoff II; Z. Metallkunde 54 (**1963**), 623.
7. Cogan, S., D. S. Holmes and R. M. Rose: On the elimination of Kirkendall voids in superconducting composites; Appl. Phys. Lett. 35 (**1979**), 557.
8. Benz, H., I. Horvath, K. Kwasnitza, R. K. Maix and G. Meyer: Worldwide cryogenics–Switzerland; Cryogenics 19 (**1979**), 435.
9. Hashimoto, Y., K. Yoshizaki and M. Tanaka: Processing and properties of superconducting Nb_3Sn filamentary wirs; Proc. of 5th Int. Cryo. Eng. Conf. Kyoto (**1974**), 332.
10. Otubo, J., S. Pourrahimi, H. Zhang, C. L. H. Thieme and S. Foner: Submicron multifilamentary high performance Nb_3Sn produced by powder metallurgy processing of large powders; Appl. Phys. Lett. 42 (**1983**), 469.
11. Eibler, R., W. Glätzle, G. Hilscher und H. Kirchmayr: Untersuchungen an extern verzinnten pulvermetallurgischen Nb_3Sn-Supraleitern; Proc. 11th Int. Plansee Seminar 1985, Vol. 2 (**1985**), 235, eds. H. Bildstein, H. M. Ortner.
12. Wees, A. C. A. van, P. Hoogendam and H. Veringa: Development of high current Nb_3Sn multifilament superconducting material following the ECN powder method; IEEE Trans. on Magn. MAG-19 (**1983**), 556.
13. McDonald, W. K., C. W. Curtis, R. M. Scalan, D. C. Larbalestier, K. Marken and D. B. Smathers: Manufacture and evaluation of Nb_3Sn conductors fabricated by the MJR method; IEEE Trans. on Magn. MAG-19 (**1983**), 1124.
14. Yoshizaki, K., O. Taguchi, F. Fujimura, M. Imaizumi, M. Wakata, Y. Hashimoto, K. Wakamoto, T. Yamada and T. Satow: Nb_3Sn superconducting cables processed by internal tin diffusion; IEEE Trans. on Magn. MAG-19 (**1983**), 1131.
15. Schwall, R. E., G. M. Ozeryansky, D. W. Hazelton, S. F. Cogan and R. M. Rose: Properties and performance of high current density Sn-core process MF Nb_3Sn; IEEE Trans. on Magn. MAG-19 (**1983**), 1135.
16. Otubo, J., S. Pourrahimi, C. L. H. Thieme, H. Zhang, B. B. Schwartz and S. Foner: Submicron filament multistrand powder metallurgy processed Cu-Nb-Sn wire; IEEE Trans. on Magn. MAG-19 (**1983**), 764.
17. Mrowiec, K., R. Bormann und H. C. Freyhardt: Reduktionszusätze in pulvermetallurgisch hergestellten Cu-Nb_3Sn-Verbunddrähten; Z. Metallkunde 74 (**1983**), 323.
18. Hazelton, D. W., G. M. Ozeryansky, M. S. Walker, B. A. Zeitlin, K. Hemachalam, E. N. C. Dalder and L. Summers: Internal tin process Nb_3Sn superconductors for 18 T; presented at the ICMC-Conf. **1985**.
19. Hillmann, H., H. Kuckuck, E. Springer, H. J. Weiße, M. Wilhelm and K. Wohlleben: Coil performance of multifilamentary Nb_3Sn conductors; IEEE Trans. on Magn. MAG-15 (**1979**), 205.
20. Sanger, P. A., E. Adam, E. Ioriatti and S. Richards: Critical properties of multifilamentary Nb_3Sn between 8 and 14 T; IEEE Trans. on Magn. MAG-17 (**1981**), 666.

Magnetoelastic Properties of Amorphous Alloys

Roland Grössinger, Herbert Sassik, Wien*)

Dedicated to the 80th birthday of Prof. Dr. Franz Lihl

The production procedures of amorphous, metallic ribbons and some measuring methods for studying magnetoelastic effects are described. It will be shown that the soft magnetic behaviour is dominated by the magnetostriction. Hints for the technical application of this new material will be given.

Magnetoelastische Eigenschaften amorpher Legierungen

Die Produktionsmethoden von amorphen metallischen Bändern sowie Meßmethoden zur Untersuchung magnetoelastischer Effekte werden übersichtsmäßig dargestellt. Es wird gezeigt, daß ihr weichmagnetisches Verhalten von der Magnetostriktion dominiert wird. Es werden Hinweise für eine technische Anwendung dieser neuen Werkstoffe gegeben.

Propriétés magnétoélastiques des alliages amorphes

On donne un aperçu des méthodes de production de bandes métalliques amorphes et des méthodes de mesure destinées à l'étude de leurs effets magnétoélastiques. On montre que leur comportement d'aimants doux est dominé par la magnétostriction. Des indications sont données en vue des applications techniques de ces nouveaux matériaux.

1. Introduction

Solid state physics is from an experimental point of view the study of physical properties of solid materials or compounds. The clearest information can be obtained investigating single crystals. In this case all effects can be related with the symmetry of the lattice directly. However for many technical applications polycrystalline materials are used. Additional the "usual" most often obtained phase of a solid material is the polycrystalline one. Consequently all directional differences cancel. This means that for e.g. the electrical resistivity or for the elastic constants a mean value is obtained. Substituting elements of a certain compound is a general technique in order to achieve special physical properties. Due to its statistical character such a substitution causes atomic positional disorder. Mixed crystal series are therefore a highly disordered system in spite of the fact that the lattice symmetry still exists. A typical example where such a crystalline system shows disorder effects, which are similar to an amorphous system, is the mixed crystal series $R(Fe, Al)_2$ (R = Y, Gd, Dy . . .). The magnetic ordering is a broad transition, the electrical resistivity is unusual high and nearly temperature independent (1). Similar effects were found in the $R_6(Fe, Mn)_{23}$ system. The origin which is there responsible for the disordered behaviour is the complex unit cell of this structure (2). These are some examples of crystalline systems where the physical properties are similar to that of an amorphous system. A clear understanding of such series where crystalline and disorder effects are superimposed is very difficult. Another approach to learn something about "amorphous" is, to study pure amorphous systems. They are due to their production procedure undercooled liquids (see chapter 2). Therefore the investigation of amorphous solids can be a link between the solid state physics of disordered crystalline and fully disordered (amorphous) systems. Investigations on metallic, magnetic, amorphous materials have shown, that their physical properties are not only interesting from basic point of view, but that some of them exhibit e.g. excellent soft magnetic properties. All these amorphous materials have a high and nearly temperature independent electrical resistivity. The main physical origin of these characteristic properties is that no grains exist and that the statistical arrangement of the atoms is similar to that of a liquid. Therefore the above mentioned behaviour is typical for the amorphous state.

*) Univ.-Doz. Dipl.-Ing. Dr. techn. Roland Grössinger, Dipl.-Ing. Dr. techn. Herbert Sassik, Institut für Experimentalphysik, Technische Universität Wien, Karlsplatz 13, A-1040 Wien

Some comments to the industrial application should give a short glance on the large possibility how to use amorphous metals (Metglasses as they are called by Allied Corp.) as softmagnetic materials but also as bracing foils, composite material and much more. Concerning the development of ideas how to apply these materials in industry and the documentation about the status of technology it will be referred to the proceedings of different conferences especially Int. Conf. on rapidly quenched metals RQ (3) to (7). The main applications are magnetic devices as transformers, induction coils, sensors by use of the magnetoelastic properties and shielding materials. Warlimont gave some excellent reviews about it (8), (9).

The main application is in the field of medium power transformers (10–100 kVA), where with an amorphous core the iron-losses should be 1/3 of that with conventional FeSi cores. The use of amorphous cores would save an energy of 48.10^9 kWh or 1.4 billions US-$ per year in the USA. In Europe the situation is not so clear because the power transformers are mainly in the 250–1000 kVA energy range, they are additionally better optimised and only very short times in low load use (10), (11). In general it is not visible when the breakthrough of amorphous cores will occur because a lot of disadvantages are obvious for amorphous Fe rich cores: lower saturation magnetisation than FeSi, higher magnetostriction, field annealing necessary, only 85% stacking factor, too low stability, too brittle and too thin for conventional machining and at present too expensive. This challenge is taken by the FeSi producers to improve FeSi cores (up to 6,5 wt %) technically and to manufacture them cheaper in relation to amorphous cores (cost calculations and the price relation concerning FeB are to be found in (12), (13) and other publications in (4), (5), (7).

Large progress can be seen in the use in tape recorders as tape heads and as special choke coils in DC power supplies (9), (10) where softmagnetic ribbons only 25 mm in width and with a magnetostriction constant $\lambda_s \cong 0$ are in use (cobalt rich ribbon). For the application of these materials in sensors the stress dependent magnetic properties, the extreme low coercivity force, the high and temperature independent electrical resistivity are of great advantage and special types of sensors are in production at present especially at Vakuumschmelze Hanau (8), (9).

2. The production of amorphous ribbons

Cooling a liquid, molten metal the solidification will be caused by the ordered arrangement of the atoms in a symmetric crystal lattice (long range order). If the cooling process is very rapid (e.g. $\geq 10^6$ K/sec.) the statistical position of the atoms in the melt will be frozen. We call the obtained metastable metal amorphous or metallic glass or glassy metal, because the frozen structure is similar to that of a glass which is also an undercooled liquid. The rapid quenching process is performed by cooling the melt on a cold substrate – a close thermal contact between the melt and the substrate is important – leading to ribbons or foils with about 10–80 μm thickness and a width of 1 mm up to present 1 m. It is also possible to produce such metallic glasses by sputtering, evaporation or electroless, chemical deposition, by plasma spraying or laser glazing (14).

2.1 Historical remarks

The first evaporated amorphous ferromagnetic film was produced in 1966 by Felsch (15) whereas the rapid quenching itself was first applied 1908 as melt spinning by Strange and Pim (16). Pond (17) extended this technique using also a rotating drum but in spite of cooling the melt on the outer surface the ribbon was spun on the inner surface of the hollow cylindrical shaped drum. The first amorphous Au-Si-metal however was obtained by rapid quenching by Paul Duwez in 1960 on Cal-Tec (18).

Because of the interesting ferromagnetic properties of alloys of 3d-metals with B, Si up from 1970 a lot of work was done: 1976 Lieberman and Graham (19) published their famous work on melt spinning Fe-Ni-B and 1979 the so-called planar flow casting (PFC) process was inserted by Narasimhan (20). From that time on the investigations concerning production and application are running rapidly. A lot of work was published on this subject (21), (22) pushed forward by the industry:

Vakuumschmelze Hanau (West Germany),

Allied Corporation (USA),

Research Inst. of Iron and Steel, Tohoku Univ. Sendai (Japan – RITU),

Krupp Ind. (West Germany),

General Electric (USA).

Important steps in this development were the EPRI – Research Project (Electric power research Inst. USA) and an European Patent of Prof. Güntherodt, Uni Basel (Switzerland) for a modular system to produce ribbons with 30 cm width (23) which can easily be changed to 1 m width (24). A lot of proceedings have been published, especially from the Int. Conference of rapidly quenched metals (3)–(7). For historical details see also (25), (26).

2.2 Technical details

The rapid quenching process (chill block casting) is realized in different technical constructions, depending on the special aim what materials and shapes should be obtained (21), (22).

Either a very high cooling rate (10^6–10^{12} K/sec.) but only a small sample mass

or continuous casting of long ribbons, foils or wires but with a lower cooling rate (10^4–10^6 K/sec.).

The system choosen must be in close correlation to the application of the samples either for technical use with a large amount of mass and long wide tapes or pure scientific use with small samples (see e.g. (14)):

a) Gun – technique:
A droplet of melt is pushed out from a nozzle by a gas shock wave on a substrate. A very thin foil with a lot of holes, about 10–50 mm in diameter is obtained by $\sim 10^{12}$ K/sec.

b) Piston and anvil/double piston method:
A droplet of melt is squeezed and quenched between two cold copper blocks to get discs of 10–50 μm thickness and 10–50 mm in diameter with a cooling rate of 10^5–10^7 K/sec.

c) Melt extraction and pedant drop melt extraction:
A rotating cooling wheel is touching directly without using a nozzle the melt in the melt-bath and drags a foil shaped ribbon away, but in an inhomogeneous manner with a low cooling rate ($\sim 10^4$ K/sec.).

d) The melt spinning by single or double roller technique:
The melt is pressed by gas through an e.g. quartz nozzle with an orifice diameter of ~0,5 mm and solidificated on a rotating wheel; thin and narrow ribbons are obtained with $\sim 10^6$ K/sec. Instabilities of the process are caused by the gas boundary layer on the wheel; these instabilities can be reduced either by using a helium atmosphere or vacuum (27). This is the standard laboratory technology.

e) Planar Flow Casting Process (20):
The distance between the wheel and the nozzle, which is usually rectangular (0,5 mm x 10–25 mm), is approximately 0,5 mm in order to stabilise the ribbon production which is nearly independent of the surrounding atmosphere and of the pressure in the nozzle, because the melt is draged out of the nozzle. With this technique long continuous ribbons are obtained with a cooling rate of 10^4–10^6 K/sec. This is at present the usual standard industry technology (23), (24).

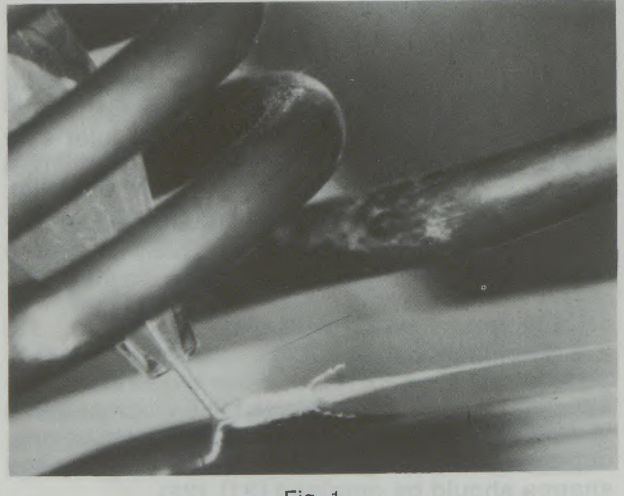

Fig. 1
Melt spinning of amorphous ribbons on a right side rotating Cu-wheel, 30 cm in diameter, surface velocity ~25 m/sec, quartz nozzle: orifice diameter 0,5 mm; Radio frequency induction heating with 30 kW, 200 kHz: stable melt puddle. Exposure time 1/2000 sec (32)

Fig. 2
The same as fig. 1, but a high speed scan (32), film number 5, showing the touching of the melt on the wheel, the melt puddle and the obtained ribbon (1 mm wide). The melt puddle was unstable, because the stream of melt was unstable with a pressing gas pressure too low

f) Advanced Planar Flow Casting:
It is a development of Allied Corporation in order to make process e) more stable by reducing the distance nozzle – wheel to ~0,1 mm. This is the present technology, to produce materials for transformer applications (see (5), especially (28), (29)).

The cold substrate is a metal wheel or drum, very often watercooled, produced of Cu, Cu-Zr, Cu-Be, Mo or steel, highly polished which should guarantee a high heat transport out of the melt/ribbon so that the product of thermal conductivity, specific heat and density should be high. The surface of the wheel must be hard in order to avoid scratches not to disturb the ribbon surface (30).

All the samples examined in our works where either obtaines by VAC and Allied Corp., by the Central Research Inst. of Physics, Budapest but mainly produced in Vienna at the only Institution and Institute in Austria using the rapid quenching technique (melt spinning, PFC). As described before the ribbon is produced on a Cu-wheel in a vacuum chamber in He, Ar atmosphere or vacuum with quartz nozzles (0,5 mm in diameter or 10 mm wide) with a substrate velocity up to 30 m/sec. at present (31). In order to study the influence of producing conditions on the quality of the amorphous ribbons we made photografic examinations by a high speed camera (HYCAM, 5000 frames per second on a 16 mm black-white film, in direct light and an exposure time of 1/12500 sec.) (32). Fig. 1 and 2 show such photographs where the occurrence of a stable (fig. 1) and an unstable (fig. 2) melt puddle is demonstrated. Note that wave like shape of the puddle, which is typical for the instability. The quality of the ribbons obtained was

tested by a simple bending technique (bending radius of amorphous ribbons is about 1 mm) and by X-ray Debye Scherrer-technique. The scattering picture is in direct connection to the structure of the metal. Fig. 3 (33) showes the picture for complete disorder, for alloys with a special short range order (liquid, amorphous) and for long range order. The scattering picture of amorphous alloys are the starting point for structural examinations to obtain a structure-model describing the order – disorder situation in glassy metals. Relaxation and stability of these metastable materials are to be examined and should be describable by the structure models (see e.g. (3), (4), (5), (7). For simple amorphous alloys as $Mg_{70}Zn_{30}$ the electrical resistivity can be calculated by application of

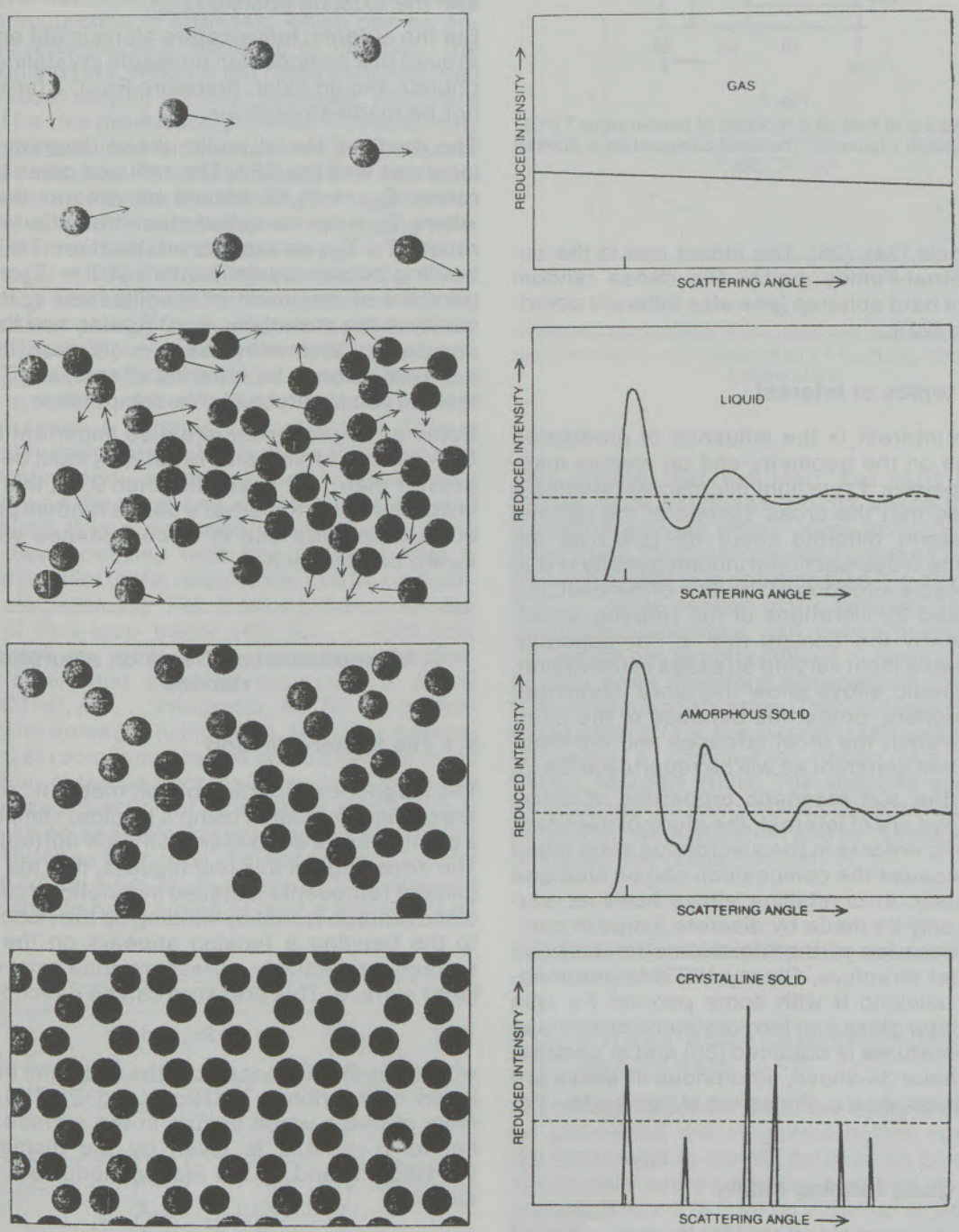

Fig. 3
Shematic X-ray scattering picture for disordered (gas), short range ordered (liquid, amorphous metal) and long range ordered, crystallographic symmetrically ordered solids. Intensity VS. scattering angle (33)

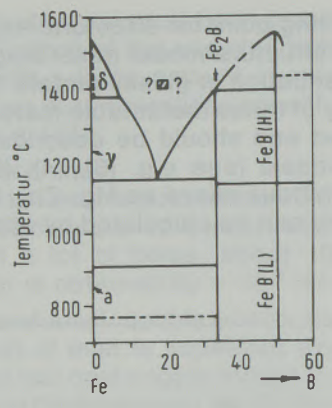

Fig. 4
Phase diagram of FeB as a function of temperature T (°C) and composition x (atom%). The ideal composition is marked by "?" (33)

such models (34), (35). The oldest one is the so-called Bernal-Finney model, the dense random packing of hard spheres (see also different contributions in (22)).

2.3 The topics of interest

Our main interest is the influence of production conditions on the geometry and on various magnetic properties. From light microscope studies it is deduced that the cross section of the ribbons is not uniform, differing about 10–15% over the length. This cross-sectional inhomogeneity is due to an unstable situation of the flow of the melt, but also caused by vibrations of the rotating wheel. Consequently the cooling rate is not constant, which causes local varying stresses in the ribbon. Ferromagnetic alloys show therefore inhomogeneous magnetic properties because of the interaction between the local stresses and the magnetostriction constant as will be reported in Ch. 3.

Not only the soft magnetic properties of amorphous alloys are of interest, the study of the onset of magnetic order is in the amorphous state much easier, because the composition can be changed continuously. In crystalline alloys however studies can only be made by discrete jumps in composition because of the stoichiometric situation and crystal structure. Glassy NiBSi is paramagnetic; by alloying it with some percent Fe spin glass, cluster glass and ferromagnetic ordering at low temperatures is obtained (36) and in contrast to amorphous 3d-alloys, amorphous 4f-alloys are hard magnetic as e.g. the series of rare earth – Fe, Co (37).

2.4 The glass forming ability

It is an experimental fact that for the production of amorphous ribbons the alloys of the 3d metals (Fe, Co, Ni) with metalloids (B, Si) with the composition $T_{80}M_{20}$ (atom%) are best suited. Additional there exist amorphous metal-metal alloys as $Zr_{40}Cu_{60}$, $Fe_{90}Zr_{10}$, $Mg_{70}Zn_{30}$. The basic understanding of the glass – forming – ability (GFA) is at present poor, but a large number of proposed models can be found (3)–(7), (8), (14), (21), (22), (23):

In most of the amorphous systems a deep eutectic temperature characterizes the composition, which can be obtained in the glassy state. Fig. 4 shows as an example the Fe-B-phasediagram. For 15–25 at% B amorphous tapes can be produced (this range depends also on the process used and the existing cooling rate).

But the eutectic temperature alone is not enough: around this composition no stable crystaline compounds should exist; therefore $Fe_{80}C_{20}$ (at%) cannot be made amorphous.

The depth of the eutectic phase diagram determines as well the GFA: The reduced glass temperature $T_{rgl} = T_{gl}/T_l$ should be greater that 0,5, where T_{gl} is the so-called glass transition temperature ($T<T_{gl}$: no rapid crystallisation; $T>T_{gl}$: by heating occurs crystallisation; at $T = T_{gl}$ = temperature of maximum in specific heat c_p the viscosity of the material $\eta = 10^{13}$ poise and the time constant of atom-movement $= 10^3$ sec., there is a critical balance for ordering effects) and T_l is the melting temperature at this composition.

Some other properties are also important for the GFA as e.g.: atomic size ratio: r_1/r_2 must be either greater than 1,12 or smaller than 0,88; this is just in agreement with Bernal's dense random packing of hard spheres and is in coincidence with the $T_{80}M_{20}$ composition.

3. Magnetoelastic effects on amorphous ribbons

3.1 The hysteresis loop

The magnetic properties of soft magnetic ribbons are generally studied using a toroidal sample with a primary and a secondary coil (pick-up) (e.g. (38)). The advantage of this technique is, that the arrangement represents a closed magnetic circuit. The disadvantage is that by winding up the ribbon, due to the bending a tension appears on the outer surface respectively a pressure zone exist on the inner surface. This pressure can be described as:

$$\sigma = 2\sigma_o x/d \qquad [1]$$

where x is the distance from the midplane (neutral layer) of the ribbon ($-d/2 \leq X \leq d/2$). The maximum stress σ which occurs in the surface plane i.e. for $x = d/2$ is given by the diameter of the toroid D and by the elastic modulus E of the sample:

$$\sigma = E \cdot d/D \qquad [2]$$

Due to (39) the total magnetization of such a toroidal sample depends on this stress σ:

$$J = J_s/2\{1 + J_sH/3\lambda_s\sigma \cdot [1 + \ln(3\lambda_s\sigma/J_sH)]\} \qquad [3]$$

There one comment should be made explaining the notation of magnetic units: The definition equation generally used is: $B = \mu_o(H + M) = \mu_o H + J$; B . . . magnetic induction, H . . . magnetic field, M . . . magnetization, J. . . . polarisation. According the fact that the magnetocrystalline anisotropy can be neglected in these materials, the magnetoelastic energy $\lambda_s\sigma$(λ_s . . . magnetostriction constant, σ . . . mechanical stress plays an important role determining the domain structure. The hysteresis loop is therefore influenced by the occurence of stresses, which can be originated external (e.g. bending) or intrinsic. The high cooling rate, which is not really constant, can cause local varying intrinsic stresses, which are typical for this production process. Consequently the hysteresis loop is different from point to point in these ribbons. The measurement of the local hysteresis is therefore a usefull tool to get informations about the constancy of the cooling rate. A special loop tracer was developped in order to allow local studies of the hysteresis (40). A low frequency ac-field (f<10Hz) is applied on the ribbon; a small pick-up coil, which is wound closely around the sample, detects the to dB/dt proportional signal. A regulating circuit corrects the input signal in order to deliver a field producing current which causes a constant dM/dt signal. This is especially important at fields close to the coercivity avoiding eddy currents. The ribbon is fixed on one side; on the other end an external stress can be applied. It is a magnetic open circuit but the small demagnetizing field (the external field is applied parallel to the ribbon axis) can be compensated electronically. Fig. 5 shows the circuit diagram of this loop tracer (40) (L1 . . . field coil, L2 . . . pick-up coil, A1 . . . current amplifier, A2 . . . differential amplifier producing a signal prop. dM/dt, A3 . . . integrator, A4, A5 . . . correction of the demagnetizing field). With this apparatus B(H) at room temperature can be measured as a function of the position studying local stresses but also as a function of an external stress. Fig. 6 shows as an example the remanence M_r and the coercivity H_c as a function of the position "z" of the pick-up coil on a $Fe_{40}Ni_{40}B_{20}$ ribbon. A low stressed region should have a high M_r and a low H_c value.

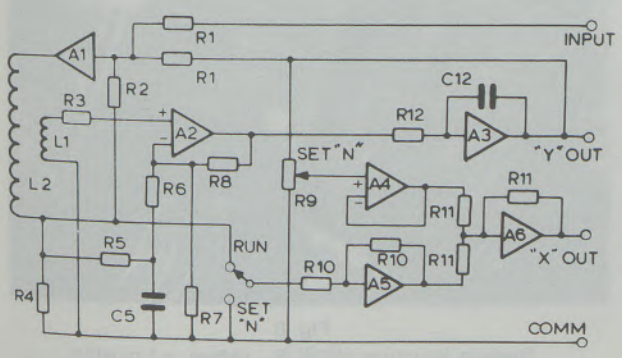

Fig. 5
Circuit diagram of the loop tracer for amorphous ribbons according to (40)

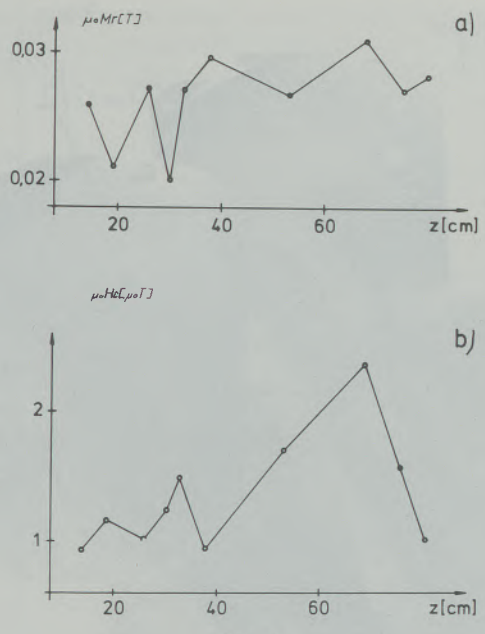

Fig. 6
Positional dependence of the remanent magnetization M_r and the coercivity H_c as measured on a $Fe_{40}Ni_{40}B_{20}$ ribbon at room temperature

This means that the $M_r(z)$ and $H_c(z)$ functions should be in antiphase. Points where this is not fulfilled are areas where cross sectional fluctuations exist. This interpretation is based on the fact that the signal is proportional to the flux $\Phi = B \cdot A$ (A . . . cross section of the sample). The rapidly quenching technique can cause fluctuations in "A" which are directly difficult to measure. Uncertainties arise therefore especially in the calibration of the magnetization. The field was calibrated using a hall probe, the magnetization was calibrated using a commercial ribbon (e.g. Metglas 2605A, Metglas 2826). The absolute accuracy is given by the reliability of the published data for the saturation magnetization and by the accuracy determining the cross section "A".

3.2 Determination of the magnetostriction constant

3.2.1 Stress dependence of the hysteresis loop

The stress dependence of the hysteresis is used for estimating the magnetostriction constant. If the hysteresis is mainly determined by the magnetoelastic energy $\lambda_s\sigma$, the sign of λ_s is very important. If $\lambda_s>0$ ($\lambda_s<0$) an external stress should cause a rotation of the domains parallel (perpendicular) to the stress axis (ribbon axis). The validity of these arguments was proved in a direct manner using the longitudinal Kerreffect for the study of the domain structure (41). Fig. 7a shows the do-

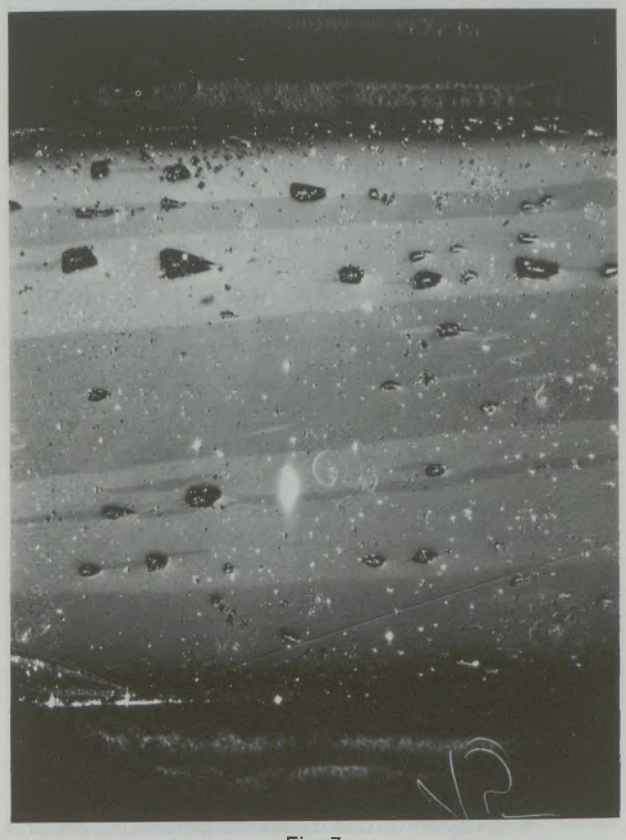

Fig. 7
Domain structure of $Fe_{80}B_{20}$ ribbon ~1 mm wide
a) without,
b) with an external stress of about 100MPa.
The stress was applied parallel to the ribbon axis

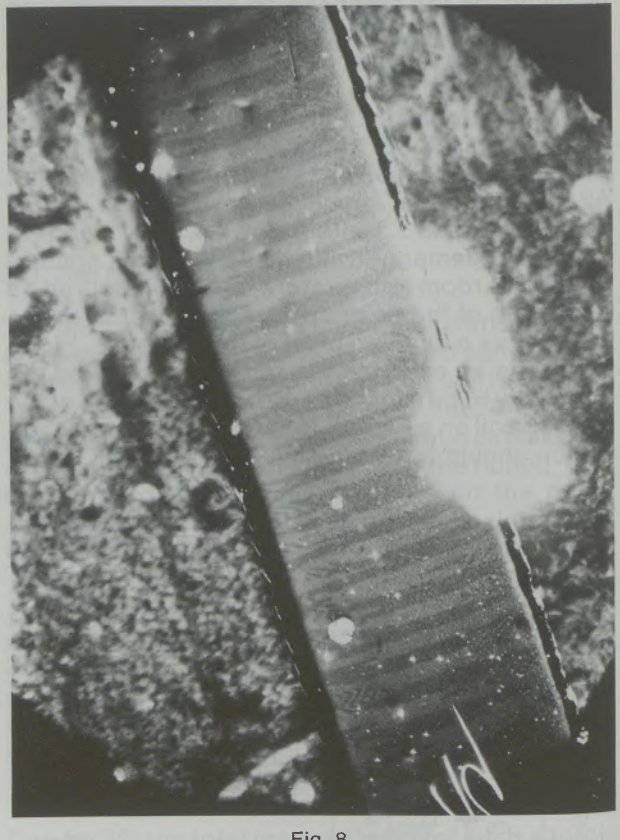

Fig. 8
Domain structure of $Co_{80}B_{20}$ ribbon ~1 m wide
a) without,
b) with an external stress of about 100MPa.
The stress was applied parallel to the ribbon axis

mains of a $Fe_{80}B_{20}$ ribbon ($\lambda_s>0$) without, and fig. 7b with an external stress of about 100MPa. The rotation parallel to the stress axis is obvious. In fig. 8a the domain pattern of $Co_{80}B_{20}$ ($\lambda_s<0$) without and also with (fig. 8b) an external stress of about 100MPa is shown. The negative sign of λ_s is responsible for the alignement of the domains perpendicular to the stress axis. Consequently for a $\lambda_s>0$ material the hysteresis steepens, whereas for a $\lambda_s<0$ material the hysteresis flattens if a stress is present. In order to demonstrate this, fig. 9 shows the stress dependence of the hysteresis loop of a $\lambda_s>0$ ($Fe_{39}Ni_{39}$(Mo, Si, B)$_{22}$) and a $\lambda_s<0$ ($Co_{75}Si_{15}B_{10}$) ribbon (42). This phenomenon was used by Becker and Kersten to determine λ_s from the stress dependence of the hysteresis loop (43). Starting from the magnetostatic energy:

$$E = -J_s H \cos\varphi \qquad [3]$$

φ . . . angle between the magnetic polarisation J_s and the ribbon axis

and introducing also the magnetoelastic energy:

$$E_\sigma = 3/2\lambda_s\sigma\sin^2\varphi \qquad [4]$$

λ_s can be calculated according to (39):

$$\lambda_s = J_s H_s / 3\sigma \qquad [5]$$

J_s . . . saturation polarisation

H_s . . . field, where saturation is achieved applying a stress σ. This method works well for $\lambda_s<0$ materials (39). If $\lambda_s>0$ this technique has to be extended. The plot of $J_R \cdot H_c$ as a function of the external stress should give a linear relation of the type (44):

$$J_R H_c = a + b\sigma \qquad [6]$$

Deviations of a linear behaviour are hints that local inhomogeneities and/or local stresses exist. From the slope "b", in close relation to formula [5] λ_s can be obtained. Differentiating formula [6] and using the stress dependence of H_c (see formulas [10], [11]) gives:

$$(dJ_R/d\sigma)H_c + J_R(dH_c/d\sigma) = b \qquad [7]$$

In the highly stressed region $dJ_R/d\sigma \rightarrow 0$ can be assumed, which leads to

$$J_R(M_r(\infty))(-3\lambda_s/\mu_o M_s^2)) = b \qquad [8]$$

From this expression λ_s can be determined:

$$\lambda_s = bJ_s^2/3J_R^2(\infty) \qquad [9]$$

$M_r(\infty)$ respectively $J_R(\infty)$ are the remanence values obtained by extrapolating $M_r(\sigma)$ ($J_R(\sigma)$) from the high stress region to $\sigma = 0$. With this procedure the influence of intrinsic stresses is canceled. Applying this method for determining λ_s from the stress dependence of the hysteresis loop gave as a surprising result a stress dependent λ_s. Fig. 10 shows $\lambda_s(\sigma)$ for $\lambda_s>0$ ribbons ($Fe_{80}B_{20}$ and $Fe_{85}B_{15}$) as well as for $Co_{80}B_{20}$ ($\lambda_s<0$) (45). The correct values for λ_s are obtained by extrapolating $\sigma \rightarrow 0$ for $\lambda_s>0$ respectively $\sigma \rightarrow \infty$ for $\lambda_s<0$ materials. This stress dependence results from the with the external stress varying alignement. In fig. 10 ad-

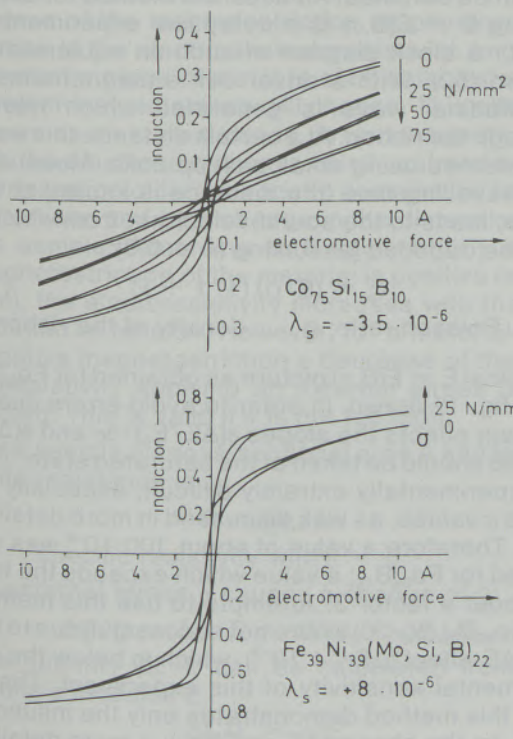

Fig. 9
Hysteresis loops of amorphous ribbons with negative and positive magnetostriction under a tensile load σ according to (42)

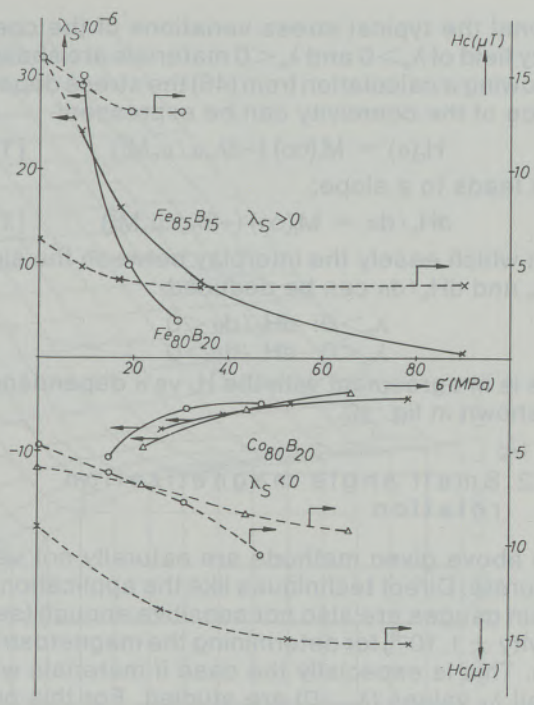

Fig. 10
a) Stress dependence of λ_s and H_c of $Fe_{85}B_{15}$ (x) and $Fe_{80}B_{20}$ (o) ($\lambda_s>0$)
b) Stress dependence of λ_s and H_c of $Co_{80}B_{20}$(x,o,Δ . . . three different samples) ($\lambda_s<0$); due to (45)

ditional the typical stress variations of the coercivity field of $\lambda_s > 0$ and $\lambda_s < 0$ materials are shown. Following a calculation from (46) the stress dependence of the coercivity can be expressed:

$$H_c(\sigma) = M_r(\infty)\,(-3\lambda_s\sigma / \mu_o M_s^2) \qquad [10]$$

This leads to a slope:

$$dH_c / d\sigma = M_r(\infty)\,(-3\lambda_s / \mu_o M_s^2) \qquad [11]$$

from which easely the interplay between the sign of λ_s and $dH_c/d\sigma$ can be deduced:

$$\lambda_s > 0:\ dH_c/d\sigma < 0$$
$$\lambda_s < 0:\ dH_c/d\sigma > 0$$

This is in agreement with the H_c vs σ dependence as shown in fig. 10.

3.2.2 Small angle magnetization rotation

The above given methods are naturally not very accurate. Direct techniques like the application of strain gauges are also not sensitive enough (sensitivity $\pm 1.10^{-6}$) for determining the magnetostriction. This is especially the case if materials with small λ_s values ($\lambda_s \rightarrow 0$) are studied. For this purpose the method of the "small angle magnetization rotation" (SAMR) was developed in order to measure λ_s in these ribbons (47), (48). The principle of this technique is the following: A constant field is applied in the ribbon axis, aligning the magnetic moments. Perpendicular to this field a small ac-field is generated in order to rotate the moments with a small deflection angle Θ out of the ribbon axis. The degree of this deflection is detected with a pick-up coil. If now an external stress is applied, two cases have to be considered:

I. $\lambda_s > 0$. The deflection angle Θ decreases.
II. $\lambda_s < 0$. The deflection angle Θ increases.

The constant field is now changed in such a manner that Θ stays constant under external stress. Knowing the variation of the constant field ΔH and the externally applied stress σ, λ_s can be determined according to (48) from:

$$\lambda_s = (-\mu_o M_s / 3)\,(\Delta H / \Delta\sigma) \qquad [12]$$

The sensitivity of this technique is $\pm 1.10^{-9}$. First attempts performed on $Fe_{80}B_{20}$ and $Co_{80}B_{20}$ gave reliable results (49).

3.3 The ΔE-effect

The magnetostriction constant does not only determine the shape of the hysteresis, it is also of great importance for the change of the elastic data under an external field or stress. For any magnetic material a field dependence of the elastic constants is expected. This effect is generally called ΔE-effect. In amorphous materials a huge ΔE-effect was detected (50). From the stress and the field dependence of the Young's modulus E according to (51) the magnetostriction constant λ_s can be estimated:

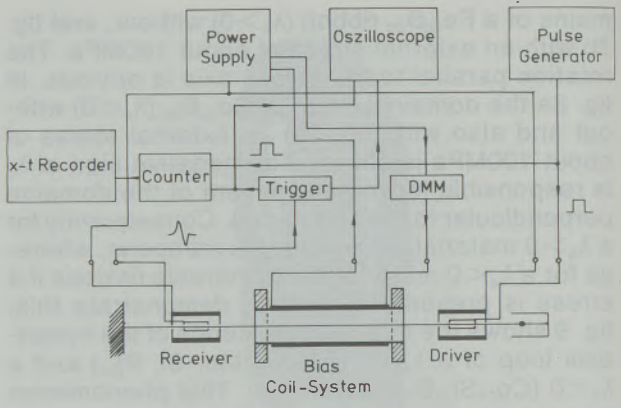

Fig. 11
Block diagram of a delay line experiment for determining $E = E(B,\sigma)$

$$B_z = \mu_o Q_\lambda M_z \cong \mu_o Q_\lambda M_s \qquad [13]$$

$$Q_\lambda = 3\lambda_s \sigma_z / \mu_o M_s^2 \qquad [14]$$

with

$$\partial(\Delta E/E_o)/\partial\sigma \,/\, \partial(\Delta E/E_o)/\partial B = -dB/d\sigma \qquad [15]$$

leading to

$$dB/d\sigma = 3\lambda_s / M_s \qquad [16]$$

Due to the above given formula from the stress and the field dependence of the Young's modulus λ_s can be obtained. An accurate method for determining $E = E(B,\sigma)$ is a delay line experiment. In fig. 11 a block diagram of such an equipment is shown (52). With a driver coil a magnetoelastic longitudinal wave is generated which travels through the ribbon. At a certain distance this wave is detected using small pick-up coils. Measuring the travelling time (the distance is known) of the wave, leads to the sound-velocity v_e from which E can be deduced (assuming ($\nu = 0.3$):

$$v_e^2 = (E/\varrho)\,(1/1 + \nu) \qquad [17]$$

ν . . . Poisson ratio; ϱ . . . density of the ribbon

A typical $E = E(B,\sigma)$ picture as obtained for $Fe_{85}B_{15}$ is in fig. 12 drawn. In order to avoid errors due to domain effects the slopes $\partial(\Delta E/E_o)/\partial\sigma$ and $\partial(\Delta E/E_o)/\partial B$ should be taken at the saturated state. This is experimentally extremly difficult, especially for large σ values, as was discussed in more detail by (53). Therefore a value of about 100.10^{-6} was obtained for $Fe_{85}B_{15}$; a value which exceeds the true λ_s about a factor 3. Attempts to use this method for $Co_{80}B_{20}$ ($\lambda_s < 0$) where not successfull due to the low ΔE-effect ($\Delta E < 1.10^{-3}$), which is below the experimental sensitivity of this experiment. Therefore this method demonstrates only the influence of λ_s on the shape of $E = E(B,\sigma)$; a more detailed theoretical analysis of $\Delta E/E_o$ as given by (54) makes clear that the formulas [15], [16] are only a first order approach.

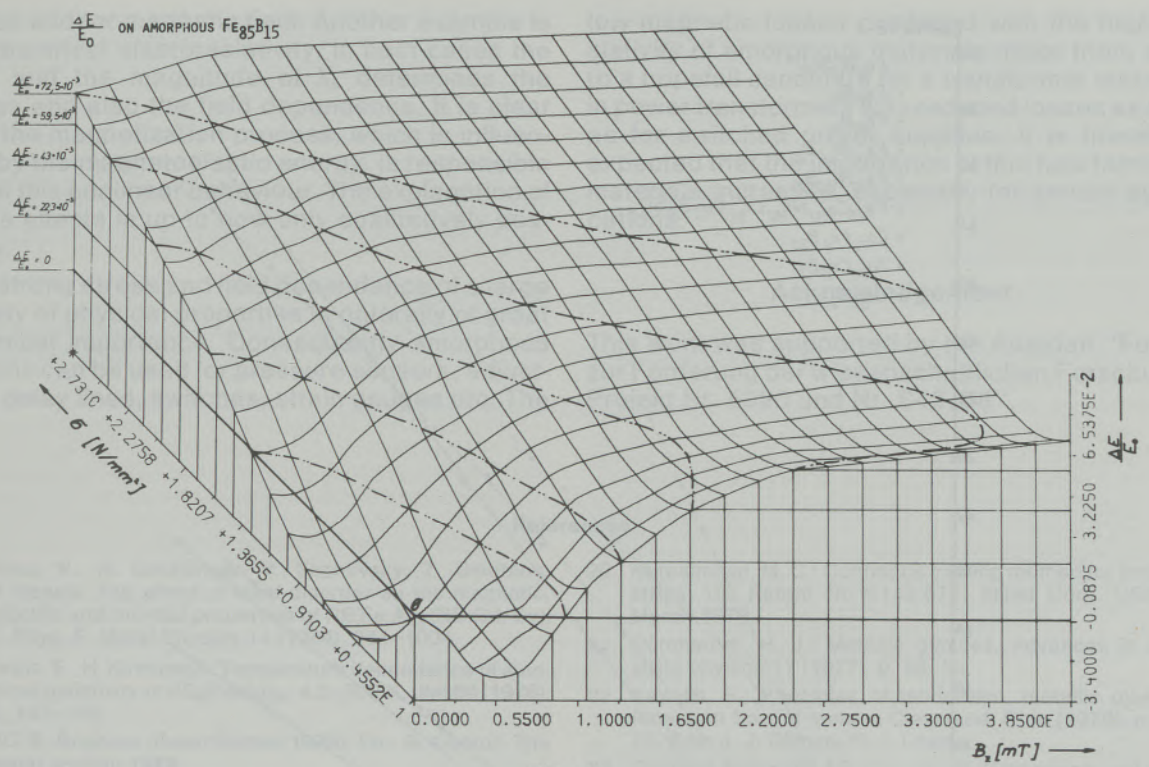

Fig. 12
$\Delta E = E(B,\sigma)$ of $Fe_{85}B_{15}$ measured at room temperature (53)

3.4 Electrical elastoresistivity

Another experiment which shows also the influence of the magnetostriction on physical properties is the electrical elastoresistivity. In general when a piece of metal is elastically distorted, its electrical resistance will change. This effect is known as elastoresistance. In ferromagnetic metals the elastoresistance is chiefly caused by the reorientation of ferromagnetic domains, by lattice distortions and by a change in the dimensions of the sample. According to Bozorth (55), if the magnetostriction of the material is positive (as for iron), the elastoresistivity increases with the application of tension. However, for a material with negative magnetostriction a decrease of the elastoresistivity applying an external stress is expected. This is valid if σ is not too high.

For a sample of cross-sectional area A and length L the resistance is

$$R = \varrho L/A \qquad [18]$$

ϱ . . . specific resistivity with $\sigma = 0$

An external stress σ causes a change of ϱ:

$$\Delta\varrho/\varrho = \Delta R/R - \Delta L/L + \Delta A/A \qquad [19]$$

The quantity $\Delta L/L$ can be calculated from the Young's modulus E:

$$\Delta L/L = \sigma/E \qquad [20]$$

Assuming an isotropic medium the change of A can be obtained:

$$\Delta A/A = -2\nu\sigma/E \qquad [21]$$

Consequently $\Delta\varrho/\varrho$ can be written

$$\Delta\varrho/\varrho = \Delta R/R - (1 + 2\nu)\sigma/E \qquad [22]$$

First experiments performed on ribbons with positive magnetostriction (Metglas 2826, 2826A and 2605A) gave linear $\Delta\varrho/\varrho$ respectively $\Delta R/R$ vs σ relations (56). More detailed investigations performed on various amorphous ribbons lead to the following conclusions (53):

I) The magnitude of the magnetization vector is of minor importance for the $\Delta R(\sigma)/R$ curves. This becomes clear because $\Delta R(\sigma)/R$ of a paramagnetic material ($Ni_{70}Cr_{10}B_{20}$) and that of a ribbon with $\lambda_s \simeq 0$ ($Fe_{7.9}Co_{61.1}Ni_{18.1}Cr_{3.2}Cu_2B_{3.1}Si_{4.6}$ and $Co_{72}Fe_8B_{20}$) is very similar (see fig. 13).

II) A material with a positive sign of λ_s shows a positive curvature of $\Delta R(\sigma)/R$ (e. g. $Fe_{80}B_{13}Si_6C$, $Fe_{85}B_{15}$, $Fe_{80}B_{20}$, $Fe_{40}Ni_{40}B_{20}$, $Fe_{20}Ni_{60}B_{20}$) (see fig. 13).

III) Materials with a negative sign of λ_s shows a negative curvature of $\Delta R(\sigma)/R$ (e. g. $Co_{80}B_{20}$) (see fig. 13).

These effects occure at stresses up to 100 MPa. From stress dependent hysteresis measurements as well as from Kerr effect studies under external stress (44) it is known, that exactly in this region the stress induced rotation of the domains occures. At higher stresses the material is magnetically saturated, therefore $\Delta R(\sigma)/R$ becomes linear at higher stress values.

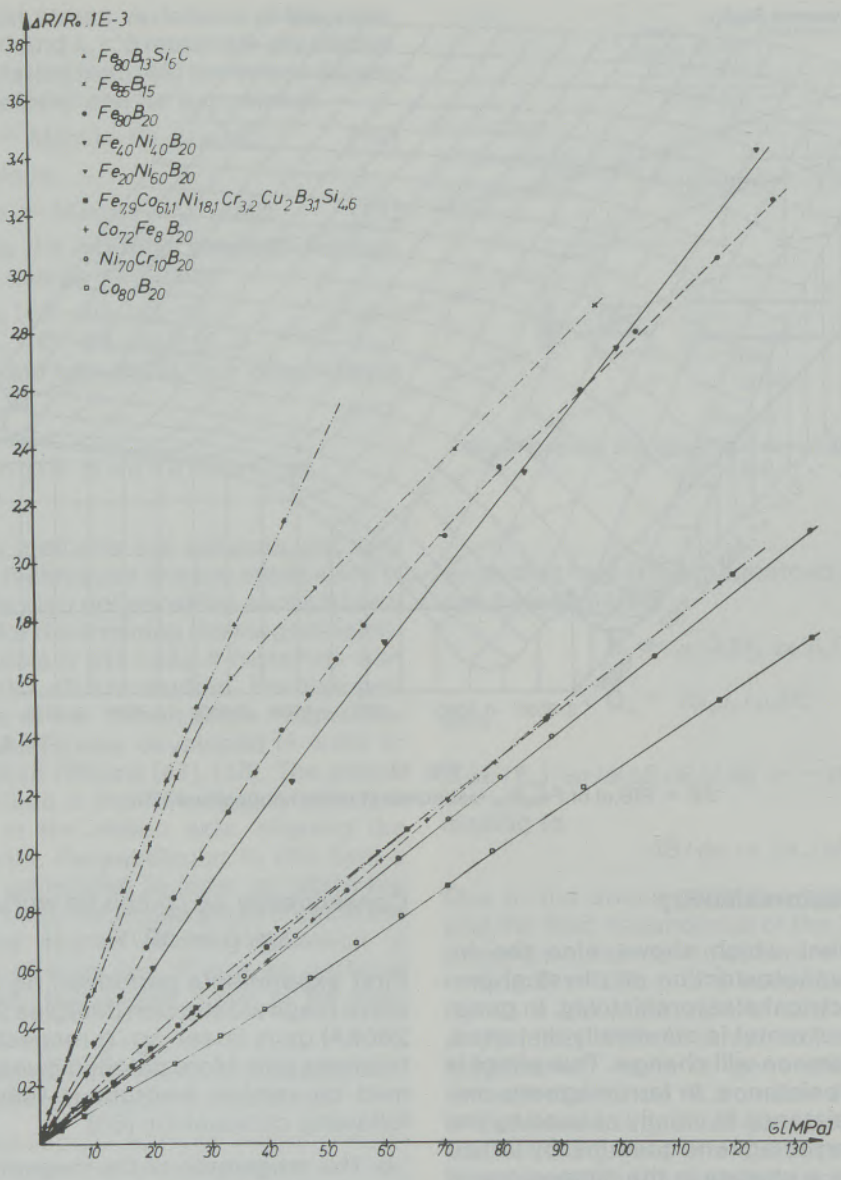

Fig. 13
$\Delta R(\sigma)$ of $Fe_{80}B_{13}Si_6C_1$ (Δ), $Fe_{85}B_{15}$ (x), $Fe_{80}B_{20}$ (●), $Fe_{40}Ni_{40}B_{20}$ (▼), $Fe_{20}Ni_{60}B_{20}$ (▽), ($\lambda_s > 0$); $Co_{72}Fe_8B_{20}$ (+), $Fe_{7.9}Co_{61.1}Ni_{18.1}Cr_{3.2}Cu_2B_{3.1}Si_{4.6}$ (■), ($\lambda_s \sim 0$); $Ni_{70}Cr_{10}B_{20}$ ($M_s \cong 0$); $Co_{80}B_{20}$ (o), ($\lambda_s < 0$)

4. Discussion and concluding remarks

In crystalline materials the domain structure is determined by intrinsic properties, like the ratio of the exchange to the anisotropy energy, but also by metallurgical parameters like e. g. the grain size, the grain boundaries, distortions and lattice defects. In soft magnetic amorphous materials the role of these metallurgical parameters is overtaken by crystalline impurities and local stresses. Due to the lack of crystalline anisotropy the magnetostriction is the most important intrinsic parameter determining the magnetization process. The special geometry (length ≫ width ≫ thickness) of these ribbons allows the investigation of the interaction of the magnetostriction with a well defined external stress on various physical properties. The most important to mention there is the hysteresis loop. The shape of the hysteresis is strongly stress dependent. This fact can be used to estimate the magnetostriction constant λ_s. The importance of λ_s in these materials needs a more accurate method for determining λ_s. The best technique with a sensitivity of $\pm 1 \cdot 10^{-9}$ is the small angle magnetization rotation, which allows the study of ribbons with nearly zero magnetostriction. Many other physical properties are influenced by λ_s and its sign too. One example here is the ΔE-effect, which shows a complex dependence of the Young's modulus E on the external

stress and/or magnetic field. Another example is the electrical elastoresistivity. In both cases the sign and the magnitude of λ_s determines the stress and also the field dependence. It is clear that the magnetization process, which is influenced by the magnetoelastic energy, is responsible for all this nonlinear behaviour. The explanation of these effects is up to now only qualitatively possible.

The strong stress and field dependence of a large variety of physical properties is naturally of great technical importance. Consequently amorphous ribbons can be used for pressure sensors, adjustable delay lines, switches, strain gauges etc. The low magnetic losses combined with the high resistivity of amorphous materials make them also to a hopefull candidate for a transformer material in power transformers with reduced losses as well as for switched power supplies. It is therefore expected that the importance of this new family of materials increases, especially for sensor applications.

Acknowledgement

This work was supported by the Austrian "Fonds zur Förderung der wissenschaftlichen Forschung, Projekt Nr. 5020 und Nr. S42/08".

References

1. Sima, V., R. Grössinger, V. Sechovsky, Z. Smetana, H. Sassik: The effect of local disorder on the magnetic, electric and thermal properties of RE(Fe Al)$_2$ (RE-Gd, Dy), J. Phys. F. Metal Physics 14 (**1984**), 981–1004.
2. Gratz, E., H. Kirchmayr: Temperature dependence of electrical resistivity of $SE_6(FeMn)_{23}$, 4,2–300 K, JMMM (**1976**), 2, 187–195.
3. RQ III, Brighton (Great Britain **1978**), Ed.: B. Cantor, The metal society **1978**.
4. RQ IV, Sendai (Japan **1981**), Eds: T. Masumoto, K. Suzuki, Ritu **1981**.
5. RQ V, Würzburg (West Germany **1984**), Eds: S. Steeb, H. Warlimont, North Holland **1985**.
6. 14. Metalltagung d. Akademie der Wissenschaften d. DDR, Dresden **1981**, Eds: Zentralforschungsinstitut f. Festkörperphysik und Werkstofforschung, H. Fidler, L. Illgen.
7. The conference on metallic glasses: Science and technology, Budapest **1980**, Eds: Central Research Institute of Physics, C. Hargitai, J. Bakonyi, T. Kemeny; KULTURA.
8. Warlimont, H.: Amorphous metals, materials and applications. Proc. of 3rd Gen. Conf. of CMD of EPS, Helv. Phys. Act. 56, 1–3 (**1983**), p. 281–291.
9. Warlimont, H.: New magnetic materials by rapid solidifying in 5), p. 1599–1609.
10. Luborsky, F. E.: Real and potential applications of amorphous ribbons. Proc. of the NATO Adv. Study Inst. on glasses; current issue, Tenerife, Spain, April 2–13, **1984**, p. 139–152.
11. Bölling, F., M. Hastenrath: Thyssen Techn. Bericht **1986**.
12. Sheppard, H. R., E. T. Norton: Amorphous metal core power transformers (economy) in 5), p. 1647–1652.
13. Rosenfelder, W.: The impact of rapidly quenched metals on the world borate industry, in 5), p. 1653–1656.
14. Handrich, K., S. Kobe: Amorphe Ferro- und Ferrimagnetika; Phys. Verlag, Weinheim **1980**.
15. Felsch, W.: Schichten aus amorphem Eisen; Z. f. Physik (**1966**) 195, p. 201.
16. Strange, E. H., Ch. A. Pim: Process of manufacturing thin sheets, foils, strips and ribbons of Zn, Pb and other metal alloys; US Patent 905.758, 1. Dez. **1908**.
17. Pond, R. B.: Metallic filaments and ribbons and making the same; US Patent 2.825.108, 4. 3. **1958**.
18. Klement, W., R. H. Willens, P. Duwez: Non crystalline structure in solidified Gold-Silicon alloys. Nature Vol 187 (**1960**), p. 809–810.
19. Lieberman, H. H., C. D. Graham: Production of amorphous alloy ribbons and effect of apparatus parameters on the ribbon dimensions; IEEE Trans. Magn. MAG 12, 6 (**1976**), 921.
20. Narasimhan, M. C.: Continous casting method for metallic strips; US Patent No 4.142.571, Allied Corp. USA, 6. March **1979**.
21. Güntherodt, H. J.: Metallic glasses, Advances in solid state physics 17 (**1977**), p. 25–53.
22. Kavesh, S.: Principles of fabrication, metallic glasses, American Soc. of metals, Cleveland, Ohio (**1978**), p. 36–73. Eds: J. J. Gilman, H. J. Leamy.
23. Concast Standard AG (CH), by W. Heinemann and H. J. Güntherodt; Process for band- and foil-shaped products, European Patent No. 0.111.728 A2, 9. 11. **1983**.
24. Güntherodt, H. J.: **1985**, priv. Comm.
25. Gonser, U.: Historical remarks and honours in 5), p. XLVII.
26. Buckel, W.: The early days of quench condensed amorphous films in 5) p. XLIX.
27. Lieberman, H. H.: Gas boundary layer effects in proc. glassy alloy ribbons in 3, **1978**, p. 34–40.
28. Güntherodt, H. J.: Introduction to rapidly solidified materials, in 5), p. 1591–1598, Vol 2.
29. Heinemann, W. A.: Rapid solidification-process technology for new material in 5), p. 27–34, Vol 1.
30. Hilzinger, H. R., S. Hock: Preparation of metallic glasses in 7), p. 71–90, Vol I.
31. Sassik, H., K. Kubaczek, H. Kirchmayr: Herstellung amorpher Metalle, berg- u. hüttenmännische Monatshefte Jg. 127, Heft 7 (**1982**), p. 236–238.
32. Scientific film Z 1787 of BHWK, Bundesstaatl. Hauptstelle für wissenschaftl. Film, Österr. Bundesinst. f. wissensch. Film **1982**, Enzyklopädia Cinematigraphica E 2732. H. Sassik, K. Kubaczek, Published details in Wiss. Film 29 (**1982**) p. 31–37. „Der Abkühlvorgang beim Schmelzspinnverf. Herstellung amorpher Metalle".
33. Chaudhari, P., B. C. Giessen, D. Turnbull: Metallic glasses, Scientific American, No 4, April **1980**, p. 242.
34. Güntherodt, H. J., H. V. Künzi: Electrical resistivity in 22), p. 247.
35. Hafner, J., E. Gratz, H. J. Güntherodt: Electrical resistivity of molten and glassy MgZn alloys International Conference on liquid and amorphous metals, LAM IV, **1980**, Grenoble. J. de Physique, **1980**, Tome 41, C 8, p. 512–514.
36. Hilscher, G., D. Haferl, H. Kirchmayr, M. Müller, H. J. Güntherodt: Breakdown of magnetism in the amorphous alloy system $(FeNi)_{77}Si_{10}B_{13}$. J. Phys. F. Metal Phys. 11 (**1981**), 2429. L. K. Varga, J. Toth, G. Hilscher, R. Grössinger, H. Sassik. Onset of magnetism in the amorphous alloy system $NiFeP_{20}$ JMMM 41 (**1984**), 131. H. Sassik, E. Bauer, H. Kirchmayr, H. J. Güntherodt, El. Resistivity and thermopower of the amorphous alloy system $(FeNi)_{77}Si_{10}B_{13}$, MRS Spring Meeting, Straßbourg, 13.–15. May **1985**, Symp. II, p. 163.

37. Apostolov, A., Ch. Christov, M. Mikhov, H. Sassik, V. Skumriev: Magnetic properties of bulk amorphous alloy Ho_4Co_3 obtained by rapid quenching in 5), Vol 2, p. 1161–1164.
38. Couroumalos, C., M. H. Price, K. J. Overshott: An electronic coercivitimeter for amorphous ribbon toroids; J. Applied Phys. 53 (**1982**), 8272–8274.
39. Hilzinger, H. R., H. Hillmann, A. Mager: Magnetostriction measurements on Co-Base Amorphous Alloys phys. stat. sol. (a) 55 (**1979**), 763–769.
40. O Dell, T. H.: A low frequency (M, B) loop tracer for amorphous ribbons; IEEE Trans. on Magn. MAG-17 (**1981**), 3364–3366.
41. Veider, A., G. Badurek, R. Grössinger, H. Kronmüller: Optical and neutron domain structure studies of amorphous ribbons; JMMM (**1986**) in print.
42. Warlimont, H., R. Boll: Applications of amorphous soft magnetic materials; JMMM 26 (**1982**), 97–105.
43. Becker, R., K. Kersten: Die Magnetisierung von Nickeldraht unter starkem Zug; Z. Phys. 64 (**1930**), 660–681.
44. Veider, A.: Untersuchungen magnetischer Bereiche amorpher Metalle mittels optischer und neutronenphysikalischer Methoden; Diplomwork, Techn. Univ. Vienna (**1984**).
45. Grössinger, R., H. Sassik, A. Lovas: The influence of processing on magnetic and mechanical properties of Fe-B and Co-B metallic glasses; JMMM 41 (**1984**), 107–109.
46. Vazquez, M., W. Fernengel, H. Kronmüller: The effect of Tensile Stresses on the Magnetic Properties of $Co_{58}Fe_5Ni_{10}Si_{11}B_{16}$ Amorphous Alloys; phys. stat. sol. (a) 80 (**1983**), 195–204.
47. Narita, K., J. Yamasaki, H. Fukunaga: Measurements of Saturation Magnetostriction of a Thin Amorphous Ribbon by Means of Small-Angle Magnetization Rotation; IEEE Trans. on Magn. MAG-16 (**1980**), 435–439.
48. Hernando, A., M. Vazquez, V. Madurga, H. Kronmüller: Modification of the saturation magnetostriction constant after thermal treatments for the $Co_{58}Fe_5Ni_{10}B_{16}Si_{11}$ amorphous ribbons; JMMM 37 (**1983**), 161–166.
49. Grössinger, R, R. Leeb, A. Veider: Analysis of the small-angle magnetization rotation for determining the saturation magnetostriction of amorphous ribbons; Proc. of Int. Symp. on Magn. of Amorphous Mat. (Sept. **1985**), Balaton (Hungary), 120–121.
50. Arai, K. I., N. Tsuya, M. Yamado: Giant $\triangle E$ effect and magnetomechanical coupling factor in amorphous $Fe_{80}P_{13}C_7$ ribbons; IEEE Trans. on Magn. MAG-12 (**1976**), 936–938.
51. O Dell, T. H.: Magnetostriction Measurements on Amorphous Ribbons by the Becker-Kersten Method; phys. stat. sol. (a) 68 (**1981**), 221–226.
52. Grössinger, R., H. Sassik, Ch. Schotzko, A. Veider: The Magnetic and Magnetoelastic Properties of Amorphous Metallic Ribbons; Z. f. Metallkunde 74 (**1983**), 577–584.
53. Grössinger, R., A. Lovas, G. Wiesinger, G. Badurek, R. Krewenka, S. Hausberger, H. Sassik, H. Kirchmayr: Influence of the Sign and Magnitude of the Magnetostriction Constant λ_s on Magnetoelastic Properties; IEEE Trans. on Magn. MAG-20 (**1984**), 1397–1399.
54. Du Tremolet de Lacheisserie, E.: Magnetoelastic properties of amorphous alloys; JMMM 25 (**1982**), 251–270.
55. Bozorth, R. M.: Ferromagnetism. D. Van Nostrand Comp., Inc. Princeton, New Jersey (**1951**), p. 749.
56. Aidun, R., S. Arajs, M. C. Martin: Electrical elastoresistivity of glassy $Fe_{40}Ni_{40}P_{14}B_6$, $Fe_{32}Ni_{16}Cr_{14}P_{12}B_6$ and $Fe_{78}Mo_2B_{20}$ at 77.4K. Mat. Science and Engn. 50 (**1981**), 143–145.

Metallography as an Implement for the Quality Control of Hard Materials: Cemented Carbides, Sintered Al_2O_3/TiC Ceramics and SiC/Si Products

Manfred Schreiner, Peter Ettmayer, Werner Wruss and Maria Simon, Wien*)

Dedicated to the 80th birthday of Prof. Dr. Franz Lihl

The accurate description of the microstructure of hard materials is one the major requirements for assessing their properties and behavior under conditions of operation. Premature failures often arise from defects in the microstructure. Light optical microscopy and electron microscopic imaging methods such as SEM, PhEEM or SEM in combination with EDAX are applied for the characterization of the microstructure. Results obtained by such investigations of cemented carbides, sintered Al_2O_3/TiC ceramics and reaction bonded SiC/Si parts are discussed.

Metallographie von Hartstofflegierungen: Hartmetalle, Al_2O_3/TiC-Sinterkeramik und infiltrierte SiC/Si-Werkstoffe

Die Beschreibung der Mikrostruktur von Hartstofflegierungen ist eine der wesentlichen Voraussetzungen, um deren Eigenschaften und Verhalten im praktischen Einsatz festzustellen. Häufig läßt sich ein vorzeitiges Versagen von Sinterteilen während des Einsatzes auf ein fehlerhaftes Gefüge zurückführen. Zur Charakterisierung des Mikroaufbaues werden in der Praxis in erster Linie lichtoptische und in zunehmendem Maße auch elektronenmikroskopische Methoden herangezogen. Die Anwendung dieser Untersuchungstechniken sowie die Möglichkeiten, damit Fehler im Aufbau von Materialien wie WC/Co-Hartmetallen, Al_2O_3/TiC-Sinterkeramiken oder infiltrierten SiC/Si-Produkten festzustellen, werden anhand von Beispielen diskutiert.

Métallographie de matériaux durs: alliages durs, céramique frittée d'Al_2O_3/TiC et matériaux de SiC/Si infiltrés

La description de la microstructure des matériaux durs est l'une des conditions essentielles de la détermination de leurs propriétés et de leur comportement dans l'utilisation pratique. Il arrive souvent que l'usure prématurée de pièces frittées au cours de leur l'emploi soit imputable à une structure défectueuse. Les caractéristiques de microstructure se déterminent principalement, dans la pratique, par les méthodes de microscopie optique et de plus en plus de microscopie électronique. On discute, au moyen d'exemples, l'application de ces méthodes d'étude ainsi que les possibilités qu'elles offrent de déceler des défauts de structure dans des matériaux tels que les alliages durs de WC/Co, les céramiques frittées d'Al_2O_3/TiC ou les matériaux de SiC/Si infiltrés.

1. Introduction

Hard materials have found widespread application in all those processes where extreme hardness in combination with a certain amount of toughness is required. Such processes include not only all metal forming and metal cutting operations, but also rock drilling and mining applications. A third sector comprises materials for wear-resistant parts where sliding friction is the lifetime limiting factor (1).

As a consequence of the evolutionary process of hard materials for the applications mentioned above, three classes of hard materials have emerged:

a) Cemented carbides or hard metals are manufactured by a sintering process with WC and other carbides such as TiC and/or TaC as the hard constituents and Co or Ni as binder metals. WC-free hard metals based on TiC, TiN with additions of Mo and/or W and with Ni as binder metals are often referred to as "cermets".

b) Ceramic materials based on Al_2O_3 with modifying additions of TiC, TiN, ZrO_2 etc. have found applications as cutting tools for high speed cutting.

c) Reaction bonded SiC/Si composites excel through their wear resistance and corrosion resistance in chemically aggressive environments.

*) Dipl.-Ing. Dr. Manfred Schreiner, a. o. Univ.-Prof. Dr. Peter Ettmayer, a. o. Univ.-Prof. Dr. Werner Wruss and Dipl.-Ing. Dr. Maria Simon, Institute for Chemical Technology of Inorganic Materials, Technical University, Getreidemarkt 9, A-1060 Vienna

Fig. 1
Micrograph of WC/Co cemented carbide with A-porosity (microporosity)

Considerable efforts have been put into analyzing the factors affecting the properties of parts made from such materials. There are numerous publications dealing with the questions as to how the contributing factors – the chemical composition, the microstructure, the grain size and the distribution of the constituents – determine the performance of the materials under actual operating conditions (2) to (5).

Mechanical properties in general are mainly a function of the microstructure of the material. The accurate description of size and distribution of the several components in a sintered material is one of the major requirements for predicting the properties and behaviour of the material under operating conditions. Defects in the microstructure such as pores, inhomogeneous distribution of the components and inclusions of impurities reduce tool life and often lead to premature failures. Therefore microstructural control of cemented carbides, of sintered ceramics and of SiC/Si products serves a dual purpose. First, it helps the manufacturer to assure himself or his customer of the uniform quality of his products, and, second, it helps to pinpoint faulty or suboptimal procedures via a "post mortem" examination of faulty materials.

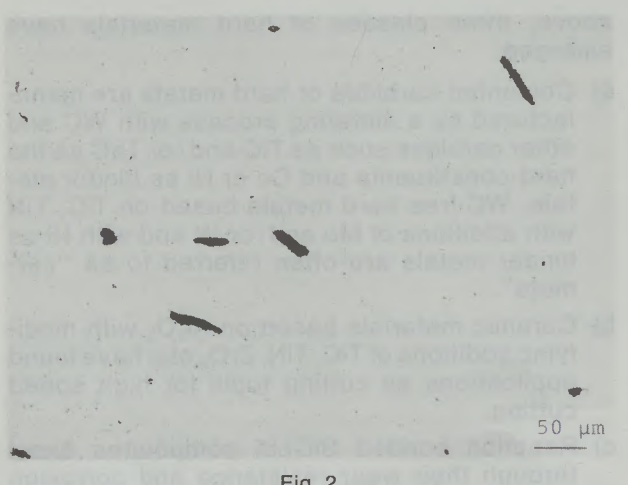

Fig. 2
Micrograph of WC/Co hard metal with B-porosity (pores 10–25 µm)

Standard metallographic procedures such as grinding, polishing, etching and evaluation of the microstructure by means of optical microscopy have been widely applied for the characterization of the materials mentioned above. Recently electron microscopic techniques as well as ion beam analytical methods have been successfully introduced and have become increasingly important. It is the purpose of this article to review the traditional metallographic methods as well as modern analytical techniques and discuss their relative potentials and limits.

2. Optical metallography

Metallographic examinations are usually carried out both on specimens sintered from the purchased powder batches in order to check the quality of the prematerials and on specimens selected from the production line in order to check the manufacturing standards and general "household standards". By this procedure trends in quality can be readily detected and immediate corrections can be made.

Cemented carbides, alumina based tools and SiC/Si parts fall into different application categories. Nevertheless, certain general principles may be applied in order to assure satisfactory performance. In all cases the products should be free from porosity, foreign inclusions or other forms of defects such as cracks or extra large grains. The distribution of the grain sizes of the several components in the sintered part should be uniform and with a well recrystallized microstructure.

Cemented carbides usually reveal two or three constituents when examined under optical microscopes: tungsten carbide – WC, cubic mixed crystals – (Ti, Ta, Nb, W)C and cobalt (nickel) binder phase (6), (7). Occasionally other usually detrimental constituents can be found by metallographic inspections. In the following a short but in no way exhaustive list of examples will be given.

One of the most common defects that can be detected by optical metallography is the porosity of the material (8). Impure prematerials or imperfect milling conditions, uneven distribution of the lubricant, contamination of the prematerial with foreign materials during handling and/or faulty dewaxing conditions are some of the causes of porosity in sintered products. Poor sintering conditions with respect to atmosphere (vacuum), temperature and/or time may cause so-called A-porosity (microporosity, fig. 1), whereas pores with an average diameter between 10 and 25 µm (B-porosity, fig. 2) originate mainly from mixing or pressing defects, hollow granulates during spray drying or inclusions of cobalt flakes. Also, foreign materials in the powder mixture which can be

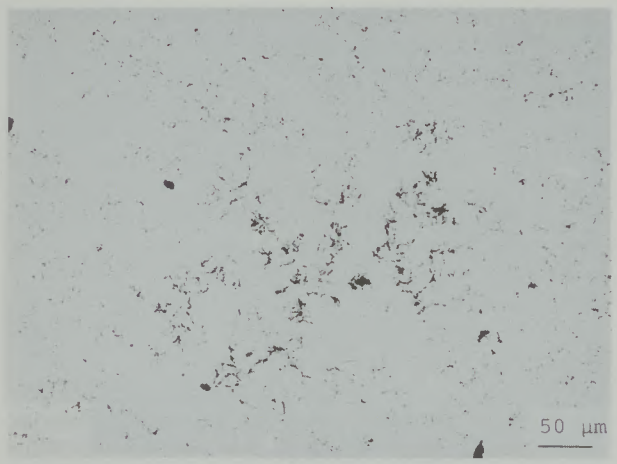

Fig. 3
Micrograph of WC/Co cemented carbide with C-porosity (free carbon)

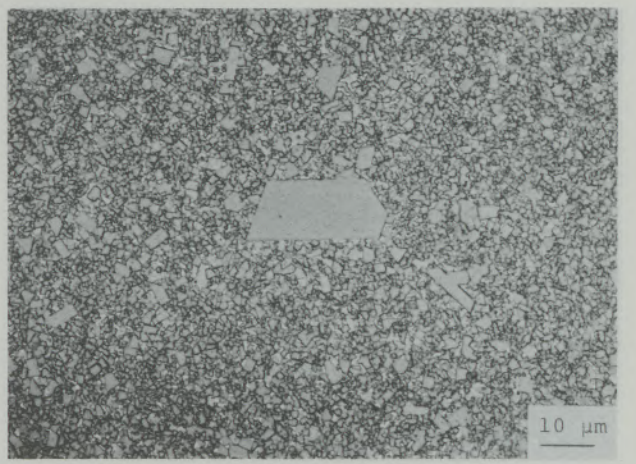

Fig. 5
Micrograph of sintered WC/Co with giant carbide crystals (oversize WC grains); etched with Murakami solution

converted into a liquid during the sintering process may be a cause of large pores (fig. 2).

Excess carbon has a detrimental effect on the rupture strength and leads to the formation of graphite (C-porosity, fig. 3). Excess carbon can be picked up during sintering, especially if the parts are supported in a bed of graphite, if the atmosphere is excessively carburizing or if the lubricant is cracked or decomposed during dewaxing. Generally, departure from the stoichiometric carbon/tungsten ratio should be avoided. Carbon deficiency leads to the formation of eta phases (e.g. W_3Co_3C) (fig. 4). Such phases have an embrittling effect and cause premature failure in service. Fine forms of η-carbides may cause problems during the grinding of sharp edges of tools. Therefore, defective oxidized prematerials and excessive uptake of oxygen during storage, milling and granulation must be avoided. Carbon loss during presintering and sintering as well as the carbon necessary for the reduction of oxides must be controlled exactly.

During the sintering process the carbide grains are surrounded by the liquid binder phase and growth of the carbide grains takes place via a solution-reprecipitation process. Although a homogeneous grain growth of the carbide grains is generally regarded as desirable, in some cases an anisotropic grain growth is observed with giant carbide crystals (fig. 5). Despite considerable research efforts this phenomenon is not yet completely understood. Overmilling and the presence of carbide agglomerates in the powder mixture seem to give rise to this effect (9) to (11).

In order to avoid discontinuous grain growth and grain growth of the carbide phase, especially in submicron grades, TaC is added as a grain growth inhibitor to the powder mixture before milling. Even small amounts of TaC (<1 wt%) are effec-

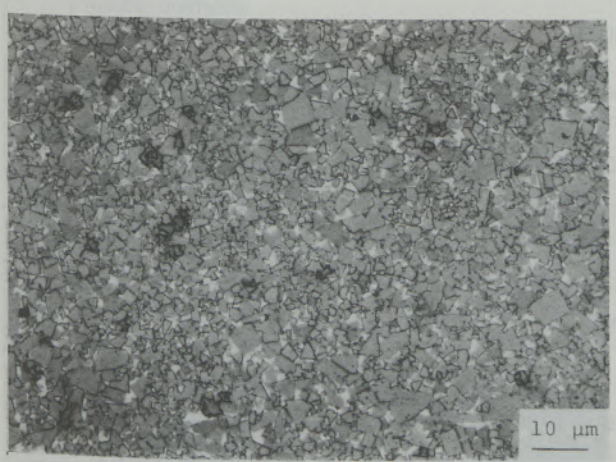

Fig. 4
Micrograph of WC/Co hard metal with η-carbides; etched with Murakami solution

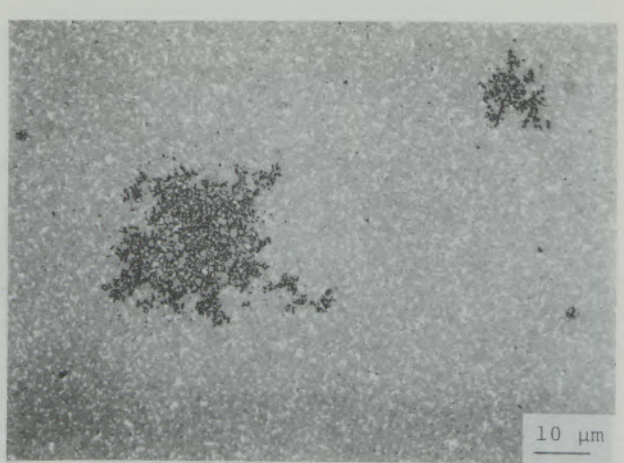

Fig. 6
Micrograph of fine grained WC/Co hard metal with TaC clusters from the TaC added as graingrowth inhibitor; etched with Murakami solution

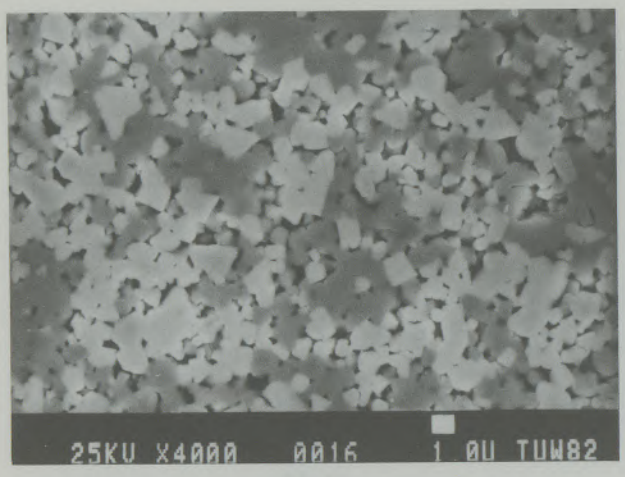

Fig. 7
SEM micrograph of cemented carbide with high contiguity of the cubic (Ti, Ta, W)C phase; Co binder etched with HCl/H_2O

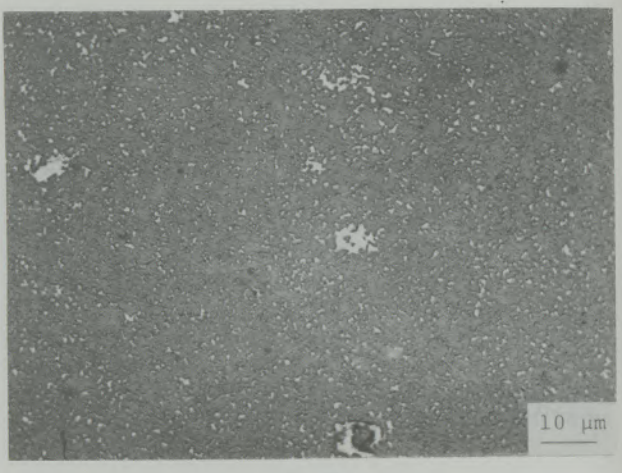

Fig. 9
Light optical micrograph of WC/Co cemented carbide with Co lakes; etched with Murakami solution

tive, but occasionally TaC contents under 0.7–1.0 wt% give rise to the formation of so-called TaC clusters (fig. 6).

High contiguity of the cubic (Ti, Ta, W)C phase (fig. 7), which may be caused by insufficient ball milling, faulty prematerials or oversintering, adversely affects the toughness of hard metals. Insufficient homogeneity of the cubic carbide component can give rise to "coring" of the cubic phase (fig. 8), which appears to be unavoidable to some extent. There is as yet no unambiguous evidence whether this effect is detrimental to the mechanical properties of a product or not (12).

Another microstructural defect arises whenever single cobalt powder particles are agglomerated during ball milling and form cobalt flakes. If such cobalt flakes are not removed from the mixed powder, so-called "cobalt lakes" (fig. 9) can be formed which are considered to be undesiderable by most carbide users.

Similar microstructural defects can be observed in microsections of sintered ceramic parts based on alumina or of reaction bonded SiC, although the manufacturing processes of such products are quite different from the liquid phase sintering process of cemented carbides. In order to improve the strength and the thermal shock resistance of such materials, alumina based ceramics are often modified by additional components such as titanium carbide (TiC), titanium nitride (TiN) or, recently, zirconia (ZrO_2) (13). The different phases can be easily detected by optical metallography (fig. 10, 11)(14). Due to the high transparency and the low reflectivity of alumina, the Al_2O_3 matrix appears gray to black and the carbide phase is bright (fig. 10). The high transparency of Al_2O_3 and the reflectivity of TiC cause carbide grains beneath the surface to become visible and the micrographs appear to be blurred and of low contrast, especially at higher magnifications (>500x). For this reason an accurate determi-

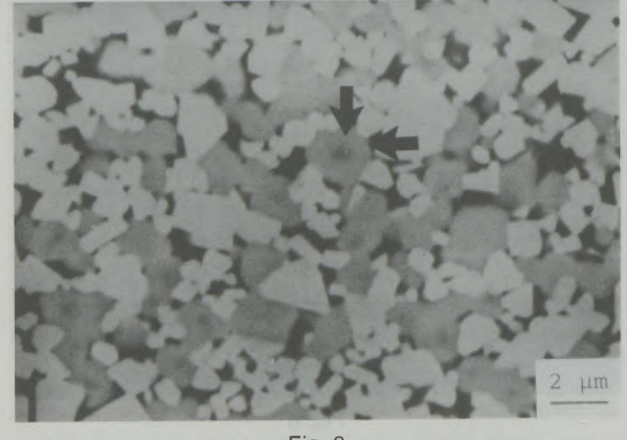

Fig. 8
SEM micrograph of a hard metal with "coring" of the cubic phase

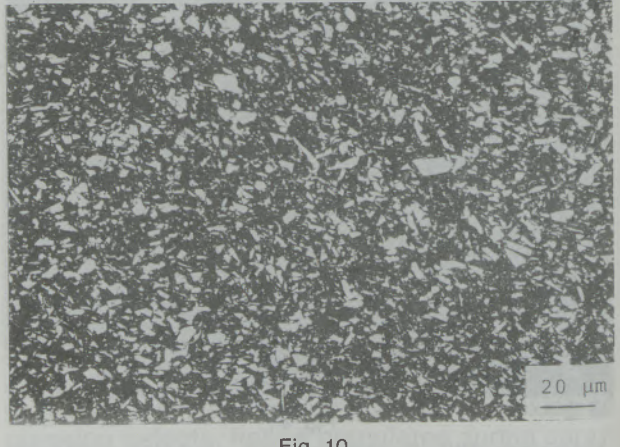

Fig. 10
Light optical micrograph of polished Al_2O_3/TiC ceramic (25 vol% TiC)

nation of the area and volume fraction of both phases is difficult. In order to overcome these difficulties the polished surface of the microsection can be coated with a thin layer of a compound having a high refractive index (14), (15). By this technique, most of the incident light is reflected at the interphase boundary between layer and ceramic material. Different phases are distinguished by different colours and a correct evaluation of the volume fraction of different phases in thus possible. A convenient way to prepare the thin layers uses the sputter technique with iron or lead as targets.

The microstructural characterization of Al_2O_3/TiC ceramics also includes the characterization of the alumina matrix with respect to its grain size. The development of that microstructure is rather difficult because of the high chemical resistance of the sintered ceramic material against conventional etching media. Usually, hot acids, molten alkaline hydroxides or high temperature treatments are applied to pure alumina materials to develop the grain boundaries for optical ceramography (16), (17). Such techniques are not suitable for the microstructural characterization of Al_2O_3/TiC products, as TiC and TiN are completely removed or decomposed by such agents. Special techniques had to be developed to etch Al_2O_3 grain boundaries without destruction of the carbide phase (18). The most important procedures for the development of the microstructure of alumina based ceramics are summarized in tab. 1. Optimal results with high reproducibility can be obtained by thermal treatment of Al_2O_3/TiC ceramics in hydrogen atmosphere followed by acidic etching of the TiC constituent (19). These techniques can also be applied for the electron microscopic characterization and will be discussed in section 3 below.

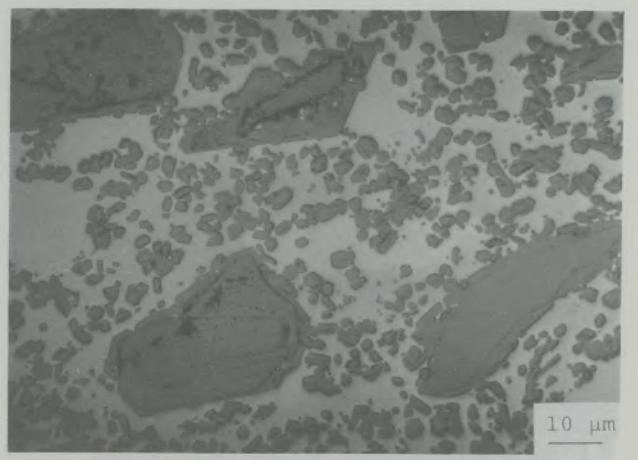

Fig. 11
Light optical micrograph of SiC/Si product; large primary SiC grains are surrounded by fine grained secondary SiC and silicon matrix; after electrolytic etching with a solution of 10% $C_2O_4H_2$ as electrolyte

Pure SiC powder is difficult to sinter to full density. For applications where a pore-free material is indispensable and the high refractoriness is of lesser importance, SiC powder or mixtures of SiC and carbon can be infiltrated with a silicon melt (20). The resulting material is fully dense and retains

Table 1

Methods for developing the microstructure of Al_2O_3/TiC ceramics for light optical and electron microscopy

	Conditions*)	Remarks	
Physical methods:			
1) Sputter techniques	1 kV, O_2, 10 mA	TiC (interference colours)	Al_2O_3
Fe-cathode	8–20 min.	red to brown	blue
Pb-cathode	1–5 min.	blue	yellow
2) Thermal treatment	1400 °C, H_2, 15 min.	Al_2O_3 grain boundaries are etched	
Chemical methods:			
NaOH	500 °C, 1–3 min.	Al_2O_3 grain boundaries are etched	
Borax	750 °C, 20–60 sec.	Al_2O_3 grain boundaries are etched	
$K_2S_2O_7$	500 °C, 0.5–2 min.	for etching TiC and partly Al_2O_3	
HF/HNO_3 (1:1)	RT, 10 min.	for TiC etching	
Combination of several techniques:			
Borax +	900 °C, 10 sec.	Al_2O_3 is etched	
$HF/HNO_3/H_2O$ (18)	RT, 2–9 min.	TiC is etched	
thermal treatment +	1400 °C, H_2, 15 min.	good reproducibility	
HF/HNO_3 (19)	RT, 5–15 min.	of the results	

*) The conditions depend mainly on the chemical composition of the material, on the purity of the components and on the observation method

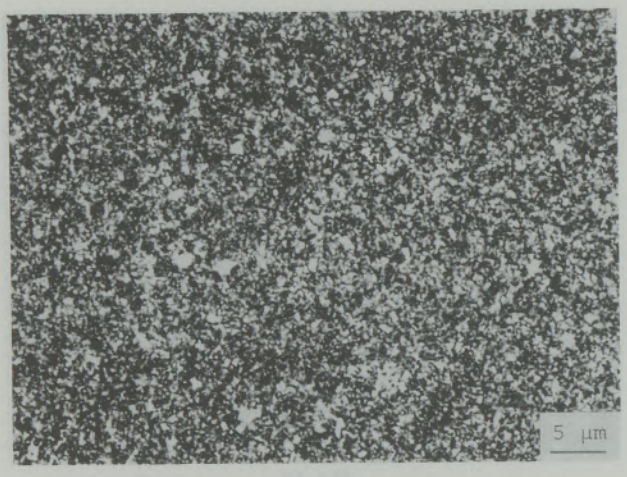

Fig. 12
Microstructure of a submicron WC/Co hard metal as seen with light optical microscopy; etched with Murakami solution

the form of the "green" SiC compact. Carbon powder that has been admixed to the SiC powder reacts with the infiltrating silicon melt and forms the so-called "secondary SiC" which fills the space between the primary SiC grains. Primary and secondary SiC can be distinguished in polarized light (21) and are beautifully set off against the bright silicon infiltrant (fig. 11).

3. Electron microscopy

The quality requirements for hard materials have become more stringent during recent years. In some cases they could be met by using extremely fine grained prematerials. Consequently, for metallographic control methods with a higher resolution than that of the light optical microscopy, which is limited to approximately 1000–1500x, are necessary. As an example, in fig. 12 and 13 micrographs of a submicron grade WC/Co hard metal are set side by side for comparative purposes: fig. 12 was taken with an optical microscope, Leitz/FRG type MM 6 (oil immersion optics 130x6.3), and fig. 13 was taken with a photo Emission Electron Microscope (PhEEM), Balzers/FL type Metioscope KE3 (22). The optical micrograph gives the general appearance of being blurred; the carbide grains are surrounded with interference fringes. The photoemission electron micrograph shows clearly defined, well faceted carbide grains, which are beautifully set off against the bright binder phase. The magnification is identical in both figures.

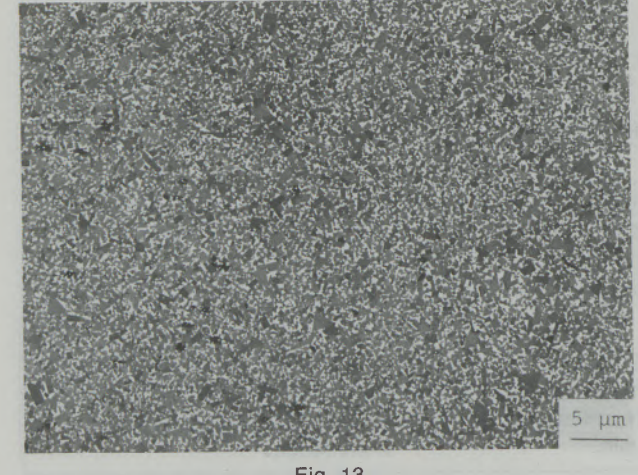

Fig. 13
Microstructure of submicron WC/Co cemented carbide seen with photo electron emission microscopy (PhEEM)

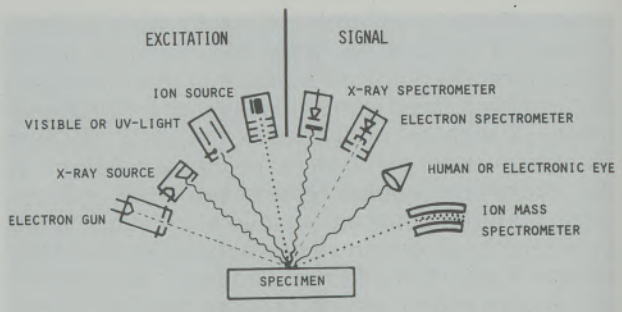

Fig. 14
Kinds of signals produced by the interaction between photons, electrons and ions with solid materials

As shown schematically in fig. 14, the PhEEM image is formed by electrons emitted from the specimen due to the effect of ultraviolet light (22). Because of the practically negligible penetration depth of the UV light, the PhEEM produces an image of an extremely thin surface layer. It is essentially a metallographic image of the surface. Different constituents or phases can be distinguished by their degree of brightness. Further, even the different orientations of the WC particles can be made observable by their different degrees of brightness. The work function of the photoelectrons depends not only on the material itself but also on the crystallographic orientation of the individual WC grains.

However, no information can be obtained from PhEEM images regarding chemical composition or average atomic number of the constituents. That may be one of the reasons that this type of microscope has found only limited application despite its high resolution limit. Transmission Electron Microscopy (TEM) and especially Scanning Electron Microscopy (SEM) are more widely used in actual metallographic applications. These instruments have proved to be highly suitable for obtaining images of fine grained hard materials. The replica technique has been used extensively to make the surface of chemically etched cemented carbides observable with TEM, while the topography of fracture surfaces has been investigated by SEM. Compared to the optical microscope, the outstanding feature of SEM is the superior depth of field. Thus, fracture surfaces, to give but one

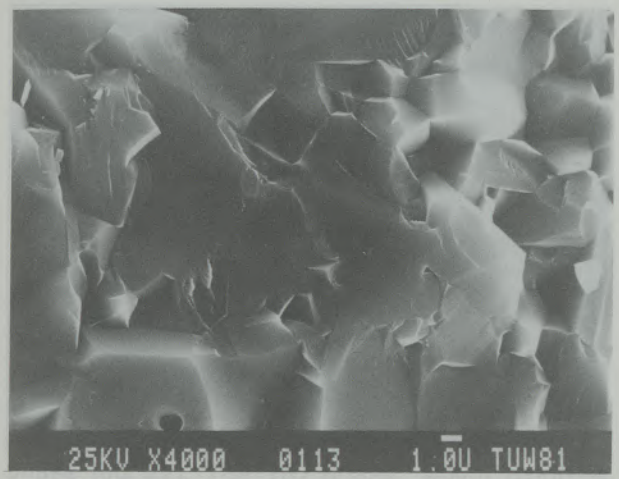

Fig. 15
SEM micrograph of the fracture of an Al_2O_3 ceramic

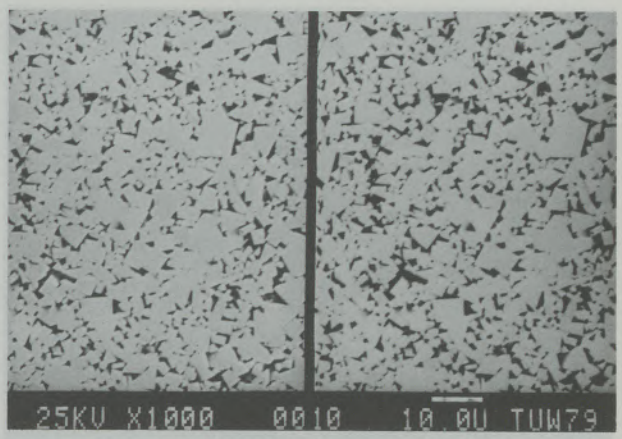

Fig. 17
Coarse grained WC/Co hard metal (unetched) as seen with SEM: a) secondary electron (SE) photomicrograph, b) backscattered electron (BE) photomicrograph

example (fig. 15, 16), can be observed at high magnifications without falling out of focus. With this method, inclusions, pores or other inhomogenities can often be identified as fracture sources (23).

SEM investigations of flat polished samples usually do not yield images of high contrast, because the yield of secondary electrons depends not only on the angle between the direction of the primary beam and the specimen surface but also on the mean atomic number of the constituents. The contrast between the different phases in a SEM micrograph of a flat polished section is therefore generally poor (24), (25), especially at higher magnifications (fig. 17, 18). The image contrast can be improved by using backscattered electrons (BE) as the image generating signal. Unfortunately, the number of BE is much smaller than that of secondary electrons, so that the signal-to-noise ratio is less favorable (fig. 17, 18).

On the other hand, secondary electrons are emitted not only from the specimen surface, but also – to a lesser degree – from below the surface to a depth of approximately 100 Å. The penetration depth depends on the energy of the primary electrons and on the mean atomic number of the specimen or the constituents. Therefore, the constituents appear to be translucent; details of the structure slightly beneath the surface and unobservable with an optical microscope become visible with SEM, depending on the energy of the primary beam and the mean atomic number of the constituents (25). A drawback with this method arises also from the interaction between the magnetic field of the ferromagnetic Co phase and the incident electron beam which gives rise to a slight deflection and, hence, an image distortion (24).

These problems cannot be completely overcome by using the characteristic x-rays for imaging (7), (24). As can be seen in fig. 14, not only secondary

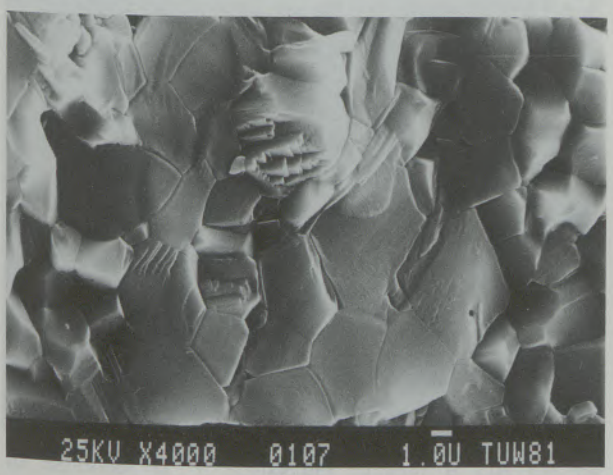

Fig. 16
SEM micrograph of the fracture of an Al_2O_3 ceramic after thermal treatment at 1200 °C for 10 min

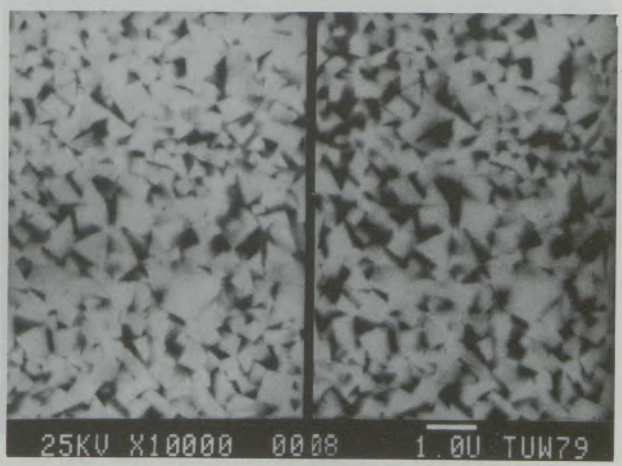

Fig. 18
Fine grained WC/Co hard metal (unetched) as seen with SEM: a) SE-image, b) BE-image

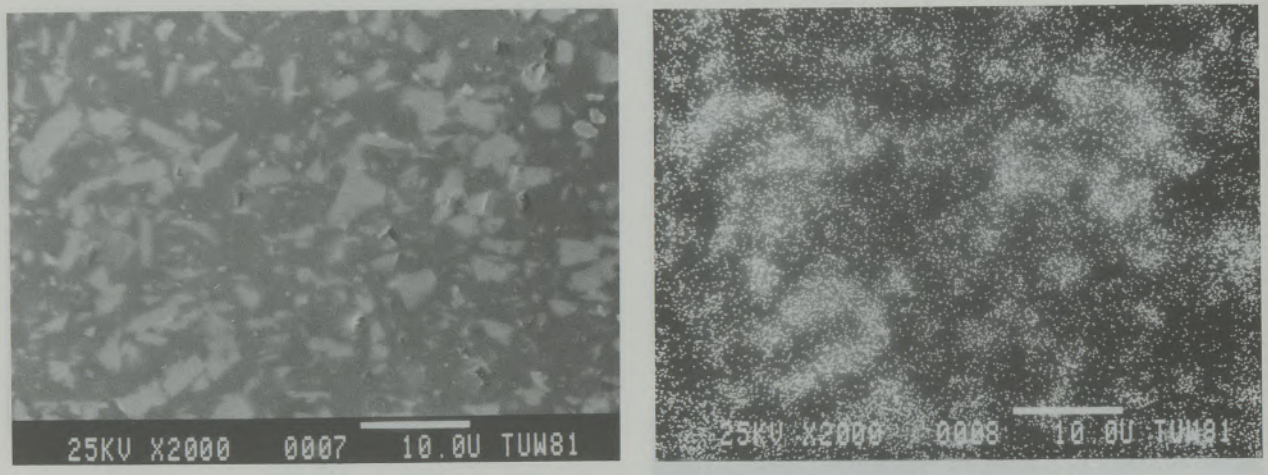

Fig. 19
SEM micrograph of a polished Al_2O_3/TiC ceramic:
a) SE-image, b) corresponding Ti distribution

or backscattered electrons but also element-specific x-rays are emitted when high energy electrons impinge on the specimen surface. Electron excitation of characteristic x-radiation has proved to be one of the most powerful methods for qualitative and quantitative analysis of microdomains: The yield of the characteristic x-rays is proportional to the concentration of the elements present in the x-ray generating domain. Because of the high penetration depth of x-rays, that region is much larger than the domain from which secondary electrons are emitted. Consequently a lower resolution is obtained by using that technique for imaging (fig. 19).

Therefore, several techniques based on deep etching, customary in the metallography of steel (26), have been applied to evaluate the microstructure of fine grained cemented carbides, sintered Al_2O_3/TiC ceramics or reaction bonded

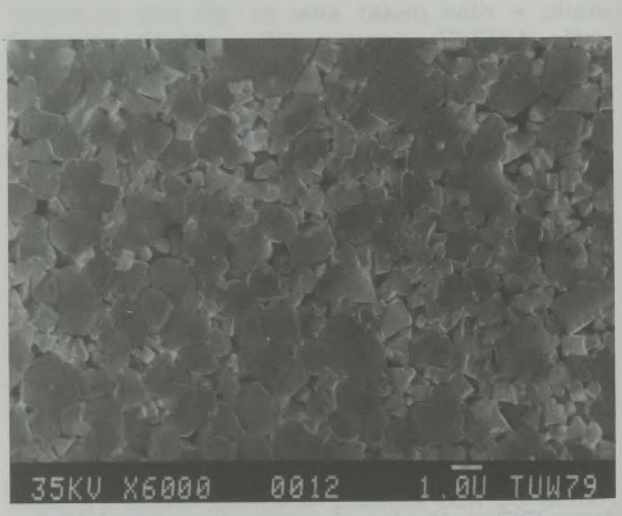

Fig. 21
SEM micrograph of fine grained WC/Co hard metal with cubic TiC phase after etching as mentioned in fig. 20

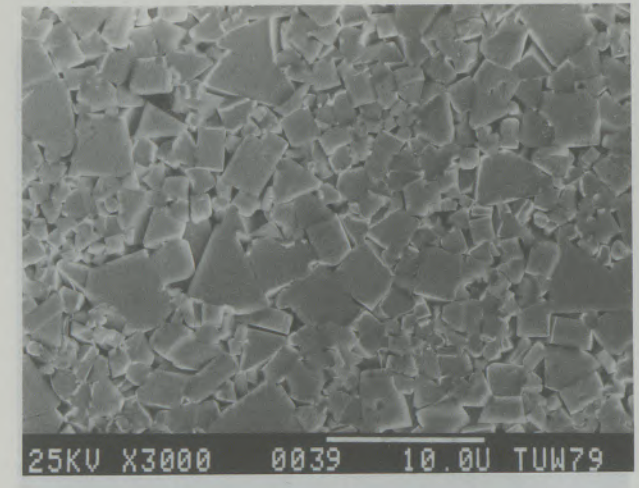

Fig. 20
Coarse grained WC/Co hard metal after etching with Murakami solution and HCl/H_2O as electrolyte, as seen with SEM

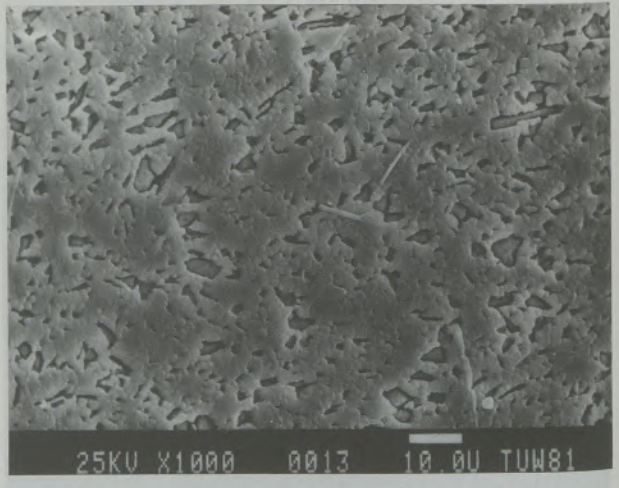

Fig. 22
SEM micrograph of Al_2O_3/TiC ceramic after thermal treatment (1400 °C, 25 min, H_2 atmosphere) and etching in HF/HNO_3 (1:1) for 5 min at room temperature

SiC/Si products by means of SEM. Fig. 20 and 21 show the result of a combination of the traditional alkaline carbide etching with electrolytic deep etching. The alkaline oxidizing ferrocyanide solution is known to attack predominantly the carbide grains. Prolongation of that etching period and subsequent electrolytic etching with HCl as electrolyte, which attacks or even dissolves the binder phase selectively, enables structural investigations even of submicron cemented carbides (24) as well as of hard metals with several constituents (fig. 21).

A similar technique has been applied to Al_2O_3/TiC products (19). A thermal treatment of the sintered materials in a hydrogen atmosphere at about 1400 °C develops the microstructure of the Al_2O_3 phase (fig. 22). The TiC phase, which oxidizes under thermals etching conditions in air, is thereby retained and may subsequently be selectively etched with solutions of HF/HNO_3 (1:1).

4. Conclusion

Classical optical microscopy will continue to hold an important position in the quality control of hard materials. Most of the structural features and defects occurring in cemented carbides, sintered ceramics based on alumina, and reaction bonded SiC products can be readily detected, observed and traced by standard metallographic procedures. Nevertheless, the more sophisticated electron microscopic techniques will see increasing use because of the superior resolution and the possibilities for analyzing defect sources. Scanning electron microscopy in particular has become an indispensable tool for investigating fracture surfaces. The application of several etching techniques to the metallography of hard materials also enables the microstructural characterization of flat polished sections.

It must also be mentioned that other electron microscopic techniques, such as EELS (Electron Energy Loss Spectroscopy) and AES (Auger Electron Spectroscopy) as well as ion beam analytical methods such as SIMS (Secondary Ion Mass Spectrometry) are being used increasingly for the characterization of microdomains, surface layers or tribological effects of wear resistant materials. Since such techniques are becoming more important in the research and development of hard materials, their value will also increase as tools for the qualitative and quantitative control of these products in the future.

Acknowledgement

The authors wish to thank Dr. L. Wegmann of Balzers AG for the PhEEM micrograph and Mrs. Cathryn L. K. Jelinek for correcting the manuscript.

References

1. Kieffer, R., F. Benesovsky: Hartmetalle; Springer Verlag Wien, **1965**.
2. Evans, D. G.: The relationship between structure and performance in carbide tools; Conference "Recent Advances in Metal Production", Sept. **1979**, Loughborough/GB, p. 39–1 to 39–19.
3. Lardner, E., G. A. Wood: Quality control and testing methods for hard metal; lit. cit. 2) p. 30–1 to 30–31.
4. Schreiner, M., P. Ettmayer, M. Simon, W. Wruss: Metallography as a quality control in the production of hard metals; Conference "Advances in Hard Metal Production", Nov. **1983**, Luzern/CH, Vol. 2, p. 29–1 to 29–24.
5. Philips, V. A.: Modern metallographic techniques and their applications; Wiley Interscience, New York **1971**.
6. Kopp, W.-U., U. Linke: Preparation and structure of sintered carbides; Pract. Met. 16 (**1979**), p. 257–267.
7. Ettmayer, P., R. Kieffer: Die Metallographie von gesinterten Hartstofflegierungen und Sonderhartstoffen; Pract. Met. Sonderband 3 (**1971**), p. 189–198.
8. Amberg, S., H. Doxner: Porosity in cemented carbide; Pow. Met. **1977**/1, p. 1–10.
9. Schmitt, T., M. Schreiner, E. Lassner, B. Lux: Über das diskontinuierliche Kornwachstum in WC/Co-Hartmetallen; Z. f. Metallk. 74 (**1983**), p. 496–499.
10. Schreiner, M., T. Schmitt, E. Lassner, B. Lux: On the origins of discontinuous grain growth during liquid phase sintering of WC/Co cemented carbides; Pow. Met. 16 (**1984**), p. 180–183.
11. Exner, H. E., A. Walter, P. Walter, G. Petzow: Auswirkungen der Wolframkarbid-Ausgangspulver auf gesinterte Wolframkarbid-Kobalt-Hartmetalle; Metall 32 (**1978**), p. 443–448.
12. Gurland, J.: Trans. Met. Soc. AIME 212 (**1958**), p. 452–455.
13. Salmang, H., H. Scholze: Die Keramik, Springer Verlag, **1968**.
14. Wellner, P., H. Hoven: Techniques for preparing sections and the structural classification of special ceramics with different porosity; Pract. Met. 18 (**1981**), p. 3–13.
15. Exner, H. E., J. Roth: Metallographic contrasting by reactively sputtered interference layers; Pract. Met. 17 (**1980**), p. 365–389.
16. Engelhardt, G., S. Kalb: Ätzverfahren zum Anätzen von Versetzungen in polykristallinem Aluminiumoxid; Ber. Dt. Keram. Ges. 51 (**1974**), p. 231–233.
17. Willmann, G., G. Heimke: Thermal etching of α-alumina and Na-β-alumina; Pract. Met. 15 (**1978**), p. 11–14.
18. Puppel, D., W. Grellner, M. Wünschmann: Combination etching process for grain size measurement of Al_2O_3/TiC sinter products; Pract. Met. 15 (**1978**), p. 528–535.
19. Schreiner, M., W. Wruss, B. Lux: Möglichkeiten der Gefügecharakterisierung von Al_2O_3/TiC-Sinterkeramiken; Pract. Met. Sonderheft 14 (**1983**), p. 101–113.
20. Sawyer, G. R., T. F. Page: Microstructural characterization of "REFEL" silicon carbides; J. Mat. Sci. 13/4 (**1978**), p. 885–904.

21. Petzow, G.: Metallographisches Ätzen; Bornträger, Stuttgart **1976**.

22. Wegmann, L.: Photoemissions-Elektronenmikroskopie; Mikroskopie 26 (**1970**), p. 99–110.

23. Mader, W., G. Grassmück, J. Blaha, P. Warbichler: Identifizierung von Poren und Inhomogenitäten im Gefüge von Sinterhartmetallen; Radex-Rundschau **1982**/3, p. 888–896.

24. Schreiner, M., G. Stingeder, P. Ettmayer, B. Lux: Scanning electron micrographs of sintered hard metal structures; Pract. Met. 17 (**1980**), p. 547–552.

25. Gahm, H., S. Karagöz, G. Kompek: Metallographic methods for the characterization of the microstructure of cemented carbides; Pract. Met. 18 (**1981**), p. 14–30.

26. Kny, E., W. Stolz, P. Stiaszny: Electrolytic deep etching – a valuable complementary method to standard metallographic procedures; Pract. Met. 14 (**1977**), p. 512–520.

Dispersionsgehärtete Al-Al_4C_3-Werkstoffe

Gerhard Jangg, Wien*)

Dedicated to the 80th birthday of Prof. Dr. Franz Lihl

In der Arbeit werden die Ergebnisse langjähriger Arbeiten zur Entwicklung von dispersionsgehärteten Al-Werkstoffen dargestellt. Es wird die Herstellung beschrieben, werden die Eigenschaften angegeben und die Verwendungsmöglichkeiten diskutiert. Zusammenhänge zwischen Gefüge und den mechanischen Eigenschaften werden angeführt.

Dispersion Strengthened Al-Al_4C_3-Materials

The paper gives the results of extended works for the development of dispersion strengthened Al-materials. The method of production is described, the properties are specified and the potential applications and connections between the structure and the mechanical properties are discussed.

Durcissement structural de matériaux d'Al – Al_4C_3

On présente dans ce rapport les résultats de nombreuses années de recherches en vue du développement de matériaux à base d'Al aptes au durcissement structural. On décrit leur méthode de production et leurs caractéristiques et on discute leurs possibilités d'applications. Les relations entre la structure et les caractéristiques mécaniques sont mises en évidence.

Wegen der hohen Alterungsbeständigkeit auch bei erhöhten Temperaturen und der hohen Warmfestigkeit beanspruchen dispersionsgehärtete Werkstoffe schon seit vielen Jahren großes Interesse. Die Verfestigung bei der Dispersionshärtung geht im wesentlichen auf ähnliche Ursachen zurück, wie bei der technisch sehr stark genutzten und gut bekannten Ausscheidungshärtung. In der Matrix eingebrachte, gleichmäßig verteilte sehr feine und harte Teilchen setzen der Verformung einen hohen Widerstand entgegen. Unterschiedlich zu den ausscheidungsgehärteten Werkstoffen liegen bei den dispersionsgehärteten Materialien aber Teilchen vor, die auch bei erhöhter Temperatur in der Matrix praktisch unlöslich sind und die daher auch bei höheren Temperaturen nicht zu Vergröberung neigen, die zu einer Verminderung ihrer Verfestigungswirkung führt. Ausscheidungsgehärtete Legierungen verlieren dagegen bekanntlich durch „Überalterung" ihre Festigkeit.

Erste Vorschläge – eine Verfestigung durch Einlagerung harter, unlöslicher Teilchen in Al –, eine Dispersionshärtung zu erreichen, stammen von E. Schmid, dessen Patente (1) Vorläufer der sehr viel später stürmisch einsetzenden Entwicklung auf dem Gebiet der Dispersionshärtung waren. Praktisch eingesetzt, zumindest im Versuchsmaßstab, wurde das von der Alusuisse (2), (3), (4) kurz nach dem Zweiten Weltkrieg entwickelte SAP-Metall, ein Al-Basis-Werkstoff mit Einlagerungen von Al_2O_3, der durch Vermahlen von Al-Pulver un-

Because of their high aging resistance also at elevated temperatures and the high hot strength, dispersion strengthened materials have been of high interest for many years. The strengthening during dispersion hardening essentially may be traced back to the same causes that are used for the technically frequently applied and well known precipitation strengthening. Very fine and hard particles placed in the matrix which are evenly distributed, show high resistance against deformation. Other than for precipitation strengthened materials, in dispersion strengthened materials particles are present that also at elevated temperatures remain practically insoluble in the matrix and do not tend to coarsening at high temperatures that would lead to a reduction of their strengthening effect. As is known, precipitation strengthened alloys lose their strength because of "aging".

First suggestions to reach strengthening by inclusion of hard, insoluble particles came from E. Schmid, whose patents (1) were precursors of a much later beginning, most vivid development in the field of dispersion strengthening. Practical use was made – a least at a trial scale – with SAP-metal developed by Alusuisse (2), (3), (4) shortly after World War II, which was an Al-based material with inclusions of Al_2O_3 obtained by milling Al-powder under oxidizing conditions under addition of milling promotors followed by extrusion. Despite the good properties obtained, it was not possible to reach technical application of SAP-metal because of the high price caused by the complicated manufacturing process. A very

*) A. o. Univ.-Prof. Dr. Gerhard Jangg, Institut für Chemische Technologie anorganischer Stoffe der TU Wien

ter oxidierenden Bedingungen und unter Zusatz von Mahlhilfsmitteln und anschließendes Strangpressen hergestellt wurde. Trotz der erzielten guten Eigenschaften konnte sich SAP-Metall wegen des durch die aufwendige Herstellungsweise bewirkten hohen Preises nicht in die Technik einführen. Einen sehr ausführlichen Überblick über das gesamte Gebiet der Dispersionshärtung und die Resultate bisheriger Anstrengungen hat M. Rühle gegeben (5).

Die SAP-Entwicklung wurde später in Wien wieder aufgegriffen und eine neue Art der Herstellung („Reaktionsmahlen") eingeführt. Aus der Erkenntnis heraus, daß die Dispersoide in den Werkstoffen sehr gleichmäßig verteilt und vor allem auch sehr fein (günstige Teilchengrößen 0,02–0,08 μm) sein müssen, wurde ein Prozeß angewendet, der auf das von INCO entwickelte „mechanische Legieren" zurückgeht (6), (7), d. h., daß die Al-Pulver in Intensivmühlen, meist Attritoren, in denen die Pulverteilchen ständig zerschlagen und wieder verschweißt werden, gemahlen werden. Miteingebrachte Dispersoide werden dabei gleichmäßig in das Materialinnere eingemahlen. Da fertige, genügend feine und geeignete Dispersoide jedoch kaum erhältlich sind, wurde von der Überlegung ausgegangen, pulverige Materialien zuzusetzen, die sich gut einmahlen lassen und während des Mahlens bzw. bei einer nachfolgenden Wärmebehandlung mit dem Al zu den gewünschten Dispersoiden umsetzen (8), (9). Als am geeignetsten haben sich Zusätze von feinem C, Ruß bzw. Graphit, erwiesen. Die Entwicklung, die in enger Zusammenarbeit mit in- und ausländischen Forschungsinstituten und Industriebetrieben vorangetrieben wird, hat einen hohen Stand erreicht, und es ist zu erwarten, daß die Werkstoffe in naher Zukunft verbreitete Anwendung finden werden.

Im vorliegenden Beitrag soll ein kurzer Überblick über den gegenwärtigen Entwicklungsstand gegeben werden.

1. Herstellung

Das Verfahrensschema des Herstellungsprozesses ist aus Abb. 1 ersichtlich. Handelsübliches, N_2-verdüstes Al-Pulver, das einen natürlichen Oxidgehalt von etwa 1% aufweist, wird zusammen mit entsprechenden Mengen (bis zu 5 Gew.-%) an feinem Ruß oder feinem Graphitpulver in einer Rührkugelmühle vermahlen. Die dabei erhaltenen Mahlgranulate werden zur Vervollständigung der Reaktion zwischen dem eingemahlenen C und dem Al zu Al_4C_3-Dispersoiden und zum Austreiben von vorhandenen gasförmigen Verunreinigungen (H_2 gebildet durch anwesende Feuchtigkeit, Al-Hydroide bzw. durch mit dem Ruß eingeschleppte Kohlenwasserstoffe) einer Wärmebehandlung unterworfen und schließlich durch Strangpressen kompaktiert. Pulverschmieden wurde ebenfalls mit Erfolg untersucht, gelingt jedoch nur unter Einhaltung sehr genauer, in der Technik kaum zu realisierender Bedingungen.

extensive survey on the total field of dispersion strengthening and the results of the efforts to-date has been given by M. Rühle (5).

The SAP-development again was taken up in Vienna lateron and a new way of producing it ("Reactionmilling") was introduced. Realizing that dispersoids in the materials have to be very evenly distributed in the materials, and, above all also have to be very fine (optimum particle size 0.02–0.08 μm), a process was applied derived from "mechanical alloying" developed by INCO (6), (7), i.e. Al-powders are ground in intensive mills, generally attritors, where the powdery particles are permanently crushed and re-welded. Co-charged dispersoids thus are evenly co-milled into the interior of the material. Since ready-made, sufficiently fine and apt dispersoids hardly are available, it was initially considered to add powdery materials that may be well co-milled and that react during milling and a consequent heat treatment with the Al to give the wanted dispersoids (8), (9). Most apt have proven additions of fine C, carbon black, resp. graphite. The development that is conducted in close cooperation with local and foreign research institutes and industrial companies has already reached a high level, and it may be expected that these materials will find extensive application in the near future.

The contribution presented here is intended to give a short survey on the present state of development.

1. Production

The flow-sheet of the manufacturing process may be seen from fig. 1. Commercial grade N_2-jet-dispersed Al-powder containing a natural oxide percentage of app. 1% is co-milled with the corresponding quantities (up to 5%/wt) of fine carbon black or fine graphite powder in an agitat-

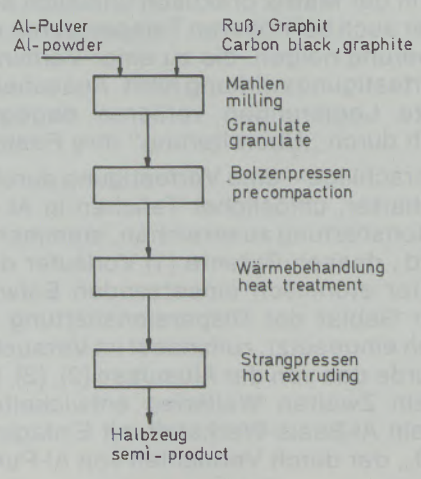

Abb./Fig. 1
Herstellungsgang für Al-Al_4C_3-Halbzeug
Flow sheet for Al-Al_4C_3 semi product

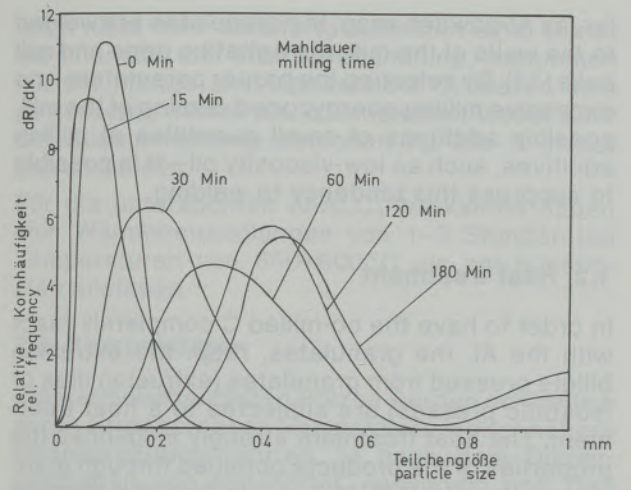

Abb./Fig. 2
Korngrößenverteilung verschieden lange gemahlener Al + 3% Ruß-Mischungen
Grain size distribution of Al + 3% carbon black mixtures milled for different lengths of time

Die Eigenschaften der erhaltenen Strangpreßprodukte hängen von sehr vielen Parametern ab, die Werkstoffe sind jedoch im Gegensatz zum früheren SAP-Metall ohne wesentlichen Ausschuß mit sehr guter Reproduzierbarkeit zu erhalten.

1.1 Mahlen

Wie erwähnt, geschieht das Vermahlen der Einsatzmischungen – Al-Pulver mit einer mittleren Korngröße von etwa 100 μm und den entsprechenden Mengen an Ruß bzw. feinem Graphit (0,25–5 Gew.-%) – in einer Rührkugelmühle (Attritor). Genauere Untersuchungen ergaben, daß die Al-Teilchen während des Mahlvorganges laufend zerkleinert und unter Einbindung des vorhandenen C wieder verschweißt werden. In den Kornverteilungskurven verschieden lange gemahlener Granulate (Abb. 2) kommt dieses Verhalten zum Ausdruck. Nach einer anfänglichen Abnahme der mittleren Korngröße werden, unter Verschwinden des Feinanteiles, gröbere Granulatkörner aufgebaut. Sobald alles Feinkorn verschwunden ist und die Granulate silberhell erscheinen, kann die Mahlung abgebrochen werden. Im allgemeinen reichen, abhängig von der Menge an zugesetztem C, etwa 40–180 Minuten Mahldauer aus. Längeres Mahlen führt zur Bildung von sehr groben, schlecht weiterverarbeitbaren Granulaten. Längere Mahldauer führt, wie am Beispiel eines Werkstoffes mit 4 Gew.-% C in (Abb. 3) gezeigt ist (10), zu keiner weiteren Verbesserung der Eigenschaften, zumindest nicht der Zugfestigkeit der aus den Granulaten stranggepreßten Produkte (11). Bei niedrigen C-Zusätzen können beim Mahlen Schwierigkeiten dadurch auftreten, daß die Al-Pulver bzw. die Granulate an die Mahlgefäßwände, die Rührarme bzw. an die Mahlkugeln anschweißen (11). Durch Wahl geeigneter Bedingungen – nicht zu hohe Mahlenergie, gute Kühlung der ing ball mill. The mill granulates thus obtained are then subjected to a heat treatment to complete the reaction between the co-milled C and the Al to Al_4C_3 dispersoids and to expel the gaseous impurities present (H_2 resulting from moisture present, Al-hydroxides, resp. hydrocarbons trailed in by carbon black), and finally, compacting is achieved by extrusion. Also, powder-forging has been successfully examined, but this is possible only under maintaining of very precise conditions that hardly can be realized technologically.

The properties of the extruded products depend on very many parameters, but contrary to the foregoing SAP-metal these materials may be obtained without considerable scrap and good reproduceability.

1.1 Milling

As already mentioned, the milling of the feed-mixes – Al-powder of a mean grain size of appr. 100 μm and the corresponding quantities of carbon black, resp. fine graphite (0.25–5% / wt.) – is accomplished in an agitating ball mill (Attritor). Exact investigations showed that the Al-particles continuously are diminuted during the milling process and are again co-welded under inclusion of the C present. This behavior can be well seen from the grain distribution graphs of granulates milled to different lengths of time (fig. 2). After an inital decrease of the mean grain size, coarser granulate grains are built up, while the fines disappear. When all the fine grain has disappeared and the granulates appear silvery-bright, milling may be stopped. In general, a milling time from 40 to 180 min. is sufficient, depending on the amount of C added. Extended milling leads to very coarse granulates that are difficult to process. Extended milling time does not lead – as shown with the example of a material with 4% / wt C (fig. 3) (10) – to an additional improvement of the properties, especially not of the tensile strength of the products extruded from the granulates (11). With low percentage additions of C difficulties arise inso-

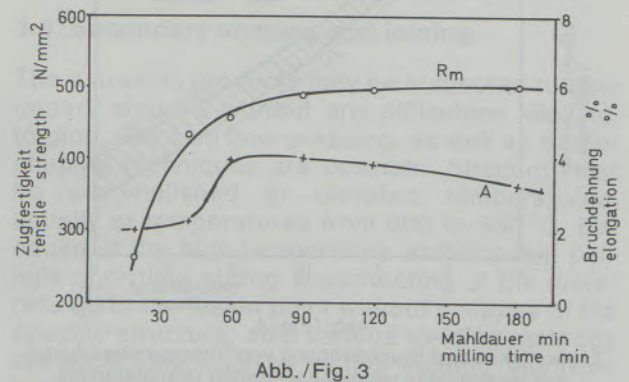

Abb./Fig. 3
Zugfestigkeit und Bruchdehnung von Strangpreßstangen aus verschieden lange gemahlenen AlC-(4 Gew. % C-)Granulaten
Tensile strength and elongation of extruded rods out of AlC-(4% / wt C-)granulates milled for different length of time

Mühle, gegebenenfalls Zusatz von geringen Mengen Mahlhilfsmitteln, wie dünnflüssiges Öl – kann diese Verschweißneigung unterdrückt werden.

1.2 Wärmebehandlung

Zur Vervollständigung der Umsetzung des eingemahlenen C mit dem Al werden die Granulate bzw. aus den Granulaten gepreßte (Matrizenpressen oder isostatisches Pressen) Strangpreßbolzen einer Wärmebehandlung unterworfen. Die Wärmebehandlung beeinflußt stark die Eigenschaften der durch das Granulatstrangpressen erhaltenen Produkte (12), (13). Neben der Umsetzung zu Al_4C_3 bewirkt die Wärmebehandlung auch eine geringe Erholung der durch das Mahlen stark verfestigten Granulate und kann auch zu geringer Rekristallisation sowie zu einer Vergröberung der Dispersoide führen. Die zuletzt genannten Prozesse verursachen eine Herabsetzung der Zugfestigkeit und eine gleichzeitige Verbesserung der Bruchdehnung.

Eingehende Untersuchungen haben einen interessanten Zusammenhang ergeben. Bis zur Vervollständigung der Bildung von Al_4C_3 nimmt sowohl die Zugfestigkeit als auch die Dehnung mit zunehmender Intensität der Wärmebehandlung (Dauer und Temperatur) zu. Weitere Wärmebehandlung führt zu einem Abfall der Zugfestigkeit und einem Anstieg der Dehnung, wobei sich R_m und A praktisch unabhängig von der Dispersoidmenge (Menge an eingemahlenem C) in einem R_m-A-Diagramm in einem schmalen Kurvenband bewegen (13) (Abb. 4). Spitzenwerte für Zugfestigkeit – bei niedriger Dehnung – werden erreicht, wenn die Al_4C_3-Umsetzung gerade erreicht ist, Erholungs- und Rekristallisationsprozesse aber

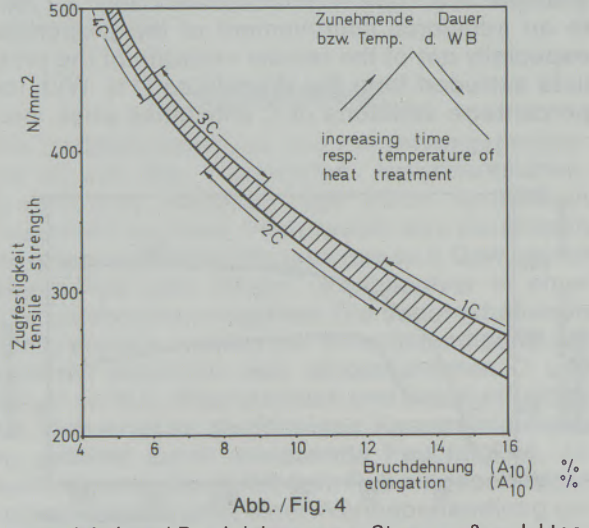

Abb./Fig. 4

Zugfestigkeit und Bruchdehnung von Strangpreßprodukten aus verschieden wärmebehandelten Granulaten mit verschiedenem C-Gehalt (Gew. % C)

Tensile strength and elongation of extruded products out of various heat treated granulates with varying C-contents (%/wt C)

far, as Al-powder, resp. the granulates are welded to the walls of the mill, the agitating arms and mill balls (11). By selecting the proper parameters – no excessive milling energy, good cooling of the mill, possibly additions of small quantities of milling additives, such as low-viscosity oil – it is possible to suppress this tendency to welding.

1.2 Heat treatment

In order to have the co-milled C completely react with the Al, the granulates, resp. the extrusion billets pressed from granulates (extrusion dies or isostatic presses) are subjected to a heat treatment. The heat treatment strongly influences the properties of the products obtained through granulate extrusion (12), (13). Aside from the reaction to Al_4C_3 the heat treatment also effects a slight recovery of the granulates strongly hardened by the milling, and may also lead to reduced recrystallization and coarsening of the dispersoids. These latter processes cause a lowering of the tensile strength and a simultaneous improvement of the elongation.

Intensive investigations have yielded an interesting connection. Until completion of the formation of Al_4C_3 as well the tensile strength as also the elongation increase with increasing intensity of the heat treatment (time and temperature). Further heat treatment leads to a decrease of the tensile strength and an increase of the elongation, whereby R_m and A remain practically independent on the quantity of dispersoid (quantity of co-milled C) in an R_m-A-diagram within a narrow band of curves (13) (fig. 4). Maximums of tensile strength – at lowest elongation – are reached, when the Al_4C_3-reaction just about is reached, however, recovery- and recrystallization processes are not very far progressed. By means of the intensity of the heat treatment, together with the quantity of C used, it is possible to obtain the wanted values of R_m, whereby the connection between R_m and A is always maintained.

For the Al-Al_4C_3-materials investigated, a heat treatments at temperatures from 550 to 600 °C for 1 to 3 hrs has been found as the optimum.

1.3 Compacting

Finally, the heat treated billets are compacted by extrusion, whereby incrased extrusion temperatures – depending on the percentage of dispersoid – of 450 to 550 °C are necessary. The extrusion process does not cause any major difficulties, it is possible to make very complicated profiles with very thin wall diameters (14). For good joining of the oxide charged granulate grains and for shearing of the oxide skins, extrusion ratios of >20:1 are necessary. Extrusion ratio and extrusion temperature influence the product properties only to a small extent. At lower extrusion temperature materials with somewhat higher

noch nicht sehr weit fortgeschritten sind. Durch die Intensität der Wärmebehandlung, zusammen mit der Menge an eingesetztem C, lassen sich gewünschte Werte für R_m einstellen, wobei aber der Zusammenhang zwischen R_m und A immer gewahrt bleibt.

Für die untersuchten Al-Al_4C_3-Werkstoffe haben sich Wärmebehandlungen von 1–3 Stunden bei Temperaturen von 550–600 °C als am günstigsten erwiesen.

1.3 Kompaktieren

Die wärmebehandelten Bolzen werden schließlich durch Strangpressen kompaktiert, wobei höhere Strangpreßtemperaturen, je nach dem Dispersoidgehalt, von 450–550 °C notwendig sind. Das Strangpressen macht keine wesentlichen Schwierigkeiten, und es gelingt, auch sehr komplizierte Profile mit sehr dünnen Wandstärken herzustellen (14). Zur guten Verbindung der oxidbehafteten Granulatkörner und zum Abscheren der Oxidhäute sind Strangpreßverhältnisse von >20:1 erforderlich. Strangpreßverhältnis und Strangpreßtemperatur beeinflussen die Eigenschaften der Produkte in nur untergeordnetem Ausmaß. Bei niedrigeren Strangpreßtemperaturen werden Materialien mit etwas höherer Zugfestigkeit, aber niedrigerer Dehnung erhalten, wobei noch ungeklärt ist (15), ob die bei niedrigerer Temperatur höheren Strangpreßkräfte eine Verfestigung bewirken, oder, ob durch das stärkere Aufheizen auf höhere Strangpreßtemperaturen schon eine gewisse Materialerholung im Granulat eintritt.

Da durch Strangpressen nur Profile erzeugt werden können, wurde auch das Pulverschmieden, mit dem direkt Formteile zu erhalten sind, versucht (16), (17), (18). Beim Pulverschmieden ist es jedoch schwierig, genügendes Abscheren der Oxidhäute zu erreichen, sodaß diese Variante wieder aufgegeben wurde.

Metallographische Untersuchungen, nur mehr elektronenoptisch möglich, zeigen ein sehr gleichmäßiges, feines Gefüge. Die Korngrößen bewegen sich im Bereich von etwa 0,2–1 μm, die recht gleichmäßig verteilten Dispersoidteilchen besitzen Teilchengrößen von etwa 0,02–0,1 μm (19), (20).

1.4 Nachverformen und Fügen

Die Strangpreßprodukte lassen sich ohne Schwierigkeiten nachverformen. Es gelingen das Walzen, das Schmieden und auch das Fließdrücken sowie ähnliche Verformungsverfahren. Die Verformung muß bei höheren Temperaturen, üblicherweise bei Temperaturen zwischen 500 und 550 °C, vorgenommen werden. Wegen der hohen Temperaturstabilität, die auch kurzzeitiges starkes Überhitzen der Werkstoffe bis zum Schmelzpunkt ohne Zusammenbrechen des speziellen Gefüges erlaubt, sind auch verschiedene

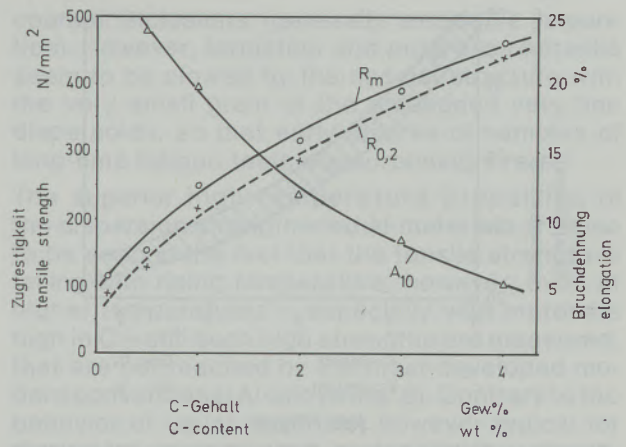

Abb./Fig. 5

Zugfestigkeit und Bruchdehnung von Strangpreßstangen aus 3^h bei 550 °C wärmebehandelten Granulaten mit verschiedenem C-Gehalt

Tensile strength and elongation of extruded rods out of granulates with varying C-content, heat treated for 3 hrs at 550 °C

tensile strength but with lower elongation are reached, whereby it is uncertain yet (15), whether the strengthening is caused by the higher extrusion force at lower temperature, or whether by stronger heating to higher extrusion temperatures already a certain material recovery in the granulate takes place.

Since it was possible to only produce profiles by extruding, it was tried to also apply powder forging that directly yields shapes (16), (17), (18). With powder forging, however, it is difficult to reach sufficient shearing of the oxide skins, so that this alternative was abandoned again.

Metallographic investigations – only possible by means of electron-optical methods – show a very even, fine structure. Grain sizes range from 0.2 to 1 μm, the quite evenly distributed dispersoid particles show particle sizes from about 0.02 to 0.1 μm (19), (20).

1.4 Secondary shaping and joining

The extrusion products may be subjected to secondary shaping without any difficulties. Rolling, forging, and also flow-pressing, as well as similar shaping techniques are possible. Shaping must be accomplished at elevated temperatures, usually at temperatures from 500 to 550 °C. Because of the high temperature stability that permits shorttime strong superheating of the materials up to the fusion point without collapse of the specific structure, also various welding methods are applicable, such as friction welding, electron-beam- and laser-beam-welding are possible. In trial runs it was possible to cast integral Al-Al_4C_3 shaped parts into Al-casting alloys obtaining good results.

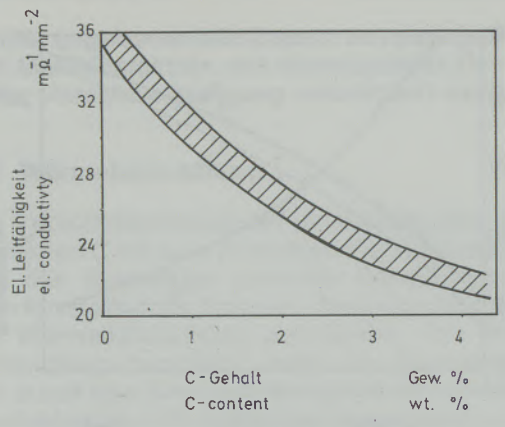

Abb./Fig. 6
Elektrische Leitfähigkeit von Al-C-Produkten in Abhängigkeit vom C-Gehalt
Electric conductivity of Al-C-products in dependance on their C-content

Schweißverfahren, wie Reibschweißen, Elektronenstrahl- und Laserstrahlschweißen, möglich. Versuchsweise gelingt auch das Eingießen von Al-Al_4C_3-Formteilen in Al-Gußlegierungen, wobei gute Verbindung erzielt wurde.

2. Eigenschaften

Die erzielbaren Eigenschaften der Al-Al_4C_3-Werkstoffe werden – ausreichendes Mahlen der Granulate und optimales Kompaktieren vorausgesetzt – vom C-Zusatz und von der Wärmebehandlung der Mahlprodukte vor dem Strangpressen bestimmt (14), (19), (21). Für Strangpreßprodukte aus 3 Stunden bei 550 °C wärmebehandelten Granulaten zeigt Abb. 5 die Abhängigkeit von Zugfestigkeit, Streckgrenze und Bruchdehnung, gemessen bei Raumtemperatur, vom C-Gehalt. Zugfestigkeit und Streckgrenze steigen mit zunehmendem C-Gehalt nahezu linear an, entsprechend fällt die Bruchdehnung ab. Für dispersionsgehärtete Werkstoffe typisch, wie ganz allgemein für Materialien im verfestigten Zustand, ist der hohe Wert für das Streckgrenze-/Zugfestigkeitsverhältnis von >0,9.

Die hohe Alterungsbeständigkeit der Produkte kommt darin zum Ausdruck, daß die Eigenschaften der Strangpreßprodukte selbst durch lange WB (gemessen bis 1000 Stunden) und bei Temperaturen bis 600 °C nur in unwesentlichem Ausmaß verändert werden. Die Abnahme an Zugfestigkeit liegt ebenso nur knapp außerhalb der Meßgenauigkeit, wie die Änderung in der Bruchdehnung.

Zunehmender Gehalt an Dispersoid bewirkt eine Herabsetzung der elektrischen Leitfähigkeit (Abb. 6), die aber selbst bei hohem Dispersoidgehalt, der sehr hohe Festigkeit der Werkstoffe bewirkt, noch relativ hoch ist. Ähnlich gutes Festigkeits-/Leitfähigkeitsverhältnis ist von handelsüblichen Al-Legierungen nicht bekannt.

Die Schlagfestigkeit nimmt mit zunehmendem C-Gehalt, der die erwähnte starke Verfesti-

2. Properties

Properties of Al-Al_4C_3-materials obtainable are determined by the C-additions and the heat treatment of the milling products prior to extrusion (14), (19), (21) – provided milling of the granulates is sufficient and compacting is optimal.

Fig. 5 shows the dependency of tensile strength, yield point and elongation, measured at room temperature on the C-content of extrusion products of granulates heat treated for 3 hrs at 550 °C. Tensile strength and yield point rise almost linear with increasing C-content, correspondingly, the elongation drops. The high value of >0.9 for the ratio of yield point/tensile strength is typical for dispersion strengthened materials, just like for all materials in general that are in a solidified state.

The high resistance against aging of the products is expressed in the fact that the properties of the extruded products are only infinitesimally changed even by very long heat treatment (measured up to 1000 hrs) and temperatures up to 600 °C. The reduction of the tensile strength is also just beyond the measuring accuracy, as the change of the elongation.

Increasing contents of dispersoid results in a reduction of the electrical conductivity (fig. 6), which is still relatively high at a high percentage of dispersoid that gives a very high strength of the materials. Comparable ratio of strength/conductivity is not known of Al-alloys that are on the market.

With increasing C-content that effects the high strengthening mentioned, the impact strength is reduced. Still, surprisingly good impact strength values of 6 (3% C) to 40 (1% C) J/cm^2 are measured (see fig. 10).

The fine and even structure of Al-Al_4C_3-materials also gives good long-time fatigue limit values (fig. 7). Ruptures exclusively start at

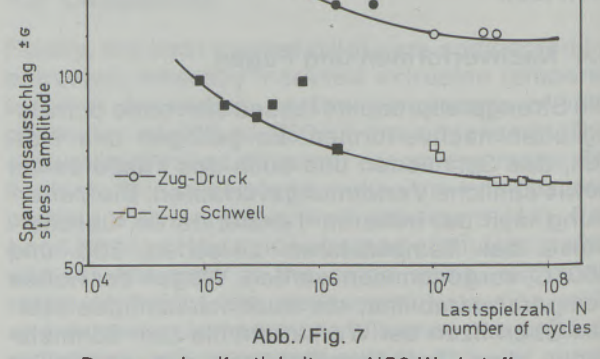

Abb./Fig. 7
Dauerwechselfestigkeit von AlC3-Werkstoffen
Longtime fatigue limit of AlC3 materials

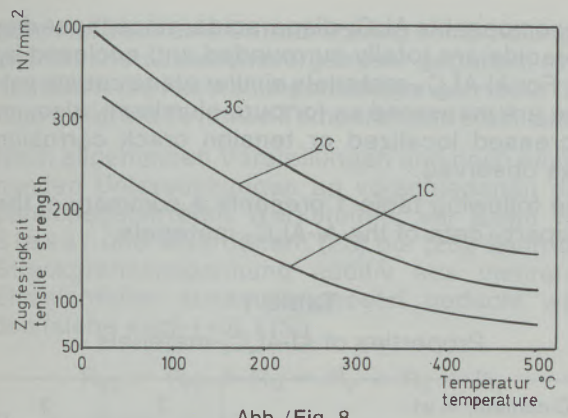

Abb./Fig. 8

Abhängigkeit der Zugfestigkeit von AlC-Werkstoffen mit verschiedenem C-Gehalt von der Temperatur

Dependance of the tensile strength of AlC-materials with varying C-content on the temperature

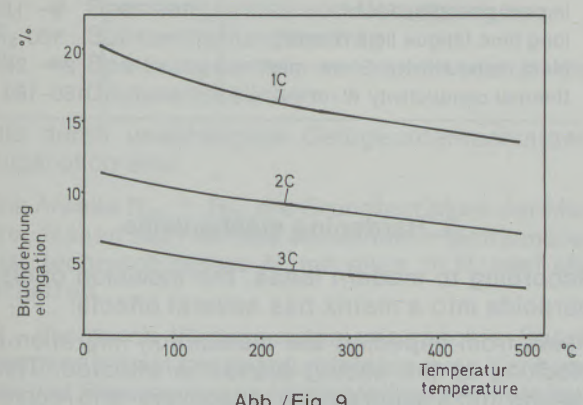

Abb./Fig. 9

Abhängigkeit der Bruchdehnung von AlC-Werkstoffen mit verschiedenem C-Gehalt von der Temperatur

Dependance of the elongation of AlC-materials with varying C-content on the temperature

gung bewirkt, ab. Es werden aber überraschend gute Schlagfestigkeitswerte von 6 (3% C) bis 40 (1% C) J/cm² gemessen (siehe Abb. 10).

Das feine, gleichmäßige Gefüge der Al-Al_4C_3-Werkstoffe gibt auch gute Dauerwechselfestigkeitswerte (Abb. 7). Brüche gehen ausschließlich von gröberen Einschlüssen (im allgemeinen vermeidbare Verunreinigungen) aus. Rißbildung und Rißfortschritt scheinen aber durch das spezielle Gefüge mit sehr kleinem Korn und den eingelagerten, sehr feinen Dispersoiden gehemmt, sodaß bei den Dauerwechselfestigkeitsmessungen vorzeitig versagende Proben überraschend selten sind.

Die überlegenen Hochtemperatureigenschaften der dispersionsgehärteten Al-Werkstoffe kommen darin zum Ausdruck, daß die Zugfestigkeit mit steigender Temperatur zwar abfällt, daß aber selbst bei höheren Temperaturen – vor allem bei Werkstoffen mit höherem C-Gehalt – noch hohe Festigkeiten gemessen werden, die auch durch die höchstentwickelten modernen konventionellen Al-Legierungen nicht erreicht

coarser inclusions (generally avoidable impurities). However, formation and progress of cracks seem to be slowed by the special structure with the very small grain of the embedded very fine dispersoids, so that early failures of samples of long-time fatigue tests are surprisingly rare.

The superior high temperature properties of the dispersion strengthened Al-materials are also to be seen in the fact that the tensile strength is falling with rising temperature, however, even at higher temperatures – especially with materials high in C – still such high strengths are measured, that are not reached by the most developed modern conventional Al-alloys (fig. 8). Contrary to the behavior of usual materials, however typical for dispersion strengthened materials, the elongation is falling with increasing temperature, despite a lowering of the strength (fig. 9). Still, a very significant increase of the impact strength with the temperature can be measured (fig. 10).

Despite of the fine structure, which favors it, the creep resistance is very good (fig. 11), since the deposited dispersoids retard the movement of the sliding planes. At room temperature, the creep resistance is very good, showing a factor of $n \approx 0.02$ ($n = -\log R\,(N/mm^2)/\log t\,(h)$). It decreases from room temperature to 200 °C, above that range the creep factor remains about constant ranging at appr. 0.04 to 0.05.

Corresponding with the high $R_{0.2}/R_m$-ratio with dispersion strengthened materials, the 0.2% creep limits are not substantially lower than the values of the creeping strength (22). As explained in (14), the creep resistance of a stronger Al-Al_4C_3-material (3% wt. C) at 500 °C, based on the same density of the materials, corresponds to about alloyed steels and exceeds that of pure-Ti and that of non-alloyed steels. It is only exceeded by high strength Ti-alloys.

Finally, it should be mentioned that the corrosion resistance of the matrix metal is practically not impaired by the inclusion of the water

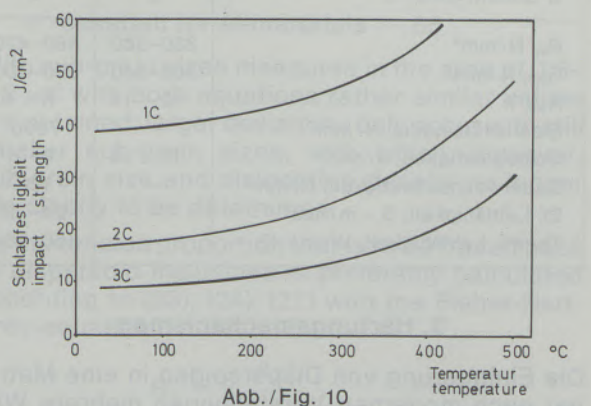

Abb./Fig. 10

Schlagfestigkeit von AlC-Werkstoffen mit verschiedenem C-Gehalt in Abhängigkeit von der Temperatur

Impact strength of AlC-materials with varying C-content in dependance on the temperature

werden (Abb. 8). Im Gegensatz zum Verhalten üblicher Werkstoffe, aber für dispersionsgehärtete Materialien typisch, fällt die Bruchdehnung mit steigender Temperatur, trotz der Erniedrigung der Festigkeit, ab (Abb. 9). Trotzdem wird ein sehr markanter Anstieg der Schlagfestigkeit mit der Temperatur gemessen (Abb. 10).

Die Kriechbeständigkeit ist trotz des feinen Gefüges, das das Kriechen begünstigt, sehr gut (Abb. 11), weil die eingelagerten Dispersoide eine Hemmung der Gleitebenenbewegung bewirkt. Bei Raumtemperatur ist die Kriechbeständigkeit mit einem Kriechfaktor von $n \approx 0{,}02$ ($n = -\log R\ (N/mm^2)/\log t\ (h)$) sehr gut. Sie nimmt zwischen Raumtemperatur und 200 °C ab, darüber bleibt der Kriechfaktor mit ca. 0,04–0,05 etwa gleich.

Die 0,2% Kriechgrenzen sind, entsprechend dem hohen $R_{0,2}/R_m$-Verhältnis bei den dispersionsverfestigten Werkstoffen, nicht wesentlich geringer als die Werte für die Zeitstandfestigkeit (22). Wie in (14) ausgeführt, entspricht die Kriechbeständigkeit eines festeren Al-Al_4C_3-Werkstoffes (3 Gew.-% C) bei 500 °C, wenn auf gleiche Werkstoffdichte bezogen, etwa der von legierten Stählen und übertrifft die von Rein-Ti und die von unlegierten Stählen. Sie wird lediglich von hochfesten Ti-Legierungen übertroffen.

Schließlich ist noch zu erwähnen, daß die Korrosionsbeständigkeit des Matrixmetalles durch die Einlagerung der wasserzersetzlichen Al_4C_3-Dispersoide praktisch nicht beeinträchtigt wird, da die Dispersoide allseitig von Al eingeschlossen sind. Bei den Al-Al_4C_3-Werkstoffen werden ähnliche Flächenabtragungswerte wie bei Rein-Al gemessen, es wird auch keine erhöhte Lochfraß- oder Spannungsriß-Korrosionsanfälligkeit beobachtet.

Folgende Tabelle 1 bringt eine Zusammenfassung der Eigenschaftswerte der Al-Al_4C_3-Werkstoffe.

Tabelle 1

Eigenschaften von Al-Al_4C_3-Werkstoffen

C-Gehalt, Gew.-%	2	3
R_m, N/mm²	320–360	380–420
$R_{0,2}$, N/mm²	300–340	350–400
A_{10}, %	12– 14	8– 10
Elastizitätsmodul, N/mm²	–	7000
Schlagfestigkeit, J/cm²	16– 19	9– 11
Dauerwechselfestigkeit, N/mm²	–	120
El. Leitfähigkeit, S · m/mm²	–	24– 25
Therm. Leitfähigkeit, W/m · K	–	150–160

3. Härtungsmechanismen

Die Einlagerung von Dispersoiden in eine Matrix hat nach modernen Vorstellungen mehrere Wirkungen:

Neben einer Behinderung des Versetzungswanderns wird eine Gleitebenenblockierung erreicht.

decomposable Al_4C_3-dispersoids, since these dispersoids are totally surrounded and enclosed by Al. For Al-Al_4C_3-materials similar plane cutting values are measured as for pure aluminum, also, no increased localized or tension crack corrosion was observed.

The following table 1 presents a summary of the property data of the Al-Al_4C_3-materials.

Table 1

Properties of Al-Al_4C_3-materials

C-content, % wt.	2	3
R_m, N/mm²	320–360	380–420
$R_{0,2}$, N/mm²	300–340	350–400
A_{10}, %	12– 14	8– 10
modulus of elasticity, N/mm²	–	7000
impact strength, J/cm²	16– 19	9– 11
long time fatigue limit N/mm²	–	120
elect. conductivity, S · m/mm²	–	24– 25
thermal conductivity W/m · K	–	150–160

3. Hardening mechanisms

According to modern ideas, the inclusion of dispersoids into a matrix has several effects:

Aside from impeding the dislocation migration a blocking of the sliding planes is effected. This results into a suppression of recovery- and recrystallization-processes, hand the fine structure caused by the conditions of the manufacture remains stabilized up to high temperatures.

According to general understanding and after extensive investigation of various dispersion strengthened materials – especially by Slesar

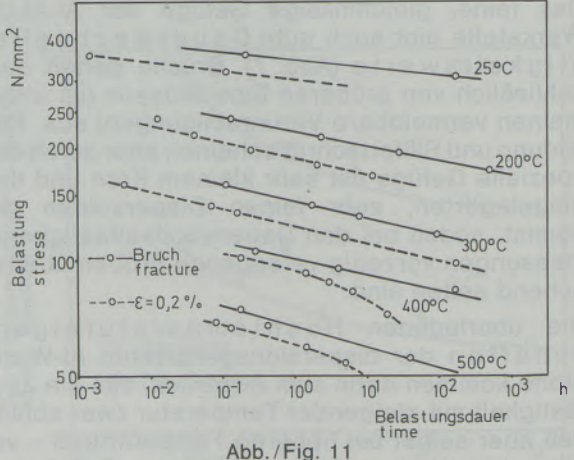

Abb./Fig. 11

Zeitstandbruch- und 0,2% Zeitstanddehnlinien von AlC3 bei verschiedenen Temperaturen

Extended time fracture- and 0.2% extended time elongation graphs of AlC3 at various temperatures

Damit ist auch eine Unterdrückung von Erholungs- und Rekristallisationsvorgängen gegeben, und das durch die Herstellungsbedingungen feine Gefüge bleibt bis zu hohen Temperaturen stabilisiert.

Nach allgemeinen Vorstellungen und nach eingehenden Untersuchungen an verschiedenen dispersionsgehärteten Werkstoffen, vor allem von Slesar und Mitarbeitern (23) bis (26), kann die Streckgrenzenspannung additiv aus mehreren Einzelanteilen zusammengesetzt gedacht werden (siehe auch (10), (15))

$$R_{0,2} = R_{PN} + R_M = R_V + R_S + R_T$$

$R_{0,2}$ = Streckgrenze
R_{PN} = kritische Schubspannung des reinen Matrixmetalles, Peierls-Nabarro-Spannung
R_M = Anteil der durch Mischkristallverfestigung eintretenden Spannungserhöhung
R_V = Spannungsanteil von Versetzungen
R_S = Subkornhärtungsbeitrag
R_T = Spannungsanteil, verursacht durch die Dispersoidteilchen

die durch unabhängige Gefügeuntersuchungen zugänglich sind.

Die Anteile $R_{PN} + R_M$, die Grundfestigkeit der Matrix, lassen sich für das verwendete Matrixmaterial, technisch reines Al, mit etwa 15 N/mm² abschätzen.

R_V, der durch Versetzungen verursachte Spannungsanteil, ist bei den durch intensives Vermahlen und Strangpressen hergestellten Werkstoffen relativ hoch. Er läßt sich aus der durch elektronenoptische Messungen aus dem Polygonisierungsgrad der Subkörner abgeschätzten Versetzungsdichte errechnen:

$$R_V = 2\alpha Gb\varrho_v^{1/2}$$

α = Festigkeit des Versetzungsnetzes, ca. 0,3
G = Schubmodul, ca. 27.000 N/mm²
b = Burges-Vektor, ca. 2,8 · 10^{-7} mm
ϱ_v = Versetzungsdichte, cm^{-2}

R_S, der Subkornhärtungsbeitrag, ergibt sich aus der elektronenoptisch an Folien zu messenden Subkorngröße nach Langford-Cohen:

$$R_S = 6\ G\ b\ d^{-1}$$

d = Subkorn- bzw. Zellgröße

bzw. nach der Hall-Petch-Beziehung

$$R_S = k\ d^{-1/2}$$

k = Konstante, für Al-Werkstoffe = 65

Bei den gemessenen Subkorngrößen im Bereich von 0,3–0,8 μm erhält man mit beiden Gleichungen etwa ähnliche Werte; größere Abweichungen ergeben sich nur bei noch kleineren Subkorngrößen, bei denen allerdings Subkorngröße und Versetzungsdichte nicht mehr eindeutig zu bestimmen sind.

R_T, der Spannungsanteil, der auf die Dispersoideinlagerungen zurückzuführen ist, wird nach (23), and coworkers (23)–(26) – the yield strength tension may be considered additively composed by several single parameters (also see (10), (15)).

$$R_{0.2} = R_{PN} + R_M + R_V + R_S + R_T$$

$R_{0.2}$ = yield strength
R_{PN} = critical shear stress of the pure matrix metal, Peierls-Nabarro tension
R_M = Percentage of tension increase caused by mixcrystal solidification
R_V = Percentage of tension caused by dislocation
R_S = Contribution by subgrain hardening
R_T = Percentage of tension caused by dispersoid particles

that are accessible to independent investigations of the micro-structure.

The percentages of $R_{PN} + R_M$, the basic strength of the matrix, may be assumed with appr. 15 N/mm² for the matrix material used, which is technically pure aluminum.

R_V, the proportion of tension caused by dislocation is relatively high with materials that have been processed by intensive milling and extrusion. It may be calculated from the degree of polygonizing of the sub-grains, permitting an estimated density of dislocation, measured by electron-optical methods:

$$R_V = 2\ \alpha\ Gb\ \varrho_v^{1/2}$$

α = strength of the dislocation grid, appr. 0.3
G = modulus of shear, appr. 27.000 N/mm²
b = Burges vector, appr. 2.8 · 10^{-7} mm
ϱ_v = density of dislocation

R_S, the proportion of sub-grain strengthening contribution is derived from the sub-grain size, measured by electron optics at foils according to Langford-Cohen:

$$R_S = 6\ G\ b\ d^{-1}$$

d = size of sub-grain, resp. cell

or following the Hall-Petch relation

$$R_S = k\ d^{-1/2}$$

k = constant for Al-materials = 65

With sub-grain sizes measured in the area of 0.3–0.8 μm with both equations rather similar values are obtained; larger deviations only occur with still smaller sub-grain sizes, with which, however, sub-grain size and dislocation density no longer are clearly to be determined.

R_t, the tension proportion that is to be traced back to dispersoid inclusions is preferably calculated according to (23), (24), (27) with the Fisher-Hart-Prey-equation:

$$R_T = k\ \frac{f^{3/2}}{r}$$

k = constant = 115
f = volume percentage of dispersoid
r = mean particle radius of dispersoids, μm

(24), (27) am besten durch die Fisher-Hart-Prey-Gleichung:

$$R_T = k \frac{f^{3/2}}{r}$$

k = Konstante = 115
f = Volumenanteil Dispersoid
r = mittlerer Teilchenradius der Dispersoide, μm

errechnet. Verfestigend wirken allerdings nur Teilchen einer bestimmten Größenkategorie von etwa 0,02–0,2 μm. Teilchen mit Größen zwischen 0,2–1,5 μm, die ebenso wie geringe Anteile noch größerer Teilchen in den dispersionsgehärteten Werkstoffen zu finden sind, haben keine verfestigende Wirkung. Die groben Teilchen verschlechtern im Gegenteil durch Bildung von Spannungsspitzen bei Belastungen z. T. stark die Plastizität.

Die Abschätzungen der Streckgrenze von Al-Al_4C_3-Werkstoffen mit verschiedenem C-Gehalt (Volumenanteil Dispersoid) aus den Meßwerten für Versetzungsdichten, Subkorngrößen, Volumenanteile und mittlere Korngrößen der Dispersoidteilchen ergaben bei verschiedenen Untersuchungen überraschend gute Übereinstimmung (10), (24), (25) (Abb. 12).

Die Untersuchungen ergaben weiter, daß der experimentell beobachtete Einfluß der Wärmebehandlung und der Strangpreßbedingungen auf die Festigkeitseigenschaften auf Gefügeänderungen des Werkstoffes zurückzuführen ist, wobei in erster Linie geringe Erholungs- und Rekristallisationserscheinungen eine Rolle spielen, die Korngrößen der Dispersoidteilchen aber auch bei längerer Wärmebehandlung unverändert erscheinen.

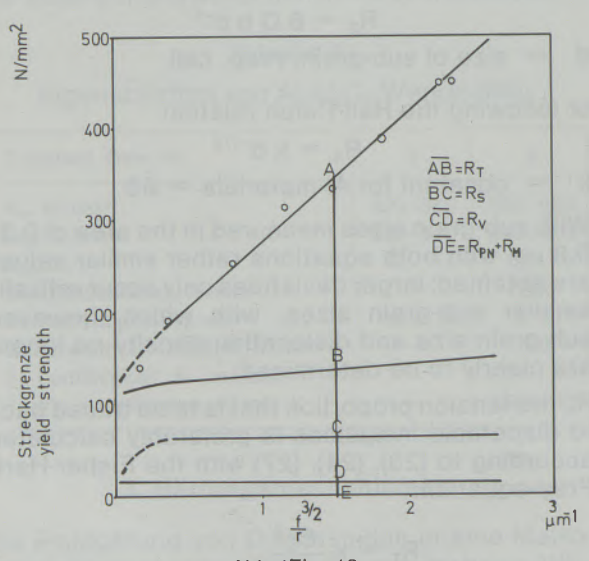

Abb./Fig. 12

Streckgrenze von AlC-Werkstoffen in Abhängigkeit von den Gefügeparametern

Yield strength of AlC-materials in dependance on the parameters of microstructure

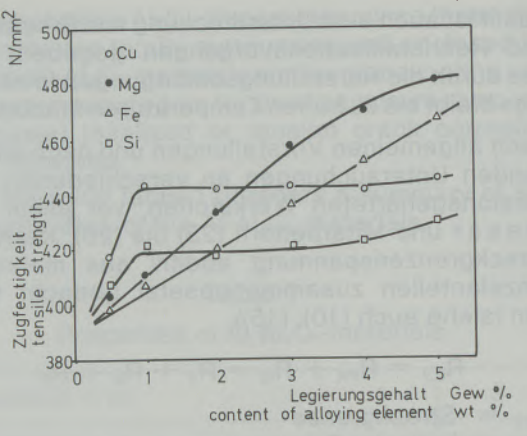

Abb./Fig. 13

Zugfestigkeit von AlC2-Werkstoffen mit Legierungsmatrix in Abhängigkeit vom Gehalt an Legierungsmetallen

Tensile strength of AlC2-materials with alloying matrix in dependance on content of alloying metals

Only particles of a certain size ranging from appr. 0.02 to 0.2 μm are strength generating. Particles with sizes ranging from 0.2 to 1.5 μm, that are found together with small proportions of still bigger particles in dispersion strengthened materials, do not show strength generating properties. Contrary, the coarse particles reduce – sometimes strongly – the plasticity by formation of tension peaks under load.

Rating of the yield strength of Al-Al_4C_3-materials with varying C-content (volume percentage of dispersoid) according to the data of displacement densities, sub-grain sizes, volume percentage and mean grain sizes of dispersoids gave a surprisingly good conformity with various investigations (10), (24), (25) (fig. 12).

Another result of the investigations was that it could be seen that the experimentally observed influence of the heat treatment and the conditions of extrusion on the strength properties can be traced back to the changes in micro-structure of the material, whereby primarily minor phenomena of recovery and recrystallization play a role, while the grain sizes of the dispersoid particles remain unchanged also after extended heat treatment.

The theoretical considerations also have a practical effect. They permit judging of the possibilities to improve the materials. According to the electron-optical measurements, in the materials there still are larger, mainly coarser particles that in the first place deteriorate the plasticity – in the first place aluminides – first of all $FeAl_3$, also dispersoid-agglomerates, however also residual non-reacted co-milled C (27). More complete reaction and better distribution of the dispersoids could still further increase the strength and the elongation at equal dispersoid contents. From theory the possibility may be derived that an additional increase of strength may be reached by using a matrix that is strengthened by mix-crystals.

Die theoretischen Überlegungen haben auch praktische Bedeutung. Sie lassen Möglichkeiten zur Verbesserung der Werkstoffe abschätzen. In den Werkstoffen sind nach den elektronenoptischen Messungen noch größere, hauptsächlich die Plastizität verschlechternde gröbere Teilchen, in erster Linie Aluminide, vor allem $FeAl_3$, daneben Dispersoidagglomerate, aber auch Reste von nicht ungesetztem, eingemahlenem C zu finden (27). Vollständigere Umsetzung und bessere Verteilung der Dispersoide könnten die Festigkeit bei gleichem Dispersoidgehalt noch weiter steigern und auch die Bruchdehnung verbessern. Aus der Theorie geht auch die Möglichkeit hervor, eine weitere Festigkeitssteigerung durch Verwendung einer mischkristallverfestigten Matrix zu erreichen.

4. Dispersionsgehärtete Al-Legierungen

Ganz in Übereinstimmung mit den erwähnten Überlegungen werden durch Zulegieren von Legierungselementen – anstelle von Rein-Al-Pulver bzw. Mischungen von Legierungspulvern (AlMg5, AlFe5, AlCu33, AlSi12) mit entsprechenden Mengen an Rein-Al-Pulver, die sich beim Intensivvermahlen, „mechanisches Legieren", bis zum atomaren Bereich mischen (u. a. 7) – z. T. beträchtliche Festigkeitssteigerungen erreicht (Abb. 13) (21), (28), (29).

Aus der Abb. 13 geht hervor, daß die verfestigende Wirkung von steigenden Legierungselementzusätzen etwa bei der Löslichkeitsgrenze aufhört, d. h., daß tatsächlich nur der Anteil R_M erhöht wird und der sich als gröbere intermetallische Verbindungen mit Al ausscheidende überschüssige Anteil an Legierungszusätzen praktisch keine Festigkeitssteigerung bringt. Der scheinbar widersprüchliche, in etwa lineare Festigkeitszuwachs mit steigendem Fe-Gehalt ist durch die Feinheit der vorliegenden $FeAl_3$-Teilchen zu erklären. Fe wurde in Form einer gesprühten AlFe5-Legierung eingeführt, in der das Fe nach elektronenoptischen Aufnahmen zum großen Teil noch metastabil gelöst vorlag (30). Die bei der Verarbeitung der Granulate zu Strangpreßprodukten entstehenden $FeAl_3$-Teilchen sind sehr fein und zum großen Teil dispersionsverfestigungswirksam, und sie altern (Kornvergröberung), wie Untersuchungen gezeigt haben, in Gegenwart von Al_4C_3-Dispersoiden nur außerordentlich langsam. $CuAl_2$-Teilchen bzw. elementare Si-Teilchen liegen dagegen in gröberer Form vor.

Dispersionshärtung und die gerade bei Al-Werkstoffen häufig angewendete Ausscheidungshärtung sind nur zum Teil additiv, da das feine Gefüge und die hohe Versetzungsdichte, die bei der Auslagerungsbehandlung entstehen und im wesentlichen die Festigkeitssteigerung bewirken, bei den dispersionsverfestigten Werkstoffen schon vorliegen. Gegenüber dispersionsverfestigten Werkstoffen mit Rein-Al-Matrix kommen

4. Dispersion strengthened Al-alloys

Fully in accordance with the considerations mentioned, it is possible to reach partially considerably higher strengths by alloying with alloying elements – instead of pure Al-powder, resp. mixtures of alloying powders (AlMg5, AlFe5, AlCu33, AlSi12) with corresponding quantities of pure-Al-powder that mix themselves during intensive-milling ("mechanical alloying") down to atomary levels (among others 7) (fig. 13) (21), (28), (29).

From fig. 13 it can be seen that the strengthening effect of increasing alloying element additions about ends at the limit of solubility, i.e. that actually only the proportion of R_M is increased and the excess part of alloying additions precipitate as coarser inter-metallic compounds with Al, practically yielding no increase in strength. The apparently contradictional, about linear increase in strength with increasing Fe-content may be explained by the fineness of the $FeAl_3$ particles present. Fe was introduced as a sprayed AlFe5-alloy, in which – according to electron-optical investigation – Fe was present to a large extent metastably dissolved (30). The $FeAl_3$-particles developing during processing of the granulates to extruded products are very fine and to a large extent dispersion strengthening effective and they age (grain coarsening) extremely slowly in presence of Al_4C_3 dispersoids, as has been shown by the investigations. $CuAl_2$-particles, resp. elemental Si-particles, however, are present in coarser form.

Dispersion strengthening and the precipitation strengthening frequently applied to Al-materials are only partially additive, since the fine microstructure and the high dislocation density that develop during precipitation treatment resulting mainly in an increase of strength are already prevailing in dispersion strengthened materials.

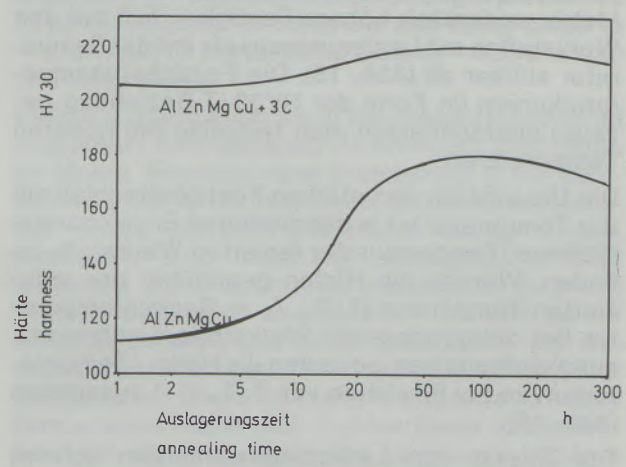

Abb./Fig. 14

Härte einer ausscheidungshärtbaren Legierung mit und ohne Al_4C_3-Dispersoidgehalt in Abhängigkeit von der Auslagerungszeit (120 °C)

Hardness of an alloy apt for precipitation strengthening with and without Al_4C_3-dispersoid-content in dependance on aging time (120 °C)

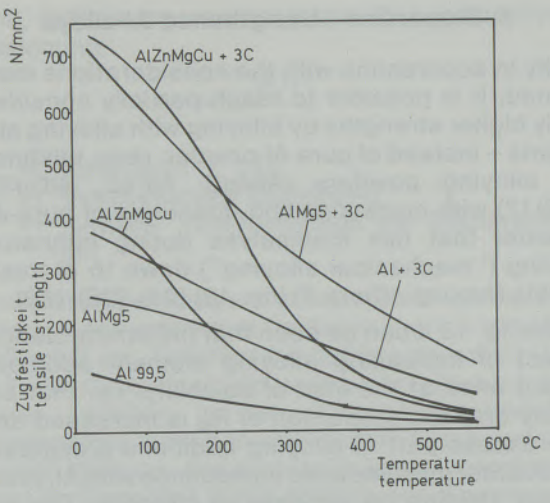

Abb./Fig. 15

Zugfestigkeit von mit 3 Gew. % C gehärteten Al-Legierungen in Abhängigkeit von der Temperatur

Tensile strength of Al-alloys strengthened with 3%/wt C in dependance on the temperature

bei gleichzeitig ausscheidungsverfestigten Materialien nur der Mischkristallverfestigungsanteil und eine durch die Ausscheidungen bedingte Erhöhung des Dispersoidteilchenanteiles zum Tragen. Ausscheidungshärtbare dispersionsverfestigte Werkstoffe sind daher auch im lösungsgeglühten Zustand schon fest, und durch die Auslagerung tritt nur mehr eine bescheidene weitere Verfestigung ein (Abb. 14). Eine wesentliche Hemmung der Ausscheidungs- und Überalterungsvorgänge durch die Anwesenheit von Al_4C_3-Dispersoid konnte nicht beobachtet werden.

Die Legierungszusätze beeinflussen aber die Warmfestigkeitseigenschaften. Die bei Normaltemperatur gegenüber Materialien mit Rein-Al-Matrix wesentlich höhere Festigkeit fällt bei den Werkstoffen mit Legierungszusatz mit der Temperatur stärker ab (Abb. 15). Die Festigkeitstemperaturkurven (in Form der HV30/T-Beziehung gezeigt) überschneiden sich teilweise bei höheren Temperaturen.

Die Ursache für den starken Festigkeitsabfall mit der Temperatur ist in der niedrigen Erweichungs-(Solidus-)Temperatur der legierten Werkstoffe zu finden. Werden die Härten gegenüber der reduzierten Temperatur (T/T_S; T_S = Solidustemperatur bei entsprechender Werkstoffzusammensetzung) aufgetragen, so laufen die Härte-/Temperaturkurven bei Erreichen von $T/T_S = 1$ zusammen (Abb. 16).

Der Zusatz von Legierungselementen scheint also bei dispersionsverfestigten Al-Werkstoffen, wenn gute Hochtemperaturfestigkeitseigenschaften angestrebt werden, eher eine Verschlechterung zu bewirken. Sinnvoll scheinen Legierungszusätze dann, wenn durch die eventuelle Verbesserung anderer Eigenschaften, z. B. der Zähig-

Compared to dispersion strengthened materials with pure-Al-matrix, with simultaneously precipitation strengthened materials only the proportion of mix-crystal-strengthening and an increase of the proportion of dispersoid-particles caused by the precipitation becomes effective. Precipitation hardenable, dispersion strengthened materials therefore already are strengthened in solution heat treated state, and by precipitation only a modest additional strengthening takes place (fig. 14). It was not possible to observe any considerable slowing of the precipitation or aging processes on account of the presence of Al_4C_3-dispersoid.

The alloying additions however influence the hot strength properties. The strength at normal temperatures compared to materials with pure-Al-matrix that is much higher, more strongly decreases with increasing temperature with materials with alloying additions (fig. 15). The strength-temperature-graphs (expressed as the HV30/T-relation) partially cross at elevated temperatures.

The reason for the strong loss in strength with rising temperature is to be found in the low softening-(solidus-)temperature of the alloyed materials. If the hardness is plotted against the reduced temperature (T/T_S; T_S = solidus temperature at corresponding composition of material), the hardness/temperature graphs converge upon reaching $T/T_S = 1$ (fig. 16).

Addition of alloying elements therefore seems to be rather detrimental for dispersion strengthened Al-materials when good high-temperature

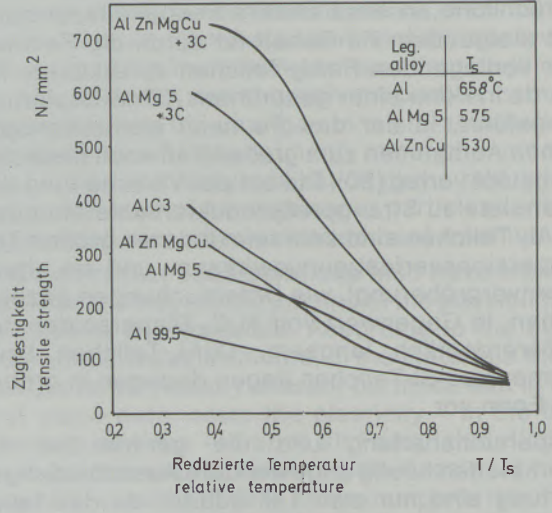

Abb./Fig. 16

Zugfestigkeit von mit 3 Gew. % C gehärteten Al-Legierungen aufgetragen über der reduzierten Temperatur (T/T_S; T_S = Solidustemperatur)

Tensile strength of Al-alloys strengthened with 3%/wt C plotted over the reduced temperature (T/T_S; T_S = solidus temperature)

keit, der Verschleißbeständigkeit u. a., die nachteilige Herabsetzung der Hochtemperatureigenschaften kompensiert wird. Interessant ist ein Zusatz auch in Fällen, in denen bei hohen Festigkeiten bei mäßigen Temperaturen eine Hochtemperaturbeständigkeit bei kurzfristiger Überhitzung gefordert wird, oder in Fällen, in denen spezielle Konstruktionsteile sowohl extrem hohe Festigkeiten bei niedrigerer als auch hohe Festigkeiten bei erhöhter Temperatur haben müssen (z. B. im Automobilbau, bei Turbinenscheiben).

5. Anwendungen

Die interessanten Eigenschaften der dispersionsgehärteten Al-Werkstoffe eröffnen diesem Material verschiedene Anwendungsmöglichkeiten, die über die heutige Verwendung von Al-Legierungen weit hinausgehen. Schon während der Entwicklung des SAP-Metalles wurden diese interessanten Anwendungsgebiete aufgezeigt. Die Einführung des SAP-Metalles ist nicht an mangelnden Eigenschaften gescheitert, sondern an dem durch die sehr komplizierte Herstellungstechnik und den großen Ausschuß verursachten hohen Preis. Das neue Herstellungsverfahren erlaubt entsprechend niedrige Preise, so daß eine rasche Einführung der Werkstoffe in die Technik erwartet werden kann. Schon jetzt besteht eine Erzeugungskapazität von 50 jato für Al-Al_4C_3-Granulate verschiedener Qualität (Fa. Eckart, BRD), und es werden verschiedenste Strangpreßprofile im Pilot-Maßstab (Fa. Erbslöh, BRD) hergestellt (14), (31).

Mögliche Anwendungen gehen aus den in dieser Arbeit beschriebenen speziellen Eigenschaften hervor. In erster Linie scheinen die Materialien für Anwendungen bei Temperaturen zwischen 350 und 550 °C interessant. In diesem Bereich sind sie in den Festigkeitseigenschaften allen handelsüblichen Al-Werkstoffen deutlich überlegen und kommen – wenn auf die Werkstoffdichte bezogen wird – Ti und Stählen zumindest nahe.

Anwendungsgebiete für in der Zwischenzeit auch von Fa. Novamet angebotene ähnliche dispersionsgehärtete Al-Werkstoffe (32) eröffnen sich im Automobilbau für wärmebeanspruchte Teile, z. B. für Zylinderköpfe, Kolben und Kolbenböden – hier scheinen besonders auch dispersionsgehärtete AlSi-Werkstoffe wegen ihres geringen thermischen Ausdehnungskoeffizienten interessant – sowie für Abgasturbinen und Kompressoren (14). Im Flugzeugbau sind die Werkstoffe für Konstruktionsteile im Gespräch, die hohen Temperaturbelastungen ausgesetzt sind (33). Weitere Anwendungsgebiete werden sich zeigen, wenn der Konstrukteur mit der Tatsache vertraut sein wird, daß die dispersionsgehärteten Al-Werkstoffe die Grenzen der Eigenschaften der üblichen Al-Werkstoffe weit sprengen und daß gewissermaßen ein „neuer" Werkstoff mit bisher noch nicht bewußt gewordenen Eigenschaftspotentialen vorliegt.

strength properties are strived for. Alloying additions seem meaningful only then, when by a probable improvement of other properties, e.g. of the toughness, or the wear-resistance, or others, the detrimental reduction of the hot strength properties is compensated. Addition also is interesting in such cases, where with high strengths at moderate temperatures high temperature strength during short time overheating is required, or in cases, where special parts of construction require extremely high strengths as well at low, as also high strengths at increased temperatures (e.g. automotive industry, turbine discs).

5. Applications

The interesting properties of dispersion strengthened Al-materials provide for this material various fields of application, that reach far beyond the presentday use of Al-alloys. Already during the development of the SAP-metal those interesting properties were indicated. The introduction of SAP-metal did not fail because of lack of the right properties, but because of the high price caused by the very complicated manufacturing technique and the large quantity of scrap. The new manufacturing process permits correspondingly low prices, so that a soon acceptance of these materials by technical application may be anticipated. Already now there exists a manufacturing capacity of 50 tpa for Al-Al_4C_3-granulates of varying grades (Mssrs. Eckart, GFR) and a variety of extruded profiles are produced on a pilot scale (Mssrs. Erbslöh, GFR) (14), (31).

Possible applications develop out of the special properties described in this paper. In the first place, the materials seem interesting for applications at temperatures from 350 to 550 °C. In this area they are superior in their strength properties to all commercial Al-materials and come close to – if referred to the material density – rather close to Ti and steels.

Fields of application for in the meanwhile offered dispersion strengthened Al-materials (32) made by Mssrs. Novamet open themselves in the automotive industry for heat stressed parts, e.g. cylinder heads, pistons, and piston heads – here, especially also dispersion strengthened AlSi-materials seem interesting because of their low thermal expansion coefficient – as well as for exhaust turbines and compressors (14). For aircraft construction, the materials are discussed for construction elements that are exposed to heavy temperature loads (33). Further fields of application will show up, once the designers become familiar with the fact that the dispersion strengthened Al-materials widely open up the limits given by the usual Al-materials and that – so to speak – a "new" material with to-day not yet made concious potentials of properties has become available.

Literaturverzeichnis / References

1. Schmid, E.: DRP 425451 und 425452 (**1926**).
2. Irmann, R.: Technische Rundschau (Bern) 41 (**1949**), S. 36.
3. Zeerleder, A. v.: Z. Metallk. 41 (**1950**), S. 228.
4. Zeerleder, A. v.: Z. Metallk. 46 (**1955**), S. 809.
5. Rühle, M.: Metall 38 (**1982**), S. 1280; 39 (**1983**), S. 519, 707.
6. Benjamin, J. St.: DBP 1909781 (**1970**).
7. Benjamin, J. St.: Met. Trans. 1 (**1970**), S. 2943.
8. Jangg, G., F. Kutner: Aluminium 51 (**1975**), S. 641.
9. Jangg, G., G. Korb, F. Kutner: VI. Int. Leichtmetalltagung Leoben, Berichtsbd. S. 61, Al-Verlag Düsseldorf **1976**.
10. Schalunov, J., M. Slesar, M. Besterci, H. Oppenheim und G. Jangg: Metall, im Druck.
11. Oppenheim, H., G. Jangg: Z. Werkstofft. 14 (**1983**), S. 179.
12. Lowschenko, F., F. Kutner, G. Jangg: Planseeb. f. Pulvermet. 25 (**1977**), S. 205.
13. Vasgyura, H.: Diss. TU Wien, **1986.**
14. Arnhold, V., J. Baumgarten: Powder Met. Int. 17 (**1985**), S. 168.
15. Slesar, M., M. Besterci, G. Jangg, H. Oppenheim: in Vorbereitung.
16. Jangg, G., W. J. Huppmann: Mod. Dev. in Powder Met. vol 14 (**1981**), S. 419.
17. Jangg, G., W. J. Huppmann: Ind. Heating (**1981**), S. 20.
18. Jangg, G., F. Kutner, W. J. Huppmann: 7. Int. Leichtmetalltagung, Leoben, Vortragsbd. **1981**, S. 240.
19. Jangg, G., F. Kutner, G. Korb: Powder Met. Ing. 9 (**1977**), S. 24.
20. Stolz, W., G. Jangg, R. Stickler: Prakt. Metallographie, Sonderbd. 6, S. 182, Dr. Riederer-Verlag, Stuttgart **1976**.
21. Korb, G., G. Jangg, F. Kutner: Draht 30 (**1979**), S. 318.
22. Kubasta, E.: 5. Int. Conf. Strength of Metals and Alloys, Vol. 3, S. 1687. Pergamon Press. Oxford **1979**.
23. Besterci, M., M. Slesar: Mittlg. des Inst. f. Pulvermetallurgie Sumperk, Bd. 1, **1983**; Sumperk, ČSSR.
24. Slesar, M., G. Jangg, M. Besterci, M. Durisin: 7. Int. Leichtmetallg. Leoben, **1981**, Berichtsb. S. 240.
25. Besterci, M., M. Slesar et al.: Int. PM-Conf. Brno **1982**, Tagungsband, S. 205.
26. Slesar, M., K. E. Easterling, M. Besterci, B. Bengtsson: V. Int. Verbundwerkstofftg. Smolenice **1983**, Tagungsband, S. 281.
27. Besterci, M., M. Slesar, M. Orolinova, G. Jangg: V. Int. Verbundwerkstofftg. Smolenice **1983**, Tagungsbd., S. 291.
28. Oppenheim, H., G. Jangg: in Vorbereitung.
29. Benjamin, J. S., R. D. Schelling: Met. Trans. A. 12a (**1981**), S. 1827.
30. Jangg, G., F. Kutner, G. Korb, F. Feher: Metall 29 (**1975**), S. 1014.
31. Fa. Krebsöge und Erbslöh-Aluminium: Firmenprospekte „Dispal".
32. Fa. Novamet: Firmenprospekte.
33. Erich, D. L., St. J. Donachie: Metal Progress (**1982**), S. 22.

Lebensdauervorhersage für hochfeste metallische Werkstoffe bei höheren Temperaturen

Robert Danzer*) und Friedwin Sturm**), Leoben

Dedicated to the 80th birthday of Prof. Dr. Franz Lihl

Bei der Lebensdauervorhersage im Bereich der Niedriglastwechselermüdung (LCF) hochfester Materialien bei hohen Temperaturen ist sowohl die Kriechschädigung (zeitabhängige Schädigung) als auch die Ermüdungsschädigung zu berücksichtigen. Nach Einführung des Dehnratenverhältnisses r ergibt sich für die Akkumulation der relativ zeitabhängigen Schädigung eine Lebensdauerregel (RTD-Regel) mit einem anpaßbaren Parameter ν. Eine Auswertung der LCF-Daten der Superlegierungen PM Astroloy, Waspaloy, MAR M 509 und In 738 LC zeigt, daß die RTD-Regel im Bereich zwischen reinem Kriechen ($r = 1$) und reiner Ermüdung ($r > 10^6$) eingesetzt werden kann. Die bei der Extrapolation auf unterschiedliche Beanspruchungsbedingungen auftretenden Streuungen sind in der Größenordnung der Streuungen im Interpolationsbereich.

Life Time Prediction of High Strength Metallic Materials at Elevated Temperatures

For the prediction of cyclic life times in the low cycle fatigue (LCF) region of high strength materials at elevated temperatures creep damage (time dependent damage) as well as fatigue damage have to be considered. By defining a value r, which depends on the ratio of the inelastic strainrates a life time prediction rule for the accumulation of time dependent damage (RTD – rule) with one adjustable parameter ν can be derived. An evaluation of LCF-data of the superalloys PM Astroloy, Waspaloy, MAR M 509 and In 738 LC show, that the RTD-rule can be used in the region between pure creep ($r = 1$) and pure fatigue ($r > 10^6$). The scatter obtained by extrapolating to different loading conditions is in the same order of magnitude as the scatter of the interpolated data.

Prévision de la tenue, aux températures élevées, de métaux hautement résistants

Lorsqu'on fait des prévisions sur la tenue de matériaux hautement résistants à des températures élevées, soumis à des essais de fatigue sous de faibles charges alternées, il faut tenir compte aussi bien de la détérioration par fluage (détérioration dépendant du temps) que de celle due à la fatigue. Après introduction du rapport d'allongement r on obtient, pour l'accumulation de la détérioration ayant une relation relative avec le temps, une règle de durée de vie à paramètre ajustable ν. L'interprétation des données de fatigue sous faible charge alternée des superalliages PM Astroloy, Waspaloy, MAR M 509 et In 738 LC montre que la règle de durée de vie peut être appliquée dans un domaine situé entre le fluage pur ($r = 1$) et la fatigue pure ($r > 10^6$). Les dispersions obtenues lors de l'extrapolation sur différentes conditions de sollicitation se trouvent dans l'ordre de grandeur des dispersions obtenues dans le domaine de l'interpolation.

1. Regeln zur Lebensdauervorhersage

Für die Beanspruchung im Bereich der Hochtemperatur-Niedriglastwechselermüdung (Low cycle fatigue – LCF) existieren eine Reihe von Lebensdauerregeln. Die verschiedenen Regeln besitzen meist mehrere Parameter, die so an Versuchsdaten angepaßt werden, daß die mittlere Abweichung zwischen den berechneten und den gemessenen Lebensdauern möglichst klein wird. Im allgemeinen beschreiben sämtliche Lebensdauerregeln die zyklische Lebensdauer in jenem Belastungsbereich genügend genau, in dem die Anpassung erfolgte. Für eine Extrapolation auf andere Belastungsbereiche fehlen meist Abschät-

*) Dipl.-Ing. Dr. Robert Danzer, Institut für Metallkunde und Werkstoffprüfung
**) A. o. Univ.-Prof. Dr. Friedwin Sturm, Institut für Physik, Abteilung für Angewandte Physik, Montanuniversität Leoben

1. Rules for life time prediction

For loads in the field of high temperature low cycle fatigue (LCF) there exists a number of life time rules. The various rules are determined by several parameters that are adapted to the experimental data in such way, that the mean deviation between the calculated and the measured life times is minimized. In general, all the life time rules describe the cyclic life time precisely enough for that load area, for which the adaptation had been effected. For extrapolating into other load areas, estimations on the exactness and the areas of validity for the single rules are mostly lacking.

It could be seen from investigations on the materials PM Astroloy, MAR M 509, Waspaloy and In 738 LC that in the area of operational load of these materials as well creep damage (time dependent damage), as also fatigue damage (time independent damage) lead to failure of the constructional

zungen über die Genauigkeit und die Gültigkeitsbereiche der einzelnen Regeln.

Aus Untersuchungen über die Werkstoffe PM Astroloy, MAR M 509, Waspaloy und In 738 LC hat sich ergeben, daß im Bereich der Betriebsbeanspruchungen dieser Werkstoffe sowohl Kriechschädigung (zeitabhängige Schädigung) als auch Ermüdungsschädigung (zeitunabhängige Schädigung) zum Versagen der Bauteile führt. Zur Lebensdauervorhersage in diesem Verformungsbereich werden folgende drei Regeln diskutiert:

I) Lineare Akkumulation der zeitabhängigen Schädigung (LATD-Regel)
II) Akkumulation der relativ zeitabhängigen Schädigung (RTD-Regel)
III) Manson-Coffin-Regel (MC-Regel)

1.1 LATD-Regel

Wenn die Schädigung ausschließlich oder überwiegend durch Kriechen bedingt ist, so kann davon ausgegangen werden, daß der Hauptschädigungsmechanismus, ausgedrückt durch die inelastische Dehnrate $\dot{\varepsilon}_{in}$, dem stationären Kriechen mit der minimalen Kriechdehnrate $\dot{\varepsilon}_{min}$ entspricht. Andere zeitabhängige Effekte, wie Korrosion von Karbiden oder Bildung von Oxiden in Korngrenzen, können ebenfalls einen ähnlichen Einfluß ausüben, sodaß die ursprüngliche Bezeichnung für die im Bereich der Kriechschädigung eingesetzte Lebensdauerregel „Lineare Akkumulation der Kriechschädigung" (1) bis (3) auf „Lineare Akkumulation der zeitabhängigen Schädigung" (Linear Accumulation rule of Time dependent Damage – LATD) erweitert wird.

Die akkumulierte Schädigung D (t) zu einer bestimmten Zeit t ist gegeben durch:

$$D(t) = \int_0^t \dot{D}(t)\, dt\,, \qquad [1]$$

wobei die Schädigung zum Zeitpunkt des Versagens D = 1 ist. Unter „Versagen" wird dabei je

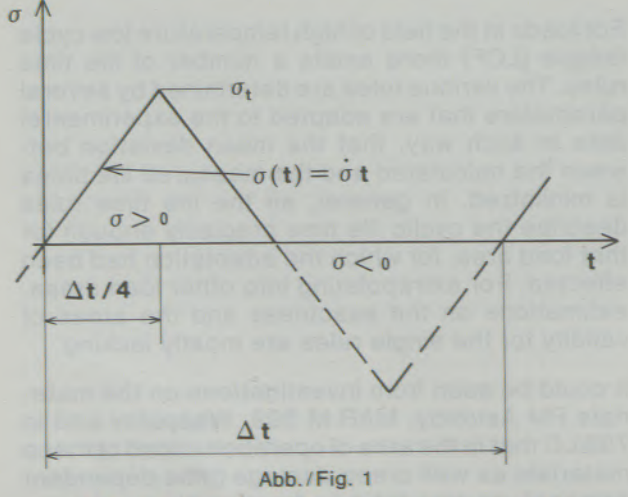

Abb./Fig. 1
Zyklische Belastung mit konstanter Spannungsrate
Cyclic load with constant strain rate

parts. The following three rules are discussed for life time predictions in this area of deformation:

I) Linear accumulation of the time-dependent damage (LATD-rule)
II) Accumulation of the relatively time-dependent damage (RTD-rule)
III) Manson-Coffin-rule (MC-rule)

1.1 LATD-rule

If the damage is exclusively or to a major part caused by creep, it may be assumed that the main damaging mechanism – expressed by the inelastic strain rate $\dot{\varepsilon}_{in}$- corresponds to stationary creep with the minimum creep strain rate $\dot{\varepsilon}_{min}$. Other time-dependent effects, such as corrosion of carbides or formation of oxides along grain boundaries may also exert a similar influence, so that the original definition for the life time rule used for the area of creep damage "Linear Accumulation of Creep Damage" (1) to (3) is extended to „Linear Accumulation rule of Time dependet Damage."

The accumulated damage D(t) at a determined time t is given by:

$$D(t) = \int_0^t \dot{D}(t)\, dt\,, \qquad [1]$$

whereby the damage at the time of failure D = 1. By "failure" we understand – depending on the specific case of application – the separation of the constructional part or the sample (fracture), the beginning of tertiary creep, the formation of cracks of a certain size or a certain decrease of the stress signal. If D(Δt) means the damage after a load cycle with a length of cycle Δt, there results N_f for the number of cycles to failure:

$$N_{f,LATD} = \frac{1}{D(\Delta t)}\,. \qquad [2]$$

In accordance with the damage analyses performed it may be assumed that with the materials investigated no damage occurs in the area of compression stress. In the area of tensile stress the rate of damage equals the reciprocal value of the time $t_{f,c}$ until failure in a creep test (4):

$$\dot{D} = \frac{1}{t_{f,c}}\,. \qquad [3]$$

$t_{f,c}$ is a function of stress σ and temperature T, which is determined by creep rupture test. From the equations [1] to [3] the following formula results for N_f:

$$N_{f,LATD} = \frac{1}{\int_0^{\Delta t} \frac{1}{t_{f,c}}\, dt}\,. \qquad [4]$$

If the creep data can be described analytically, e.g. by a power rule, an exponential rule or a Spera-formulation:

$$t_{f,c} = A(T) \cdot \sigma^{-n} \qquad [5]$$

nach Anwendungsfall die Trennung des Bauteils oder der Probe (Bruch), der Beginn von tertiärem Kriechen, die Bildung von Rissen einer bestimmten Größe oder ein bestimmter Abfall des Spannungssignals verstanden. Bedeutet D (Δt) die Schädigung nach einem Belastungszyklus mit einer Zyklusdauer Δt, so ergibt sich für die Anzahl der Zyklen bis zum Versagen N_f (Number of cycles to failure):

$$N_{f,LATD} = \frac{1}{D(\Delta t)} \cdot \qquad [2]$$

In Übereinstimmung mit durchgeführten Schadensanalysen kann angenommen werden, daß bei den untersuchten Werkstoffen im Druckspannungsbereich keine Schädigung auftritt. Im Zugspannungsbereich ist die Schädigungsrate gleich dem Reziprokwert der Zeitdauer $t_{f,c}$ bis zum Versagen im Kriechversuch (time to failure in a creep test) (4):

$$\dot{D} = \frac{1}{t_{f,c}} \cdot \qquad [3]$$

$t_{f,c}$ ist eine Funktion von Spannung σ und Temperatur T, die im Kurzzeitkriechversuch (creep rupture test) ermittelt wird. Aus den Gleichungen [1] bis [3] ergibt sich für N_f folgender Ausdruck:

$$N_{f,LATD} = \frac{1}{\int_0^{\Delta t} \frac{1}{t_{f,c}}\, dt} \cdot \qquad [4]$$

Wenn die Kriechdaten analytisch dargestellt werden können, etwa durch ein Potenzgesetz, ein Exponentialgesetz oder einen Spera-Ansatz:

$$t_{f,c} = A(T) \cdot \sigma^{-n} \qquad [5]$$

$$t_{f,c} = A(T) \cdot \exp(-\sigma/\sigma_0) \qquad [6]$$

$$t_{f,c} = t_0 \cdot f_1(T) \cdot f_2(\sigma) \qquad [7]$$

so kann das Integral in Gleichung [4] entsprechend dem Belastungszyklus direkt berechnet werden. In allen übrigen Fällen müssen die Daten numerisch ausgewertet werden.

Bei einem zyklischen, spannungskontrollierten Versuch (konstante Temperatur, Mittelspannung ist Null) mit konstanter Spannungsrate $\dot{\sigma}$ ist die Spannung im ersten Viertel des Zyklus bis t = Δt/4 (siehe Abb. 1):

$$\sigma(t) = \dot{\sigma} \cdot t \,. \qquad [8]$$

Wenn das Kriechverhalten des Materials durch ein Potenzgesetz nach Gleichung [5] beschrieben werden kann, ergibt sich für die Schädigungsrate:

$$\dot{D} = \frac{1}{t_{f,c}} = \frac{1}{A \cdot \sigma^{-n}} = \frac{1}{A \cdot \dot{\sigma}^{-n}} \cdot t^n \qquad [9]$$

$$t_{f,c} = A(T) \cdot \exp(-\sigma/\sigma_0) \qquad [6]$$

$$t_{f,c} = t_0 \cdot f_1(T) \cdot f_2(\sigma) \qquad [7]$$

the integral of equation[4] can be calculated directly according to the load cycle. In all other cases the data have to be evaluated numerically.

During a cyclic, stress-controlled test (constant temperature, mean stress is zero) with constant strain rate $\dot{\sigma}$ the stress during the first quarter of the cycle until t = Δt/4 (fig. 1):

$$\sigma(t) = \dot{\sigma} \cdot t \,. \qquad [8]$$

If the creep behavior of the material may be described by a power rule according to equation [5], the following results for the rate of damage:

$$\dot{D} = \frac{1}{t_{f,c}} = \frac{1}{A \cdot \sigma^{-n}} = \frac{1}{A \cdot \dot{\sigma}^{-n}} \cdot t^n \qquad [9]$$

and for the accumulated damage after a quarter cycle according to equation [1]:

$$D(\Delta t/4) = \frac{1}{A \cdot \dot{\sigma}^{-n}} \int_0^{\Delta t/4} t^n\, dt = \frac{(\Delta t/4)^{n+1}}{(n+1) \cdot A \cdot \dot{\sigma}^{-n}}$$

$$= \frac{\Delta t}{4(n+1)} \cdot \frac{1}{A\, \dot{\sigma}^{-n} (\Delta t/4)^{-n}} \qquad [10]$$

$$= \frac{\Delta t}{4(n+1)} \cdot \frac{1}{A\, \sigma_t^{-n}} = \frac{\Delta t}{4(n+1)} \cdot \frac{1}{t_{f,c}(\sigma_t, T)} \,.$$

With this D(Δt/4) can be calculated directly from the value for $t_{f,c}$ as determined by creep test under maximum tensile strain σ_t and temperature T.

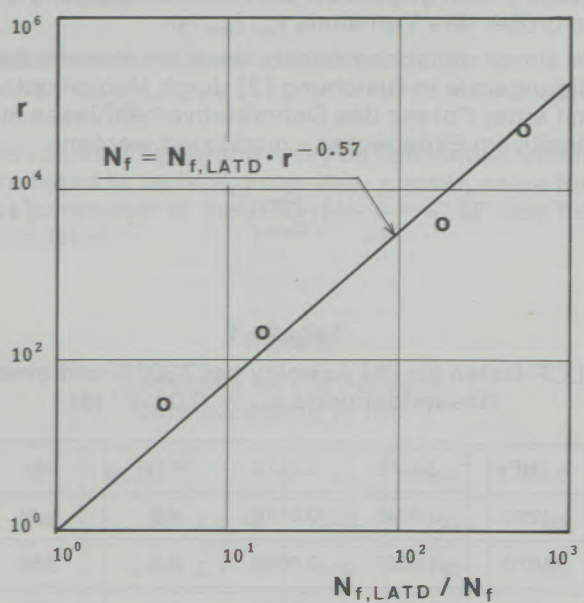

Abb./Fig. 2
r-Wert für PM Astroloy, LCF-Daten nach Tabelle 1
r-value for PM-Astroloy, LCF-data according to tab. 1

und für die nach einem Viertelzyklus akkumulierte Schädigung nach Gleichung [1]:

$$D(\Delta t/4) = \frac{1}{A \cdot \dot{\sigma}^{-n}} \int_0^{\Delta t/4} t^n dt = \frac{(\Delta t/4)^{n+1}}{(n+1) \cdot A \cdot \dot{\sigma}^{-n}}$$

$$= \frac{\Delta t}{4(n+1)} \cdot \frac{1}{A\, \dot{\sigma}^{-n} (\Delta t/4)^{-n}} \qquad [10]$$

$$= \frac{\Delta t}{4(n+1)} \cdot \frac{1}{A\, \sigma_t^{-n}} = \frac{\Delta t}{4(n+1)} \cdot \frac{1}{t_{f,c}(\sigma_t, T)}$$

Damit kann D ($\Delta t/4$) direkt aus dem im Kriechversuch ermittelten Wert für $t_{f,c}$, bei der maximalen Zugspannung σ_t und der Temperatur T berechnet werden.

Aus Symmetriegründen ergibt sich für den Fall, daß Druckspannungen keine Schädigung bewirken, für die Schädigung je Zyklus:

$$D(\Delta t) = D(\Delta t/2) = 2D(\Delta t/4) = \frac{\Delta t}{2(n+1) \cdot t_{f,c}(\sigma_t, T)} \cdot \qquad [11]$$

1.2 RTD-Regel

In vielen Fällen ist die Verformung zeitabhängig und die inelastische Dehnrate $\dot{\varepsilon}_{in}$ bei der Maximalspannung größer als $\dot{\varepsilon}_{min}$, wie etwa im Bereich des primären Kriechens. In diesem Verformungsbereich bei gleichzeitigem Einfluß von Kriechschädigung und Ermüdungsschädigung kann die von C. J. Franklin (5) vorgeschlagene Lebensdauerregel mit Akkumulation von relativ zeitabhängiger Schädigung (Accumulation of Relative Time dependent Damage – RTD) angewandt werden. Dabei wird angenommen, daß die Schädigungsrate umso größer gegenüber der Kriechschädigung ist, je größer das Verhältnis $\dot{\varepsilon}_{in}/\dot{\varepsilon}_{min}$ ist.

In einem einfachen Ansatz kann die Kriechschädigungsrate in Gleichung [3] durch Multiplikation mit einer Potenz des Dehnratenverhältnisses mit positivem Exponenten ν modifiziert werden:

$$\dot{D} = \frac{1}{t_{f,c}} \cdot \left(\frac{\dot{\varepsilon}_{in}}{\dot{\varepsilon}_{min}}\right)^{\nu}. \qquad [12]$$

Out of reasons of symmetry, the following results for damage per cycle, in case that compression stresses do not cause damage.

$$D(\Delta t) = D(\Delta t/2) = 2D(\Delta t/4) = \frac{\Delta t}{2(n+1) \cdot t_{f,c}(\sigma_t, T)} \cdot \qquad [11]$$

1.2 RTD-rule

In many cases, deformation is time dependent and the inelastic strain rate $\dot{\varepsilon}_{in}$ at maximum tension is higher than $\dot{\varepsilon}_{min}$, as e.g. in the area of primary creep. For this area of deformation at simultaneous influence of creep damage and fatigue damage the life time rule suggested by C. J. Franklin (5), with accumulation of Relative Time dependent Damage, RTD, may be applied. It is hereby assumed that the rate of damage is the bigger compared to creep damage, the bigger there is the ratio $\dot{\varepsilon}_{in}/\dot{\varepsilon}_{min}$.

In a simple formulation the rate of creep damage in equation [3] may be modified by multiplying with a power of the inelastic strain rate with positive exponent ν:

$$\dot{D} = \frac{1}{t_{f,c}} \cdot \left(\frac{\dot{\varepsilon}_{in}}{\dot{\varepsilon}_{min}}\right)^{\nu}. \qquad [12]$$

Therefore the following results for the number of cycles to failure:

$$N_{f,RTD} = \frac{1}{\int_0^{\Delta t} \frac{1}{t_{f,c}} \cdot \left(\frac{\dot{\varepsilon}_{in}}{\dot{\varepsilon}_{min}}\right)^{\nu} dt} \qquad [13]$$

If as a measure for the ratio of the strain rates a value r is introduced, the following holds (6):

$$r(t) = \frac{\int_0^t \dot{\varepsilon}_{in}\, dt}{\int_0^t \dot{\varepsilon}_{min}\, dt} \qquad [14]$$

with

$$r(\Delta t) = r(\Delta t/2) = \frac{\Delta \varepsilon_{in}}{\Delta \varepsilon_{min}}, \qquad [15]$$

and there may – as a comparison with numerical evaluation shows – for saw-toothshape cycles a mean value of the ratio of the strainrates be lifted

Tabelle 1

LCF-Daten für PM Astroloy bei 730 °C und einer Gesamtdehnrate $\dot{\varepsilon}_{tot} = 0.01\ s^{-1}$ (8)

σ_t [MPa]	$\Delta\varepsilon_{in}/2$	$\Delta\varepsilon_{tot}/2$	Δt [s]	N_f
1250	0.0045	0.0116	4.6	48
1070	0.0027	0.0090	3.6	150
845	0.0012	0.0060	2.4	620
660	0.0003	0.0041	1.6	9800

Table 1

LCF-data for PM Astroloy at 730 °C and a total rate of expansion $\dot{\varepsilon}_{tot} = 0.01\ s^{-1}$ (8)

σ_t [MPa]	$\Delta\varepsilon_{in}/2$	$\Delta\varepsilon_{tot}/2$	Δt [s]	N_f
1250	0.0045	0.0116	4.6	48
1070	0.0027	0.0090	3.6	150
845	0.0012	0.0060	2.4	620
660	0.0003	0.0041	1.6	9800

Damit ergibt sich für die Anzahl der Zyklen bis zum Versagen:

$$N_{f,RTD} = \frac{1}{\int_0^{\Delta t} \frac{1}{t_{f,c}} \cdot \left(\frac{\dot{\varepsilon}_{in}}{\dot{\varepsilon}_{min}}\right)^{\nu} dt} \quad [13]$$

Wird als Maß für das Verhältnis der Dehnraten ein Wert r eingeführt (6):

$$r(t) = \frac{\int_0^t \dot{\varepsilon}_{in}\, dt}{\int_0^t \dot{\varepsilon}_{min}\, dt} \quad [14]$$

mit

$$r(\Delta t) = r\,(\Delta t/2) = \frac{\Delta \varepsilon_{in}}{\Delta \varepsilon_{min}}, \quad [15]$$

so kann, wie ein Vergleich mit numerischen Auswertungen gezeigt hat, für symmetrische sägezahnförmige Zyklen ein mittlerer Wert des Dehnratenverhältnisses aus dem Integral in Gleichung [13] herausgegeben werden, so daß sich für $N_{f,RTD}$ näherungsweise folgender Ausdruck ergibt:

$$N_{f,RTD} = \frac{1}{\int_0^{\Delta t} \frac{dt}{t_{f,c}}} \cdot r^{-\nu} = N_{f,LATD} \cdot r^{-\nu}. \quad [16]$$

Für r = 1 (reine Kriechverformung) enthält die RTD-Regel als Grenzfall die LATD-Regel. Der Parameter ν der RTD-Regel ist an die Versuchsdaten anzupassen. Mit den im Versuch gemessenen Lebensdauern N_f lassen sich entsprechend Gleichung [16] aus den nach Gleichung [4] berechneten Werten für $N_{f,LATD}$ und den nach Gleichung [15] berechneten Werten für r mittlere Werte für den Parameter ν ermitteln:

$$\nu = \log\,(N_{f,LATD} / N_f) \,/\, \log r. \quad [17]$$

Gilt die Monkmant-Grant-Regel (7)

$$t_{f,c} \cdot \dot{\varepsilon}_{min} = c_{MG}, \quad [18]$$

out of the integral of equation [13], thus resulting into an approximated formulation for $N_{f,RTD}$ as follows:

$$N_{f,RTD} = \frac{1}{\int_0^{\Delta t} \frac{dt}{t_{f,c}}} \cdot r^{-\nu} = N_{f,LATD} \cdot r^{-\nu}. \quad [16]$$

For r = 1 (pure creep deformation) the RTD-rule contains the LATD-rule as a case in the limit. The parameter of the RTD-rule has to be adapted to the experimental data. With the life times N_f measured in the experiment it becomes possible by means of equation [16] to determine mean values of parameter ν out of the values calculated for $N_{f,LATD}$ calculated according to equation [4], and the values for r calculated according to equation [15]:

$$\nu = \log\,(N_{f,LATD} / N_f) \,/\, \log r. \quad [17]$$

If Monkmant-Grant-rule (7) holds

$$t_{f,c} \cdot \dot{\varepsilon}_{min} = c_{MG}, \quad [18]$$

whereby c_{MG} is called Monkmant-Grant-constant (which may be stress dependent, however), the following results for r-value:

$$r(\Delta t) = r\,(\Delta t/2) = \frac{\Delta \varepsilon_{in}}{\int_0^{\Delta t/2} \dot{\varepsilon}_{min}\, dt} = \quad [19]$$

$$= \frac{\Delta \varepsilon_{in}}{c_{MG} \int_0^{\Delta t/2} \frac{dt}{t_{f,c}}} = \frac{\Delta \varepsilon_{in}}{c_{MG}} \cdot N_{f,LATD}.$$

Out of the LCF-data for PM Astroloy (8) in tab. 1, a power formulation for $t_{f,c}$ (σ in MPa and $t_{f,c}$ in s)

$$t_{f,c} = 5.1 \cdot 10^{43}\, \sigma^{-13.5} \quad [20]$$

and Monkmant-Grant-constant

$$c_{MG} = 0.063 \quad [21]$$

the values of $N_{f,LATD}$ and r may be calculated, which are listed in table 2. From this, a mean value for the parameter of the RTD-rule, $\nu = 0.57$ may be calculated.

Tabelle 2

Lebensdauern für PM Astroloy; Daten nach Tabelle 1

N_f	$N_{f,LATD}$	r	ν	$N_{f,MC}$	$N_{f,RTD}$
48	200	$2.9\ 10^1$	0.43	50	30
150	2.400	$2.1\ 10^2$	0.52	140	120
620	110.000	$4.0\ 10^3$	0.62	650	930
9800	5,000.000	$4.8\ 10^4$	0.58	9600	11.000

Table 2

Life-times for PM Astroloy; data according to tab. 1

N_f	$N_{f,LATD}$	r	ν	$N_{f,MC}$	$N_{f,RTD}$
48	200	$2.9\ 10^1$	0.43	50	30
150	2.400	$2.1\ 10^2$	0.52	140	120
620	110.000	$4.0\ 10^3$	0.62	650	930
9800	5,000.000	$4.8\ 10^4$	0.58	9600	11.000

wobei c_{MG} als Monkmant-Grant-Konstante bezeichnet wird (die aber auch spannungsabhängig sein kann), so ergibt sich für den r-Wert:

$$r(\Delta t) = r(\Delta t/2) = \frac{\Delta\varepsilon_{in}}{\int_0^{\Delta t/2} \dot{\varepsilon}_{min}\, dt} = \frac{\Delta\varepsilon_{in}}{c_{MG} \int_0^{\Delta t/2} \frac{dt}{t_{f,c}}} = \frac{\Delta\varepsilon_{in}}{c_{MG}} \cdot N_{f,LATD} \quad [19]$$

Aus den LCF-Daten für PM Astroloy (8) in Tabelle 1, einem Potenzansatz für $t_{f,c}$ (σ in MPa und $t_{f,c}$ in s)

$$t_{f,c} = 5.1\ 10^{43}\ \sigma^{-13.5} \quad [20]$$

und der Monkmant-Grant-Konstante

$$c_{MG} = 0.063 \quad [21]$$

lassen sich die Werte für $N_{f,LATD}$ und r berechnen, die in Tabelle 2 eingetragen sind. Daraus läßt sich ein mittlerer Wert für den Parameter der RTD-Regel, $\nu = 0.57$, berechnen.

In Abb. 2 ist r als Funktion des Verhältnisses $N_{f,LATD}/N_f$ in doppeltlogarithmischer Darstellung wiedergegeben. Für den in Tabelle 1 ausgewählten Datensatz ergeben sich r-Werte größer als 1, sodaß keine reine Kriechschädigung ($r = 1$) vorliegt. Die Werte für $N_{f,LATD}$ besitzen daher nur eine rechnerische Bedeutung. Zur Abschätzung der Lebensdauer sind die Werte für $N_{f,RTD}$ nach Gleichung [16] heranzuziehen, die ebenfalls in Tabelle 2 eingetragen sind.

1.3 MC-Regel

Im reinen Ermüdungsbereich treten keine zeitabhängigen Verformungen auf (niedrige Temperaturen) und das Niedriglastwechsel-Ermüdungsverhalten kann durch die Manson-Coffin-Regel (9), (10) beschrieben werden:

$$N_{f,MC} = \alpha \cdot (\Delta\varepsilon_{in}/2)^{-b}. \quad [22]$$

Die beiden Parameter a und b sind an die Versuchsdaten anzupassen. Ist die Temperaturabhängigkeit der beiden Parameter bekannt, so kann die MC-Regel auch bei höheren Temperaturen angewandt werden, wobei zusätzlich auch noch eine Frequenzabhängigkeit berücksichtigt werden kann. Um Vergleichswerte für die RTD-Regel zu erhalten, werden die Lebensdauern nach der Standardform der MC-Regel nach Gleichung [22] ohne Modifikation berechnet. Aus den LCF-Daten in Tabelle 1 ergibt sich für PM Astroloy bei 730 °C folgende Manson-Coffin-Regel:

$$N_{f,MC} = 0.0014\ (\Delta\varepsilon_{in}/2)^{-1,94}. \quad [23]$$

Die nach dieser Gleichung errechneten Werte für $N_{f,MC}$ sind in Tabelle 2 eingetragen. $N_{f,MC}$ besitzt gegenüber den Meßergebnissen, N_f, geringere

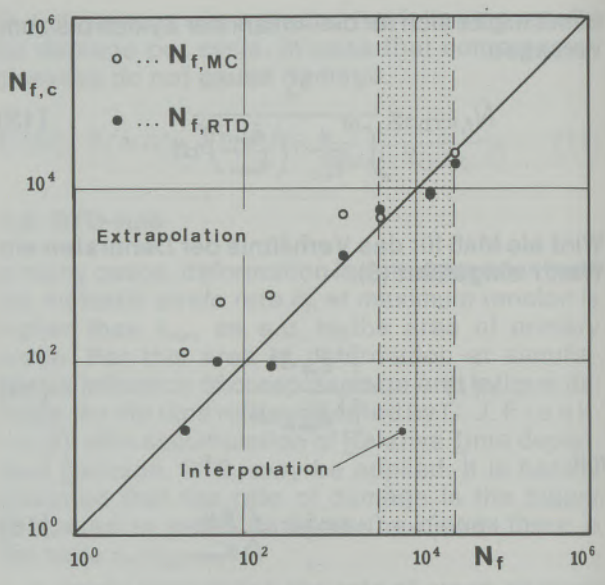

Abb./Fig. 3

Berechnete Lebensdauern $N_{f,c}$ aufgetragen über den gemessenen Lebensdauern N_f für die Kobaltbasis Superlegierung MAR M 509, Interpolation und Extrapolation für die RTD-Regel und die MC-Regel

Calculated life-times $N_{f,c}$ plotted over the measured life-times N_f for cobalt based superalloy MAR M 509, interpolation and extrapolation for RTD-rule and MC-rule

In fig. 2, r is rendered as a function of the ratio $N_{f,LATD}/N_f$ in double-logarithmic presentation. For the set of dates selected in table 1 the r-values show up greater than 1, so that no pure creep damage ($r = 1$) is prevailing. The values for $N_{f,LATD}$ are only of calculatory importance. For estimation of the life time, however, the values for $N_{f,RTD}$ according to equation [16] have to be used, which are also listed in table 2.

1.3 MC-rule

In the mere area of fatigue no time-dependent deformations appear (low temperatures) and the low cycle fatigue behavior may be described by the Manson-Coffin-rule (9), (10):

$$N_{f,MC} = \alpha \cdot (\Delta\varepsilon_{in}/2)^{-b}. \quad [22]$$

The two parameters a and b have to be adapted to the test data. If the temperature dependance of the two parameters is known, it is possible to apply the MC-rule also at higher temperatures, whereby also a frequency dependance may be taken into consideration. In order to obtain comparable values for the RTD-rule, the life-times are calculated with the standard form of the MC-rule according to equation [22] without modification. From the LCF-data of table 1, the following Manson-Coffin-rule results for PM Astroloy at 730 °C:

$$N_{f,MC} = 0.0014\ (\Delta\varepsilon_{in}/2)^{-1,94}. \quad [23]$$

The values found for $N_{f,MC}$ according to this equation are listed in table 2. $N_{f,MC}$ shows smaller de-

Tabelle 3

LCF-Daten für MAR M 509 bei 900 °C (11)

$\Delta\sigma/2$ [MPa]	$\Delta\varepsilon_{in}/2$	$\Delta\varepsilon_{tot}/2$	Δt [s]	N_f
228	0.0004	0.0021	0.05	3.600
216	0.0003	0.0016	0.05	14.000
209	0.0001	0.0018	0.05	27.000

Abweichungen als $N_{f,RTD}$. Dies ist darauf zurückzuführen, daß bei der MC-Regel im Interpolationsbereich zwei Parameter angepaßt werden (a und b) und bei der RTD-Regel nur ein Parameter (ν).

2. Genauigkeit der Lebensdauerregeln

Um die Genauigkeit der verwendeten Lebensdauerregeln quantitativ zu beschreiben, werden zwei Größen: S und C/M berechnet. S ist der mittlere Fehler aus den Logarithmen der berechneten Lebensdauern $N_{f,c}$ und der gemessenen Lebensdauern N_f nach folgender Gleichung:

$$S = \left(\frac{1}{n-1} \sum_{j=1}^{n} \left(\log N_{f,c} - \log N_f \right)_j^2 \right)^{\frac{1}{2}}. \qquad [24]$$

n bedeutet dabei die Gesamtzahl der j = 1,2 . . . n Experimente. S entspricht bei einer Gaußverteilung der Standardabweichung. C/M ist definiert als der größte Wert der Verhältnisse $N_{f,c}/N_f$ und $N_f/N_{f,c}$ innerhalb einer Meßreihe:

$$C/M = \text{Maximum} \left(N_{f,c}/N_f \text{ und } N_f/N_{f,c} \right) \qquad [25]$$

Innerhalb des Interpolationsbereiches, in dem die Parameter angepaßt werden, ist das Streuband, ausgedrückt durch S und C/M, umso kleiner, je größer die Anzahl der Parameter ist. Im Extrapolationsbereich, in dem die Lebensdauerregeln auf außerhalb des Anpaßbereiches liegende Beanspruchungsbedingungen (z. B. hohe und niedrige Frequenzen) angewandt werden, ist zu fordern, daß sich das Streuband nicht wesentlich vergrößert.

3. Vergleich der Lebensdauervorhersagen mit Meßergebnissen

Die Genauigkeit und die Geltungsbereiche der einzelnen Lebensdauerregeln können so über-

Tabelle 4

Berechnete Lebensdauern für die Daten nach Tabelle 3 (Interpolation)

N_f	r	$N_{f,LATD}$	$N_{f,RTD}$	$N_{f,MC}$
3.600	$2.6\ 10^3$	310.000	6.000	4.700
14.000	$3.1\ 10^3$	580.000	10.000	9400
27.000	$2.7\ 10^3$	1,000.000	20.000	27.000

Table 3

LCF-data for MAR M 509 at 900 °C (11)

$\Delta\sigma/2$ [MPa]	$\Delta\varepsilon_{in}/2$	$\Delta\varepsilon_{tot}/2$	Δt [s]	N_f
228	0.0004	0.0021	0.05	3.600
216	0.0003	0.0016	0.05	14.000
209	0.0001	0.0018	0.05	27.000

viations than $N_{f,RTD}$, compared to the measured data N_f. This may be traced back to the fact that with the MC-rules in the area of interpolation two parameters are adapted (a and b) and with the RTD-rule only one parameter (ν).

2. Accuracy of the life-time rules

In order to quantitatively describe the accuracy of the life-time rules used, two quantities: S and C/M are calculated. S is the mean error of the logarithms of the calculated life-times $N_{f,c}$ and the measured life-times N_f according to the following equation:

$$S = \left(\frac{1}{n-1} \sum_{j=1}^{n} \left(\log N_{f,c} - \log N_f \right)_j^2 \right)^{\frac{1}{2}}. \qquad [24]$$

n means the total number of the j = 1, 2, . . .n experiments, S corresponds to the standard deviation of a Gauss-distribution. C/M is defined as the greatest value of the ratios $N_{f,c}/N_f$ and $N_f/N_{f,c}$ within a series of measurements:

$$C/M = \text{Maximum} \left(N_{f,c}/N_f \text{ und } N_f/N_{f,c} \right) \qquad [25]$$

Within the area of interpolation, in which the parameters are adapted, the scattering band – expressed by S and C/M – is the smaller, the bigger there is the number of parameters. In the area of extrapolation, where the rules of life time are applied to wear conditions outside the area of adaptation (e.g. high and low frequencies), it must be required that the scattering band is not substantially increased.

3. Comparison of life time predictions and results of measurements

The accuracy and the area of validity of the single rules of life time may be controlled in such way that

Table 4

Calculated life-times for the data according to tab. 3 (interpolation)

N_f	r	$N_{f,LATD}$	$N_{f,RTD}$	$N_{f,MC}$
3.600	$2.6\ 10^3$	310.000	6.000	4.700
14.000	$3.1\ 10^3$	580.000	10.000	9400
27.000	$2.7\ 10^3$	1,000.000	20.000	27.000

Tabelle 5

Berechnete Lebensdauern für MAR M 509 (Extrapolation)

N_f	$N_{f,RTD}$	$N_{f,MC}$
20	16	130
50	100	500
190	91	670
1900	1700	5200
S	0.27	0.87
C/M	2.1	10

prüft werden, daß einige LCF-Daten dazu verwendet werden, um die Parameter, ν bzw. a und b, anzupassen und die übrigen Meßdaten, um die Güte der extrapolierten Lebensdauern zu ermitteln.

3.1 Kobaltbasis Superlegierung MAR M 509

Das Kriechverhalten dieses Werkstoffes kann im Temperaturbereich von 850 °C bis 1100 °C durch ein Potenzgesetz beschrieben werden (11) und die Monkmant-Grant-Konstante kann mit etwa $c_{MG} = 0.1$ abgeschätzt werden. Aus den LCF-Daten in Tabelle 3 ergibt sich für den Parameter $\nu = 0.5$ und als Manson-Coffin-Regel

$$N_{f,MC} = 0.058 \; (\Delta\varepsilon_{in}/2)^{-1.46} . \qquad [26]$$

Die berechneten Werte für r, $N_{f,LATD}$, $N_{f,RTD}$ und $N_{f,MC}$ sind in Tabelle 4 eingetragen. Da alle drei Werte für r größer als 10 sind (4), kommt den Werten für $N_{f,LATD}$ nur rechnerische Bedeutung zu. Im Interpolationsbereich besitzen die Werte für $N_{f,RTD}$ die Abweichungen S = 0.21 und C/M = 1.7 und die Werte für $N_{f,MC}$ die Abweichungen S = 0.15 und C/M = 1.5. Bei der Extrapolation auf einen anderen Datensatz bei geänderten Versuchsbedingungen, ergeben sich die in Tabelle 5 angegebenen Werte für die Lebensdauern (N_f . . . Meßergebnis). In Abb. 3 sind die berechneten Lebensdauern $N_{f,c}$

Table 5

Calculated life-times of MAR M 509 (extrapolation)

N_f	$N_{f,RTD}$	$N_{f,MC}$
20	16	130
50	100	500
190	91	670
1900	1700	5200
S	0.27	0.87
C/M	2.1	10

several LCF-data are used to adapt the parameters ν, resp. a and b, and the other measured data to determine the quality of the extrapolated life times.

3.1 Cobalt base superalloy MAR M 509

The creep behavior of this material in the temperature interval from 850 °C to 1100 °C may be described by means of a power rule (11) and the Monkmant-Grant-constant may be assumed with appr. $c_{MG} = 0.1$. From the LCF-data in table 3, for the parameter $\nu = 0.5$, and as Manson-Coffin rule there results

$$N_{f,MC} = 0.058 \; (\Delta\varepsilon_{in}/2)^{-1.46} . \qquad [26]$$

The calculated values for r, $N_{f,LATD}$, $N_{f,RTD}$ and $N_{f,MC}$ are listed in table 4. Since all three values for r are greater than 10 (4), only calculatory importance holds for the values for $N_{f,LATD}$. In the area of interpolation, the values for $N_{f,RTD}$ show the deviations S = 0.21 and C/M = 1.7 and the values for $N_{f,MC}$ the deviations S = 0.15 and C/M = 1.5. Upon extrapolation to another set of data under changed testing conditions, the values listed in table 5 result for life times (N_f . . . result of measurement). In fig. 3 the calculated life times $N_{f,c}$ as a function of the measured life times N_f are plotted, whereby the straigth line under 45° corresponds to a con-

Tabelle 6

LCF-Daten für In 738 LC bei 850 °C (12)

σ_t [MPa]	Δt [s]	$\Delta\varepsilon_{tot}$	$\Delta\varepsilon_{in}$	N_f	r
261	1.0	$50\ 10^{-4}$	$0.6\ 10^{-4}$	54.000	$1.2\ 10^{5}$
343	1.4	$70\ 10^{-4}$	$3.2\ 10^{-4}$	6.200	$6.8\ 10^{4}$
427	2.0	$100\ 10^{-4}$	$8.0\ 10^{-4}$	480	$1.7\ 10^{4}$
751	2.6	$130\ 10^{-4}$	$25.2\ 10^{-4}$	160	$3.1\ 10^{1}$
892	4.0	$200\ 10^{-4}$	$84.5\ 10^{-4}$	19	$3.0\ 10^{0}$

Table 6

LCF-data for In 738 LC at 850 °C (12)

σ_t [MPa]	Δt [s]	$\Delta\varepsilon_{tot}$	$\Delta\varepsilon_{in}$	N_f	r
261	1.0	$50\ 10^{-4}$	$0.6\ 10^{-4}$	54.000	$1.2\ 10^{5}$
343	1.4	$70\ 10^{-4}$	$3.2\ 10^{-4}$	6.200	$6.8\ 10^{4}$
427	2.0	$100\ 10^{-4}$	$8.0\ 10^{-4}$	480	$1.7\ 10^{4}$
751	2.6	$130\ 10^{-4}$	$25.2\ 10^{-4}$	160	$3.1\ 10^{1}$
892	4.0	$200\ 10^{-4}$	$84.5\ 10^{-4}$	19	$3.0\ 10^{0}$

Tabelle 7

Streuung der extrapolierten Lebensdauern für In 738 LC (13)

	$N_{f,RTD}$	$N_{f,MC}$
Interpolation	S = 0.30 C/M = 3.5	S = 0.17 C/M = 1.8
Extrapolation (140 Werte)	S = 0.28 C/M = 5.2	S = 0.41 C/M = 23.2

als Funktion der gemessenen Lebensdauern N_f aufgetragen, wobei die Gerade unter 45° einer Übereinstimmung der beiden Werte entspricht. Es ist deutlich zu erkennen, daß beide Lebensdauerregeln im Interpolationsbereich eine große Genauigkeit besitzen, aber im Extrapolationsbereich nur die RTD-Regel brauchbare Ergebnisse liefert, wobei sich der Streubereich gegenüber dem Interpolationsbereich nur geringfügig vergrößert hat.

3.2 Nickelbasis Superlegierung In 738 LC

Die Kriechdaten von In 738 LC lassen sich durch einen Spera-Ansatz beschreiben (12) ($t_{f,c}$ in s, Temperatur T in K und Spannung σ in MPa):

$$t_{f,c} = t_o \cdot f_1(T) \cdot f_2(\sigma)$$
$$t_o = 1.6\ 10^{-11}$$
$$f_1(T) = \exp\ (6.1\ 10^4/T) \qquad [27]$$
$$f_2(\sigma) = 10^{-(1.8 \log \sigma + 7.5 \cdot 10^{-3} \sigma + 1.15 \cdot 10^{-7} \sigma^2)}$$

und die minimale Kriechdehnrate durch

$$\dot{\varepsilon}_{min} = 0.16\ (t_{f,c})^{-1.12} \qquad [28]$$

Aus den in Tabelle 6 angeführten Daten aus fünf Ermüdungsversuchen bei einer Temperatur von 850 °C und $\dot{\varepsilon} = 0.01\ s^{-1}$ lassen sich die Werte für r berechnen. Als mittlerer Wert für den Parameter ν der RTD-Regel ergibt sich $\nu = 0.64$, wenn angenommen wird, daß Druckspannungen keine Schädigung bewirken. Für die Manson-Coffin-Regel ergibt sich:

$$N_{f,MC} = 2.7\ 10^{-3} (\Delta\varepsilon_{in}/2)^{-1.62} \qquad [29]$$

Tabelle 8

LCF-Daten für Waspaloy bei 600 °C (8)

σ_t [MPa]	$\Delta\varepsilon_{in}/2$	$\Delta\varepsilon_{tot}/2$	Δt [s]	N_f
737	0.00091	0.00500	6.7	2.900
689	0.00045	0.00425	5.7	5.200
626	0.00008	0.00350	4.7	14.000
583	0.00005	0.00325	4.3	19.000

Table 7

Scattering of the extrapolated life-times of In 738 LC (13)

	$N_{f,RTD}$	$N_{f,MC}$
Interpolation	S = 0.30 C/M = 3.5	S = 0.17 C/M = 1.8
Extrapolation (140 measurements)	S = 0.28 C/M = 5.2	S = 0.41 C/M = 23.2

cordance of the two values. It can be clearly seen that both of the life time rules are of high exactness in the area of interpolation, in the extrapolation area, however, only the RTD-rule gives useful results, whereby the scattering range is only little increased compared with the area of interpolation.

3.2 Nickel based superalloy In 738 LC

The creep data of In 738 LC may be described by a Spera-formulation (12) ($t_{f,c}$ in s, temperature T in K and tension σ in MPa):

$$t_{f,c} = t_o \cdot f_1(T) \cdot f_2(\sigma)$$
$$t_o = 1.6\ 10^{-11}$$
$$f_1(T) = \exp\ (6.1\ 10^4/T) \qquad [27]$$
$$f_2(\sigma) = 10^{-(1.8 \log \sigma + 7.5 \cdot 10^{-3} \sigma + 1.15 \cdot 10^{-7} \sigma^2)}$$

and the minimum creep strain rate by

$$\dot{\varepsilon}_{min} = 0.16\ (t_{f,c})^{-1.12} \qquad [28]$$

From the data of five fatigue tests listed in table 6, run at a temperature of 850 °C and $\dot{\varepsilon} = 0.01\ s^{-1}$, the values for r may be calculated. As a mean value for the parameter ν of the RTD-rule there results $\nu = 0.64$, when there is assumed that compression stresses cause no damage. For the Manson-Coffin rule there holds:

$$N_{f,MC} = 2.7\ 10^{-3} (\Delta\varepsilon_{in}/2)^{-1.62} \qquad [29]$$

Upon evaluation of 140 measurement data (13) there result the scattering bands listed in table 7. It becomes clearly visible that within the LCF-area

Table 8

LCF-data for Waspaloy at 600 °C (8)

σ_t [MPa]	$\Delta\varepsilon_{in}/2$	$\Delta\varepsilon_{tot}/2$	Δt [s]	N_f
737	0.00091	0.00500	6.7	2.900
689	0.00045	0.00425	5.7	5.200
626	0.00008	0.00350	4.7	14.000
583	0.00005	0.00325	4.3	19.000

Bei einer Auswertung von 140 Meßergebnissen (13) ergeben sich die in Tabelle 7 angeführten Streubänder. Es zeigt sich deutlich, daß im beobachteten LCF-Bereich (Temperaturen von 750 °C bis 900 °C, Frequenzbereich über 6 Größenordnungen bei 850 °C, verschiedene Belastungszyklen) die zeitabhängigen Verformungen einen wesentlichen Einfluß besitzen, wobei jedoch Verformungen, die ähnlich dem stationären Kriechen ablaufen, mit Werten von $r < 10$, nur in 30 Fällen aufgetreten sind.

3.3 Nickelbasis Superlegierung Waspaloy

Die in Tabelle 8 angegebenen LCF-Daten bei 600 °C ergeben mit dem Exponentialgesetz für $t_{f,c}$ (8)

$$t_{f,c} = 1.4\ 10^{12} \exp(-5/60) \qquad [30]$$

und der Monkmant-Grant-Beziehung

$$t_{f,c} \cdot \dot{\varepsilon}_{min} = 2.3\ 10^{-3} \exp(5/271) \qquad [31]$$

für die RTD-Regel den Ausdruck:

$$N_{f,RTD} = N_{f,LATD} \cdot r^{-0.65} \qquad [32]$$

und für die MC-Regel:

$$N_{f,MC} = 37.4\ (\Delta\varepsilon_{in}/2)^{-0.63}. \qquad [33]$$

Die bei der Extrapolation auf weitere 29 Datensätze aus LCF-Versuchen errechneten Werte für $N_{f,MC}$ und $N_{f,RTD}$ sind in Abb. 4 als Funktion der gemessenen Lebensdauern aufgetragen. Dabei ergeben sich für die RTD-Regel Streuwerte mit

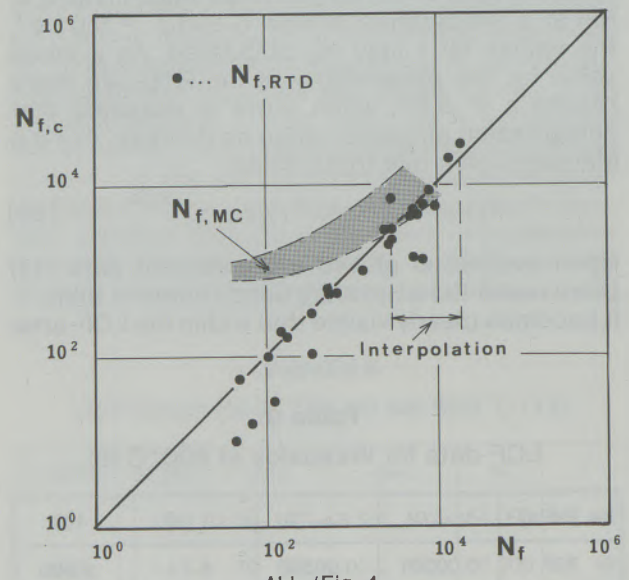

Abb./Fig. 4

Nach der RTD-Regel und der MC-Regel berechnete Lebensdauern $N_{f,c}$ aufgetragen über den gemessenen Lebensdauern N_f für die Nickelbasis Superlegierung Waspaloy

Calculated life-times $N_{f,c}$ according to RTD-rule and MC-rule, plotted over the measured life-times N_f for nickel based superalloy Waspaloy

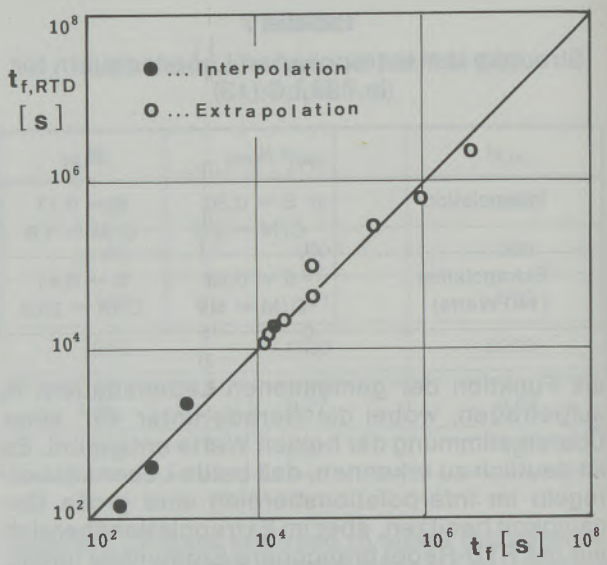

Abb./Fig. 5

Nach der RTD-Regel berechnete Zeitdauer bis zum Versagen $t_{f,RTD}$ aufgetragen über den gemessenen Zeitdauern t_f für die Nickelbasis Superlegierung PM Astroloy

Time to failure $t_{f,RTD}$ calculated according to the RTD-rule plotted over the measured time length t_f for nickel based superalloy PM Astroloy

observed (temperatures from 750 °C to 900 °C, frequency range of 6 orders of magnitude at 850 °C, various load cycles) the time-dependent deformations are of essential influence, whereby deformations that happen similar to stationary creep, with values of $r < 10$, only occured in 30 cases.

3.3 Nickel based superalloy Waspaloy

The LCF-data at 600 °C listed in table 8 result for $t_{f,c}$ (8) with the exponential rule

$$t_{f,c} = 1.4\ 10^{12} \exp(-5/60) \qquad [30]$$

and the Monkmant-Grant relation

$$t_{f,c} \cdot \dot{\varepsilon}_{min} = 2.3\ 10^{-3} \exp(5/271) \qquad [31]$$

for the RTD-rule the formulation:

$$N_{f,RTD} = N_{f,LATD} \cdot r^{-0.65} \qquad [32]$$

and for the MC-rule:

$$N_{f,MC} = 37.4\ (\Delta\varepsilon_{in}/2)^{-0.63}. \qquad [33]$$

The values for $N_{f,MC}$ and $N_{f,RTD}$ calculated by extrapolation to additional 29 sets of data out of LCF tests are plotted in fig. 4 as a function of the life times measured. Thereby scattering values with S = 0.28 and C/M = 4.3 (with the interpolation S = 0.17 and C/M = 1.6) result for the RTD-rule, and for the MC-rule S = 0.61 and C/M = 17.0 (with interpolation S = 0.02 and C/M = 1.1).

S = 0.28 und C/M = 4.3 (bei der Interpolation S = 0.17 und C/M = 1.6) und für die MC-Regel S = 0.61 und C/M = 17.0 (bei der Interpolation S = 0.02 und C/M = 1.1).

3.4 Nickelbasis Superlegierung PM Astroloy

Um die Möglichkeit der Extrapolation zu längeren Zeiten darzustellen, werden die nach der RTD-Regel berechneten Werte für $N_{f,RTD}$ in Zeiten $t_{f,RTD}$ umgerechnet und mit den gemessenen Zeitdauern t_f verglichen (Abb. 5). Der Parameter ν ist entsprechend den Werten in Tabelle 1 aus experimentellen Daten ermittelt, bei denen die Versuchsdauern weniger als fünf Stunden betragen haben. Wie Abb. 5 zeigt, ist es möglich, mit der RTD-Regel Lebensdauern bis zu Zeiten von 1000 Stunden vorauszusagen (Faktor 200) (8).

4. Zusammenfassung

Bei der Lebensdauervorhersage für hochfeste Werkstoffe, wie sie im Turbinenbau bei der Auslegung der Scheiben (PM Astroloy und Waspaloy) und Schaufeln (MAR M 509 und In 738 LC) Verwendung finden, ist sowohl die zeitabhängige Schädigung als auch die Ermüdungsschädigung zu berücksichtigen. Für die Prognose werden drei Regeln angewandt, deren Gültigkeitsbereiche durch entsprechende Werte des Dehnratenverhältnisses r abgegrenzt werden können.

Eine systematische Anwendung der drei Lebensdauerregeln auf zahlreiche Untersuchungsergebnisse hat gezeigt, daß die RTD-Regel bei r-Werten von 1 bis rund 10^6 angewandt werden kann. Die LATD-Regel, die Verformungsmechanismen, die ähnlich dem stationären Kriechen ablaufen, entspricht, gilt bei r = 1 und kann bis r = 10 angewandt werden. Die MC-Regel ohne Frequenzmodifikation soll bei r-Werten kleiner als 10^6 nicht eingesetzt werden, da in diesem Bereich die zeitabhängigen Effekte nicht vernachlässigt werden können.

Die LATD-Regel besitzt keinen anzupassenden Parameter, und die zyklische Lebensdauer kann direkt aus den stationären Kriechdaten berechnet werden. Die RTD-Regel besitzt einen Parameter ν und die MC-Regel zwei Parameter a und b. Aus den LCF-Daten der einzelnen Werkstoffe werden einige Datensätze zur Anpassung der Parameter verwendet und die übrigen Daten werden zur Extrapolation und zum Vergleich der berechneten Lebensdauern mit den gemessenen Werten herangezogen. Es zeigt sich, daß die RTD-Regel im Extrapolationsbereich ausreichend genaue Ergebnisse liefert und sich die Streuung der Werte gegenüber dem Interpolationsbereich nicht wesentlich vergrößert.

*

Diese Arbeit wurde vom Fonds zur Förderung der wissenschaftlichen Forschung in Österreich unter Projekt Nummer 5058 unterstützt.

3.4 Nickel based superalloy PM Astroloy

In order to present the possibility of extrapolation at extended times, the values for $N_{f,RTD}$ calculated according to the RTD-rule are transformed in times $t_{f,RTD}$ and compared with the measured times t_f (fig. 5). Corresponding to the values in table 1, the parameter ν has been determined from experimental data, where the length of time for the tests have been less than five hours. As fig. 5 shows, it is possible to predict life times up to 1000 hrs (factor 200) (8) by means of the RTD-rule.

4. Summary

For life time predictions of high-strength materials, such as are used for the construction of turbines for dimensioning discs (PM Astroloy and Waspaloy) and blades (MAR M 509 and In 738 LC), as well time-dependent damage as also damage from fatigue have to be considered. For a prognosis, three rules are applied, the validity of which can be limited by corresponding values of the ratio r of the inelastic strain rates.

Systematic application of the three life-time rules to numerous results of investigations have shown that the RTD-rule may be applied at r-values from 1 to appr. 10^6. The LATD-rule that corresponds to mechanisms of deformation similar to stationary creep, holds at r = 1 and may be applied up to r = 10. The MC-rule without frequency modification should not be used for r-values smaller than 10^6, since in this area time dependent effects cannot be neglected.

The LATD-rule has no adaptable parameter and the cyclic life time may be directly calculated from the stationary creep data. The RTD-rule has a parameter ν and the MC-rule has two parameters a and b. From the LCF-data of the single materials several sets of data are used for adaptation of the parameters and the other data are used for extrapolation and for comparison of the calculated lifetimes and the measured values. There it shows that the RTD-rule yields sufficiently exact results in the area of extrapolation and that the scattering of the values compared with the area of interpolation is not increased essentially.

*

This work was subsidized by „Fonds zur Förderung der wissenschaftlichen Forschung" in Austria under project no. 5058.

Literaturverzeichnis/References

1. Robinson, E. L.: Effect of Temperature Variation on the Long-Time Rupture Strength of Steels. Trans. ASME 74 (**1952**), S. 777–780.
2. Taira, S.: Creep in Structures, ed. N. J. HOFF, Springer-Verlag, Berlin (**1962**), S. 96–119.
3. Spera, D. A.: The Calculation of Elevated Temperature Cyclic Life Considering Low Cycle Fatigue and Creep. NASA TN D-5317 (**1969**).
4. Danzer, R.: The Validity Region of the Linear Creep Damage Accumulation Rule. Res Mechanica 13 (**1985**), S. 63–76.
5. Franklin, C. J.: Cyclic Creep and Fatigue Life Time Prediction in „High Temperature Alloys for Gas Turbines", ed. D. COUTSOURADIS et al, Appl. Science Publ. Ltd., London (**1978**), S. 513–547.
6. Danzer, R.: The Influence of Creep on the High Temperature Deformation Behaviour of Metals. Res. Mechanica 12 (**1984**), S. 259–273.
7. Ilschner, B.: Hochtemperatur – Plastizität, Springer-Verlag, Berlin (**1973**).
8. Danzer, R., und J. Bressers: A New Method to predict the Life under High-Temperature Low Cycle Fatigue Conditions. Fatigue & Fracture of Engineering Materials & Structures, im Druck.
9. Manson, S. S.: Behaviour of Materials under Conditions of Thermal Stress. NASA TN 2933 (**1953**).
10. Coffin jr., L. F.: A Study of the Effects of Cyclic Thermal Stresses on a Ductile Metal. Metal. Trans. ASME 76 (**1954**), S. 931–950.
11. Remy, L., F. Rezai-Aria, R. Danzer and W. Hoffellner: Evaluation of Life Prediction Methods in High Temperature Fatigue. ASTM–STP (**1986**).
12. Danzer, R., B. Buchmayr and G. B. Thomas: The Influence of Creep on the High Temperature Cyclic Life of In 738 LC. in "High Temperature Alloys for Gas Turbines **1982**", ed. R. BRUNETAUD et al, D. Reidel Publ. Co., Dordrecht, Boston, London (**1982**).
13. Danzer, R.: Life Time Prediction of the Gas Turbine Materials PM Astroloy, MAR M 509, Waspaloy, In 738 LC in the Creep-Fatigue Interaction Regime. COST 50/III, Joint Research Report (Nov. **1985**).

Determination and Description of Pore Structure in Ceramics

Dieter Vollath, Karlsruhe*)

Dedicated to the 80th birthday of Prof. Dr. Franz Lihl

This review explains the determination of pore structure of sintered material by image analysis and mercury porosimetry. Based on the experimental results a model for the pore structure of sintered ceramics is given.

Bestimmung und Beschreibung der Porenstruktur in Keramiken

Dieser Überblick erklärt die Bestimmung von Porenstruktur von gesintertem Material mittels Bildanalyse und Quecksilber Porositätsbestimmung. Aufgrund der Versuchsergebnisse wird ein Modell für die Porenstruktur gesinterter Keramiken präsentiert.

Détermination et description de la structure des pores dans la céramique

On résume et on explique dans cet article les modes de détermination de la structure des pores dans les matériaux frittés au moyen de l'analyse d'images et de la méthode du mercure. En se basant sur les résultats expérimentaux, on présente un modèle de structure poreuse des céramiques frittées.

1. Introduction

Bodies made from oxide ceramics are never fabricated so as to be completely dense. The fabrication of high density material would be extremely difficult in the powder metallurgical techniques applied. Also it would not be reasonable because the porosity often is required to adjust materials properties. In principle, the porosity of a sintered body can be subdivided into two categories:

- Open porosity, which is the fraction with a connection to the outside. This fraction is mainly responsible for all phenomena relating to the gas exchange between the workpieces and their environment.
- Closed porosities.

The sum total of these two contributions reflects the total porosity. The way in which the homogeneity of the porosity distribution is determined will not be described here. This applies in particular to the homogeneity coefficient and the autocorrelation function characterizing the distribution (1), (2).

2. Determining open porosity

The open porosity fraction is determined by penetration techniques. One of these methods is mercury porosimetry. In this method, mercury under high presure is forced into a specimen evacuated in advance. A channel size distribution can be determined from the pressure input p and the volume of mercury forced into the specimen. The mercury forced through channels connecting the pores into the pores under the pressure p does not completely fill the pores, but approximates the shapes of the pores to a surface characterized by the minimum radius r of the mercury meniscus. This radius corresponds to the smallest channel into which mercury can penetrate in a measurement at the pressure p. Under the assumption of cylindrical channels this size D = 2 r is obtained from formula (3):

$$D = -4\,\sigma \cos \Theta / p.$$

σ is the surface tension of the mercury and Θ is the contact angle of mercury with the solid. For σ and Θ the values of σ = 473 dyne/cm and = 130° were selected in accordance with Winslow and Shapiro (4). If different values are chosen for these materials constants, this may result in differences in size up to a maximum of 20‰.

Fig. 1 reflects the results of one such measurement. In this diagram the volume of the mercury forced into the open porosity was plotted in a cumulative plot against the logarithm of the channel size. In this example we see a marked rise of the pore volume accessible from the outside in the region of meniscus radii between 0.2 and 0.1 μm and in the range below 0.01 μm. If the mercury

*) Univ.-Doz. Dr. Dieter Vollath, Kernforschungszentrum Karlsruhe GmbH., Institut für Material- und Festkörperforschung III, Postfach 3640, D-7500 Karlsruhe

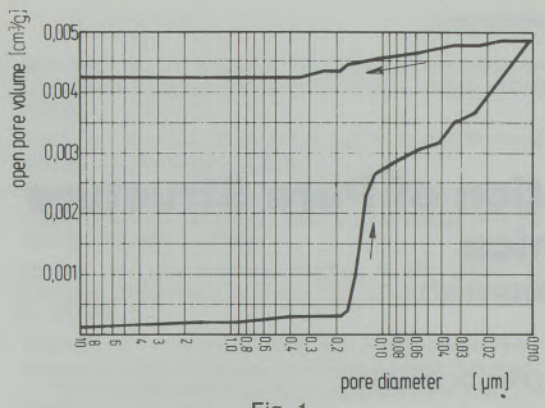

Fig. 1
Example showing the hysteresis in mercury intrusion porosimetry

pressure is reduced after the maximum pressure has been attained, the mercury, under the pressure of its surface tension, is again forced out of the pores. If one carries out an experiment of this kind, one recognizes pronounced hysteresis between the pore volume when raising the pressure and that associated with pressure reduction.

The plot of the specimen volume depicted in fig. 1 which can be filled by channels up to a given size plotted versus the channel size. The volume fraction of the channels can be determined as the pressure is reduced. If the difference is formed between the maximum volume filled by mercury and the mercury volume contained in the specimen at a reduced pressure, this furnishes the volume of all channels whose diameters are smaller than would correspond to twice the meniscus radius at the pressure p. Differentiation of the curve of the channel volumes and subsequent division by the cross section areas of the channels allows an estimate to be made of the length of the channels as a function of channel size. Of course, this procedure is no longer very meaningful in the range of very small channels, because these small volume changes can no longer be determined exactly enough.

3. Determining pore size distributions by image analysis

Measuring size distributions of pores in samples prepared ceramographically constitutes a determination of the size distributions of all pores in the area of a section. Hence, the measurement cannot distinguish closed pores from open ones. However, only those pores are accessible to this type of measurement which also fall in the range of enlargement of the microscope used.

As in any particle size determination, measurements are only meaningful after proper definition; also in pore size determination an adequate definition of pore size has to be found. As long as the pores are largely spherical the pore size can be characterized by the diameter of the circle of intersection. For this reason, the maximum chord length in the scanning direction of the image analyzer may be used as a measure of pore size. From this linear measured result one can then calculate the sizes of the spheres from which this distribution of the size of intersection was obtained.

In the general case however, we are interested to obtain information on the shape of the pores. Depending on the method of production our material may have pores of significant different shapes stemming from different steps in the production. This means, we have to determine the size of pores with respect to a given shape, e.g., circles or triangles.

To perform such a measurement we shall "deform" the pores by means of the Minkowski sets operations (5).

We assume, a binary picture (set) B with particles representing e.g. the pores P in it and a set of structuring elements (templets) S representing the class of shapes, in which we are interested.

In this case, S shall be added to B according to the rules the Minkowski addition

$$B' = B \oplus S$$

The Minkowski addition (dilation) is the union of the vectorial sums of all position vectors of the sets B and S to be joined.

In geometrical terms, this can be imagined such that the origin of S passes along the contour of the pores P within the image B. The area covered in this process then constitutes the resulting figure. The Minkowski subtraction (erosion) is described by an appropriate inversion formula as proposed by Hadwiger (5).

$$B'' = B \ominus S = \overline{B} \oplus \tilde{S}$$

$\tilde{S}$ is the set S reflected about the origin. In this case the origin of S passes along the contour of the pores P. $\tilde{S}$ always moves within P. The area covered by S, which is part of P, is canceled out. It is now plausible without difficulty that, depending on which figures S is selected, different results are obtained. The decisive factor is, however, and this has been indicated by Delfiner (6) that by the process of the Minkowski subtraction the particles can be classified by the shape of S. If one wishes to classify a particle P according to a sequence of homothetic test patterns S_i, this sequence must be so ordered that each pattern with the number i is an element of the pattern with the number $i + 1$ and hence an element of each pattern with a number greater than i (7).

$$S_i \subset S_{i+j} \qquad i, j \in N$$

The size of the maximum inscribable test pattern is characterized by the fact that the pattern with the number i is still the element of P, but not the pattern with the number $i + 1$ or greater.

$$P = P(S_i) \Leftrightarrow S_i \subset P \,.\, \Lambda \,.\, S_{i+j} \,.\, P \qquad j > o$$

The element S is now the greatest inscribable element if after the Minkowski subtraction involv-

ing S_i a rest of P is left but after the Minkowski subtraction involving S_{i+1} nothing, i.e., only a null set is left of P.

$$P = P(S_i) \Leftrightarrow P \ominus S_i \neq \varnothing \,.$$
$$\Lambda \,.\, P \ominus S_{i+j} = \varnothing \qquad j > o$$

Using the method described, it is possible to classify pores by shape and size. To make, e.g., a distinction between rather spherical and rather tetrahedron shaped pores, this analysis can be performed once with a triangle and once with a square as the elements S (7), (8). For triangular patterns it must be considered in addition that in a discrete cartesian coordinate system four congruent equilateral rectangular triangles exist which can be converted into each other by rotation. These four possible orientations must be taken into account in the measurement.

After the measurements have been made with triangles and squares, the individual results of measurements have to be assigned to these figures.

Two assumptions can be made for this separation. Asuming that the shapes of the pores can be described rather well by triangles or squares, one subsequently supposes that in each figure into which a square can be inscribed also a triangle of equal size can be inscribed (inclusions). This means that these triangles cannot be counted. However, also a square of half the lateral length can be inscribed into each triangle.

Since in this case the square is the smaller figure, it is eliminated from counting. If the figures cannot be so well assigned, another assumption is made. On this assumption the figure is evaluated as being a square in case one can inscribe either a triangle of equal edge length or if the area of an

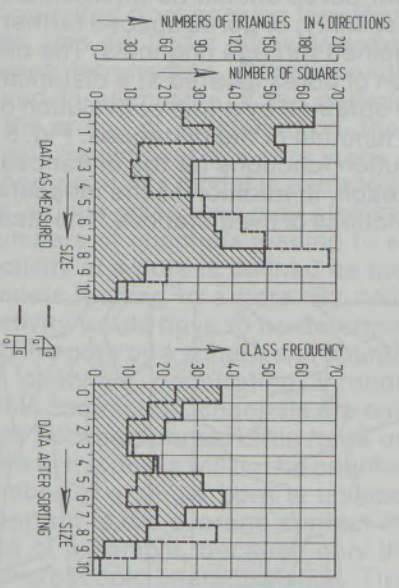

Fig. 2
Classification of pores of a pellet by size and shape (granulated powder)

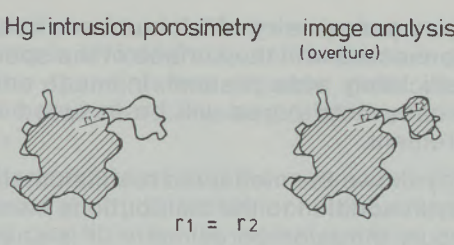

Fig. 3
Comparison of the methods for measurement of porosity by Hg-intrusion porosimetry and image analysis

inscribable square is greater than that of the inscribed triangle. Consequently, figures having the same area constitute the limit case.

Fig. 2 shows measured results obtained from sample made of granulated powder. In the left part of the figure the roughly measured data are entered with the result of the four orientations of the triangles added up. In the right part the classification by shape and size has been entered. Since approximated triangular pores have to be treated here, the assumption of inclusions could be used for evaluation.

We see that in the sample under consideration the greatest pores are rather triangular than square. If we compare these results with measurements obtained from single-pressed material, we could recognize major differences. In this case the dominance of the rather round pores would be apparent.

Additionally, we obtain very interesting insights into the pore structure, if we use a circular structuring element. In this special case we can directly compare these results from image analysis with the results obtained by mercury prosimetry.
This measurements are done by an image transformation called "ouverture" (9). We obtain the transformed image B' in this case by

$$B' = (B \ominus S) \oplus S$$

The result of this transformation applied, e. g., to a pore using a circle as structuring element S is shown in the right hand side of fig. 3.

Hence, especially in this case it is better to get away from pore counting and measure the area fractions instead. In this type of measurement the area fractions of pores are determined whose surfaces are characterized by a minimum radius of curvature, the radius of the circular structuring element S. This radius of curvature at the same time is the radius of the smallest pore considered in each step of the measurement. If this radius of curvature ist selected as a parameter, one obtains a dependence of the pore volume on the radius of curvature, similar as in a mercury porosimeter. Fig. 3 shows a comparison of the principle of measurement applied to mercury porosimetry and the image analysis technique chosen.

If the same radius of the meniscus is used in both cases, only the large pore will be filled in the case

of mercury porosimetry which had been assumed to be connected with the surface of the specimen by a sufficiently wide channel. In image analysis in this case both pores will be included in the measurement.

Fig. 4 (1) shows the measured results obtained in this way in addition to the distributions measured by mercury intrusion porosimetry. It is seen that pores measured by image analysis are much larger than the channels between the pores. This is confirmed by the pore model outlined in fig. 5a which is based on large pores interconnected by narrow channels. In plotting the measured results it was not taken into account in this case that the pore size reflects only sections in three-dimensional structures because, in this representation, it was primarily important to establish a comparison of sizes which, in this double logarithmic plot, is hardly influenced by the conversion to three-dimensional structures.

It is seen that in the sample available, most channels are in the size range of the smallest measurable channels. One restriction must be made with respect to the descriptions given above. In the diagram of the channel volumes not only the volumes of the channels can be found but, in addition, also the volumes of small bulges of pores which are also filled with mercury at the same time as the channels. However, introducing such a distinction would create major difficulties in a precise definition; hence, this conceptual distinction should not be maintained.

The hysteresis of the mercury intrusion porosimetry depicted in fig. 1 is in combination with the results of image analysis fig. 4 only possible, if the pore structure is like that in fig. 5a. A structure like such plotted in fig. 5b is based on the measured result impossible in our type of materials.

This means, in the material represented here, we find larger pores interconnected by fine channels. The diameter of these channels then represent the quantity determined by means of the mercury pressure.

4. Determining distances between pores

If we count the number of pores before and after application of a dilation using a structuring element S, the difference between these two counts gives the number of pores within a neighborhood described by S. This can be used to determine the distance between pores if we use a circular structuring element.

However, this definition admits the existence of channels inside the sphere interconnecting the individual pores. The definition is rather arbitrary insofar as a strict distinction is made between pores and channels which does not exist in practice. But it can be seen from the measured results (fig. 3) that the diameters of the channels connecting the pores are generally smaller than 1 μm. Since our measurement by image analysis does not take into account pores smaller than approx. 1.4 μm, this definition is unequivocal from the point of view of measuring techniques. Similar constraints are met when measuring the distance distribution of pores.

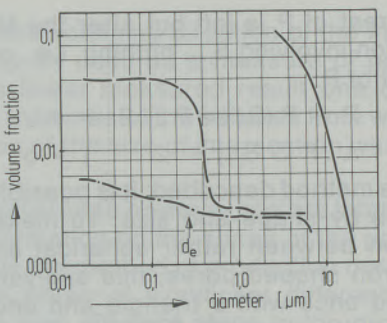

Fig. 4
Size distribution of open porosity, channels and total porosity
—— total porosity (image analysis)
– – – open porosity (mercury intrusion porosimetry)
-.-.- channel volume

Fig. 6 shows one such distance distribution by way of example. This distribution was normalized in such a way that the sum total of all distances smaller than the lower limit was assumed to be unity. In this distribution a dominating role of short distances is evident (1), (10).

The distances measured in this way must not be mixed up with the lengths of the channels, because the channels must not be assumed to extend straight from pore to pore. When estimating the channel lengths one must also consider the curvature in the calculation. This means that the channels are longer by the tortuosity than would correspond to the diameter of the largest spheres inscribable between the pores. Next it must be stated that there is no reason why only directly adjacent pores should be interconnected. There is a possibility, of pores spaced farther apart also being joined through channels. The distance distribution of pores located at a distance of n-pores can be obtained by n-fold convolution of the distribution function of the distances. Fig. 6 shows the distribution functions for the distances of 2 and 4 pores each, in addition to the measured distribution functions of the distances. The mean distance

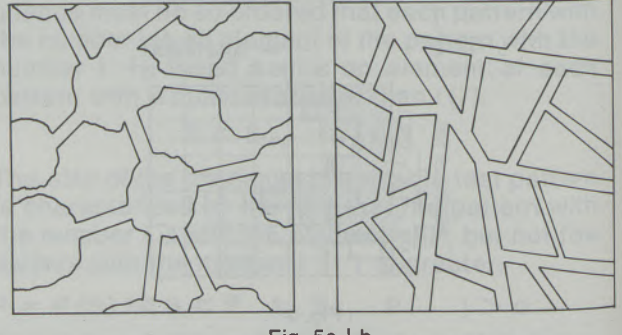

Fig. 5a+b
Different types of pore networks

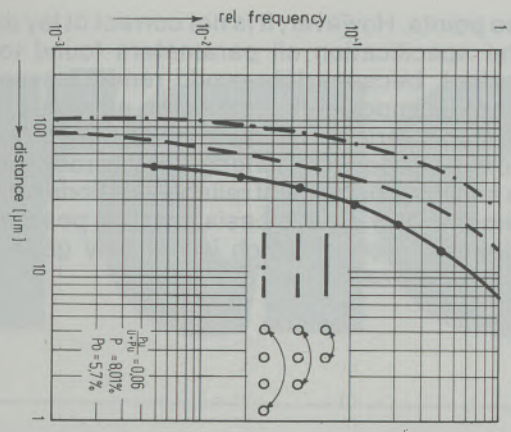

Fig. 6
Distances between pores and their next and following neighbors

between 2 pores each is 12.5 μm, that between the next but ones is 25.4μm, and the pores located at a distance of 4 pores are 41.2 μm away. However, also these distances must still be enlarged by the tortuosity because the channels certainly do not constitute the shortest connection between two pores. Only by additionally assuming the existence of such long channels it is possible to explain the relatively large channel volumes as determined by mercury intrusion porosimetry.

5. Determining the mean connectivity of pores

The pores of the open porosimetry are interconnected by channels. Each pore must have at least two connections to make it a real open porosity. If a pore has only one connection, it is the end of a channel. If one imagines that a porous structur may have originated from packing together isolated particles, one will find a porosity node in the center of each tetrahedron. Consequently, four channels lead to each pore. If the particles are packed in the shape of a octahedron, there are eight channels leading out of a pore in the center of the octahedron. If this model is extrapolated to particles of various sizes, one may also arrive at different numbers of channels leading to a pore. The connectivity of a pore is defined as the number of channels leading to a pore. By definition, this connectivity would have to be determined by surrounding the pore by a sphere and counting the number of channels penetrating through this sphere. In this connection, channels are only connecting lines between pores. Little bags our bulges attached to the pores will not be counted. The contact number of a single pore is unimportant; what is important is the average contact number of the pores of a sample, because only this will affect the microscopic characteristics. The term connectivity has been introduced here to describe the three-dimensional pore structure. In principle, this description could have been achieved also through the genus of the pore system (11). However, this is an integral quantity which, e. g., may describe the sintering process quite well, but leads to a number furnishing relatively little information.

A method of determining the mean connectivity is gas permeation (12). In this technique, a specimen is held gas-tight by its lateral surface and the amount of gas is measured which can be forced through this pellet at a given differential pressure. One difficulty of the method lies in the fact that the gas flow occurs in the highly pressure dependent region of viscous flow. This will affect the accuracay of evaluation. In addition, high-density material may involve the difficulty of there being too few or no through channels for gas flow. In that case, these measurements can no longer be carried out. These problems do not occur in the application of the gas effusion method in which the pellets are filled with helium and the outflowing helium is traced as a function of time.

By proper selection of the filling pressure it can be ensured that the gas flow will occur always in the pressure independent region of molecular flow. These measurements and the respective theory for evaluation are described in detail by M e n g e l and V o l l a t h (13). Since in this method the outflow of the gas from the pores is measured, it is not neccessary for the sample to have a finite gas permeability. The only precondition is the existence of open porosity.

Input quantities for the evaluation of gas effusion experiments, in addition to the development of the gas release as a function of time, are porosity, pore size distribution and the distances between the pores. For the distances between the pores additional assumptions must be made about the frequency of direct connections to neighbors located at geater distance. If the connectivity were to be determined by calculating the absolute number of pores by means of pore size distribution and the overall length of channels as determined by mercury intrusion porosimetry, the product of channel length per pore multiplied by the connectivity would be found out. The connectivity can only be determined by the additional results from gas effusion measurements (13).

Contact numbers found in our experiments are normally between 3 and 4 (14). In special cases contact numbers up to about 40 are found. Contact numbers larger than 8 can not be explained by simple geometrical models. We have found that those high contact numbers are always connected with specimen containing cracks (14).

6. Conclusions

A material is not fully characterized by measurement of individual structural parameters. Only if a connection can be established between these parameters, the structure can truly be understood. However, this requires high efforts in mea-

surement and the mathematical description of the structures. This has been shown in this paper using the example of pore structure. Characterizing sample material is not an end in itself. Instead, it is to help in the verification whether a material is fabricated uniformly and to specifications. Minor differences in pore structure may, e. g., greatly affect thermal conductivity or the gas exchange behavior. And it is these parameters which influence the behavior of the material so much that there should not be any deviations in those points. However, it is not correct ot lay down in the specification all parameters found to be important, because this would render economic fabrication impossible. Finding an adequate optimum in this variety of parameters is based, first of all, on the precise knowledge of interdependencies and the existence of reliable methods of measurement. Only on this basis it will be possible to fabricate a product which is not only good, but also economical.

References

1. Vollath, D.: Methods of Characterizing Fuel Structure. J. Nucl. Mat. 81 (**1979**), 115.
2. Vollath, D.: The Application of a Normalized Correlation Function in Image Analysis. J. Microscopy 122 (**1981**), 35.
3. Washburn, E.: Proc. Nat. Acad. Sci. 7 (**1971**), 115.
4. Winslow, N. M., J. J. Shapiro: ASTM Bull. 226 (**1959**), 39.
5. Hadwiger, H.: Minkowskische Addition und Subtraction beliebiger Punktmengen und die Theoreme von Erhard Schmidt, Math. Zeitschrift 53 (**1950**), 210.
6. Delfiner, P.: Generalization of the Concept of Size, J. Microscopy 95 (**1972**), 203.
7. Vollath, D.: Optical Methods in Nuclear Fuel Characterization, J. Nucl. Mat. 106 (**1982**), 71.
8. Vollath, D.: Das Bildanalysensystem PACOS, Praktische Metallographie 19 (**1982**), 7, 94.
9. Serra, J.: Stereology and Structuring Elements, J. Microscopy 95/1 (**1972**), 93.
10. Mengel, P., D. Vollath: Determination of the Three Dimensional Characteristic of Pore Network, J. Microscopie 37 (**1980**), 381.
11. DeHoff, R. T., in R. T. DeHoff, F. N. Rhines: ORO-4212-16 (**1975**).
12. Rhines, F. N., R. T. DeHoff, E. D. Whitney: ORO-4212-1- (**1975**).
13. Mengel, P., D. Vollath: Charakterisierung des Porennetzwerkes in UO_2-PuO_2-Brennstofftabletten, J. Nucl. Mat. 81 (**1979**), 143.
14. Vollath, D., H. Wedemeyer: Influence of Process Parameters on the Fabrication of UO_2-PuO_2 Pellets using the Granulation Process, J. Nucl. Mat. 106 (**1982**), 191.

RUNDSCHAU
radex
RADENTHEIN, IM DEZEMBER 1986

Inhalt — Heft 4

Theoretische und praxisbezogene Versuchsergebnisse von Gasspülsteinen für Stahlgießpfannen

Helmut Preyer, Urmitz; Hans Höffgen, Urmitz; Bernd Grabner, Radenthein

Gasspülsteine unterschiedlicher Konzeption wurden in einem Wassermodell auf das Spül- und Homogenisierungsverhalten getestet. Während Steine mit „gerichteter Porosität" auch bei höheren Gasmengen ein ruhiges Blasverhalten aufwiesen, kam es bei Steinen mit erhöhter Porosität zur Koaleszenz der Gasblasen in horizontaler und vertikaler Richtung. Weiters wurden von Praxiseinbauten Spülsteine mit „gerichteter Porosität" auf das Verschleißverhalten hin untersucht.

Theoretical and Practical Results of Trials with Permeable Plugs

Purge plugs with different gas injection systems were tested in a water model for the purging and homogenizing effect. Whilst plugs with "directed porosity" showed a constant detachment of gas bubbles with plugs with high open porosity a horizontal and vertical coalescence was observed. Further the wear behaviour of some purge plugs with "directed porosity" after service was investigated.

Résultats d'essais théoriques et pratiques de bouchons poreux pour poche de coulée

Des bouchons poreux de différents principes ont subi un essai de simulation dans de l'eau pour définir les comportements de bullage et d'homogénéisation. Alors que des bouchons à «porosité dirigée» montrent un comportement de bullage régulier, meme dans le cas de débit élevé, d'autres bouchons à porosité non dirigée (porosité élevée) montrent une «agglomération» de bulles d'air les directions horizontale et verticale. Actuellement, nous effectuons des essais d'usure réels de bouchons à «porosité dirigée».

1. Einleitung

Das Einblasen von Inertgas in Metallschmelzen gehört zum Stand der Technik. Auf die Gründe, die zur Einführung der verschiedenen Verfahren führten, soll hier nicht weiter eingegangen werden, da diese bereits häufig in der Literatur beschrieben wurden (1) bis (6). Auch die verschiedenen Spülsteintypen und Formate wurden bereits in der Literatur beschrieben. Abb. 1 zeigt die historische Entwicklung und die derzeit zur Anwendung kommenden Spülsteintypen.

Hiebei wird das Gas beim Fugenspüler durch den freien Spalt zwischen Blech und dichter Keramik in die Stahlschmelze geleitet. Bei Spülsteinen mit ungerichteter Porosität wird das Inertgas durch den erhöhten Anteil offener Poren in die Stahlschmelze geleitet. Im Gegensatz hiezu wird bei Spülsteinen mit gerichteter Porosität das Gas durch eine bestimmte Anzahl von Kanälen mit definiertem Durchmesser in die Schmelze geleitet.

Bei Fugenspülsteinen besteht die Gefahr, daß bei fortschreitendem Verschleiß flüssiger Stahl nach Beendigung der Spülbehandlung in die Fuge dringen kann. Ausbruchsteine von Spülsteinen mit ungerichteter Porosität zeigen in der Regel eine Infiltration von Stahl / Schlacke in einer Stärke von 20 bis 30 mm. Neben der Gefahr von Spülaussetzern besteht der stark verschleißfördernde Nach-

1. Introduction

The injection of inert gas into metal melts is today's state of art. The reasons for the application of the different processes is known from the literature (1)–(6), as well as the different types and shapes of permeable plugs. Fig. 1 shows the development and the different types of the presently applied permeable plugs.

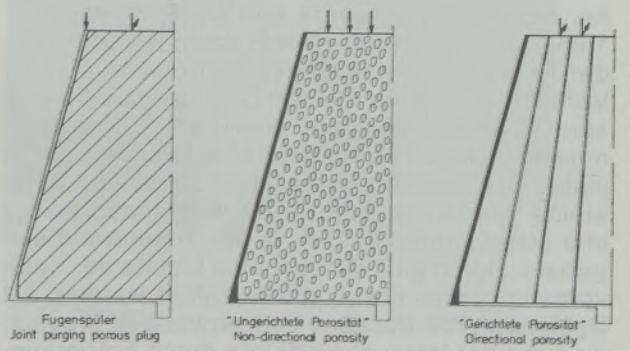

Abb. / Fig. 1

Derzeit in der Stahlwerkspraxis angewandte unterschiedliche Spülsteintypen

Presently in steel plants applied different types of permeable plugs

teil, daß diese infiltrierten Bereiche zwischen den Spülbehandlungen durch Spüldruck abgesprengt werden. Durch die Verwendung von dichter, hochverschleißfester Keramik zeigen Spülsteine mit gerichteter Porosität nur einen Infiltrationsbereich von 3 bis 5 mm.

Um den Einfluß der unterschiedlichen Spülsteintypen auf die Ausbildung der Gasblasen bzw. des Blasenschwarmes zu eruieren, wurden bereits Modellversuche (7) durchgeführt. In dem in (7) beschriebenen Modell wurden die Vorgänge, die beim Einbringen von Gas in Flüssigkeiten ablaufen, unter niedrigen Drücken bzw. Gasmengen, abhängig von der Modellgröße, beobachtet. Demnach unterscheidet man in Abhängigkeit vom Gasdurchsatz verschiedene Strömungsbereiche. Bei schwacher Gaszufuhr entstehen an den Gasaustrittsöffnungen einzelne Blasen, deren Größe direkt von den Eigenschaften des Systems (z. B. Porengröße, ferrostatischer Druck und Viskosität der Flüssigkeit) abhängt. Bei steigender Gaszufuhr bleibt die Blasengröße bis zu einem kritischen Wert konstant, während sich die Blasenfrequenz ändert. Oberhalb dieses kritischen Wertes erhöht sich die Blasengröße, während die Blasenfrequenz konstant bleibt. Die Größe der Primärblasen hängt jetzt vorwiegend vom Gasdurchsatz ab. Neben dem Gasdurchsatz ist aber auch der Abstand der Gasaustrittsöffnung von ausschlaggebender Bedeutung, da bei geringen Poren- bzw. Kanalabständen die austretenden Gasblasen in horizontaler Richtung miteinander koaleszieren können. Bei weiterer Steigerung des Gasdurchsatzes kommt es zur Koaleszenz der Gasblasen in vertikaler Richtung. Der Einzelblasenbereich geht in den Bereich des geschlossenen Gasstrahles über (7).

2. Versuchsdurchführung

Ziel der Modellversuche in einem größeren, den tatsächlichen Praxisverhältnissen angenäherten Wassertank war es, die Vorgänge beim Einblasen von Gas in Flüssigkeiten auch bei hohen Drücken und Gasmengen beobachten zu können.

Als Modellanlage diente ein Wassertank (D = 1,05 m, H = 2,0 m) mit einer Füllmenge von 1,3 m^3, der in seinen Abmessungen den geometrischen Verhältnissen einer kleinen Stahlgießpfanne entsprach. Als Meßanlage wurden Geräte (Druckmanometer, Durchflußmeßgeräte) verwendet, die in vielen Stahlwerken gebräuchlich sind. Die Spülsteine wurden sowohl im Behälterboden (mittig und außermittig) als auch in der Seitenwand eingebaut. Durch eine Glasscheibe konnte der Spülvorgang beobachtet und fotografiert werden. Als Spülgas wurde trockene Luft verwendet. Die Auswertung der Versuche erfolgte durch Fotografieren, visuelle Betrachtungen und Videoaufzeichnungen.

Als geometrische Einflußgrößen wurden der Kanaldurchmesser bei Spülsteinen mit gerichteter

Through the plugs with joints the gas is pressed between the steel case and a dense refractory brick into the melt. In purge brick with non-directional porosity the gas is pressed through the increased amount of open pores. In brick with "directed porosity" the gas is pressed through a certain number of small channels with a defined diameter.

With joint purge brick it may occur at advanced wear that after purging steel may penetrate into the joint. As post mortem investigations showed, in purge brick with high open porosity, the penetration depth of steel and slag may reach appr. 20–30 mm. Beside the possibility of purge failures the infiltrated parts of the purge brick may lead to the spalling of this zone, especially under gas pressure. By using a dense refractory product with high wear resistance purge brick with directed porosity show an infiltration depth of appr. 3–5 mm.

In order to investigate the influence of the various types of purge brick on the formation of gas bubbles, model trials were already performed (7). In this model the parameters for the penetration of gas into liquids were investigated under low pressures resp. low amounts of gas, depending on the size of the model. According to this investigation different regimes of gas flow depending on the gas pressure and amount can be differed. With low amounts of gas single bubbles are formed at the orifice, the bubble size depending on the properties of the system (like pore size, viscosity of the liquid gas pressure). With rising amount of gas remains constant into a critical value with changing frequency of bubbles. Above this critical value the size of the bubbles is increased at constant bubble frequency. The size of the primary bubble depends mainly on the amont of gas. Besides the amount of gas the distance of the orifices is of great importance because of the possibility of a horizontal coalescence of the bubbles. A further increase of the amount of gas causes the formation of a gas jet by vertical coalescence of the bubbles – the regime of single bubble formation is transferred into a gas jet (7).

2. Performance of the trials

The aim of the water model trials in a greater scale (similar to real size) was the observation of the processes of gas purging at higher amounts and pressures of gas.

As model a water tank with a diameter of 1.05 m a height of 2.0 m resp. a volume of appr. 1.3 m^3 was used, in the dimensions being similar to a small steel casting ladle. As measuring devices manometers and flow meters were used being known in most steel plants. The purge brick were installed in the bottom of the model (in the center

Porosität, die Anordnung der Spülkanäle im Spülstein sowie die Anordnung des Steines im Reaktionsgefäß berücksichtigt. Des weiteren sollte untersucht werden, ob zwischen Spülsteinen mit „ungerichteter Porosität" im Vergleich zu Steinen mit „gerichteter Porosität" hinsichtlich des Spülverhaltens, insbesondere in bezug auf Blasenbildung und Blasengröße sowie Einflüsse auf die Rührwirkung, starke Abweichungen auftreten.

An feuerfesten Gasspülsteinen, bei denen das Spülgas durch künstlich erzeugte Kanäle (sogenannte gerichtete Porosität) geleitet wird und die umliegende Keramik gasundurchlässig ist, wurde der Einfluß des Spülkanaldurchmessers auf die Blasengröße untersucht. Dazu wurden Steine mit Kanaldurchmessern von 0,6 mm, 0,7 mm, 1,0 mm, 1,5 mm und 2,0 mm angefertigt. Diese wurden bei vergleichbaren, abgestuften Gasvolumenströmen im Wassermodell beobachtet und fotografiert. Des weiteren wurden Spülsteine mit

and eccentric) as well as in the sidewall. Through a glas window the trials could be observed and photographed. As gas air was used. The documentation and evaluation of the trials was performed by visual observation, photographs and video records.

As geometrical parameters the channel diameter of purge brick, the situation of the channels and the location of the plug installation were recorded. Additionally possible differences of plugs with higher open porosity versus directed porosity regarding the bubbling behaviour, especially formation and size of bubbles and the influence in mixing efficiency were investigated.

For purge plugs with directed porosity the influence of the channel diameter on the size of the bubbles was also observed. For this purpose plugs with 0.6 mm, 0.7 mm, 1 mm, 1.5 mm and 2 mm channel diameter were produced. These

MODELLUNTERSUCHUNGEN AN GASSPÜLSTEINEN
MODEL TRIALS WITH PURGING BRICKS

Abb./Fig. 2
Spülstein mit ungerichteter Porosität
Druck: 0,3 bar; Volumenstrom: 33,3 Nl/min
Purge brick with high open porosity
Pressure: 0.3 bar; gas volume: 33.3 Nl/min

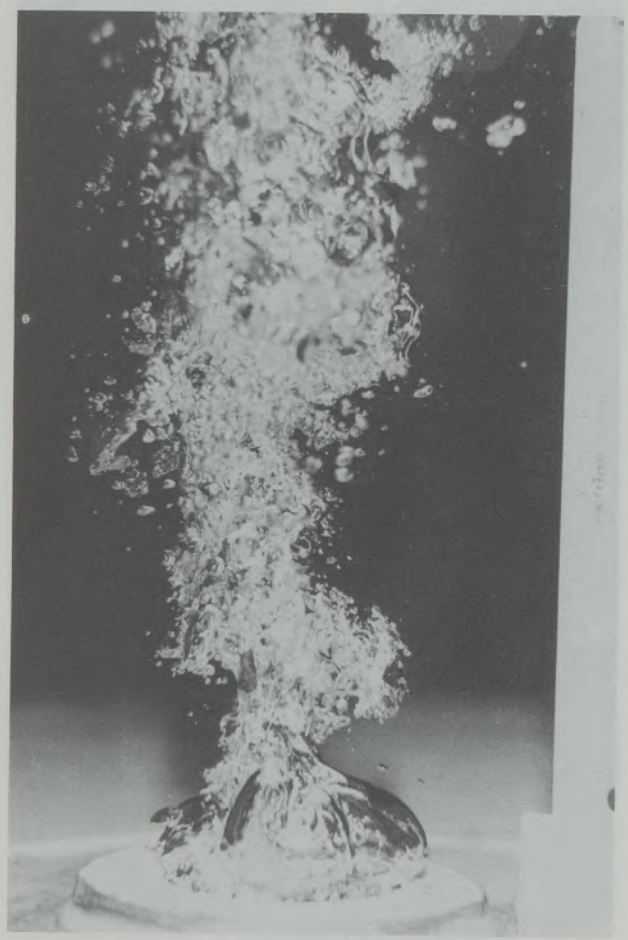

Abb./Fig. 3
Spülstein mit ungerichteter Porosität
Druck: 0,5 bar, V: 66,67 Nl/min, erste Bildung von Großblasen
Purge plug with high open porosity
Pressure: 0.5 bar, gas volume: 66.67 Nl/min, first formation at great bubbles

einer erhöhten offenen Porosität (sogenannte ungerichtete Porosität) unter gleichen Bedingungen überprüft und mit den Ergebnissen mit der gerichteten Porosität verglichen. Weiterhin wurde die geometrische Anordnung der Spülkanäle im Spülstein und deren Einfluß auf die räumliche Ausdehnung eines Gasblasenschwarmes nach dem Austritt aus dem Spülstein ermittelt. Dazu wurden Spülsteine verwendet, bei denen die Spülkanäle unterschiedliche Neigungswinkel aufwiesen.

Um den Einfluß der geometrischen Anordnung des Spülelementes im Reaktionsgefäß zu ermitteln, wurden Meßsonden in die Modellanlage eingebaut. Nach Zugabe von Elektrolyten wurde die Änderung der elektrischen Leitfähigkeit über der Zeit gemessen (9). Dadurch ließ sich die Homogenisierungsleistung sowohl verschiedener Spülsteintypen als auch bei unterschiedlicher geometrischer Anordnung im Gefäß gut feststellen.

plugs were observed and photographed, purging with comparable amounts of gas in the water model. Also plugs with high open porosity were tested under the same conditions and the results compared with these of the "directed porosity" plugs. Also the influence of the geometrical arrangement of the channels in the plug on the volumetic expansion of the bubble swarm were investigated. For this purpose purge plugs with different angles of inclination were used.

In order to evaluate the influence of the location of the plug in the water model, measuring devices were applied. After the addition of an electrolyte the change of the electrical conductivity within the time was measured. With this device the effect of homogenisation of various types of purge brick as well as the effect of different locations of the plugs in the water model could be investigated.

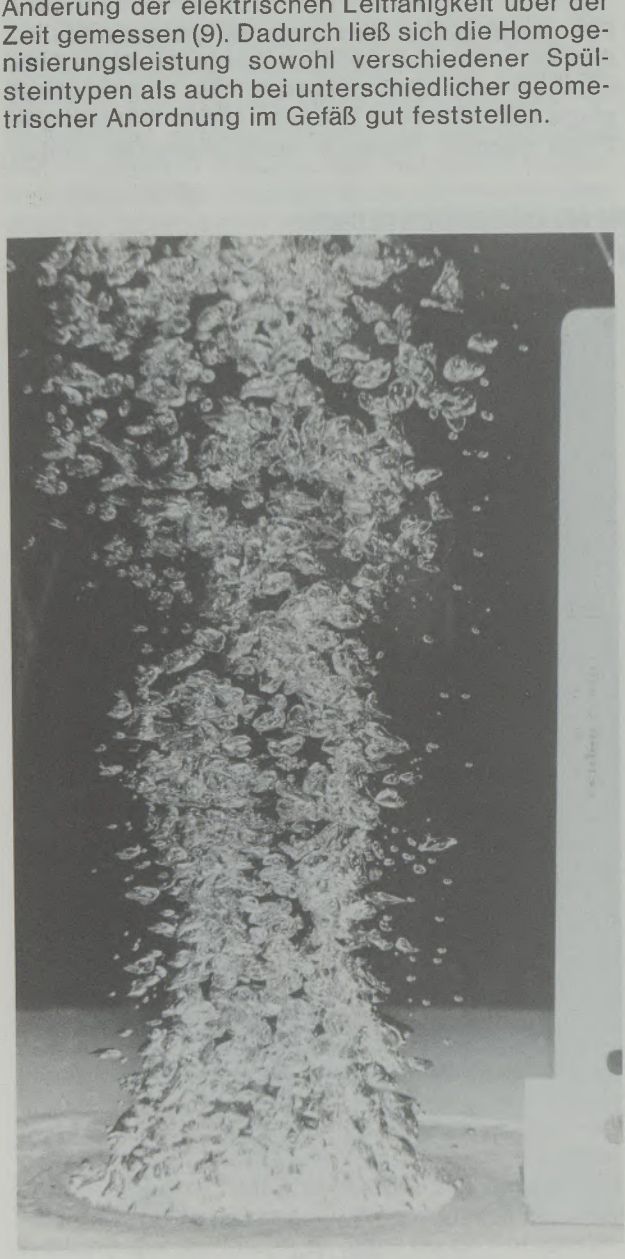

Abb./Fig. 4
Spülstein mit gerichteter Porosität
Druck: 0,4 bar; Volumenstrom: 33,3 Nl/min
Purge brick with directed porosity
Pressure: 0.4 bar; gas volume: 33.3 Nl/min

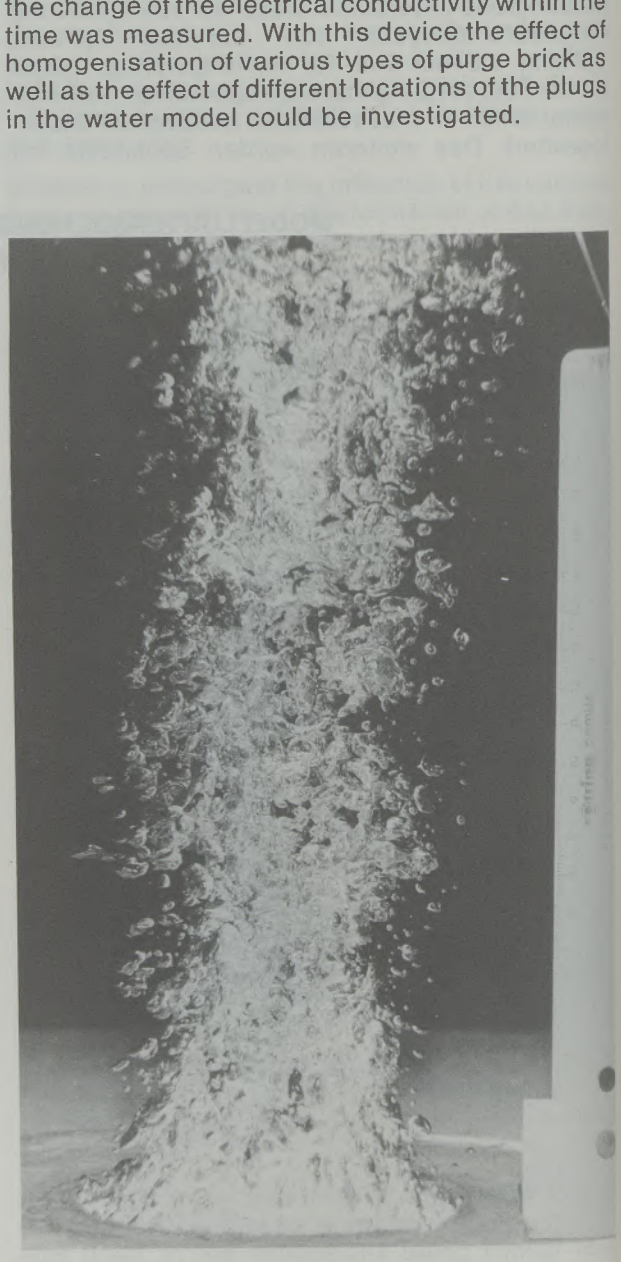

Abb./Fig. 5
Spülstein mit gerichteter Porosität
Druck: 1 bar; Volumenstrom: 66,67 Nl/min
Purge brick with directed porosity
Pressure: 1 bar; gas volume: 66.67 Nl/min

3. Ergebnisse

Bei Versuchen im Labormaßstab, also bei sehr geringen Drücken und Volumenströmen, ist bisher oft festgestellt worden, daß kleine Porendurchmesser, wie z. B. bei der ungerichteten Porosität, auch Blasenschwärme mit kleinen Gasblasen erzeugen (7), (8). Dies ist dadurch bedingt, daß im Einzelblasenbereich die Blasengröße von den Bedingungen des Systems abhängt. Dieser Einzelblasenbereich ist aber durch geringe Drücke und Volumenströme begrenzt und kommt daher in der Praxis selten zur Anwendung. Schon während des Überganges zum geschlossenen Gasstrahl änderte sich das Spülverhalten der untersuchten Steine. Während bei Steinen mit gerichteter Porosität viele Blasen mit relativ geringem Durchmesser entstehen (Abb. 4, 5, 8, 9), kommt es bei Steinen mit ungerichteter Porosität zur Koaleszenz in horizontaler und vertikaler Richtung (Abb. 2, 3, 6, 7).

Schon bei relativ niedrigem Druck (im Modell bei 0,5 bar) kam es bei Steinen mit ungerichteter Po-

3. Results

According to former trials in a small scale with low gas pressures and gas volumes it was stated that small pore diameters f.e. plugs with high open porosity cause bubble swarms with small bubble diameters (7), (8). The reason is in the conditions of the system in the regime of constant bubble size. This regime is stable only at low gas pressures and volumes and is only sometimes applied under practical conditions. Already during the transition to the jet regime the different types of purge plugs showed a different bubbling behaviour. Where as plugs with directed porosity showed the formation of bubble swarms with relative small bubble diameters (fig. 4, 5, 8, 9), plugs with a high open porosity caused a coalescence of the bubbles in horizontal and vertical direction (fig. 2, 3, 6, 7).

Already at relative low gas pressures (0.5 bar in the model) the formation of great bubbles from plugs with high open porosity was observed. The gas does not emanate constantly but is pulsating

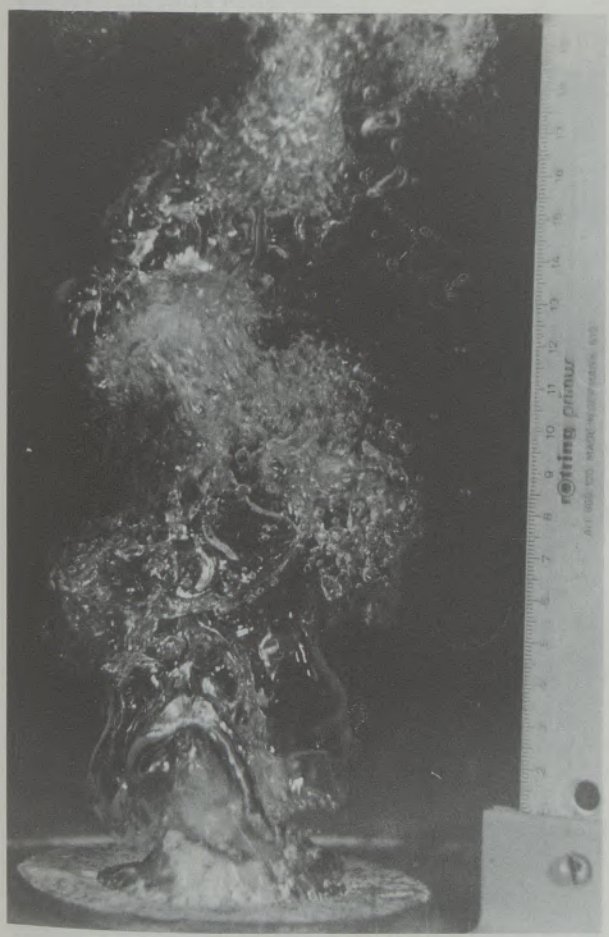

Abb./Fig. 6
Spülstein mit ungerichteter Porosität
Druck: 1 bar; Volumenstrom: 160 Nl/min
Purge brick with high open porosity
Pressure: 1 bar; gas volume: 160 Nl/min

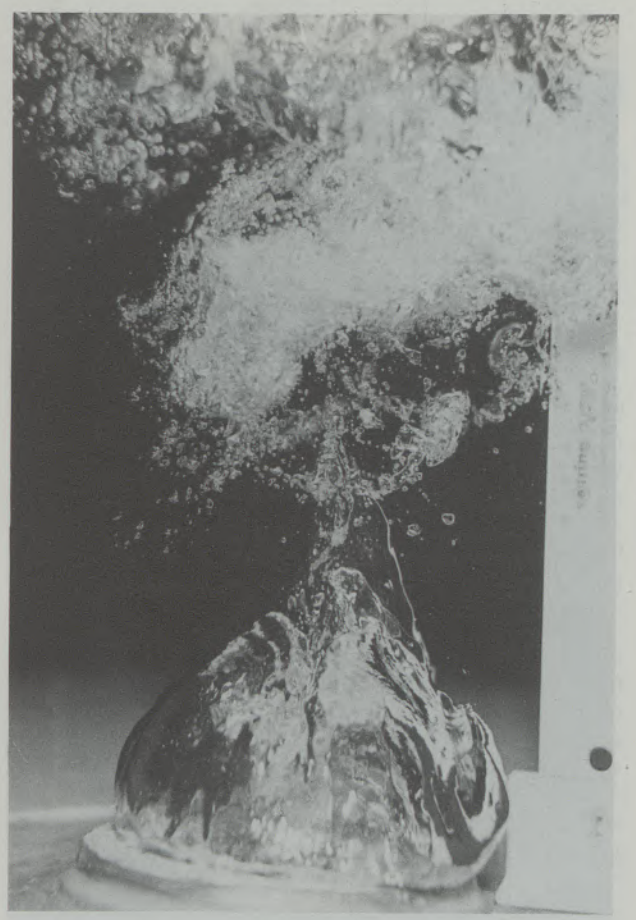

Abb./Fig. 7
Spülstein mit ungerichteter Porosität
Druck: 2 bar; Volumenstrom: 250 Nl/min
Purge brick with high open porosity
Pressure: 2 bar; gas volume: 250 Nl/min
Back-attack-effect

rosität zur Bildung von Großblasen. Der Gasstrahl strömt nicht mehr gleichmäßig aus, sondern pulsiert sehr stark. Bei höherem Gasdruck konnte man ein Zurückschlagen der Gasblasen auf den Spülstein beobachten (back-attack-effect, Abb. 7). Dieses Zurückschlagen der Gasblasen auf den Spülstein ist eine mögliche Ursache für das Ausfallen eines Spülsteines. Neben einem höheren Verschleiß durch Erosion besteht die Gefahr des Zusetzens der spülenden Poren durch Stahlpartikel, welche mit dem Zurückschlagen der Gasblasen in die Poren infiltrieren. Dieser back-attack-effect kann demnach als möglicher Grund für das in der Praxis häufig vorliegende konkave Verschleißbild vermutet werden.

Diese Erscheinung hat erfahrungsgemäß Auswirkungen auf die Haltbarkeit eines Spülsteines. Neben der schon erhöhten Verschleißanfälligkeit eines Spülers mit „ungerichteter Porosität" durch die gegebene Porosität trägt die höhere Erosion zur Verschlechterung der Haltbarkeit bei.

Daraus folgt, daß Steine mit ungerichteter Porosität nicht beide Forderungen der Metallurgen, große Mengen kleiner Gasblasen bei gleichzeitig

strongly. At higher gas pressures (fig. 7) a back-attack-effect of the gas bubbles could be observed. This back-attack-effect is a possible reason for difficulties in the purging behaviour. Besides a higher wear rate caused by erosion of the porous refractory material there is also the possibility of penetration of steel drops, being pressed into the pores by the back-attack-effect. This is also a possible reason for the concave shaped "hot face" of purge plugs with high open porosity, often observed in steel plant practice.

This effect may influence the life of a purge plug. Besides a higher wear rate of a purge plug with high open porosity also a more intensive erosion causes a decrease of the life of a porous plug.

It also can be assumed by these results that plugs with high open porosity cannot meet both demands of the metallurgists of high amounts of small gas bubbles together with a simultaneous high kinetic efficiency.

In order to evaluate the influence of the geometrical situation of the plug, some additions were mixed into the water for better visibility of the

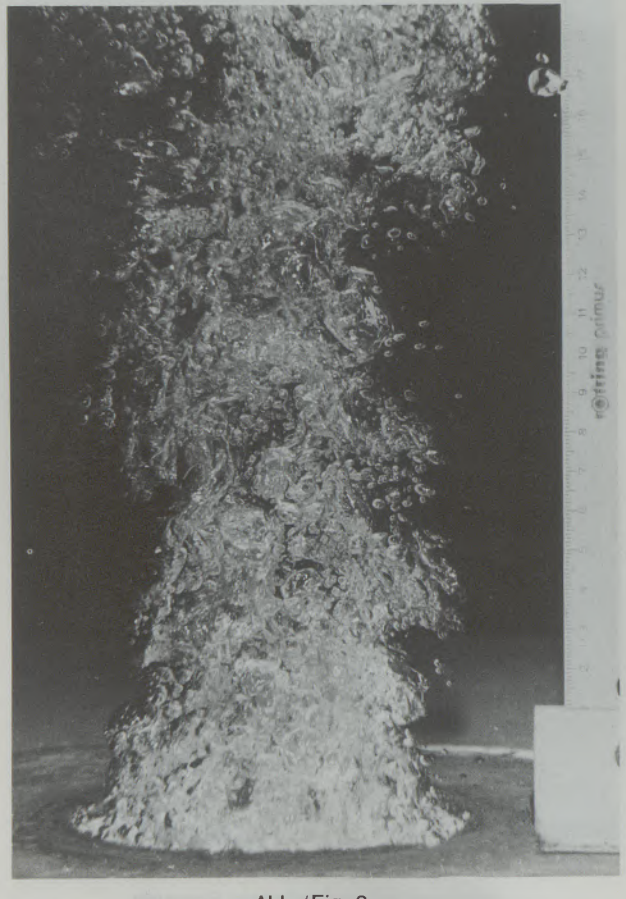

Abb./Fig. 8
Spülstein mit gerichteter Porosität
Druck: 1,2 bar; Volumenstrom: 100 Nl/min
Purge brick with directed porosity
Pressure: 1.2 bar; gas volume: 100 Nl/min

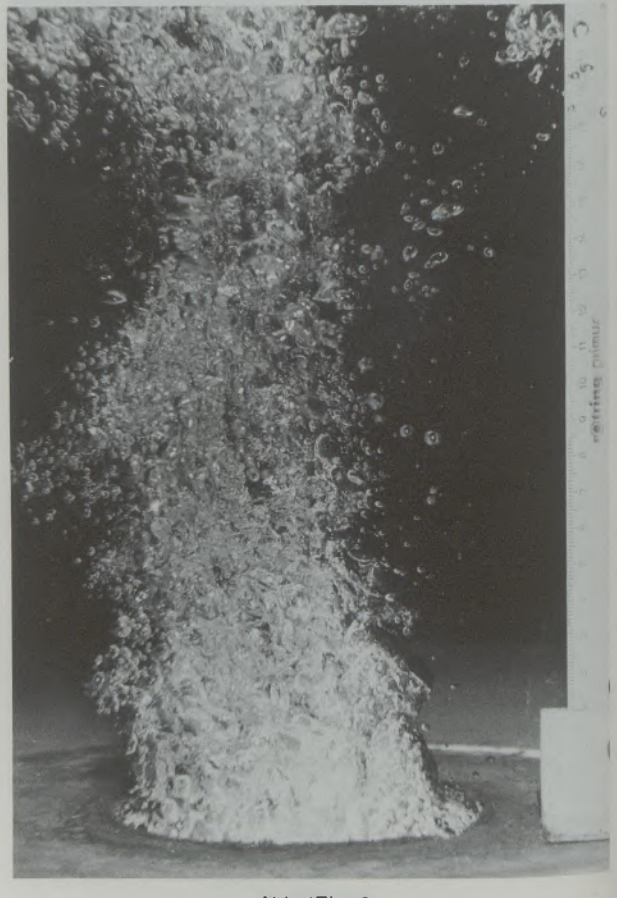

Abb./Fig. 9
Spülstein mit gerichteter Porosität
Druck: 2 bar; Volumenstrom: 150 Nl/min
Purge brick with directed porosity
Pressure: 2 bar, gas volume: 150 Nl/min

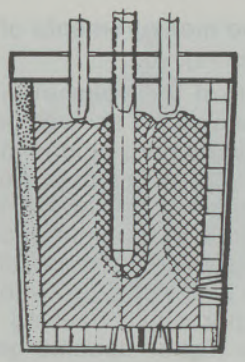

Abb./Fig. 10
Blasenbild bei Spülsteineinbau in der Seitenwand
Formation of the bubble swarm observed at location in the side wall

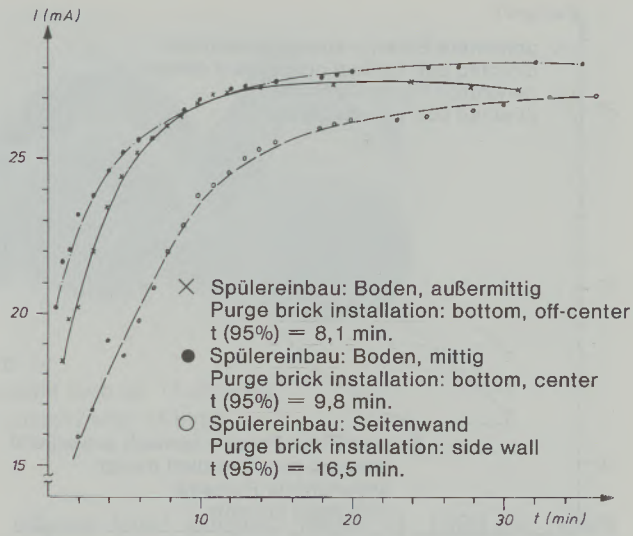

Abb./Fig. 11
Modellversuch: Homogenisierungsleistung in Abhängigkeit der geometrischen Anordnung von Spülsteinen im Wassermodell
Model trial: Effect of homogenisation depending on geometrical location of the purge brick in the model

ger guter kinetischer Wirkung, erfüllen. Diese Forderungen werden aber von Steinen mit gerichteter Porosität erfüllt.

Um den Einfluß der geometrischen Anordnungen des Spülers feststellen zu können, wurden der Modellflüssigkeit Stoffe zugegeben, die die Strömungen im Gefäß sichtbar machten. Untersucht wurden folgende Kriterien:

- Homogenisierungsleistung von Spülern mit „ungerichteter Porosität" und Spülern mit „gerichteter Porosität" bei Einbau im Behälterboden mittig.
- Einfluß der geometrischen Anordnung eines Spülers durch:
  - Einbau im Behälterboden mittig,
  - Einbau im Behälterboden außermittig,
  - Einbau im unteren Drittel der Seitenwand.

Zur Dokumentation wurden Leitfähigkeitsmessungen und Videoaufzeichnungen herangezogen. Dabei zeigten die Ergebnisse der unterschiedlichen Auswertungen gute Übereinstimmungen. So stellte sich heraus, daß bei Steinen mit „ungerichteter Porosität" die Rührwirkung im Gefäß nicht durch eine gleichmäßige Strömung erreicht wird. Durch das Pulsieren des Gasstrahles kommt es zur Ausbildung zonaler Turbulenzen, die die Flüssigkeit verwirbeln. Die Videoaufnahmen zeigten, daß damit eine homogene Durchmischung nicht gewährleistet ist. Im Gegensatz dazu konnte man bei Steinen mit gerichteter Porosität eine gleichmäßige Badströmung beobachten, die zu einer kontinuierlichen Badumwälzung führt.

Beim Einbau von Spülern in die Mitte des Behälterbodens kommt es auf dem Boden im Randbereich zu Ablagerungen (tote Zonen). Bei außermittigem Bodeneinbau trat diese Erscheinung nicht auf. Hier wurde der gesamte Gefäßinhalt von der Badströmung erfaßt. Die schlechteste Badumwälzung erzeugt ein in der Seitenwand eingebauter Spüler. Das Spülgas steigt sofort nach dem Austritt aus dem Spüler entlang der Seitenwand auf (Abb. 10).

An der Badoberfläche stehen zwei gegeneinander gerichtete Strömungen, die in dem dem Spüler

currents in the model. Following criterias were investigated:

- efficiency of homogenisation of plugs with high open porosity and "directed porosity" placed in the center of the model bottom,
- placed eccentric in the model bottom,
- placed in the lower part of the side wall (appr. the third part).

For documentation the electrical conductivity was measured as well as video records were used. The results of the different evaluations showed good correspondence. It was stated, that with plugs with high open porosity the mixing efficiency in the model was achieved not by homogenious currents but by turbulences caused by the pulsation of the gas jet. Plugs with "directed porosity" showed a homogenious current with a continuous mixing effect.

The location of the plugs in the center of the bottom showed the formation of zones with no current and segregation of the additions. With eccentric location of the plug these phenomena were not observed and the whole volume of the model was moved by the currents. The worst mixing behaviour showed plugs located in the side wall. The gas rises instantly after leaving the plug surface (fig. 10).

At the surface of the bath two opposite currents were observed causing turbulences in the corresponding areas of the surface. Therefore a higher wear rate of the ladle lining in this region can be expected. At the bottom of the model segregations of the added particules were observed and

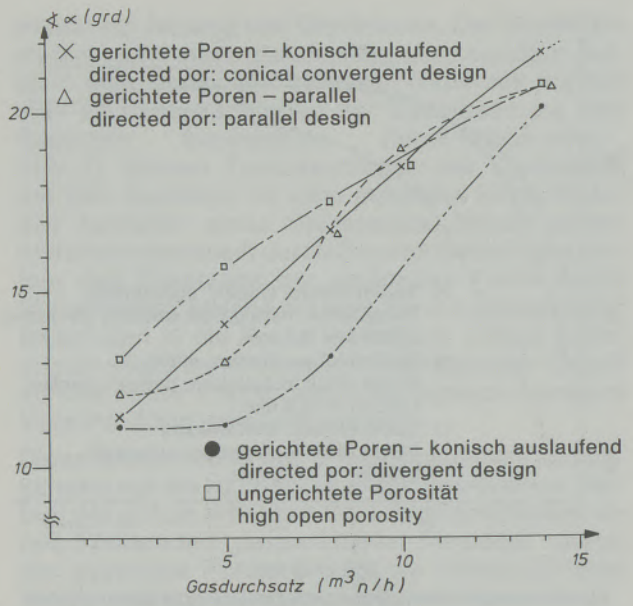

Abb./Fig. 12
Abhängigkeit des Spülwinkels vom
1. Gasdurchsatz
2. Spülkanalanordnung
Relation between angle of the bubble swarm and
1. gas volume
2. design of channels

gegenüber liegenden Bereich zu Turbulenzen an der Oberfläche führen. Hiedurch ist mit einem erhöhten Verschleiß der Feuerfestauskleidung in diesem Bereich zu rechnen. Auf dem Behälterboden kam es zu starken Ablagerungen der zugesetzten Partikel. Diese Beobachtungen wurden durch die Leitfähigkeitsmessungen bestätigt (Abb. 11).

Bei der Beobachtung der räumlichen Ausdehnung des aufsteigenden Blasenschwarmes konnten nur im Bereich des relativ geringen Gasdurchsatzes Differenzen festgestellt werden. Mit steigendem Gasdurchsatz nähert sich die Blasenschwarmausdehnung unabhängig vom Spülsteintyp einem Maximalwert. Den gleichmäßigsten, annähernd linearen Anstieg in der Ausdehnung mit dem größten Ausdehnungswinkel erreichte der Standardspülstein mit „gerichteter Porosität". Diese starke Ausdehnung verstärkt die Badumwälzung und ergibt eine verbesserte Schlackenarbeit sowie eine größere Badoberfläche für Entgasungsreaktionen (Abb. 12).

4. Diskussion der Ergebnisse

Faßt man alle vorliegenden Ergebnisse sowie Ergebnisse von begleitenden Versuchen, die hier nicht näher erläutert werden sollen, zusammen, so kommt man zu folgenden Aussagen:

Das Einsatzgebiet von Spülern mit ungerichteter Porosität dürfte vorwiegend dort zu finden sein, wo eine relativ kurze Spülbehandlung vorwiegend

confirmed by the measurements of the electrical conductivity (fig. 11).

The observation of the volumetric expansion of the rising bubble swarms showed only differences of the various types purge plugs in the regime of low amounts of gas. With increasing gas volumes the expansion of the bubble swarm is approaching a maximum value independent of the type of porous plug. A constant increase of the volume of the swarm was also achieved with porous plugs with "directed porosity", causing a high mixing intensity and a higher specific gas surface for degassing reactions (fig. 12).

4. Conclusions

Summarizing all results discussed in this paper and the results of many marginal trials the following conclusions may be discussed:

The application of plugs with high porosity may mainly be in ladles with relatively low treatment time for homogenisation of temperature and chemical composition. For higher treatment times and special applications like ladle furnace, vacuum treatment etc. the application of purge plugs with "directed porosity" can be recommended. Besides the advantages like great bubble swarms with low bubble diameters for an improved metallurgical reaction and a continuous bath agitation there is also a lower wear rate because of the dense ceramic structure of this type of brick. These results were confirmed also under steel plant conditions. In many cases steel plants are using purge brick with directed porosity for heats with higher purging time or for special treatments.

The consequent development of the experience – distance of gas orifices caused the variation of different shapes of plugs as shown in fig. 13.

Subsequently the life of the plugs could be improved by these measurements, in same cases the same life of the plug as the lining life of the ladle bottom was achieved.

The life of the porous plugs is almost always connected with the applied quality of the well block and the nozzle, which should be balanced by using special ceramic materials. Regarding these con-

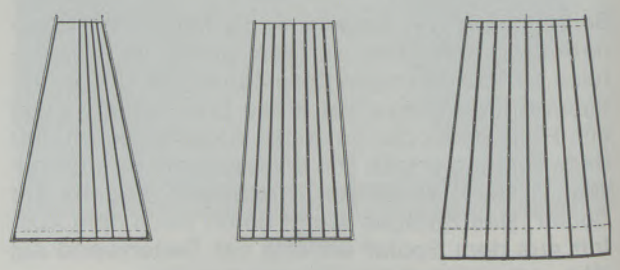

Abb./Fig. 13
Spülsteinformate mit gerichteter Porosität
Shapes of purge brick with directed porosity

Abb./Fig. 14
Spülsteine mit gerichteter Porosität nach ca. 14 Chargen
Purge brick with directed porosity after 14 heats

dem Temperaturausgleich dient. Für längere Spülbehandlungen sowie für Spezialbehandlungen, wie z. B. Ladle Furnace, Vakuumbehandlung usw., empfiehlt sich die Verwendung von Spülern mit gerichteter Porosität. Diese bieten neben den schon erwähnten Vorteilen, wie große Blasenschwärme mit kleinen Blasendurchmessern zur Verbesserung metallurgischer Reaktionen sowie einer kontinuierlichen Badumwälzung aufgrund der dichten Keramik, auch ein verbessertes Verschleißverhalten. Diese Ergebnisse haben sich auch in der Praxis bestätigt. In vielen Fällen verwenden Stahlwerke zum Spülen von Chargen mit längerer Behandlungsdauer oder Sonderbehandlungen heute vorwiegend Spüler mit gerichteter Porosität.

Die konsequente Weiterführung der Erfahrung „Abstand der Gasaustrittsöffnung" führte zu der Entwicklung der in nachstehender Abb. 13 dargestellten Formate.

In der Folge konnte die Haltbarkeit erneut entscheidend verbessert werden. Unter bestimmten Voraussetzungen kann hiebei die Haltbarkeit des Bodens der Stahlgießpfanne erreicht werden.

Die Haltbarkeit der Spülsteine muß jedoch im Zusammenhang mit dem verwendeten Lochstein und eventuell der Hülse gesehen werden. Nur ein abgestimmtes Feuerfestmaterial eines Spülsteines kann jedoch die Haltbarkeitswünsche erfüllen. Durch die Verwendung von Spezialkeramiken für die Lochsteine und Hülsen kann diesen Ansprüchen weitgehend entsprochen werden. Unter Berücksichtigung dieser Kriterien konnten schon Gesamtspülzeiten von 1800 Minuten mit einem Spülstein erreicht werden. Bei sehr langen Spülbehandlungen ist es nach wie vor in einigen Fällen notwendig, den Spülstein während einer Pfannenreise zu wechseln. Stand der Technik ist heute, daß dies wie im Pfannenschieberbereich zwischen den einzelnen Chargen, d. h. im heißen Zustand, von außen erfolgt. Hier sollte in jedem Falle ein Spülsystem mit Hülse verwendet werden, wobei dann mit dem Spülstein auch die Hülse gewechselt werden muß. Dies hat den Vorteil, daß beim Einbau eines neuen Spülsteines in einen

ditions total purging times of 1800 min were achieved with one plug. For long treatment times it is still necessary to change the plug within a ladle campaign. Today's state of the art is the change of the plug between the heats from outside like the slide gate materials. In these cases a purging set with a nozzle should be applied, changing plug and nozzle at the same time. This is advantageous for the protection of the new plug by the nozzle when the well block is partly worn, resulting in a higher security of the system and a longer life of the plug.

Tabelle/Table 1

	hochtonerdehältig/ high alumina Urblock 1850 W	basisch/basic PERcast CMS
Al_2O_3 (%)	97	7
MgO (%)	–	54
Cr_2O_3 (%)	–	20
RG/BD (g/cm³)	2,85	2,9
KDF/CCS (N/mm²)	30	40–70 nach Vorbrand after prefiring

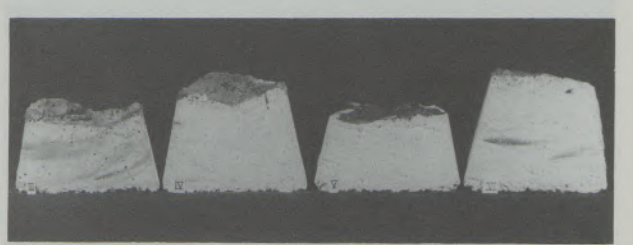

Abb./Fig. 15
Verschleißbild und Infiltrationstiefe von Spülsteinen mit gerichteter Porosität auf Basis Al_2O_3
Wear and penetration behaviour of purge brick with directed porosity

48.279 6×

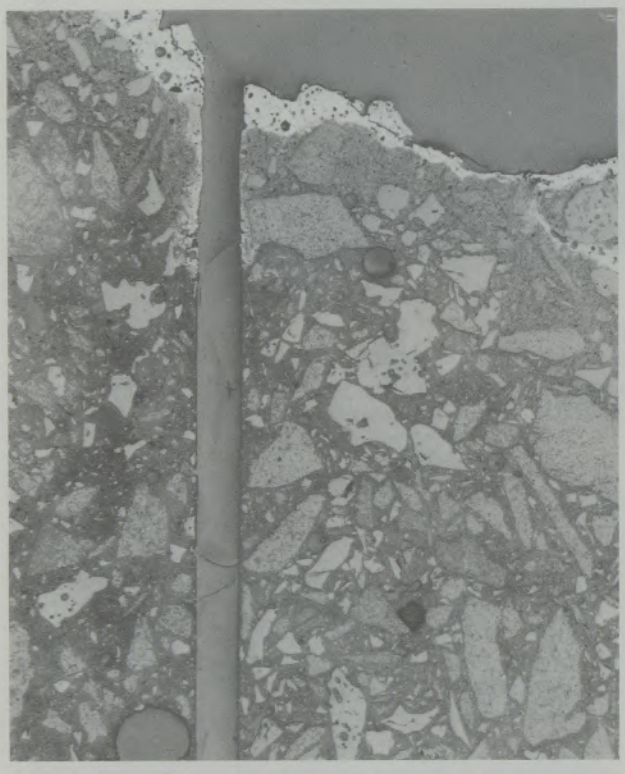

Abb./Fig. 16
Übersichtsaufnahme – Spülkanal an der „Feuerseite"
Mini-tuyere at the "hot face"

48.280 6×

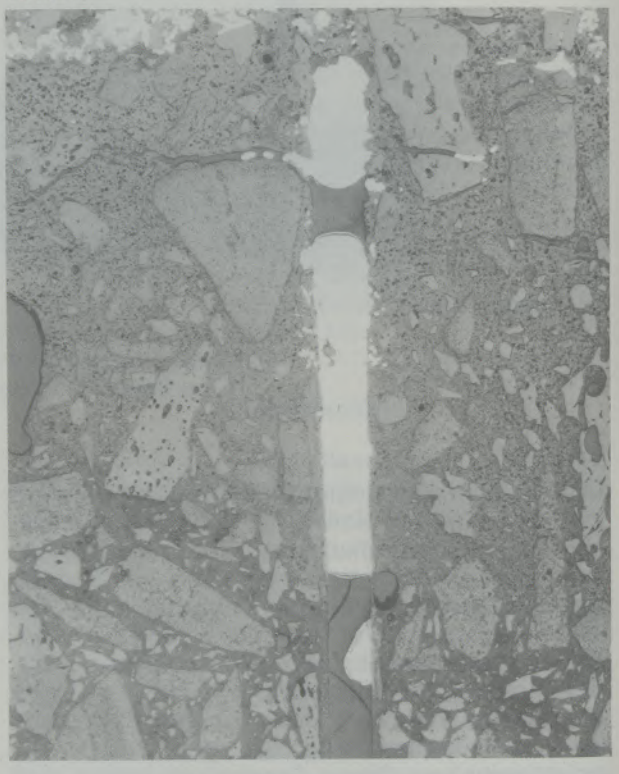

Abb./Fig. 17
Übersichtsaufnahme – Spülkanal an der „Feuerseite"
Mini-tuyere at the "hot face"

48.281 6×

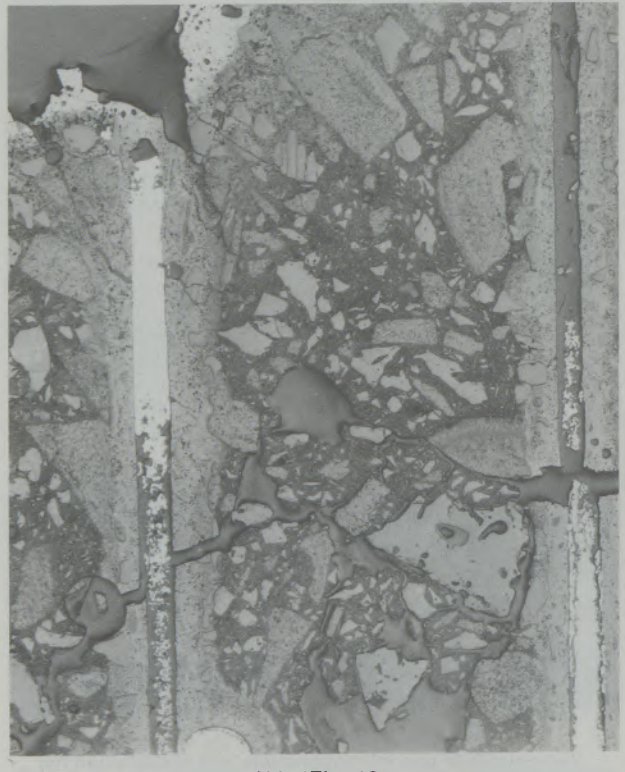

Abb./Fig. 18
Übersichtsaufnahme – Spülkanal an der „Feuerseite"
Mini-tuyere at the "hot face"

48.282 6×

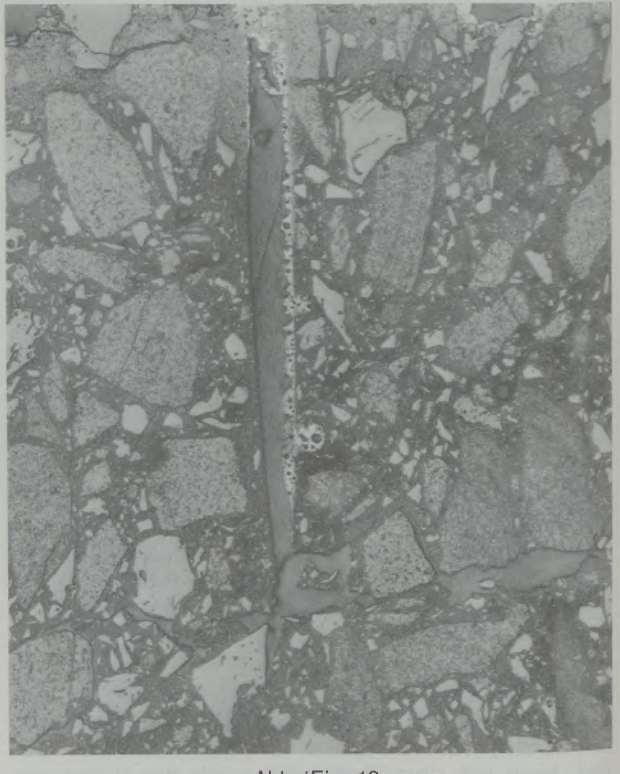

Abb./Fig. 19
Übersichtsaufnahme – Spülkanal an der Feuerseite
Mini tuyere at the "hot face"

48.283 150× (90×)

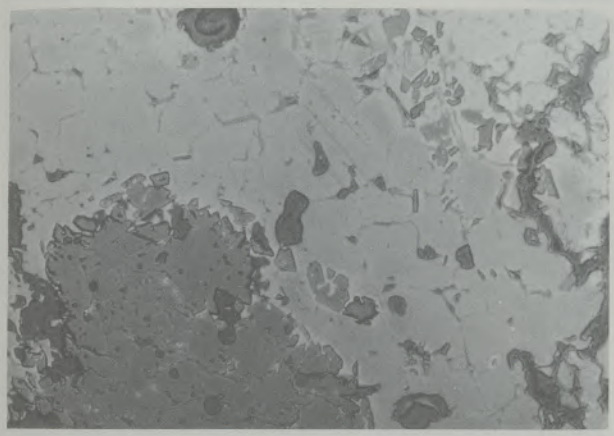

Abb./Fig. 20
Abbau der Korundkomponente durch Eisen-Oxide
Corrosion of corundum by iron oxides

48.284 150× (90×)

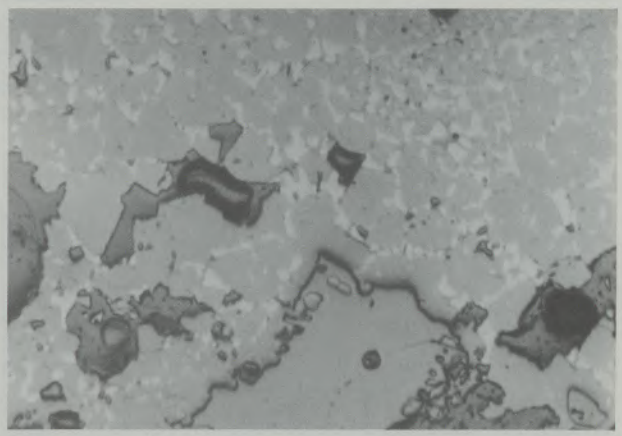

Abb./Fig. 21
Abbau der Korundkomponente über Spinellbildung durch Eisen-Oxide
Corrosion of corundum by iron oxides – formation of spinels

48.285 750× (450×)

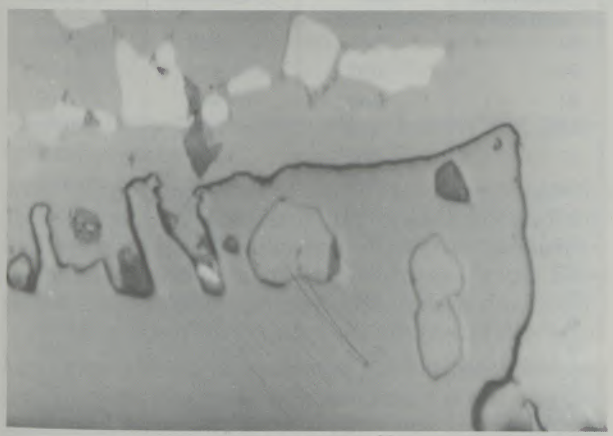

Abb./Fig. 22
Abbau der Korundkomponente
Corrosion of corundum

48.286 300× (180×)

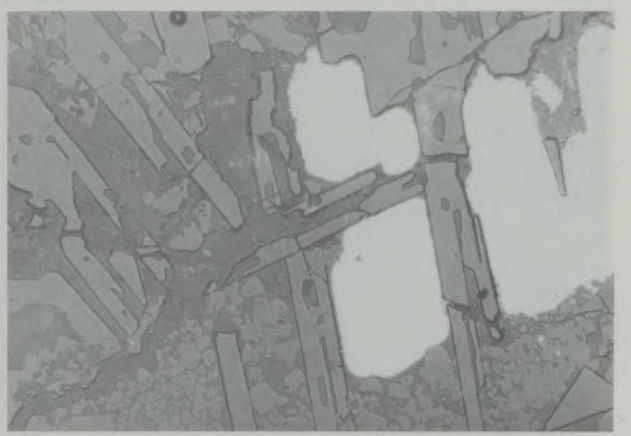

Abb./Fig. 23
Abbau der Korundkomponente
Corrosion of corundum

48.287 300× (180×)

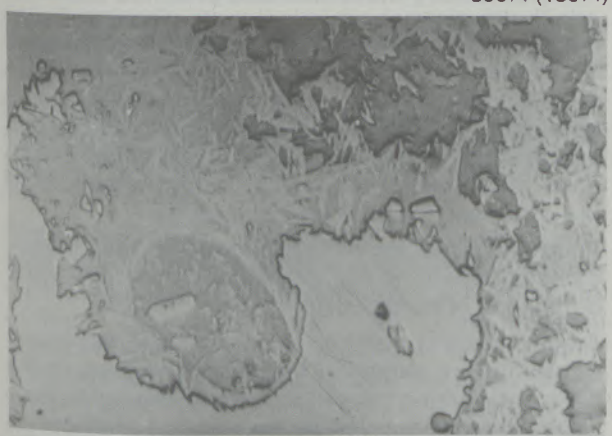

Abb./Fig. 24
Abbau der Korundkomponente über Ca-Aluminate
Corrosion of corundum by calcium-aluminates

48.288 750× (450×)

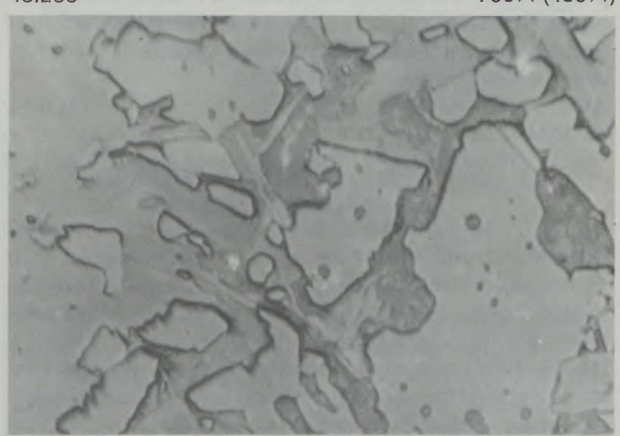

Abb./Fig. 25
Abbau der Korundkomponente über Ca-Aluminate
Corrosion of corundum by calcium-aluminates

48.289 750× (450×)

Abb./Fig. 26
Ca-Aluminate mit unterschiedlichen chemischen Zusammensetzungen
Calcium aluminates with different chemical compositions

48.290 750× (450×)

Abb./Fig. 27
Bildung von Ca-Aluminaten (CA_2)
Formation of Ca-aluminates (CA_2)

48.291 150× (90×)

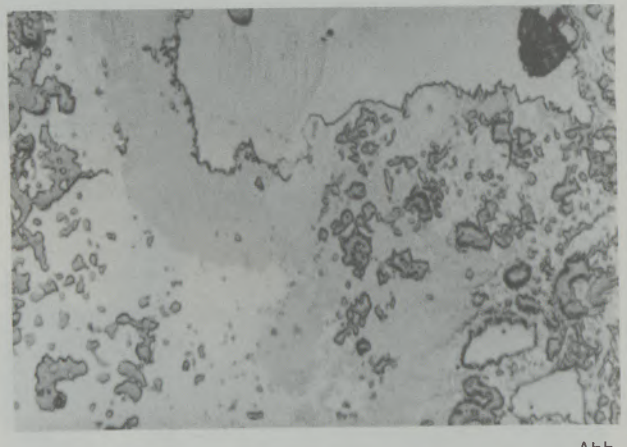

Element	ZAF	% Element	% Oxide
Si	782	17.057	36.487
Fe	837	4.971	7.107
Al	846	15.144	28.615
Mn	818	291	376
Cr	836	039	056
Ca	915	14.586	20.409
Mg	742	000	000
Na	607	2.507	3.380
K	1.210	113	136
Ti	806	159	265
P	1.117	1.345	3.083
S	812	030	075
O	204	43.747	000
Total		99.989	99.989

Abb./Fig. 28
a) Randliche Glasphasenbildung an Korundkörnern
Zonar formation of a glassy phase on corundum grains
b) Chemische Zusammensetzung der „feuerseitigen" Glasphase
Chemical composition of the "glassy phase"

bereits teilweise verschlissenen Lochstein der neue Spülstein durch eine neue Hülse geschützt und so die Funktionstüchtigkeit gewährleistet sowie die Haltbarkeit erhöht wird.

5. Eingesetzte feuerfeste Produkte und Praxisergebnisse

Spülsteine mit gerichteter Porosität werden, entsprechend den derzeit gängigen Zustellpraktiken, in der Sekundärmetallurgie in einer hochtonerdehaltigen und einer basischen Qualität gefertigt. Der Rohmaterialeinsatz sowie eine spezielle Binderkombination gewährleisten für beide Materialtypen ein gutes Festigkeitsniveau bei gleichzeitig hoher Gefügeelastizität.

Über erste Ergebnisse von Einbauversuchen wurde bereits in der Literatur berichtet (4), insbe-

5. Refractory materials and practice results

Purge plugs with directed porosity are produced in a high-alumina and a basic quality, according to the presently applied lining practice in secondary steelmaking. The raw materials and a special binder system guarantee a high level of refractoriness and strength as well as a high elasticity of the structure for both types of plugs.

About first results of installations there already exist publications (4), especially about the wear behaviour of basic purge plugs.

Among a great number of service results, where naturally is a range of variation because of the different working conditions, some examples were choiced to characterize the wear behaviour of high alumina purge plugs with directed porosity.

From a 125-to-BOF-ladle purge plugs after appr. 14 heats (appr. 300 min purging time) were in-

Tabelle/Table 2

RMA 1–3:
Chemische Zusammensetzung der Ca-Aluminate
Chemical composition of Ca-aluminates

RMA 1

Spectrum: FA7167/Ca-Al-Phase

Element	ZAF	% Element	% Oxide
Si	614	650	1.390
Fe	840	3.108	4.443
Al	907	39.116	73.911
Mn	821	000	000
Cr	835	100	146
Ca	919	14.024	19.622
Mg	824	000	000
Na	658	252	340
K	1.216	070	084
Ti	808	041	069
P	1.114	000	000
S	821	000	000
O	217	42.645	000
Total		100.004	100.004

RMA 2

Spectrum: FA7167/Zon. Stengel, hell

Element	ZAF	% Element	% Oxide
Si	606	464	993
Fe	863	17.928	25.632
Al	793	34.553	65.289
Mn	845	052	068
Cr	905	000	000
Ca	934	5.651	7.906
Mg	684	000	000
Na	515	000	000
K	1.214	058	070
Ti	860	017	028
P	1.106	006	014
S	819	009	023
O	293	41.286	000
Total		100.024	100.024

RMA 3

Spectrum: FA7167/dkl. Stengel

Element	ZAF	% Element	% Oxide
Si	598	352	752
Fe	858	14.090	20.144
Al	826	37.547	70.946
Mn	841	000	000
Cr	890	049	072
Ca	927	5.588	7.819
Mg	724	000	000
Na	553	000	000
K	1.204	002	002
Ti	852	044	073
P	1.095	080	182
S	811	005	012
O	297	42.248	000
Total		100.003	100.003

sondere über das Verschleißverhalten von basischen Spülsteinen.

Unter einer großen Zahl von Praxisergebnissen, deren Streuung aufgrund der unterschiedlichen Betriebsbedingungen in den einzelnen Stahlwerken entsprechend groß ist, wurden einige Beispiele ausgewählt, um den Verschleiß der hochtonerdehaltigen Spülsteine zu charakterisieren.

Aus einer 125-t-Pfanne eines Konverterstahlwerkes wurden Spülsteinproben nach einer durchschnittlichen Haltbarkeit von ca. 14 Chargen (~300 Spülminuten) entnommen und untersucht.

Der überwiegende Anteil der Kanäle war frei bzw. die Infiltrationstiefe von Stahl gering. Die folgenden Abbildungen 16 bis 19 zeigen die Ausbildung der Spülkanäle an der Innenseite der Spülsteine.

Abhängig von der Schlackenarbeit sowie von der anhaftenden Restschlacke, sind unterschiedliche Verschleißmechanismen bei der Al_2O_3-Komponente wirksam.

Im Kontakt mit Eisenoxiden ist der bereits bekannte Abbau des Korundes über die Bildung von FeO · Al_2O_3-Hercynitspinellen zu beobachten (Abb. 20 bis 22).

Stellenweise sind „feuerseitig" noch skelettförmige Korundrelikte erhalten, wobei Stahl restraumfüllend neben Spinellen und Ca-Aluminaten vorliegt (Abb. 23). Aus den CaO-haltigen Schlackenkomponenten resultiert eine Umbildung des Al_2O_3 in Ca-Aluminate der Zusammensetzung CaO · $(Al_2O_3)_2$ und CaO · $(Al_2O_3)_6$ (CA_2 CA_6) mit unterschiedlich hohen Eisenoxidgehalten. Diese in den folgenden Abbildungen 24 bis 27 ersichtliche Mineralparagenese ist oft im Kontaktbereich Ansatz–Steingefüge nachzuweisen. Die

vestigated (fig. 14, 15). Most channels were free of penetration of steel or slag resp. the penetration depth was low. The fig. 16–19 show the channels inside the purge plugs at the "hot face".

Depending on the practice and composition of the slag different wear mechanismus can be observed.

In contact with iron oxide the well known decomposition of the corundum with the formation of FeO · Al_2O_3-Hercynite-spinel is observed (fig. 20–22). Sometimes at the "hot face" skeleton relicts of corundum are still existent with spinel and calcium-aluminates and steel (fig. 23). The high-lime slag components cause a recrystallization of Al_2O_3 into Ca-aluminates of the composition CaO

RMA-Analysen lassen den unterschiedlichen Chemismus der überwiegend in stengeliger Form auskristallisierten Ca-Aluminate erkennen.

Stellenweise sind die Wechselwirkungen mit den Schlackenkomponenten so intensiv, daß es zu einem ,,dichten'' Reaktionssaum, bestehend aus Spinellen, Ca-Aluminaten und Glasphase, um die ,,feuerseitigen'' Korundkörner kommt (Abb. 28).

In allen Fällen jedoch liegt die Infiltrationstiefe bzw. die Reaktionszone zwischen dem Steingefüge und den Schlackenkomponenten bzw. Eisenoxiden im Bereich von wenigen mm.

In der derzeitigen Anwendungsbreite der Sekundärmetallurgie, mit Einbeziehung des Pfannenofens, stehen für die unumgängliche Spülgasbehandlung sowohl von der Materialseite als auch von der Konzeption der Gaseinführung her nunmehr optimierte Systeme zur Verfügung. Diese werden ergänzt durch Vorrichtungen für schnellere Spülsteinwechsel sowie zusätzliche Sicherheitseinrichtungen. Hiemit wird dem Stahlwerker für die Pfanne ein Paket an Problemlösungen für die sekundärmetallurgische Arbeit angeboten.

· $(Al_2O_3)_2$ and $CaO \cdot (Al_2O_3)_6$ (CA_2 and CA_6) with varying iron oxide contents. This mineralisation is often observed in the contact zone between slag and refractory material, as shown in the fig. 24–27. The RMA-analysis recognize the different chemical compositions of the mostly fringe crystal shape of the Ca-aluminates.

In some samples the reactions with the slag components are very intensive, showing a dense reaction zone around the corundum crystals formed by spinels, Ca-aluminates and a glassy phase (fig. 28).

In all investigated samples the penetration depth resp. the reaction zone between the refractory component and the slag is in the range of few millimeters.

For inert gas treatment in secondary steelmaking now optimized systems of refractory materials as well as gas injection conceptions are offered. These are completed by devices for quick change of the plugs and additional security devices, being a package of problem solutions for secondary steelmaking ladles.

Literaturverzeichnis/References

1. Winkler, H. J.: ,,Gasspül-Systeme in Stahlwerken'', Fachberichte Hüttenpraxis Metallverarbeitung; Vol. 21, No. 10, **1983**, S. 769–775.
2. Knüppel, H.: ,,Desoxidation und Vakuumbehandlung von Stahlschmelzen''; Band II, Verlag Stahleisen GmbH, Düsseldorf.
3. Deilmann, W., E. Klimanek: ,,Erfahrungen bei der Spülgasbehandlung des Stahles in der Gießpfanne''; Radex-Rdsch., Heft 2, **1986**, S. 127–136.
4. Grabner, B., H. Höffgen: ,,Einsatz und Verschleiß von Spülsteinen in der Sekundärmetallurgie''; Radex-Rdsch., Heft 3, **1983**, S. 179–209.
5. Ganzow, J., N. Müller, A. Pfeiffer, K. Wünneberg: ,,Metallurgische Vorgänge beim Sauerstoffaufblasverfahren mit Inertgasbodenspülung''; Stahl und Eisen 104, **1984**, Nr. 16, S. 767–773.
6. Gruner, H., H. E. Wiemer, W. Fix, K. Wünneberg: ,,Neue metallurgische Einsichten beim Sauerstoffaufblasverfahren und verbesserter Prozeßkontrolle mit Sublanze und Bodengasspülung''; Stahl und Eisen 104, **1984**, Nr. 11, S. 527–532.
7. B. E., M. E. Byung-Don You: ,,Modelluntersuchungen über die Blasenbildung und das Eindringen von Flüssigkeiten in die Lanze bei der Gas- und Feststoffinjektion''; an der Universität Leoben eingereichte Dissertation, Mai **1983**.
8. Grabner, B., W. Polanschütz: ,,Modelluntersuchungen über den Einfluß des Gefüges von Gasspülsteinen auf die Ausbildung der Gasblasen''; Radex-Rdsch., Heft 1/2, **1985**, S. 522–545.
9. Persönliche Information von Doz. Dr. Polanschütz.

The Behaviour of Hydrogen in Steelmaking by the Plasma Melting Process

Josef Knauder, Wilfried Krieger and Kilian Jandl, Linz*)

Treatment of the special problems involved in taking hydrogen samples from liquid steel. Reproducibility of hydrogen determinations on immersion probe samples and on samples obtained by means of the copper mould. The behaviour of hydrogen during melt-down, oxidizing refining, reducing refining and tapping when melting unalloyed or low-alloy steels in the plasma melting furnace. Modes of operation to adjust simultaneously low hydrogen, phosphorus and sulphur contents.

Verhalten des Wasserstoffes bei der Stahlerzeugung im Plasmaschmelzofen

Behandlung der Problematik der Wasserstoffprobenahme aus flüssigem Stahl. Reproduzierbarkeit von Wasserstoffbestimmungen an Tauchsondenproben sowie an mittels Kupferkokille erhaltenen Proben. Verhalten von Wasserstoff beim Einschmelzen, Frischen, Feinen und beim Abstich bei der Erschmelzung von un- bzw. niedriglegierten Stählen im Plasmaschmelzofen. Verfahrenswege zur gleichzeitigen Einstellung niedriger Gehalte an Wasserstoff, Phosphor und Schwefel.

Comportement de l'hydrogene au cours de l'elaboration de l'acier au four a plasma

On traite des problèmes particuliers du prélèvement d'échantillons d'hydrogène à partir de l'acier liquide. Reproductibilité des déterminations de l'hydrogène au moyen d'échantillons prélevés à la sonde à immersion ou à la coquille de cuivre. Comportement de l'hydrogène lors de la fusion, de l'affinage oxydant, de l'affinage réducteur et de la coulée en poche dans le cas de l'élaboration d'aciers non alliés ou faiblement alliés au four à plasma. Modes opératoires pour le réglage simultané de faibles teneurs en hydrogène, phosphore et soufre.

1. General

In October 1983 a 45-ton plasma melting furnace was put into operation in the electric steel plant of the Metallurgical Division in Linz. First results have been reported in the meantime (1)–(3).

Figure 1 shows the basic design of the plasma furnace. The four plasma torches located around the furnace circumference are of oblique arrangement to the bath surface and move on carriages which support them and which may be adjusted in two levels. The plasma arc itself is produced between the cathode in the torch and the melt which is in electric contact with the bottom anode. Each of the four plasma torches operated with direct current has a separate power supply, thus ensuring that they are completely independent of each other in operation.

The principles of the use of low-temperature gas plasma in metallurgy have formed the basis for various papers (2), (3). Within the scope of the subject paper let us simply mention that at the core proper of the plasma arc, at powers between 1 and 10 MW, temperatures are as high as 15.000 to 30.000 K, depending on the type of plasma gas used (Ar, He, H_2, N_2), while the arc temperature of a conventional electric arc furnace is approximately 3.800 K.

The technical data of the plasma melting furnace shown in fig. 1 are as follows:

Capacity	45 tons
Vessel diameter	5.8 m
Installed power	36 MVA
Capacity of torches	4 × 7.5 MW
Torch voltage	800 V max.
Torch current	10.800 A max.

The plasma furnace has been used so far for the production of a wide range of steels from unalloyed to high-alloy grades, processed in the rolling mills, in the forge and in the foundry. Results obtained have already been reported (1)–(4).

Specifically, this paper deals with the behaviour of hydrogen when melting unalloyed and low-alloy steels in the plasma furnace. A special aspect in

*) Dipl.-Ing. Dr. mont. Josef Knauder, Dipl.-Ing. Dr. mont. Wilfried Krieger, both Research, Development and Quality Section
Dipl.-Ing. Kilian Jandl, Electric Steel Plant
VOEST-Alpine AG/Linz

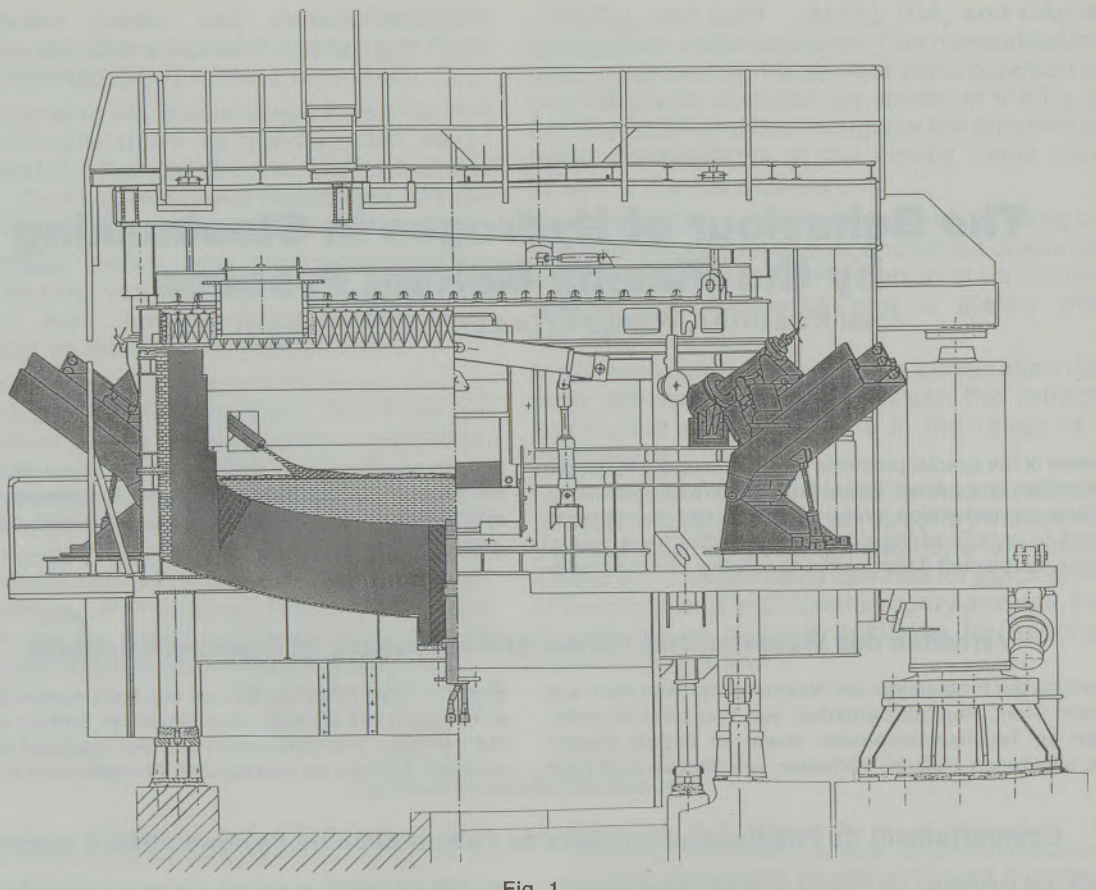

Fig. 1
45-ton Plasma melting furnace

this connection is the adjustment of low sulphur contents combined with the requirement of low phosphorus contents.

2. Hydrogen sampling/reproducibility of parallel tests

To cope with the task of systematically investigating the behaviour of hydrogen in the plasma furnace, first of all the question of a suitable hydrogen sampling method had to be answered, since it is well known that hydrogen sampling presents a problem (5), (6). Among the special criteria of selection were easy handling, good reproducibility of the values and a minimum of cost. Previous work (5) has demonstrated an immersion probe technique (fig. 2) which has proved highly successful for hydrogen sampling in the LD vessel and in the ladle. By means of the immersion probe the samples are drawn directly from the heat. In contrast to the immersion probe, sampling with the copper mould (7) (fig. 2) comprises, first, intermediate sampling by means of a sample spoon and, subsequently, pouring into the copper mould. Intermediate sampling presents a problem, as the hydrogen values may be influenced by the environment (atmosphere, slag).

In order to enable statements to be made on the reproducibility of both techniques, the following investigation of production heats was carried out. The comparison between immersion probe samples and copper mould samples (fig. 3) was made on samples from the ladle. Sampling was carried out before or after vacuum treatment. As shown in fig. 3, the agreement of the values within the range of 1 to 6×10^{-4}% can be regarded as satisfactory.

Another investigation referred to the reproducibility of hydrogen values, achievable in parallel sampling with the immersion probe. The respective tests were carried out both in the ladle and in the plasma furnace. In this respect also, the results achieved are satisfactory both in the ladle and in the plasma furnace. With the use of statistics, this may be expressed in terms of standard deviation (8). The standard deviation (s) is calculated by the formula

$$s = \left[\frac{1}{2N} \cdot \sum_{i=1}^{N} (x_{i,1} - x_{i,2})^2 \right]^{1/2}$$

$x_{i,1}$, $x_{i,2}$ individual values of the ith comparative determination

N number of comparative determinations

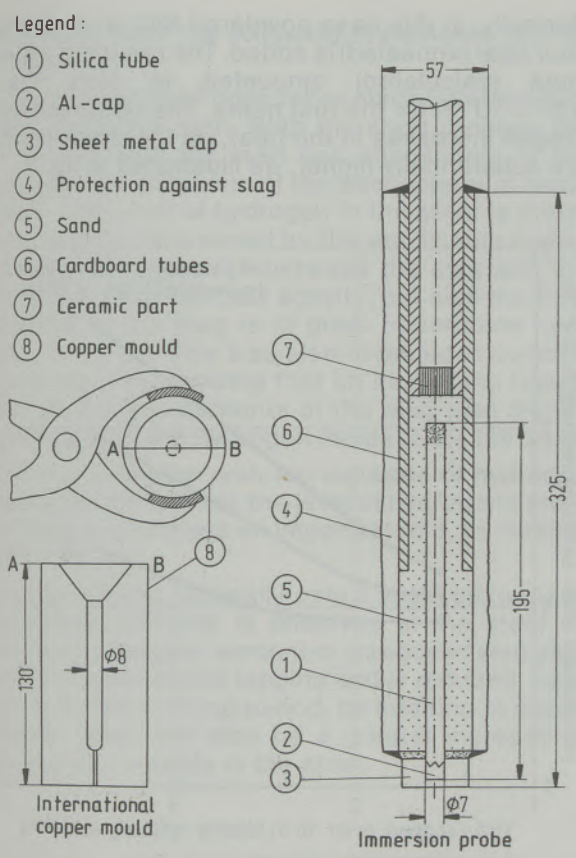

Fig. 2
Methods for taking hydrogen samples from liquid steel (dimensions in mm)

The deviations determined in this way gave the following values for the individual comparisons made:

- Comparative sampling copper mould – immersion probe 0.32 × 10^{-4}%.
- Comparison of immersion probes (parallel samples) in the ladle 0.23 × 10^{-4}%.
- Comparison of immersion probes (parallel samples) in the plasma furnace 0.21 × 10^{-4}%.

3. Effects on hydrogen behaviour in the plasma furnace

The following study, as already mentioned at the beginning, is confined to unalloyed and low-alloy steels produced in a similar way as in the electric arc furnace, that is as build-up heats.

3.1 Melt-down

The composition of the scrap is selected, depending on the requirements regarding the final analysis of the type of steel to be produced. The amounts of lime, also introduced during melt-down, depend on the phosphorus content aimed at in each particular case. Fig. 4 clearly shows that the hydrogen contents in the steel after melt-down increase with increasing lime rate and increasing water input that is associated with it. If there are exceptionally stringent requirements concerning the phosphorus contents, the melt-down slag will be tapped off and a fresh lime/fluor spar mixture will be added. This results in a further increase of the hydrogen content.

3.2 Oxidizing refining

Oxidizing refining in the plasma furnace is done, analogously to the electric arc furnace, by introducing gaseous oxygen into the steel bath by means of a lance. During this process CO is

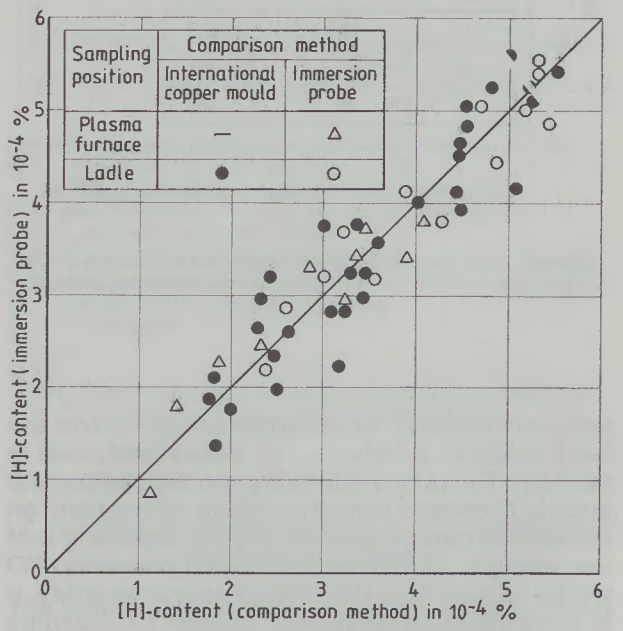

Fig. 3
Deviations of hydrogen contents in comparative sampling between copper mould and immersion probe and in parallel sampling with the immersion probe

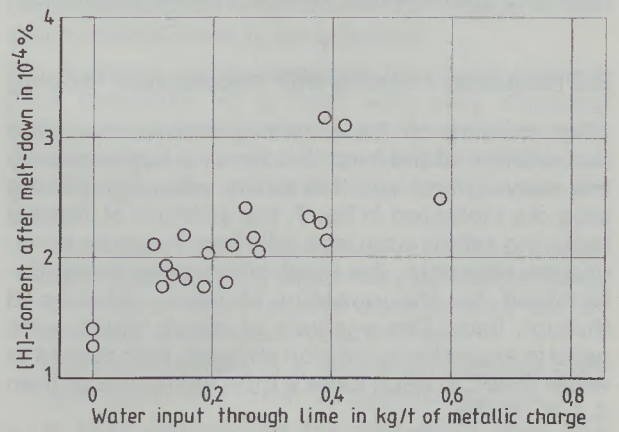

Fig. 4
Correlation between hydrogen content after melt-down and water input through lime in the plasma melting furnace

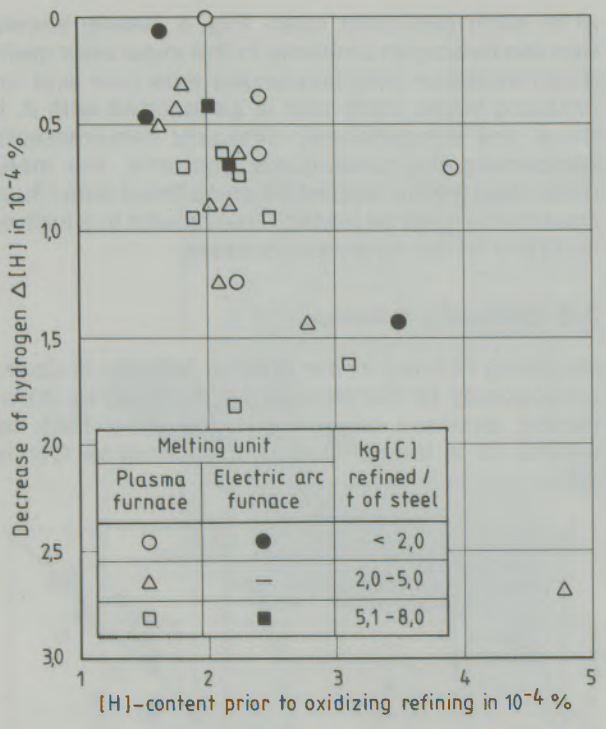

Fig. 5
Change Δ[H] during oxidizing refining as a function of the hydrogen content before oxidizing refining in the plasma melting furnace

formed in the heat, which, when escaping from the heat, leads to a reduction of gases contained in the heat. The removable hydrogen depends on the level of hydrogen before oxidizing refining and on the refined carbon quantity (fig. 5). Assuming that according to stoichiometric mass conversion CO will be formed from the refined carbon quantity, it is possible to calculate the evolved CO quantity per ton of steel.

Accordingly, fig. 6 shows that even with higher initial hydrogen contents before oxidizing refining low hydrogen contents are obtained when using high gas quantities or refined carbon quantities.

3.3 Reducing refining with subsequent tapping

After drawing off the oxidizing refining slag, the deoxidation of the heat is done and subsequently the alloying and addition of the reducing refining slag. As indicated in fig. 7, the addition of lime for reducing refining causes a further increase in hydrogen contents, the level of increase being determined by the quantity of water introduced through lime. The analysis of alloys which were used in annealed condition showed, with regard to water input, in each case a total value of less than 0.1×10^{-4}%.

A special situation is created in cases where during reducing refining, to obtain lowest sulphur contents, a further reduction of the slag takes place. Normally, in this case powdered SiC is used and fluor spar (annealed) is added. The resulting water input (calculated) amounted to less than 0.2×10^{-4}% for the test heats. The observed hydrogen increases in the heat, on the other hand, are substantially higher, as illustrated in fig. 7.

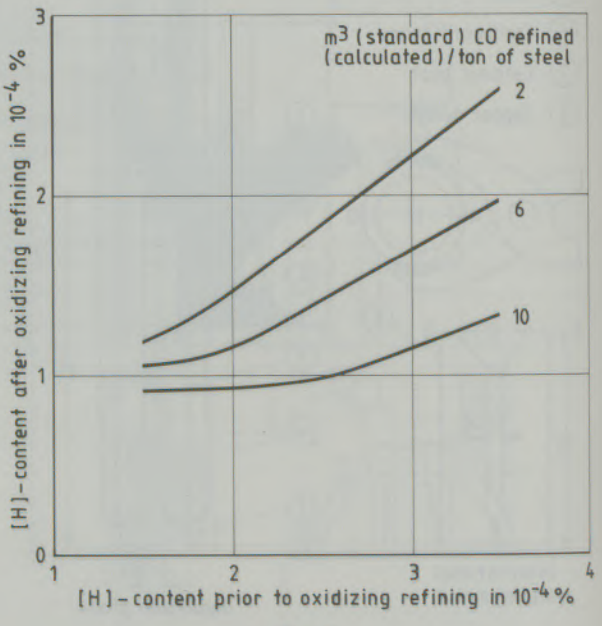

Fig. 6
Influence of refined CO quantity and of hydrogen content before oxidizing refining on the hydrogen content after oxidizing refining in the plasma melting furnace

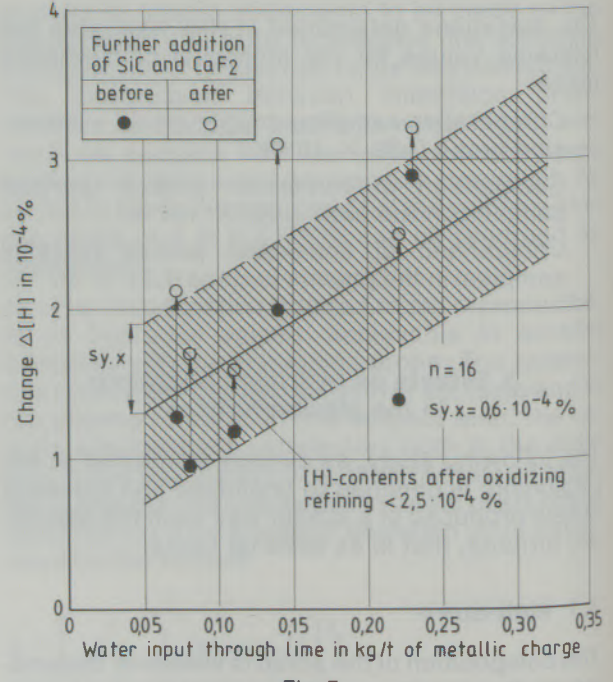

Fig. 7
Increase in hydrogen Δ[H] between end of oxidizing refining and end of normal reducing refining period by water input through refining lime and further increase in hydrogen contents by further addition of SiC and CaF_2

In this context the following statements can be made:

A transition of hydrogen takes place between gas, slag and steel bath. With the short process periods and with the inert gas atmosphere in the furnace, the influence of the atmosphere is negligible. The level of hydrogen in the steel is therefore largely determined by the equilibrium hydrogen content obtained between the slag and the bath. Not only the CaO activity, but also the FeO content of the slag is of great importance here (10), (11), (12). This was also revealed in our own tests (fig. 8b), showing that an increasing reduction of the iron contents of the slag also significantly raises the hydrogen increases in the steel.

But in connection with the increase of hydrogen contents in the steel, the level of hydrogen before reduction also plays an important role, as illustrated in fig. 8a.

During tapping, normally only a slight increase in hydrogen contents is observed in the steel. If, however, a greater amount of unreduced slag gets into the ladle during tapping and is reduced, as in the reducing refining period, by addition of deoxidizers, there will also be a greater increase of hydrogen contents in the steel.

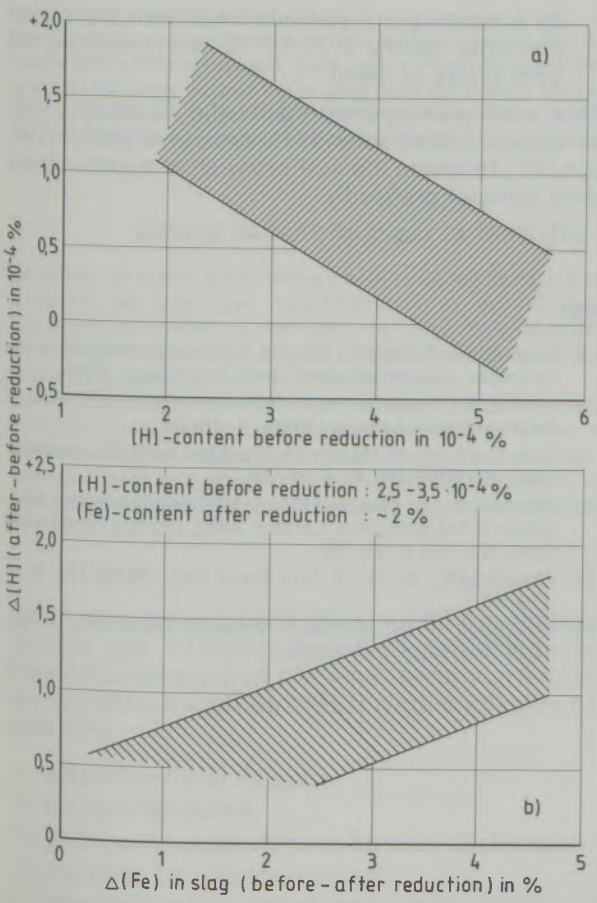

Fig. 8
Change Δ[H] by a reduction with SiC during the reducing refining period in the plasma melting furnace

Mode of operation	Melt-down		Oxidizing refining	Reducing refining+ tapping		Steel desulphurization (Ca Si)	Vacuum treatment
	H_2O input through the charge	lime additional	m^3(standard) CO/t_{ch}	H_2O input through lime	additional reduction	H_2O input through lime	Recirculation factor
A	0,42 kg /t_{ch}	0,17 kg /t_{ch}	5,6	0,13 kg /t_{ch}	Si C	0,025 kg /t_s	8
B	0,22 kg /t_{ch}	none	9,5	0,11 kg /t_{ch}	none	none	7

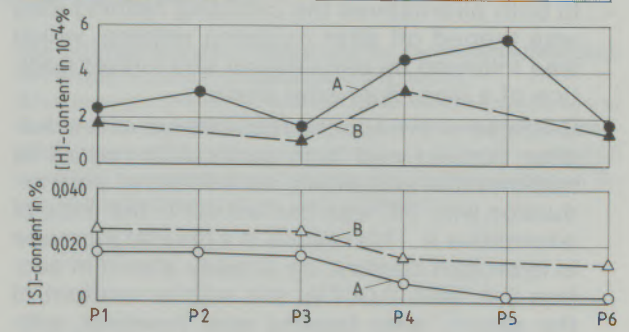

P 1 Plasma melting furnace after melt-down
P 2 Plasma melting furnace after further addition of lime
P 3 Plasma melting furnace after oxidizing refining
P 4 Ladle after tapping
P 5 Ladle after steel desulphurization
P 6 Ladle after vacuum treatment
t_{ch} ton of metallic charge
t_s ton of steel

Fig. 9
Hydrogen- and sulphur behaviour for different modes of operation in the plasma melting furnace

4. Special modes of operation and attainable hydrogen contents

The results described in section 3 were obtained in melting unalloyed or low-alloy types of steel. With regard to the phosphorus and sulphur contents, values below 0.020% are specified.

Many types of steel are increasingly required to have lower phosphorus and sulphur contents, with the simultaneous requirement that lowest hydrogen contents have to be adjusted.

Fig. 9 shows, as an example, hydrogen and sulphur behaviour of a heat with very stringent requirements (alternative A) and normal requirements (alternative B). When comparing the two procedures, the following statements can be made:

- After melt-down, alternative A shows a higher hydrogen content, which may be explained by the higher rates of lime addition and the increased water input, respectively.

  But this resulted in a melt-down sulphur content which was lower by approx. 0.010%.
- In both alternatives the melt-down slag was tapped off after melt-down, in order to minimize rephosphorization. In addition, a lime/fluor spar mixture was added in the case of alterna-

tive A, which further increased the hydrogen content in the steel, due to the water input caused by it.

- As already shown in fig. 6, if hydrogen contents before oxidizing refining are low, the hydrogen contents after oxidizing refining will be about 1×10^{-4}%, even if great quantities of carbon are refined. This case is illustrated by alternative B.
- In both alternatives the oxidizing refining slag was tapped off after oxidizing refining, which was followed by deoxidation and further addition of a lime/fluor spar mixture.

  Because of the special requirement of low sulphur content and high purity with regard to non-metallic inclusions, an additional slag reduction with SiC was carried out in the case of alternative A. This results in a greater increase in hydrogen content, as already stated in section 3.3. With 0.007%, the sulphur content of the sample after tapping was, however, substantially lower than for alternative B (0.015%).
- In the case of alternative A, steel desulphurization was carried out after tapping, for which purpose a fresh top slag was added, leading to a further increase in the hydrogen level. At favourable slag ratios (~ 0.5% Fe) the sulphur content was 0.0015% after desulphurization.
- For both alternatives a sufficiently high recirculation factor was provided for at the DH plant, in order to obtain low hydrogen contents. In this connection and in a number of further tests it was found that the removal of hydrogen depends also to a great degree on the initial content.
- Finally, it may be stated that the phosphorus content of the final sample was 0.008% for alternative A and 0.014% for alternative B.

5. Summary

Within the scope of development of the 45-ton plasma melting furnace of VOEST-ALPINE AG the hydrogen behaviour during melting of unalloyed and low-alloy types of steel was studied. The main consideration in carrying out the tests was to meet the requirement of low hydrogen levels, even if lowest phosphorus and sulphur contents are adjusted. The observations made can be summarized as follows:

- When producing steel with phosphorus and sulphur contents <0.020%, the hydrogen contents after tapping are approx. 3×10^{-4}% in the plasma furnace, provided that dried slag-forming agents and alloys are used.
- When steels are produced with phosphorus contents <0.010% and at the same time with sulphur contents <0.003%, the hydrogen contents after tapping and subsequent steel desulphurization amount to about 5×10^{-4}%, because of the higher quantity of slag-forming agents added.
- By a subsequent vacuum treatment, hydrogen contents below 2×10^{-4}% are obtained for both types of steel.

This work was sponsored by the Austrian „Forschungsförderungsfonds für die gewerbliche Wirtschaft", to whom the authors wish to express here their special gratitude.

References

1. Steipe, O., W. Krieger, K. Antlinger, D. Peterek: Giesserei 73 (**1986**), Heft 14–15, p. 427/32.
2. Lugscheider, W., F. Wallner: The Eigth Intern. Conf. on Vacuum Metallurgy, Eisenhütte Österreich. Linz 30. Sept. – 4. Oct. **1985**, Vol. 1, p. 554/568.
3. Lugscheider, W., G. Scharf: In: Gmelin-Durrer: Metallurgy of Iron, Vol. 8; Trenkler, H., W. Krieger: Practice of steelmaking 2, Springer Verlag Berlin – Heidelberg – New York – Tokyo **1985**, p. 199a/218a, 186b/192b.
4. Steipe, O., D. Peterek, W. Lugscheider: The Eigth Intern. Conf. on Vacuum Metallurgy, Eisenhütte Österreich, Linz 30. Sept. – 4. Oct. **1985**, Vol. 1, p. 899/915.
5. Knauder, J., K. Reischl, J. Gruber: Colloquium on "Trace elements in steels" of "Eisenhütte Österreich", Stahleisen-Bericht (**1985**), p. 14/16.
6. Schwarz, W., H. Zitter: Radex-Rdsch., (**1964**), No. 4, p. 226/32.
7. Stahl-Eisen-Prüfblatt 1710–66. Sampling to determine the hydrogen content of liquid steel. Issue Sept. **1966**.
8. Dörffel, K.: Statistics in analytic chemistry. VEB-Verl. of Basic Industry, Leipzig (**1966**), p. 88/96.
9. Vom Ende, H., K. Hagen, H. Trenkler: Arch. Eisenhüttenwes. 40 (**1969**) No. 6, p. 27/36.
10. Mitchell, A., S. Chattopadhyay: In: Spring meeting. Institution of Metallurgists. London **1982**. (Spring Residential Conf. No. 19.) p. 22/35.
11. Plocklington, D. N.: J. Iron Steel Inst. (**1973**) No. 6, p. 419/25.
12. Klotzbach, G., W. Jäniche, H. Vorwerk: Techn. Mitt. Krupp, 19 (**1961**) No. 3, p. 107/21.

Der energieoptimierte exzentrische Bodenabstich am Elektrolichtbogenofen

Harald Berger und Ernst Zajicek, Linz

Der exzentrische Bodenabstich am Lichtbogenofen hat bezüglich schlackenfreien Abstichs, verringerter Gasaufnahme und geringen Temperaturverlustes sowie weiter vergrößerter wassergekühlter Wandflächen bedeutende Vorteile gebracht.
Es sind jedoch auch Nachteile mit dem konventionellen exzentrischen Bodenabstich verbunden, wie z. B. die relativ große Entfernung des Stahlvolumens im Erker von der Energiequelle des Lichtbogens, eine Vergrößerung der Stahlbadoberfläche und ein absolut hoher Bedarf an feuerfestem Mauerwerk durch die Ausmauerung des Erkers.
Der letzte Umstand tritt besonders bei der sicherheitsbedingten Anhebung des Erkerabdeckpanels hervor.
Beim energieoptimierten exzentrischen Bodenabstich, wie er im folgenden beschrieben wird, werden die erwähnten Nachteile unter Beibehaltung aller erwiesenen Vorteile wesentlich gemildert durch eine Heranführung des Stahlvolumens im Erker an das Energiezentrum des Lichtbogens.

Eccentric Bottom Tapping at the Electric Arc Furnace under Optimized Energy Conditions

Eccentric bottom tapping at the EAF has important advantages regarding slag-free tapping, reduced gas pick-up and low temperature losses as well as water-cooled wall panels which have been further extended in size.
Nevertheless, conventional eccentric bottom tapping also involves some disadvantages, such as the relatively large distance of the steel volume in the oriel from the energy source of the electric arc, an increase of the steel bath surface and the refractory demand which is absolutely high due to the oriel lining.
The last-mentioned aspect is especially prominent with regard to the lifting of the oriel cover panel which has become necessary for safety reasons.
With energy-optimized eccentric bottom tapping (EBT) as is described in the following, the advantages are kept up while the disadvantages referred to are essentially alleviated by approaching the steel volume in the oriel to the energy source of the electric arc.

Coulée excentrique par le fond des fours à arcs avec optimisation d'energie

La coulée en poche excentrique par le fond des fours à arcs a apporté des avantages considérables en ce qui concerne une coulée sans laitier, la diminution de l'absorption de gaz et de la perte de chaleur ainsi qu'un accroissement supplémentaire des surfaces de parois refroidies à l'eau.
Mais la coulée excentrique par le fond conventionnelle comporte aussi des inconvénients, comme par exemple la distance relativement grande entre le volume d'acier contenu dans le chenal et la source d'énergie de l'arc électrique, un accroissement de la surface de l'acier et un besoin nécessairement élevé en garnissage réfractaire pour le revêtement du chenal.
Ce dernier inconvénient se fait particulièrement sentir lors du relèvement du panneau de couverture du chenal dicté par les impératifs de sécurité.
Dans le cas d'une coulée en poche excentrique avec optimisation d'énergie, comme on le décrit ci-après, on réduira considérablement les inconvénients décrits, tout en conservant les avantages, en plaçant le volume d'acier se trouvant dans le chenal au centre d'énergie de l'arc électrique.

Die in den Jahren 1983/84 eingeführte Abstichtechnik des exzentrischen Bodenabstiches an Elektrolichtbogenöfen hat eine Reihe von Vorteilen qualitativer und betrieblich-wirtschaftlicher Art gebracht:

- schlackenfreier Abstich;
- kurze Abstichzeit;
- geringe Gasaufnahme in kurzem Gießstrahl;
- geringer Temperaturverlust;
- kleiner Ofenkippwinkel, dadurch Vergrößerung der wassergekühlten Wandkühlflächen möglich.

The method of eccentric bottom tapping at electric arc furnaces which has been introduced in 1983/84, shows a number of advantages as regards quality and shop management:

- slag-free tapping;
- short tapping time;
- low gas pick-up in the short tapping stream;
- low temperature loss;
- small furnace tilting angle, enabling extension of the water-cooled wall panels.

The disadvantages of this method are the extended, refractory-lined hearth and wall zone, caused

Nachteilig muß die durch den erkerartigen Anbau an den Gefäßunterteil vergrößerte, feuerfest gemauerte Herd- und Wandzone, die vergrößerte, wärmestrahlende Stahlbadoberfläche sowie der Umstand angesehen werden, daß sich das Stahlbadvolumen im Erker in relativ großem Abstand von der Energiequelle des Lichtbogens befindet.

Diese Nachteile wurden in Kauf genommen, um die beim Vorläufer des exzentrischen Bodenabstiches, dem zentrischen Bodenabstich, auftretenden Schwierigkeiten im Zusammenhang mit dem schlackenfreien Abstich sowie der Abstichlochpflege zu umgehen. Um die Nachteile zu minimieren, wurde der Abstich so dicht wie nur möglich an die Ofenwand herangeführt (1).

Überlegungen, die Nachteile des im ganzen zweifellos vorteilhaften exzentrischen Bodenabstiches zu mindern, führten zur Konzeption eines energieoptimierten exzentrischen Bodenabstiches, der zum Patent angemeldet wurde (2).

Beschreibung des energieoptimierten exzentrischen Bodenabstiches

Der energieoptimierte exzentrische Bodenabstich ist gekennzeichnet durch:

- Verringerung der Entfernung des flüssigen Stahlvolumens im Erker von der Energiequelle des Lichtbogens;
- Verringerung der Wärmeabfuhr aus dem Erker durch Vergrößerung des Abstandes des Erkerabdeckpanels von der Badoberfläche.

Konstruktiv erreicht man dies durch eine Abflachung des sonst kreisförmigen Umrisses des Gefäßoberteiles im Bereich des Abstichloches (Abb. 1). Durch diese Maßnahme ist es möglich, das Abstichloch in einem geringeren Abstand zur Mittelachse des Gefäßes anzuordnen als bei einem Oberteil mit kreisförmigem Grundriß, ohne dabei die Zugänglichkeit des Abstichloches zur Lochpflege zu behindern. Diese gegenüber dem herkömmlichen exzentrischen Bodenabstich geringere Exzentrizität des Abstichloches führt zu einer Verringerung der oben angeführten Nachteile eines solchen Abstichsystems unter Beibehaltung aller Vorteile und ermöglicht in besonders vorteilhafter Weise die Einhaltung der folgenden wesentlichen Gestaltungsmerkmale eines Schmelzgefäßes mit exzentrischem Bodenabstich:

- geringe Exzentrizität des Abstichloches;
- großer vertikaler Abstand zwischen Badoberfläche und Erkerabdeckpanel;
- kurze wassergekühlte Wandpanels im Erkerbereich, damit die Strahlung des Lichtbogens auch das Stahlvolumen im Erker erreicht;
- geringe Höhendifferenz zwischen den Niveaus des Herdbodens und des Erkerbodens.

Durch die Einhaltung dieser Konstruktionsprinzipien gelangt man zu einer geometrischen Form

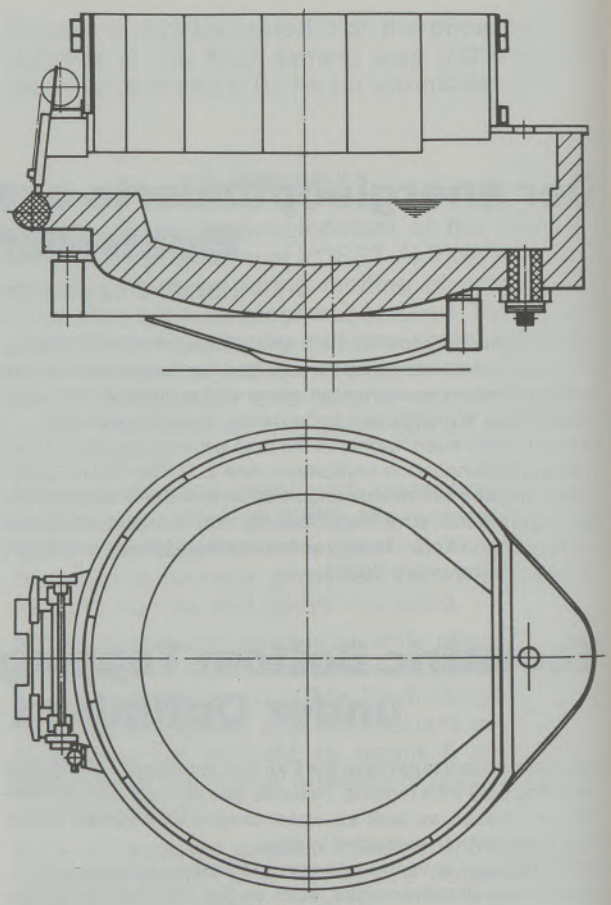

Abb./Fig. 1

by the oriel-like attachment to the shell bottom part, the extented, heat-radiating steel bath surface, as well as the fact that the steel bath volume in the oriel is located at a relatively large distance from the energy source of the electric arc.

These disadvantages, however, have been accepted in order to by-pass the difficulties which had arisen in connection with centric bottom tapping, the tapping mode which had preceded eccentric bottom tapping, in connection with slag-free tapping as well as tap-hole maintenance. In order to keep the disadvantages to a minimum, the tapping hole has been situated as close as possible to the furnace wall (1).

Considerations with the aim to alleviate the disadvantages of eccentric bottom tapping, which, as a whole is advantagous, resulted in the conception of energy-optimized eccentric bottom tapping for which numerous applications for protective rights as well as one patent are available (2).

Description of energy-optimized eccentric bottom tapping

Energy-optimized eccentric bottom tapping is characterized by the following:

- shorter distance of the liquid steel volume in the oriel from the energy source of the electric arc;

des Schmelzbades, bei der thermische und metallurgische Homogenität weitgehend gegeben sind. Ein großer vertikaler Abstand zwischen Badoberfläche und Erkerabdeckpanel ist außerdem aus Sicherheitsgründen unbedingt erforderlich, um sicherzustellen, daß beim Kippen des Ofens während des Abstichvorganges flüssiger Stahl das Abdeckpanel nicht berührt. Beim anfänglich ausgeführten Abstand von etwa 500 mm zwischen Bad und Panel kam es zu schweren Explosionen, worauf der Abstand auf etwas über 1000 mm angehoben werden mußte. Durch diesen Umstand ist auch keine erhöhte Wärmebelastung der wassergekühlten Wandelemente im abgeflachten Teil des Gefäßes, welche ja näher zu den Elektroden liegen, zu erwarten, da sie während des Einschmelzvorganges durch Schrott geschützt sind und in der Flachbadphase eine wesentliche Wärmebelastung in der Höhe dieser Elemente nicht auftritt. Der Lichtbogen strahlt nämlich unter diesen Elementen hindurch in den Erker, sollte er nicht von schaumiger Schlacke eingehüllt sein.

Die Chargierbarkeit wird durch das eingezogene Gefäßoberteil nicht beeinträchtigt. Der Schrottkorb wird in einer aus der Ofenmitte um 150 bis 250 mm (je nach Ofengröße) Richtung Schlackentür versetzten Stellung geöffnet. Bei der Verwendung von Schrottkörben, wie sie für die jeweilige Ofengröße üblich sind, ergibt sich dadurch ein genügend großer Sicherheitsabstand zwischen Schrottkorbdurchmesser und Panelinnenkante von 400 bis 500 mm.

Beim Neubau von Stahlwerken ist allerdings die Verwendung von ovalen Schrottkörben denkbar. Dadurch ist eine weitere Verringerung der Exzentrizität des Abstichloches möglich, wodurch sich die Vorteile des energieoptimierten Prinzips im folgenden Vergleich zwischen konservativem exzentrischem Bodenabstich und energieoptimiertem exzentrischem Bodenabstich noch vergrößern würden.

Vergleich zwischen exzentrischem Bodenabstich konservativer und energieoptimierter Bauweise

Im Rahmen dieses Vergleiches sollen folgende für die Wirtschaftlichkeit und für die thermischen und metallurgischen Bedingungen im Ofen entscheidenden Kenngrößen untersucht werden:

- Abstand zwischen Abstichloch und Ofenmitte;
- Fläche der ff-Ausmauerung über Badspiegel bzw. Schaffplatte;
- Fläche der wassergekühlten Wandelemente;
- Verhältnis der beiden oben angeführten Flächen;
- Badoberfläche.

Vorerst soll der Abstand zwischen Ofenmitte und Abstichloch untersucht werden (Abb. 2). An den auseinanderstrebenden Geraden zeigt sich, daß der absolute Betrag der Abstandsverkürzung mit größer werdendem Ofendurchmesser steigt. Die

- less heat dissipation from the oriel by increased distance of the oriel cover panel from the bath surface.

Both these features are obtained by flattening the otherwise circular contour of the shell upper part in the area of the tap-hole (fig. 1). By this measure it is possible to situate the tap-hole closer to the central axis of the shell, which is in contrast to a shell upper part designed with circular lay-out, without impeding the accessibility of the tap-hole for maintenance purposes. The fact that the eccentricity of the tap-hole is less compared with conventional eccentric bottom tapping practice, leads to a reduction of the disadvantages of such a tapping system as referred to above, while all advantages are kept. Moreover, all essential design features of a melting furnace can be kept in a most advantageous way:

- low eccentricity of the tap-hole;
- large vertical distance between bath surface and oriel cover panel;
- short, water-cooled wall panels in the oriel area, to ensure that the radiation of the electric arc reaches the steel volume in the oriel;
- minor difference in level between the hearth bottom and the oriel bottom.

When these design principles are adhered to, a geometrical shape of the melting bath is obtained, providing thermal and metallurgical homogeneity to a large extent. A big vertical distance between the bath surface and the oriel cover panel is an absolute must for reasons of safety, in order to prevent liquid steel from getting into contact with the cover panel during tapping when the furnace is tilted. The distance of about 500 mm referred to earlier between bath and panel, caused heavy explosions and as a consequence, the distance had to be increased to slightly above 1000 mm. Due to this design, no increased thermal load of the water-cooled wall panels which are located closer to the electrodes in the flattened part of the shell is to be expected, as they are protected by scrap during melting down and as no essential thermal load occurs at the level of these elements in the flat bath phase. The reason for this being the fact that the electric arc radiates into the oriel below these elements in case it is not shrouded by foamy slag.

Charging as such is not hindered by flattened design of the shell upper part. The scrap bucket is opened in a position which is displaced from the furnace centre by 150 to 250 mm (depending on furnace size) in direction of the slag door. When using scrap buckets which are standard for the individual furnace size, the safety distance resulting between scrap bucket diameter and panel inner edge is 400 to 500 mm.

With newly erected steel shops, the use of oval-shaped scrap bucket is possible. Thus, the eccentricity of the tap-hole can be further reduced, which means that the advantages of the energy-

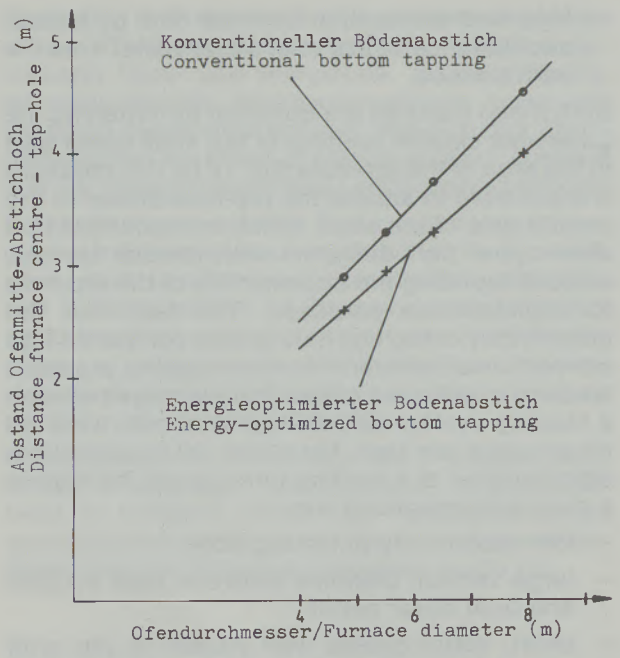

Abflachung des ursprünglich kreisförmigen Ofengrundrisses und damit die Annäherung des Abstichloches an das Ofenzentrum ergeben sich aus dem für den jeweiligen Ofendurchmesser üblichen Schrottkorbdurchmesser und der Sicherheitsdistanz von 400 bis 500 mm zwischen Schrottkorbdurchmesser und Panelinnenkante. Beim konservativen Bodenabstich ist der Abstand des Abstichloches zum Ofenzentrum gegenüber dem energieoptimierten Konzept bei den untersuchten Ofengrößen (4,8 m; 5,6 m; 6,4 m; 8 m) von 11,5 Prozent (4,8-m-Ofen) bis 13,8 Prozent (8-m-Ofen) größer. Der kleinere Abstand beim energieoptimierten Konzept entspricht der Forderung, den Erker möglichst nahe an die Energiequelle zu rücken.

Die restlichen vier Kriterien sollen an Hand eines Lichtbogenofens mit einem Ofendurchmesser von 6,4 m verglichen werden (Tabelle 1).

Es wurde zugrunde gelegt, daß die Stahlbadoberfläche 100 mm unterhalb der Schaffplatte liegt. Die Öfen sind mit unterhalb der Stahlpanels angeordneten Kupferpanels ausgerüstet, deren Unterkante 350 mm über dem Badspiegel liegt. Weiters sind die verglichenen Öfen für eine 2-Korb-Schrottchargierung ausgelegt. Für die Chargierung wird ein Schrottkorb mit einem Durchmesser von 5,1 m verwendet. Die Verringerung des Ofenvolumens durch die Abflachung des Gefäßoberteiles wird durch eine Erhöhung desselben um 50 mm ausgeglichen.

Betrachtet man die feuerfest ausgekleidete Fläche des Ofengefäßes, welche über dem Badspiegel liegt, so zeigt sich, daß die Gefäßform nach dem energieoptimierten Konzept mit 9,3 Prozent weniger Fläche feuerfesten Materials auskommt als beim konventionellen Erkerabstich. Dies ergibt sich aus dem kleineren Gefäßumfang.

optimized principle become even more obvious when comparing between the conventional eccentric bottom tapping and the energy-optimized eccentric bottom tapping mode.

Comparison of eccentric bottom tapping of conventional and energy-optimized design

This comparison aims at the investigation of characteristics which are decisive for the economy as well as for the thermal and metallurgical conditions in the furnace:

- distance between tap-hole and furnace centre;
- area of refractory lining above bath level and / or sill plate;
- area of water-cooled wall elements;
- relation of the two above areas;
- bath surface.

First of all, the distance between furnace centre and tap-hole is to be investigated (fig. 2). The two disparating straight lines show that the absolute rate of the shorter distance increases as the furnace diameter increases. The flattening of the furnace lay-out which has originally been circular, and thus the approach of the tap-hole to the furnace centre, result from the scrap bucket diameter standard for the individual furnace diameter and the safety distance of 400 to 500 mm between the scrap bucket diameter and the panel inner edge. With conventional bottom tapping, the distance between the tap-hole and the furnace centre is larger by up to 11.5% (4.8 m furnace) and by up to 13.8% (8 m furnace) compared with the energy-optimized design of the furnace sizes investigated (4.8 m; 5.6 m; 6.4 m; 8 m). The shorter distance of the energy-optimized concept complies with the request to situate the oriel as close as possible to the energy source.

The remaining 4 criteria should be compared on basis of an electric arc furnace with a furnace diameter of 6.4 m (table 1).

The investigation has been based on the assumption that the steel bath surface is 100 mm below sill level. The furnaces are equipped with copper panels located below the steel panels. The bottom edge of these copper panels is 350 mm above the bath level. In addition, the furnaces which have been compared are designed for 2-bucket scrap charging. For charging, a scrap bucket of a diameter of 5.1 m is used. The reduction of the furnace volume due to the flattening of the shell upper part is compensated by extending the height by 50 mm.

When investigating the refractory-lined surface of the furnace shell, which is located above the bath level, it shows that for the shell when designed according to the enery-optimized concept, 9.3% less of refractory-lined surface are required than for the conventional eccentric bottom tapping which is due to the smaller shell circumference.

Tabelle/Table 1

Vergleich der wichtigsten Betriebskennzahlen bei energieoptimiertem und konservativem Bodenabstich sowie bei Siphonabstich, dargestellt für einen 6,4-m-Ofen

Comparison of the most important operatings characteristics of energy-optimized and conventional bottom tapping as well as siphon tapping, based on a 6.4 m furnace

Kriterium / Arten des Abstichs / criterion / kind of tapping	Fläche des ff-Materials über Badspiegel; surface of refr. material above bath level		Fläche des ff-Materials über Schaffplatte; surface of refr. material above sill level		Fläche der wassergek. Wand; surface of water-cooled wall		Flächenverhältnis wassergek. Wand: ff-Material über Badspiegel; surface ratio water-cooled wall: refr. mat. above bath level	Flächenverhältnis wassergek. Wand: ff-Material über Schaffplatte; surface ratio water-cooled wall: refr. mat. above sill level	Badoberfläche 100 mm unter Schaffplatte; bath surface 100 mm below sill level	
	[m²]	%	[m²]	%	[m²]	%			[m²]	%
Energieoptimierter Bodenabstich energy-optimized bottom tapping	10,8	100	9,1	100	49,6	100	4,59	5,45	22,05	100
Konservativer Bodenabstich conventional bottom tapping	11,8	109,3	10,0	109,9	49,0	98,8	4,15	4,9	23,18	105,1
Siphonabstich (mit Kupferpanels) siphon tapping (with copper panels)	11,8	109,3	10,3	113,2	39,8	80,2	3,2	3,67	19,56	88,7

Durch den geringeren Abstand zwischen Ofenmitte und äußerster abstichseitiger Ausmauerung steigt der Badspiegel beim Kippen des Ofens nach energieoptimiertem Konzept weniger als beim konservativen Erker. Dadurch kann das Erkerpanel bei Anwendung der gleichen Sicherheitsgrundsätze um ca. 100 mm tiefer gesetzt werden, was eine weitere Reduzierung der ausgemauerten Fläche um 0,3 m² oder 2,8 Prozent gegenüber dem konservativen Erker bringt. Im Vergleich nach Tabelle 1 wurde beim Abstand zwischen Badspiegel und Erkerpanel jedoch zugunsten einer erhöhten Sicherheit diese Reduzierung um 100 mm nicht berücksichtigt.

Interessant ist auch die Tatsache, daß ein mit Cu-Panels ausgerüsteter Lichtbogenofen mit Siphonabstich die gleiche ff-Fläche über Bad wie ein Ofen mit Erkerabstich aufweist, d. h., daß der ursprüngliche Vorteil des konservativen Erkers in Bezug auf ff-Fläche durch die aus Sicherheitsgründen notwendige Anhebung des Erkerpanels verlorenging.

Allerdings befindet sich die bestrahlte Fläche in einem größeren Abstand zu den Elektroden, sodaß der ff-Verbrauch beim Erkerofen dennoch günstiger ist.

Im Vergleich der wassergekühlten Wandflächen zeigt sich ein nur unwesentlicher Unterschied zwischen den beiden Ofenformen mit exzentrischem

Owing to the shorter distance between the furnace centre and the outmost lining of the tapping side, the bath level rises less when tilting the furnace according to the energy-optimized concept than with conventional bottom tapping. Thus, it is possible to place the oriel panel by about 100 mm lower based on the same safety principles, which means a further reduction of the lined surface by 0.3 m² or 2.8% compared with the conventional method. According to table 1, this reduction by 100 mm has not been taken into consideration for the distance between the bath level and the oriel panel in favour of a higher degree of safety.

Another aspect which seems worth mentioning is the fact that an electric arc furnace equipped with copper panels with siphon tapping has the same refractory-lined surface above tha bath as a furnace with eccentric bottom tapping which means that the original advantage of the conventional oriel regarding the refractory-lined surface was lost by lifting of the oriel panel for safety reasons.

The distance between the radiated surface and the electrodes is larger however, which means that the refractory consumption of a furnace with eccentric bottom tapping is still more favourable.

When comparing the water-cooled wall panels, the difference between the two furnace designs with eccentric bottom tapping is minor. Despite

Bodenabstich. Trotz eines kleineren Umfanges der wassergekühlten Wandauskleidung ist die Fläche beim energieoptimierten Erker auf Grund der notwendigen Gefäßerhöhung zur Erreichung des gleichen chargierfähigen Ofenvolumens geringfügig größer. Die wassergekühlte Wandfläche ist beim Siphonabstich wesentlich geringer. Dies resultiert hauptsächlich aus der Tatsache, daß das Herdvolumen zu 100 Prozent chargierfähig ist und daher das Volumen (und damit die Wandfläche) über Schaffplatte bei gleichem Gesamtvolumen kleiner ist.

Das Flächenverhältnis zwischen wassergekühlter Wand und ff-Ausmauerung über Schaffplatte von 5,45:1 beim energieoptimierten Erker kommt nahe an das Flächenverhältnis von Öfen mit konservativem exzentrischem Bodenabstich vor der durch die Unglücksfälle notwendig gewordenen Anhebung des Erkerpanels heran. Das Verhältnis lag bei diesen Öfen über 6:1. Der entsprechende Wert liegt beim betrachteten Ofen mit konservativem Erker und angehobenem Erkerabdeckpanel bei 4,9:1 und ist daher ungünstiger.

Die Badoberfläche kann als Maß für die Wärmeabstrahlung nach außen angesehen werden. Auch bei diesem Vergleich liegt der Ofen nach dem energieoptimierten Konzept naturgemäß günstiger als der konservative Erkerofen.

Abschließend sei auch noch erwähnt, daß die Investitionskosten beim Ofen mit einem energieoptimierten Erker etwas niedriger als beim konservativen Erkerofen liegen und die Gefäßform festigkeitsmäßig leichter beherrschbar ist.

Zusammenfassung

Durch die Verringerung der Exzentrizität des Abstichloches bei Lichtbogenöfen mit exzentrischem Bodenabstich nach dem energieoptimierten Konzept können wesentliche für den wirtschaftlichen Betrieb sowie für die Schmelzenführung entscheidende Daten gegenüber einem konservativen exzentrischen Bodenabstich verbessert werden. Es verringert sich bei gleichen Bedingungen die Fläche der feuerfesten Ausmauerung über dem Badspiegel ebenso wie die Badoberfläche.

Während ersteres einen geringeren ff-Materialverbrauch erwarten läßt, bringt die kompaktere Badform eine verringerte Wärmeabstrahlung und eine verbesserte thermische und metallurgische Homogenität der Schmelze. Außerdem wird das Flächenverhältnis von wassergekühlter Wand zu feuerfester Ausmauerung über Badspiegel zu günstigeren, höheren Werten hin verschoben.

the small circumference of the water-cooled wall lining the surface in case of the energy-optimized oriel is slightly larger which is due to the lifting of the shell to achieve the same chargeable furnace volume. The water-cooled wall surface is considerably smaller with siphon tapping. This is mainly due to the fact that the hearth volume is chargeable to 100% and that the volume (and thus the wall surface) above sill level is smaller, the overall volume remaining the same.

The relation of surface between water-cooled wall and refractory lining above sill level of 5.45:1 with energy-optimized bottom tapping gets close to the surface ratio of furnaces with conventional eccentric bottom tapping prior to lifting of the oriel panels which became necessary after some accidents had happened. With these furnaces, the ratio was above 6:1. The respective value of the furnace investigated with conventional oriel and lifted oriel cover panel is around 4.9:1, and therefore less favourable.

The bath level can be regarded as measure for heat radiation toward the outside. This investigation too proved that the furnace which is operated according to the energy-optimized concept is more favourable than the conventional bottom tapping furnace.

Finally, it should be mentioned that the investment cost are slightly lower for a furnace with energy-optimized bottom tapping than for the conventional bottom tapping furnace and that the strength of the shell shape can more easily be controlled.

Summary

By reducing the eccentricity of the tap-hole of electric arc furnace with eccentric bottom tapping according to the energy-optimized concept, data which are important for economical operation as well as heat practice can be essentially improved as compared with conventional eccentric bottom tapping. The surface of the refractory lining above the bath level as well as the bath surface decreases under identical conditions.

While from the first less refractory consumption may be expected, the more compact bath shape results in a reduced heat radiation and improved thermal and metallurgical homogeneity of the heat. Moreover, the ration of surfaces between water-cooled wall and refractory brickwork above the bath level is shifted towards more favourable, higher values.

Literaturverzeichnis/References

1. Baare, R.-D., J. Overgaard und E. Rasmussen: Schlackenfreier Abstich, ein Hauptproblem bei der Herstellung von Qualitätsstahl; Stahl und Eisen 104 (1984), Nr. 1.

2. AT-Patent 380102 und korrespondierende Auslandsschutzrechte; Gegenstand: Elektroofen; Patentinhaber: VOEST-Alpine AG, Linz.

Industrieller Energieeinsatz und Umwelt

Heinz Jungmeier, Radenthein

Zwischen Energieeinsatz und Umweltbelastung der Luft besteht engster Zusammenhang. Größter Effekt durch bessere Energienutzung; hier liegen große Reserven und Chancen: Neben Senken der Schadstoffbelastung gleichzeitig große Impulse für die Wirtschaft (intelligentes Produkt). Von großer Bedeutung wäre weltweit die richtige Bewertung des Rohstoffes Energie.

Industrial Use of Energy and Environment

There is a close relation between energy-input and environmental load of the air. The maximum effect attainable is reached by improved energy usage; these are the large reserves and chances: Aside from reduction of pollutants, simultaneous large impulses result for the economy (intelligent product). The realistic appraisal of the raw material energy worldwide would be of prominent importance.

L'énergie dans l'industrie et environnement

Il existe un rapport très étroit entre l'utilisation de l'énergie et la pollution de l'air. Impact plus marqué par une meilleure utilisation de l'énergie. Ici se trouvent des grosses réserves et des opportunités: d'un coté, la réduction des éléments polluants et, de l'autre, de grandes répercussions sur l'économie (produit conçu intelligement). Une estimation exacte de la matière première énergie serait de la plus haute importance dans le monde entier.

Neben markanten Erscheinungen der industriellen Entwicklung, wie die bahnbrechenden Erfindungen der Buchdruckerkunst, der Dampfmaschine und des schmiedbaren Stahles, oder Einführung der Arbeitsteilung, Gründung der Arbeiterbewegung, Krieg und Wiederaufbau, hat und wird Weniges die industrielle Entwicklung so nachhaltig beeinflussen, wie die Reflexion an der Umwelt.

Nicht analytisches Denken, sondern anthropogene Naturkatastrophen jüngster Vergangenheit, haben eine neue, ungeheure Bewußtseinsbildung über die Grenzen menschlichen Tuns gebracht. Beispiele wie Umkippen der Seen, Grundwasserverunreinigungen, Smogkatastrophen, Seveso, Bhopal, Tschernobyl und die Rhein-Katastrophe sind ins Fleisch gegangen. Noch nie hat ein Naturphänomen so nachhaltig gewirkt wie saurer Regen und Waldsterben. Das verstehen alle!

Um die Problemstellung überhaupt begreifen zu können, ist es notwendig, Rechenschaft über die letzten 150 Jahre der Entwicklung abzulegen.

Welche wesentliche globale Entwicklung ist heute erkennbar?

In Abb. 1 ist die Entwicklung der Weltbevölkerung dargestellt. Vorher fast parallel zur Abszisse verlaufend, verläuft die Kurve nun fast parallel zur Ordinate.

Von 1975 bis 2010 eine Verdoppelung von 4 auf 8 Mrd. Menschen. Es ist eine Entwicklung, von der die Fachleute sagen, daß sie durch nichts aufzuhalten sein wird, als durch Katastrophen.

Jetzt aber können wir eine in höchstem Maße faszinierende Entdeckung machen: Die wichtig-

Aside from noteworthy phenomena of the industrial development – such as the pioneer inventions like the art of printing, the steam engine and the forgeable steel, the introduction of the division of labor, the foundation of the labor movement, war and period of reconstruction – few things will influence the industrial development as profoundly as the environmental reflexes.

It was not analytical thinking, but anthropogeneous catastrophies in nature of the near past that have created a new profound consciousness regarding the limits of human doing. Examples like ecological collapses of lakes, contaminations of ground water, smog catastrophies, Seveso, Bhopal, Tschernobyl and the River Rhine desaster have gone under the skin. Never before has a natural phenomenon acted as lasting as acid rain and the dying forests. That is understood by all!

In order to come to an understanding of the problems, it is necessary to analyze the development of the past 150 years.

What essential global development may be realized today?

In fig. 1 the development of the global population is shown. First, it ran almost parallel with the abscissas, now it runs almost parallel with the ordinate.

From 1975 until 2010 mankind will double from 4 to 8 billion men. This is a development, for which experts say that nothing other than catastrophies may stop it.

Right now, however, we discover a highly fascinating fact: The most important data of our civili-

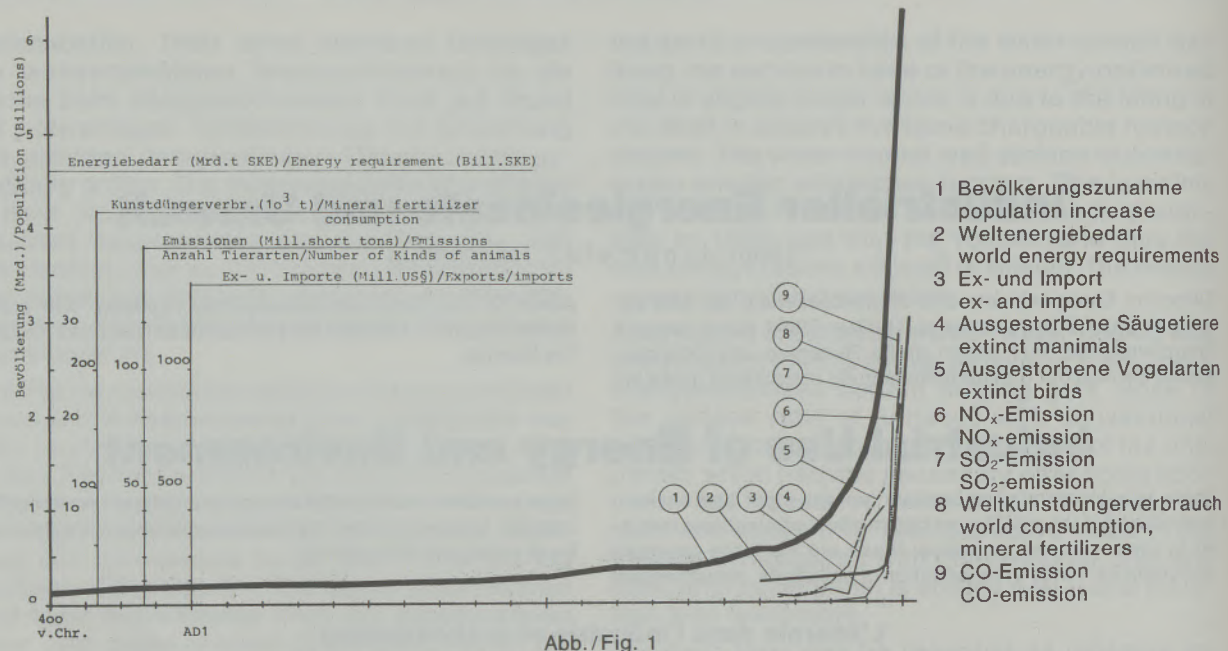

Abb./Fig. 1
Entwicklung seit Chr. Geburt / Development since A. D. zero

sten, meßbaren Größen unserer Zivilisation, über der Zeit aufgetragen, ergeben eine ähnliche Steigerungscharakteristik:

Bevölkerung
Energieverbrauch
SO_2-Emissionen
NO_x-Emissionen
Aussterben der Arten
Düngerproduktion (1), (2), (13)
etc.

Was heißt das? Es heißt, daß wir heute um die Jahrtausendwende zu Zeugen einer unvorstellbaren Entwicklung der Menschheitsgeschichte werden.

Heute, vor unseren Augen vollzieht sich in immer kürzeren Zeitabständen jeweils eine Verdoppelung der Probleme (Müll, Energie, Luftbelastung etc.), wenn nicht etwas ganz Entscheidendes dagegen unternommen wird. Niemand kann sich der Faszination dieser Aussage entziehen! Was sind die Konsequenzen?

Energie und Umwelt

Abb. 1 zeigt die Entwicklung des Energieverbrauches. Sie zeigt aber auch die Korrelation zu den Umweltproblemen.

Beispielsweise:

1985 ⟶ 13 Mrd. t SKE verbraucht ≙ in einem Tag verheizt, was in 2,8 Mio. Jahren gebildet wurde.

2000 ⟶ 21 Mrd. t SKE verbraucht.

Energie ist untrennbar mit der technischen Entwicklung verbunden und muß als einer der wesentlichsten Faktoren der Umweltbeeinflussung gesehen werden. Energie und Umwelt kann man nur als Paar sehen, das sich nicht voneinander trennen läßt.

zation that may be measured, plotted over the time, reveal a similar characteristic of increase:

Population
Energy consumption
SO_2-emission
NO_x-emission
Extinction of species
Production of fertilizers (1), (2) (13)
etc.

What does this mean? This means that we in our days at the turn of the millenium become witnesses of an unimaginable development of the history of mankind.

Today, and in front of our eyes, there occurs the doubling of the problems in ever decreasing periods (waste, energy, air contamination etc.) – unless clearly decisive steps against this development are done. Nobody may escape the fascination of this statement! What are the consequences?

Energy and environment

Fig. 1 shows the development of the energy consumption. However, it also shows the correlation with the environmental problems.

For example: Until 1985 some 13 billion tons of hard coal units were fired; in one day the quantity was fired, that took 2.8 million years to form. Until 2000 some 21 billion tons of hard coal units will be fired.

Energy is inseparably connected with technical development, and must be considered as one of the most essential factors of environmental in-

Alle Energieumsetzvorgänge, also die Erzeugung und Nutzung von Energie, üben größten Einfluß auf die Umweltsituation. Damit ist hier ein wichtiger Schlüssel zur Lösung von Umweltproblemen zu finden. Bei jedem Verbrennungsvorgang werden Schadstoffe verschiedenster Art frei und belasten die Umwelt. Dies hat spätestens mit dem ersten Entzünden von Feuer begonnen, um Staub, Kohlenwasserstoffe (C_xH_y), Kohlenoxide (CO_x), Stickoxide (NO_x), Schwefeloxide (SO_x) und Ruß etc. freizusetzen. Durch die beispiellose technische Entwicklung der letzten 150 Jahre, vor allem seit 1945, stiegen der Energieverbrauch und damit in vielfältigster Weise die Umweltbelastung an: von einer störenden Begleiterscheinung zur lebensbedrohenden, wie wir es beim Waldsterben, Smogkatastrophen u. a. Erscheinungen erleben. Ein Zeitalter hat begonnen, in dem Energie und Umwelt eine zentrale Rolle spielen werden: Einerseits wegen der begrenzten Verfügbarkeit von Energie, andererseits wegen der begrenzten Belastbarkeit unserer Umwelt. Hier wird ein Phänomen sichtbar: Nicht die Technik an sich ist schuld, sondern deren bedenkenlose Anwendung!

Das Abgasproblem entsteht nicht daraus, daß 1 Auto konstruiert wurde oder 1 Kraftwerk. Wenn aber 10 das gleiche machen wie einer, so bedeutet dies eine Verzehnfachung des Problems. Wenn 1000, 10.000 oder 100 Mio. Autos Emissionen abgeben, so führen solche Erscheinungen bei einer bestimmten Größe zwangsläufig zum Kollaps.

Wenn nur einer elektrische Energie verwendet, sind die elektrischen Energievorräte fast unendlich, wenn aber 100 Millionen von Kienspan auf elektrische Beleuchtung umstellen, gehen diese unendlichen Energievorräte in endliche und begrenzte über; dies gilt auch für den Luftvorrat.

Seit einigen Jahrzehnten steht alles im Zeichen der Masse: Massenverkehr, Massenmedien, Massenballungen, Massenbevölkerung, Massentourismus, Massenbeheizung (früher 1 Raum), Massenbelastungen, Massenemissionen.

Eine weitere Erkenntnis der letzten Jahre liegt darin, daß von Luftschadstoffen nicht nur die unmittelbare Umgebung vom Emittenten betroffen ist, sondern auch weiter entfernte Gebiete. Es konnte nachgewiesen werden, daß Luftschadstoffe in wenigen Tagen über Tausende Kilometer transportiert werden, womit das Problem länderübergreifend und global wird.

Außerdem kommen nicht nur die primär emittierten Schadstoffe zur Wirkung. Durch Zusammenwirken einzelner Schadstoffe miteinander, unter Einfluß des Sonnenlichtes, entstehen Reaktionsprodukte, sogenannte Photooxidantien, die z. T. äußerst toxisch sind (26).

Karl H. Becker beschreibt in seiner Arbeit (3) bereits 1970, daß Ozonkonzentrationen schon ab 0,1 ppm giftig sind, während sich die toxische Wirkung der Blausäure erst ab 100 ppm bemerkbar macht (3).

fluence. Energy and environment may only be seen as a pair that cannot be separated.

All energy conversion processes, that is, the production and use of energy, exercise a maximum of influence on the environmental situation. With this, here is found an important key to the solution of environmental problems. With each combustion process noxious substances of varying kinds are set free and become a burden for the environment. This has begun as early when the first fire was lit, when dust, hydrocarbons (C_xH_y), carbon oxides (CO_x), nitric oxides (NO_x), sulfur oxides (SO_x) and soot were set free. During the overboarding technical development of the past 150 years, especially of those since 1945, the energy consumption has increased, and with this, also the most manifold load on the environment: from a disturbing phenomenon to a life-threatening one, as we live to see it with the dying forests, smog catastrophies and other phenomena. An age has begun, during which energy and environment will play a central role: On one hand, because of the limited availability of energy, on the other hand, because of the limited load capacity of our environment. Here a phenomenon becomes visible: It is not the fault of technology but of its reckless application!

The waste gas problem does not develop from the fact that one car was constructed, or one power station. However, if the same is done by ten people, the problem becomes ten-fold. If 1000, 10,000 or 100 million cars produce emissions, such phenomena, lead to collapses after a certain magnitude is reached.

If only one person uses electric energy, the electric energy reserves are near infinite; however, if 100 million people change over from candle light to electric illumination, those infinite energy reserves are converted to limited ones; this also holds for our air reserves.

Since a few decades all is running under the sign of mass: Mass transportation, mass-media, megalopolis, mass-population, mass-tourism, mass-heating (before: only one room), mass-load, mass-emissions.

Another realization of the past years is the fact that not only the immediate surroundings of an emitting source, but also more distant areas are victims. It could be proven that air pollutants travel thousands of kilometers in a few days, thus making the problem inter-national and global.

Also, not only the primarily emitted noxes become effective. Through reactions of single pollutants with each other under the influence of sunlight, new substances result, the so-called photooxidants, that partially are highly toxic (26).

Karl H. Becker describes in his paper (3) already in 1970 that ozone is already poisonous in concentrations up from 0.1 ppm, while hydrocyanic acid becomes noticeable only up from 100 ppm (3).

Die wichtigsten Emissionsquellen von Luftschadstoffen:

The most important emission sources of air pollutants:

Verursacher / sources	SO_2	%	NO_x	%	CO	%	C_xH_y	%	Staub / dust	%
Kal. Kraftwerke / caloric power stations	95.000	29,3	20.000	9,7	5.000	0,5	1.400	1,2	8.000	16,6
Verkehr / traffic	14.000	4,3	146.000	70,9	700.000	65,4	104.000	85,7	10.000	20,8
Industrie / industry	150.000	46,3	30.000	14,6	7.000	0,5	3.000	2,5	9.000	18,8
Kleinabnehmer / individuals	65.000	20,1	10.000	4,9	360.000	33,6	13.000	10,7	21.000	43,8
Gesamtemission / total emission	324.000		206.000		1,070.000		121.400		48.000	

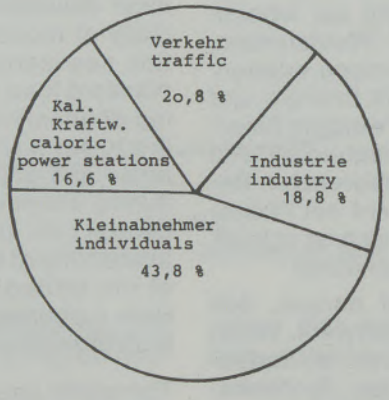

Abb. / Fig. 2
Wichtigste Luftschadstoffe in Österreich (Tonnen), lt. Energiebericht 1984
(Schwermetalle, Halogene etc. ausgeklammert)
Air pollutants in Austria (tons), according to Energy report 1984
(with exception of heavy metals, halogenes, etc.)

Aus Abb. 2 ist ersichtlich, daß die Menge der einzelnen Schadstoffe je nach Verursacher sehr unterschiedlich und ihre Entstehung in jedem Falle mit einem Energie-Umsetzvorgang verbunden sind. Während die Industrie noch der Hauptverursacher von Schwefeldioxidemissionen ist, ist bei Stickstoffoxiden, Kohlenwasserstoffen der Verkehr dominierend, beim Staub die Kleinverbraucher. Über die Gefährlichkeit der einzelnen Schadstoffe ist hiebei keine Aussage getroffen (4).

Im folgenden sei auf die Energie- und Luftemissionen der Industrie näher eingegangen.

Wichtige industrielle Energieträger

Feste Brennstoffe: Steinkohle, Braunkohle, Holz, Petrolkoks (5).

Flüssige Brennstoffe: Heizöl schwer (HS), Heizöl leicht (HL), Heizöl mittel (HM), Heizöl extra leicht (HEL).

Gasförmige Brennstoffe: Erdgas.

Elektrische Energie.

Technisch reiner Sauerstoff zur Anreicherung der Verbrennungsluft.

From fig. 2 it may be seen that the quantities of the single pollutants vary quite much with the sources. Their origin is always found with a process of energy transformation. While industry still is the main source of sulfur dioxide emissions, traffic dominates with nitric oxides and hydrocarbons; for dust, it is the individual small energy consumer. The dangerousness of the single pollutants is hereby not classified (4).

In the following, the energy- and air-emissions of industry are discussed in detail.

Important industrial sources of energy

Solid fuels: Hard coal, lignite, wood, petrol coke (5).

Liquid fuels: Heavy oil, light oil, middle and special light oil.

Gaseous fuels: Natural gas.

Electric energy.

Technically pure oxygen to upgrade the combustion air.

The choice of type of energy for a certain process depends on a number of factors. Availability, na-

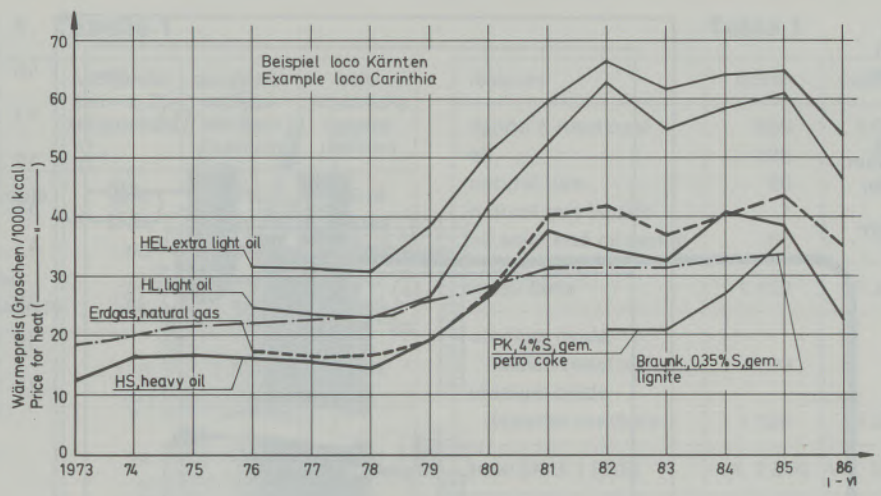

Abb./Fig. 3
Entwicklung der Wärmepreise für diverse industrielle Energieträger
(Beispiel loco Kärnten)
Development of the prices for heat for various industrial sources of energy.

Welcher Energieträger für ein Verfahren gewählt wird, hängt von vielen Faktoren ab. Verfügbarkeit, volks- und betriebswirtschaftliche Gesichtspunkte, technologische, strategische, nicht zuletzt umweltrelevante und vor allem geographische Überlegungen sind anzustellen.

Wenn es nur um die Erzeugung von Wärme geht, so sind die industriell eingesetzten Energieträger grundsätzlich in weitem Bereich substituierbar; Unterschiede bei der Verbrennung diverser Energieträger sind aber unbedingt zu beachten (Spitzen-Verbrennungstemperatur, Flammenform, Rauchgasvolumina, Wärmeübergang etc.).

Elektrische Energie wird zur Wärmeerzeugung vorwiegend in Lichtbogenöfen, weniger in Induktions- und Widerstandsöfen eingesetzt. Die technischen Einrichtungen sind dem jeweiligen Energieträger anzupassen. Moderne Brennerkonstruktionen gestatten Mehrkanalausführung (Abb. 4) den gleichzeitigen oder wechselseitigen

tional-economic of operational points of view, also technological, strategic, and not to the least, environmental and above all, geographic aspects must be considered.

If needed only for the production of heat, the industrial sources of energy basically are interchangeable to a great extent; differences upon combustion of the various energy carriers have to be duly considered (peak combustion temperature, flame shape, flue gas volumes, heat transition, etc.).

Electric energy is used for heat production mainly in electric arc furnace, to a smaller extent in induction and resistance furnaces. The technical equipment has to be adapted to the prevailing energy carrier. Modern burner designs with multichannel constructions (fig. 4) permit simultaneous or alternating use of solid, liquid or gaseous fuels.

Solid fuels are mill-dried and injected into the combustion chamber. This results in an excellent

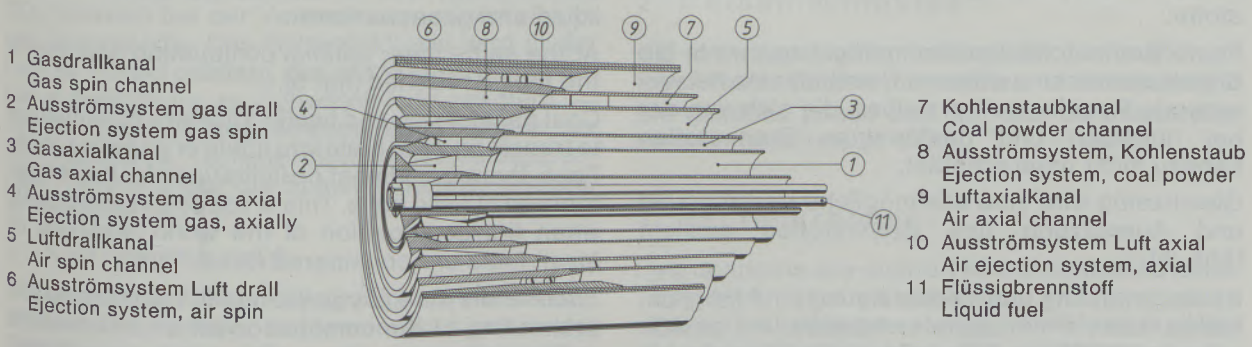

Abb./Fig. 4
Ausströmsystem Fünfkanal-Drehofenbrenner
Ejection system, five-channel rotary kiln burner

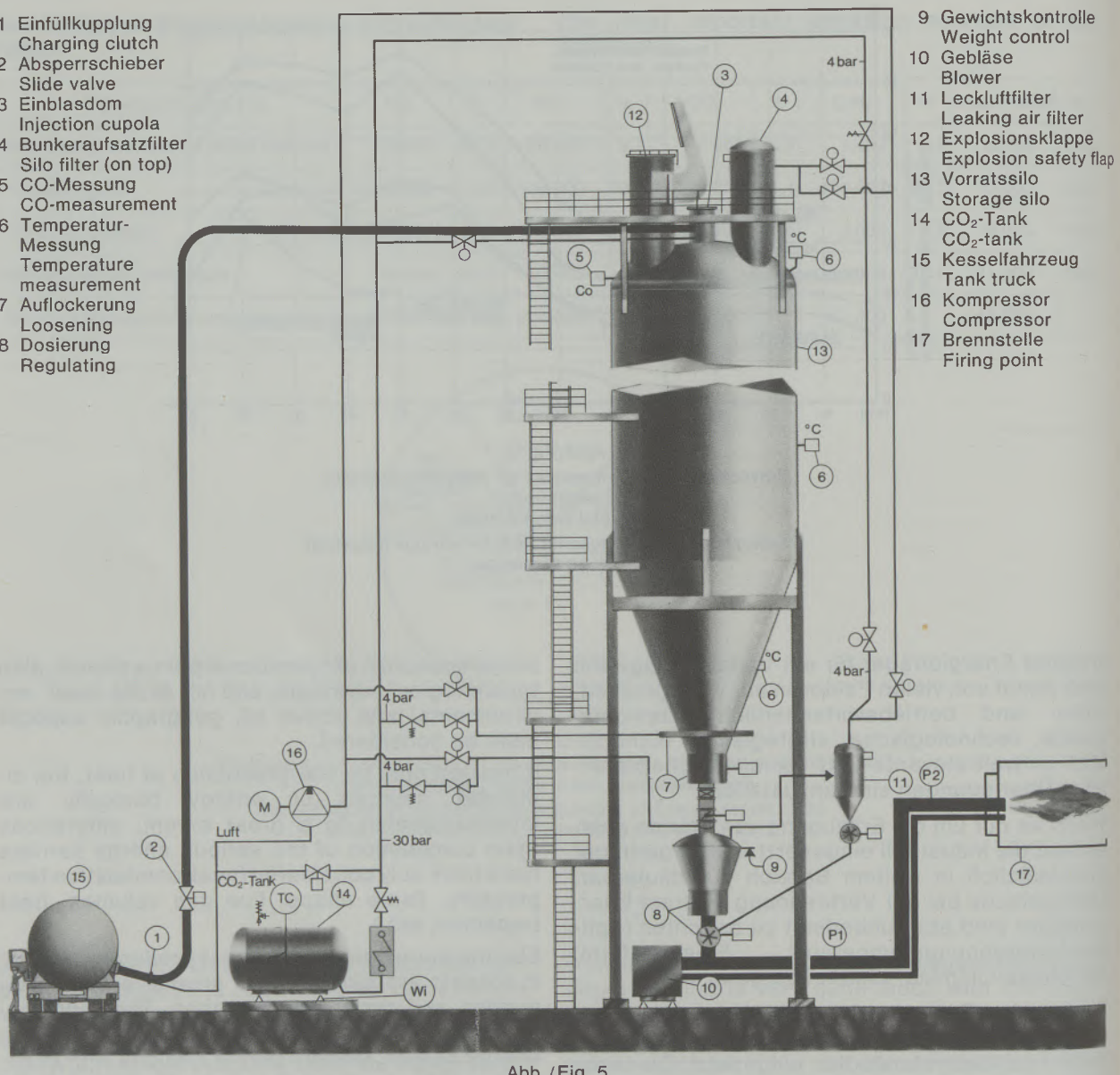

Abb./Fig. 5
Lager- und Fördersystem für Kohle
Storing and conveying system for coal

Einsatz fester, flüssiger und gasförmiger Brennstoffe.

Feste Brennstoffe werden mahlgetrocknet in die Brennkammer eingeblasen. Damit ist eine hervorragende Regelbarkeit erzielbar, die sich von der bei flüssigen und gasförmigen Brennstoffen nahezu nicht unterscheidet.

Gleichzeitig wird eine bestmögliche Verbrennung und Ausnutzung des Brennstoffes erreicht (Abb. 5).

Kohlevergasung und Verflüssigung sind Möglichkeiten, feste Brennstoffe in flüssige und gasförmige überzuführen. Dem industriellen Einsatz von festen Brennstoffen sind damit kaum Grenzen gesetzt. Dies ist auch deshalb von großer Bedeu-

controllability that is almost the same as with liquid and gaseous fuels.

At the same time, optimal combustion and use of the fuel is reached (fig. 5).

Coal gasification and liquification are possibilities to transform solid fuels into liquid or gaseous form. Thus, there are almost no limitations for the industrial use of solid fuels. This is especially important, when the composition of the world reserves of fossil fuels are considered (table 1) (6).

Technically pure oxygen is used in addition to the preheating of the combustion air as an effective means to increase the combustion temperatures. Thus the percentage of nitrogen to be heated as a ballast is reduced and fuel is conserved. This

Tabelle 1

	nachgewiesen – z. Zt. abbauwürdig	geschätzte noch gewinnbare Reserven	wahrscheinliche Gesamtreserven
Braun- und Steinkohle	866	6.050	6.916
Erdöl	133	562	695
Erdgas	65	361	426
Erdgasflüssigkeiten	7	40	47
Ölschiefer- und Ölsande	58	505	563
Fossile Brennstoffe	1.129	7.518	8.647
Uranoxid in Spaltreaktoren	29	58	87
Uranoxid in Brüterreaktoren	1.158	4.320	6.520
Gesamt (Mrd. t SKE)	ca. 2.300	ca. 12.000	ca. 15.000

Table 1

reserves	proven	estimated	probable
lignite & hard coal	866	6.050	6.916
oil	133	562	695
natural gas	65	361	426
natural gas liquids	7	40	47
oil shist and oil sands	58	505	563
fossil fuels	1.129	7.518	8.647
uranium oxide fission reactors	29	58	87
uranium oxide breeder reactors	1.158	4.320	6.520
total (mrd. t SKE)	ca. 2.300	ca. 12.000	ca. 15.000

tung, wenn man die Zusammensetzung der Weltvorräte bei fossilen Brennstoffen betrachtet (Tabelle 1) (6).

Technisch reiner Sauerstoff wird neben der Vorwärmung der Verbrennungsluft und Brennstoffersatz als wirkungsvolle Möglichkeit zur Erhöhung der Verbrennungstemperaturen eingesetzt. Der zu erwärmende Stickstoffballast wird verringert und eine Brennstoffersparnis erzielt. Damit können die aus dem Brennstoff resultierenden Schadstoffe beim Anwender gesenkt werden (z. B. Schwefel) (10). Obwohl sich die Verbrennung von festen, flüssigen, gasförmigen Brennstoffen im Detail unterscheiden, sind durch die genannten Maßnahmen die Voraussetzungen geschaffen, um sich technologisch weitgehend an die erforderlichen Prozeßbedingungen anpassen zu können. Somit ist bei der Auswahl des Energieträgers nach betriebswirtschaftlichen und umweltrelevanten Gesichtspunkten ein großer Freiheitsspielraum gegeben. Hier den optimalen Weg zu finden, ist heute für jeden Industriebetrieb von größter Bedeutung.

Die wichtigsten Verbrennungsschadstoffe

1. Schwefeldioxid:

SO_2 entsteht bei der Verbrennung schwefelhaltiger Brennstoffe. Das Schwefeldioxid wird in der Luft zu Trioxid oxidiert, das mit Wasserdampf unter Nebelbildung zu Schwefelsäure reagiert. → Saurer Regen, Smog. Mittlere Verweilzeit in der Atmosphäre ca. 10 Tage, daher große Verlagerungen. Tabelle 2 gibt die Schwefelgehalte diverser Brennstoffe an.

2. Kohlenmonoxid:

CO entsteht bei der unvollständigen Verbrennung fossiler Brennstoffe. Kohlenmonoxid ist in der Gasphase reaktionsträge, es kann erst bei höheren Temperaturen, oder an metallischen Katalysatoren zu CO_2 oxidiert werden.

also gives the possibility to reduce the pollutants deriving from the fuel (e.g. sulfur) (10). Although the combustions of solid, liquid and gaseous fuels differ in detail, the measures mentioned make it possible to adapt to a large extent to the process parameters required. Out of this, a large field of free choice according to operational and environmental aspects is resulting. It is of maximum importance for every industrial enterprise to find the optimum way here and today.

The most important combustion pollutants

1. Sulfur dioxide:

SO_2 develops upon combustion of sulfur containing fuels. In air, sulfur dioxide is oxidized to sulfur trioxide that reacts with water vapor to sulfuric acid, resulting into acid rain, smog. Mean prevailing time in air: appr. 10 days, therefore, travelling long distances. Table 2 shows sulfur contents of various fuels.

2. Carbon monoxide:

CO develops during incomplete combustion of fossil fuels. Carbon monoxide is slow reacting in the gaseous phase and can only be oxidized at metallic catalysts to CO_2.

3. Hydrocarbons:

Hydrocarbons are emitted as uncombusted fuels. They also occur as emissions after processes where a reducing gas atmosphere is required out of technological reasons. The possibilities to decompose the single hydrocarbons differ greatly and are only little known.

Tabelle 2

Brennstoff	Schwefelgehalt (%)	Bemerkung
HS	2,0	ab 1985 stufenweise bis auf 1% im Jahre 1995 (Österreich)
HM	1,0	
HL	0,5	
HEL	0,3	ab 1987 0,15% (Österreich)
Erdgas	0 –0,3	
Steinkohle	0,6–4,0	und darüber
Braunkohle	0,3–2,0	und darüber
Petrolkoks	0,8–6,0	
Holz	0	

Table 2

Fuel	sulfur content (%)	note
heavy oil	2.0	since 1985, stepwise reduction down to 1% in 1995 (Austria)
light oil	1.0	
middle oil	0.5	
special light	0.3	from 1987 0.15% (Austria)
natural gas	0 –0.3	
hard coal	0.6–4.0	and higher
lignite	0.3–2.0	and higher
petrol coke	0.8–6.0	
wood	0	

3. Kohlenwasserstoffe:

Kohlenwasserstoffe werden als unverbrannte Kraftstoffe emittiert. Sie treten auch als Emissionen nach Prozessen auf, in denen aus technologischen Gründen reduzierende Rauchgasatmosphären herrschen müssen. Die Abbaumöglichkeiten der einzelnen Kohlenwasserstoffe sind sehr verschieden und wenig bekannt.

4. Stickstoffoxide NO_x:

Mittlere Verweilzeit in der Atmosphäre ca. 1 Tag, d. h. lokal von größerer Bedeutung. 10x raschere Reaktivität wie SO_x.

Thermisches NO_x: Die Bildung hängt von den Parametern Flammentemperatur, Verweilzeit und Sauerstoffpatialdruck ab.

Promptes NO_x: Quelle ist der Stickstoff in der Verbrennungsluft. Bei der Verbrennung der Kohlenwasserstoffe entstehen Zwischenprodukte, die mit dem Luftstickstoff reagieren.

Brennstoffe NO_x: Stickstoffquellen sind die vielen organischen Stickstoffverbindungen des Brennstoffes.

Stickstoffoxid-Emissionen können aber auch aus rein chemischen Prozessen stammen. Alle Reaktionen, die die Bildung und den Zerfall von Stickstoffoxiden beeinflussen, sind sehr temperaturabhängig. Eine nennenswerte thermische NO_x-Bildung setzt bei Temperaturen von ca. 1300 °C ein. Danach steigt sie sehr stark an. NO_2 ist ein giftiges Gas, das bereits in geringer Konzentration als brauner Dunst auf weite Strecken sichtbar ist (7), (8).

5. Staub:

Staub kann als Flugasche aus der Verbrennung emittiert werden oder tritt als unerwünschter Rauchgasbestandteil nach Brennprozessen auf. Sowohl von seiner jeweiligen chemischen Zusammensetzung her, als auch nach der emittierten Menge, ist er ein mehr oder minder gefährlicher Schadstoff. Nach dem Kornaufbau wird Staub unterschieden: grob, lungengängig, Aerosol (9).

Mit dem gemeinsamen Auftreten von Stickstoff-

4. Nitric oxides NO_x:

Mean prevailing time in the atmosphere appr. 1 day, i.e. locally of greater importance. Ten times higher reactivity than SO_x.

Thermic NO_x: The formation depends on the parameters flame temperature, reaction time and oxygen partial pressure.

Prompt NO_x: Source is nitrogen of combustion air. During combustion of the hydrocarbons intermediary products result that react with the nitrogen of the air.

Fuel NO_x: Sources are the many organic nitrogen compounds of the fuel.

Nitrogen emissions may also result from straight chemical processes. All reactions that cause formation and decomposition of nitric oxides are highly temperature dependent. Noticeable thermic NO_x-formation starts at temperatures around 1300 °C. After that, it very quickly rises. NO_2 is a poisonous gas that becomes visible as a brown haze already at low concentrations and over a long distance (7), (8).

5. Dust:

Dust may be fly ash from the combustion or appears as an unwanted component of the flue gases after firing processes. As well as from the chemical composition, as also from the quantity it is a more or less dangerous pollutant. With regard to grain sizing it is classified into coarse, lung afflicting, aerosol (9).

Upon common appearance of nitric oxide and hydrocarbons and under the influence of sunlight, the process of photo-oxidation commences, whereby aldehydes and ozone are formed. It is accepted as proven that the nitric oxides catalyzed the photo-oxidation of carbohydrates.

oxiden und Kohlenwasserstoffen kommt unter dem Einfluß der Sonneneinstrahlung die Photooxidation in Gang, wobei u. a. Aldehyde und Ozon entstehen. Es gilt als sicher, daß Stickstoffoxide die Photooxidation von Kohlenwasserstoffen katalysieren.

Komplexe Mechanismen in der Atmosphäre führen zu Reaktionsketten, deren umweltschädigende Zwischen- und Endprodukte überproportional mit der Quellenintensität anwachsen. Die entstandenen Reaktionsprodukte können stark toxisch sein und dürften nach neuesten Vermutungen möglicherweise mit dem sogenannten „Waldsterben" in Zusammenhang stehen (3), (26).

Für den industriellen Energieeinsatz bedeutet dies, daß die dabei entstehenden Schadstoffe vermieden bzw. auf ein Mindestmaß begrenzt werden müssen (25).

Möglichkeiten zur Minderung von Luftschadstoffen

Hier ist zu unterscheiden, ob die Schadstoffe schon ausgeschieden werden können, bevor sie in das Verfahren eingebracht werden (z. B. Schwefel), ob sie durch eine entsprechende Prozeßführung in ihrer Entstehung gemindert (CO, C_xH_y, NO_x) oder erst am Ende des Verfahrens – vor Kamineintritt – aus dem Rauchgas gefiltert werden (after pipe).

Entstaubung:

Staub ist in Fliehkraftabscheidern (Zyklonen), Filtern verschiedenster Bauart, trocken, naß, elektrostatisch etc. abscheid- und filterbar. Durchwegs werden heute bei den industriellen Anlagen Reingasstaubgehalte von 40 mg/Nm³ vorgeschrieben, in vielen Anlagen auch schon 20 mg/Nm³ und darunter erreicht. Entsprechende Wartung vorausgesetzt, sind sie als Stand der Technik anzusehen (9).

Schwefel wird im allgemeinen über schwefelhältigen Brennstoff, das Produkt oder prozeßbedingte Stoffe in das System eingebracht und vorwiegend als SO_2, aber auch als SO_3 emittiert.

Schwefeldioxid kann aus dem Rauchgas abgeschieden werden: Trockenadditivverfahren, Naßwäscher. Solche Verfahren haben hohe Investitions- und Betriebskosten. Wenn es dabei nicht gelingt, aus den Filterabgängen ein wiederverwertbares Produkt zu erzeugen (H_2SO_4, S, Baustoffe etc.), so ergeben sich Deponie- und Grundwasserprobleme. Rauchgasgips als Schwefelträger ist beispielsweise auf dem europäischen Markt kaum mehr abzusetzen.

Bevor Entschwefelungsanlagen in Betracht gezogen werden, sollten alle Möglichkeiten ausgeschöpft werden, den Schwefel vorher auszuscheiden. Wo es gelingt, die Menge des dem System zugeführten Schwefels zu verringern, beispielsweise durch Senken des Schwefels im Heizöl, ist dies in vielen Fällen die ideale Lösung.

Complex mechanisms in the atmosphere lead to reaction chains, whose polluting intermediate and final products increase overproportional with the intensity of the source. The products developed may be strongly toxic and according to the latest assumption, possibly have to be seen in connection with the so called "dying of forests" (3).

With respect to industrial use of energy this all means that the development of the pollutants must be avoided or reduced to a minimum (25).

Possibilities to reduce air pollutants

Here it has to be differentiated between the possibilities to eliminate the pollutants already prior to the process (c.f. sulfur), or if they can be reduced by appropriate type of process technology (less generation of CO, C_xH_y, NO_x), or whether they may only be screened out of the flue gas at the end of the process prior to entering into the stack (after pipe).

Dedusting:

Dust may be removed by means of centrifugal force separators (cyclones), filters of varying designs, dry, wet, electrostatically etc. Generally, in industrial installations, today the dust contents of purified flue gases are limited with 40 mg/Nm³; actually, many units already reach 20 mg/Nm³. Properly serviced, they are considered as state of the art (9).

Desulfurization:

Sulfur is brought into the system through sulfur containing fuels, or through the product of the process itself, or through reagents necessary for the process; it is mainly emitted as SO_2, but also as SO_3.

Sulfurdioxide can be eliminated from the flue gases by dry-additive processes or by wet screening. These processes require high sums for investment and operation. Unless it is possible to convert the filter tailings into usable products (H_2SO_4, S, building materials, etc.), problems of disposals and ground water arise. Flue gas gypsum, for instance cannot be sold on the European market any more.

Prior to considering the installation of desulfurization plants, all possibilities to eliminate the sulfur prior to the process have to be tried. It is the ideal solution to lower the quantity of sulfur brought into the process, for instance by using low-sulfur fuel oil.

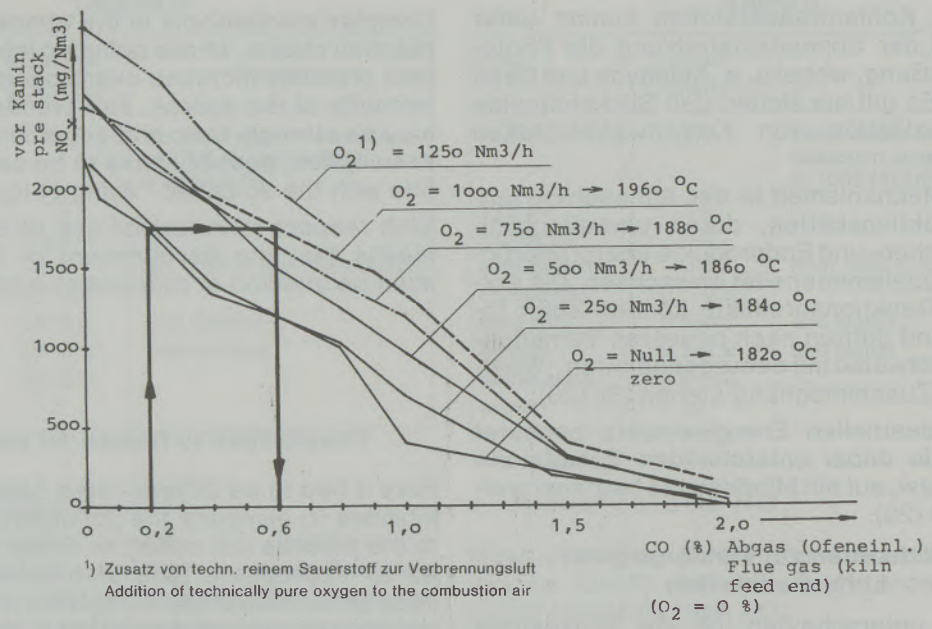

Abb./Fig. 6
NO_x in Abhängigkeit vom CO-Gehalt bei einem Drehrohrofen für Magnesit
NO_x depending on CO-content in a magnesite rotary kiln

Nachverbrennung:

Kohlenwasserstoffe und Kohlenmonoxid können im Unterschied zu SO_2 durch die Steuerung des Brennprozesses weitgehend beeinflußt werden. Probleme ergeben sich vor allem dort, wo aus technologischen Gründen bestimmte Rauchgasatmosphären erforderlich sind. Auftretendes CO und C_xH_y-Bestandteile im Rauchgas können durch thermische Nachverbrennung oxidiert werden.

Die hiefür notwendige Temperatur hängt von der Zusammensetzung der Kohlenwasserstoffe ab. Das Problem bei diesem Verfahren liegt darin, daß das gesamte Rauchgasvolumen z. T. erheblich über 1000 °C erhitzt werden muß. Dies ergibt einen hohen Energieverbrauch, der nur teilweise und mit teuren Abgaskühlanlagen kompensiert werden kann.

Entstickung (Denox):

Der Stickstoffoxidemissionsanteil der Industrie wird heute mit 13% angegeben (Prof. Lenz, TU Wien).

So wie für die Entstehung von NO_x eine Reihe von Parametern zutreffend sind, siehe Pkt. 4, können diese verändert werden, um in einem gewissen Bereich die Entstehung der Stickstoffoxide zu minimieren (Primärmaßnahmen).

Mit einer Senkung der Spitzenverbrennungstemperaturen oder durch Vermindern des O_2-Angebotes in der Verbrennungsluft, kann die NO_x-Bildung verringert werden. Im Beispiel Abb. 6 ist dies bei

After combustion:

Contrary to SO_2, it is possible to considerably influence the carry-off of carbohydrates and carbonmonoxide through regulation of the combustion process. Problems result especially there, where out of technological reasons it is necessary to maintain certain conditions of the combustion gas atmosphere. CO and C_xH_y components of the combustion gas can be oxidized by thermal after combustion.

The temperature necessary for this process depends on the composition of the hydrocarbons. The problem of this process is situated in the fact that all of the combustion gas has to be heated (in certain cases) substantially higher than 1000 °C. This again results in a high energy consumption increase that can only be compensated partially by expensive waste gas cooling systems.

Denoxing:

Nitrogen oxide emission percentage caused by the industry is assumed to be at 13% today (Prof. Lenz, Technical University, Vienna).

In the same way as there are several parameters relevant for the development of NO_x (see sub 4), they may also be altered in order to minimize the generation of nitric oxides (primary measures).

einem Magnesitdrehofen bis zu einem CO-Gehalt im Rauchgas von 2,0% dargestellt.

Reduzierende Atmosphäre reduziert gebildete NO_x, sodaß sie nicht emissionswirksam werden. Produktverträglichkeit vorausgesetzt, könnten demnach, bei genauer Kenntnis der Gefährlichkeit der NO_x einerseits und CO andererseits, ohne zusätzliche Anlagenteile kurzfristig Minimierungen der Gesamtmenge beider Schadstoffe allein durch die Prozeßführung erreicht werden (7), (8), (10).

Die zu ergreifenden Maßnahmen sind für jeden Prozeß verschieden und können nur in engstem Zusammenhang mit dem Produkt und anderen relevanten Emissionen gesehen werden.

Denox-Filter werden heute in verschiedenen Ausführungen angeboten. Hier sei nur auf Primärmaßnahmen hingewiesen, die in jedem Falle optimiert werden müssen, bevor man an den Einbau eines Denox-Filters denkt.

NO_x-arme Brenner, mehrstufige Verbrennung, Rauchgasrückführungen sind weitere Möglichkeiten. Neue Technologien, wie flammenlose Verbrennung in zirkulierender Wirbelschicht bei niedrigstmöglichen Temperaturen, sind bereits als Stand der Technik anzusehen. Sie unterdrücken die Bildung von Stickoxiden durch minimale Verbrennungstemperatur; in erster Stufe stöchimetrische Verbrennung, in zweiter Stufe durch Ver-

By lowering the peak combustion temperatures or by reducing the O_2 concentration of the combustion air, NO_x-formation may be reduced. In example of fig. 6 this is demonstrated with a magnesite rotary kiln with a CO-content of flue gas of 2%.

Reducing air reduces the NO_x formed so that they do not become emission efficient. Provided it is compatible with the product, it is therefore possible – upon exact knowledge about the dangerousness of the NO_x on one hand and CO on the other hand –, to reach in short time a minimizing of the total volume of both pollutants only by adapting the process (7), (8), (10), without any additional installations.

The measures to be taken will vary with the relevant processes and may only be seen in close correlation with the product and other relevant emissions.

Denox-filters are offered in varying designs today. Here, it is only referred to primary measures that have to be optimized in every single case before thinking of an installation of a denox-filter.

Low-NO_x-burners, multiple stage combustion, flue-gas recirculation are additional possibilities. New technologies, such as flameless combustion in the circulating fluidized bed may already be

Tabelle 3

	Einsparpotential:
Raumwärme:	
Einfamilienhäuser	62–80%
Mehrfamilienhäuser	39–59%
Kleinverbraucher	39–59%
Industrie	20–40%
Prozeßwärme:	
Haushalte	28–30%
Kleinverbraucher	10–15%
Industrie	20–33%
Beleuchtung und stationäre Antriebe:	
Haushalte	20–40%
Kleinverbraucher	20–30%
Industrie	20–33%
Verkehr:	
Pkw	50%
Lkw	30%
„Energiewende“:	
Raumheizung	70%
Autos	60%
Industrielle Prozeßwärme	30%
Elektrische Haushaltsgeräte	65%
Elektrische Antriebe	30%

Table 3

	Savings potential
Room heating:	
One family houses	62–80%
Multiple family houses	39–59%
Small users	39–59%
Industry	20–40%
Process heat:	
Homes	28–30%
Small users	10–15%
Industry	20–33%
Illumination & stationary drives:	
Homes	20–40%
Small users	20–30%
Industry	20–33%
Traffic:	
Cars	50%
Trucks	30%
“Energy conversion”:	
Room heating	70%
Automotive traffic	60%
Industrial process heat	30%
Electrical appliances	65%
Electrical drives	30%

brennung mit geringem Luftüberschuß auf ein Minimum (80 bis 200 mg/Nm³) (Abb. 7).

Die zirkulierende Wirbelschicht und ähnliche Verfahren werden heute für alle Brennstoffe eingesetzt, in der Kraftwerkstechnik und in der Prozeßtechnologie (Kalzination von Tonerde etc.) (11).

Senken des Energieverbrauches als Schlüssel

Effizienteste Möglichkeit zum Mindern verbrennungsbedingter Schadstoffe ist das Senken des Energieverbrauches. Zielsetzungen, wie noch 1976 in einschlägiger Tagung ausgesprochen, daß Standard-Energieverbrauch der USA, der zwei- bis dreimal über dem der Europäer liegt, erreicht werden muß, sind heute undenkbar (Abb. 8).

Dabei gehen mindestens 55% des Energieeinsatzes zum Abdecken der Verluste (Abb. 9, 10).

Primäre Fragestellung kann überall nur lauten: Wie kann ich meinen Prozeß mit weniger Energie ablaufen lassen?

Die Möglichkeiten zur besseren Energienutzung sind zahllos und die erzielbaren Potentiale beachtlich (Tabelle 3).

Dabei sind zwei Zielsetzungen gleichzeitig erreichbar: Senken von Primärenergie (Kosten) und Schadstoffemissionen (12), (14).

considered as state of the art. They suppress the formation of nitric oxides by a minimum combustion temperature; in the first stage a stoichiometric combustion, in the second stage by combustion with a small excess of air at a minimum (80–200 mg/Nm³) (fig. 7).

Circulating fluidized bed and similar processes are used for all kinds of fuels today, as well in power station technology as in process technology (calcining of alumina, etc.) (11).

Reduction of energy consumption as the key

The most efficient possibility to reduce pollutants originating from combustions clearly is the reduction of energy consumption. Goals that have been mentioned in a relevant convention in 1976, where the standard energy consumption of the USA that is two to three times that of the European, should be reached, are unthinkable today (fig. 8).

At least 55% of the energy input cover the losses (figs. 9, 10).

The primary question can only be: How is it possible that I run my process with less energy?

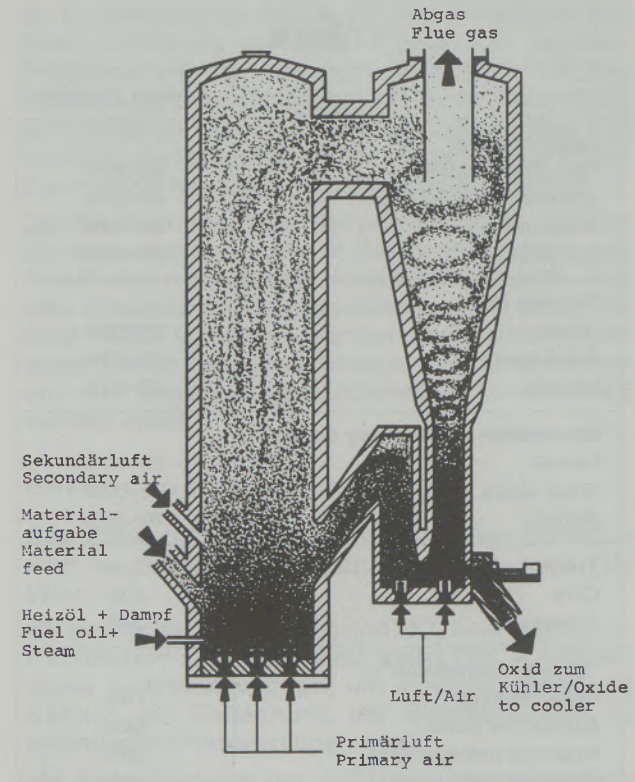

Abb./Fig. 7
Prinzip der zirkulierenden Wirbelschicht
Principle of circulating fluidized bed

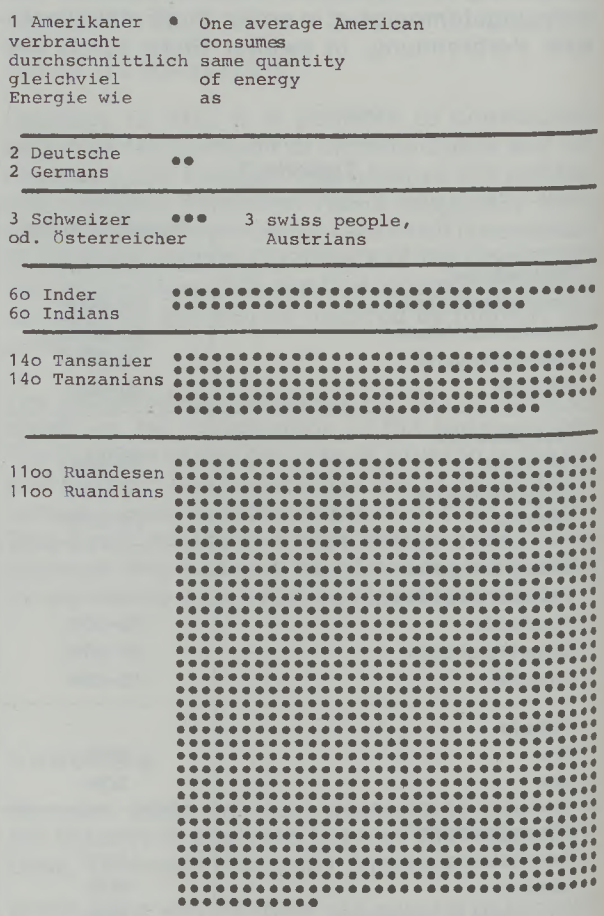

Abb./Fig. 8
Energieverbrauch als Maßstab für Fehlentwicklung
Energy consumption as a measure for misdevelopment

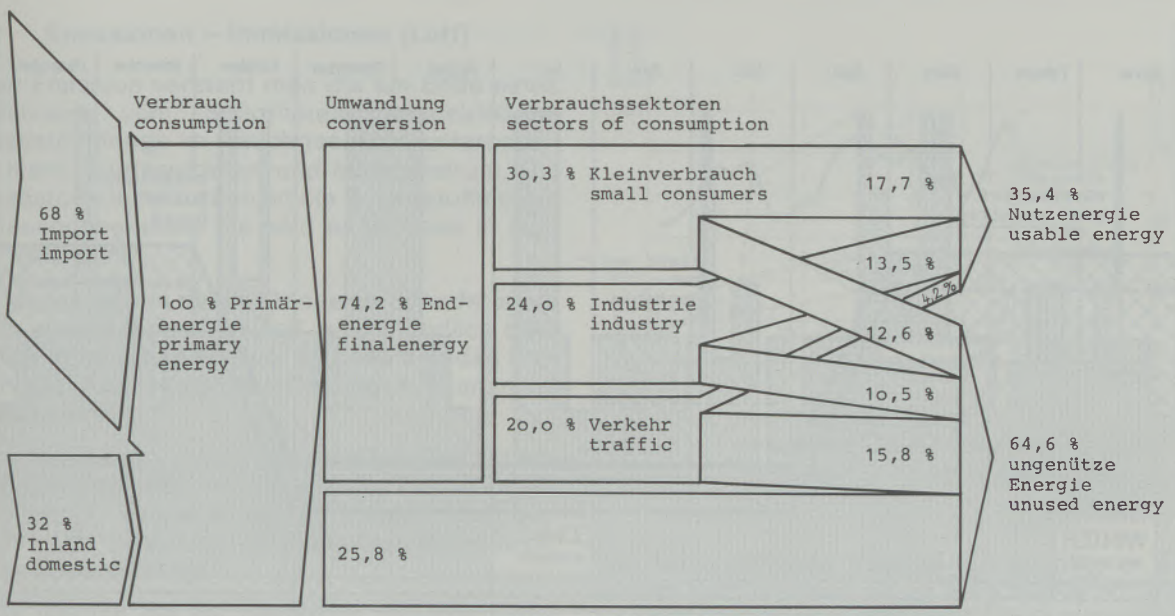

Abb./Fig. 9
Energiebilanz Österreichs 1983 (vereinfacht)
Austrian energy balance sheet 1983 (simplified)

Für die Industrie nur einige Anhaltspunkte zur Energieeinsparung:

durch

- Energiemanagement
- Neue Verfahren für Verbrennung und Prozesse
- Isolation
- Abwärme-Rückgewinnung und Nutzung
- Einsatz moderner Meß-Regeltechnik
- Fahrweise der Aggregate
- Müllverbrennung mit energetischer Nutzung
- Recycling
- niedrigere Luftüberschußzahlen
  etc.

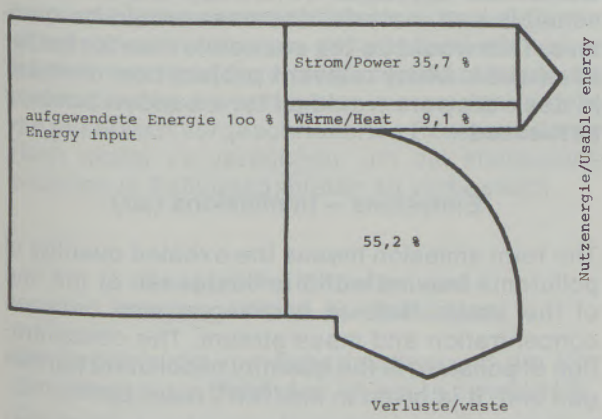

Abb./Fig. 10
Energienutzung der Wärmekraftwerke der Energieversorgungsunternehmen Österreichs 1983
Energy utilization of Austrian power companies 1983

The possibilities for improved use of energy are numerous, the potentials attainable are considerable (table 3).

In this connection two goals may be reached simultaneously: Lowering of consumption of primary energy (cost reduction) and lowering of emission of pollutants (12), (14).

Here are a few indicators for industrial energy saving:

by

- energy management
- new methods for combustion and processes
- insulation
- heat recovery and utilization
- application of new measuring and control techniques
- operation of installations
- trash incineration with energy utilization
- recycling
- reduced air excess
  etc.

Ad waste heat:

Only in case that the process cannot be organized without generation of waste heat, a waste heat use should be tried. The degree of efficiency here is not very high, only 10–20%. Because of limited storage possibility a synchronous user has to be found (fig. 11). Therefore: "The best waste heat is that one, that does not generate and therefore need not be recovered."

Wherever it seems possible, industrial waste heat should be used as long-distance heat to eliminate trade and home emissions and to reduce the pri-

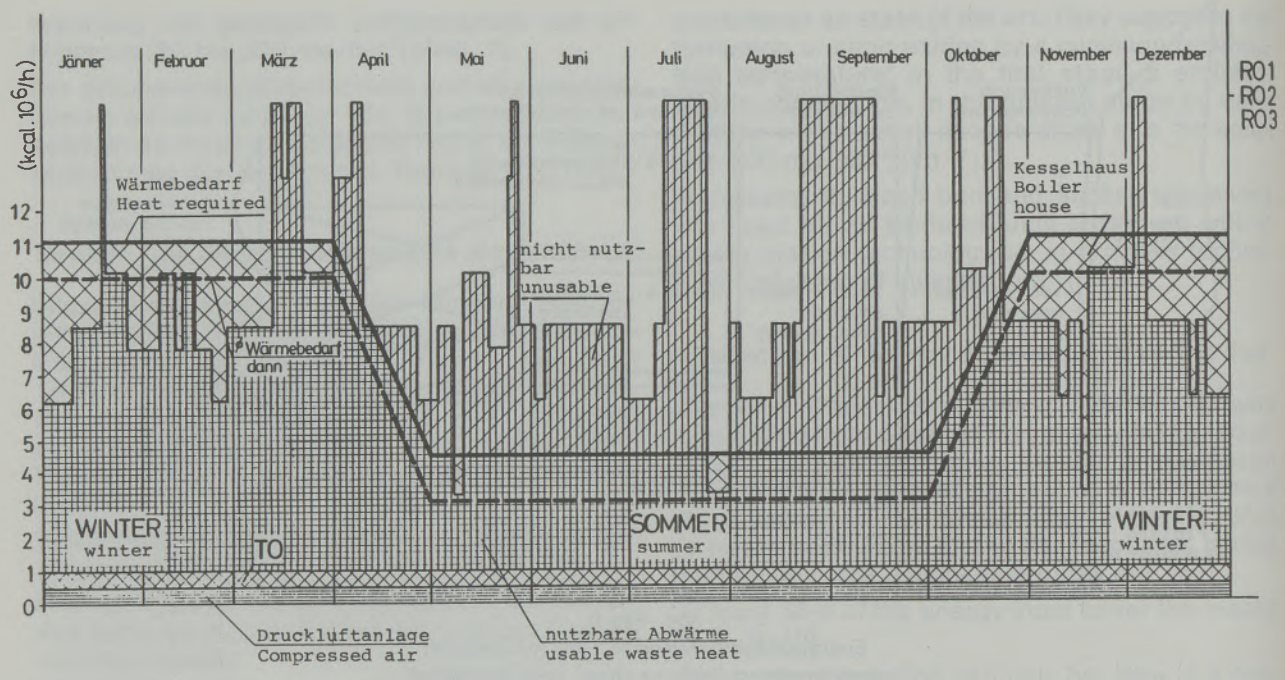

Abb./Fig. 11
Magnesithütte: Rotieröfen-Abwärmenutzung
Magnesite plant: Rotary kilns waste heat recovery
Wärmeangebot – Wärmebedarf 1979
Available heat – heat required 1979

Zur Abwärme:

Nur dann, wenn sich der Prozeß ohne Abwärmeanfall nicht gestalten läßt, ist eine Abwärmeverwertung anzustreben. Der Wirkungsgrad hiebei ist nicht hoch, oft nur 10 bis 20%. Dabei muß wegen begrenzter Speicherfähigkeit ein synchroner Abnehmer gefunden werden (Abb. 11). Deshalb: „Beste Abwärme ist die, die nicht anfällt und daher nicht zurückgewonnen werden muß."

Wo es aber möglich erscheint, ist industrielle Abwärme als Fernwärme zur Eliminierung der Gewerbe- und Hausbrandemissionen und Senkung des Primärenergieverbrauches nicht zu vernachlässigen (siehe auch „Kraft-Wärmekopplung").

Der Verbesserung der Energienutzung sind grundsätzlich nur die theoretischen Grenzen gesetzt. Diese Grenzen asymptotisch zu erreichen, ist die Herausforderung für die nächsten Technikergenerationen. Dinge komplizierter zu machen ist keine Kunst, aber sie vereinfachen, mit weniger Energie auskommen etc. bedarf es Kreativität.

Der „Rückzug aus dem Erdöl" hat bereits begonnen, erste Erfolge seit 1974 sichtbar. **Entscheidend aber wäre eine weltweite echte Bewertung der Energie – so wie sie diesem edelsten Rohstoff zukäme; sie würde die betriebswirtschaftliche Initialzündung zur besseren Nutzung darstellen. Viele einschlägige Projekte, die heute in Schreibtischladen schlummern, würden schlagartig aktuell.**

mary energy consumption (see also "power-heat coupling").

Basically, only the theoretical limits will limit the improvement of energy utilization. It is the challenge for the next generations of technicians to asymptotically approach these limits. It is no special art to make things more complicated, however, to simplify them, to get along with less energy, requires creativity.

The "retreat from oil" already has begun, the first successes became visible since 1974. **A true worldwide appraisal of energy as this most valuable raw material deserves would be decisive. This would be the economic fuse for better evaluation. Many relevant project now dormant in desk drawers would all for a sudden become actualized.**

Emissions – Immissions (air)

The term emission means the exhaled quantity of pollutants leaving with the flue gases at the end of the stack. Here, it is differentiated between concentration and mass-stream. The concentration of pollutant is the quantity of pollutant per flue gas unit. It is given in mg/Nm^3, resp. ppm.

The mass-stream is the quantity of pollutants that is given off within a defined time, e.g. hourly or annually; it is the product of concentration times flue gas volume under standard conditions.

Emissionen – Immissionen (Luft)

Unter Emission versteht man die am Ende eines Verfahrens vom Schornstein ausgestoßene Schadstoffmenge im Rauchgas. Man unterscheidet hiebei Konzentration und Massenstrom. Die Schadstoffkonzentration ist die Schadstoffmenge je Rauchgaseinheit. Sie wird angegeben in mg/Nm³ bzw. ppm.

Der Massenstrom ist die Menge an Schadstoffen, die in einer bestimmten Zeit, also stündlich oder jährlich abgegeben wird; er ist demnach das Produkt aus Konzentration x Rauchgasvolumen im Normzustand.

Unter Immission versteht man die auf eine schadstoffbelastete Fläche niedergehenden Schadstoffmengen. Früher in mg/m² ausgedrückt, beispielsweise bei der mittels Bleikerzenmethode erfaßten Bleiimmission.

Heute werden die mit modernen dauerregistrierenden Konzentrationsmeßgeräten erfaßten Immissionen in mg/Nm³ angegeben. Diese Meßgeräte sind in der Anschaffung derzeit noch teuer und wartungsintensiv.

Den Zusammenhang zwischen bestimmten Emissionen und der Immission herzustellen, ist nur begrenzt möglich. Dazwischen liegen die gesamte Meteorologie und Topografie, diffuse Emittenten und die Fernverfrachtung von Schadstoffen.

In Abb. 12 wurde erstmalig versucht, eine direkte Korrelation zwischen den Emissionen eines dominierenden Industriebetriebes und dem Zuwachs der Bäume in einer Entfernung von ca. 6 km herzustellen. Der Jahresring-Zuwachs (cm²) wurde über die Auswertung von Bohrkernen ermittelt. Alter der Bäume ca. 100 Jahre, damit 30 Jahre alt bei Inbetriebnahme des Werkes.

Problem: Neben Luft-Immissionseinflüssen auch solche aus Klima, Wetter (Niederschläge) etc.

Mit der sogenannten „Politik der hohen Kamine" hatte man früher versucht, hohe Schadstoffemissionen so zu verdünnen, daß die Immissionen erträglich wurden. Diese Möglichkeit hat heute nur mehr dort ihre Berechtigung, wo es darum geht, die gesetzlich vorgeschriebenen Restemissionen noch weiter zu verdünnen, um die Immissionssituation in Ballungsgebieten zu verbessern.

Gesetzliche Situation und Vorgangsweise der Behörden

Die Begrenzung von Schadstoffen und die Vorgangsweise der Behörden ist heute zweigeteilt.

Einerseits werden die Emissionsgrenzwerte festgelegt (Konzentrationen, Massenströme oder beides), andererseits die Immissionsgrenzwerte.

Luftgüteklassen:

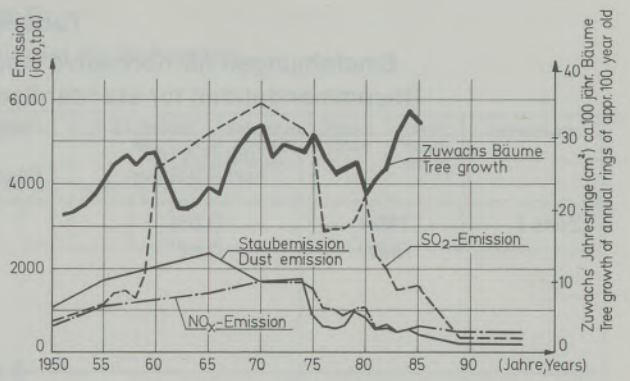

Abb./Fig. 12
Emissionen – Zuwachs der Bäume
Emissions – Growth of trees

The term immission means the quantity of pollutants settling down on an area that is polluted. Formerly, this was given in mg/m², as for example with the lead-candle method to indicate the lead-immission.

Today, immissions that are registered with continuously registering concentration measuring instruments, are listed in mg/Nm³. These control instruments still are expensive and have to be continuously serviced.

It is only possible to a limited extent to correlate certain emissions and the immission. Inbetween there is all of the meteorology, the topography, diffuse emittants and the long distance drift of pollutants.

In fig. 12 it was tried for the first time to establish a direct correlation between the emissions of a dominating industrial installation and the growth of trees in a distance of appr. 6 kms. The annual ring-growth (cm²) was evaluated by means of drilled cores. The age of the trees averaged 100 years, they were 30 years old when the industrial operation was started up.

There is a problem that aside from immission influences there are also such resulting from climate, weather (precipitations), etc.

With the "policy of high stacks" it had been tried in the past to dilute high concentrations of pollutants to such a degree that the immissions became bearable. This possibility today is only given and justified in such areas where it is tried to still dilute the remaining emissions already below the legal values in order to improve the immission situation in areas of high population densities.

Legal situation and methods of authorities

The limitation of pollutanta and the procedures of the authorities are split up into two directions.

On one hand, emission limits are defined (concentrations, mass streams or both), on the other hand immission limits are set.

Air quality classification:

Tabelle/Table 4

Empfehlungen für normative Immissions-Grenzkonzentrationen (15)
Recommendations for standardized immission limit concentrations (15)

		mg SO_2/m^3 April–Oktober	November–März		mg Staub/m^3 mg dust/m^3
Zone I	TMW HMW	0,05 0,07	0,10 0,15	TMW	0,12 darf an sieben Tagen pro Jahr, die jedoch nicht aufeinanderfolgen sollten, überschritten werden (may be exceeded on seven days p. yr., but not in one row)
Zone II	TMW HMW	0,20 0,20 darf nur 3mal pro Tag überschritten werden (may be exceeded only 3 times a day)		TMW	0,20
Zone III	TMW HMW	0,30 0,30 darf nur 3mal pro Tag überschritten werden (may be exceeded only 3 times a day)		TMW	0,30

Tabelle 5

Die neuen Umweltgesetze

Kraftfahrzeugverkehr:

Unverbleites Normalbenzin (91 ROZ) und unverbleites Superbenzin (95 ROZ).
Einführung der Pkw-Abgasnorm US-Standard 1983 mit 1. 1. 1987 bzw. 1. 1. 1988.
Verringerung der Lkw-Abgasemission um 20 Prozent unter die ECE-Norm R 49 zunächst freiwillig, ab 1. 1. 1988 obligatorisch (CO, HC, NO_x).
Verringerung des Schwefelgehaltes im Dieseltreibstoff.

Luftreinhaltung bei stationären Anlagen:

Weitere Senkung des Schwefelgehaltes im Heizöl
Altölgesetz-Novelle.
Dampfkessel-Emissionsgesetz wird Luftreinhaltegesetz mit neuer Durchführungsverordnung.
Smogalarmgesetz.

Chemikaliengesetz
Düngemittelgesetz
Pflanzenschutzmittelgesetz
Sonderabfallbeseitigungskonzept
Flußreinhalteprogramm
Umweltverträglichkeitsprüfung
Verpackung
Verursacherprinzip

Table 5

The new environmental control laws

Automotive traffic:

Non-leaded standard gasoline (91 ROZ) and non-leaded extra gasoline (95 ROZ).
Introduction of car exhaust standards of 1983 (USA) as of Jan. 1, 1987, resp. Jan. 1, 1988.
Reduction of truck emissions by 20% below ECE standard R 49 first on a voluntary basis, obligatory as of Jan. 1, 1988 (Co, HC, NO_x).
Reduction of the sulfur content of diesel fuel.

Clean air & stationary units:

Additional reduction of the sulfur content of heavy oil.
Revision of the law on used oils.
Steam boiler emission law if converted into law on keeping air clean, together with new ordinances.
Smog alarm law.

Law on chemicals
Fertilizer law
Plant protection chemicals law
Special waste removal concept
Keeping rivers clean program
Environmental compatibility examination
Packing
Principle of originator

Auch das Forstgesetz baut auf Immissionsgrenzwerte auf (17). Vorsicht ist hier geboten: Würde man generell von Immissionsgrenzwerten ausgehen, so wären diejenigen Betriebe, die sich in Ballungszentren befinden, in ihren Emissionen stärker zu begrenzen als diejenigen, die als

Also the Austrian Forest Law is based on immission limit concentrations (17). This calls for caution: If immission limit concentrations would become the rule, this would mean that those operations that are located in centers of high density population would have to be more limited in their

Tabelle 6

Emissionskataster (Beispiel für Schwefel)

Schwefel

Emitt.-Nr.	Bereich/Anlage/Emissionsquelle	Energieeinsatz/Jahr HS t	HL t	HEL t	Gas m^3	x s %	Bh/Jahr	Abgasmenge Nm^3/h	IST-Emission[1] SO_2 mg/Nm^3	kg/Bh	jato	SOLL-Emission SO_2 mg/Nm^3	kg/Bh	jato	Maßnahmen, Verbesserungen	Projektkosten	Termin, Probebetrieb	Bemerkungen

[1]) plus zusätzl. Schwefelemissionen aus Produkt oder Bindemittel etc.

Table 6

Emission survey (example sulfur)

Sulfur

emittant no	area/plant/source	energy use/yr HS t	HL t	HEL t	gas m^3	x s %	S/hr/year	flue gas vol Nm^3/h	actual emission[1] SO_2 mg/Nm^3	kg/hr	tpa	allowable emission SO_2 mg/Nm^3	kg/hr	tpa	improvements	costs	deadline trial op.	notes

[1]) plus additional sulfur emissions from product or binder, etc.

Punkteemittenten auf dem freien Land liegen. Der Gleichheitsgrundsatz bliebe auf der Strecke, und eine Wettbewerbsverzerrung müßte die Folge sein. Letzten Endes können aber immer nur Emissionen – als Verursacher – begrenzt werden, weshalb der Überprüfung von Immissionen nur als wichtige zusätzliche Information angesehen werden sollte (20).

Das Dampfkessel-Emissionsgesetz (DKEG) begrenzt die Emissionen von Feuerungsanlagen abgestuft nach Leistung. Emissionen sollen künftig laufend nach dem Stand der Technik reduziert werden. Diese Forderung wird derzeit heftig diskutiert (Rechtsunsicherheit) (16), (18).

Wo entsprechende nationale Regelungen fehlen, wird auch die TA-Luft (BRD) herangezogen.

Bei austauscharmen Wetterlagen (Inversion) steigen die Immissionskonzentrationen auf das 5- bis 10fache und noch mehr an. Für diese kritischen Fälle ist ein Smogalarmgesetz (19) im Begutachtungsverfahren (Tabelle 5).

Beispiel zur Vorgangsweise der Behörden in Kärnten bei Sanierungsprojekten:

- Lufthygienische Studie: Immissionen – Emissionen, Schadstoffausbreitung, Meteorologie (21).
- Gewerberechtliche Überprüfung des Betriebes.
- Emissionskataster für alle Schadstoffe, Tabelle 6.
- Überprüfung der Emittenten.
- Vorschlag eines Verbesserungskonzeptes zur Erreichung der Emissions- und Immissionsgrenzwerte (Betrieb).
- Bescheid: Bis Tag X zu sanieren (22).

emissions than those that are situated in the open country as spot-emittants. This would mean the end of the egality principle shifting competition in an unfair way. In the end, only the emissions may be limited – to reduce the cause – whereby the immission control should only be an important additional source of information (20).

The steam boiler emission law limits emissions of burner installations stepwise according to output. In the future, emissions should continuously be limited according to the prevailing state of the art. This requirement is being discussed at the moment (legal insecurity) (16), (18).

In cases where corresponding national regulations are missing, also the TA-Air regulation of GFR is used.

During low-exchange weather situations (inversion) immission concentrations may rise to the five to tenfold and even more. For these critical situations a smog-alarm law (19) is presently under consideration (table 5).

Example for the method of the procedere of the authorities in Carinthia for sanitizing projects:

- Air hygienic study: immissions – emissions, spreading of pollutants, meteorology (21).
- Trade law commissioning of the operation.
- Emission survey (example) (table 6).
- Control of the emittants.
- Operation offers concept of improvement to reach limits.
- Ordinance from authority: to be effected until day X (22).

Zusammenfassung

Engster Zusammenhang zwischen Energieverbrauch und Emissionen; dies gilt nicht nur in der Industrie, sondern überall. Enorme Reserven in besserer Energienutzung: Vorsichtig geschätzt mindestens 50% ohne Komfortverlust.

Herausforderung an Generationen von Technikern, denn nur die Technik kann hier Lösungen bringen.

Damit verbunden sind große Impulse für die Wirtschaft (Arbeitsplätze). Von großer Bedeutung wäre weltweit die richtige Bewertung des Rohstoffes Energie, um diese Entwicklung zu beschleunigen.

Umweltschutz ist integrativ zu sehen, wenn er effizient sein soll, d. h. jeweils das ganze System ist zu hinterfragen. Nur zum geringen Teil after pipe.

Große Verantwortung des Technikers: In Übereinstimmung mit den Naturgesetzen auf die „Anwendung der Technik" achten!

Denn: „Steht die Wissenschaft mit dem Leben im Widerspruch, hat stets das Leben recht" (Justus Liebig). In vielen Fällen wird aber – und das muß deutlich ausgesprochen werden, eine Änderung der Konsumgewohnheiten stattfinden müssen. Das dürfte nicht leicht sein. Bestes Beispiel ist das Auto: „Alle wollen zurück zur Natur, keiner zu Fuß."

Hier wird man falsch verstandene Freiheit neu interpretieren müssen, denn: Die Freiheit des Menschen liegt nicht darin, daß er tun kann was er will, sondern darin, daß er nicht tun muß, was er nicht tun will (J. J. Rousseau), (23), (24).

Summary

There is an intimate correlation between energy consumption and emissions; this holds not only for the industry, but everywhere. There are tremendous reserves contained in improved energy utilization: Careful estimate: at least 50% without any loss in comfort.

It is also a challenge for generations of technicians, since only technology can bring about solutions.

Connected with this development are great impulses for the economy (creation of jobs). A worldwide true appraisal of the raw material energy would be of great importance to speed up this development.

Environmental control must be seen integratively, should it be efficient, i.e. in every case the whole system has to be discussed. Solutions "after pipe" may be sought after only to a minor extent.

There is a high responsibility of the technician: "Application of technology" must be seen in concordance with the laws of nature!

Because: "When science is contradictory to life, life always will remain right" (Justus Liebig). It also has to be said clearly that in many cases a change of old consumers' habits will have to take place. That will not be very easy. The automobile is the best example: "Everybody wants to get back to nature, but not afoot."

Here a wrongly understood freedom will have to be interpreted in a new way, since: The freedom of man is not based on the fact that he may do what he wants, but that he need not do, what he does not want to do (J. J. Rousseau), (23), (24).

Literaturverzeichnis / References

1. Gruhl, H.: Ein Planet wird geplündert – Die Schreckensbilanz unserer Politik.
2. Global 2000 – Der Bericht an den Präsidenten – 49. Auflage, November **1983.**
3. Becker, K. H.: Physikalisch-chemische Probleme der Luftverunreinigung, **1970.**
4. Energiebericht und Energiekonzept **1984** von der Österreichischen Bundesregierung.
5. Mays, J. P.: Die Verwendung von Delayed Type Petrolkoks als Brennstoff in Zementwerken.
6. Agst, J.: Informations- und Studienmappe 1 – Die Brennstoffe, 6. Auflage, August **1982.**
7. NO_x-Symposion Karlsruhe, 21.–22. Februar **1985,** Internationale Betriebserfahrungen, Universität Karlsruhe (TH).
8. Symposium „Stickoxide", TU Wien, 2.–3. Mai **1984.**
9. Löffler, F.: Fortschritte und Entwicklungstendenzen bei der Gasreinigung mit Faserfiltern.
10. Jungmeier, H.: Primärenergie-Substitution und SO_2-, NO_x-Emissionsminderung bei Sauerstoffzusatz im Drehrohrofen. – Radex-Rundschau (**1985**) 3, S. 624–637.
11. Wargalla, G., und J. Lotze: „Umweltfreundliche Verbrennung von Ballastkohle in der zirkulierenden Wirbelschicht", Erzmetall 38 (**1985**), Nr. 6.
12. Österreichische Gesellschaft für Ökologie – Energie 2030 – Der sanfte Weg – Eine umweltfreundliche Variante der künftigen Energieversorgung Österreichs.
13. Bischoff, G., und W. Gocht: Das Energiehandbuch, 3. Auflage, Köln/Berlin, Oktober **1978.**
14. Meyer-Abich, Meixner, Luhmann, Lieb, Lersch, Hampicke: Energiesparen – Die neue Energiequelle – Wirtschaftspolitische Möglichkeiten und alternative Technologien.
15. Akademie der Wissenschaften „Schwefeloxide in der Atmosphäre; Luftqualitätskriterien SO_2", herausgegeben vom Bundesministerium für Gesundheit und Umweltschutz.
16. Luftreinhalteverordnung für Kesselanlagen **1986** (LRV-K 1986): Begutachtung.
17. Bundesgesetzblatt, 199. Verordnung: Zweite Verordnung gegen forstschädliche Luftverunreinigungen.
18. Bundesgesetzblatt, 209. Verordnung: Begrenzung der Emissionen von Dampfkesselanlagen (2. Durchführungsverordnung zum DKEG), ausgegeben am 30. Mai **1984.**
19. Entwurf eines Bundesgesetzes über den Schutz der Gesundheit des Menschen vor schädlichen Luftverunreinigungen bei austauscharmen Wetterlagen (Smogalarmgesetz).

20. Jungmeier, H.: Die Auswirkungen gesetzlicher Umweltschutzregelungen auf die Industrie am Beispiel der ÖAMAG in Kärnten, Vortrag am Österreichischen Eisenhüttentag am 29. Mai **1984** in Leoben.
21. Lufthygienische Schwerpunktstudie Radenthein vom Amt der Kärntner Landesregierung, Abteilung 19, **1984.**
22. Jungmeier, H.: Das Umweltsanierungskonzept der ÖAMAG Radenthein.
23. Schurt, J.: Vom Umweltdenken zum Umwelthandeln; ÖGNU 6/**84.**
24. Blank, U.: Zur Logik ingenieurwissenschaftlicher Arbeit, VDI-Z, 23/24/**1980**.
25. Krapfenbauer, A.: Waldsterben – Hauptverursacher Oxidantien, Dezember **1985.**
26. Umweltfonds: Studie zu den Emissionen organischer Luftschadstoffe (Kohlenwasserstoffe).

Die Reaktions-, Porendiffusions- und Wärmeleitkoeffizienten verschiedener Magnesite und ihr Einfluß auf die Zersetzungszeit

Eckehard Specht, Hartmut Kainer, Rudolf Jeschar*), Clausthal-Zellerfeld

Für die Zersetzung von Magnesiten verschiedenster Herkunft wurden die Reaktions-, Porendiffusions- und Wärmeleitkoeffizienten experimentell ermittelt und ihre Temperatur- und Materialabhängigkeit diskutiert. Die Versuchsanlage und das dazugehörige Auswerteverfahren, für das die Messungen der Form der Abbaugradkurve und der Körpertemperaturen benötigt werden, wurden kurz erläutert. Ferner wurde der Einfluß der drei Stoffgrößen sowie der Wärme- und Stoffübergangsbedingungen auf die Zersetzungstemperatur und die Zersetzungszeit dargestellt.

Reaction, Pore Diffusion and Thermal Conduction Coefficients of Various Magnesites and their Influence on the Decomposition Time

For the decomposition of magnesites of different origin the reaction –, pore diffusion – and thermal conduction – coefficients have been determined experimentally and their dependence on temperature and material have been discussed. The experimental apparatus and the consequent evaluation procedure, for which the measurement of the form of the curves of decomposition and the temperature of the test specimen are necessary, have briefly been explained. Further more, the influence of the three material values and of the heat and mass transfer conditions on the decomposition temperature and decomposition time are dealt with in detail.

Coefficients de réactivité, de diffusion poreuse et de conductibilité thermique de différentes magnésites et leur influence sur la duree de décomposition

On a déterminé expérimentalement les coefficients de réactivité, de diffusion poreuse et de conductibilité thermique de différentes magnésites afin d'en étudier la décomposition et on a discuté leur relation avec la température et la nature du matériau. On a décrit brièvement l'installation expérimentale et la méthode d'interprétation applicable à celle-ci qui sert à mesurer la forme de la courbe de dégradation et les températures des éprouvettes. On a ensuite donné une représentation de l'influence des trois grandeurs des matériaux ainsi que des conditions thermiques et de transformation sur la température de décomposition et la durée de celle-ci.

1. Einleitung

Das Erdalkalicarbonat Magnesit ($MgCO_3$) ist ein bedeutender natürlicher Rohstoff für viele Industriezweige. Es wird jedoch nur in geringer Menge thermisch unbehandelt weiterverarbeitet. Der überwiegende Anteil des carbonatischen Rohgesteins wird vor der endgültigen Verwendung in verschiedensten Reaktoren gebrannt. Dabei erfolgt unter großem Energiebedarf die Zersetzung des Carbonates, d. h. die Abspaltung des CO_2, und man gewinnt das Magnesiumoxid (MgO). Dieses wird je nach Reinheit und im Brennprozeß erzielter Dichte in der Bauindustrie z. B. für Estrich, in der keramischen Industrie zur Herstellung von feuerfesten Baustoffen sowie Hochwert-

*) Dr.-Ing. E. Specht, Dr.-Ing. H. Kainer und Prof. Dr.-Ing. R. Jeschar, Institut für Energieverfahrenstechnik der Technischen Universität Clausthal, D-3392 Clausthal-Zellerfeld

1. Introduction

The alkaline-earth carbonate magnesite ($MgCO_3$) is an important raw material for many branches of industry. But it is further processed only in thermally untreated small quantities. Before its final utilization the greater part of the natural carbonate rock is burned (calcined) in different kinds of reactors. In this treatment the decomposition of the carbonate takes place with a high input of energy, with splitting-off of CO_2, to yield the magnesium oxide. According to the purity and the density obtained in the firing process, the MgO is used as reactant in the building industry, as for example for flooring plaster, in the ceramic industry for the production of refractory building materials, as well as for high quality ceramics and for pollution control.

To achieve a better optimization of calcining processes it is important to know the decomposition

keramiken und im Bereich des Umweltschutzes als Reaktionsmittel eingesetzt.

Zur Optimierung der Brennverfahren ist es wichtig, das Zersetzungsverhalten des einzelnen Carbonatstückes unter den jeweiligen Prozeßbedingungen zu kennen. Die Zersetzungsgeschwindigkeit eines Carbonatstückes wird durch die fünf Teilvorgänge Wärmeübertragung an den Körper, Wärmeleitung in den Körper, chemische Kinetik der Zersetzungsreaktion, Diffusion des dabei entstandenen CO_2 durch die poröse Oxidschicht an die Körperfläche und Stoffübergang in die Umgebung bestimmt. Zur Berechnung der Zersetzungsgeschwindigkeit können die von V o s t e e n (1) und J e s c h a r (2), (3) angegebenen, analytisch lösbaren Gleichungen verwendet werden. Zu ihrer Lösung werden Reaktions-, Porendiffusions-, Wärmeleit-, Wärmeübergangs- und Stoffübergangskoeffizienten benötigt. Letztere beiden Koeffizienten können für die meisten Strömungen als bekannt angesehen werden. Zahlenwerte für die drei erstgenannten Stoffwerte liegen jedoch bisher für die Magnesitzersetzung noch nicht vor (4). Im Fall des Wärmeleitkoeffizienten ist dies nicht weiter von Bedeutung, da dieser bei den meisten mineralischen Stoffen in etwa gleich ist. Der Wärmeleitkoeffizient des Magnesiumoxids kann somit ohne allzu großen Fehler abgeschätzt werden. Dagegen können Vergleichswerte für den Porendiffusions- und besonders für den Reaktionskoeffizienten nicht herangezogen werden, da diese nur für sehr wenige Mineralien bekannt sind.

In der vorliegenden Arbeit werden deshalb diese drei Stoffwerte in Abhängigkeit von der Temperatur sowie von der Herkunft und Genese für verschiedene Magnesite ermittelt. Dazu wird eine Methodik beschrieben, mit der sich die gesuchten Stoffwerte eines bestimmten Magnesits bei einer vorgegebenen Temperatur aus einem einzigen Zersetzungsverlauf bestimmen lassen. Wie mit Hilfe der von J e s c h a r (2), (3) angegebenen Formeln schon für Kalksteine in (4), (5) gezeigt wurde, üben die Stoffwerte einen unterschiedlichen Einfluß auf die Form des Zersetzungsverlaufes aus, sodaß von dieser auf die Stoffwerte geschlossen werden kann. Voraussetzung hierfür ist jedoch die Kenntnis des Wärme- und Stoffüberganges sowie der Körpertemperaturen. Aufgrund dieser Bedingungen wurde eine Versuchsanlage konzipiert, mit der Zersetzungsverläufe definiert angeströmter Carbonatkörper bei verschiedenen konstanten Temperaturen und CO_2-Umgebungskonzentrationen gemessen werden können.

2. Zersetzungsmodell von Magnesit

Bei der Zersetzung von Magnesit handelt es sich um eine endotherme topochemische Reaktion des Typs

$$\underset{\text{fest}}{MgCO_3} \rightarrow \underset{\text{fest}}{MgO} + \underset{\text{gasf.}}{CO_2} + \Delta H_R$$

Reaktionsenthalpie.

behavior of each individual piece of carbonate under given process conditions. The rate of decomposition of a piece of carbonate is determined by the following five sub-processes: namely heat transfer to the material, heat conduction inside the material, chemical kinetics of the decomposition reaction, diffusion of the splitted CO_2 through the porous oxide layer to the surface of the material, and mass transfer. For computation of the rate of decomposition the analytically solvable equations of V o s t e e n (1) and of J e s c h a r (2), (3) can be used. It is necessary, however, to know the pore diffusion, thermal conduction, heat transfer and mass transfer coefficients for the solution of these equations. The heat transfer coefficient and the mass transfer coefficient are known for flow around bodies. But for the three first mentioned properties there are no numerical values available for the decomposition of magnesite (4). This does not matter for the coefficient of thermal conduction, because it has nearly the same value for most of the mineral substances. This way it is possible to approximate the thermal conduction coefficient. But for the pore diffusion coefficient and especially for the reaction coefficient it is not possible to use comparative values, because they are only very poorly authenticated values for minerals.

In this paper these three properties have therefore been determined in dependence on the temperature, the origin and the genesis of various magnesites. For this purpose a method will be described, whereby the wanted material values of a particular magnesite can be determined for a given temperature from a single curve of decomposition. The same way as it has been shown for the example of limestone in (4), (5) with the aid of J e s c h a r s formulae (2), (3), the properties exercise a different influence on the form of the decomposition curve so that these properties can be inferred therefrom. However, this requires knowledge of the heat and mass transfer as well as of the temperatures of the material. On the basis of these considerations an experimental installation was designed with which it is possible to measure the decomposition behavior of carbonate specimens under specific flow conditions at different constant temperatures and CO_2 ambient concentrations.

2. Decomposition model of magnesite

The decomposition of magnesite is an endothermic topochemical reaction of the following type:

$$\underset{\text{solid}}{MgCO_3} \rightarrow \underset{\text{solid}}{MgO} + \underset{\text{gaseous}}{CO_2} + \Delta H_R \quad \text{reactionenthalpy}$$

This is a dissociation reaction in which the conversion takes place at a moving phase layer. The decomposition mechanism is explained with reference to a partly decomposed piece of carbonate with the shape of a sphere. As shown in fig. 1 schematically the specimen comprises an unde-

Dies ist eine Abbaureaktion, bei der der Umsatz an einer wandernden Phasenfront stattfindet. Der Zersetzungsmechanismus wird an einem teilzersetzten, kugelförmigen Carbonatstück erläutert. Entsprechend Abb. 1 besteht im teilzersetzten Zustand der Carbonatkörper aus einem unzersetzten Carbonatkern, der von der porösen Oxidschicht umgeben ist. Im Calcinationsreaktor mit der Temperatur T_u wird Wärme durch Strahlung und Konvektion (symbolisiert durch α) auf die Oxidschicht mit der Oberflächentemperatur T_o übertragen. Die Wärme gelangt infolge Leitung (λ_{Ox}) durch die poröse Oxidschicht mit der Porosität ψ zur Reaktionsfront, an der sich die Zersetzungstemperatur T_f einstellt. Da während des Zersetzungsvorganges die Reaktionsenthalpie die innere Energie um ein Mehrfaches überwiegt, ist der weitere Wärmefluß in den unzersetzten Kern sehr gering, sodaß die Temperatur im Kern nur unwesentlich niedriger ist als die Temperatur an der Phasenfront. Durch das entsprechende Wärmeangebot erfolgt dann die chemische Reaktion (k), für deren Triebkraft eine Gleichgewichtsabweichung ($p_{Gl}-p_f$) des CO_2-Patialdruckes notwendig ist. Das freiwerdende CO_2 diffundiert (D^p) durch die poröse Oxidschicht an die Oberfläche und geht schließlich konvektiv (β) in die Umgebung über, in der der CO_2-Partialdruck p_u vorliegt.

Die vier physikalischen Transportvorgänge und die chemische Kinetik an der Reaktionsfront sind also miteinander gekoppelt. Diese Verknüpfung läßt sich anschaulich durch eine Reihenschaltung der einzelnen Widerstände darstellen (4), (5).

Der Zersetzungsmechanismus von Magnesit ist identisch mit dem von Kalkstein, der in (4), (5) untersucht worden ist. In diesen beiden Arbeiten sind die Gleichungen zur mathematischen Beschreibung des Zersetzungsvorganges schon ausführlich behandelt worden. Im folgenden wird daher nur noch auf die wesentlichsten Gleichungen eingegangen.

Der Zersetzungsverlauf läßt sich mathematisch durch analytisch lösbare Gleichungen beschreiben, wenn folgende Annahmen getroffen werden:

- Die Carbonatstücke können als Kugeln, Zylinder oder Platte angesehen werden.
- Die Wärmezufuhr erfolge symmetrisch, sodaß für alle Vorgänge eine eindimensionale Betrachtung möglich ist.
- Die chemische und strukturelle Zusammensetzung des Rohsteines sei homogen.
- Die Reaktion beginne gleichmäßig an der Oberfläche, und es bilde sich stets eine geometrisch glatte Zersetzungsfront aus, die kontinuierlich ins Innere des Körpers hineinwandert. Makroskopisch gesehen, trifft diese Annahme sicherlich zu. Mikroskopisch gesehen, setzt die Reaktion bevorzugt an den Rändern der einzelnen Kristallite ein. Dadurch ist die tatsächliche Reaktionsfläche etwas größer als die angenommene ebene Reaktionsfläche. Die

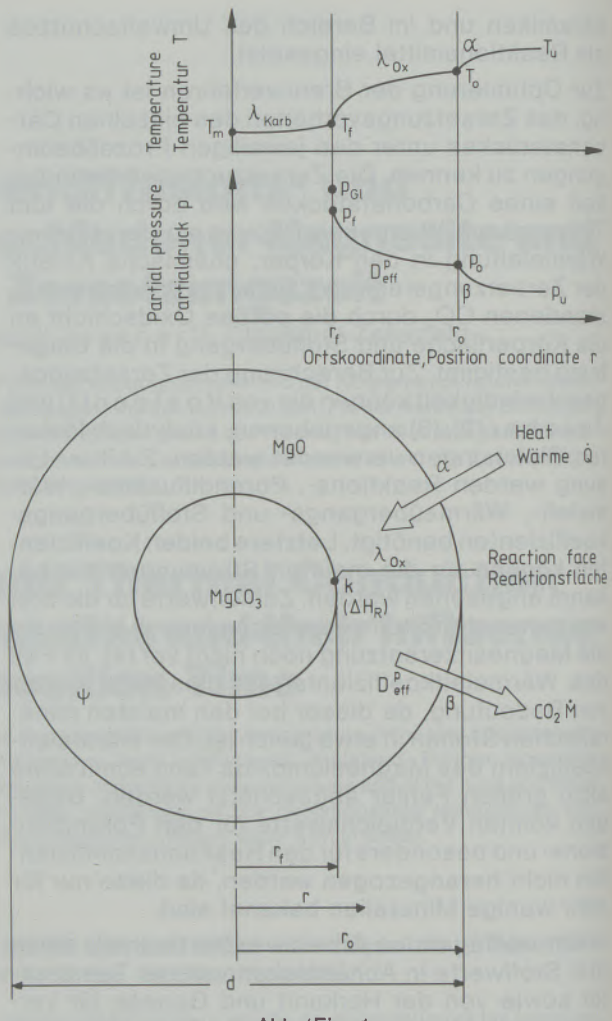

Abb. / Fig. 1
Modell der Zersetzung von Magnesit
Model of the decomposition of magnesite

composed core of carbonate surrounded by the porous oxide layer. In the calcination reactor with the temperature T_u the heat is transferred by radiation and convection (symbolized by α) to the oxide layer with the surface temperature T_o. By conduction (λ_{Ox}) the heat passes through the porous oxide layer with the porosity ψ to the reaction layer where the decomposition temperature T_f is established. During the decomposition process the reaction enthalpy predominates the internal energy. Therefore, the further heat flow into the undecomposed core is very slight, so that the temperature in the core is only very little lower than the temperature at the reaction layer. Sustained by the appropriate supply of heat, the chemical reaction (k) then takes place, for the driving force of which a deviation ($p_{Gl}-p_f$) from equilibrium of the CO_2 partial pressure is necessary. The released CO_2 diffuses (D^p) through the porous oxide layer to the surface and reaches by convection (β) the ambient atmosphere with the CO_2 partial pressure (p_u).

Abweichung dieser beiden Flächen sei in dem Reaktionskoeffizienten k enthalten.

- Der Wärmeübergang kann mit einem effektiven Wärmeübergangskoeffizienten beschrieben werden, der Strahlung und Konvektion beinhaltet.
- Der Zustand der Umgebung (p_u, T_u) sei konstant.
- Die Stoffwerte sowie die Wärme- und Stoffübergangskoeffizienten seien innerhalb des jeweils untersuchten (engen) Temperaturbereiches konstant.
- Die innere Energie (Speicherwärme) sei während der Zersetzungszeit gegenüber der Reaktionsenthalpie vernachlässigbar.

Für den Wärme- und Stoffübergang gelten die Ansätze

$$\dot{Q} = \alpha \cdot A_o \cdot (T_o - T_u) \qquad [1]$$

und

$$\dot{M} = \frac{\beta}{R_C \cdot T} \cdot A_o \, (p_o - p_u) \; . \qquad [2]$$

Hierin bedeuten $\dot{Q}$ den Wärmestrom, α den gesamten, sich aus Strahlung und Konvektion zusammensetzenden Wärmeübergangskoeffizienten, A_o die Oberfläche des unzersetzten Körpers, $\dot{M}$ den Massenstrom des CO_2, R_C die Gaskonstante des CO_2, β den Stoffübergangskoeffizienten sowie T_o und T_u und p_o bzw. p_u die Temperaturen und CO_2-Partialdrücke an der Oberfläche bzw. in der Umgebung. Der Wärme- und Stofftransport durch die Oxidschicht wird durch das Fourriersche bzw. 1. Ficksche Gesetz beschrieben

$$\dot{Q} = - \lambda_{Ox} \cdot A(r) \cdot \frac{dT}{dr} \qquad [3]$$

bzw.

$$\dot{M} = - \frac{D^p_{eff}}{R_C \cdot T_s} \cdot A(r) \cdot \frac{dp}{dr} \; . \qquad [4]$$

Hierin sind λ_{Ox} der Wärmeleitkoeffizient des Oxids, r der Radius bzw. die Ortskoordinate des Körpers, A(r) die örtliche Fläche, T_s die mittlere Temperatur der Oxidschicht und D^p_{eff} ein effektiver Porendiffusionskoeffizient.

Der CO_2-Transport in den Poren kann, je nach Porengröße, durch Knudsen-Diffusion oder (nicht äquimolare) Ficksche Diffusion erfolgen. Beiden Transportmechanismen kann zusätzlich eine konvektive Strömung überlagert sein, wenn der Partialdruck in den Poren den Umgebungsdruck übersteigt. Der sich einstellende Transportmechanismus wird von der Porenstruktur (Größe und Ausbildung der Poren) bestimmt, die von der Materialart und der Temperatur abhängt. Da immer eine Porengrößenverteilung vorliegt, können an ver-

The four physical transport processes and the chemical kinetics at the reaction front are consequently interconnected. This connection can be visualized in analogy with individual resistance connected in series (4), (5).

The decomposition mechanism of magnesite is identical with the decomposition mechanism of limestone, which has been investigated in (4), (5). The equations for the mathematical description of the decomposition behavior have been presented in detail in these two reports. This is the reason why in the following only the main equations are dealt with.

The decomposition behavior may mathematically be described by analytically solvable equations, if the following assumptions are made:

- The pieces of carbonates are to be regarded as spheres, cylinders or plates.
- The heat supply is symmetrical, so that all processes can be treated as one-dimensional.
- The chemical and the structural composition of the raw material is homogeneous.
- The reaction starts uniformly on the surface, always forming a geometrically smooth decomposition front, which advances continuously into the interior of the body. Macroscopically, this assumption is certainly correct. Microscopically, the edges of the individual crystals are the preferred locations where the reaction starts. This is the reason why the actual reaction surface is somewhat larger than the assumed smooth surface. The difference is incorporated in the reaction coefficient k.
- The heat transfer can be described by an effective heat transfer coefficient, which comprises radiation and convection.
- The ambient state (p_u, T_u) is constant.
- The properties as well as the heat transfer coefficient and the mass transfer coefficient are constant within the small temperature range, which has been investigated.
- The internal energy (stored energy) is negligible in comparision with the reaction enthalpy during the decomposition time.

The following statements are valid for the heat and mass transfer

$$\dot{Q} = \alpha \cdot A_o \cdot (T_o - T_u) \qquad [1]$$

and

$$\dot{M} = \frac{\beta}{R_C \cdot T} \cdot A_o \, (p_o - p_u) \; . \qquad [2]$$

Here $\dot{Q}$ stands for the heat flow, α for the total heat transfer coefficient, which contains radiation and convection, A_o for the surface of the undecomposed initial material, $\dot{M}$ for the mass flow of the CO_2, R_C for the gas constant of the CO_2, β for the mass transfer coefficient, T_o and T_u for the surface and

schiedenen Orten in der Oxidschale unterschiedliche Transportmechanismen auftreten. Alle diese Effekte sind mathematisch sehr schwierig zu beschreiben. Sie werden daher in einem effektiven Porendiffusionskoeffizienten D^p_{eff} zusammengefaßt, sodaß der CO_2-Transport durch das 1. Ficksche Gesetz erfaßt werden kann.

Zur Beschreibung des umgesetzten CO_2-Massenstroms wird der Reaktionsansatz

$$\dot{M} = \frac{k}{R_C \cdot T_f} \cdot A_f \cdot (p_{Gl} - p_f) \qquad [5]$$

gewählt. Hierin bedeuten k den Reaktionskoeffizienten, A_f die Reaktionsfläche und $(p_{Gl}-p_f)$ die an ihr bestehende Gleichgewichtsabweichung des Partialdrucks. Wärme- und Massenstrom sind über die Reaktionsanthalpie Δh_R miteinander verknüpft

$$\dot{Q} = - \dot{M} \cdot \Delta h_R \quad . \qquad [6]$$

Der Ort r_f der Reaktionsfront ergibt sich aus der Stoffbilanz, daß der freiwerdende CO_2-Strom gleich der CO_2-Abnahme im Körper ist

$$\dot{M} = - A_f \cdot K_C \cdot \frac{dr_f}{dt} \quad . \qquad [7]$$

K_C ist die Volumenkonzentration des CO_2 im Ausgangsmaterial. Den Zusammenhang zwischen dem Gleichgewichtsdruck und der Temperatur erhält man aus der thermodynamischen Beziehung

$$p_{Gl} = f\,(T) \quad . \qquad [8]$$

Führt man den wie folgt definierten Abbaugrad

$$A = \frac{M(t)}{M_{t=0}} = 1 - \left(\frac{r_f}{r_o}\right)^b \qquad [9]$$

ein, worin $M_{t=0}$ die Anfangsmasse des CO_2 im Ausgangsmaterial und M die reagierte Masse des CO_2 bedeuten, mit dem Formfaktor b = 1, 2, 3 für Platte, Zylinder und Kugel, so ergibt sich aus den Gleichungen [1] bis [9] die zu jedem Abbaugrad A zugehörige Zersetzungszeit aus den beiden gleichwertigen Beziehungen

$$t = R_\alpha \cdot f_3\,(A) + R_\lambda \cdot f_4\,(A) \qquad [10]$$

$$t = R_\beta \cdot f_3\,(A) + R_D \cdot f_4\,(A) + R_k \cdot f_5\,(A). \qquad [11]$$

Hierin sind R_α der Wärmeübergangswiderstand

$$R_\alpha = \frac{K_C \cdot \Delta h_R}{T_u - T_f} \cdot \frac{r_o}{\alpha \cdot b} \quad , \qquad [12]$$

ambient temperature, p_o and p_u for the CO_2 partial pressure on the surface and in the ambient atmosphere. The heat and mass transfer through the oxide layer are described by the law of Fourier and the 1. law of Fick

$$\dot{Q} = - \lambda_{Ox} \cdot A(r) \cdot \frac{dT}{dr} \qquad [3]$$

and

$$\dot{M} = - \frac{D^p_{eff}}{R_C \cdot T_s} \cdot A(r) \cdot \frac{dp}{dr} \quad . \qquad [4]$$

Here λ_{Ox} stands for the coefficient of thermal conduction of the oxide, r for the radius or for the position coordinate, respectively, A(r) for the local surface, T_s for the mean temperature of the oxide layer and D^p_{eff} for the effective pore diffusion coefficient.

The CO_2 transport into the pores may take place – depending on the pore size – by Knudsen diffusion or by (non-equimolar) Fick diffusion. If the partial pressure in the pores exceeds the ambient pressure, a convective flow may additionally be superimposed on both of these transport mechanisms. The transport mechanism, which is actually established, will depend very much on the pore structure – size and shape of the pores. The pore size in turn depends on the crystallographic structure and thus on the temperature of the oxide layer. Moreover, because there is always a distribution of pore sizes, different transport mechanisms may occur in different parts of the oxide shell. All these effects are very difficult to describe mathematically. They are therefore lumped together in an effective pore diffusion coefficient D^p_{eff}, so that CO_2 transport can be described by means of Fick's first law.

The converted CO_2 mass flow is obtained from the chosen formulation

$$\dot{M} = \frac{k}{R_C \cdot T_f} \cdot A_f \cdot (p_{Gl} - p_f), \qquad [5]$$

where k stands for the reaction coefficient, A_f for the reaction surface and $(p_{Gl}-p_f)$ for the deviation of equilibrium from the partial pressure at the reaction surface. The heat flow and the mass flow are coupled by the reaction enthalpy Δh_R

$$\dot{Q} = - \dot{M} \cdot \Delta h_R \quad . \qquad [6]$$

The till now unknown position r_f of the reaction front is obtained from the balance of matter (mass balance), namely, that the released CO_2 flow is equal to the CO_2 decrease in the body

$$\dot{M} = - A_f \cdot K_C \cdot \frac{dr_f}{dt} \quad , \qquad [7]$$

where K_C stands for the volume concentration of CO_2 in the initial substance. The connection be-

R_λ der Wärmeleitwiderstand

$$R_\lambda = \frac{K_C \cdot \Delta h_R}{T_u - T_f} \cdot \frac{r_o^2}{\lambda_{Ox} \cdot 2 \cdot b}, \qquad [13]$$

R_β der Stoffübergangswiderstand

$$R_\beta = \frac{K_C \cdot R_C \cdot T_o}{p_{Gl,f} - p_u} \cdot \frac{r_o}{\beta \cdot b}, \qquad [14]$$

R_D der Diffusionswiderstand

$$R_D = \frac{K_C \cdot R_C \cdot T_s}{p_{Gl,f} - p_u} \cdot \frac{r_o^2}{2 \cdot D^p_{eff} \cdot b} \qquad [15]$$

und R_k der Reaktionswiderstand

$$R_k = \frac{K_C \cdot R_C \cdot T_f}{p_{Gl,f} - p_u} \cdot \frac{r_o}{k}. \qquad [16]$$

Für die Abbaugradfunktionen ist einzusetzen

$$f_3(A) = A \quad \text{(f. Platte, Zylinder, Kugel)}$$
$$f_4(A) = A^2 \quad \text{(f. Platte)} \qquad [17]$$

$$f_4(A) = A + (1 - A) \cdot \ln(1 - A) \quad \text{(f. Zylinder)} \qquad [18]$$

$$f_4(A) = 3 \cdot [1 - (1 - A)^{2/3}] - 2 \cdot A \quad \text{(f. Kugel)}$$

$$f_5(A) = 1 - (1 - A)^{1/b} \quad \text{(f. Platte, Zylinder, Kugel).} \qquad [19]$$

Die Zersetzung kann also entweder als Wärmetransportproblem (Gleichung [10]) oder als Stofftransportproblem (Gleichung [11]) gesehen werden. Anhand der Widerstände (Gleichungen [12] bis [16]) ist zu erkennen, daß als Triebkraft beim Wärmetransport die Temperaturdifferenz zwischen Umgebung und Reaktionsfront und beim Stofftransport die Differenz zwischen Gleichgewichtsdruck und Umgebungspartialdruck wirkt. Da jedoch für die praktischen Berechnungen die Temperatur an der Reaktionsfront und damit der Gleichgewichtsdruck nicht bekannt sind, muß die Zersetzungszeit iterativ aus den Gleichungen [10] und [11] unter Zuhilfenahme der Gleichgewichtsbeziehung [8] ermittelt werden. Mißt man nun die Temperatur an der Reaktionsfront, wobei die Einhaltung der zuvor getroffenen Voraussetzungen gegeben sein muß, so können über die Gleichungen [10] und [11] die gesuchten Stoffwerte experimentell ermittelt werden.

Es zeigt sich nun, wie an späterer Stelle noch ausführlich dargestellt wird, daß sich die Tempe-

tween equilibrium pressure and the temperature results form the thermodynamic relation

$$p_{Gl} = f(T). \qquad [8]$$

The degree of conversion is defined as follows

$$A = \frac{M(t)}{M_{t=0}} = 1 - \left(\frac{r_f}{r_o}\right)^b, \qquad [9]$$

$M_{t=o}$ stands for the initial mass of the CO_2 in the starting substance, M for the reacted mass of CO_2 and b for the shape factor, which is b = 1, 2, 3 for plate, cylinder and sphere [1–9]. The decomposition time corresponding to any particular value of the degree of conversion is obtained from the two equivalent relationships

$$t = R_\alpha \cdot f_3(A) + R_\lambda \cdot f_4(A) \qquad [10]$$

$$t = R_\beta \cdot f_3(A) + R_D \cdot f_4(A) + R_k \cdot f_5(A). \qquad [11]$$

R_α stands for the heat transfer resistance

$$R_\alpha = \frac{K_C \cdot \Delta h_R}{T_u - T_f} \cdot \frac{r_o}{\alpha \cdot b}, \qquad [12]$$

R_λ stands for the heat conduction resistance

$$R_\lambda = \frac{K_C \cdot \Delta h_R}{T_u - T_f} \cdot \frac{r_o^2}{\lambda_{Ox} \cdot 2 \cdot b}, \qquad [13]$$

R_β stands for the mass transfer resistance

$$R_\beta = \frac{K_C \cdot R_C \cdot T_o}{p_{Gl,f} - p_u} \cdot \frac{r_o}{\beta \cdot b}, \qquad [14]$$

R_D stands for the diffusion resistance

$$R_D = \frac{K_C \cdot R_C \cdot T_s}{p_{Gl,f} - p_u} \cdot \frac{r_o^2}{2 \cdot D^p_{eff} \cdot b} \qquad [15]$$

and R_k stands for the reaction resistance

$$R_k = \frac{K_C \cdot R_C \cdot T_f}{p_{Gl,f} - p_u} \cdot \frac{r_o}{k}. \qquad [16]$$

The following has to be used for the function of the degree of conversion

$$f_3(A) = A \quad \text{(for plate, cylinder, sphere)}$$
$$f_4(A) = A^2 \quad \text{(for plate)} \qquad [17]$$

$$f_4(A) = A + (1 - A) \cdot \ln(1 - A) \quad \text{(for cylinder)} \qquad [18]$$

$$f_4(A) = 3 \cdot [1 - (1 - A)^{2/3}] - 2 \cdot A \quad \text{(for sphere)}$$

ratur an der Reaktionsfront und damit der Gleichgewichtsdruck während der Zersetzung unter bestimmten Bedingungen nur geringfügig verändern. Die Widerstände R_i bleiben daher während der Zersetzung nahezu konstant. Die Gleichungen [10] und [11] lassen sich somit zu den folgenden Geradengleichungen [20] und [21] umformen:

$$\frac{t}{f_3(A)} = R_\alpha + R_\lambda \cdot \frac{f_4(A)}{f_3(A)} \qquad [20]$$

$$\frac{t - R_\beta \cdot f_3(A)}{f_5(A)} = R_k + R_D \cdot \frac{f_4(A)}{f_5(A)} \cdot \qquad [21]$$

Aus dem Ordinatenabschnitt dieser Geradengleichungen*) kann man somit R_α bzw. R_k ablesen und aus der Steigung R_λ bzw. R_D. Der Widerstand R_β läßt sich aus dem Stoffübergang berechnen. Es sei an dieser Stelle schon darauf hingewiesen, daß R_β gegenüber den anderen vier Widerständen vernachlässigbar ist. Die gesuchten Stoffwerte λ_{Ox}, D^p_{eff} und k können dann aus den Gleichungen [13], [15] und [16] ermittelt werden, da die Temperatur T_f an der Reaktionsfront aus der Messung bekannt ist. Zur experimentellen Bestimmung der Stoffwerte müssen also konstante Umgebungsbedingungen vorliegen und der zeitliche Abbaugradverlauf (z. B. durch Wägung) und die Reaktionstemperatur, die zugleich Kerntemperatur ist, gemessen werden. Bevor die dazugehörige Versuchsanlage vorgestellt wird, sei noch eine Gleichung angegeben, mit der man den Einfluß der einzelnen Widerstände R_i auf die Zersetzungszeit berechnen kann.

Wie Vosteen (1) und Jeschar (3) gezeigt haben, lassen sich die beiden obigen Gleichungen entkoppeln, wenn man den Gleichgewichtsdruck nicht mit der Temperatur der Reaktionsfront, sondern mit der bekannten Umgebungstemperatur bildet und entsprechend die Zersetzungsgeschwindigkeit proportional der Differenz zwischen dem Gleichgewichtsdruck bei Umgebungstemperatur und dem Umgebungspartialdruck ($p_{Gl,u} - p_u$) setzt.

Für die Endzersetzungszeit τ bei A = 1 erhält man dann die Gleichung

$$\tau = \tau_\beta + \tau_D + \tau_k + \tau_\alpha + \tau_\lambda \qquad [22]$$

mit

$$\tau_\beta = \frac{K_C \cdot R_C \cdot T_o}{p_{Gl,u} - p_u} \cdot \frac{r_o}{b \cdot \beta}, \qquad [23]$$

$$\tau_D = \frac{K_C \cdot R_C \cdot T_s}{p_{Gl,u} - p_u} \cdot \frac{r_o^2}{2 \cdot b \cdot D^p_{eff}}, \qquad [24]$$

$$f_5(A) = 1 - (1 - A)^{1/b} \qquad [19]$$

(for plate, cylinder, sphere).

The decomposition can therefore be conceived either as a heat transport problem (equation [10]) or as a mass transport problem (equation [11]). With reference to the resistances (equation [12] to [16]) it is apparent that the driving force acting in the case of heat transport is the temperature difference between the ambience and the reaction layer, while in the case of mass transport it is the difference between the equilibrium pressure and the ambient partial pressure. For practical calculation purposes the temperature at the reaction layer and with that the equilibrium pressure are not known. So the decomposition time must be determined iteratively from the equations [10] and [11] with the aid of the equilibrium relationship [8]. Now, if the temperature at the reaction front for which the above-mentioned assumptions must be satisfied, are measured, we can, via the equations [10] and [11], experimentally determine the wanted material values.

It now emerges – as it will be explained in more detail later on – that the temperature at the reaction front and therefore the equilibrium pressure changes only slightly during decomposition under certain conditions. Therefore the resistances R_i remain virtually constant during the decomposition. Hence the equations [10] and [11] can be transformed into the linear equations [20] and [21]:

$$\frac{t}{f_3(A)} = R_\alpha + R_\lambda \cdot \frac{f_4(A)}{f_3(A)} \qquad [20]$$

$$\frac{t - R_\beta \cdot f_3(A)}{f_5(A)} = R_k + R_D \cdot \frac{f_4(A)}{f_5(A)} \cdot \qquad [21]$$

From the intercepts of these equations*) with the axis of ordinates we can then read R_α or R_k, and from the gradient we can read R_λ or R_D. The resistance R_β can be calculated from the mass transfer and may therefore be presumed to be known. It should be noted that R_β is usually very small in comparison to the four other resistances. The required material values λ_{Ox}, D^p_{eff} and k can then be determined from the equations [13], [15] and [16], because the temperature T_f at the reaction front is known by measurement. For the experimental determination of the material values it is therefore necessary to have constant ambient conditions, and the time-related progress of the degree of decomposition must be determined (by weighing, for example) and the reaction temperature (which is also the core temperature) has to be

*) Ebenso ergeben sich Geradengleichungen, wenn man die Gleichungen [10] und [11] anstatt durch $f_3(A)$ bzw. $f_5(A)$ jeweils durch $f_4(A)$ dividiert. Die Gleichungen [20] und [21] eignen sich jedoch zur Auswertung besser.

*) Linear equations are likewise obtained if the equations [10] and [11] are divided by $f_4(A)$ instead of by $f_3(A)$ and $f_5(A)$ respectively. However, in this case the equations [20] and [21] are more suitable for evaluation.

$$\tau_k = \frac{K_C \cdot R_C \cdot T_f}{p_{Gl,u} - p_u} \cdot \frac{r_o}{k}, \quad [25]$$

$$\tau_\alpha = \frac{K_C \cdot \Delta h_R}{p_{Gl,u} - p_u} \cdot \frac{p_{Gl,u} - p_{Gl,f}}{T_u - T_f} \cdot \frac{r_o}{b \cdot \alpha} \quad [26]$$

und

$$\tau_\lambda = \frac{K_C \cdot \Delta h_R}{p_{Gl,u} - p_u} \cdot \frac{p_{Gl,u} - p_{Gl,f}}{T_u - T_f} \cdot \frac{r_o^2}{2 \cdot b \cdot \lambda_{Ox}} \cdot \quad [27]$$

Das Verhältnis

$$\Omega_i = \frac{\tau_i}{\tau} \quad [28]$$

gibt nun den Anteil jedes einzelnen Vorganges i an der Gesamtzeit an. Dieser integrale Zeitanteil Ω_i ist somit ein Maß für die Bedeutung des betreffenden Teilvorganges. Mit dem Zeitanteil Ω_i kann abgeschätzt werden, ob für bestimmte Verhältnisse einzelne Vorgänge besonders hervortreten und somit für eine Änderung der Zersetzungszeit einen wirksamen Einfluß ausüben. Die Zeitanteile werden an späterer Stelle in Abhängigkeit der Temperatur und Partikelgröße angegeben, nachdem die Stoffwerte vorgestellt sind.

3. Versuchsanlage

Das Schema der verwendeten Versuchsanlage zur Messung des Zersetzungsverlaufes ist in Abb. 2 dargestellt. Die Carbonatkörper hängen an einer Unterflurwaage, mit der der Gewichtsverlust und damit der Abbaugrad kontinuierlich registriert werden kann. Um die Probe definiert anströmen und damit den konvektiven Wärme- und Stoffübergang bestimmen zu können, ist diese von einem zylindrischen Strömungskanal (Durchmesser 140 mm, Höhe 600 mm) umgeben. Dieser befindet sich in einem elektrisch beheizten Kammerofen. Mit einer Thyristorregelung kann die Ofentemperatur auf ± 1 K konstant gehalten werden. Durch den Kanal wird heißes Gas aus dem Ofenraum gesaugt. Durch die Gasentnahme wird gleichzeitig eine CO_2-Anreicherung im Kanal vermieden, sodaß immer ein konstanter CO_2-Umgebungspartieldruck vorliegt. Die Bestimmung der Gasgeschwindigkeit im Strömungskanal erfolgt mit Hilfe einer außerhalb des Ofens nachgeschalteten Blendenmeßstrecke. Die Körpertemperaturen werden mit PtRh(10)-Pt-Thermoelementen gemessen, die in feinen Bohrungen stecken. Diese sind bei allen untersuchten Körpern im Kern und

measured. Before the experimental apparatus for this purpose will be described, another equation is presented with which the influence of the individual resistances R_i on the decomposition time can be calculated.

As Vosteen (1) and Jeschar (3) have shown, the two above equations can be decoupled by associating the equilibrium pressure, not to the temperature of the reaction front, but to the known ambient temperature, and by correspondingly taking the decomposition rate as proportional to the difference between the equilibrium pressure at ambient temperature and ambient partial pressure ($p_{Gl,u} - p_u$).

For the final decomposition time τ for A = 1 we therefore obtain equation [22].

$$\tau = \tau_\beta + \tau_D + \tau_k + \tau_\alpha + \tau_\lambda \quad [22]$$

with

$$\tau_\beta = \frac{K_C \cdot R_C \cdot T_o}{p_{Gl,u} - p_u} \cdot \frac{r_o}{b \cdot \beta}, \quad [23]$$

$$\tau_D = \frac{K_C \cdot R_C \cdot T_s}{p_{Gl,u} - p_u} \cdot \frac{r_o^2}{2 \cdot b \cdot D_{eff}^p}, \quad [24]$$

$$\tau_k = \frac{K_C \cdot R_C \cdot T_f}{p_{Gl,u} - p_u} \cdot \frac{r_o}{k}, \quad [25]$$

$$\tau_\alpha = \frac{K_C \cdot \Delta h_R}{p_{Gl,u} - p_u} \cdot \frac{p_{Gl,u} - p_{Gl,f}}{T_u - T_f} \cdot \frac{r_o}{b \cdot \alpha} \quad [26]$$

and

$$\tau_\lambda = \frac{K_C \cdot \Delta h_R}{p_{Gl,u} - p_u} \cdot \frac{p_{Gl,u} - p_{Gl,f}}{T_u - T_f} \cdot \frac{r_o^2}{2 \cdot b \cdot \lambda_{Ox}} \cdot \quad [27]$$

The ratio

$$\Omega_i = \frac{\tau_i}{\tau} \quad [28]$$

indicates the portion or share of each individual process i of the total time. This integral time share Ω_i is therefore a measure of the importance of the sub-process in question. With the aid of this time share it is possible to estimate whether, for particular conditions, individual processes are especially prominent and thus have a significant influence on the decomposition time. The time shares will, after having presented the material values, in due course be indicated as functions of temperature and particle size.

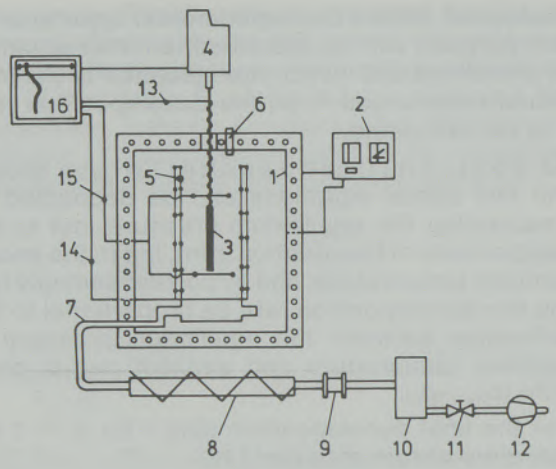

Legende/Legend:

1. Kammerofen
   chamber furnace
2. Ofentemperaturregler
   furnace temperature regulator
3. Karbonatprobe
   carbonate specimen
4. Waage
   balance
5. Strömungskanal
   flow channel
6. CO_2-Einspeisung
   CO_2-feed
7. Absaugung
   exhaust
8. Gaskühler
   gas cooler
9. Normblende
   standard orifice
10. Ausgleichsgefäß
    expansion tank
11. Regelventil
    control valve
12. Pumpe
    pump

Thermoelemente für:
Thermocouples for:

13. Körpertemperatur
    body temperature
14. Kanaltemperatur
    channel temperature
15. Gastemperatur
    gas temperature
16. Meßwerterfassung
    data logging system

Abb./Fig. 2

Experimentelle Apparatur zum Messen des Zersetzungsverhaltens von Karbonaten

Experimental apparatus for measuring the decomposition behavior of carbonates

teilweise auch über den Querschnitt verteilt angebracht. Die Wandtemperaturen des Strömungskanals werden an verschiedenen Orten ebenfalls mit PtRh(10)-Pt-Thermoelementen bestimmt. Dabei zeigt sich, daß der Strömungskanal eine einheitliche Temperatur besitzt. Die Gastemperatur wird mit einem Absaugthermoelement und mit Thermoelementpaaren unterschiedlicher Perlengröße ermittelt, mit deren Anordnung sich der Strahlungseinfluß rechnerisch eliminieren läßt.

Die Versuche wurden an Zylindern mit Durchmessern von 20 mm, 25 mm und 46 mm durchgeführt, wobei das Verhältnis Länge zu Durchmesser bei den Zylindern zwischen 5 und 12 lag. Sie können daher für die Auswertung als unendlich ausgedehnt und damit eindimensional angesehen werden. Wie schon die Versuche von Kalkstein ergaben, hat die Körperform (Platte, Zylinder, Kugel) keinen Einfluß auf die zu untersuchenden Stoffwerte (4), (5). Die chemische Zusammensetzung der untersuchten Magnesite ist in Tabelle 1 aufgeführt.

3. Experimental apparatus

The experimental apparatus for measuring the decomposition behavior is shown schematically in fig. 2. The carbonate specimens are suspended from a weighing device with which the loss in weight and therewith the degree of decomposition can be continuously recorded. In order to have well-defined flow conditions around the specimen and thus be able to determine the convective heat and mass transfer, the specimen is enclosed within a cylindrical flow channel (140 mm diameter, 600 mm height), which in turn is mounted in an electrically heated chamber furnace in which the temperature is always constant. Hot gas is drawn from within the kiln through the top opening of the flow channel. This extraction prevents a build-up of a CO_2 concentration in the flow channel, so that the CO_2 ambient partial pressure is always the same. The determination of the gas velocity in the flow channel is based on measurement through an orifice gauge installed outside the furnace. The temperatures of the specimen are measured by means of PtRh(10)-Pt thermocouples. These are mounted in small-diameter drilled holes, namely, in the core of all the specimens and furthermore at several other points at the cross-section of some of them. The wall temperatures of the flow channel are measured at various points likewise with PtRh(10)-Pt thermocouples and also with NiCr-Ni thermocouples. These measurements show that the flow channel has a uniform temperature. The gas temperature is determined with a suction thermocouple and with pairs of thermocouples with different sizes of junction, by means of which the radiation influence can be eliminated in the calculations.

The tests have been performed on cylinders with diameters of 20 mm, 25 mm and 46 mm. The length/diameter ratios of the cylinders ranged from 5 to 12, so that they could be regarded as infinitely long and thus be treated as one-dimensional cases. The chemical composition of the investigated magnesites is given in table 1.

4. Decomposition behavior

Typical curves of the decomposition of magnesite have often been represented in the literature. This is the reason why here only four measured curves of decomposition are plotted in fig. 3, with the corresponding ambient temperature and core temperature, and that, beginning with a very low ambient temperature of 550 °C, at which the decomposition just starts and continuing with a gradual temperature rise of 50 K in each case. From these four examples it can be drawn that the temperature at the reaction layer is only increasing a little bit during the decomposition process after a short starting period. Because of the slight temperature increase the decomposition temperature T_f and the equilibrium pressure p_{GL} may be regarded as approximately constant. The as-

Tabelle/Table 1

Chemische Analyse und Dichte der untersuchten Magnesite
Chemical analysis and density of magnesites investigated

Magnesit/magnesite $MgCO_3$							
Chem. Analyse/chem. analysis	kryptokristallin/crypto crystalline				kristallin/crystalline		
	Griechenland/Greece				Österreich/Austria		Türkei/Turkey
in Gew.-%/by wt-%	Euböa	Euböa	Euböa	Euböa	Millstatt	Breitenau	–
CaO	0,28	–	0,99	0,69	0,38	0,84	1,89
MgO	46,12	–	45,90	47,15	45,45	42,50	45,40
SiO_2	0,45	–	0,61	0,064	1,27	0,58	0,35
Fe_2O_3	1,19	–	0,06	0,13	1,71	4,34	0,08
Al_2O_3	0,06	–	1,13	0,016	0,07	0,40	0,19
K_2O	0,012	–	–	0,003	0,008	–	–
Na_2O	0,01	–	–	0,014	0,023	–	–
BaO	0,002	–	–	0,002	0,003	–	–
SrO	0,001	–	–	0,001	0,001	–	–
Mn_2O_3	0,11	–	–	0,005	0,095	–	–
SO_3	0,00	–	–	0,003	0,00	–	–
Glühverlust/loss on ignition	51,78	51,60	51,0	51,50	51,03	51,1	51,6
Summe/total	99,42	–	99,69	99,58	100,04	99,79	99,51
Dichte in/density in g/cm³	2,95	2,80	2,54	2,36	2,96	3,00	2,80

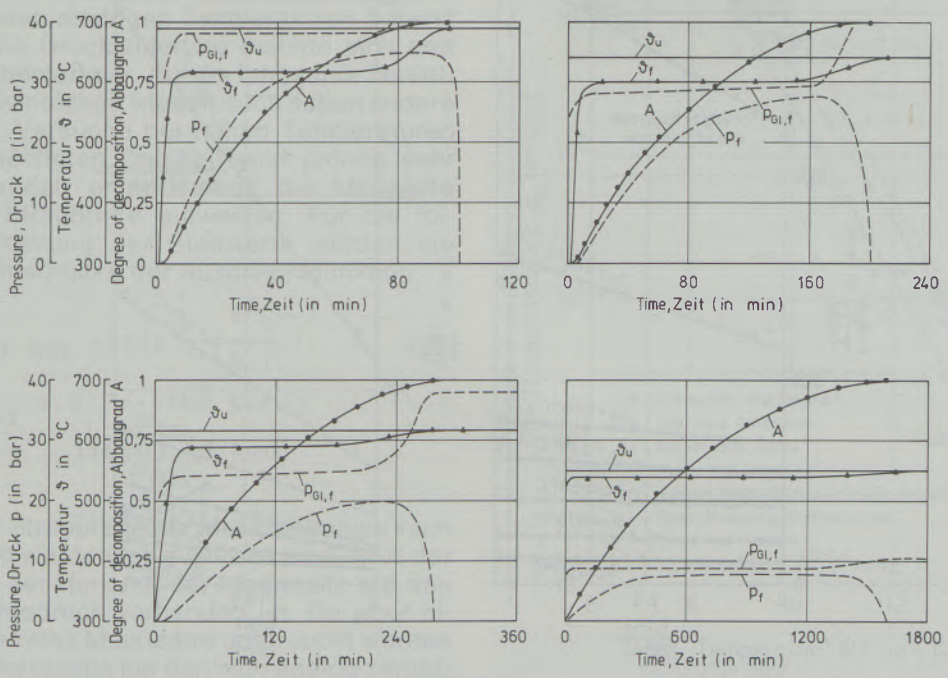

Abb./Fig. 3

Kurven für den Zersetzungsgrad, die Temperatur und den Druck in Magnesitzylindern aus Euböa mit 25 mm Durchmesser ($p = 2{,}54$ g/cm³), bei verschiedenen Temperaturen zersetzt

Curves for degree of decomposition, temperature and pressure in magnesite cylinders of 25 mm diameter from Euboia ($p = 2.54$ g/cm³), decomposed at different temperatures

4. Zersetzungsverläufe

Die typischen Zersetzungsverläufe von Magnesiten sind in der Literatur schon häufig dargestellt worden. Hier werden deshalb in Abb. 3 nur vier gemessene Abbaugradverläufe mit den dazugehörigen Temperaturen in der Umgebung und an der Reaktionsfront gezeigt, und zwar beginnend bei einer äußerst niedrigen Umgebungstemperatur von 550 °C, bei der die Zersetzung gerade anfängt, mit einer stufenweisen Temperaturerhöhung um jeweils etwa 50 K. An diesen vier Beispielen ist zu erkennen, daß die Temperatur an der Reaktionsfront, nach einer kurzen Anlaufphase, während des Zersetzungsvorganges nur noch minimal ansteigt. Aufgrund dieses geringen Temperaturanstiegs kann man die Zersetzungstemperatur T_f und damit den Gleichgewichtsdruck p_{Gl} näherungsweise als konstant ansehen. Damit ist die zur Linearisierung der Abbaugradverläufe entsprechend den Gleichungen [10] und [11] notwendige Voraussetzung von konstanten Widerständen (Gleichungen [12] bis [16]) erfüllt. Auf die Höhe der Zersetzungstemperatur sowie des CO_2-Partialdruckes in der Oxidschicht wird an späterer Stelle noch ausführlich eingegangen werden.

Die gemessenen Abbaugradverläufe wurden entsprechend den Gleichungen [20] und [21] linearisiert. Abb. 4 zeigt beispielhaft für einige Magnesitzylinder solche Abbaugradverläufe. Man erkennt, daß sich die Meßwerte sehr gut durch

sumption of constant resistances (equation [12] to [16] is therefore met, which is necessary for the linearizing action of the curves of the decomposition degree according to equation [10] and [11]. The level of the decomposition temperature and of the CO_2-partial pressure in the oxide layer will be considered in detail later on.

The measured behavior curves for the degree of decomposition have been liniarized in accordance with equation [20] and [21]. By way of example, fig. 4 shows such linearized diagrams for some magnesite cylinders. It is apparent that the measured values may be very satisfactorily approximated by straight lines, which confirms the validity of the equations established. From the ordinate intercept values we can now determine the reaction coefficient and the effective heat transfer coefficient via equations [16] and [12], and from the gradients we can determine the diffusion coefficient and the heat conduction coefficient via equations [15] and [13]. The effective heat transfer coefficient in the experimental apparatus is of no further interest here. The three material values will now be discussed.

5. Material values

5.1. Equilibrium pressure

The equilibrium pressure will first be considered, because it is directly proportional to the decom-

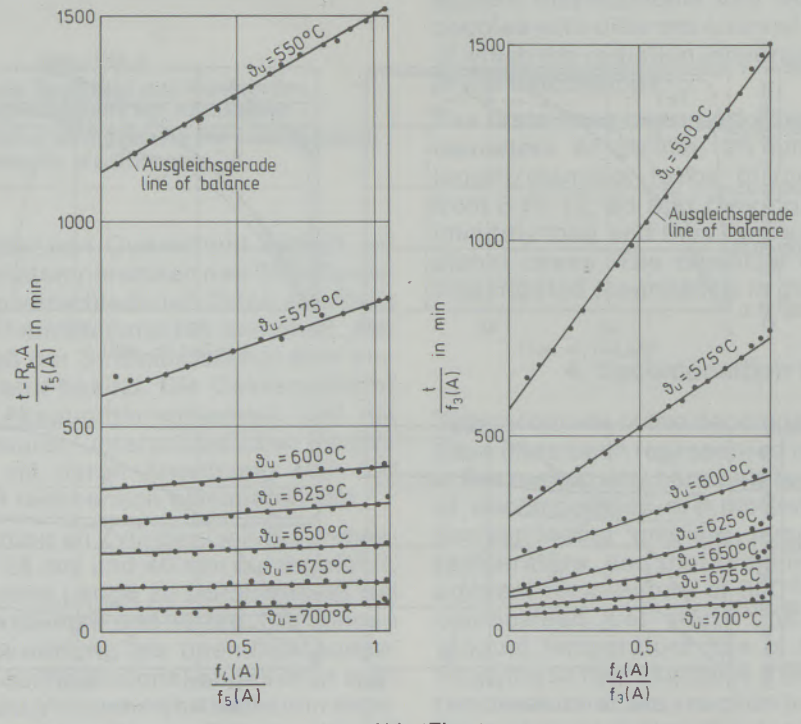

Abb./Fig. 4

Linearisierte Zersetzungsdiagramme für Zylinder (d = 25 mm, l = 120 mm), aus Euböa-Magnesit (p = 2,54 g/cm³) bestehend

Linearized decomposition diagramms for cylinders (d = 25 mm, l = 120 mm) consisting of Euboia magnesite (p = 2.54 g/cm³)

Geraden annähern lassen. Dies bestätigt die Gültigkeit der aufgestellten Gleichungen. Aus den Ordinatenwerten lassen sich über die Gleichungen [16] und [12] der Reaktions- sowie der effektive Wärmeübergangskoeffizient bestimmen und aus der Steigung der Gleichungen [15] und [13] der Diffusions- sowie Wärmeleitkoeffizient. Der effektive Wärmeübergangskoeffizient in der Versuchsanlage ist hier nicht weiter von Interesse. Die drei Stoffwerte werden im folgenden diskutiert.

5. Stoffwerte

5.1. Gleichgewichtsdruck

Zuvor wird auf den Gleichgewichtsdruck eingegangen, da dieser der einzige Stoffwert ist, der der Zersetzungszeit direkt proportional ist (vgl. Gleichungen [22] bis [27]). Abb. 5 zeigt die von Goldsmith und Heard (6), Graf und Goldsmith (7), Harker und Tuttle (8), Marc und Simek (9) gemessenen Gleichgewichtsdrücke sowie die von Haul und Markus (10) und Barin und Knacke (11) aus thermodynamischen Größen berechneten Gleichgewichtsdrücke. Ferner sind in dem Bild eigene Werte enthalten, die mit der in (5) beschriebenen Versuchsanlage ermittelt wurden. Die Streuung der einzelnen Meßpunkte ist erheblich. Wie sich bei den eigenen Messungen des Gleichgewichtsdruckes, die aufgrund der Konzeption der Versuchsanlage nur unterhalb 1 bar durchgeführt werden konnten, zeigte, ist die Reaktionsgeschwindigkeit der Magnesitzersetzung bei diesen niedrigen Temperaturen äußerst langsam. Eine Druckänderung machte sich erst nach Tagen bemerkbar. Auf die langsame Zersetzungsgeschwindigkeit wiesen auch schon andere Autoren hin. Versuche bei hohen Temperaturen und damit höchsten Drücken sind jedoch sehr schwierig, sodaß entsprechend die Meßwerte eine große Streubreite aufweisen. Für die folgende Bestimmung der Stoffwerte werden die Gleichgewichtsdrücke der Ausgleichsfunktion

$$p_{Gl} = p_{Gl\,max} \cdot \exp\left(-\frac{\Delta\tilde{h}_R}{R \cdot T}\right) \qquad [29]$$

mit $p_{Gl\,max} = 2{,}7 \cdot 10^8$ bar

und $\Delta\tilde{h}_R = 116400$ kJ/kmol

benutzt.

Aufgrund der Streubreite der Meßergebnisse kann nicht ermittelt werden, ob eventuell ein Einfluß der Genese und der Herkunft der Magnesite auf den Gleichgewichtsdruck vorhanden ist. Da aber einerseits sehr reine Magnesite untersucht worden sind und andererseits bei den sich analog zersetzenden Kalksteinen kein Einfluß der Materialart festgestellt werden konnte (5), wird davon ausgegangen, daß Gleichung [29] für alle Magnesitsorten gültig ist. Sollte ein bestimmter Magnesit einen abweichenden Gleichgewichtsdruck besitposition time (cf. equations [22] to [27]. Fig. 5 shows the equilibrium pressure which have been measured by Goldsmith and Heard (6), Graf and Goldsmith (7), Harker and Tuttle (8), and Marc and Simek (9), as well as the computed equilibrium pressures from thermodynamic values by Haul and Markus (10) and Barin and Knacke (11). Fig. 5 further contains some values, which have been determined with the aid of the experimental apparatus, explained in (5). The distribution of the measuring points is considerable. From our own measurements of the equilibrium pressure, which have been executed only beneath 1 bar, because of the conception of the experimental apparatus, it has been the result that the reaction rate of the magnesite decomposition is very slow at this low temperatures. A change of the pressure will not be perceptible until a few days. The slow decomposition rate has also been reported by other authors. Experiments with high temperatures and therefore with high pressures are very difficult, so that the measured va-

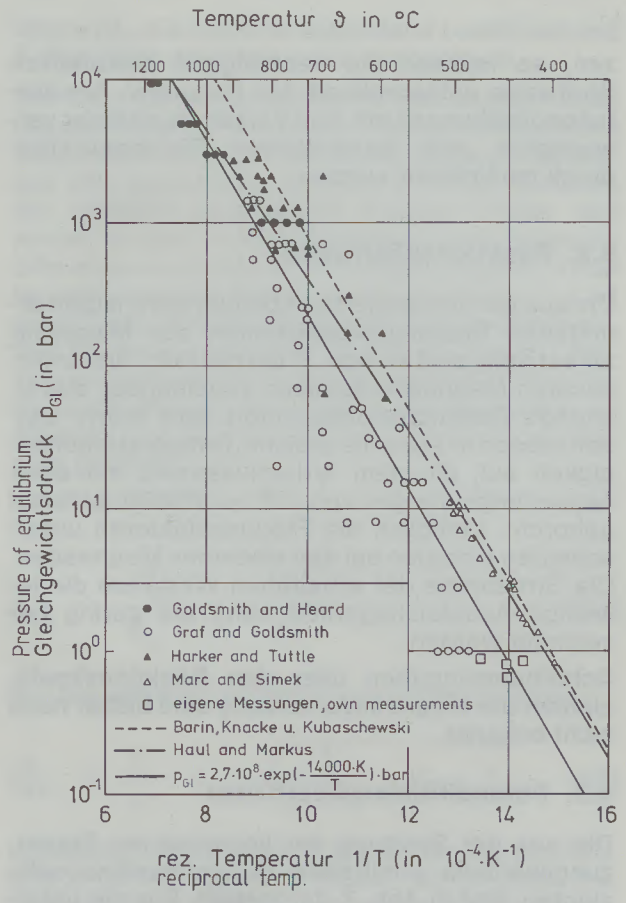

Abb./Fig. 5

Gleichgewichtsdruck als Funktion der Temperatur im System $MgCO_3/MgO/CO_2$

Equilibrium pressure as a function of temperature in the system $MgCO_3/MgO/CO_2$

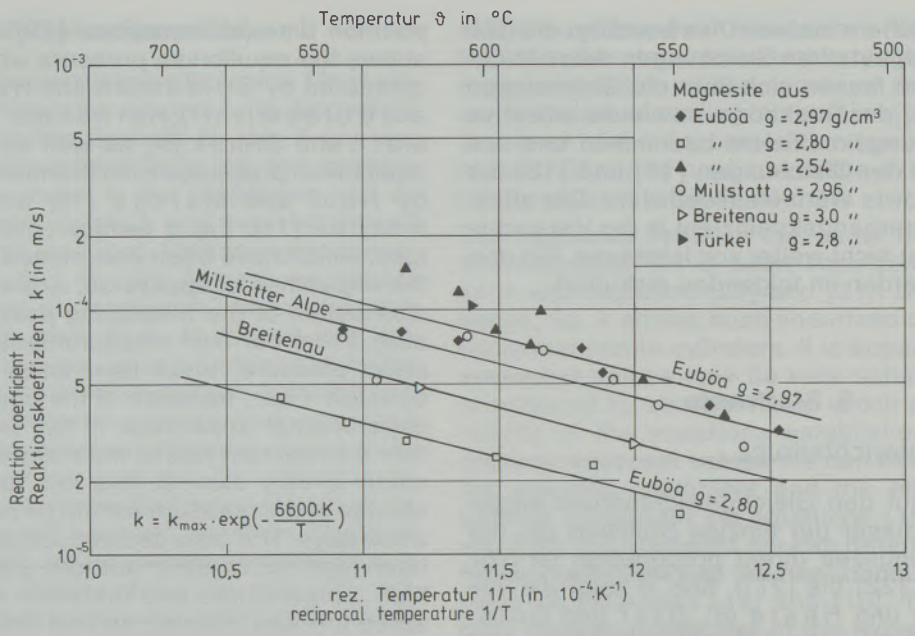

Abb./Fig. 6
Reaktionskoeffizienten verschiedener Magnesite
Reaction coefficients of various magnesites

zen, so müssen die nachfolgend diskutierten Stoffwerte entsprechend den benutzten Auswertungsgleichungen mit dem Verhältnis des hier verwendeten zum tatsächlichen Gleichgewichtsdruck multipliziert werden.

5.2. Reaktionskoeffizient

Die aus den linearisierten Abbaugradverläufen ermittelten Reaktionskoeffizienten der Magnesitzersetzung sind in Abb. 6 dargestellt. Die untersuchten Magnesite besitzen voneinander abweichende Reaktionskoeffizienten. Ihre Werte weisen jedoch in etwa die gleiche Temperaturabhängigkeit auf, die dem Arrheniusansatz mit einer Aktivierungsenergie von $\Delta\tilde{E} \approx 55000$ kJ/kmol gehorcht. Lediglich die Frequenzfaktoren unterscheiden sich also bei den einzelnen Magnesiten. Die Streubreite der erhaltenen Werte um die jeweilige Ausgleichsgerade kann als gering bezeichnet werden.

Schrifttumsangaben über den Reaktionskoeffizienten der Magnesitzersetzung sind bisher noch nicht bekannt.

5.3. Porendiffusionskoeffizient

Die aus der Steigung der linearisierten Zersetzungsverläufe ermittelten Porendiffusionskoeffizienten sind in Abb. 7 dargestellt. Für die untersuchten Magnesite ergeben sich zum Teil sehr unterschiedliche Werte, deren Bandbreite etwa eine Zehnerpotenz beträgt. Der Breitenauer Magnesit mit den kleinsten Porendiffusionskoeffi-

lues have this scattering. For all magnesites the equilibrium pressure of the compensation function

$$p_{Gl} = p_{Gl\ max} \cdot \exp\left(-\frac{\Delta\tilde{h}_R}{R \cdot T}\right) \qquad [29]$$

is used for determining the material values, with

$$p_{Gl\ max} = 2{,}7 \cdot 10^8 \text{ bar}$$

$$\Delta\tilde{h}_R = 116400 \text{ kJ/kmol}$$

Because of the scattering of the measured points it cannot be ascertained wether any influence of the genesis and origin of the magnesites is available on the equilibrium pressure. Because on the one hand very pure magnesites have been investigated and on the other hand there is no influence on the origin of the analogous decomposing limestones (5), it will be postulated, that equation [29] is valid for all kinds of magnesite. If a certain magnesite should have a different equilibrium pressure, it will be necessary to multiply the following discussed properties corresponding to be applied equations with the ratio of the postulated to the real equilibrium pressure.

5.2. Reaction coefficient

The reaction coefficients determined from the linearized decomposition behavior curves are represented in fig. 6, and it is apparent that they differ from one kind of magnesite to another. Their values nevertheless exhibit nearly the same dependence on the temperature responding to the Arrhenius equation with a activation energy of $\Delta\tilde{E}$

zienten fiel beim Herstellen der Versuchskörper durch seine besonders große Härte auf, während dagegen der Euböa-Magnesit mit der Dichte 2,54 g/cm³ sich besonders leicht bearbeiten ließ. Die Porendiffusionskoeffizienten sind stark temperaturabhängig. Man kann für alle Magnesite eine näherungsweise gleiche Temperaturabhängigkeit ihrer Porendiffusionskoeffizienten annehmen, die sich durch den Exponentialansatz

$$D^p_{eff} = D^p_{min} \cdot \exp\,(0{,}0165 \cdot K^{-1} \cdot T_s) \quad [30]$$

darstellen läßt, worin D^p_{min} ein materialabhängiger Koeffizient und T_s die mittlere absolute Oxidtemperatur sind.

Die sich mit diesen Porendiffusionskoeffizienten aus den zuvor aufgeführten Gleichungen ergebenden CO_2-Partialdrücke an der Reaktionsfront sind in Abb. 3 dargestellt. Der Partialdruck steigt mit der Zersetzungsdauer an, da der Diffusionsweg immer länger und zu dessen Überwindung ein immer größeres Partialdruckgefälle benötigt wird. Man erkennt, daß selbst für den Euböa-Magnesit (ϱ = 2,54 g/cm³) mit den höchsten Porendiffusionskoeffizienten der CO_2-Partialdruck weit mehr als 1 bar beträgt. Es wird daher im folgenden untersucht, ob der CO_2-Transport durch die Oxidschale überwiegend durch Diffusion oder durch die Strömung hervorgerufen wird, die aufgrund des Gesamtdruckgradienten vorhanden ist.

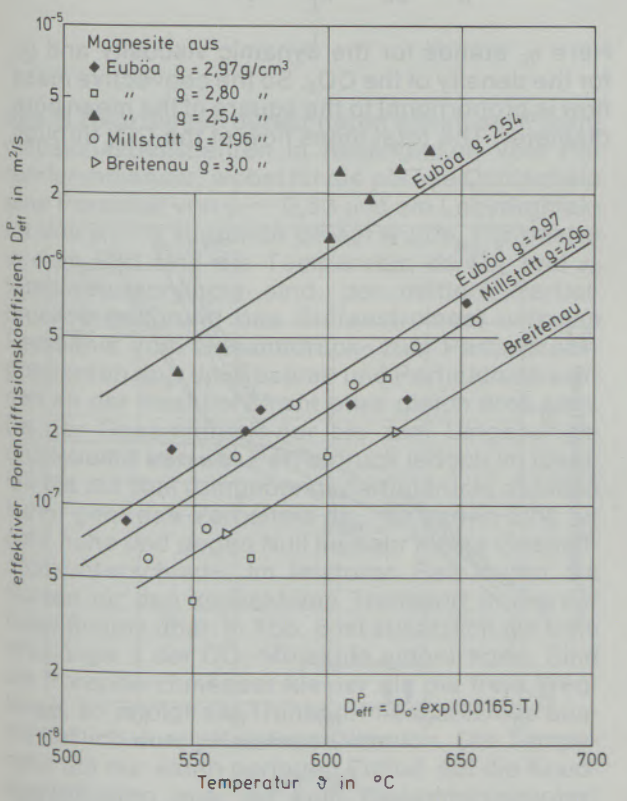

Abb./Fig. 7
Porendiffusionskoeffizienten verschiedener Magnesite
Pore diffusion coefficients of various magnesites

≈ 55000 kJ/kmol. Only the frequency factors differ between the kinds of magnesite. The scattering of the obtained values around the compensation line can be considered as small.

Data about reaction coefficients of magnesite are not known in literature yet.

5.3. Pore diffusion coefficient

The pore diffusion coefficients determined from the gradient of the linearized decomposition behavior curves are represented in fig. 7. The various investigated magnesites have partially differing values, which scatter range extends about the factor 10. It is remarkable, that the Breitenauer magnesite with the lowest pore diffusion coefficients shows the biggest hardness while preparing the test specimen, in comparison to this the Euboia magnesite with the density ϱ = 2,54 g/cm³ could be prepared easily. The pore diffusion coefficients depends very much on temperature. For all magnesites the same dependence on temperature may be assumed for their pore diffusion coefficients, with an approximation by the exponential function

$$D^p_{eff} = D^p_{min} \cdot \exp\,(0{,}0165 \cdot K^{-1} \cdot T_s) \quad [30]$$

where D^p_{min} is a material dependend coefficient and T_s the mean absolute oxide temperature.

The CO_2 partial pressures at the reaction layer resulted from the previously mentioned equations are plotted in fig. 3. The partial pressure increases with the duration of decomposition, because the diffusion path length become longer and longer, so that an always higher partial pressure difference is needed for the mass transport. It can be seen, even for the Euboia magnesite (ϱ = 2,54 g/cm³) with the highest pore diffusion coefficients, that the partial pressure is lying far above 1 bar. Therefore it will be researched whether the CO_2 transport through the oxide layer is caused by diffusion or by flow proceeding from the total pressure gradient.

The Knudsen diffusion is described with the equation

$$\dot{m}_{Kn} = \frac{D^p_{Kn}}{R_C \cdot T} \cdot \frac{dp}{dr} \quad . \quad [31]$$

For the diffusion coefficient you have to place

$$D^p_{Kn} = \frac{\psi}{\mu} \cdot \bar{d}_p \cdot \sqrt{\frac{8}{9 \cdot \pi}} \cdot R_C \cdot T \cdot \quad [32]$$

according to (14). Here ψ stands for the porosity and μ for the labyrinth factor, which gives the deviation from the real path length in the pores to the length of a straight path through the material. The magnitude of the mass flow by Knudsen diffusion is proportional to the mean pore diameter d_p. Because the gas diffusion by Fick in the decom-

Für den Stofftransport durch Knudsen-Diffusion gilt

$$\dot{m}_{Kn} = \frac{D^p_{Kn}}{R_C \cdot T} \cdot \frac{dp}{dr} \cdot \qquad [31]$$

Der Koeffizient der Knudsen-Diffusion beträgt nach (14)

$$D^p_{Kn} = \frac{\psi}{\mu} \cdot \bar{d}_p \cdot \sqrt{\frac{8}{9 \cdot \pi} \cdot R_C \cdot T} \cdot \qquad [32]$$

Hierin sind ψ die Porosität und μ der Labyrinthfaktor, der die Abweichung der realen Porenlänge von der Länge einer geraden Röhre durch den Körper beschreibt. Die Höhe des Stoffstromes ist bei der Knudsen-Diffusion also proportional dem mittleren Porendurchmesser $\bar{d}_p$. Da die Gasdiffusion in der zersetzten Carbonatschale nicht-äquimolar ist, lautet für sie das 1. Ficksche Gesetz

$$\dot{m}_{Fi} = \frac{D^p_{Fi}}{R_C \cdot T} \cdot \frac{p_g}{p_g - p} \cdot \frac{dp}{dr}, \qquad [33]$$

worin p_g den Gesamtdruck bedeutet. Der Koeffizient der Fickschen Porendiffusion beträgt nach (14)

$$D^p_{Fi} = \frac{\psi}{\mu} \cdot D_{CL} \qquad [34]$$

mit D_{CL} als binärem Diffusionskoeffizienten des Gemisches CO_2-Luft. Der Ficksche Diffusionsstrom ist also unabhängig vom Porendurchmesser. Im Übergangsbereich zwischen Fickscher und Knudsen-Diffusion kann

$$\frac{1}{\dot{m}_D} = \frac{1}{\dot{m}_{Kn}} + \frac{1}{\dot{m}_{Fi}} \qquad [35]$$

gesetzt werden (12), (13). Der konvektive Transportstrom läßt sich näherungsweise aus dem Hagen-Poiseulleschen Gesetz herleiten, wenn man davon ausgeht, daß die Strömung aufgrund der kleinen Durchmesser und damit Reynoldszahlen laminar ist und die Strömungswiderstände nur durch die Wandreibung hervorgerufen werden und nicht durch Umlenkungen und Querschnittsveränderungen

$$\dot{m}_{Kon} = \frac{\psi}{\mu} \cdot \frac{d_p^2 \cdot \varrho_C}{32 \cdot \eta_C} \cdot \frac{dp_g}{dr} \cdot \qquad [36]$$

Hierin bedeuten η_C die dynamische Zähigkeit und ϱ_C die Dichte des CO_2. Die konvektive Massenstromdichte ist also proportional dem Quadrat des mittleren Porendurchmessers. Der gesamte Stoffstrom des CO_2 durch die poröse Schale setzt sich aus der Diffusion und dem konvektiven Transport zusammen

$$\dot{m} = \dot{m}_D + \dot{m}_{Kon} \cdot \qquad [37]$$

posed oxide layer is non-equimolar, the 1. Fick law has to be applied in the form

$$\dot{m}_{Fi} = \frac{D^p_{Fi}}{R_C \cdot T} \cdot \frac{p_g}{p_g - p} \cdot \frac{dp}{dr} \qquad [33]$$

where p_g stands for the total pressure. For the diffusion coefficient you have to place now

$$D^p_{Fi} = \frac{\psi}{\mu} \cdot D_{CL} \qquad [34]$$

according to (14), too, with D_{CL} as binary diffusion coefficient of the mixture CO_2-air. Fick's diffusion flow is independ on the pore diameter. In the transition region between Fick diffusion and Knudsen diffusion can be set (12), (13)

$$\frac{1}{\dot{m}_D} = \frac{1}{\dot{m}_{Kn}} + \frac{1}{\dot{m}_{Fi}} \cdot \qquad [35]$$

The convective mass flow may be derived approximately from the law of Hagen-Poiseulle, if a laminar flow is assumed caused by the small pore diameter and therefore of low Reynolds numbers and if the flow resistance are proceeding only by wall friction and not by turns and modifications of the pore cross-section

$$\dot{m}_{Kon} = \frac{\psi}{\mu} \cdot \frac{d_p^2 \cdot \varrho_C}{32 \cdot \eta_C} \cdot \frac{dp_g}{dr} \cdot \qquad [36]$$

Here η_C stands for the dynamic viscosity and ϱ_C for the density of the CO_2. So the convective mass flow is proportional to the square of the mean pore diameter. The total mass flow of the CO_2 through

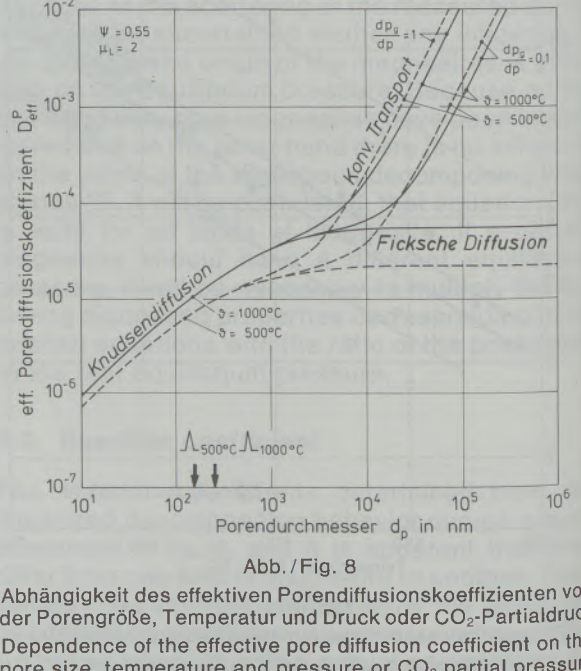

Abb./Fig. 8

Abhängigkeit des effektiven Porendiffusionskoeffizienten von der Porengröße, Temperatur und Druck oder CO_2-Partialdruck

Dependence of the effective pore diffusion coefficient on the pore size, temperature and pressure or CO_2 partial pressure

Um, wie zuvor beschrieben, die Zersetzungszeit analytisch herleiten zu können, wurde für den gesamten Stoffstrom der Ansatz

$$\dot{m} = \frac{D^p_{eff}}{R_C \cdot T} \cdot \frac{dp}{dr} \qquad [4]$$

benutzt, in dem D^p_{eff} der effektive Porendiffusionskoeffizient ist, in dem alle drei Transportmechanismen enthalten sind. Aus den Zersetzungsverläufen kann folglich auch nur dieser effektive Porendiffusionskoeffizient bestimmt werden. Mit Hilfe der Gleichungen [31] bis [37] läßt sich jedoch aus diesem gemessenen Diffusionskoeffizienten auf den vorhandenen Transportmechanismus schließen. Diese Gleichungen in Gleichung [4] eingesetzt, ergibt für den effektiven Porendiffusionskoeffizienten

$$D^p_{eff} = \frac{\psi}{\mu} \cdot \left[\frac{1}{\frac{1}{\frac{p_g}{p_g - p} \cdot D_{CL}} + \frac{1}{\sqrt{\frac{8}{9 \cdot \pi} \cdot R_C \cdot T \cdot d_p}}} + \frac{R_C \cdot T \cdot d_p^{-2}}{32 \cdot \nu_C} \cdot \frac{dp_g}{dp} \right] \cdot \qquad [38]$$

Abb. 8 zeigt diesen berechneten effektiven Porendiffusionskoeffizienten in Abhängigkeit vom Porendurchmesser, wobei für die poröse Oxidschale eine Porosität von $\psi = 0{,}53$ und ein Labyrinthfaktor von $\mu = 2$ zugrunde gelegt wurde. Parameter in dem Bild sind die Temperatur, da D_{CL} und ν_C temperaturabhängig sind, der mittlere Partialdruck $\bar{p}$ (aufgrund des Stefanstromes) und das Verhältnis vom Gesamtdruck- zum Partialdruckgradienten dp_g/dp. Gesamt- und Partialdruck werden an der Reaktionsfront etwa gleich groß sein. Da der Gesamtdruck nur bis zum Umgebungsdruck von 1 bar, der Partialdruck jedoch im Idealfall bis auf Null (Umgebungspartialdruck) abfallen kann, geht das Verhältnis dp_g/dp gegen Eins für sehr hohe und gegen Null für sehr kleine Gesamtdruckunterschiede. Im letzteren Fall laufen die Kurven für den konvektiven Transport in die der Gasdiffusion über. In Abb. 8 ist zusätzlich die freie Weglänge Λ der CO_2-Moleküle eingetragen. Sind die Porendurchmesser kleiner als die freie Weglänge, so erfolgt der Transportmechanismus ausschließlich durch Knudsen-Diffusion. Die Temperatur übt nur einen geringen Einfluß auf die Knudsen-Diffusion aus. Ist kein Gesamtdruckunterschied vorhanden und sind die Porendurchmesser wesentlich größer als die freie Weglänge, so ist der effektive Diffusionskoeffizient unabhängig

the porous layer is superposed on diffusion and convective flow

$$\dot{m} = \dot{m}_D + \dot{m}_{Kon}. \qquad [37]$$

In order to deduce the decomposition time analytically, as described above, the equation

$$\dot{m} = \frac{D^p_{eff}}{R_C \cdot T} \cdot \frac{dp}{dr} \qquad [4]$$

was appointed for the total mass flow, in which D^p_{eff} is the effective pore diffusion coefficient containing the three transport mechanisms. Hence, it is only possible to determine this effective pore diffusion coefficient from the curves of decomposition. But with the aid of the equations [31] to [37] you can infer from the measured diffusion coefficients to the real diffusion mechanism. Setting these equations in equation [4] you get for the effective pore diffusion coefficient

$$D^p_{eff} = \frac{\psi}{\mu} \cdot \left[\frac{1}{\frac{1}{\frac{p_g}{p_g - p} \cdot D_{CL}} + \frac{1}{\sqrt{\frac{8}{9 \cdot \pi} \cdot R_C \cdot T \cdot d_p}}} + \frac{R_C \cdot T \cdot d_p^{-2}}{32 \cdot \nu_C} \cdot \frac{dp_g}{dp} \right] \cdot \qquad [38]$$

Fig. 8 shows this computed effective pore diffusion coefficient in dependence on the pore diameter, whereby a porosity of $\psi = 0{,}53$ and a labyrinth factor of $\mu = 2$ has been taken us a basis for the porous oxide layer. Parameter in the figure are the temperature, because D_{CL} and ν_C depend on temperature, the mean partial pressure $\bar{p}$ (because of the Stefan flow) and the ratio of the total pressure gradient to the partial pressure gradient dp_g/dp. Total and partial pressure will nearly be equal at the reaction front. Because the total pressure may only drop down to the ambient pressure of 1 bar, however, the partial pressure may drop down to zero (ambient partial pressure) in an ideal case, the ratio dp_g/dp is tending towards one for very big, and towards zero for very small differences of the total pressure. In the last case, the curves for the convective transport passes into the curves for the gas diffusion. In addition to this, the free path lengths Λ of the CO_2 molecules are plotted in fig. 8. If the pore diameters are smaller than the free path lengths the transport mechanism takes places only by Knudsen diffusion. The temperature has not much influence on the Knudsen diffusion. If there is no difference of the total

vom Porendurchmesser. Es liegt Ficksche Gasdiffusion vor. Auf diese hat die Temperatur den größten Einfluß. Tritt dagegen schon eine kleine Gesamtdruckdifferenz auf (z. B. $dp_g/dp = 0{,}01$), so wird der Stofftransport im Bereich $\bar{d}_p > \Lambda$ nur noch durch Konvektion hervorgerufen. Werden die Porendurchmesser kleiner als die freie Weglänge der Moleküle, ergeben sich jedoch solch große Reibungswiderstände, daß der konvektive Transport gegenüber der Knudsen-Diffusion vernachlässigbar wird.

Um den Diffusionsmechanismus beurteilen zu können, muß also die Größe der Poren im Magnesiumoxid bekannt sein. Deshalb wurde die Porengrößenverteilung in einigen Proben nach Beendigung der Zersetzung mit einem Quecksilberporosimeter (Druckbereich 0 bis 2000 bar) gemessen. Der integralen Porenhäufigkeitsverteilung wird bei 50% ein mittlerer Porendurchmesser $\bar{d}_p$ zugeordnet. Diese bei Raumtemperatur ermittelten Werte sind in Abb. 9 in Abhängigkeit der Temperatur, bei der die Proben gebrannt wurden, aufgetragen. Die mittleren Porendurchmesser der porösen Magnesitschale liegen im Bereich 5 nm bis 50 nm. Mit diesen Durchmessern ergibt sich aus Abb. 8, daß der CO_2-Transport in der Oxidschale nur durch Knudsen-Diffusion erfolgt.

Die mittleren Porendurchmesser der verschiedenen Magnesite unterscheiden sich erheblich. Sie steigen jedoch, bis auf eine Ausnahme, mehr oder weniger stark mit der Brenntemperatur an. Dies deutet darauf hin, daß die Poren umso größer sind, je höher die Temperatur der Oxidschale während des Brennprozesses ist. Hierauf ist die starke

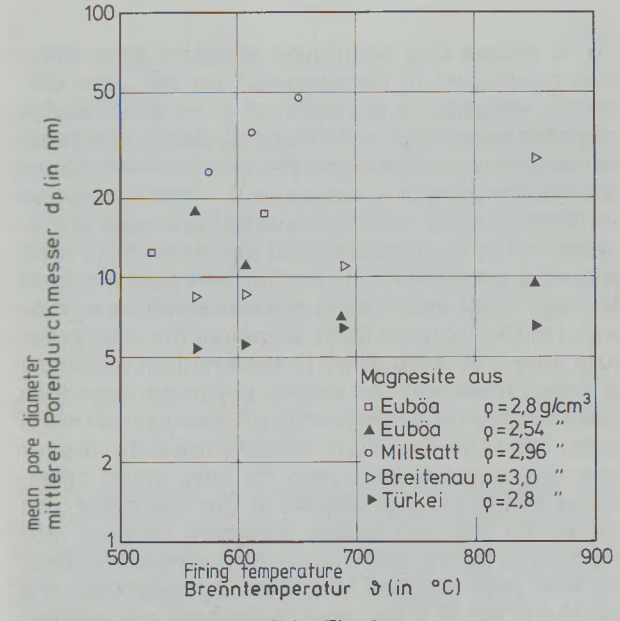

Abb./Fig. 9

Mittlerer Porendurchmesser des Magnesiumoxides in Abhängigkeit von der Brenntemperatur

Mean pore diameter of the magnesite oxide in dependence on the firing temperature

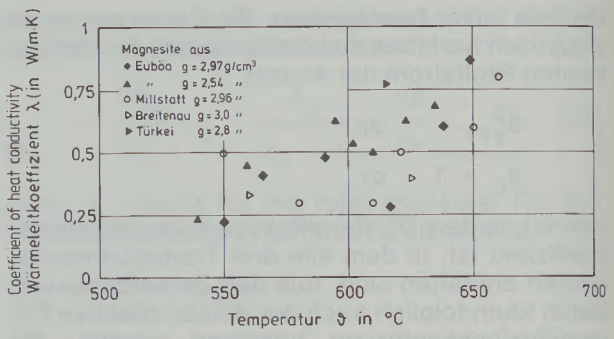

Abb./Fig. 10

Wärmeleitkoeffizient der porösen MgO-Schicht

Thermal conduction coefficient of the porous MgO layer

pressure and if the pore diameters are much bigger than the free path lengths, the effective diffusion coefficient is independend on the pore diameter. Then you have gas diffusion by Fick, which is most influenced by the temperature. But if there even exists a small difference of the total pressure (for example $dp_g/dp = 0.01$), then the mass transport in the range $d_p > \Lambda$ will only be caused by convection. If the pore diameters become smaller than the free path lengths of the molecules, then such a big friction resistance results that the convective transport, compared to the Knudsen diffusion, may be neglected.

In order to estimate the diffusion mechanism, it is necessary to have knowledge about pore sizes in the magnesite oxide. This is the reason why the pore size distribution of some test specimens have been measured after the decomposition with a mercury porosimeter (pressure range 0–2000 bar). A mean pore diameter $\bar{d}_p$ is assigned to the integral pore frequency distribution at 50%. These values, determined at ambient temperature are those, plotted in fig. 9 in dependence on the temperature, at which the test specimen had been calcined. The mean pore diameters of the porous magnesite shell are in the range of 5 nm to 50 nm. With these diameters it follows from fig. 8 that the CO_2-transport in the oxide shell may only take place by Knudsen diffusion.

The mean pore diameters of the particular magnesites differ apparently. Except for one exception they increase more or less with the calcining temperature. This indicates, the higher the temperature of the oxide shell during the calcining process the bigger the pore size will be. The strong dependence on the temperature of the pore diffusion coefficient can be explained by that, according to fig. 7.

5.4. Heat conduction coefficient

The heat conduction coefficients, determined from the linearized curves of the decomposition behavior, are represented in fig. 10. According to equation [13] the heat conduction coefficient is

Temperaturabhängigkeit des Porendiffusionskoeffizienten entsprechend Abb. 7 zurückzuführen.

5.4. Wärmeleitkoeffizient

In Abb. 10 sind die aus den linearisierten Zersetzungsverläufen bestimmten Wärmeleitkoeffizienten dargestellt. Entsprechend Gleichung [13] ist der Wärmeleitkoeffizient proportional der Temperaturdifferenz zwischen Umgebung und Reaktionsfront. Diese Temperaturdifferenz betrug bei den meisten Versuchen nur wenige Kelvin. Da

proportional to the temperature difference between the ambience and the reaction front, which has been only a few Kelvins during most of the experiments. So the heat conduction coefficient can not be determined very exactly with the thin specimen used here, because on the one hand, the temperatures of the ambience (wall temperature of the channel) exhibit differences of up to 5 degrees and, on the other hand, the temperature of the reaction front rises a few degrees during the decomposition. There is no discernible dependence of the measured values on the temperature of material, shown in fig. 10.

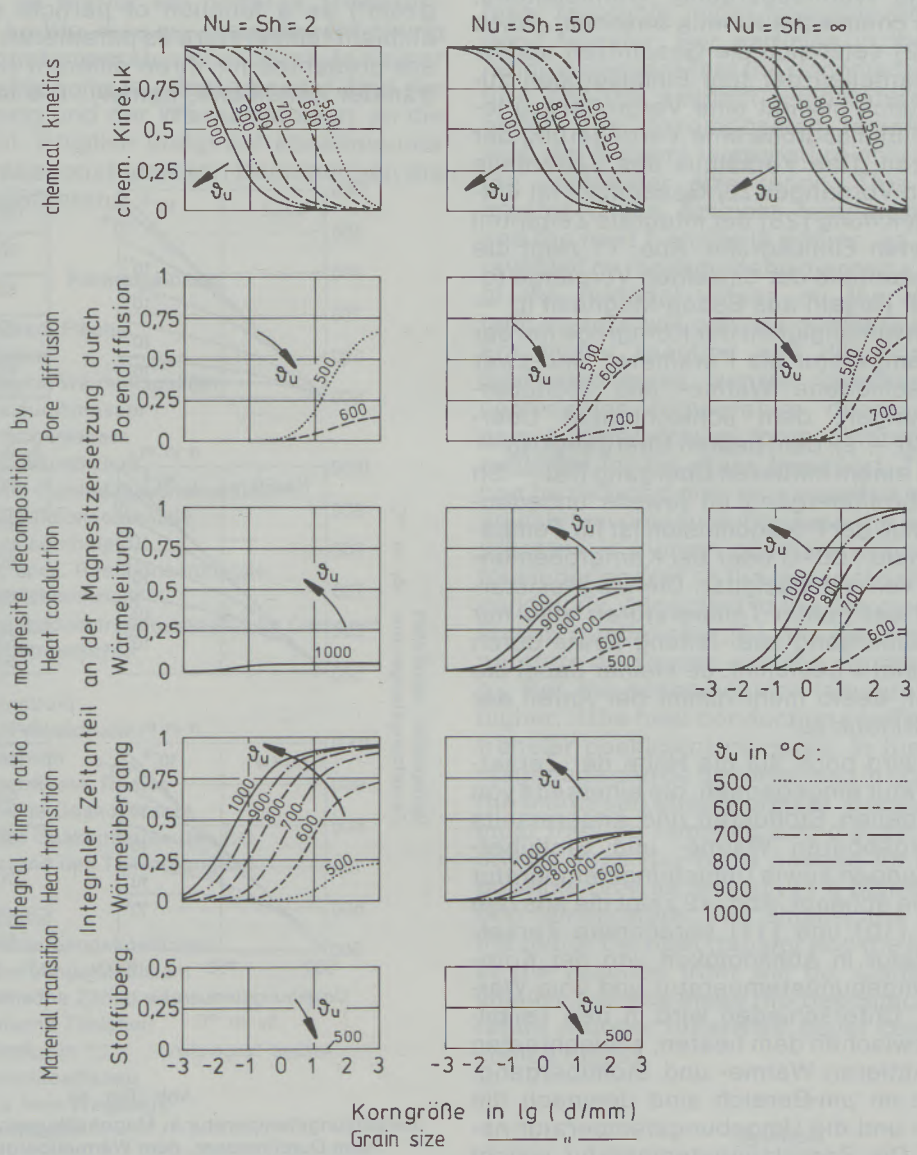

Abb./Fig. 11

Integrale Zeitanteile der prinzipiellen Prozesse, die in Zusammenhang mit der Zersetzung von Magnesit stehen
Integral time portions of the principal processes involved in the decomposition of magnesite

aber einerseits die Temperaturen der Umgebung (Kanalwandtemperaturen) Unterschiede bis zu 5 Kelvin aufwiesen und andererseits die Temperatur der Reaktionsfront während der Zersetzung um ein paar Kelvin stieg, kann der Wärmeleitkoeffizient mit den hier benutzten dünnen Körpern nicht sehr genau bestimmt werden. Eine Temperatur- oder Materialabhängigkeit ist aus den in Abb. 10 gezeigten Werten nicht erkennbar.

6. Wirkung der Einflußgrößen

Im folgenden wird auf den Einfluß der einzelnen Stoffwerte und der Wärme- und Stoffübergangsbedingungen auf den Zersetzungsvorgang eingegangen.

Die Zersetzungszeit wird durch die fünf Einflußgrößen Stoff- und Wärmeübergang, Wärmeleitung, Diffusion und chemische Kinetik bestimmt. Nach Gleichung [22] setzt sich die Gesamtzeit additiv aus den Zeitanteilen der fünf Einflußgrößen zusammen. Folglich bewirkt eine Vergrößerung jeder einzelnen Einflußgröße eine Verringerung der Zersetzungszeit. Das Verhältnis des Zeitanteils des jeweiligen Vorganges zur Gesamtzeit ist entsprechend Gleichung [28] der integrale Zeitanteil der betrachteten Einflußgröße. Abb. 11 zeigt die integralen Zeitanteile der einzelnen Vorgänge repräsentativ für Kugeln aus Euböa-Magnesit (ϱ = 2,54 g/cm³) in Abhängigkeit der Korngröße mit der Umgebungstemperatur als Parameter, und zwar für drei verschiedene Wärme- und Stoffübergangsbedingungen, dem schlechtesten Übergang (Nu = Sh = 2), dem besten Übergang (Nu = Sh = ∞) und einem mittleren Übergang (Nu = Sh = 50). Der Stoffübergang ist jeweils unbedeutend. Der Einfluß der Porendiffusion ist für Temperaturen oberhalb 700 °C oder bei Korngrößen unterhalb 1 cm vernachlässigbar. Die Magnesitzersetzung wird bei hohen Temperaturen also nur durch Wärmeübergang und -leitung sowie durch chemische Kinetik bestimmt. Je kleiner dabei die Korngröße ist, desto mehr nimmt der Anteil der chemischen Kinetik zu.

Zum Schluß wird noch auf die Höhe der Zersetzungstemperatur eingegangen, die einerseits von den vorgegebenen Stoffdaten und andererseits von den vorgebbaren Wärme- und Stoffübergangsbedingungen sowie Umgebungstemperatur und Korngröße abhängt. Abb. 12 zeigt die aus den Gleichungen [10] und [11] berechnete Zersetzungstemperatur in Abhängigkeit von der Korngröße, der Umgebungstemperatur und vom Wärmeübergang. Unterschieden wird in den Teilbildern wieder zwischen dem besten, schlechtesten und einem mittleren Wärme- und Stoffübergang. Bei Partikeln im μm-Bereich sind demnach die Zersetzungs- und die Umgebungstemperatur nahezu gleich. Die Zersetzungstemperatur weicht von der Umgebungstemperatur etwa erst bei Partikeln im cm-Bereich ab, und zwar umso stärker, je höher die Umgebungstemperatur und je schlech-

6. Effect of the influencing variables

The influence of the individual material values and of the heat and mass transfer conditions on the decomposition process will now be considered.

The decomposition time is determined by the five influencing variables: mass transfer, heat transfer, heat conduct, diffusion, chemical kinetics. According to equation [22], the total time is composed additively of the time shares of the five influencing variables. Consequently, an increase in any individual influencing variable results in a shortening of the decomposition time. The ratio of the time share of a particular process to the total time is, according to equation [28], the integral time share of the influencing variable under consideration. Fig. 11 shows the integral time shares (or portions) of the individual processes for spheres consisting of Euboia magnesite (ϱ = 2.54 g/cm³) as a function of particle size, with the ambient temperature as parameter. The diagrams are presented for three different heat and mass transfer conditions, namely, the least favorable

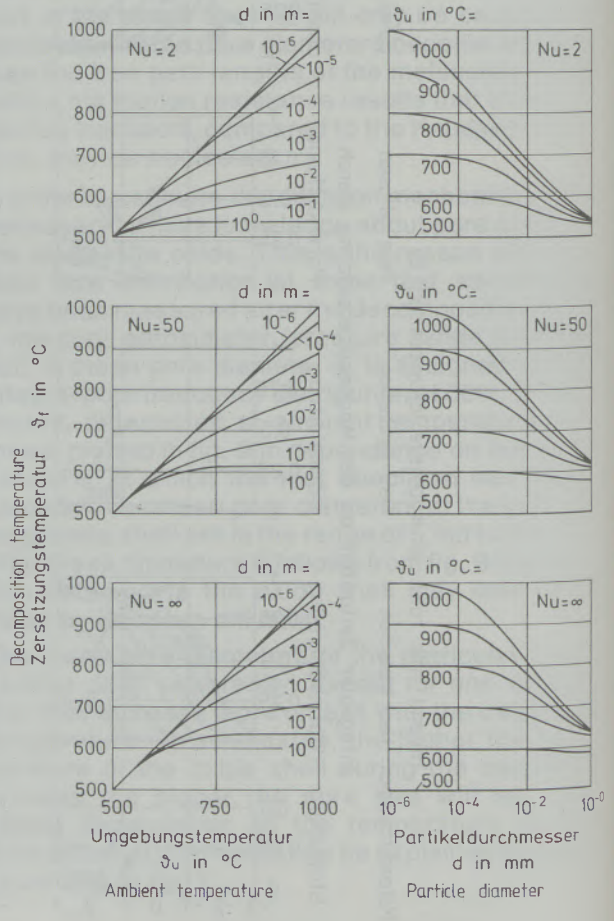

Abb./Fig. 12

Zersetzungstemperatur in Magnesitkugeln in Abhängigkeit vom Durchmesser, dem Wärmeübergang und der Umgebungstemperatur

Decomposition temperature in magnesite spheres in dependence on diameter, heat transfer and ambient temperature

ter der Wärmeübergang ist, wie man an den rechten Teilbildern besonders gut erkennen kann. Der Einfluß der Stoffwerte auf die Zersetzungstemperatur wird nur qualitativ beschrieben. Mit steigendem Reaktions- und Diffusionskoeffizienten sinkt die Zersetzungstemperatur, da nun für den Stofftransport ein niedrigeres Triebkraftgefälle ($p_{Gl}-p_u$) ausreicht. Dieses kann nur kleiner werden, wenn der Gleichgewichtsdruck abnimmt, weil der Umgebungspartialdruck als konstant vorgegeben und damit unabhängig von den Stoffdaten und Übergangsbedingungen ist. Entsprechend der thermodynamischen Gleichgewichtsbeziehung [8] nimmt mit p_{Gl} auch die Zersetzungstemperatur ab. Steigen der Wärmeleit- und der Wärmeübergangskoeffizient, erhöht sich die Zersetzungstemperatur. In diesem Fall kann durch das vergrößerte Wärmeangebot mehr Magnesit zersetzt werden. Da nun mehr CO_2 abtransportiert werden muß, ist hierfür ein höheres Triebkraftgefälle ($p_{Gl}-p_u$) nötig, was nur über eine Erhöhung der Zersetzungstemperatur möglich ist. Je kleiner die Körperabmessung ist, desto besser sind der Wärmeübergang und der Wärmetransport an die Reaktionsfront. Folglich steigt mit abnehmender Korngröße unter sonst gleichen Bedingungen die Zersetzungstemperatur.

Formelzeichen

A	Abbaugrad, Fläche
b	Formfaktor
c	spezifische Wärmekapazität
d	Partikeldurchmesser
d_p	Porendurchmesser
D	Diffusionskoeffizient
D^p_{eff}	effektiver Porendiffusionskoeffizient
Δh_R	spez. Reaktionsenthalpie
ΔH_R	Reaktionsenthalpie
$\Delta \tilde{h}_R$	molare spez. Reaktionsenthalpie
k	Reaktionskoeffizient
K_c	Volumenkonzentration des CO_2 im Carbonat
$\dot{m}$	Massenstromdichte
M	Masse
$\dot{M}$	Massenstrom
p	Druck, Partialdruck
$\dot{Q}$	Wärmestrom
r	Ortskoordinate, Radius
R	allgemeine Gaskonstante
R_c	spezielle Gaskonstante des CO_2
R_i	Widerstand des Teilvorganges i
t	Zeit
T	Temperatur
α	Wärmeübergangskoeffizient
β	Stoffübergangskoeffizient
ν	kinematische Zähigkeit
η	dynamische Zähigkeit
ϑ	Temperatur in °C
λ	Wärmeleitkoeffizient
Λ	mittlere freie Weglänge
μ	Labyrinthfaktor
ϱ	Dichte
τ	Zersetzungszeit
ψ	Porosität
Ω	integraler Zeitanteil

(Nu = Sh = 2), the most favorable (Nu = Sh = ∞) and a moderately good transfer (Nu = Sh = 50). The mass transfer in each case is negligible. The magnesite decomposition is determined at high temperatures only by heat transfer and conduction such as chemical kinetics. The smaller the particle size becomes, the higher the share of the chemical kinetics will be.

Finally, the attained decomposition temperature will be considered. On the one hand, it depends on the given material data, and on the other hand, it depends on the presupposing heat and mass transfer conditions as well as on the ambient temperature and the particle sizes. Fig. 12 shows the decomposition temperature – calculated from equations [10] and [11] – as a function of the ambient temperature and of the particle size for different values of the heat transfer. The diagrams relate to the above-mentioned three cases of least favorable, most favorable and moderately good transfer. For particles in the micron size range it appears that the decomposition temperature and the ambient temperature are virtually equal. The decomposition temperature differs from the ambient temperature only for particles in the centimeter size range. This difference is greater if the ambient temperature is higher and the heat transfer is poorer, as is very clearly revealed by the right-hand diagrams. The influence of the material values on the decomposition temperature will only be qualitatively described. For higher reaction and diffusion coefficients (and also mass transfer coefficients) the decomposition temperature decreases because now a lower driving force difference ($p_{Gl}-p_u$) is sufficient for the mass transport. This difference can be reduced only as a result of lowering of the equilibrium pressure, because the ambient partial pressure is a given constant value and is therefore independent on the material data and transfer conditions. According to the thermodynamic equilibrium relationship [8], the decomposition temperature decreases with the equilibrium pressure p_{Gl}. But, the decomposition temperature becomes higher, if the heat conduction coefficient and heat transfer coefficient increase. In that case, more magnesite can be decomposed in consequence of the increased supply of heat. Because more CO_2 must then be removed and discharged, a larger driving force ($p_{Gl}-p_u$) is needed for this, which is possible only as a result of a higher decomposition temperature. The smaller the particle size, the better the heat transfer and the heat transport at the reaction front will be. Consequently, for smaller particle sizes the decomposition temperature – under otherwise equal conditions – becomes higher.

Symbols

A	degree of decomposition, surface
b	shape factor
c	specific thermal capacity

Indizes

C	CO_2
Carb	Carbonat
D	Diffusion
eff	effektiv
f	Reaktionsfront
Fi	Ficksche Diffusion
g	gesamt
Gl	Gleichgewicht
k	chemische Reaktion
Kn	Knudsen-Diffusion
m	Kern, Mitte
max	maximal
min	minimal
o	Oberfläche
Ox	Oxid
p	Pore
R	Reaktion
s	mittlerer Wert der Oxidschicht
u	Umgebung
α	Wärmeübergang
β	Stoffübergang
λ	Wärmeleitung
–	gemittelt

Literaturverzeichnis/References

1. Vosteen, B.: Die physikalische und chemische Kinetik der thermischen Zersetzung von Kalk. Dissertation TU Braunschweig, **1970.**
2. Jeschar, R.: Kopplung von Wärme- und Stofftransport mit chemischen Reaktionen im porösen Einzelkörper. VDI-Bildungswerk Nr. Bw 2060 (**1971**), S. 1–6.
3. Jeschar, R.: Über den Einfluß von Wärme- und Stoffübergang bei heterogenen Reaktionen zwischen Gasen und dichten Festkörpern. Arch. Eisenhüttenwesen 43 (**1972**), S. 109–114.
4. Kainer, H.: Kopplung von Wärme- und Stoffaustausch mit chemischer Kinetik bei der Zersetzung von natürlichen Karbonaten. Dissertation TU Clausthal **1982**.
5. Kainer, H., E. Specht, R. Jeschar: Die Porendiffusions-, Reaktions- und Wärmeleitkoeffizienten verschiedener Kalksteine und ihr Einfluß auf die Zersetzungszeit. Zement–Kalk–Gips, 39 (**1986**), S. 259–268.
6. Goldsmith, J. R., H. C. Heard: Subsolidus phase relations in the system $CaCO_3$–$MgCO_3$. Journal Geology 69 (**1961**), S. 45–74.
7. Graf, D. L., J. R. Goldsmith: Dolomite-magnesian calcite relations at elevated temperatures and CO_2 pressures. Geochimica et Cosmochimica Acta 7 (**1955**), S. 109–128.
8. Harker, R. J., O. F. Tuttle: The thermal dissociation of calcite, dolomite and magnesite. Am. Jour. Sci. 253 (**1955**), S. 209–224.
9. Marc, R., A. Simek: Über die thermische Dissoziation des Magnesiumkarbonates. Z. anorg. Chemie 82 (**1913**), S. 21–49.
10. Haul, A. W., J. Markus: On the thermal decomposition of dolomite. J. appl. Chem. 2 (**1952**), S. 298–306.
11. Barin, I., O. Knacke, O. Kubaschewski: Thermochemical properties of inorganic substances Supplement. Springer-Verlag Berlin/Heidelberg/New York, **1977**.
12. Koch, H.: Einfluß der Porenstruktur auf die Diffusion von Gasen in porösen Feststoffen mit bimodaler Porenstruktur. Dissertation TU Berlin **1979.**

d	particle diameter
d_p	pore diameter
D	diffusion coefficient
D^p_{eff}	effective pore diffusion coefficient
Δh_R	specific reaction enthalpy
ΔH_R	reaction enthalpy
$\Delta \tilde{h}_R$	molar specific reaction enthalpy
k	reaction coefficient
K_C	volume concentration of CO_2 in carbonate
$\dot{m}$	mass flow density
M	mass
$\dot{M}$	mass flow
p	pressure, partial pressure
$\dot{Q}$	heat flow
r	position coordinate, radius
R	universal gas constant
R_C	special gas constant of CO_2
R_i	resistance of the sub-process i
t	time
T	temperature
α	heat transfer coefficient
β	mass transfer coefficient
ν	kinematic viscosity
η	dynamic viscosity
ϑ	temperature in °C
λ	heat conduction coefficient
Λ	mean free path
μ	labyrinth factor
ϱ	density
τ	decomposition time
ψ	porosity
Ω	integral time share

Subscripts

C	CO_2
Carb	carbonate
D	diffusion
eff	effective
f	reaction layer or reaction front
Fi	diffusion of Fick
g	total
Gl	equilibrium
k	chemical reaction
Kn	diffusion of Knudsen
m	core, center
max	maximum
min	minimum
o	surface
Ox	oxide
p	pore
R	reaction
s	mean value of the oxide layer
u	ambient, ambience
α	heat transfer
β	mass transfer
λ	heat conduction
–	average

13. Hugo, P.: Gastransport im Übergangsgebiet zwischen Knudsen-Bereich und Laminarströmung. Ber. Bunsenges. physik. Chem. 79 (**1975**), S. 748–758.
14. Krischer, O., W. Kast: Die wissenschaftlichen Grundlagen der Trocknungstechnik. Springer-Verlag Berlin **1978**, 1. Band, 3. Auflage.